10-4248 765

## UNITED STATES AIR FORCE

SUMMER RESEARCH PROGRAM - 1991

SUMMER FACULTY RESEARCH PROGRAM (SFRP) REPORTS

VOLUME 3

PHILLIPS LABORATORY
CIVIL ENGINEERING LABORATORY

# RESEARCH & DEVELOPMENT LABORATORIES

5800 UPLANDER WAY
CULVER CITY, CA 90230-6608

SUBMITTED TO:

LT. COL. CLAUDE CAVENDER
PROGRAM MANAGER

AIR FORCE OFFICE OF SCIENTIFIC RESEARCH

BOLLING AND TONCE LABOR WASHINGTON, D.C.

nurs estimate

4,7p.

ARCH (AFSC)

The state of the s

by and Integram Manager

## REPORT DOCUMENTATION PAGE

Form Approved

OMB NO 0704-0188 Public reporting burden for this collection of information is estimated to scenario in scenario information in scenario information of scenario information in scenario information of scenario inform 1. AGENCY USE ONLY (Leave blank) 2. REPORT DATE 3 REPORT TYPE AND DATES COVERED 9 January 1902 30 Sep 30-30 Sep 91 4. TITLE AND SUBTITLE 5. FUNDING NUMBERS 1991 Summer Faculty Research Program (SFRP) Volumes 2-5b F49620-90-C-0076 6. AUTHOR(S) Mr Gary Moore 7. PERFORMING ORGANIZATION NAME(S) AND ADDRESS(ES) 8. PERFORMING ORGANIZATION REPORT NUMBER Research Development Laboratories (RDL) 5800 Uplander Way 02 0169 Culver City CA 90230-6608 AFOSR-TR-9. SPONSORING/MONITORING AGENCY NAME(S) AND ADDRESS(ES) 10. SPONSORING / MONITORING AGENCY REPORT NUMBER AFOSR/NI Bldg 410 Bolling AFB DC 20332-6448 Lt Col V. Claude Cavender 11. SUPPLEMENTARY NOTES 12a. DISTRIBUTION / AVAILABILITY STATEMENT 12b. DISTRIBUTION CODE UNLIMITED 13. ABSTRACT (Maximum 200 words) The purpose of this program is to develop the basis for continuing research of interest to the Air Force at the institution of the faculty member; to stimulate continuing relations among faculty members and professional peers in the Air Force; to enhance the research interests and capabilities of scientific and engineering educators; and to provide follow-on funding for research of particular promise that was started at an Air Force laboratory under the Summer Faculty Research Program. During the summer of 1991 170 university faculty conducted research at Air Force laboratories for a period of 10 weeks. Each participant provided a report of their research, and these reports are consolidated into this annual report. 14. SUBJECT TERMS 15. NUMBER OF PAGES 16. PRICE CODE 19. SECURITY CLASSIFICATION 17. SECURITY CLASSIFICATION SECURITY CLASSIFICATION 20. LIMITATION OF ABSTRACT OF REPORT OF THIS PAGE OF ABSTRACT UNCLASSIFIED UNCLASSIFIED

UNCLASSIFIED

#### UNITED STATES AIR FORCE

#### SUMMER RESEARCH PROGRAM -- 1991

## SUMMER FACULTY RESEARCH PROGRAM (SFRP) REPORTS

#### VOLUME 3

# PHILLIPS LABORATORY CIVIL ENGINEERING LABORATORY

# RESEARCH & DEVELOPMENT LABORATORIES 5800 Uplander Way Culver City, CA 90230-6608

Program Director, RDL Gary Moore

Program Manager, AFOSR Lt. Col. Claude Cavender

Program Manager, RDL Claude Baum

Program Administrator, RDL Gwendolyn Smith

#### Submitted to:

AIR FORCE OFFICE OF SCIENTIFIC RESEARCH

Bolling Air Force Base

Washington, D.C.

December 1991



Accesio	n For	
NTIS	CRA&I	Z
DTIC	TAB	
U.ant		
Justitio	ation	
By Dist ibstion/		
Amilability Codes		
Dist	Avan and Speci	
12	İ	

#### **PREFACE**

Reports in this document are numbered consecutively beginning with number 1. Each report is paginated with the report number followed by consecutive page numbers, e.g., 1-1, 1-2, 1-3; 2-1, 2-2, 2-3.

This document is one of a set of 13 volumes describing the 1991 AFOSR Summer Research Program. The following volumes comprise the set:

<u>VOLUME</u>	TITLE			
1	Program Management Report			
	Summer Faculty Research Program (SFRP) Reports			
2	Armstrong Laboratory, Wilford Hall Medical Center			
3	Phillips Laboratory, Civil Engineering Laboratory			
4	Rome Laboratory, Arnold Engineering Development Center, Frank J. Seiler Research Laboratory			
5	Wright Laboratory			
Graduate Student Research Program (GSRP) Reports				
6	Armstrong Laboratory, Wilford Hall Medical Center			
7	Phillips Laboratory, Civil Engineering Laboratory			
8	Rome Laboratory, Arnold Engineering Development Center, Frank J. Seiler Research Laboratory			
9	Wright Laboratory			
High School Apprenticeship Program (HSAP) Reports				
10	Armstrong Laboratory			
11	Phillips Laboratory, Civil Engineering Laboratory			
12	Rome Laboratory, Arnold Engineering Development Center			
13	Wright Laboratory			

### 1991 FACULTY RESEARCH REPORTS

## Phillips Laboratory, Civil Engineering Laboratory

•	mber Report Title	Author
	Phillips Laboratory	
	Astronautics Laboratory (ASTRO)	
1	Some Relationships of Acoustically Measurable Parameters to Microstructural Damage and Mechanical Properties of Solid Rocket Propellants	Dr. David Elliott
2	Research in Vibration Identification, Isolation, and Suppression for Large Space Structures	Dr. Ephrahim Garcia
3	Analytical and Experimental Investigation of the Mode Dampings in Laminated Composite Beams	Dr. Hany Ghoneim
4	The Synthesis and Properties of Energetic Salts with Potential for Development as Solid Rocket Propellants	Dr. Vincent Giannamore
5	Drop Size Instrumentation for Rocket Injector Tests	Dr. William Grissom
6	Liquid Jet Injection Processes in Liquid Rocket Engines	Dr. Stephen Heister
7	XAFS of AP and AP/Binder Systems	Dr. Richard Hoffman
8	Polymeric Ionic Conductors Electrolytes for Solid Polymer Batteries	Dr. Iris Howard
9	Model Reduction and Control of ASTREX	Dr. Ashok Iyer
10	Research in Emerging Technologies at Phillips Laboratory	Dr. Peter Langhoff
11	Mechanical Testing of Isogrid Structures	Dr. Christopher Rotz
12	Nonlinear Adaptive Control of ASTREX System Using Gaussian and Multilayer Neural Networks	Dr. Sahjendra Singh
	Geophysics Laboratory (GEO)	
13	Some Aspects of Remote Sensing	Dr. Frank Battles
14	Theoretical Studies of Collisional Vibrational Relaxation of OH	Dr. Ronald Bieniek
15	The Form of Cyclonic Precipitation and its Thermal Impact	Dr. Stanley Gedzelman
16	A Geographic Information Systems Implementation Analysis for the Geographics Directorate/A mospheric Structure Branch/Phillips Laboratory	Dr. William Hamilton
	P. G. A. M. A. C. P. A. C. A. L. A. P. B. C. G. S. C.	D 41 1 771 C

Dr. Arkady Kheyfets

17 E. Carton Moment of Rotation in Ashtekar's Theory of Gravitation

Report Number Report Title Author				
	Phillips Laboratory (cont.)			
18	Criteria for Excitation of Parametric Instability in the Ionosphere by Obliquely Incident HF Heater	Dr. Spencer Kuo		
19	Atmospheric Dynamics	Dr. Arvind Marathay		
20	Preliminary Analysis of the Western Norilsk Lake Baikal Deep Seismic Sounding Profile	Dr. Keith Priestley		
21	Structural and Vibrational Analyses of the Wake Side Plasma Sensor for the Wake Shield Facility	Dr. Joseph Rencis		
22	A Preliminary Investigation of High Resolution Interferometry of the Solar Disk	Dr. Edward Seykora		
23	Improved HITRAN Data for Molecular Oxygen	Dr. Richard Tipping		
	Weapons Laboratory (WL)			
24	Coherent Laser Radar and Array Imaging	Dr. Richard Anderson		
25	Experimental Techniques for Heterodyne Laser Speckle Imaging	Dr. James Boger		
26	Fiberoptic Interferometer Studies	Dr. Douglas Christensen		
27	Construction and Initial Operation of the Working Fluid Experiment	Dr. John M. Gahl		
28	Finite Element Analysis of Hardened Aircraft Shelters	Dr. Walter Gerstle		
29	Alternating Directions Optimization An Approach to Linear Equation Solving	Dr. Jerald Kabell		
30	Space Debris Impact Effects on Spacecraft Materials	Dr. Jon Shively		
31	Nuclear and Plasma Physics with Antiprotons at SHIVA Star	Dr. Gerald Smith		
32	Constitutive Modeling of Slurry Infiltrated Fiber Concrete (SIFCON)	Dr. David Stevens		
33	Surface Deactivation Efficiencies for $O_2(^t\Delta)(g)$ Quenching on a Range of Coil Related Materials	Dr. Philip Whitefield		
	Civil Engineering Laboratory			
	Engineering Services Center (ESC)			
34	Estimation of Contaminant Transport Parameters from Laboratory Studies: Batch and Column Techniques with Sorbing Organic Solutes	Dr. William Ball		

Rep Nur	ort n <u>ber Report Title</u>	<u>Author</u>
	Civil Engineering Laboratory (cont.)	
35	Microbial Degradation of 4-Nitrophenol	Dr. Joseph Dreisbach
36	Extraction of Aromatic Polymers from Montmorillonite Clay Using Supercritical Fluids	Dr. Larry Gerdom
37	Data Acquisition and Instrumentation Integration for the Tyndall AFB Anti- Penetration Laboratory	Dr. Bobby Green
38	The Comparison of Complexation-Ultrafiltration to Chelation Ion Exchange in the Treatment of Spent Electroless Nickel Plating Baths	Dr. Douglas Klarup
39	Feasibility Study to Use the Gyratory Testing Machine for Field Compaction Control of Aggregate Base Course in Flexible Airfield Pavements	Dr. Cheng Liu
40	Use of a Centrifuge in Investigation of Dynamic Phenomena in Partially Saturated Sands	Dr. Teresa Taylor
41	Draft Test Methods to Assess the Performance of External Vapor-Phase Leak Detection Devices for Underground Storage Tanks: A Validation and Modification Study	Dr. Brian Vogt
42	Microbial Chlorobenzene Degradation	Dr. In-Soon You

SOME RELATIONSHIPS OF ACOUSTICALLY MEASURABLE PARAMETERS TO MICRO-STRUCTURAL DAMAGE AND MECHANICAL PROPERTIES OF SOLID ROCKET PROPELLANTS

> David M. Elliott, Ph.D. Associate Professor Arkansas Tech University Russellville, AR 72801 (501) 968-0338

#### ABSTRACT

This work consists of an analysis of the results of a previous experimental program which measured acoustical as well as mechanical parameters of an inert solid rocket propellant subjected to complex uniaxial loading histories. The objective of the current work was to determine additional relationships between acoustic parameters and microstructural damage and mechanical properties which might be used to enhance the fundamental understanding of the micromechanics of solid rocket propellants and lead ultimately to a non-destructive test to measure the microstructural damage accumulated over complex time dependent loading histories. It was found that, of the two acoustic parameters measured, relative attenuation is a better measure of microstructural damage than is a sound speed parameter. For constant strain rates, relative attenuation was found to be Gaussian in strain. This result was used as the basis for a new model to predict volume dilatation as a function of strain. While not yet verified by comparison to experiment, this model appears to give reasonable results. It was found that the energy dissipated within the sample during cyclic loading was correlated with microstructural damage as measured by relative attenuation. Three such correlations are presented. secant modulus of this inert solid rocket propellant was found to be linearly correlated with relative attenuation and to exhibit a definite shift with strain rate.

#### INTROLUCTION

Elastomeric composite materials like those used in solid rocket propellants suffer microstructural damage when subjected to mechanical strain above a certain threshold level. Microstructural damage in these materials is characterized by the formation and subsequent growth of vacuoles (voide) within the material. The mechanical properties of solid rocket propellants necessary for structural and operational analysis are intimately related to the extent of microstructural damage.

The most commonly used measure of microstructural damage in the past has been volume dilatation. Dilatation measurements are difficult and require a dilatometer which is not available at the Phillips Laboratory. Previous work by C.T. Liu and others has shown that microstructural damage is related to the acoustically measurable parameters of sound speed and relative attenuation (db/cm). A series of tests was run where both mechanical and acoustical data were taken at constant strain rates and under various cyclic loadings. This work considered the effects of different loading histories and strain rates on cumulative damage and on constitutive behavior and residual strength.

The objective of the present work is to determine additional relationships between acoustic parameters and both microstructural damage and mechanical properties. These relationships might then be used to enhance the fundamental understanding of the micromechanics of solid rocket propellants and lead ultimately to a non-destructive test to measure the microstructural damage accumulated over complex time dependent loading histories.

#### DISCUSSION OF THE PROBLEM

The results of a series of experiments performed in 1986 by the Lockheed Research Laboratory in Palo Alto, California for the Air Force Rocket Propulsion Laboratory were made available to the author for this project. This series consisted of seventeen separate tests. Uniaxial tensile specimens of an inert composite solid propellant were subjected to three different loading regimes: constant strain rate tests at 0.005, 0.05, and 0.5 per minute; cyclic loading of triangular shape increasing in steps of 3 percent maximum strain from 0 to 21 percent followed by a final pull to failure; and block cyclic loadings consisting of five repetitions at each of the maximum strains used in the cyclic loadings before a final pull to failure. There were two block cyclic tests. In

one, the strain blocks began at 3 percent and progressed to 21 percent before the final pull to failure (Lo-Hi). In the other, the strain blocks began at 21 percent and proceeded downward to 3 percent before the final pull to failure (Hi-Lo). The strain rate used in both the cyclic and the block cyclic tests was 0.05 per minute. All tests were done at ambient temperature. Table 1. Lists all of the Lockheed data runs.

During each of these tests, both mechanical and acoustical data were taken. The mechanical data consisted of load (lbs), vertical crosshead displacement (inches), and transverse displacement (inches). The acoustical data were generated and measured by transducers mounted on opposite transverse faces of the specimens. Bursts of nominal 528 kHz voltage were applied to one transducer. The other transducer measured the energy after it had passed through the specimen. The data consisted of source signal (volts), received signal (volts) and the delay in traversing the specimen (ns). Based on these data, the following parameters were calculated: Stress (psi), X-strain (in/in), total attenuation (db), relative attenuation (db/cm), transverse strain (in/in), fractional change in sound speed, and fractional change in volume (dilatation). See Table 2.

C.T. Liu et al (1,2) have utilized the results of these tests to investigate many of the effects of strain rate and loading regime on cumulative damage and on mechanical properties of this composite material. They observed that the onset of dewetting corresponds to the beginning of the deviation from linearity in the stress-strain curve. They noted that both relative attenuation and volume dilatation are functions of strain rate and of temperature. Perhaps their most important observation from a practical standpoint is that the damage level in the material depends on the entire loading history. In other words, they found that the extent of microstructural damage is a path function and not a point function. Another very interesting observation made by these authors is that cyclic (but not block cyclic) loading produces a noticeable increase in the strength (maximum stress) of the material.

While the pioneering work by Liu et al produced very significant new insights, Dr. Liu felt that, with further effort, still more might be learned from t e existing data. As a consequence, the present work was undertaken with the following specific objectives:

- 1. Examine the literature and the experimental data to determine whether the sound speed parameter or relative attenuation is the better measure of accumulated microstructural damage.
- 2. Examine the method used by Lockheed to calculate volume dilatation and devise modifications to improve the agreement with other available experimental data.
- 3. Study the relationships between the energy dissipated during cyclic loadings and microstructural damage.
- 4. Seek additional relationships between microstructural damage and gross mechanical properties.

#### RESULTS

#### Acoustic Parameters as Measures of Microstructural Damage

Two calculated quantities, relative attenuation and sound speed parameter, have been considered as measures of microstructural damage. Both of these were calculated by Lockheed from the original data as shown in Table 2. Figures 1 and 2 show both of these acoustical parameters plotted against longitudinal strain for a typical constant strain rate run. The most striking observation is that the shapes of these two curves are remarkably similar.

Knollman, Martinson, and Bellin (3,4,5,6) have developed quantitative physical models relating the acoustic parameters of relative attenuation and sound speed parameter to specific aspects of microstructural damage. These authors found that the number density of vacuoles, the average size of vacuoles, and volume dilatation were functions of relative attenuation and the sound speed parameter. Relative attenuation is the attenuation of the acoustic energy across the sample in decibels divided by the width of the sample (db/cm). The sound speed parameter, S, is given by:

$$S = \frac{\Delta C_L / C_{L_0}}{1 - \Delta C_L / C_{L_0}} \tag{1}$$

Where  $C_L$  = Longitudinal sound speed,

 $C_{L_0}$  = Longitudinal sound speed in unstrained material, and

 $\Delta C_L = C_{L_0} - C_L.$ 

Figure 3 shows relative attenuation plotted against the sound speed parameter for a typical constant strain rate run. The apparent correlation suggests that these parameters might not be independent.

The relations found by these authors are given by the following three equations: (3)

$$\frac{\Delta V}{V_0} = \frac{1}{b} \left( \frac{\Delta C_L / L_c}{1 - \Delta C_L / C_{L_0}} \right) \tag{2}$$

$$\overline{a} = \left(\frac{b}{m} \Delta \alpha \frac{1 - \Delta C_L / C_{L_0}}{\Delta C_L / C_{L_0}}\right)^{1/3}$$
(3)

$$\bar{n} = \frac{3m}{4\pi b^2 \Delta \alpha} \left( \frac{\Delta C_L / C_{L_0}}{1 - \Delta C_L / C_{L_0}} \right)^2$$
(4)

Where  $\frac{\Delta V}{V_0}$  = Volume dilatation,

$$b = \frac{3}{8(1-2v_0)},$$

 $v_0$  = Poisson's ratio for unstrained material,

 $\Delta \alpha$  = Relative Attenuation,

a = Average vacuole size,

 $\overline{n}$  = Average number density of vacuoles, and

m = A function of Poisson's ratio for the unstrained material and the wave number of the acoustic wave

In the Lockheed experiments, relative attenuation was calculated from measured voltage ratios across the width of the sample and the gage width. Sound speeds were calculated based on the measured delay time of pulses traversing the sample and on the measured width of the sample as it varied with strain. Volume dilatation was calculated from equation 2 using a value of Poisson's ratio for the unstrained material of 0.49.

Close examination of the Lockheed data reveals an apparent error in the

reported values of the transverse displacement. If the values of crosshead displacement and transverse displacement are used with the appropriate gage dimensions to calculate the ratio of transverse strain to longitudinal strain and these values are plotted against the transverse strain (X-Strain), the resultant curve, Figure 4, does not exhibit the expected behavior. The curve would be expected to begin at a value of 0.5 at very low strain and decrease monotonically with increasing strain. (7)

If the transverse displacement values are not correct, the calculated sound speed will be in error as will any other calculated quantity whose value depends on transverse displacement. In particular, the values of dilatation given in the Lockheed results are thought to be in error. The values of relative attenuation are not impacted by errors in transverse displacement because they are based on the gage width.

Another fact that should be considered when deciding which acoustic parameter might be the better measure of microstructural damage is that sound speed is impacted by the nonlinear elastic properties of the pure binder while relative attenuation is not. (4) As a result, sound speed varies with strain at very low strains before the onset of microstructural damage (dewetting). This effect is responsible for the sound speed parameter going negative at low strains. See Figure 1. Examination of plots of sound speed parameter and relative attenuation versus strain reveals that the sound speed parameter results are considerably more erratic than are relative attenuation results. This is particularly evident at the higher values of strain. See Figure 2.

For the above reasons, relative attenuation is judged to be a better measure of microstructural damage than the sound speed parameter. In addition, there is reason to believe that relative attenuation is directly proportional to the dewetting distribution function (the fraction of particles dewetted). The next section explores this possible relationship in more detail.

The general shape of the relative attenuation versus strain curves, ignoring the erratic behavior at high strains, for the constant strain rate runs bears a remarkable resemblance to the Gaussian or normal distribution function. To investigate this possible relationship, the relative attenuation data were normalized and plotted versus strain on arithmetic normal probability graph paper. Figure 5 shows one such

plot. If the resultant plot is a straight line, then relative attenuation is normally distributed with

- $\mu = mean, and$
- $\sigma =$  standard deviation.

Arithmetic normal plots of normalized relative attenuation versus strain were made for eight constant strain rate runs. The results are given in Table 3. It is evident from the table that both the mean and the standard deviation are functions of strain rate.

#### Volume Dilatation Calculations

In the Lockheed results, volume dilatation is directly proportional to the sound speed parameter. See equation 2. These dilatation results, therefore, have the same problems as the sound speed parameter. Figures 6 and 7 show the Lockheed results for two constant strain rate runs. Besides the obvious problems at strains above about 30 percent, these values of dilatation are much too large.

Several attempts were made to improve the dilatation results. One method used a strain dependent Poisson's ratio rather than the fixed value of 0.49. Values of Poisson's ratio as a function of strain were inferred from dilatation versus strain data for a similar material. These data were based on dilatometer results obtained at another laboratory. Another method used a more accurate but far more complex expression for dilatation as a function of sound speed change. Both methods individually and in combination produced disappointing results and this effort was discontinued.

Dilatation is historically the most prevalent method of assessing microstructural damage in filled elastomeric composite materials and a wealth of data are available, at least for uniaxial tension. It would be highly useful, therefore, if some method could be found to relate dilatation to acoustically measurable parameters like sound speed or relative attenuation. The potential for nondestructive determination of cumulative microstructural damage under complex loading histories clearly exists.

If both the dewetting distribution function and the rate of growth of vacuoles once they are formed were known as functions of strain, dilatation could be calculated. The author has measured both the dewetting distribution function and the rate of growth of vacuoles in an

elastomer-glass bead composite by optical means. (8) The dewetting distribution function for uniaxial strain found in that work had a shape very similar to the relative attenuation functions presented in the Lockheed results. Based partly on that similarity, it is hypothesized that relative attenuation is directly proportional to the dewetting distribution function. If this is true, the dewetting distribution function can be found by normalizing the relative attenuation results. The Lockheed relative attenuation results were found to be approximately Gaussian. The means and standard deviations for eight constant strain rate runs were determined and are given in Table 3.

If the dewetting distribution function and the rate of vacuole growth are known, a first approximation calculation of dilatation can be made as shown below.

First, the following assumptions are made:

- 1. All particles are spherical with the same diameter,  $\delta_0$ ,
- 2. No interaction between particles.
- 3. The dewetting density function is Gaussian in strain with parameters  $\mu, \sigma$  which depend on  $\delta_0, \dot{\epsilon}$ .

Then, let

- 1.  $g(e_0)$  = the fraction of the total particles which dewet in a unit strain interval  $de_0$ ,
- 2.  $V_{void} = V_{void}(\delta_0, \epsilon, \epsilon_0) = \text{volume of void, and}$
- 3.  $N_0$  = number of particles per unit volume.

Then,

$$d(\frac{\Delta V}{V_0}) = N_0 g(e_0) V_{void}(\delta_0, e, e_0) de_0$$
 (5)

and the dilatation is given by

$$\frac{\Delta V}{V_0} = \int_0^{\epsilon} N_0 g(\epsilon_0) V_{void}(\delta_0, \epsilon, \epsilon_0) d\epsilon_0$$
 (6)

According to assumption 3, the dewetting density function is given by

$$g(\mathbf{e}_0) = \frac{1}{\sqrt{2\pi}\sigma} e^{-\frac{1}{2}} \left(\frac{\mathbf{e}_0 - \mu}{\sigma}\right)^2 \tag{7}$$

Where  $\epsilon_0$  = "dewetting strain"

To calculate the void volume, all vacuoles are assumed to be ellipsoidal in shape and are considered here as "single dewetted". The void volume is then given by

or for a half-ellipsoid,

$$V_{void} = \frac{2}{3}\pi \left(\frac{\delta_0}{2}\right)^2 \left(b - \frac{\delta_0}{2}\right) \tag{8}$$

The moment a vacuole is formed, its semi-major axis is larger than the radius of the included particle. Let C be the ratio of the semi-major axis just after the vacuole forms to the radius of the included particle and let K be the rate at which the semi-major axis grows with strain. Then the semi-major axis of the vacuole is given by

$$b = \left(\frac{\delta_0}{2}\right) \left[K(e - e_0) + C\right] \tag{9}$$

Where K and C are determined from direct observation. Putting the results of equations 7,8, and 9 into equation 5 and integrating gives

$$\frac{\Delta V}{V_0} = \frac{V_f}{2} \int_0^{\epsilon} \frac{1}{\sqrt{2\pi}\sigma} e^{-\frac{1}{2}} \left( \frac{e' - \mu}{\sigma} \right)^2 \left[ (K(\epsilon' - \epsilon_0) + C) - 1 \right] de' \tag{10}$$

Where e' = a dummy variable of integration, and

$$V_f = \frac{4\pi N_0}{3} \left(\frac{\delta_0}{2}\right)^3 = \text{volume fraction of filler.}$$

Evaluation of the integral in equation 10 is straightforward. The calculations were carried out on a personal computer with the spreadsheet program Quatro Pro. Using values of 3.0 for K and 1.17 for C based on the author's previous work<sup>(8)</sup> and assuming a value of 0.8 for the volume fraction of solids, preliminary curves of dilatation versus strain were prepared. Figure 8 shows the results. Dilatation was calculated for strain rates of 0.05, 0.5, and 5 percent per minute using the average values of mean and standard deviation given in Table 3. The effect of strain rate is clearly evident.

It should be emphasized that the values of the constants used here are very preliminary first estimates. Still, the general shape of the dilatation versus strain curves is what one would expect and the dilatation values obtained are not unreasonable. The spreadsheet implementation of equation 10 makes it easy and fast to vary any

parameter or combination of parameters and observe the effect on the calculated dilatation versus strain curve.

The lack of measured dilatation data for the material used in the Lockheed experiments precludes verification of the dilatation model at this time. Simultaneous measurements of acoustical parameters and those mechanical parameters necessary to evaluate dilatation would provide verification. Direct measurement of the dewetting distribution function by optical or other means would prove or disprove the hypothesized Gaussian dewetting distribution function.

#### Energy Dissipated and Microstructural Damage

During the cyclic loading and block cyclic loading, the samples were subjected to triangular strain cycles where the strain increased at a constant rate to a given value and then returned essentially to zero at the same rate. The energy dissipated during one of these cycles is the difference between the areas under the loading and unloading stressstrain curves. This dissipated energy is sometimes called the hysteresis energy. Because the hysteresis energy is dissipated within the sample, it seems reasonable to suppose that this energy might be related to an increase in microstructural damage. To investigate such possible relationships, relative attenuation was taken as a measure of microstructural damage and plotted against the hysteresis energy. types of such plots were made. The first type shows the maximum value reached during the loading and unloading parts of the cycle versus the energy dissipated during that cycle for the cyclic loading runs. Figure 9 shows a typical result. The second type shows the change in relative attenuation during a cycle versus the energy dissipated during that cycle, again for the cyclic loading runs. Figure 10 shows the results for all three cyclic loading runs. The third and last type shows relative attenuation at the end of each cycle versus the cumulative Figure 11 shows these results for all three of the energy dissipated. cyclic loading runs and for the 21 percent strain block only in both of the block cyclic runs.

Based on the results shown in Figures 9,10, and 11; the following correlations are apparent:

 The maximum damage level reached during both the loading and unloading portions of a strain cycle is correlated with the energy dissipated during that cycle.

- 2. The increase in damage that occurs during a strain cycle is correlated with the energy dissipated during that cycle.
- 3. The damage occurring over a series of sequential strain cycles is correlated with the cumulative energy dissipated during those cycles.

#### Microstructural Damage and Gross Mechanical Properties

It is well known that some gross mechanical properties of elastomeric composite materials are related to the extent of microstructural damage that the material has suffered. The Mullins softening effect, for example, has been known for decades. Liu et al<sup>(1)</sup> have written that the transition away from linear behavior in the stress-strain curve is associated with the onset of dewetting. Many correlations of microstructural damage with gross mechanical properties probably exist and their continued study should aid considerably in understanding and predicting the deformation and failure of these materials.

The data available from the constant strain rate Lockheed runs can be used to investigate the correlation between the secant modulus and microstructural damage. Figure 12. shows three curves of secant modulus plotted against relative attenuation. Each of the curves shown is for one of the runs at a particular strain rate. The runs selected were judged to be typical of all of the runs at that particular strain rate. It is observed from the figure that the secant modulus appears to be linearly correlated with damage as measured by relative attenuation over a wide range of relative attenuation (at least 40 db/cm). It is also apparent that there is a definite "shift" with strain rate.

#### CONCLUSIONS

1. Ultrasonic assessment of microstructural damage in elastomeric composite materials is an extremely powerful tool whose full potential remains to be explored. The data currently available from application of this tool to solid rocket propellants, however, are meager. The theoretical analyses available for relating acoustic parameters to microstructural damage need to be substantially improved. This method, with further work, holds the potential for non-destructive analysis of the state of damage existing in solid rocket propellants after complex loading histories.

- 2. Relative attenuation is a better measure of microstructural damage than is the sound speed parameter.
- 3. The data points of relative attenuation as a function of strain measured in the Lockheed constant strain rate runs appear to be generated by a Gaussian distribution. That is the change in relative attenuation with strain appears to be normally distributed and is characterized by a mean and a standard deviation. The mean and, to a lesser extent, the standard deviation, are functions of strain rate.
- 4. Volume dilatation as a function of strain can be calculated using parameters obtainable from relative attenuation. The method appears to give reasonable results and it is more sensitive and much easier to accomplish than the dilatometer method. It is likely that the acoustic parameters used in this model can be related to fundamental physical and chemical properties such as particle size distribution and bond strength. Further work is needed to establish these relationships.
- 5. Energy dissipated within an elastomeric composite material by mechanical deformation is well correlated with microstructural damage as measured by relative attenuation.
- 6. The secant modulus of the solid rocket propellant used in the Lockheed experiments is linearly correlated with microstructural damage as measured by relative attenuation.

#### REFERENCES

- Liu, C.T., Bellin, J.L., and Holsinger, R.W., "Effect of Load History on the Cumulative Damage in a Composite Solid Propellant", AIAA/ASME/ASCE/AHS 28 Structures, Structural Dynamics and Materials Conference 27th: 1986: San Antonio, TX.
- Liu, C.T., "Effects of Cyclic Loading Sequence on Cumulative Damage and Constitutive Behavior of a Composite Solid Propellant", AIAA/ASME/ASCE/AHS 28 Structures, Structural Dynamics and Materials Conference, 1987: Monterey, CA.
- 3. Knollman, G.C., Martinson, R.H., and Bellin, J.L., "Ultrasonic Assessment of Cumulative Internal Damage in Filled Polymers', <u>J. Appl. Phys.</u> 50(1), January, 1979.
- 4. Knollman, G.C. and Martinson, R.H., "Nonlinear Elastic Effects in the Ultrasonic Assessment of Cumulative Internal Damage in Filled Polymers", J. Appl. Phys. 50(12), December 1979.
- 5. Knollman, G.C., Martinson, R.H., and Bellin, J.L., "Ultrasonic Assessment of Cumulative Internal Damage in Filled Polymers (II)", J. Appl. Phys. 51(6), June 1980
- 6. Martinson, R.H., Bellin, J.L., and Holsinger, R.W., "Damage Assessment in Filled Polymers by Ultrasonics" citation unknown.
- 7. Bills, K.W., Jr., Sweeny, K.H., and Salcedo, F.S., <u>J. Appl.</u>

  <u>Polymer Sci.</u>, 4, 259, 1960
- 8. Elliott, D.M. and Ledbetter, W.B., "Microstructural Damage and its Influence on the Dilatation-Strain Properties of a Filled Elastomeric Composite Material", CPIA Publication No. 158, Vol. I, 1967.

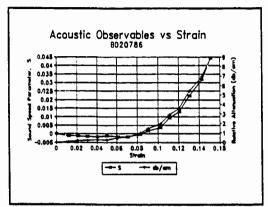


Figure 1

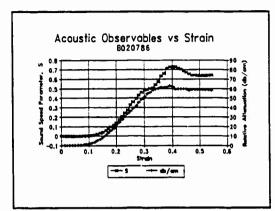


Figure 2

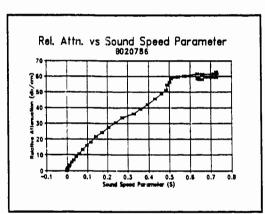


Figure 3

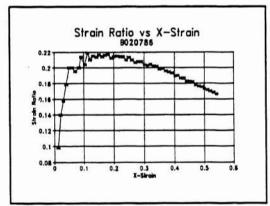


Figure 4

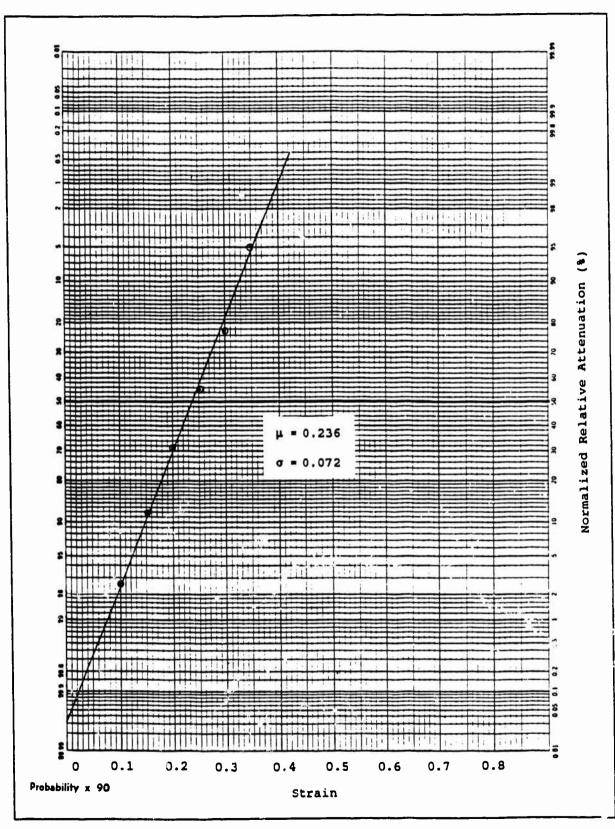
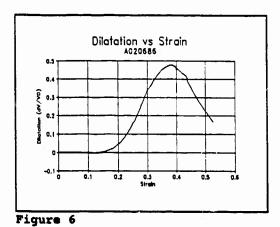


Figure 5 Normalized Relative Attenuation vs. Strain for Run C020786



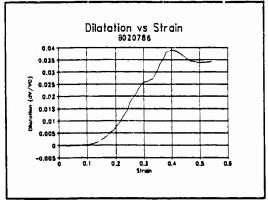


Figure 7

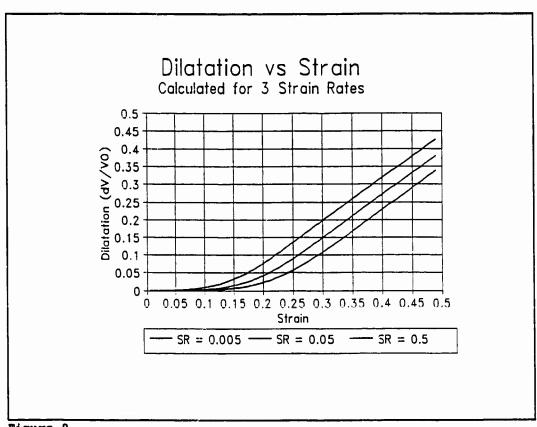


Figure 8

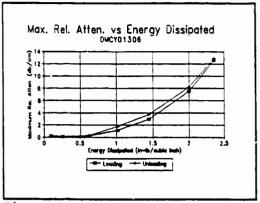


Figure 9

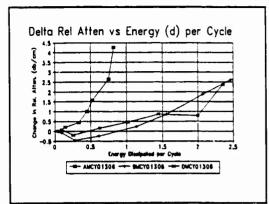


Figure 10

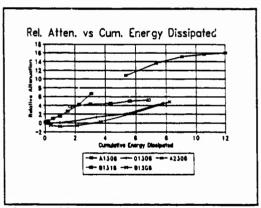


Figure 11

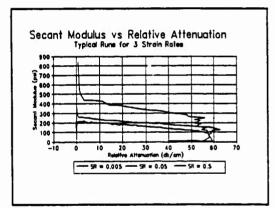


Figure 12

CONSTANT STR	TN DATE DING		
Strain Rate = 0.05	Strain Rate = 0.05		
A020686 B020586 C020586	A020586 B020786 C020786 C012986 D012986 F012986		
Strain Rate = 0.5 G012986 H012986 I012986			
CYCLING RUNS			
Cyclic Loading (Strain Rate = 0.05)	Block Cyclic Loading (Strain Rate = 0.05)		
A013086 B013086 D013086	A020386 B013186		

Table 1. Lockheed Data Runs

Measured Quantities	Calculated Quantities
o Load o Crosshead Displacement o Transverse Displacement o Source Signal o Time Delay o Received Signal	o Stress o X-Strain o Total Attenuation o Relative Attenuation o Fractional Contraction o Sound Speed Parameter o Volume Dilatation

Table 2. Measured and Calculated Quantities from Lockheed Data Runs

INDIVIDUAL RUN VALUES			
Strain Rate	Run Number	<u>Mean</u>	St. Deviation
0.005 0.005	A020686 B020686	0.266 0.262	0.070 0.082
0.050 0.050 0.050 0.050 0.500	B020786 A020586 C020786 D012986 H012986 I012986	0.225 0.225 0.236 0.231 0.186 0.192	0.075 0.063 0.072 0.077 0.071 0.065
AVERAGE VALUES			
Strain Rate	Run Number	Mean	St. Deviation
0.005 0.050 0.500	- - -	0.264 0.229 0.189	0.076 0.072 0.068

Table 3. Mean and Standard Deviation of Relative Attenuation for Constant Strain Rate Runs

#### **ACKNOWLEDGMENTS**

I would like to thank the Air Force Systems Command, the Air Force Office of Scientific Research, and the Phillips Laboratory for sponsoring this project. Arkansas Tech University provided additional financial support for which I am grateful. Special thanks are due to Dr. C.T. Liu for serving as focal point and for his encouragement and guidance throughout the project. Dr. Seng Chung spent numerous hours analyzing data and preparing plots; I very much appreciate his efforts. Dr. John Rusek and Mr. Wayne Roe of Phillips Laboratory and Mr. David Miller of Research & Development Laboratories were particularly helpful in a number of ways and I want to acknowledge their efforts and to thank them too.

# 1991 USAF-RDL SUMMER FACULTY RESEARCH PROGRAM/ GRADUATE STUDENT RESEARCH PROGRAM

Sponsored by the

#### AIR FORCE OFFICE OF SCIENTIFIC RESEARCH

Conducted by the

Research and Development Laboratories, Inc.

#### FINAL REPORT

#### RESEARCH IN VIBRATION IDENTIFICATION, ISOLATION, AND SUPPRESSION

#### **FOR LARGE SPACE STRUCTURES**

Prepared by:

James Michael Argento Robert Alan Carlin

Marco David D'Amore Ephrahim Garcia, Ph.D.

Academic Rank:

Assistant Professor

Department and

Department of Mechanical Engineering

University:

Vanderbilt University, Nashville, TN

Research Location:

Edwards Air Force Base

Phillips Laboratory, ASTREX division Edwards AFB, Lancaster, California

Date:

August 23, 1991

#### I. INTRODUCTION

The loads and vibrations that impinge upon a payload during launch have historically been the focus of structural and design engineers. My summer research focused on one particular Air Force satellite, and the possibility of reducing the loads from the two launch vehicles currently used: the Titan IV, and the Space Shuttle. The first step in this ongoing project was to learn about the structure of this satellite and perform an eigenanalysis using Nastran, NASA's Structural Analysis program. The next step involves a parametric study of the passive and/or active system that would be required to reduce said loads. It is assumed that this vibration isolator would be positioned between the satellite and the Inertial Upper Stage (IUS) upon which the satellite sits during launch in both vehicles.

Every satellite and its own substructures must be designed in such a way that they can withstand "launch cycle loads", and be able to perform their duties once they reach orbit. A considerable savings could be gained if these loads were reduced by some means. The savings are numerous and could include a decreased mass for the main load bearing members in the satellite, and in turn, an increased allowable mass for other components, such as electronics and propellant for attitude rockets. Another benefit is longer satellite life, since more propellant could mean a greater number of attitude adjustments while on orbit. The electronics on board might also exhibit longer life and have an even greater endurance, since the dynamic loading on the circuitry during launch would be reduced. With this in mind, the investigation into a vibration isolator for satellite sytems has great potential.

#### DISCUSSION

Modeling The satellite chosen for this study is a geosynchronous Air Force satellite (Figure 1.1). Several Nastran models of this satellite have been analyzed in the past to obtain a reasonable structural analysis and mode shapes. The models used initially in this investigation had on the order of 18,000 degrees of freedom (DOFs), and were used to obtain mode shapes and a general feel for the dynamics of the satellite and its components. Once this was accomplished, it was determined that much simpler models would suffice, since the scope of this investigation involves only a parametric study of the vibration isolator. In the process, we are aiming to obtain similar responses to that given by the more complex models.

One of these simpler models was designed using MSC/PAL2, another finite element analysis package, and has approximately 150 DOFs in its current configuration (Figure 1.2). This model consists of the main load bearing members and mass simulators at the top, using very similar dimensions to those used in the Nastran models. Other components have obviously been left out of this model, but we have already obtained similar mode snapes to those in the 18,000 DOFs models for the components modelled, and continue to work on the details of this model.

Another modelling case being studied is a simple 2-D, undamped, lumped parameter model (Figure 1.3). This four DOF model and its equations of motion can be used to study the trends and tradeoffs of the isolator in a general way. The equivalent mass, stiffness and inertia of the modelled components (i.e.  $m_1 J_1$ ,  $k_1$ ) can be adjusted until they match those exhibited in previous models. The trends exhibited by the isolator can be studied in the same way, by adjusting  $k_2$ . The equation of motion, in matrix form, is:

$$..$$

$$M x + K x = B y$$

where

ŧ

$$M = \begin{bmatrix} m_1 + 4J_1/d_1^2 & m_1 - 4J_1/d_1^2 & 0 & 0 \\ m_1 - 4J_1/d_1^2 & m_1 + 4J_1/d_1^2 & 0 & 0 \\ 0 & 0 & m_2 + 4J_2/d_2^2 & m_2 - 4J_2/d_2^2 \\ 0 & 0 & m_2 - 4J_2/d_2^2 & m_2 + 4J_2/d_2^2 \end{bmatrix}$$

$$K = \begin{bmatrix} 4k_1 & 0 & -4k_1 & 0 \\ 0 & 4k_1 & 0 & -4k_1 \\ -4k_1 & 0 & 4(k_1+k_2) & 0 \\ 0 & 4k_1 & 0 & 4(k_1+k_3) \end{bmatrix}$$

$$B = \begin{bmatrix} 0 & 0 \\ 0 & 0 \\ 4k_3 & 0 \\ 0 & 4k_3 \end{bmatrix}$$

Damping terms (i.e. c<sub>1</sub> and c<sub>2</sub>) will be added in future studies, and in turn, can be varied to study trends in the isolator design.

Excitation The load cycle of the launch vehicle is of key importance in this study. We will be using an internal report published by the Aerospace Corporation, which contains data obtained from the Titan IV booster during several previous missions. While much of this data is not intended for external release, we have obtained permission to use it and will discuss only that information which is deemed appropriate for a report such as this. There are several flight event times during a Titan IV launch that involve significant transients in the loading induced onto the payload. These are liftoff, stage I ignition, solid rocket motor separation, payload fairing separation, stage I shutdown, stage II ignition and stage II. shutdown. While these events cover short periods of time during the launch cycle, they are the most important time periods, since large magnitude changes in the loading forces occur. The largest strains, and thus, the largest deformations will also occur at these times. The other time periods are relatively sedentary, and are probably unimportant in our study. The data obtained includes accelerations (i.e. g forces) in the principal directions of roll, pitch and yaw as recorded by several accelerometers at locations close to the payload compartment. This information will be used when we begin to evaluate the parameters of the isolation system.

Passive Control As mentioned earlier, the most significant elements of the launch load cycle are a select few time periods during which transients play an important role. In our passive control considerations, we will be looking to optimize our isolator design with the following considerations: designing the isolator strictly for these transients vs. designing the isolator for the transients and the time periods in between, during which the excitation is more sedentary. The available data indicates that the excitation forces during the sedentary periods are in a higher frequency range than the transients, but their amplitude is of a much smaller magnitude, making these secondary loads. While both cases will be considered in our optimization, the inclusion of the sedentary loads will probably prove unneccessary. The optimization process will involve tuning our system parameters (i.e.  $k_s$  and  $c_s$ , shown in Figure 1.4) until we achieve an overall minimum of displacement  $(x_s)$  of the bottom of the satellite.

Active Control A greater isolator performance could most likely be achieved by including active control. A feedback control loop would allow for an on-line "active" isolator, and

would prove more robust for this satellite suspension system. By generating a force F<sub>G</sub> (see Figure 1.4), such that

$$F_G = -k_G x_s$$

that is, a force proportional to the velocity of the satellite, we could greatly reduce the excitation forces being transmitted to the satellite. Once the active control is properly tuned, the effects on the passive control would also be analyzed.

#### RESULTS

Since this project will continue for approximately one more year, the results will not be complete for some time. As of mid-August however, we have obtained results from the extensive Nastran model, such as natural frequencies and mode shapes for 0 to 300 Hz. We are examining the Nastran results for mode shapes that may prove significant in determining which parts of the satellite might violate tolerances within the payload fairing shroud during launch. We have found two modes (14.8 and 30.4 Hz) in which the equipment compartment at the top of the satellite displaces as a rigid body with the supporting trusses in a swaying motion. Other modes involve the displacement of the main solar panel, configured as a cylinder around the main load bearing trusses of the satellite. The displacements of the solar paddles at the base of the satellite, which are stowed upward during launch, are also of concern. The current rigid assembly used as the interface between the satellite and the launch vehicle, has not allowed the satellite to violate any of the payload fairing tolerances, and the isolation system we intend to define during this investigation must conform in the same way. Information on the allowable deflections within the payload fairing has been obtained and will be used as a guide for our research.

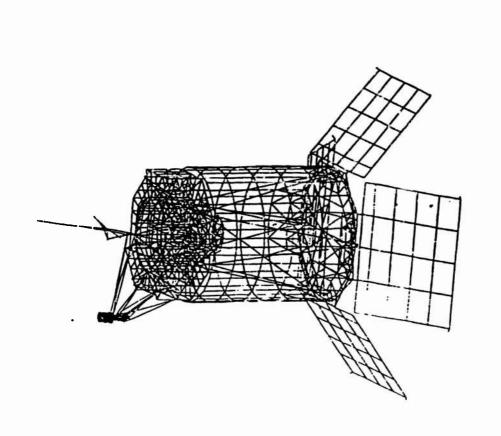


Figure 1.1
Geosynchronous Air Force Satellite, Nastran Model

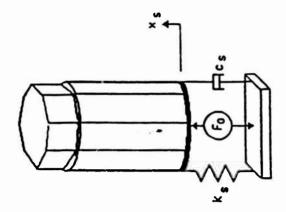


Figure 1.4 Schematic of satellite and passive/active vibration isolator

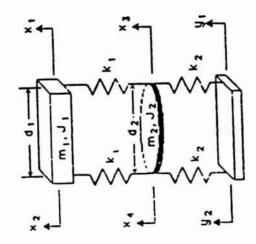


Figure 1.3 2-Dimensional, 4 DOF lumped parameter model

#### II. INTRODUCTION

The field of large space structures is very diverse. It encompasses modelling, testing, fabrication and operation of extremely complex mechanisms. Before anything can be built, however, extensive testing must be done to ensure that no unforeseen problems occur. To this end, modal analysis is used to determine a particular structure's natural frequencies of vibration, damping ratios, and mode shapes. However, each test requires that enormous amounts of data be collected in order to obtain a reasonable identification of these properties.

In order to reduce the amount of space necessary to store the tests, as well as save time in processing the data, the technique of data compression has been introduced. Although the idea of data compression is not new, it has not previously been used in parameter identification. The basic premise behind data compression (DC) is that data is eliminated from the original signal, thereby saving a combination of volume, time, and/or bandwidth (see section b).

Preliminary studies have shown that this application can be very useful in both ground tests and on-orbit identification. Telemetry data is, by necessity, extremely redundant; partial compression will not only save disk space (allowing more tests for less initial monetary outlay) but will not be much of a hindrance in analysis.

#### DISCUSSION

<u>Data Compression: Background</u> The definition of data compression states that it is simply a reduction in the amount of storage space needed to save a given data set. This data can be in several forms. It can be physical, such as the volume that data takes up on a computer's hard drive; an interval of time, such as the time needed to transmit the data; or a part of the electromagnetic spectrum, like the bandwidth necessary to transmit the data. These three forms are interrelated, using the following analogy:

#### Volume = $f(time \times bandwidth)$

Therefore, a reduction in volume affects either the transmission time or bandwidth. The parameter of interest - in our case, the volume - determines where the compression operation is performed in the system.

Data compression is performed for one of two major reasons. The first reason is to bypass a design constraint, such as limited storage space; the second is to obtain a significant

savings in the design of a new system. In the performance aspect, data compression methods can be grouped into two 'classes' - reversible (called redundancy reduction) and irreversible (called entropy reduction). Irreversible techniques deal with the entropy of a system, where the entropy is defined as the average information. An example of an irreversible compression algorithm is the use of a threshold when obtaining responses of a system. In this case, the data is only transmitted when a particular sample exceeds the threshold. If very few values cross that level, a large amount of compression is achieved, but the original signal can't be reconstructed. Reversible techniques, on the other hand, allow for the restoration of the original data by removing only that data which is redundant. An example of this method is the elimination of repetitive data - for example, a square wave. In a redundancy-reduction operation, only the significant points - such as the 'corners' of the square wave - are retained, along with their relative positions in the original signal. <sup>1</sup>

Algorithm Background For our studies, a redundancy reduction algorithm was used to obtain significant amounts of compression of frequency response functions. This algorithm was implemented using a PC-based matrix manipulation program called MATLAB. MATLAB was chosen for both its comprehension and its functionality. A block diagram of the steps used in the modal analysis procedure may be seen in Figure 2.1. Time history responses are fast Fourier transformed into transfer functions and then averaged. This averaged transfer function (TF) can then either be analyzed (the right 'fork' of Figure 2.1) or it can first be compressed and then analyzed. Figure 2.2 shows the steps taken in the compression and analysis of the data. The TF is first compressed, and the compression ratio is calculated. The compression ratio, CR, is defined as:

# CR = number of data points before compression number of data points after compression

This means that for a CR of 30, only 1 data point in 30 is saved, and the compressed TF has only  $\frac{1}{30}$ th of the spectral lines of the original TF. The data is next decompressed using a new algorithm based on the compression algorithm. At this point, the data is analyzed using one of two methods. The first method requires that each 'peak' in the TF be separately identified and run through a SDOF Nyquist circle fit algorithm to obtain natural frequencies and damping ratios. The other method necessitates using an inverse fast Fourier transform to return the data to a time history format and then entering it into the Eigensystem Realization Algorithm (ERA).

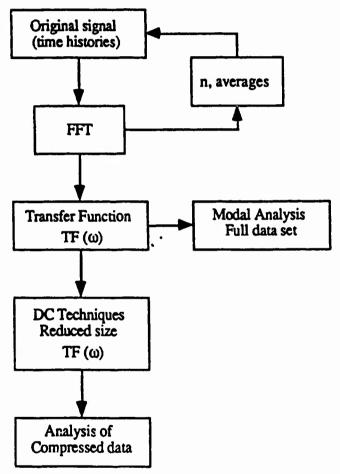


Figure 2.1. Steps used in the modal analysis procedure.

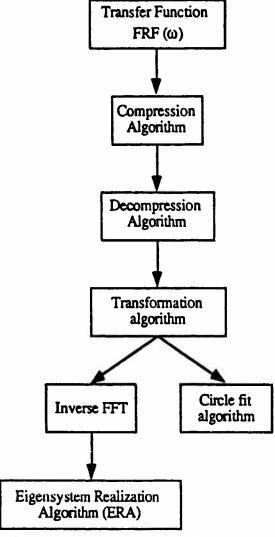


Figure 2.2. Steps used in the compressed data analysis procedure.

Initially, several frequency response functions were modelled in MATLAB, for both single- and multiple-degree-of-freedom (SDOF and MDOF, respectively) cases. Modal models were chosen for ease of reliability comparisons. The single degree of freedom test was done using a TF with a natural frequency of 10 Hz and a damping ratio of 0.02. Compression ratio values between 4 and 64 were obtained, and the results may be shown in Table 2.1, below. Please note that the actual identified value of the damping was determined to be 0.0195, and that the % errors are measured with respect to this value.

CR, comp. ratio	ω,	ω, % error	ζ,	ζ, % error
	decompressed	•	decompressed	
	(Hz)		(% critical)	
4	10.000	· 0.00	1.95	0.00
8	10.000	0.00	1.95	0.00
22	10.000	0.00	2.15	10.26
32	10.039	0.39	2.33	19.49
64	9.961	0.39	3.53	81.03

Table 2.1. Analysis of a SDOF model with respect to varying compression ratios.

Note that for large compression ratios, the modal parameter errors are relatively small. The maximum error obtained in the frequency determination is less that 0.5% at all times. This is not the case for the errors induced in the damping term. However, for compression ratios as high as 32, the error was only roughly 20%.

The multiple degree of freedom test was done with a TF which had natural frequencies of 1, 2, 10, and 16 Hz with  $\zeta$ =0.02 for modes 1 and 2, and  $\zeta$ =0.01 for modes 3 and 4. Results were obtained only for a compression ratio of approximately 4.0 and may be seen in Table 2.2.

Mode	Natural frequency, Hz	% Error	Damping ratio	% Еггог
1	1.0254	2.54	0.0238	19.00
2	2.0215	1.08	0.0217	8.50
3	10.0:95	0.20	0.0112	12.00
4	16.0156	0.10	0.0101	1.00

Table 2.2. Identified natural frequencies and damping ratios, MDOF system, CR ≈ 4.0.

Astrex background The Phillips Laboratory at Edwards AFB is equipped with a one-half-scale model of a typical SDI satellite, shown in Figure 2.3. This model is called the ASTREX - Advanced Space Structures Technology Research Experiment. In order to prove the feasibility of the data compression technique in modal analysis, testing was performed with the help of the technicians at Edwards. The CDAC - Computer-controlled

Data Acquisition system - was used in conjunction with another matrix manipulation program called MATRIX<sub>x</sub> to obtain time history data for several positions on the model. These time histories were fast Fourier transformed and averaged to create usable transfer functions. At this time, analysis of these transfer functions has begun, but it is only preliminary. Initial analysis of one member from 0-40 Hz has shown 19 modes of vibration in this small frequency range. ERA was used to obtain a stability plot for the uncompressed data; this can be seen in Figure 2.4. Figure 2.5 shows the stability plot obtained by ERA for the compressed data, and Figure 2.6 shows a comparison of both stability plots. It can be seen from Figure 2.6 that the results obtained after compression are almost identical to those obtained before compression. This is a very good indication that the compression technique is reliable.

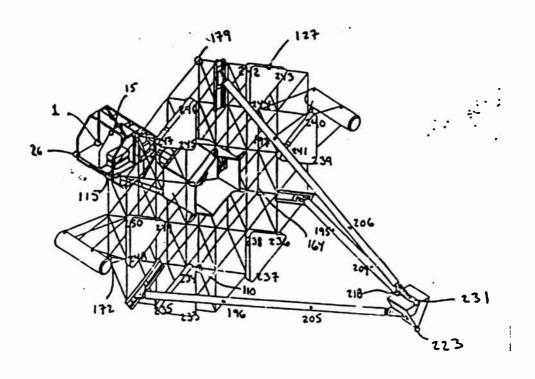


Figure 2.3. Diagram of the ASTREX test structure.

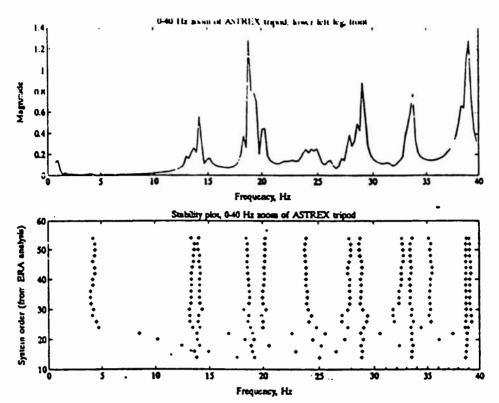


Figure 2.4. ERA stability plot, ASTREX structure, uncompressed data, 0-40 Hz.

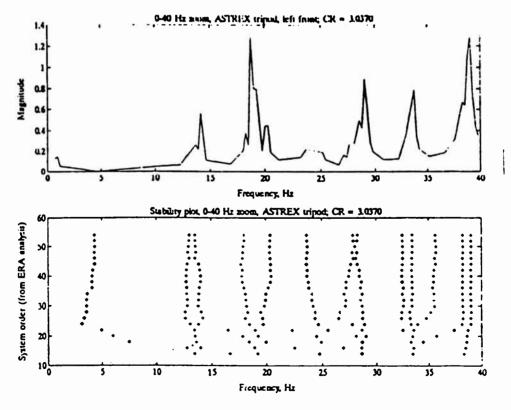


Figure 2.5. ERA stability plot, compressed data, ASTREX structure, 0-40 Hz.

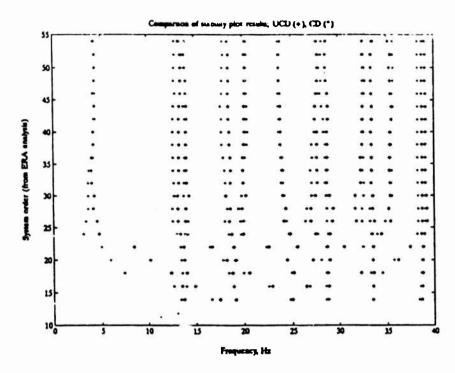


Figure 2.6. Comparison of stability plots, compressed and uncompressed data.

### CONCLUSIONS

It can be seen from the data presented here that data compression in modal analysis is a viable area of research. The identification of modal parameters is robust with respect to data compression. Also, a significant savings in volume, as well as time, is feasible with the use of certain compression methods. Potential applications for this theory are too numerous to mention, but include the topics of on-orbit testing, telemetry, and health monitoring.

### REFERENCES

- [1] Lynch, Thomas J. <u>Data Compression: Techniques and Applications.</u> New York: Van Nostrand Reinhold, 1985.
- [2] Ewins, D.J. Modal Testing: Theory and Practice. Letchworth, England: Research Studies Press Ltd./Brüel & Kjaer, 1986.
- [3] Garcia, E, "System Identification for the Microcomputer Environment," M.S. Thesis, Department of Mechanical and Aerospace Engineering, State University of New York at Buffalo, Buffalo, New York, 14260.
- [4] Juang, J.-N. and Pappa, R.S., "An Eigensystem Realization Algorithm for Modal Parameter Identification and Model Reduction," AIAA Journal of Guidance, Control, and Dynamics, Vol. 8, No. 5, Sept.-Oct. 1985, pp. 620-627.

### III. INTRODUCTION

A very critical area is the suppression of vibrations in spacecraft with long flexible appendages. Many outside stimuli are responsible for such motions, such as dynamics induced by thermal gradients brought about by solar heating, solar winds, and or the vibrations induced by a slewing maneuver. The problems induced by such motions tend to wreak havoc with such systems used for signal transmission-performed by antenna arrays. Not only can these dynamics cause accuracy problems in the performance of such systems but also high amplitude motions may prove fatal to these systems.

The ASTREX Facility (Advanced Structures Technology Research Experiment) is a structure specifically designed to investigate the aforementioned areas of research. The motivation of this study is to research and design a control algorithm for this structure using the existing actuators. The goal of these controllers will be to suppress vibrations using the reaction wheel and gas-jet thrusters. The induced slewing load will be a model which may prove important when using the thrusters for vibration suppression. The thrust of the vibration suppression scheme is to reduce the line of sight (LOS) error of the structure due to a disturbance response.

#### DISCUSSION

Modeling In order to investigate the ASTREX and develop a control model, a finite element model of the structure must be developed. A full order model consisting of 2394 degrees of freedom (DOFs) was constructed using Cosmic NASTRAN. A diagram of the undeformed model can be seen in Fig. 3.1 at the end of this section. This diagram was produced via NASTRAN.

It is evident that this structure, as stated earlier, needs a very complicated FEM model to accurately perform a dynamic analysis of the structure and thus is the reason for having 399 nodal locations. However, while this makes for a very precise model to predict the experimental modes of the structure, the mass and stiffness matrices extracted from an analysis are unmanageable and not to be considered for use in the control design. Therefore the structural model must be reduced enough so that they can be manipulated into a state space model. The idea is to take the large mass and stiffness matrices and reduce them while still having them retain the ability to produce the lower modes given by the full order model or as close to these modes as possible.

The method of reduction chosen was Guyan reduction. This a very well known and common reduction method which was easily incorporated into the NASTRAN model via the ASET command. The way the ASET card works is that the node location that you desire to keep is entered in along with the retained DOFs associated with that node. The key to using the Guyan reduction is to choose the nodes and the corresponding DOFs at those points to render a good approximation to the full order model. Many trial runs were done to check which nodal locations should be kept with regards to the sensitivity of the model. The ultimate goal was to get a very accurate model with very small order, not forgetting that the line of sight investigation (LOS) is the main goal of this study. Therefore, the main nodes to be kept are those with which pointing is an issue, such as the secondary reflector, trackers, and positions on the primary structure where mirrors would be located.

MODE NUMBER	FULL ORDER 2394	958	472	197	58
1	3.519	3.521	3.529	3.529	3.528
. 2	5.146	5.154	5.156	5.156	5.233
3	13.014	13.135	13.150	13.155	13.549
4	13.178	13.273	13.292	13.298	13.675
5	16.501	17.028	17.234	17.239	18.643
6	18.277	18.979	19.224	19.246	19.252
7	19.188	19.222	19.330	19.352	19.732
8	20.200	20.304	20.406	20.428	21.282
9	25.347	27.167	27.544	27.587	29.503
10	26.765	28.626	29.256	29.348	31.177

TABLE 3.1 Frequencies for Guyan reduced models

The lower modes, not including the rigid body pedestal modes, are tripod modes (motion between the secondary and the primary via the tripod configuration). It is for these reasons that it is felt that much time and effort should be concentrated in controlling these modes in order to control the LOS between the secondary and primary structures. For verification of this fact, refer to Table 3.1 and compare the modes of the model with 472 DOFs to the model with 197 DOFs. The model with 472 DOFs contains all primary and

tripod nodes that the 197 DOF model contains. However the 472 DOF model contains all DOFs for the tertiary structure as well as the components connecting the tertiary to the hub. It is readily discerned from scrutinizing these two reductions that the large difference in DOFs had insignificant effect on the model to warrant the inclusion of these nodes in the model.

The 958 DOF model is an attempt to see that the inclusion of all nodes and corresponding DOFs for the primary had a significant effect on the lower eigenvalues. The reason for this model was to see whether or not perhaps a loss of mass in the reduced mass matrix caused an error when the eigenanalysis was performed using the new reduced mass and stiffness matrices. As is shown in Table 3.1, this run has little difference than the other runs at 472 and 197.

These previous examples of reductions were never considered to be a feasible model from the onset because of the large order matrices they would produce. They were simply done, as expressed earlier, for verification of the pertinent nodes to render a good model. Having done these studies, I was able to come up with a small but good approximation to the full order model of order 58. The model, as shown from Table 3.1, has a model that is as good, if not better than, the models of several magnitudes larger. The reason this final model was developed is to approximate the induced slewing loads in the structure, as well as the applied actuator loads, in order to arrive at a high fidelity model.

It should be pointed out that by no means does the author propose to develop a control using a 58 by 58 matrix or a 116 by 116 state matrix. Via the incorporation of damping from experimental data, the model of the system will be transformed into a modal model. This will also allow the model to be reduced even further through a modal reduction method in which the desired modes are kept along with their corresponding eigenvectors (mode shapes). This will finally allow manageability for a control study. This is also due to the fact that damping information is only available for the modes between 0 to 140 Hz.

Once the desired mass(M) and stiffness(K) matrices were extracted from NASTRAN a small program was written to transform them into a format that was readable by MATLAB. Doing an eigenanalysis

 $(M^{-1} K - \lambda I)u = 0$ 

the eigenvalues( $\lambda$ ) and eigenvectors (u) were calculated, thus producing a diagonal matrix of eigenvalues (diag( $\omega^2_i$ )) and also a matrix of eigenvectors, U=(u<sub>i</sub>). Using this eigenvector matrix, a mass weighted similarity transformation matrix (S<sub>m</sub> = M<sup>-1/2</sup>U) was formed which has the following properties.

$$S^{T}_{m} M S_{m} = I$$
  
 $S^{T}_{m} D S_{m} = diag(2\zeta\omega)$   
 $S^{T}_{m} K S_{m} = diag(\omega^{2}_{t})$ 

The D is the damping matrix and the  $\zeta$  is damping ratio. From the methods expressed in Section II, the damping ratios may be found and by using the second equation above, the damping matrix may be formulated using this transformation matrix. Knowing what eigenvector is associated with what mode and what the order of M and K was as determined by NASTRAN, the second order system can be produced and then ultimately transformed into state space form.

$$\dot{\mathbf{x}} = \begin{bmatrix} 0 & \mathbf{I} \\ -\mathbf{M}^{-1}\mathbf{K} & -\mathbf{M}^{-1}\mathbf{D} \end{bmatrix} \mathbf{x} + \begin{bmatrix} 0 \\ -\mathbf{M}^{-1} \end{bmatrix} \mathbf{f}$$

### RESULTS

In addition to the work mentioned above, a model of the torque wheel was produced via SIMULAB and a model of the thruster is presently under development. These models will be used to develop a control scheme by using a comparison of Linear Velocity Feedback (LVF) and Linear Quadratic Gaussian (LQG) methods. The ultimate goal is to suppress the lower modes of vibration, which predominantly affect the tripod, in order to improve line of sight accuracy. Also, the effects of slewing induced vibrations will be considered in this study. Due to space considerations, the aforementioned material has not been included.

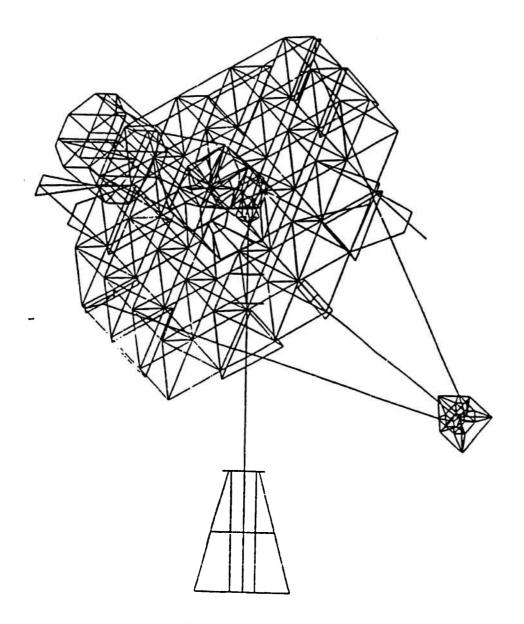


Figure 3.1. Full order finite element model of the ASTREX structure.

# Analytical and Experimental Investigation of The Mode Dampings in Laminated Composite Beams

## H. Ghoneim

## Abstract

A viscoelastic constitutive equation which accounts for damage is proposed. The equation is implemented into a finite element program and used to predict the mode dampings of a cantilever laminated beam. The results are compared with the corresponding experimental ones for a graphite epoxy laminated beam. The effect of the frequency and amplitude of vibration as well as damage is addressed. Discussion of the results and conclusion are presented.

## Introduction

The embedded sensors and actuators used to control the unwanted vibration in smart structures provide a secondary potential pay off: health monitoring [1]. Adopting the premise that material damping in general increases with increasing damping [2,3], the sensors embedded in smart structures can be used to monitor damping and consequently the state of damage of the structure. However, this application requires a good understanding of the material damping and its sensitivity to factors such as the frequency and amplitude of vibration, damage, and embedded and/or bonded sensors and actuators.

Crawley and Luis [4] studied the coupling effect between a structure and a piezoelectric sensor (embeded and/or bonded) on the the vibration response of a beam. Damping effect was not included. Allen et al [5] presented a model of a damage dependent damping in a laminated composite beam. Their model assumed that the undamaged state of the material is elastic and not viscoelastic. More over, the study was confined to the first mode damping.

In this report, we present a preliminary analytical/experimental study of damping in a laminated composite graphite epoxy beam. The sensitivity of

damping to the frequency and amplitude of vibration as well as damage is included in the study. A nonlinear viscoelastic constitutive equation is presented to model the mechanical behavior of the laminate including the damping. The model incorporates a single internal state variable which accounts for the damage. The constitutive equation is implemented into a finite element program and used to predict the first three mode damping for both damaged and undamaged laminated composite cantilever beams. The results are compared with the corresponding experimental ones, and finally discussion and conclusion are presented.

## The Model

In order to analytically investigate the mode dampings of a structure, we need the proper constitutive equation which describes the mechanical behavior of the material under consideration. We also need to implement this equation into a numerical code, such as the finite elment method, to solve the appropriate boundary value problems and calculate the mode dampings.

## The constitive equation

To account for the strain rate sensitivity and damping we adopt a nonlinear Maxwell model. Consequently, for isothermal, small, and uniaxial deformation, we have

$$\sigma = E(\varepsilon - \varepsilon^{v}) \tag{1}$$

where  $\sigma, \varepsilon, \varepsilon^{\nu}$  and E are the axial stress, strain, viscous strain and elastic modulus, respectively. The evolution of the viscous strain is assumed to follow the power law [6], i.e.,

$$\dot{\varepsilon}^{\mathbf{v}} = C \left(\frac{\mathbf{\sigma}}{R}\right)^{\mathbf{n}} \tag{2}$$

where C is a scalar parameter, n is a strain rate sensitivity parameter, and R is the drag stress which represent the resistance of the material to flow. As R increases, the flow resistance increases and consequently the material becomes less viscous and more elastic. In general, an evolution equation with a hardening-recovery format is needed for R. When no viscoplastic deformation occurs, R may be expressed as

 $R = a + b \{1-Exp(-\epsilon)\}$ or for very small strains:

$$R = a + b \in$$
 (3)

Ghoneim and Matsuoka have shown that, in general, the constitutive equations (1) and (2) are capable of describing the thermomechanical behavior of amorphous polymers (including the rubbery and glassy stages) over a wide range of strain rates and temperatures [7]. However, for a more accurate presentation, more vicous elements may be needed, i.e;

$$\dot{\varepsilon}^{v} = \sum_{i} C_{i} \left( \frac{\sigma}{R_{i}} \right)^{n_{i}} \tag{4}$$

To incorporate the effect of damage, we follow the continuous damage approach [8]. We adopt a single internal state variable, D. It represents the corrected area of cracks and cavities (damage) per unit surface normal to the axial direction: D=0 corresponds to the undamaged state, D=1 corresponds to rupture of the element into two parts, and 0<D<1 characterizes the damage state. Incorporating the damage variable, D, into equations (1) and (2) the proposed viscoelastic constitutive equation, for a single viscous element, beacomes [9]

$$\dot{\sigma} = (1 - D) E \dot{\varepsilon} - E C \left( \frac{\sigma}{(1 - D)R} \right)^n$$
 (5)

Where the dot represents differentiation with respect to time.

## The Finite Element equations

For our preliminary study, we confine our analysis to beams which obeys the elementary Bernoulli-Euler Theory. The governing equation is

$$M'' + \rho A \ddot{y} = p \tag{6}$$

where M is the bending moment,  $\rho$  is the mass density, A is the cross section area, y is the transverse displacement of the neutral axis, and p is the beam transverse force per unit length. The superscript prime indicates differentiation with respect to the axial coordinate, x. Substituting from (1) into (6), we can get

$$(EI \ y'')'' + \rho \ A \ \ddot{y} = p - M^{v''}$$
 (7)

where EI is the flexure stiffness of the beam, and Mv is an equivalent viscous moment.

$$M^{\mathbf{v}} = \int_{\mathbf{A}} \mathbf{E} \, \mathbf{\epsilon}^{\mathbf{v}} \, \mathbf{z} \, \mathrm{d}\mathbf{A}$$

where z is the beam transverse coordinate direction. Applying Galerkin finite element method to the governing equation (7), we get

$$[M] \ddot{Y} + [K] \underline{Y} = \underline{F} + \underline{F}^{V}$$
(8)

where [M], [K],  $\underline{Y}$  and  $\underline{F}$  are the standard mass matrix, stiffness matrix, nodal tranverse displacement vector, and nodal load vector, respectively. The equivalent visous load vector  $\underline{F}^{v}$  is given by

$$\underline{F}^{\mathbf{v}} = -\sum_{n=1}^{e} \int \underline{\Psi}^{n} \mathbf{M}^{\mathbf{v}} d\mathbf{x}$$

where  $\underline{\Psi}$  is the shape function vector. Cubic Hermits functions are chosen for  $\underline{\Psi}$ . The Newmark method [10] is adopted for the time marching solution of (8). It should be pointed out that the resulting algebraic equations are nonlinear, and consequently the successive iteration method is applied at each time step in order to get the current nodal displacement vector.

Also, it should be mentioned that, as a first step, we restrict our analysis to regular symmetric cross-ply laminated beams. And, since the contribution of the matrix material to damping is substantially greater than that of the graphite fibers, we assumed that all the material damping of cross-ply laminates is attributed to the 900 plies. Hence, the standard constitutive equation of elasticity ( Hooke's law ) is applied for the 00 plies, and the proposed viscoelastic equations for the 900 plies.

## The Experimental Work

The experimental work is carried out to assess the material parameters of the proposed constitutive equation (5) and to examine its capability to predict the mode daming of both the undamaged and damaged beams. The composite laminated used in all our experiments have been hand laid up using a standard graphite epoxy ( Thornel 300 ) prepreg tape lay out and hot press curing processes.

## Assassement of The Material Parameters

An independent set of experiments, tensile tests at various strain rates, is carried out to find the material parameters of the proposed constitutive equation (E, n, a, and b) for the 90° ply. Test results, at three different strain rates are displayed in Fig. 1. The experiments are conducted on MTS880 Hydraulic Axial-Torsional Testing Machine, and the samples were prepared in accordance with the ASTM recommendations.

The values of the stress at  $\varepsilon=0.2\%$  for the 8.33E-5 and 8.33E-6 strain rates are used to obtain the value of n. And the stress-strain diagram at the strain rate of 8.33E-5 is utilized to determine the values of E, a and b. The assessed values are presented in table 1. (column # 1). The predicted stress-strain diagrams at strain rates=8.33E-6 and 8.33E-7, together with the corresponding experimental curves are displayed in Figures 2. and 3, respectively. In general, the agreement is good. However, at a very small strain ( $\varepsilon<0.1\%$ ) the predicted results are too elastic.

Since most dynamic tests, in particularly modal damping tests, are run within this range of strain. It is imperative to add another viscous element, as in equation (4), which accounts for damping at this range. In the absence of sufficient experimental data at this range of strain, the added new material parameters are assumed based on experimental observations. These values are presented in table 1 (column # 2). The new value of n is assumed to be very close to unity scince at very small strains the mode damping becomes independent of the amplitude of vibration. Also, for simplicity, R is assumed constant and consequently the value of C/R becomes equivalent to the daming coefficient of a linear vicous element. Note that when n=1 the viscoelastic model degenerates to the standard linear Maxwell model.

#### be

It should pointed out that special tests have to be devised to provide data about the rate sensitivity of the 900 ply at this very small range of strain, and consequently to obtain the necessary material parameters of the second viscous element in a more scientific way.

## Modal Damping Tests

Because of its relative simplicity, a cantilever beam is selected as the current test configuration. Proper care is taken to apply a constant clamping torque for all the tests.

In order to reduce the system damping, as upon using shaker or piezo-ceramic actuators, impulse testing using a pendulum weight is selected as the source of excitation. The weight imparts a constant impact to the beam near the clamp. Because of its high mechanical compliance, very low damping coefficient and very high sensitivity, a piezo film glued to the base near the clamp is used as a sensor. The data from the piezo film are aquired, processed and displayed using the HP33660A dynamic signal analyzer.

Though, using the piezo ceramics as sensors and actuators is very appealing and are widely used in smart structures, understanding the coupling effects between the ceramic and the structure is crucial before using them for our modal damping test. Consequently, this idea was abandoned for now.

The laminated beam is 10"long, 1" wide, and has an approximate thickness of 0.06". The stacking sequence of the laminate is  $[0,0,90,90,90,90,90]_S$  Since it is recommended, for better sensitivity, to stick the piezo films, on  $0^0$  plies, They have been added at the outer surfaces of the laminated beam.

Damaged beams have been prepared by embedding NiTi alloy wires in between the 90° plies during the lay up process, then pulling them out after curing. Upon pulling, the NiTi wires experience a considerable reduction in their diameters and can be pulled out with a relative ease, leaving the laminated beams with cylindrical cavities running across the thickness of the beams. Only one configuration of damage is considered in this study. Three layers of wires (20 each) are embedded at the center of the beam and between the third and the fourth 90° plies. The wires are spread over a length of 1.5" and located at x=3.5" to x=5". A magification of the resulting damaged section is shown in Figure 4.

It should be pointed out that though this method introduces a nonrealistic damage, it nonetheless provides a controllable damage - a great obstecale for many researchers working in this area. Also, by changing the number, size, location and shape of the embedded wires, this method can be exapanded to introduce controllable realistic types of damage. For example,

wires with thin flat cross sections embedded between the plies can be used to introduce delamination. The current damage is reasonable for this preliminary study, which investigates the effect of damage, in general, on the mode damping.

## Results and Discussion

The experimental and analytical results of the first three mode damping are displayed in table 2. In both cases damping is calculated using the logarithmic increment method. Because of the amplitude dependence of daming, the values presented are the average values over the strain range  $\varepsilon=1E-5$  to 1E-6. To emphasize the amplitude ependence of the mode damping, the first mode damping at a higher strain range ( $\varepsilon=1E-4$  to 1E-5) is reported as well.

The reported analytical results are obtained using the developed finite element program. The modeled beam is initially deformed with the appropriate mode shape and released from rest. The resulting transient response of the transverse displacement at the tip of the beam is used to calculate the corresponding mode damping. The free decay response and the corresponding frequency response at the first natural frequency are displayed in Figures 5. and 6., respectively. The magnitude of the initial displacement is adjusted such that the resulting strain near the base, where the piezo film is located, is within the corresponding experimental strain range recorded by the piezo film.

The experimental results indicate that damping in general increases upon introducing damage. Moreover, the results show that the second and the third mode dampings increase much more than the first one. This is in accordance with the premise that a large increase in the local loss factor (damping), as in the case of the presence of a local damage, will only have an effect on the overall loss factor of a given mode of vibration (damping mode) if it coincides with an area of a high stored enery. Figure 7. shows the modal strain enery variation, for the first three modes, with the beam length. The relative location of the introduced damage is marked by thick lines. It is clear that the damage coincides with an area of a high strain energy for the second and the third modes only. This finding confirms the validity of the methodolgy developed by Griffin and Yost [1], at least in concept, for dedecting the damaged developed in vibrating beams.

The analytical results, on the other hand, indicates that the developed model, though needs adjustments and refinements, possesses a promising potential. The model fails to provide reasonable quantitative results. It also fails to predict the correct strain rate sensitivity. The experimental results indicates that the third mode damping increases substantially, while the analytical results shows that it considerably declines. However, the model can predict the strain dependency of the mode damping - it increases with increasing the magnitude of the strain. Also, the model successfully simulates the effect of damage on the mode damping. Ingeneral the predicted mode damping increases with damage. And, thore important, the second and third mode dampings experience more relative increase than the first one.

## Conclusion

- 1) The developed viscoelastic constitutive equation needs to be modified in order to properly simulate the strain rate sensitivity of the mode damping. Also, experimental work to obtain the strain rate sensitivity of polymeric materials at a very small strain needs to be devised. The experiments are needed to provide for a better understanding of the strain rate sensitivity, and consequently damping, at a very small strian levels as well as to provide the necessary data required to assess the material parameters of the modified model.
- 2) Using the embeded NiTi wire approach is a good technique to introduce a controlled damage. By varying the number and size, the location and the shape of the wires, the effect of the intensity, location and type of damage can be studied.
- 3) The adoption of the continuous damage approach is A simple and usefull for a qualitative analytical study of the damping related damage.

## Reference

- [1] Griffin, S., and Yost, B., "Health Monitoring of Smart Structures"
- [2] Plunkett, R., "Damping in Fiber Reinforced Laminated Composites at High Strain," J. Composite Material Supplement, Vol. 14, pp. 109-117, 1980.
- [3] Edberg, D. L., "Material Damping of Sample Structures in a Simulated Space Environment," J. of Spacecraft and Rockets, Vol. 23, pp. 288-296, 1986.
- [4] Crawley, E. F., and Luis, J., "Use of Piezoelectric Actuators as Elements of Intelligent Structures," AIAA Journal, Vol. 25, pp. 1373-1385, 1987.
- [5] Allen, D. H., Harris, C. E., and Highsmith, A. L., "prediction and Experimental Observation of Damage Dependent Damping in Laminated Composite Beams", ASME DE-Vol. 5, pp. 253-264, 1987.
- [6] Ghoneim, H., "Analysis and Application of a Coupled Thermoviscoplasticity Theory," ASME J. of Applied Mechanics, 1990.
- [7] Ghoneim, H., and Matsuoka, S., "A constitutive Equation for Amorphous Polymers Including the Rubbery and Glassy Stages," Submitted to J., of Rheology.
- [8] Lemaitre, I., "A Continuous Damage Mechanics Model for Ductile Fracture,", ASME J. of Engineering Materials and Technology, Vol.107, pp. 83-89, 1985.
- [9] Lemaitre, J., "Local Approach of Fracture," Engineering Fracture Mechanics, Vol. 25, pp. 523-537, 1986.
- [10] Zienkiewicz, O. C., The Finite Element Method, McGraw-Hill, London, 1977.

Material Parameters	Units	Element #1	Element #2
С	1/sec	1.0	1E-4
n		60	1.2
а	psi	300	10
b	psi	1.53E6	0

Table. 1. Material Parameters

Mode #	Analytical		Experimental	
	undamaged	damaged	ndamaged	damaged
1	1.6E-3	1.9E-3	1.5E-3	1.7E-3
2	.54E-3	.68E-3	1.3E-3	1.7E-3
3	.11E-3	.14E-3	1.7E-3	2.3E-3
1*	2.7E-3	3.9E-3	2.1E-3	2.3E-3
<u></u>				

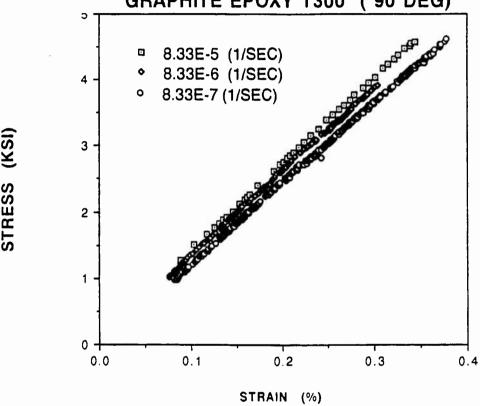
Table. 2.

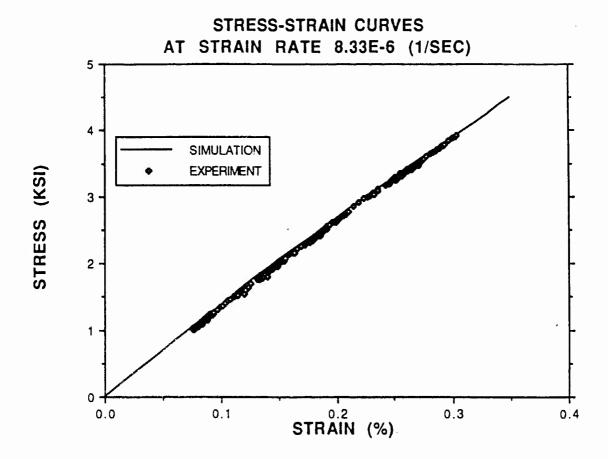
Mode Dampings
(1\* is for the higher strain range)

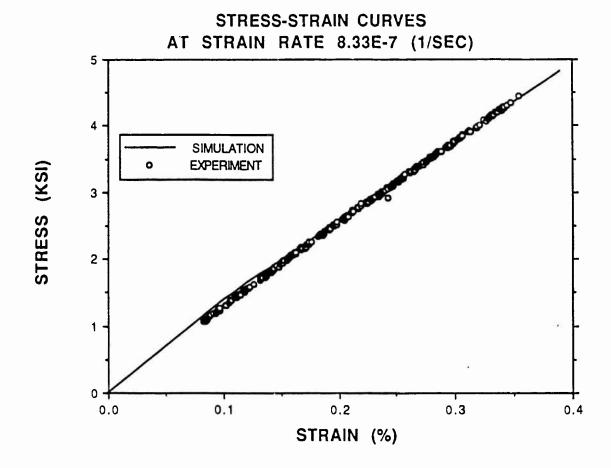
## Figure Captions

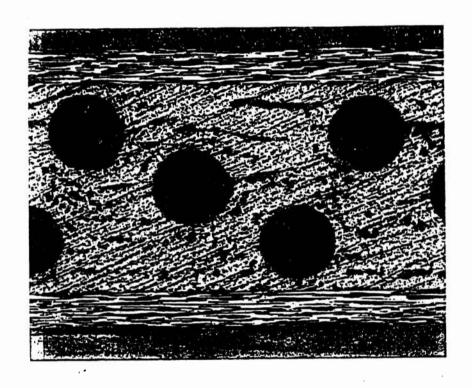
- Fig.1. The Experimental Stress-Strain Diagrams at Different Strain Rates.
- Fig.2. Comparison of the Predicted and Experimental Stress-Strain at Strain Rate = 8.33E-6 1/sec.
- Fig.3. Comparison of the Predicted and Experimental Stress-Strain at Strain Rate = 8.33E-7 1/sec.
- Fig.4. A Magnified Photo Picture of a Section of the Damaged Laminated Beam
- Fig.5. The Predicted Free Response at the Tip of the Laminated Cantilever Beam.
- Fig.6. The Predicted Frequency Response.
- Fig.7. The Modal Strain Energy Variation with the Beam Length.

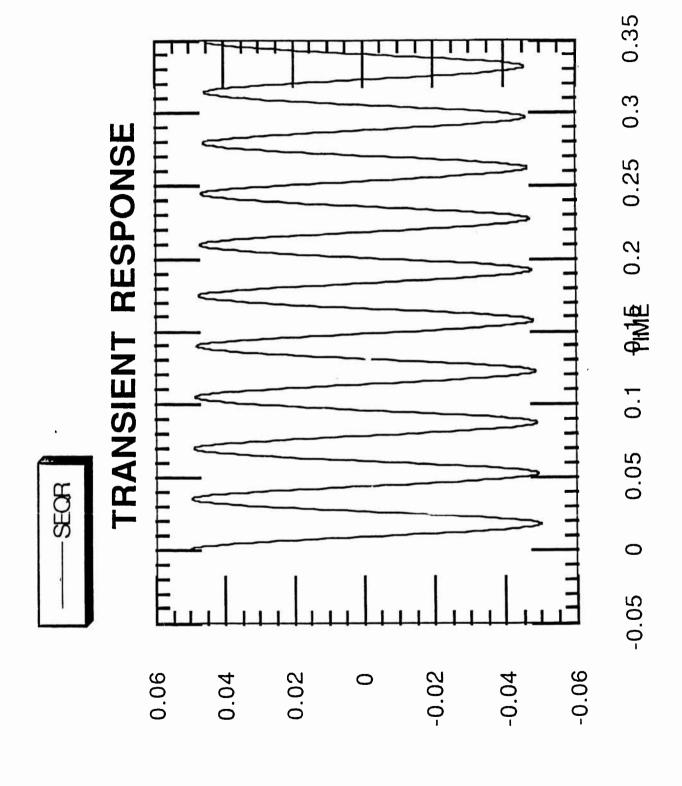
# TENSILE TEST AT DIFFERENT STRAIN RATES GRAPHITE EPOXY T300 (90 DEG)

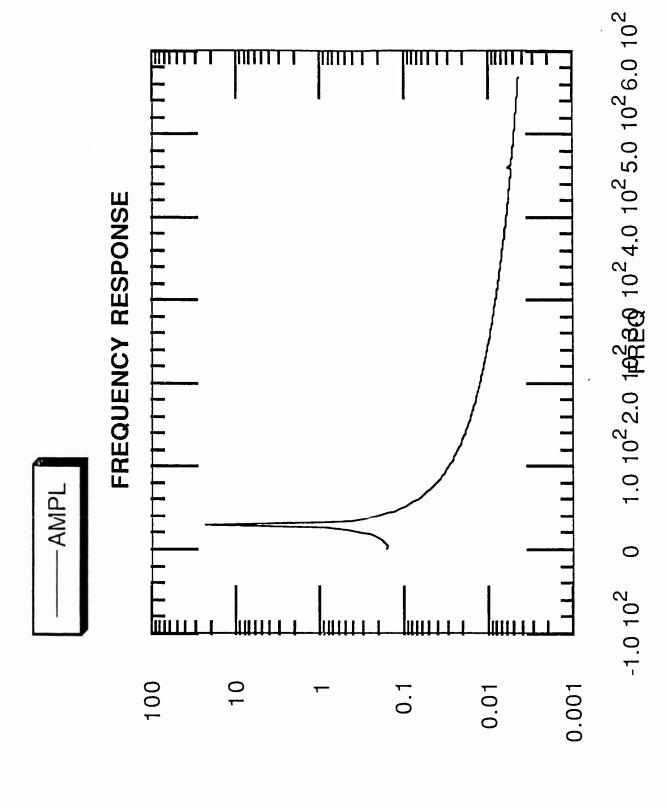


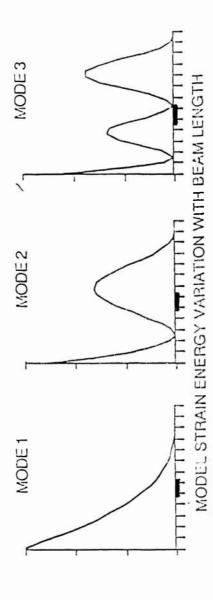












## THE SYNTHESIS AND PROPERTIES OF ENERGETIC SALTS WITH POTENTIAL FOR DEVELOPMENT AS SOLID ROCKET PROPELLANTS

#### Dr. Vincent P. Giannamore

ABSTRACT: Energetic salts with potential for use in solid propellants have been investigated. Three nitroformate salts have been prepared. Each combines a cation which can serve as a fuel with the oxidizing nitroformate anion. The characterization of these compounds is reported as well as some of their thermal properties and sensitivity to impact and friction. Triaminoguanidinium nitroformate, while highly energetic, is probably too sensitive to warrant further development. Guanidinium nitroformate, however, appeared to be a candidate for further development as a propellant ingredient. Hexaamminecobalt(III) nitroformate may have been prepared but more investigations are required for its characterization and demonstration of its value as a propellant ingredient.

INTRODUCTION: Formulators of solid rocket propellants are continuously striving to increase rocket system capabilities by devising higher energy formulations. At the same time, some demands have been made for tactical rockets that are relatively smokeless and have more environmentally benign effluents. This would require rocket propellants that do not employ metal fuels nor produce hydrogen chloride as an exhaust product. Finally, safety is a primary consideration for propellant formulations.

One current requirement is for formulations suitable for orbital defense systems. These systems must be small, high energy, and stable

over long periods of time. Another requirement is for formulations having low explosive hazard and generating minimum smoke for use in small air-launch missiles to improve aircraft operations safety. Environmental concerns make it desirable to eliminate halogens from propellant formulations. Yet, any new formulations must still be capable of satisfying operational thrust-time requirements.

Present propellants are not well-adapted to meet these requirements. For example, most formulations include metals which contribute to the formation of smoke. Yet, in the absence of metals, satisfactory specific impulse levels are difficult to attain. Those propellants which do have adequate specific impulse usually contain halogens. Thus, there is a need to examine new or relatively unknown materials for use in solid propellants.

Screening tests are desired for nonhalogen containing energetic oxidizing salts that might provide adequate energetics, combustion traits, thermal stability, chemical compatibility, and safety for future solid propellant propulsion needs. The current study includes the synthesis of some of these salts, determination of some of their properties, and screening them for impact and friction sensitivity. In short, the purpose of the study is to identify salts which have the potential for development as propellant ingredients for use in formulations capable of meeting future mission requirements.

DISCUSSION: Salts containing the nitroformate anion,  $C(NO_2)_3$ , and those containing the dinitramide anion,  $N(NO_2)_2$ , were considered for investigation. However, lack of ammonium dinitramide as an energetic salt precursor prevented dinitramide investigations.

Nitroform compounds had been of considerable interest to propellant chemists at one time. For example, hydrazinium nitroformate (HNF) was extensively investigated during the period 1960 - 1968. Interest in these compounds waned when difluoroamino propellants began to be developed, but interest has resurfaced recently (1).

Three compounds were chosen for investigation. The first was triaminoguanidinium nitroformate (TAGNF),  $C(NHNH_2)_3C(NO_2)_3$ . Theoretical  $I_{SP}$  calculations for smokeless propellant formulations using this compound gave values as high as 254 seconds (2). When metal fuels were included, even higher values could be projected. Since it also contains no halogens, TAGNF seemed a likely candidate for investigation.

TAGNF is a known compound, but more precise details concerning its friction and drop weight impact sensitivities were desired. In addition, it was hoped that new high purity samples would show improved thermal stability versus the products of the earlier synthesis. Also, present test methods data for friction sensitivity and differential scanning calorimetry could be readily compared to that of other propellant ingredients. These tests were not performed on the previously prepared TAGNF.

The second compound chosen for investigation was the related salt guanidinium nitroformate (GNF),  $C(NH_2)_3C(NO_2)_3$ . It was of interest for the same reasons as TAGNF, i.e., high theoretical  $I_{SP}$  and absence of halogen content. This compound was also known and the problems to be solved were identical to those stated above for TAGNF. The possibility of cosalt formation from TAGNF-GNF mixtures was also of interest.

The third salt chosen for investigation was hexaamminecobalt(III)

nitroformate. As far as can be determined, this appears to be a previously unknown compound. Although the compound contains a metal, the high molecular weight cation makes the percentage of metal in the compound relatively small. A method for synthesis of this compound had to be devised. Its sensitivity to impact and friction would need to be determined and its thermal properties studied. As a new compound, more extensive characterization of this compound than of the other two would be appropriate.

RESULTS: The synthesis of TAGNF was based upon a method which had been reported by Carignan and Satriana for other triaminoguanidine salts (3). In this synthesis the acid corresponding to the desired anion is reacted with the free base triaminoguanidine (TAG). TAG was prepared by the action of sodium hydroxide on the nitrate salt of TAG. Because TAG has a strong tendency to oxidize in air (4), the literature procedure required modification before satisfactory results could be obtained. Little or no yield of TAG was obtained from the nitrate unless the reaction was performed under nitrogen. For the same reason, it was found that freshly prepared TAG gave the best results in the subsequent reaction with nitroform to form TAGNF. When TAG which had been stored for more than a day or two was used in this reaction, it was necessary to wash it with cold, anhydrous methanol to remove the red oxidation product prior to reaction with the nitroform.

TAGNF was obtained in the form of fluffy yellow needles which also showed a strong tendency to oxidize over time when stored in air. The onset of this oxidation did not occur as rapidly as that of the TAG but the oxidation appeared to be more complete once it did occur. The

melting point was obtained from thermograms obtained by differential scanning calorimetry (DSC). The average value was 82.43 °C.

An infrared spectrum was obtained on an FT-IR with a photoacoustic cell (PAS-FTIR). The spectrum was consistent with TAGNF. Ir particular, absorptions due to the presence of NH<sub>2</sub> and NO<sub>2</sub> were noted. It should be noted in connection with this that the frequencies of the infrared absorptions attributed to the nitroformate anion were consistent among the spectra of all nitroformate salts reported in this study.

In addition to an endothermic transition at the melting point reported above, the DSC thermograms of the TAGNF samples also showed a large exothermic transition at an average temperature of 111.47 °C. The heat flow associated with this transition was of the order of 5 to 7 mcal/sec. The average enthalpy change was 560.6 cal/g, which is equivalent to 143.0 Kcal/mole.

As reported below, considerable problems were encountered due to the presence of water in GNF crystals obtained directly from its preparative reaction. Water did not appear to be a problem with TAGNF. A sample of TAGNF was kept in a vacuum dessicator for more than one week. At the end of this period neither its melting point nor DSC had changed significantly. In addition, there was no indication of significant water content in the infrared spectrum obtained on a sample which had not been subjected to any special drying procedures.

TAGNF proved to be very sensitive to impact and friction. The sensitivity number (E50) for impact was 44 Kg-cm. For friction the E50 was 3.7 Kg. These are values which indicate the level at which one-half

of the samples tested would be expected to explode. However, a positive friction test was obtained on one out of five samples at 1.5 Kg. Sample holders for both the impact and friction tests were shattered during some of the trials. The

technician reported that such sharply explosive behavior was especially rare. The synthesis of GNF was straightforward. Addition of guanidinium carbonate to aqueous solutions containing excess nitroform caused GNF to precipitate in the form of fluffy yellow needles similar to those formed by TAGNF. The reaction was driven by the formation of CO<sub>2</sub> gas. Excess nitroform was used because it had been previously reported to stabilize HNF (1). While the nature of the reaction indicates that nearly quantitative yields might be expected, the great solubility of GNF in water makes isolated yields much lower. It should be noted that nitroform was available only in the form of a 32.3% aqueous solution.

In contrast to the TAG compounds, GNF showed no apparent tendency to oxidize. However, significant problems were encountered due to water incorporated in the crystals. The infrared spectrum obtained on a sample as formed in the reaction showed the expected absorptions due to NH<sub>2</sub> and to the nitroformate anion. However, the spectrum also showed indications for the presence of water. Researchers at Rocketdyne Corporation had reported a melting point of around 128 °C for GNF (5). However, DSC thermograms showed that freshly prepared samples melted at an average temperature of 82.74 °C. This was also confirmed using a standard Thomas-Hoover melting point apparatus.

Attempts to obtain anhydrous GNF concentrated on finding a method

to recrystallize the salt from some solvent other than water. This method was considered desirable because it was hoped that the crystals formed would be in some form other than needles which are undesirable for propellant processing. Unfortunately, GNF proved to be extremely soluble in all polar solvents tested and insoluble only in hydrocarbons and freon 113.

Recrystallization was accomplished by three methods. Mixed solvent systems consisting of various combinations of liquids were tried. For example, GNF was dissolved in a minimum amount of isopropyl alcohol, a solvent in which it is very soluble. Then, toluene, in which GNF is insoluble, was added to the solution until crystals of GNF began to form. Another method was to cool solutions of GNF in various solvents below room temperature to induce crystallization. Related to this was the method whereby solvent was evaporated from the GNF solutions. Both of the latter two methods work best when the original solution is saturated. However, GNF was so soluble in most solvents that it was difficult to prepare saturated solutions. All of this work was complicated by the fact that the thermal sensitivity of hydrated GNF made heating it inadvisable. Nevertheless, recrystallization was accomplished by all of these methods and by combinations thereof using a number of different solvents. However, the GNF crystals obtained always contained water as indicated by melting point determination. This also proved true when freshly dried solvents were used and when the GNF solutions were allowed to stand over drying agents before recrystallization. Occasionally, some improvement in melting point was noted but values approaching 120 °C with narrow ranges were never

observed. The crystals were always in the form of needles, although in some cases the needles were very small. Drying was only accomplished by placing the hydrated GNF samples in a vacuum dessicator over anhydrous magnesium perchlorate. Samples treated in this way no longer melted at the lower temperature. DSC showed that the only transition which occurred when these samples were heated occurred at an average temperature of 126.09 °C. Because of certain technical factors connected with the DSC, reliable figures for the enthalpy change associated with the transition could not be obtained. In the Thomas-Hoover capillary melting point apparatus the transition appeared to be a melt coincident with decomposition. I.e., the sample turned liquid and simultaneously began to evolve a gas. The thermograms showed these transitions to be exothermic although a slight endothermic shoulder may be noted in one of the thermograms. Melting unaccompanied by other phenomena would be expected to be endothermic. Infrared spectra (PAS-FTIR) obtained on the dry samples showed that the peaks indicative of the presence of water had disappeared, while the characteristic amino and nitroformate absorptions remained. Once dried, the GNF showed only a slight tendency to pick up water from the atmosphere.

Impact and friction sensitivity tests were performed on both the hydrated and anhydrous species. GNF proved to be insensitive to both friction and impact within the limits of the tests regardless of the water content. The anhydrous sample was not initiated by a 6 Kg weight dropped from a height of 50 cm which indicated a sensitivity number greater than 300 kg-cm for impact. The sensitivity number for friction appeared to be 10.8 kg or better.

One attempt was made to form a cosalt of GNF and TAGNF. Highly concentrated solutions of TAGNF and GNF in isopropyl alcohol were prepared and mixed. The solutions were concentrated by evaporating solvent in a stream of nitrogen and were cooled. Only GNF precipitated. Curiously, judging by the melting point, this GNF appeared to be closer to anhydrous than any other sample which had not been dried in vacuo.

Hexaamminecobalt(III) nitroformate was prepared by the reaction of Hexaamminecobalt(III) chloride with nitroform. The best method appeared to be to mix aqueous solutions of nitroform and cobalt salt and refrigerate the solution for several days. The crystals formed as long brown needles. Smaller fragments appear to be slightly orange. Another method used was to mix the solid chloride with the nitroform solution. This presented practical difficulties in distinguishing between unreacted chloride and product as well as in separating them. Since the thermal sensitivity of the compound was not known, heating did not seem advisable. More work is indicated in this area so that a synthetic method can be perfected.

Three product samples were obtained, each by slightly different methods. The appearance of the product when not allowed to crystallize slowly was not much different than that of the chloride starting material. However, observation of samples of each compound while being heated in a capillary melting point apparatus confirmed that the samples were not identical to the chloride. Both the product samples and the starting material go through a series of color changes before decomposition. However, those exhibited by the product samples were different than those of the starting material and occurred at

temperatures more than 100 °C lower than those of the starting material. Identification of the product as hexaamminecobalt(III) nitroformate was based primarily on PAS-FTIR and cannot be considered conclusive without further analysis. The spectra obtained show absorptions at frequencies corresponding to the frequencies at which the spectra of the other nitroformate salts displayed absorptions attributed to nitroformate anion. The presence of the hexaamminecobalt(III) cation was inferred by the spectra's remarkable similarity to an Aldrich Library spectrum of hexaamminecobalt(III) chloride.

Nevertheless, it was not be shown by this method that the cation to anion ratio was 1:3. This information would be better obtained by NMR and/or by elemental analysis. Time did not permit these analyses to be completed. Each of the product samples obtained display some minor differences in their IR spectra and considerable differences in the DSC thermograms. These might be explained by contamination with impurities, replacement of different numbers of chloride ions by nitroformate ions, or some other cause. Once again, this indicates the need for more complete analysis to establish the purity as well as confirming the identity of the product. This will be one of the subjects of follow-up research to be proposed. Sensitivity of this compound to impact and friction has not yet been established.

CONCLUSION: Methods for the synthesis of all three compounds have been established, although improvements in crystallization methods would be desirable. Characterization and identification of TAGNF and GNF seems conclusive. There appears to be good evidence that a nitroformate salt of hexaamminecobalt(III) had been formed but more rigorous

characterization is required.

Both GNF and TAGNF were shown by their DSC thermograms to be very energetic species. TAGNF was considerably more rapid than GNF and its decomposition was more exothermic than many established propellants. In this respect both compounds seemed worth further study by propellant formulators.

The sensitivity data for GNF was encouraging. Impact and friction tests indicate that it should be safe to handle if reasonable caution is exercised. Lack of any transitions below 120 °C is an indication that it may have sufficient thermal stability for a number of applications. The crystal form of the material appears to be its major disadvantage.

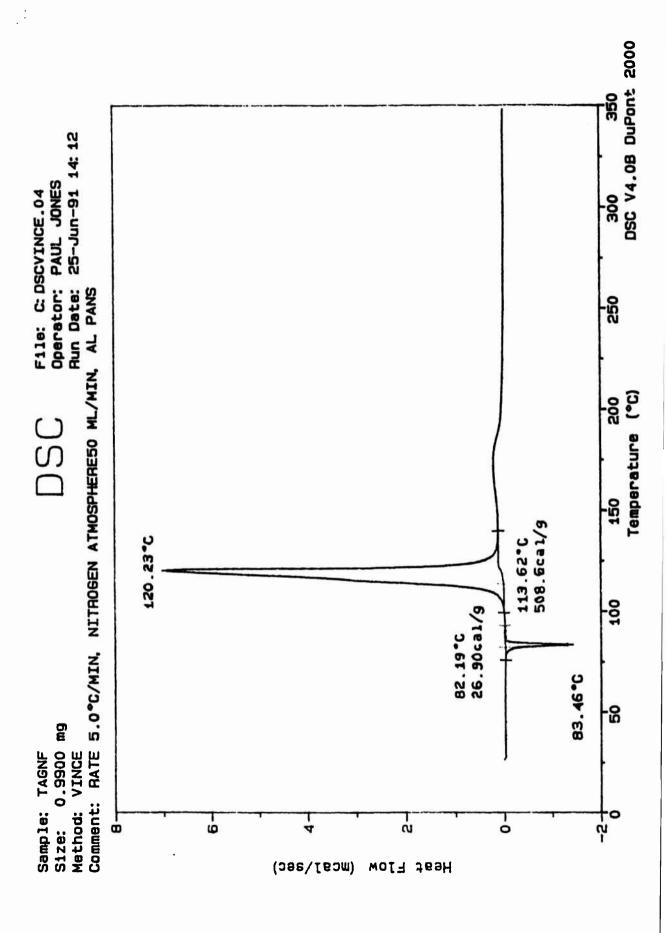
By contrast, TAGNF did not appear to be a reasonable candidate for further work. It has low thermal stability making it difficult to work with and preventing its use in certain applications. Its major drawback, however, is its sensitivity to explosive initiation by friction. Even if the E50 values were to be considered an acceptable risk, the erratic nature of the sensitivity would make it a very hazardous compound to handle.

Hexaamminecobalt(III) nitroformate appears to be promising and may indicate that complex salts of other transition metals are desirable targets for investigation. Much more work needs to be done on this compound, however, as discussed in the previous section.

Examples of IR spectra and DSC thermograms referred to in the text are shown on the following pages.

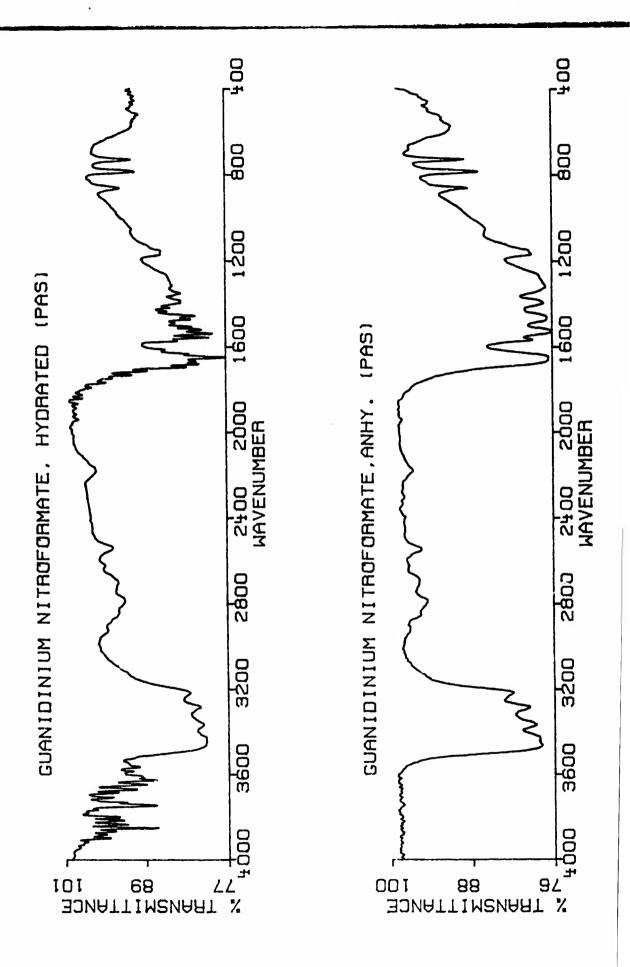
#### REFERENCES:

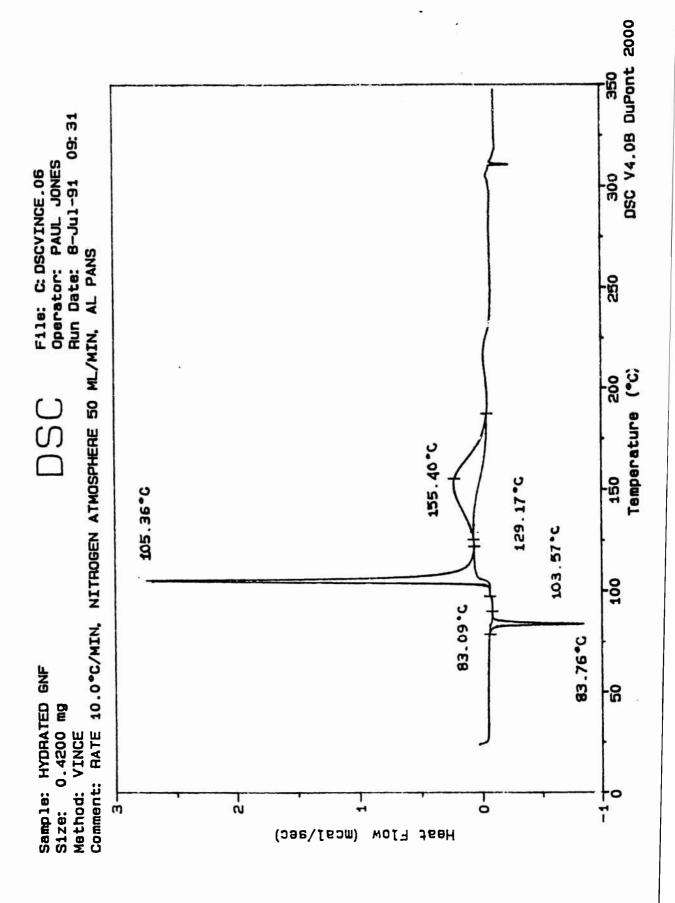
- (1) Roberto, F. Consultant's Report on Hydrazine Nitroform Literature, 21 May 1991.
- (2) Merrill, C. personal communication.
- (3) Carignan, Y. P.; Satriana, D. R. J. Org. Chem. 1967, 32, 285.
- (4) Benjamin, L. E. J. Org. Chem. 1964, 29, 3729.
- (5) personal communication through Claude Merrill.

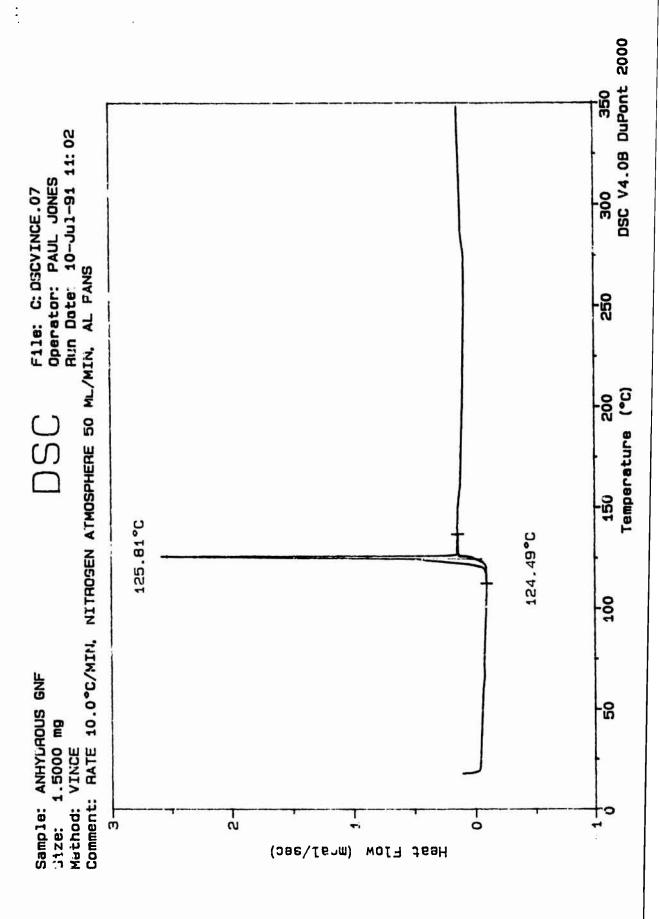


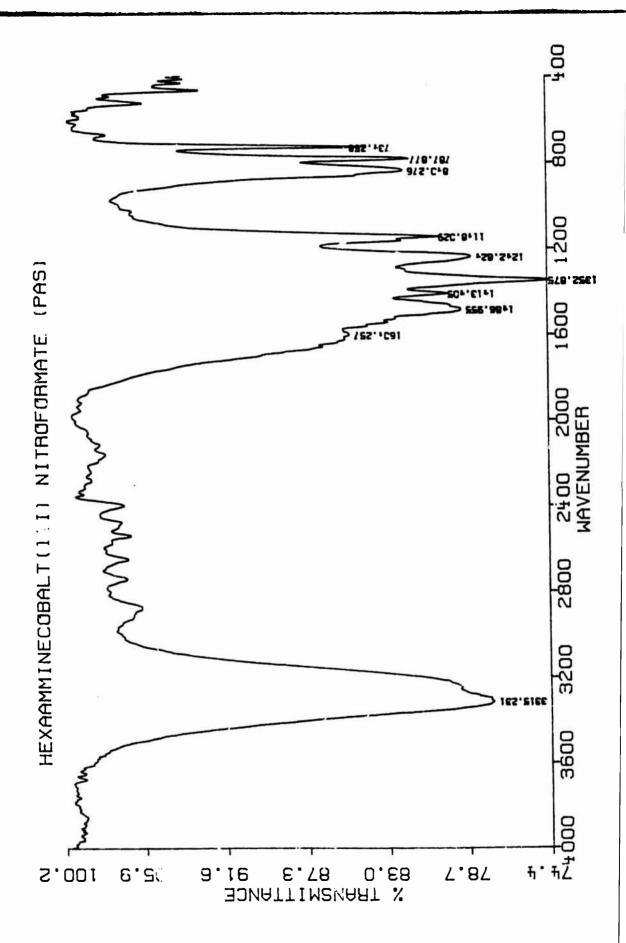
•:

()

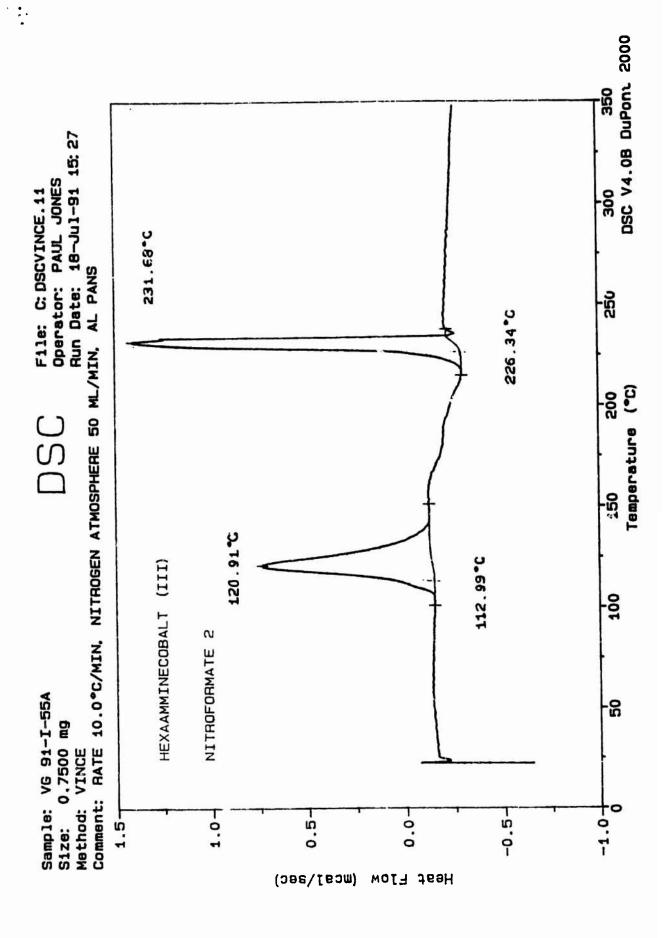


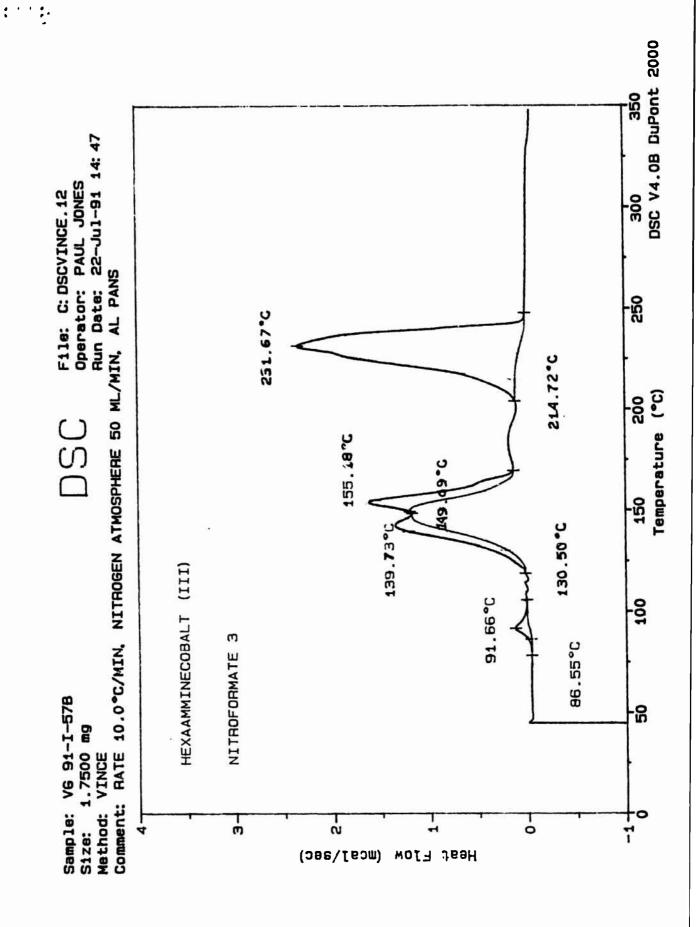






.:





# DROP SIZE INSTRUMENTATION FOR ROCKET INJECTOR TESTS

William M. Grissom Assistant Professor of Physics Morehouse College

#### ABSTRACT

Three drop sizing instruments were studied for tests in liquid rocket injector sprays. These included two commercial instruments, a Malvern Particle Analyzer and a Phase Doppler Particle Analyzer, as well as a Coaxial Beam Particle Analyzer developed by the author. The main effort involved design and construction of an improved Coaxial Beam Particle Analyzer.

#### INTRODUCTION

Liquid rocket injectors produce a spray of fuel and/or oxidizer drops in the combustion chamber. It is known empirically that changes in injector design have a large effect upon the performance and stability of liquid rocket engines. This is attributed to differences in the drop size distributions produced by the injector. It is thought that smaller drops give higher performance, but tend to cause combustion instability. Present liquid rocket combustion models show a strong sensitivity to the drop size distributions input to the model [1].

A high-pressure (2000 psi) chamber of 2 ft diameter exists at the Phillips Lab to test liquid rocket injectors at ambient pressures characteristic of rocket combustion chambers. Instrumentation in the chamber consists of a linear array of square tubes to sample the mass distributions in the spray, a bucket to collect the total flow, and pressure and temperature sensors. A 5½" D window and three 2½" D windows located 30°, 110°, and 180° from the larger window allow optical access.

Presently the lab has a Malvern 2600 particle sizer. Plans were made to acquire a Phase Doppler Particle Analyzer (PDPA), however acquisition was postponed due to a protest by a competing manufacturer. The initial plan was that I work with the PDPA sizer during the summer appointment. However, the protest voided this plan.

As an alternative, it was suggested that I bring my Coaxial Beam Particle Analyzer (CBPA) from Morehouse College. Given the size of the instrument, the extensive redesign required to match the window placement and working depths in the pressure chamber, and that the design had not been updated from the original prototype, it was decided that a more productive approach would be to design and construct a new version which would be more compact, more user friendly, less expensive, and could remain at the Phillips Lab at the end of the summer program. This decision allowed me to implement many of the changes conceived during the four years spent developing the instrument.

#### BACKGROUND

The earliest attempts at measuring drop size distributions in rocket injector sprays used either photographic [2,3] or hot-wax techniques [4]. Ferrenberg and Varma [1] discuss the difficulties with these methods and data correlations reported. Azzopardi gives a thorough review of most drop sizing techniques up to 1978 [5]. Since 1978 the main developments have been the Polarization Ratio [6,7], PDPA [8], and Pulse Intensity [9-11] techniques.

The Malvern 2600 Particle Analyzer at the lab works by passing a collimated laser beam through the spray and measuring the time averaged intensity of the forward scattered light about the beam axis. A single drop, or a monodisperse

spray, gives the well-known Airy diffraction rings [5], the intensity versus angle being described by a Bessel function. In a poly-disperse spray the angular intensity distribution is the sum of contributions from all drops in the spray, weighted by the total cross-section area of all drops in each size class.

The Malvern detector consists of 31 photodiode rings which measure the intensity at 31 different scattering angles. The analysis iteratively searches for the number distribution among 31 drop size classes which best fits the measured angular intensity distribution. The main difficulty with the Malvern instrument is that it gives a weighted average along the entire beam path through the spray. In most sprays there are large variations in drop size from the center to edge of the spray.

The PDPA is a descendant of the more common Laser Doppler Velocimeter [12]. In both instruments a pair of coherent laser beams are crossed at an acute angle, forming a series of closely spaced interference fringes. A particle passing through the fringes flickers on and off at a frequency proportional to the velocity component perpendicular to the fringes. The signal detected is termed the "doppler burst". The PDPA detects the doppler burst at three different angles around 70°. A phase shift in the doppler burst between any two detectors results, which is proportional to the drop diameter.

The PDPA gives both a drop size distribution and velocity distribution, as well as size-velocity correlations at specific points in a spray. Averaging over a line through the spray gives good agreement with Malvern data.

The CBPA, developed by the author at Morehouse College [13], is a type of Pulse Intensity technique. These instruments determine the drop size by measuring the scattered pulse as a drop crosses a laser beam. The main problem

is that the scattered intensity depends upon the path the drop follows across the beam. Since the laser beam has a Gaussian intensity distribution, a drop passing far from the beam center gives a smaller pulse height than if it passed through the center.

An obvious solution is to define the center of the laser beam such that measurements are triggered only when a drop passes through the center. The CBPA uses a smaller laser beam of a different color, coaxial with the main beam, to define the main beam center.

#### COAXIAL BEAM PARTICLE ANALYZER DESIGN

### **Optics:**

The original CBPA design [13] consisted of pin-mounted components on rails, with both transmitter and receiver contained on a single 2'x4' table. While this approach was useful for the original prototype, it is a costly means of mounting optical components. The new design bolts all components to the table, at an optic axis of 2 inches above the table. The transmitter and receiver are placed on separate 1'x2' tables. This allows more freedom in selecting the scattering angle and was virtually mandated by the placement of the chamber windows 110° apart.

The improved CBPA transmitter is shown in Figure 1. A 3 mW, 633 nm, polarized He-Ne laser is expanded to 25 mmD with a x40 microscope objective in a spatial filter (SF) and collimated by two series lenses (L1 and L2). A 5 mW, 674 nm diode laser is expanded to 25 mmD with a x10 microscope objective (L3) and collimated by two series lenses (L4 and L5). The two expanded beams are combined coaxially by an edge filter (EF1). A final lens (L6) focuses the beams at

the "probe volume" 500 mm away.

L2 and L5 are mounted in focusing holders, allowing adjustment of each beam diameter at the probe volume. The diode laser beam is focused to a small diameter to locate the center of the He-Ne "main beam". L2 can also be translated transverse to the optic axis, allowing the He-Ne laser beam to be moved laterally. Both lenses are weak (f = 400 mm), allowing precise adjustments using inexpensive translators.

The original transmitter used 50 mmD beams to insure that the beams could be focused sufficiently small at the probe volume. This was found to be over conservative. The present 25 mmD optics are more compact and less expensive.

The improved CBPA receiver is shown in Figure 2. A 50 mmD lens (L7) collects light scattered from the probe volume 500 mm away and images it onto the "main slit" (S1). The slit width, together with the beam diameter defines the size of the probe volume. A x10 microscope objective (L8) refocuses the light transmitted through the main slit. The two colors are separated by an edge filter (EF2). The 633 nm light from the main beam is transmitted through interference filter F1 to the "main photomultiplier" (PMT1).

The 670 nm light from the locater beam is reflected by EF2 and re-imaged onto the "locater slit" (S2). The locater slit views only the center of the main slit, ignoring drops which are partially obscured by the edges of the main slit. The locater photomultiplier (PMT2) triggers a measurement only when a drop passes through the center of the main beam and is centered in the view of the main slit.

The optics are aligned by placing a piece of paper at the probe volume, using the spray translator (with the photomultipliers turned off). Removable

main slit on screen SN. 1.8 is adjusted to focus the image of the main slit at a magnification of  $M_2 = i_2/f_8 - 1$ , where  $f_8$  is the 14.8 mm focal length of L8 (x10 objective), and  $i_2$  is the distance from L8 to SN. L7 is adjusted to focus the image of the probe volume at the screen (simultaneously forming a focused image at the main slit). The probe volume magnification at the main slit is  $M_1 = i_1/o_1$ , where  $o_1$  is the distance from the probe volume to L7 and  $i_1$  is the distance from L7 to S1. Therefore, the total magnification of the probe volume at the screen is  $M_1 M_2$ . This is checked by placing a reticle with a fine scale at the probe volume.

The main and locater beams are focused to the desired diameters (using L2 and L5), while viewing the magnified images on the screen. The diameters are approximated by eye, which differs slightly from the exact  $e^{-2}$  diameters. The main beam diameter is made as large as possible without allowing coincident drops in the probe volume. The locater beam diameter is made about 1/4 of the main beam. Generally, an  $800 \mu mD$  main beam and a  $200 \mu mD$  locater beam are ideal. L2 is then translated transverse to the optic axis to make the main beam and locater beam concentric.

It is desirable to collect scattered light over a large angle to average the Mie interference pattern [14]. The interference fringes limit the resolution for small drops. The present 50 mmD collection lens was chosen to allow viewing of different points in the spray through the 125 mmD window, without obscuring the collection cone. This f/10 collection angle causes some ambiguity in measuring drops below about 20  $\mu$ mD. An alternate lens 100 mmD (f/5) was purchased to allow well defined measurements to at least 10  $\mu$ mD. However, measurements with this lens would be confined to the centerline of the spray.

The chamber windows allow freedom to move in only a single direction, along the beam axis, about +/- 38 mm. A single axis motorized translator moves the transmitter table. The receiver table rests on a floating platform, consisting of two crossed linear slides. The transmitter and receiver tables are coupled, so that they maintain the same relative position. The tables remain at a constant vertical height, since the injector can be translated vertically.

The transmitted light from the main beam is collected and focused onto a pinhole in front of a photodiode (PD2). The main beam before the spray is also sampled with a photodiode (PD1). This allows determination of the beam transmittance through the spray. Using the scattered tomography analysis [13] corrections are easily made for beam attenuation through the spray.

# Signal Processing:

The photomultiplier dynode chains were hand-wired with zener diodes and capacitors to insure linearity for large pulses. This provides increased dynamic range over commercially available dynode chains.

The photomultiplier currents are amplified by a "current to voltage" or "transimpedance" amplifier. A low offset operational amplifier (OP27) with switch-selectable feedback resistor (R<sub>f</sub>) is used for the main beam signal, with subsequent x10 voltage amplification. A fixed resistor and single stage is used for the locater signal, as it serves only as a trigger. Generally, R<sub>f</sub> is increased when the drops in the spray are much smaller than those used for calibration.

The voltage signals are digitized by a Rapid Systems R2000 20 MHz, 8 bit digital O-scope. A locater pulse triggers storage of both pre- and post-trigger values of the main pulse. The digitized pulse is fit to a Gaussian curve. The pulse peak is proportional to the drop area and the width is inversely

proportional to the velocity component transverse to the beam.

Since the pulse amplitude is approximately proportional to the square of the drop diameter, care must be taken to provide a wide dynamic range. The programmable gain feature of the digitizer is used. Measurements are made at three gain ranges, with the highest 100 times the lowest.

The computer program (AQ21.BAS) was developed at Morehouse College in QuickBASIC. It can be run either in the QuickBASIC environment or from the DOS command line (type "AQ21") by changing parameters in ASCII file "AQ.IN" (or subroutine "SETUP").

Time traces of the collected pulses are plotted periodically. When the total number of pulses requested has been collected the drop size histograms and velocity histograms are plotted. These can then be fit to a function and stored in a file. The data files are automatically named by type, date and number, starting with the values in file "FILE.BUFF".

The data files are in a comma-delimited form for easy importation into a spreadsheet (Quattro Pro) for plotting and analysis. The spreadsheets take a while to load on the present PC/AT. For more rapid data review, program DISPLAY.BAS can be used (place data disk in drive A: and type "DISPLAY"). This program allows fitting the histograms to various probability functions.

Presently a 12 MHz PC/AT compatible computer with coprocessor is used. It takes about 10 min for a 2000 point histogram. A 486 PC would decrease the time by a factor of 10. One is included with the PDPA system and will be used when it arrives. Microsoft's BASIC compiler has been ordered. It should increase the speed by another 120%, so that eventually it will take less than 30 seconds to measure a drop size distribution. Competitive Single Particle

Counters use a Digital Signal Processor, but these require tedious assembly language programming, which hasn't been warranted.

For calibration, a uniform stream of drops is generated by vibrating a thin glass pipet with a speaker. At certain frequencies the jet breaks into a stream of uniform drops from 100-300  $\mu$ mD. Knowing the drop generation frequency and flow rate, the drop diameter is easily calculated.

#### SYSTEM DEVELOPMENT

To minimize costs, components were carefully selected from 16 different vendors. Vere Electronics supplied the optical tables. Thor Labs provided most optical mounts. Newport provided the focusing mounts and several lens mounts. A retail telephoto lens was chosen for the collecting lens, allowing focusing and focal length adjustments at low cost. Edmund Scientific provided most of the other lenses. The lasers came from MWK Industries. The filters were from Ealing Electro-Optics and Reynard Enterprises. Hamamatsu supplied the R453 photomultipliers, modular power supply, and \$1227-66BR photodiodes. The motorized translators were from Techno. Other vendors were Central Scientific, Keithley Metrabyte. King Photo, Melles Griot, Newark Electronics, The Programmer's Shop, and Radio Shack. The electronics were wired in-house by Ed Cole and Bob Douglas.

Ordering the components was an introduction to the government acquisition system. The government requires that every line item be typed on a separate form (DD1348-6), in duplicate. Given the several hundred line items needed to complete the system, this would have taken considerable time with a typewriter, as was the normal procedure. A computer program existed to print

the forms, but it didn't work correctly. Since the source code was unavailable, I decided to write my own program in QuickBASIC. The time spent developing the code was more than repaid in time saved. This program (F1348.BAS) has been well received at the Phillips Lab.

The total system, consisting of the CBPA, translation system, calibration system, and spray mount cost less than \$10K. An additional \$3K is required for a 20 MHz A/D. Presently one brought from Morehouse College is used. Considering that the lowest cost Single Particle Counter from other sources exceeds \$60K, the Phillips Lab has obtained a cost effective drop sizing instrument.

As of this writing most components have arrived. The optic tables were received three weeks after the promised delivery date, delaying final assembly of the components. Consequently, there has not been time to thoroughly test the system. However, the optic design appears sound. One question was the use of a diode laser to replace the yellow He-Ne laser used in the Morehouse College instrument. Although it gives a narrow fan-shaped beam, it can be focused sufficiently small to serve as the locater beam. If problems arise, a yellow or green He-Ne laser can be ordered to replace it. This would require only the replacement of several optical filters.

The existing Malvern 2600 Particle Sizer has been tested and found to give results comparable to the CBPA in a Delavan WDB-20 spray, 6 inches downstream, flowing water at 40 psi.

I presented a paper at the Fifth International Conference on Liquid Atomization and Spray Systems in Gaithersburg, MD, July 17, describing the CBPA [13] (travel funded by the DOE Minority Institution Research Travel

Program). The two competitors for the PDPA instrument, Aerometrics and Dantec, demonstrated their instruments. This experience proved valuable, as I was later asked to make a technical evaluation of the PDPA Protest for the Phillips Lab.

The PDPA instrument will require the entire window areas of the pressure chamber to bring the laser beams in and transmit the scattered light. There will be no freedom to make measurements at any points in the spray other than on the centerline of the chamber.

A related program at the Phillips Lab is to study the evaporation of a stream of uniform size drops at super-critical pressures. As support for this project, I worked with Doug Talley to generate a uniform drop stream using my drop generator. We used a video imaging system in the Chem Lab to obtain a visual record, demonstrating the operating principles.

#### CONCLUSIONS

The Coaxial Beam Particle Analyzer has been completed. Due to delays in component deliveries, time did not allowed thorough testing of the instrument. However, the system is user friendly, so that personnel at the Phillips lab will be able to operate the instrument. Thorough drawings and notes have been provided for future reference.

The Phase Doppler Particle Analyzer has been studied. It is fairly easy to operate and gives repeatable results. However, being a sophisticated instrument, it requires an operator experienced in optical diagnostics to understand the limitations and correctly interpret the results. It will be able to measure only on

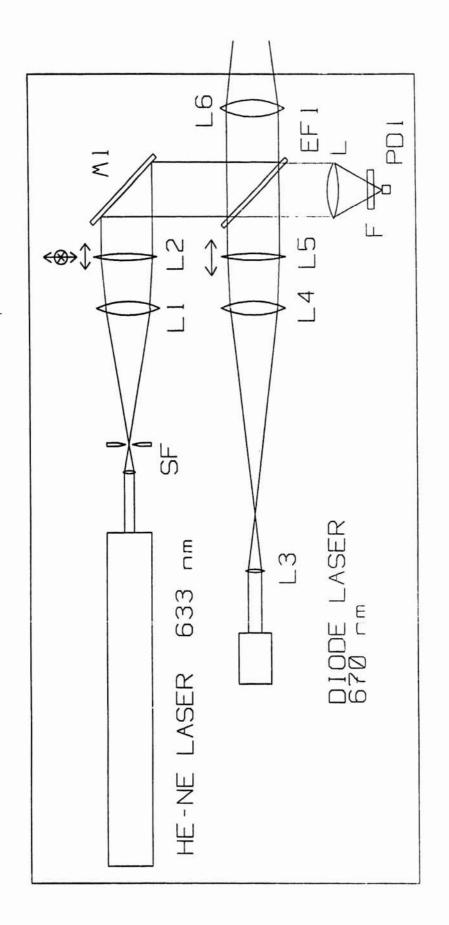
the centerline of the chamber due to window constraints.

The Malvern Particle Sizer has been tested and found to give results comparable to the CBPA. Operation of this instrument is straight-forward. However, the data is not as detailed as with the CBPA and PDPA Single Particle Counters.

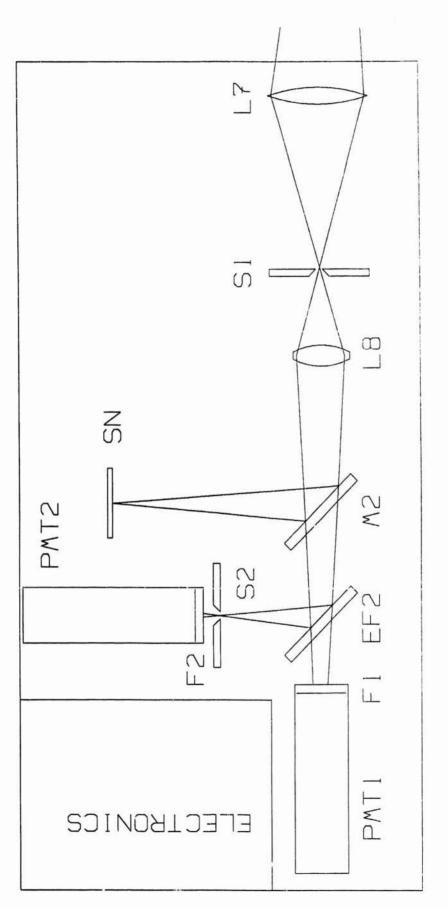
#### REFERENCES

- 1. Ferrenberg, A.J. and Varma, M.S., "Atomization Data Requirements for Rocket Combustor Modeling", 21st JANNAF Combustion Meeting, CPIA Publ. 412, Vol. 1, Oct 1984, p. 369.
- 2. Ingebo. R.D., "Drop-size Distributions for Impinging-Jet Breakup in Airstreams Simulating the Velocity Conditions in Rocket Combustors", NASA TN-4222, March 1958.
- 3. Heidmann, M.F. and Foster, H.H., "Effect of Impingment Angle on Drop-size Distribution and Spray Pattern of Two Impinging Water Jets", NASA TND-372, July 1961.
- 4. Zajac, L.J., "Droplet Breakup in Accelerating Gas Flows, Part I: Primary Atomization", NASA CR-134478, October 1973.
- 5. Azzopardi, B.J., "Measurement of Drop Sizes", Int. Journal of Heat and Mass Transfer, 22, (1979), p. 1245.
- 6. Beretta, F., et. al. "Drop Size and Concentration in a Spray by Sideward Laser Light Scattering Measurements", Combustion Science and Technology, Vol. 36 (1984), pp. 19-37

- 7. Presser, C., Santoro, R.J., and Semerjian, H.G., "Velocity and Droplet Size Measurements in a Fuel Spray", AIAA-86-0297, January 1986.
- 8. Bachalo, W.D. and Houser, M.D., "Phase/Doppler Spray Analyzer for Simultaneous Measurements of Drop Size and Velocity Distributions", Optical Engineering, Vol. 23, no. 5, pp.583-590, Sept/Oct 1984.
- 9. Holve, D. and S.A. Self, "Optical Particle Sizing for in situ Measurements, Part II", Applied Optics 18, 1646 (1979)
- 10. Mizutani, Y., et. al., "Doppler-Mie Combination Technique for Determination of Size-Velocity Correlation of Spray Droplets", Combustion and Flame, 44, 1982.
- 11. Hess, C.F. "Nonintrusive Optical Single-Particle Counter for measuring the Size and Velocity of Droplets in a Spray", Applied Optics, Vol. 23, no. 23 (December 1984), pp 4375-4382.
- 12. Chigier, N., ed. Combustion Measurements, Hemisphere, 1991.
- 13. W.M. Grissom, "A Coaxial Beam Drop Sizing Instrument for Dense Sprays", 5th Int'l Conf. on Liquid Atomization and Spray Systems, Gaithersburg, MD (July 1991).
- 14. Van de Hulst, H.C., Light Scattering by Small Particles, Wiley, 1957.



ransmitter Optics F i gure



Receiver Optics

# LIQUID JET INJECTION PROCESSES IN LIQUID ROCKET ENGINES

# S. D. Heister, Assistant Professor AFOSR Summer Faculty Program Final Report

Purdue University, School of Aeronautics & Astronautics

25 July, 1991

#### ABSTRACT/SUMMARY

This report summarizes efforts completed during the time period 16 May - 26 July, 1991 while on assignment within the AFOSR Summer Faculty Program at Phillips Laboratory Rocket Propulsion Division at Edwards Air Force Base, California. A review of the current state-of-the-art in the analysis of liquid jet injection processes as applied to liquid rocket engine injectors has been conducted. Fundamental physical mechanisms and analytic treatments of atomizing jets is discussed herein. In addition, an improved correlation technique is described and recommended for future data reduction of atomizing jet experiments. It is anticipated that this correlation technique will improve descriptions of experimental results thus making correlations more useful for the design of future liquid rocket engine injectors.

## 1. INTRODUCTION

Developing a detailed knowledge of injection processes is crucial to describing the performance and stability of liquid rocket engines (LREs). Atomization characteristics of liquid sprays entering the chamber serve as inputs to droplet evaporation and combustion models which will ultimately describe the overall series of events taking place in the LRE combustion chamber. A knowledge of spray characteristics is also required to assess the compatibility of the injector design with chamber wall materials. In addition, pressure drops occurring through injector elements serve as vital inputs to feed system, injector, and combustion chamber design.

Injection processes are also known to play a dominant role in both low and high frequency combustion stability problems encountered during the development of LRE's. Low frequency oscillations caused by a coupling of the chamber with the feed system are strongly dependent on the inertance (discharge coefficients) of injector elements as discussed by Harije and Reardon (1972). In addition, results of Reba and Brosilow (1960) indicate that chamber pressure oscillations can cause a profound influence on the character of the spray pattern during injection. This fact suggests that a coupling of the injection process with vaporization/combustion processes in the chamber could explain some forms of high frequency instabilities.

For these reasons, it is essential to develop an understanding of both steady-state and oscillating behavior of liquid jet injection processes. The JANNAF subcommittee formed to address combustor stability emphasizes this as one of the more crucial areas to develop an understanding of these phenomenon (see Jensen (1990)). Analytic techniques are required to predict atomization characteristics for arbitrary geometrics for both steady and unsteady flows. Correlation of experimental data with important physical parameters is also required to enhance the usefulness of this information.

This document provides an assessment of the current state-of-the-art in using analytic techniques to describe physical processes during liquid jet injection and atomization. A review of previous research is described in the next section, followed by a new technique aimed at improving existing correlations with experimental data. Conclusions from the study are provided in Section 4.

## 2. REVIEW OF LIQUID JET INJECTION LITERATURE

# 2.1 Jet Injection Flow Regimes

Before we begin our review, it is useful to characterize the various flow regimes encountered when injecting a liquid jet into a gaseous medium. If the pressure differential across the orifice is very small, a dripping-type flow will result, much like that in a dripping faucet. As the pressure differential is increased, a true liquid column will be formed. We can describe the breakup of this column by introducing these distinct categories: As indicated in Figure 1. The categories are:

1) Rayleigh breakup regime: This mode, shown in Figure 1 is categorized by droplets larger than the diameter of the orifice. This breakup mechanism is present only in jets injected at low Reynold's number

$$Re = \rho_1 U_1 a/\mu_1$$

where  $\rho$ ,  $U_1$ , and  $\mu$  are density, velocity and viscosity; a is the orifice radius and subscript 1 refers to properties within the liquid phase. Rayleigh (1878) showed that droplets formed in this mode were driven by a capillary instability resulting from an initial inbalance between surface tension and dynamic pressure forces within the jet. Since low Re implies very low velocity or high viscosity jets, aerodynamic forces in this regime are typically negligible. Note that since surface tension forces are also important in this regime, therefore the Weber number

We = 
$$P_1U_1^2 a/\sigma$$

where  $\sigma$  is the surface tension, is also important.

Wind induced regime: As the jet Reynold's number is increased, viscous forces at the jet periphery generate smaller wavelength instabilities and the size of resulting droplets decreases below the orifice diameter (see Fig. 1). Since gas phase viscous forces are now a contributor, clearly the gas phase Reynold's number:

$$Re_g = \rho_g U_1 a/\mu_g$$

should also be considered. In addition, some authors (such as Lefebvre (1989)) suggest the liquid/gas  $(\wp_i/\rho_g)$  density ratio as another important parameter. The wind induced regime is characterized by the small surface waves which appear on the surface of the jet. Weber (1931) was the first to include the effect of gas phase viscosity in an attempt to extend Rayleigh's benchmark analysis. Some authors (such as Bracco (1985)) have subdivided the wind induced regime into two subclasses based on droplet size.

3) Atomization Regime: As the jet Reynold's number is increased further, the point at which droplets first appear gets closer to the orifice until droplet formation appears essentially at the orifice exit. High speed jets in LREs inevitably fall into this atomization regime in which the droplets formed from the jet are much smaller than the diameter of the orifice. Some of the primary variables used in describing an atomizing jet are detailed in Figure 2. The core length, z<sub>c</sub> is the distance at which the innermost portion of the jet disintegrates into droplets. The cone or spray angle α, distinguishes the outermost boundary of the spray and is important in calculating

mixing with adjacent injector elements inside a LRE and assessing chamber wall compatibility. Finally, the droplet size distribution is critical to describing evaporation, gas phase mixing, and combustion processes occurring downstream of the orifice.

The following section provides a critical review of literature pertaining to the atomizing jet.

# 2.2 Atomizing Jet Literature Review

Injection of a high velocity liquid jet into a quiescent gas is a fundamental two-phase flow problem in fluid mechanics with application not only to LRE injectors, but also gas turbine and diesel engines, agricultural spraying, painting processes and even fire hoses. For this reason, there are hundreds of literature citations discussing aspects of this problem. The review cited here is by no means comprehensive but is intended to focus on material relevant to LRE injectors. There are numerous review articles and books; for example: Ghafourian et. al. (1991), Lefebvre (1989), McCarthy and Molloy (1974), Reitz and Bracco (1982) and most notably Bracco (1985).

A full analytic description of this complex flowfield has eluded researchers to this point. Even with the advent of new CFD techniques, numerical solution of the governing equations has not been accomplished due to the complexity introduced by the free surface. Since pressure changes across this surface are related to the local radius of curvature, very fine grids are required, hence, computational times are exorbitant for all but the simplest cases. Numerical techniques based on the volume of fluid (VOF) approach are currently under development. Since VOF approaches are in a sense approximate (they permit an arbitrary gas/liquid volume ratio in a given cell but must interpolate to locate the free surface within the cell) there is still a great need for alternate approaches to address this difficult problem.

For the reasons given above, previous efforts have focused on the stability theory approach pioneered by Rayleigh (1878) or on correlations of experimental data. Before exploring these areas, it will first be necessary to investigate the physical phenomena responsible for generating the atomization process. In reviewing the applicable literature, the following mechanisms have been suggested as contributions to the atomization process:

- 1) Aerodynamic forces at the periphery of the jet (Castleman (1932)).
- 2) Changes in the jet velocity profile due to a change from a no slip boundary condition at the edge of the duct to a free surface condition outside the orifice (Rupe (1962)).

- 3) Instability driven by small changes in supply pressure (Giffen and Muraszeu (1953)).
- 4) Instability driven by changes in liquid boundary layer (Shkadov (1970)).
- 5) Turbulent fluctuations within the jet (DeJuhasz (1931)).

In a careful series of experiments, Reitz and Bracco (1982) argued that supply pressure variations, jet turbulence levels, and liquid boundary layer instabilities could not explain the observed atomization behavior. The strong influence of their results on gas density indicates that aerodynamic forces at the gas/liquid interface are important to the characterization of the atomization regime. In addition, orifice geometry (and hence velocity profile within the jet) was shown to have a strong influence on atomization results. In fact, numerous authors have indicated the importance of the orifice L/D to spray characteristics.

# 2.2.1 Analytic Efforts

At this point it is obvious that a correct analytic description of an atomizing jet must include the effect of the velocity profile within the jet as well as aerodynamic forces arising on the jets periphery. Unfortunately, a model of this type incorporating the dynamics of a free surface has not yet been created. In spite of this deficiency, many prior treatments have included some of the important features of this problem and have contributed significantly to our knowledge of this flowfield.

As mentioned previously, most of the analytic treatments have investigated the stability of the liquid/gas interface under certain assumptions. Rayleigh (1878), Ranz (1958), and others have presumed that the resultant droplet size is proportional to the wavelength of the most unstable disturbance propagating along the interface. Using this approach, the mean drop size and core length can be obtained up to some proportionality constant. The spray angle can be assumed to be proportional to the radial velocity perturbation at the jet's periphery then completing a simplified description of the spray.

To illustrate the procedure used in a linear stability analysis and highlight variables important to jet breakup, we will follow the generalized approach of Sterling and Sleicher (1975). To highlight the dimensionless parameters which occur in the analysis we will present Sterling and Sleichers' results in dimensionless form: Velocities will be nondimensionalized against a reference jet velocity,  $U_o$ , lengths will be reported with respect to the orifice radius, a, and densities will be unity in dimensionless variables. In addition, we shall choose a coordinate system which travels at velocity  $U_o$  (traveling with

fluid in the jet) and assume incompressible flow in both fluids.

Under these assumptions, the geometry associated with the analysis is given in Figure 3 where primes denote dimensional quantities and the subscripts ()<sub>1</sub> and ()<sub>g</sub> refer to liquid and gas phases, respectively. The variable  $\eta'$  measures the deflection of the surface from the line r' = a'. The velocity components are written as the sum of the mean velocity and a fluctuation, where the "hatted" quantities are assumed to be small fluctuations in dimensional form. Since the coordinate system follows the liquid we have

$$u' = \hat{u}, v' = \hat{v}$$
 in liquid phase  
 $u'_g = U(r) + \hat{u}_g, v'_g = \hat{v}_g$  in gas phase
$$(1)$$

The unsteady Navier-Stokes equations are assumed to hold in the liquid phase, while in the gas phase, viscosity is neglected. Rayleigh (1878) showed that only axisymmetric disturbances are unstable so we may neglect any variations in the circumferential direction. Under these assumptions, substitution of Eq. (1) into the Navier-Stokes (and continuity) equations with the appropriate nondimensionalization described above gives:

$$\frac{\partial u}{\partial z} + \frac{1}{r} \frac{\partial}{\partial r} (rv) = 0$$

$$\frac{\partial u}{\partial t} = -\frac{\partial P}{\partial z} + \frac{1}{Re} \left[ \frac{\partial^2 u}{\partial z^2} + \frac{1}{r} \frac{\partial}{\partial r} \left[ r \frac{\partial u}{\partial r} \right] \right] \text{ Liquid Phase}$$

$$\frac{\partial v}{\partial t} = -\frac{\partial P}{\partial r} + \frac{1}{Re} \left[ \frac{\partial^2 v}{\partial z^2} + \frac{1}{r} \frac{\partial}{\partial r} (rv) \right]$$
(2)

where terms involving products of perturbations have been ignored. Note that  $u = u'/U'_o$ ,  $v = v'/U'_o$ , and  $P = P'/(\rho'_1 U'^2_o)$  in these dimensionless equations. Following a similar procedure for the gas phase, we may write:

$$\frac{\partial u_g}{\partial z} + \frac{1}{r} \frac{\partial}{\partial r} (r v_g) = 0$$

$$\frac{\partial u_g}{\partial t} = -\frac{\partial P_g}{\partial z} - U \frac{\partial u_g}{\partial z} - v_g \frac{dU}{dr}$$

$$\frac{\partial v_g}{\partial t} = -\frac{\partial P_g}{\partial r} - U \frac{\partial v_g}{\partial r}$$
(3)

where  $U = U'(r)/U'_o$  and gas viscosity has been neglected.

The dimensionless boundary conditions at the interface include continuity of surface velocity (both phases), a continuity condition (no mass flux across interface), and the requirement that normal stress be continuous. In addition, we require that perturbation quantities vanish at the jet centerline and far from the interface in the gas phase. For the liquid phase, these conditions become:

$$v(1, z) = \frac{\partial \eta}{\partial t}$$

$$\frac{\partial u}{\partial r} + \frac{\partial v}{\partial z} \Big|_{1,z} = 0$$

$$P(0, z) = u(0, z) = v(0, z) = 0$$
(4)

while for the gas phase, we have:

$$v_{g}(1, z) = \left[ \frac{\partial \eta}{\partial t} + U \frac{\partial \eta}{\partial z} \right]_{1, z}$$

$$v_{g}, U_{g}, P_{g} \to 0 \text{ as } r \to \infty$$
(5)

and the normal stress condition at the interface gives (see Clift, et. al. (1978))

$$-\underline{P} - P + \frac{2}{Re} \frac{\partial v}{\partial r} = -\varepsilon P_g - \frac{1}{We} \left[ \frac{1}{R_1} + \frac{1}{R_2} \right]$$
 (6)

where  $\underline{P}$  is the undisturbed pressure in the jet,  $\varepsilon = \rho_g'/\rho_e'$  is the gas-liquid density ratio, We is the Weber number as defined previously, and  $R_1$  and  $R_2$  are dimensionless radii of curvature in axial and circumferential directions.

These radii of curvature may be written in terms of  $\eta$  if we consider the surface to have a wave-type shape:

$$\eta = \eta_{10} e^{\omega t + ikz} \tag{7}$$

where w is the dimensionless frequency of the surface waves  $(w = w'a'/U'_o)$  and k is the dimensionless wave number (k = k'a') of the disturbance. Under this assumption one can show that

$$\frac{1}{R_1} + \frac{1}{R_2} = 1 - \eta + \eta k^2 \tag{8}$$

which is accurate to terms containing  $\eta^2$  as is consistent with a linear analysis. Substituting

Eq. 8 into Eq. 6 and noting that the undisturbed jet pressure is simply  $\underline{P} = 1/We$  we obtain:

$$-P + \frac{2}{Re} \frac{\partial v}{\partial r} = -\varepsilon P_g + \frac{\eta (1 - k^2)}{We}$$
 (9)

which is the linearized surface stress condition in dimensionless form. Note that the dimensionless variables  $R_e$ , We, and  $\varepsilon$  describe the pressure fluctuations present for a given size disturbance  $(\eta, k)$ .

The gas phase equations can be simplified by introducing the velocity potential

$$\nabla \phi_{\mathbf{g}} = \overrightarrow{\mathbf{V}}_{\mathbf{g}} \tag{10}$$

such that Eq. 3 can be written:

$$\frac{\partial^2 \phi_g}{\partial r^2} + \frac{1}{r} \frac{\partial \phi_g}{\partial r} + \frac{\partial^2 \phi_g}{\partial z^2} = 0$$

$$\frac{\partial \phi_g}{\partial t} + U \frac{\partial \phi_g}{\partial z} = -P_g$$
(11)

and the boundary conditions (Eq. (5)) become:

$$\frac{\partial \phi_{g}}{\partial r} \bigg|_{1,z} = \left[ \frac{\partial \eta}{\partial t} + U \frac{\partial \eta}{\partial z} \right] \bigg|_{1,z} \qquad \text{Gas Phase} 
\frac{\partial \phi_{g}}{\partial r}, \frac{\partial \phi_{g}}{\partial z}, P_{g} \to 0 \text{ as } r \to \infty \qquad \text{Boundary Conditions}$$
(12)

Since our analysis considers viscous forces in the liquid phase, the velocity cannot be expressed in terms of a potential alone. If we let the innotational portion of the velocity be represented by a stream function,  $\psi$ , we may write the liquid velocity vector:

$$\vec{V} = \nabla \phi + \nabla \times \vec{B} \qquad \vec{B} = (0\hat{r}, -\frac{\psi}{r}\hat{\theta}, 0\hat{z})$$
 (13)

using this notation, we have:

$$u = \frac{\partial \phi}{\partial z} - \frac{1}{r} \frac{\partial \psi}{\partial r} \; ; \; v = \frac{\partial \phi}{\partial r} + \frac{1}{r} \frac{\partial \psi}{\partial z}$$
 (14)

making use of several vector identities, Eqs. 13 and 2 become:

$$\frac{\partial^2 \phi}{\partial r^2} + \frac{1}{r} \frac{\partial \phi}{\partial r} + \frac{\partial^2 \phi}{\partial z^2} = 0$$

$$P = -\frac{\partial \phi}{\partial t} \qquad \text{Liquid Phase}$$

$$\frac{\partial^2 \psi}{\partial r^2} - \frac{1}{r} \frac{\partial \psi}{\partial r} + \frac{\partial^2 \psi}{\partial z^2} - \text{Re} \frac{\partial \psi}{\partial t} = 0$$
(15)

and the interface conditions (Eqs. 4 and 9) may be rewritten:

$$\left[ \frac{\partial \phi}{\partial r} + \frac{1}{r} \frac{\partial \psi}{\partial z} \right] \Big|_{1,z} = \frac{\partial \eta}{\partial t} \Big|_{1,z}$$

$$\left[ \frac{1}{r} \frac{\partial^2 \psi}{\partial z^2} - \frac{\partial}{\partial r} \left( \frac{1}{r} \frac{\partial \psi}{\partial r} \right) + \frac{2}{r} \frac{\partial^2 \phi}{\partial r \partial z} \right]_{1,z} = 0 \qquad \text{Liquid Phase Boundary Conditions}$$

$$\frac{\partial}{\partial r} (\phi, \psi) = \frac{\partial}{\partial z} (\phi, \psi) = 0 \text{ as } r \to 0$$

$$\left[ -P + \frac{2}{Re} \frac{\partial^2 \phi}{\partial r^2} - \frac{1}{r^2} \frac{\partial \psi}{\partial z} + \frac{1}{r} \frac{\partial^2 \psi}{\partial r \partial z} \right]_{1,z} = -\varepsilon P_g + \frac{\eta(1 - k^2)}{We}$$

$$\left[ -\frac{1}{Re} \frac{\partial^2 \psi}{\partial r^2} - \frac{1}{r^2} \frac{\partial \psi}{\partial z} + \frac{1}{r} \frac{\partial^2 \psi}{\partial r \partial z} \right]_{1,z} = -\varepsilon P_g + \frac{\eta(1 - k^2)}{We}$$

which completes the development of all governing equations and boundary conditions in terms of  $\phi$ ,  $\phi_g$  and  $\psi$ . The resulting relations (Eqs. 11, 12, 15, 16) indicate that the size of the perturbations, and hence the stability of the jet, is determined by the parameters Re,  $\varepsilon$ , and We as noted above. The analysis continues by assuming wave-type solutions for  $\phi$ ,  $\phi_g$ , and  $\psi$  which gives a Bessel function dependence for the radial variation of these parameters. Constants in the equations for  $\phi$ ,  $\phi_g$ , and  $\psi$  are determined from boundary conditions and the normal stress condition provides the dispersion relation between  $\omega$  and k of the form:

$$\omega^2 F(k, \epsilon, Re) + \omega G(k, U, \epsilon, Re) + H(k, U, We) = 0$$
 (17)

where the functions F, G, and H contain ratios of Bessel functions and are quite complex in the most general case.

As a result of this complexity, many authors have considered various limiting cases as a simplification to Eq. 17. For example, Rayleigh neglected all viscous effects, gas velocity, and pressure and derived the following dispersion relation

$$\omega^2 = \frac{k}{We} (1 - k^2) \frac{I_1(k)}{I_0(k)}$$
 (18)

where  $I_0$  and  $I_1$  are zeroth and first order modified Bessel functions of the first kind. Rayleigh argued that the disturbance having the maximum growth rate (frequency) would be predominant so he proceeded to find the wave number which maximized  $\omega$  in the equation above. By using the first few terms in the Bessel function expansions, he found the most destructive wave number,  $k_m$ , as:

$$k_m \approx 0.697$$

which gives the dimensionless wavelength ( $\lambda$ ) of the disturbance

$$\lambda = 2\pi/k_m = 9.01$$

which means the disturbance should generate waves of a length about equal to nine orifice radii. Assuming the jet breaks into packets of this length, the resulting drop diameter  $d_d$  would be

$$d_d = 3.78$$
 or  $d'_d = 3.78 a'$ 

which gives a droplet diameter roughly twice the diameter of the orifice.

Other researchers have investigated other limiting forms of Eq. 17 using the technique of Rayleigh described above. The primary assumption in these analyses is that the resultant droplet size will be proportional to the wavelength of a disturbance which maximizes the growth rate obtained from solution of Eq. 17. Weber (1931) considered large wavelength (k < 1) disturbances but included the effects of gas density and velocity. Sterling and Sleicher (1975) improved upon Weber's result by including an arbitrary constant (in Eq. 17) to account for viscous effects in the gas phase.

These authors also showed that the dimensionless core length for a disturbance of the type in Eq. 7 would be:

$$Z_{c} = -\ln \eta_{o}/\omega_{m} \tag{19}$$

where  $\omega_m$  is the maximum growth rate and  $\eta_o$  is the initial amplitude of the disturbance. Since  $\eta_o$  is not known, correlation with test data is required to calculate core lengths from Eq. 19.

For the atomization regime, we expect very small droplets which implies that we expect k >> 1 to generate these small wavelength disturbances. Analysis of Eq. (17) in this limit was first due to Taylor (see Batchelor (1958)). For k >> 1,  $\epsilon << 1$ , the applicable form of the dispersion relation (Eq. (17)) becomes:

$$\omega = 2\sqrt{\varepsilon} \text{ We F(We/k, Ta)}$$
 (20)

where Ta is the Taylor number:

$$Ta = \varepsilon^{-1} (Re/We)^2 = \frac{\rho_1'}{\rho_g'} \left[ \frac{\sigma'}{\mu_1' U_o'} \right]^2$$
 (21)

and the function F must be evaluated numerically. As a result of this landmark analysis, many researchers have attempted to correlate experimental data with Taylor number. Note that results are independent of a length scale since in this regime k' << a' the jet surface is approximated by a planer sheet.

In addition, Taylor reasoned that the spray angle could be determined from the transverse velocity perturbation:

$$\tan (\alpha/2) = \frac{v'}{U'_{\alpha}} = v = A\sqrt{\epsilon} F(We/k_m^*, T_a)$$
 (22)

where A is an undetermined constant and  $k_m^*$  is a scaled wave number corresponding to the fastest growing disturbance:

$$k_{m}^{*} = k_{m} \left[ \frac{\sigma'}{\rho'_{g} U_{o}^{'2}} \right]$$
 (23)

Figure 4, excerpted from Bracco (1985) indicates the dependence of  $F_m$  and  $\omega_m^*$  on Taylor number, where  $\omega_m^*$  is given by:

$$\omega_{\rm m} = 2\sqrt{\varepsilon} \left[ \frac{\rho_{\rm g}' U_{\rm o}'^3}{\sigma'} \right] \omega_{\rm m}^* \tag{24}$$

The droplet size may be inferred as by Rayleigh provided that the  $k_m^*$  value for a given  $\omega_m^*$  and defined from Eq. 20.

## 2.2.2 Velocity Profile Effects

For all the efforts described in the previous subsection, velocity variations within the jet itself have been ignored. Unfortunately, Reitz and Bracco (1982), McCarthy and Molloy (1974) and others have highlighted the importance of jet velocity profile on the breakup process. Figure 5 shows a series of experiments conducted by McCarthy and Molloy at fixed Re and We values. By varying nozzle length, injection velocity profiles could be varied from essentially slug flow to a near fully developed flow pattern. While the analyses described in the previous section would predict identical behavior for these four jets, it is obvious that velocity profile effects can have a profound influence on jet stability.

Experimental evidence indicates that jets with fully developed laminer velocity profiles are more unstable than jets with flat profiles approximating a slug flow. It is interesting to note that fully developed turbulent jets have been shown to be more stable than the laminer jet owing to the fact that the turbulent velocity profile is "fuller" than the laminer case.

Recent linear stability analyses by Leib and Goldstein (1986) and Hevert, et. al. (1991). Both results indicate that jet stability decreases as the exit condition varies from slug flow to a fully developed Hagan-Pousille profile. The additional instability is generated by relaxation within the jet due to a sudden change from a "no-slip" boundary condition within the nozzle to a free surface condition at the orifice exit.

## 3. CORRELATION OF EXPERIMENTAL RESULTS

As is evidenced by the discussion in the previous section, the jet atomization regime must be characterized not only by flow variables governing the process (Rel, We, Ta,  $\varepsilon$ ), but also must include the effects of injector geometry and its subsequent influence on the jet velocity  $\varepsilon$  ofile at the orifice exit. To date, existing correlations have made use of flow variables only and have not attempted to include the effect of injection element geometry. As a result, these correlations will hold only for the geometry utilized in the particular test and will have limited usefulness for one interested in alternate geometries. For this reason, we are motivated to find correlating parameter(s) which incorporate both flow variables and injector geometry.

A unique approach to the treatment of viscous forces both inside and outside the injector element will be outlined for the simple geometry shown in Figure 6. The nondimensionalization employed in the previous section is assumed here with the

exception that all velocities will be normalized with respect to the mass-weighted average velocity at the jet exit

$$\bar{u}_{o} = \int_{0}^{a'} u_{o}' r' dr' / a'^{2}$$
(1)

It is well known that viscous forces generate vorticity in a boundary layer and that this vorticity leads rise to a net circulation,  $\Gamma$ , which effectively represents the integral of vorticity throughout the boundary layer (see Schlicting (1958)). In addition, the impulse of the jet into the quiescent gas gives rise to an additional vorticity component as a result of viscous forces acting at the periphery of the jet. In other words, we could envision a circulation at the exit plane of the form

$$\Gamma = \Gamma_{\rm RL} + \Gamma_{\rm I} \tag{2}$$

where  $\Gamma_{BL}$  arises from vorticity generated in the injector passage and  $\Gamma_{I}$  results from the jet impulse into the gas. Note that  $\Gamma$  should represent the two types of disturbances known to affect the behavior of atomizing jets since it contains not only the effect of aerodynamic interaction with the gas, but also the effect of velocity profile development within the injector passage.

Our motivation here is to develop a simple estimate of  $\Gamma$  based on conditions typically measured during an experiment in order to compare with spray characteristics from such an experiment. Since  $\Gamma$  represents destabilizing influences and We measures stabilizing effects due to surface tension, we would expect the parameter  $\Gamma$  We (or some other combination) to correlate well with experimental data. If such a correlation could be developed, it would be highly usefully since it would include both the effects of flow variably and injector geometry. With these ideas in mind, we shall develop expressions for  $\Gamma_{\rm I}$  and  $\Gamma_{\rm BL}$  below.

Following Heister and Karagozian (1990), we can write the circulation due to jet impulse as:

$$\Gamma_{\mathbf{I}}' = \mathbf{I}'/(2\pi \mathbf{a}' \mathbf{p}_{\mathbf{g}}') \tag{3}$$

where primes denote dimensional quantities and I' represents the impulse per unit length (thrust per unit velocity) of the jet:

$$I' = \rho_1' \overline{u}_0'^2 \pi a'^2 / \overline{u}_0'$$
 (4)

Combining (3) and (4) and nondimensionalizing, we have

$$\Gamma_{\rm I} = \frac{1}{2 \, \varepsilon} \tag{5}$$

where  $\varepsilon = \rho_g'/\rho_1'$  as before. Therefore,  $\Gamma_I$  should measure the strong effect of gas density noted by Reitz and Bracco (1982).

The calculation of  $\Gamma_{BL}$  is a bit more involved since it represents a history of velocity profile development over the length of the injector element. From Sabersky, et. al. (1971) we may write:

$$\Gamma_{\rm BL} = \oint_{\rm c} \vec{v} \cdot \vec{dr} = \int_{\rm s} \left[ \frac{\partial v}{\partial x} - \frac{\partial u}{\partial r} \right] ds = \int_{\rm s} w ds$$
 (6)

where we have used Stokes theorem to transform the result from a line integral to a surface integral and assumed axisymmetric flow in the channel. The quantity w in Eq. 6 represents the vorticity component in the tangential direction (out of the page in Fig. 6). One can show that for a 2-D steady flow, w obeys Laplace's equation:

$$\Delta^2 \mathbf{w} = 0 \tag{7}$$

The task at hand is to determine w throughout the domain and integrate per Eq. 6 to get  $\Gamma_{BL}$ . Solution of Eq. 7 is straightforward using analytic or numerical techniques provided we can assign the proper boundary conditions. Assuming plug flow at the inlet (z=0) all velocity derivatives vanish, so we must have w(0, r) = 0. Similarly, at the duct centerline the axisymmetric assumption gives  $\partial v/\partial x = \partial u/\partial r = w(z, 0) = 0$ .

At the edge of the duct (r = 1) the term  $\partial v/\partial x$  vanishes since v itself vanishes. In this case, we may write (in dimensional form):

$$w'(z', 1) = -\frac{\partial u'}{\partial v'}(z', 1) = -\tau'_w/\mu'_1$$
 (8)

where  $\tau_{w}$  is the shear stress:

$$\tau'_{\rm w} = -c_{\rm f}(z)\rho'_{\rm l}\bar{u}_{\rm o}^{'2}$$
 (9)

Combining Eqs. (8) and (9) gives:

$$w(z, 1) = \operatorname{Re} c_f(z) \tag{10}$$

where in general,  $c_f = c_f(Re_z) = c_f(z)$  is the wall friction which depends on z. For example, the flat plate result is of the form:

$$c_f(z) = A/\sqrt{Re_z} = \frac{A}{Re\sqrt{z}}$$
 (11)

where A is a constant.

The boundary condition for the vorticity at the exit of the duct is the most difficult since we have no way of knowing apriori the degree of velocity profile development at this location. For this reason, it is useful to perform calculations on a very long duct so we can assume fully developed flow at the exit of the form

$$u = 2(1 - r^2), v = 0, w(L, r) = 4r$$
 (12)

By solving on this extended domain, we can simply integrate Eq. 6 over the length of interest.

Note that the unknown constant A in Eq. 11 will need to be assumed for the solution to proceed. An iterative procedure will be required to give the A value which corresponds to the discharge coefficient measured in the test. Nevertheless, computational or analytic solution of Eq. 7 is very economical and this type of iteration will not be prohibitive.

Note that  $\Gamma_{BL}$  contains Reynold's number dependence through the boundary condition at the wall (Eq. 10) and also contains duct length dependence through the integral in Eq. 6. Therefore the total circulation,  $\Gamma$ , will reflect geometric and flow variable variations in both the liquid and gas phase. For this reason, use of this approach appears to have merit in correlating atomizing jet measurements such as spray angle and core length.

# 4. CONCLUSIONS

This paper has summarized previous analytic efforts regarding high speed (atomizing) liquid jets. Results of the review indicate that velocity profile relaxation and aerodynamic interactions at the liquid/gas interface are the primary contributers to the atomization process. A general outline of the linear stability analysis used to predict trends in jet breakup has been provided.

While velocity profile relaxation has been theorized to have a major effect on jet dynamics, no correlations of experimental data have been developed to reflect this important parameter. For this reason, a vorticity/circulation method has been proposed to include the effects of injector geometry and hence velocity profile development.

Preliminary analysis of this technique indicates that jet circulation contains many of the features required to correlate data such as gas phase density, liquid phase Reynolds number, and injector geometry. For this reason, this approach appears to have merit in correlating measurements from injector characterization experiments.

## REFERENCES

Batchelor, G. K. (Editor), "Collected Works of G. I. Gaylor," Cambridge University Press, 1958.

Bracco, F. V., "Modeling of Engine Sprays," 1985 SAE Congress SAE 850394, 1985.

Castleman, R. A., "The Mechanism of the Atomization Accompanying Solid Injection," NACA Report No. 440, 1932.

Clift, R., Grace, J. R., and Weber, M. E., <u>Bubbles, Drops and Particles</u>, Academic Press, 1978.

DeJuhasz, K. J., "Dispersion of Sprays in Solid Injection Oil Engines," Transactions of the ASME, Vol. 53, p. 65, 1931.

Ghafourian, A., Mahalingam, S., Dindi, H., and Daily, J. W., "A Review of Atomization in Liquid Rocket Engines," AIAA-91-0283, 29th Aerospace Sciences Meeting, 1991.

Giffen, E., and Muraszew, A., Atomization of Liquid Fuels, John Wiley and Sons, 1953.

Harije, D. J., and Reardon, F. H. (Ed.), Liquid Propellant Rocket Instability, NASA SP-194, 1972.

Hevert, S., Mahalingam, S., and Daily, J. W., "Velocity Profile Effects on the Stability of a Liquid Jet," University of Colorado-Boulder Center for Combustion Research, CCR Report 91-06, 1991.

Heister, S. D., and Karagozian, A. R., "Vortex Modeling of Gaseous Jets in a Compressible Crossflow," AIAA Journal of Propulsion and Power, Vol. 6, No. 1, pp. 85-92, 1990.

Jensen, R., (Ed.), "JANNAF Subcommittee on Combustion Stability - Annual Report," 27th JANNAF Combustion Meeting, Cheyenne, Wyoming, 1990.

Lefebvre, A. H., Atomization and Spraysundere, Hemisphere Publishing Company, 1989.

Leib, S. J., and Goldstein, M. E., "The Generation of Capillary Instabilities on a Liquid Jet," Journal of Fluid Mechanics, Vol. 168, pp. 479-500, 1986.

McCarthy, M. J. and Molloy, N. A., "Review of Stability of Liquid Jets and the Influence of Nozzle Design," Chemical Engineering Journal, Vol. 7, pp. 1-20, 1974.

Ranz, W. E., "On Sprays and Spraying," Canadian Journal of Chemical Engineering, Vol. 36, p. 175, 1958.

Rayleigh, Lord, "On the Instability of Jets," Proc. of London Mathematical Society, Vol. 10, pp. 4-13, 1878.

Reba, I., and Brosilow, C., "Combustion Instability Liquid Stream and Droplet Behavior. Part III: The Response of Liquid Jets to Large Amplitude Sonic Oscillations," Polytechnic Institute of Brooklyn, WADC Technical Report No. 59-720, Part III, 1960.

Reitz, R. D., and Bracco, F. V., "Mechanism of Atomization of Liquid Jet," Physics of Fluids, Vol. 25, pp. 1730-1742, 1982.

Rupe, J. H., "On the Dynamic Characteristics of Free - liquid Jets and a Partial Correlation with Orifice Geometry," JPL Tech. Report No. 32, 1962.

Sabersky, R. H., Acosta, A. J., and Hauptman, E. G., <u>Fluid Flow, Second Edition</u>, McMillan Publishing Co., 1971.

Schlicting, H., Boundary Layer Theory, McGraw-Hill Publishing Company, 1955.

Sterling, A. M., and Sleicher, Ca. A., "The Instability of Capillary Jets," Journal of Fluid Mechanics, Vol. 68, pp. 477-495, 1975.

Shkadov, V. Ya., "Wave Formation on the Surface of a Viscous Liquid Due to Tangential Stress," Fluid Dynamics, Vol. 5, p. 423, 1970.

Weber, C., "Disintegration of Liquid Jets," Z. Agnew Math. Mech., Vol. 11, No. 2, pp. 136-159, 1931.

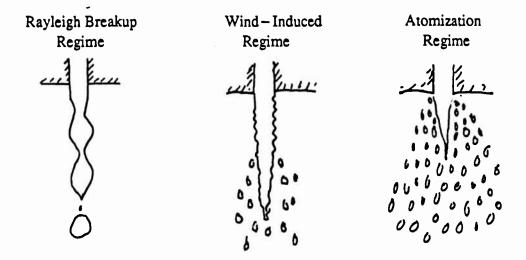


Figure 1. Breakup and Atomization Regimes Observed for a Liquid Jet

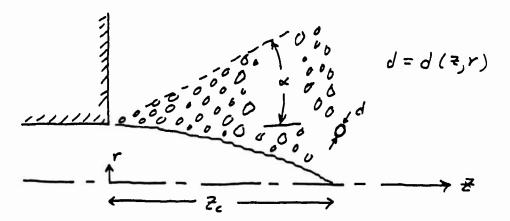


Figure 2. Primary Variables used in Describing an Atomizing Jet

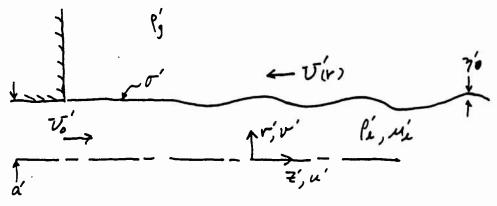


Figure 3. Nomenclature for Jet Stability Analysis

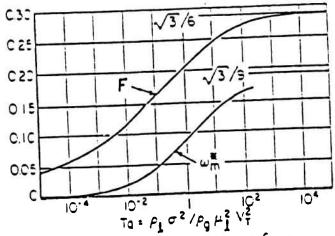


Figure 4. Dependence of Function F and Scaled Maximum Growth Rate, wm on Taylor Number

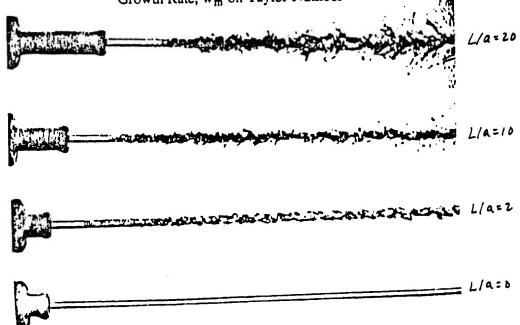


Figure 5. Effect of Jet Velocity Profile on Jet Stability Re = 4750, We = 15,300

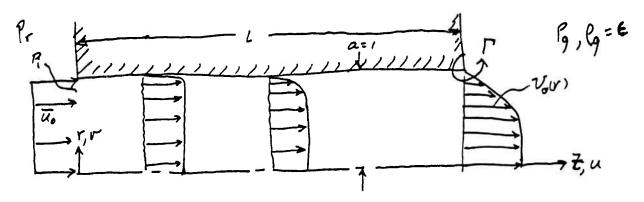


Figure 6. Injector Element Geometry and Circulation Generated Due to Boundary Layer Vorticity

# RDL AFOSR FINAL REPORT

R. W. Hoffman

Phillips Laboratory Edwards AFB Ca

22 August, 1991 Research Paper

#### **ABSTRACT**

### XAFS of AP and AP/Binder Systems

Techniques of Lytle detection in x-ray fluorescence were applied to 26 distinct chemical samples at the Cl edge, 1 at the K edge, and 7 at the Ti edge. The specimens commonly pressed from powders, 2.5 um particle size in the case of AP to thi knesses of about 1/32 in., thus obtaining samples for further ex, diments of adding binders or remaining uncoated. A special sample holder was designed and constructed to aid in the specimen transfer. The sample thickness necessitated fluorescent detection with an estimated probing depth of 25 um. experiments were carried out on beam line X-19A at Brookhaven Laboratory and are National in the process of quantitatively evaluated. Differences in the XANES spectra between binders are noted, and tentatively related to the steric chemistry and to the local structure and valence of the Cl containing samples. Several new polymeric materials were also examined.

#### Introduction

The prime commitment to the RDL/AFOSR Summer Research Program was to make XAFS techniques available to the Phillips Laboratory, Edwards AFB and especially to certain persons who would be trained or updated in many phases of Synchrotron Radiation (SR) research involving absorption fine structure spectroscopy. The persons participating directly in this activity were Dr. John Rusek and Dr. Kevin Chaffee, Phillips Laboratory, and Professor Richard Hoffman and Mr. Guy DeRose, participants in the Summer Research Participation Program. A secondary goal was to explore the conductivity limits for the samples used in Scanning Tunneling Microscopy using the STM existing in the Phillips Laboratory, and will not be discussed in this paper.

The preliminary steps necessary to be able to carry out an XAFS actual sample data acquisition at a synchrotron include

Synchrotron Selection Beam Line selection

User proposal and approval

Safety approval

User financing

Experimental design, including sample preparation and selection of spectroscopy and apparatus availability.

Scheduling of experimental time with beam line personnel, including beam line training in safety and operation

For orientation, background information taken from the NSLS literature and relabeled as Figure 1 is reproduced on the following page.

The steps above must be completed prior to actually obtaining data and will not be discussed in detail in this report. In our case 5 days were scheduled from 7-12 August, 1991. AP, various standards, and other runs were completed at Brookhaven National Laboratory at the National Synchrotron Light Source (NSLS), Upton NY during that time. The items to be discussed in this report are concerned with the equipment alignment, data acquisition, and some of the problems arising during the actual run period. Additional details as to the data reduction will be found in the report by Guy A. DeRose to RDL.

Figure 1 . Hoor plan of the National Synchrotron Light Source experimental area.

## X-ray Absorption Fine Structure

XAFS is the short hand algorithm for both Extended X-ray Adsorption Fine Structure (EXAFS) and X-ray Absorption Near Edge Structure (XANES) or as is it sometimes called Near Edge X-ray Absorption Fine Structure (NEXAFS). EXAFS as practiced for surfaces is called SEXAFS and uses Auger electron detection. EXAFS, the earlier technique is the generation of outgoing spherical photoelectron waves of varying wavelengths following photoemission and the subsequent backscattering from nearby atoms in coordination shells and the analysis of the resulting raw data to provide elemental coordination distances and numbers crystalline and modestly disordered samples. All XAFS techniques are commonly practiced using the high intensity SR sources (typically 10 billion photons per second). Bremstrahlung radiation arising from bending magnets forms the white radiation of the beam line used (X-19A) for these experiments. The beam line has Si (111) oriented single crystals used as a monochromator to be wavelength tuneable to scan the absorption as a function of energy through and between various edges and is a polarized x-ray source, not used in these first experiments since the samples were powders of all orientations. This beam line was selected for its specialization to energies and its availability with known personnel. It was well suited to our needs since a feedback system made vertical translation of the sample unnecessary as the energy was scanned. suffered from having very limited on-line data analysis. Figure 2 on the following page give X-19A beam characteristics and other data.

#### XAFS Techniques

The XAFS information may be obtained in transmission, fluorescence emission, photoelectron emission, with electron or ion detection using ion chambers or other detectors. One of the most common and versatile is the Lytle detector, a combination of transmission and fluorescence geometries, commonly using ion chambers and optimized for the 3d transition series and using Soller slits and x-ray K beta filtering techniques. For our experiments the Soller slits serve no useful purpose and no simple filters exist and were not used in either In the design of the the CWRU or UK (X-19A) detectors. experiment, proper consideration of the sample and detection geometry must be taken into account to optimize the data for easier analysis. While certain corrections may be made during

the data analysis, it is better to have good data in the beginning. In addition to the noise questions, one important parameter is the depth in the sample to be probed. For the Cl edge in most of the materials studied here, the absorption length is about 17 um at energies above the Cl edge energy. Since we found in preliminary experiments in preparing samples it was not possible to press sample powders to make proper specimens with thicknesses less the 35 um for transmission due to the soft radiation (2.623 KeV) used. As the samples were not electrically conducting, and we wished to probe a distance greater than 100 A in order to study buried interfaces, the fluorescent technique was selected and will be emphasized in this report. As stated earlier, we did not take advantage of the polarization of the X-ray beam in this run, but hope to examine oriented samples in the future.

## SR Experience during August, 1991

Dr. John Rusek, Dr. Kevin Chaffee, Prof. Hoffman, and Mr. Guy DeRose went to the NSLS at BNL to make the measurements. We traveled from EAFB to BNL as a group. Since we had 5 days of beam time and we needed to operate 24 hours per day, we operated in two 12 hr shifts. Except for a major unscheduled beam dump (no X-rays) for a construction mishap and another for natural lightning strikes causing power failures for a total of some 36 hours, we were able to make full use of the NSLS facility and finished most of the samples that were available. Some beam time loss due to beam decay is expected. Taken from our log and end of run report, some statistics follow; more are available upon request.

#### Table I Beam Statistics 7-12 Aug., 1991

Possible time available	(8 hr shifts)	15
No beam for many reasons	(8 hr shifts)	6
Beam available	(shifts)	9
Initial set up time	(shifts)	1.5

### Sample Preparation

Consistent with the necessity of using fluorescent radiation and a Lytle detector we investigated the pressing of AP and other materials into pellets in a die similar to a KBr press. Mr. David Cooke fabricated a very useful die that made samples nominally 3/8 in: in diameter. The samples were made 1/32 in. thick by filling the die with some 100 mg of AP. These samples were pressed to an oil pressure of about 1000 psig in a Carver press in Cell No 6 at the Chemistry Lab at Phillips Laboratory We produced about 150 samples which were strong enough to withstand handling and shipment and thus serve as reproducible samples. Mr Tracy Reed assisted with the final pressing.

This die was successful in making samples not only of AP but other standards, perchlorates and polymer samples for XAFS studies. Earlier studies to optimize pressing conditions showed a rather wide range of conditions possible, but a particle size of 2.5 um was selected for AP. The pellet samples were removed from the die by light pressing. For AP the final pellet density increased slightly with particle size decrease and increased with increasing pressure of pressing. The final density was about 1.7 gm/cm or about 90% of the bulk crystalline density with a volume contraction of about 3 times. Upon extrusion from the die, the first exposed (Upper or Top surface) had a few fine cracks and some surface debris and was noted in the earlier studies. TiO2, a standard (calibration) sample was not able to be pressed and required the addition of a binder. It and a CuClO4 sample were vise pressed at BNL. The pelletizing technique provided samples of low mass that were easily transported and handled, and is recommended for future use. An appropriate sample holder was designed and fabricated to facilitate the sample insertion into the Lytle detector at the beam line. The geometry is shown in Figure 3 which follows. Reference 1 may be consulted for more details about XAFS experimental design.

### Apparatus and Procedures used at ENL

Most of the operating hardware for the XAFS data acquisition and a Lytle detector was available as part of the X-19A apparatus. We provided the CWRU Lytle detector, samples, and operating experience. Some beam line specifications were reproduced in Fig 2. It is important to contact beam line personnel until the user is familiar with the beam line operation. In our case, Dr. Kumi Panigraphi, a former student,

Beamline: X19A
Ring: X-Ray
Operational Status: Operational

Participating Institutions:

NSLS, U. of Kentucky, U. of Michigan, BNL - Department of

Applied Science (members of the X19A Stewardship Group)

Local Contact:

Fu-Long Lu (516)282-5619, 2338 @ BNL

Spokesperson:

Stephen Cramer (BITNET address: CRAMER@BNLCLI)

Research Program:

X-ray absorption spectroscopy, EXAFS

Energy Range (keV)	Crystal Type	Resolution ΔE(eV) @8 keV, Si(111) @12 keV, Si(220)	Flux (photons/sec.)	Spot Size (mm)	Total Horizontal Angular Acceptance (mradians)
2.1 - 7.9	Si(111)	8.1 - 0.7	-10 <sup>11</sup>	40H x 5V	2.4(unfoc.)
3.4 - 12.9	Si(220)	12 - 0.8	@ 5 keV	unfocused	1.3(foc.)
Ì			(100 mA, 2.5 GeV)	-1 mm diam focused	
7.6 - 13.4	Si(111)	8.1 - 0.7	$-5 \times 10^{11}$	40H x 5V	2.4(unfoc.)
12.5 - 23.0	Si(220)	12 - 0.8	@ 11 keV	unfocused	1.3(foc.)
			(100 mA, 2.5GeV)	-1 mm diam focused	

Largest value corresponds to 2 mm slit. Small value is for 0.1 mm slit.

## Optical Configuration

### a) Monochromator

NSLS boomerang-type double flat crystal monochromator; fixed exit geometry; first crystal is water-cooled; operates at UHV; two presettable Bragg angle ranges of 14.5° - 70° and 8.5° - 15°; located 9.3 meters from the source. Operates primarily in low energy, Si(111), unfocused configuration.

#### b) Mirror

Cylindrical aluminum focusing mirror, electroless nickel plated and overcoated with rhodium, for focusing beam onto sample at 18.5 meters from the source; 3 mradian incidence angle; 23 keV high energy cutoff; mirror may be dropped out of beam path for unfocused mode; located 10.5 meters from the source.

### c) Windows

Beamline is UHV up to window located inside radiation hutch; a 6 µm graphite filter is in the beam at all times; the exit window for non-vacuum operation is 10 mil Be.

#### Experimental Apparatus

Positioning table using stepper motor controls, two perpendicular translations and effectively three mutually perpendicular rotations. Germanium array detector available by special arrangement with S.P. Cramer.

#### Computer System Hardware and Software

MicroVAXII computer with CAMAC interface running Micro-VMS operating system; Ethernet link to AMD cluster and major networks.

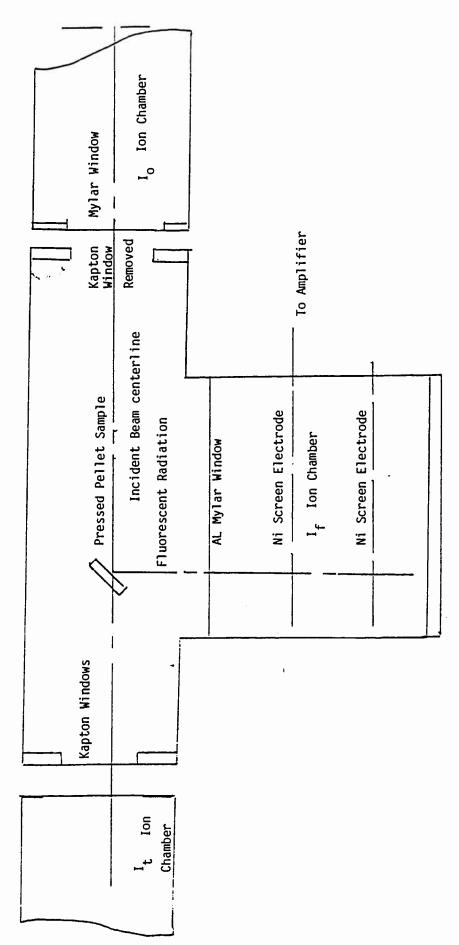
December 5, 1990

Figure 2 X-19A Beam Line Data

and other beam line people were very helpful. Although many beam lines are similar in their operation, differences exist between PRT groups resulting in differences in data collection and beam line operation. Most beam lines provide documentation and help to new users in order to obtain useful data from the beginning. In our case the CWRU Lytle detector failed near the beginning of our time necessitating the use of the University of Kentucky X-19A ion chamber and electronics being wedded mechanically to the sample chamber of the CWRU instrument. This was successfully accomplished at NSLS. To minimize the absorption of the X-rays of low energy in the air path, we selected a uhv beam line and filled the Lytle detector with helium in the sample region. Helium was also sent to the Io (first) ion chamber after it was repaired. The second (If) ion chamber was filled with nitrogen gas to absorb most of the K beta radiation and maximize the signal. The analog signals from the ion chambers are amplified and sent to a voltage to frequency converted before the signals were recorded by the beam line computers. Background (offset) readings are taken after any X-ray changes. The tuning of the Bremstrahlung is accomplished by computer control of monochromator and proper alignment of the X-ray beam. This alignment must be carried out at the beginning and minor realignment done each time a new electron fill is made to the storage ring, approximately once each shift. Part of alignment procedure is to adjust, by calibration with a known standard sample, the position of the monochromating crystals to calculated edge energy by following a predetermined (computer) procedure.

The computer for the X-19A operation was able to preload scans for various energies and predetermined integration times to reduce the total time at the expense of a given scan time. This procedure also set the energy resolution of the monochromator. As the data evolved, it was obvious that the XANES region would be more important in showing differences than the EXAFS region so the scans were adjusted to optimize to provide better energy resolution near the edge of interest.

Realignment to find the position of the beam so that the sample may be placed in the proper position, calibration of the energy, and using standard known samples—for phase and amplitude information necessary for the—data reduction usually takes about half of the total available beam time; thus making use of the 24 hour a day 7 days a week schedule is required. Fortunately, the persons going to NSLS for this run all had prior SR experience.



(CWRU) Lytle Detector for Fluorescence Detection of XANES and EXAFS Figure 3

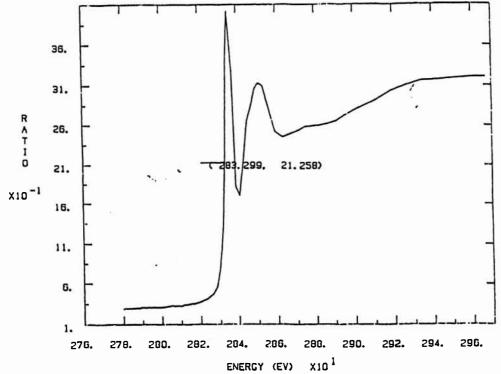
#### Analog Results

As stated earlier, no on-line data reduction exists on X-19A so that only data in the form of analog plots were available to bring back. These have been examined with the results—reported below. All together some 143 separate scans—were carried out. Many of these were—for beam alignment purposes and—covered only the Cl edge region. Later edge scans were set up to include both the Cl and Ar edges for a reference energy built in to each scan. Finally some full data scans from—below the Cl edge to above the K—edge—were set—up to—minimize—the statistical—errors while maximizing—the number of specimens—that could be—examined in a given time. These—later scan parameters were used when time was limited curing the last two days.—In all, the following samples were examined as shown in Table II below:

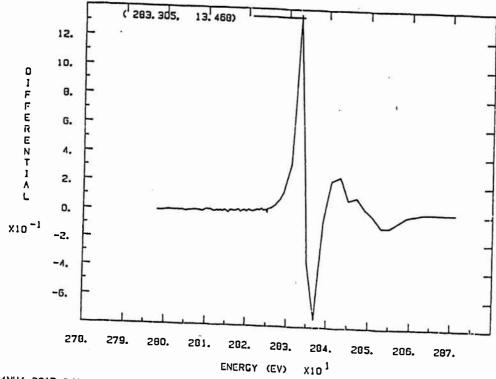
Table II Sample Summary Scan Data

Sample File	No. of Samples	No. of Scans
AP CLO4NH4	1	30
CLNH4	1	10
CLEDGE	2	22
STD Various		
KC1 KCL & CLK	1	8
AP/binders Various	17	37
New Polymers SYN Var	. 4	12
TI CVD Various	2	5
TI STD Various	5	12
Various polymer		
window films	3	3
Totals	36	109

Representative data are shown in Figures 4-8 for both energy calibration, XANES (Multiple scattering), and EXAFS (Single scattering) regions. Details are not given here, but file numbers are on the figures and some details are given in the Figure Caption list.



CLO4NH4.301W 3/1 8-AUG-91 Figure 4a CLedge scan for energy calibration



CLO4NH4. 3010 3/1 8-AUG-91 Figure4b Differentiation of population

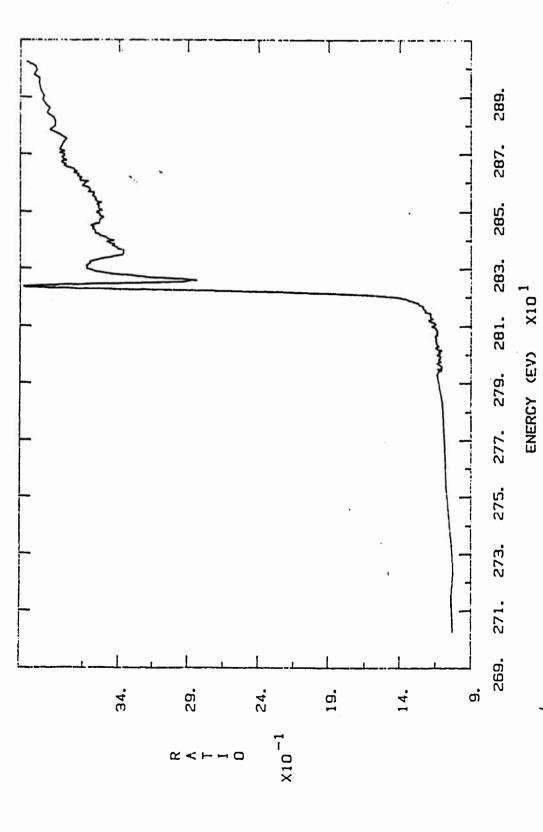
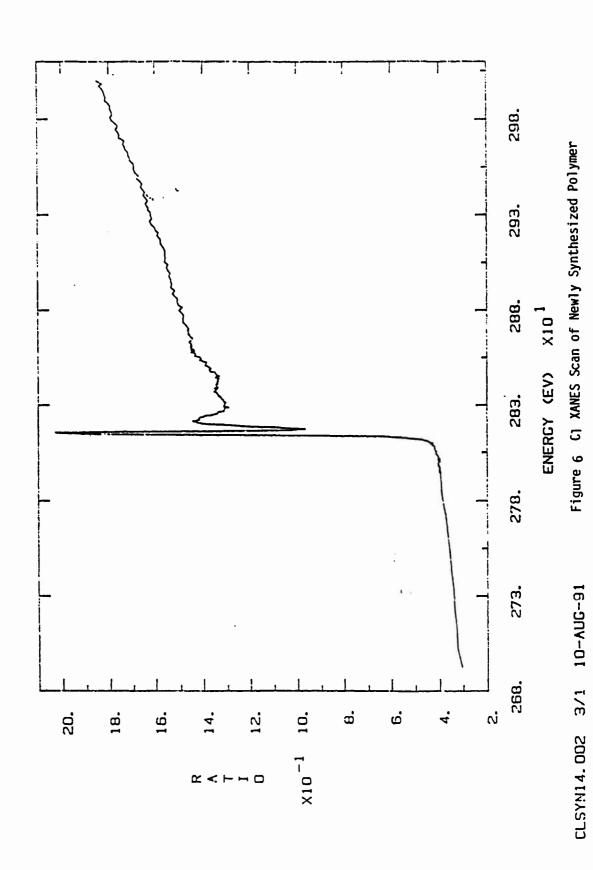


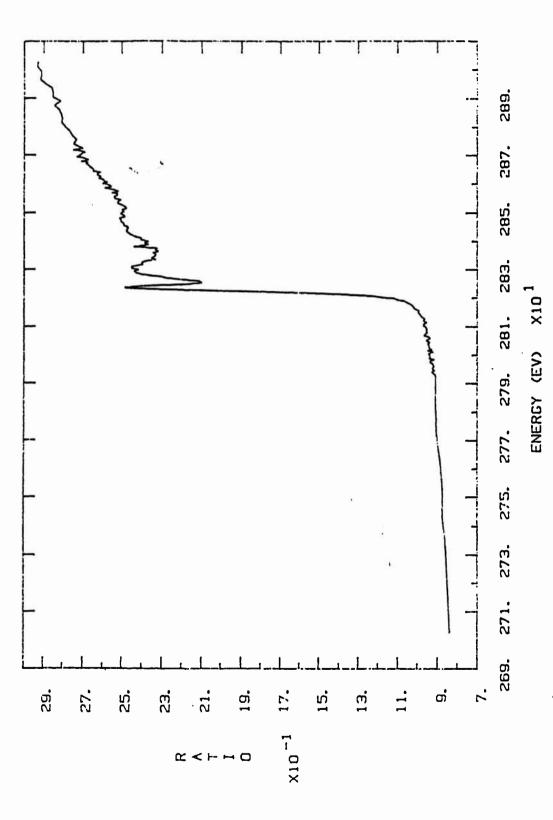
Figure 5 Cl XANES Scan of Chlorohydroquinone

СLСLHQ. 302<sup>№</sup> 3/1 11-AUG-91

7-13



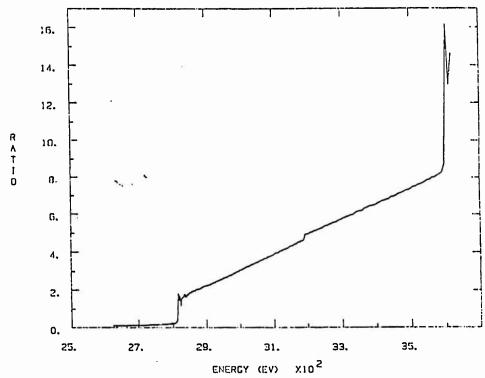
7-14



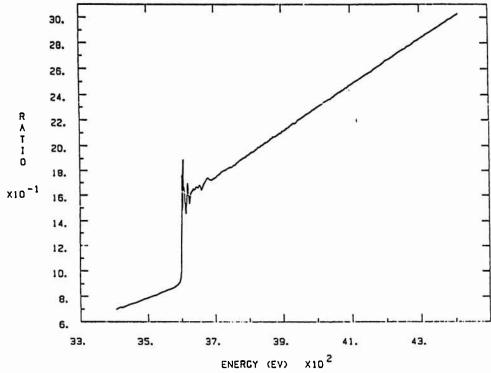
CLPACP. 001W3/1 11-AUG-91

Figure 7 Cl XANES Scan Of AP/Binder

7-15



CLK. 001 3/1 9-AUG-91 Figure 8 a KCl Cl edge full scan showing A and K edges and Cl EXAFS-



KCL. 002 3/1 11-AUG-91 Figure 8b KCl K edge full scan showing K XANES and EXAFS

From the analog data, certain qualitative information may be For EXAFS, quantitative information may be deduced by carefully fitting the file data by averaging scans to reduce noise, performing background subtraction and energy calibration to obtain the inner potential, then transforming from energy to k space followed by a Fourier transform to obtain the (uncorrected) Function which is similar to Radial Structure Distribution Function and allows one to select the coordination spheres for proper fitting. This is a long process of interactive data processing involving both standard data from known coumpounds with a similar coordination and varying degrees of sophistication depending on the program used. It is our purpose to make these programs available to the personnel at Phillips Laboratory as needed for their future work.

It follows for this report that only analog examination is possible at this time. Nevertheless, we have formed the following conclusions based on our first C1 edge experience.

- 1. It is possible to work at the Cl K-edge with a Lytle detector minus Soller slits and filter. This poses no additional difficulty providing the small adsorption length for the soft radiation is taken into account. Beam line X-19A is an appropriate line for the Cl and Ti edge. The beam must be detuned drastically (70%) to reduce the third harmonic in the incident beam to less than 1/1000 and the contribution from all K emission lines is observed and may need to be corrected in the data analysis.
- 2. After changing samples, a decreasing intensity Ar edge is found which arises from the impurities in the air that can enter the Lytle detector sample chamber. This edge provides an automatic energy calibration for the Ar edge and, hence, an energy reference for the Cl edge, assuming linearity in the monochromator. We will test this approach since the reference energy for each scan elimanates one additional beam line vagary.
- 3. The Cl EXAFS region shows rapid damping and will be difficult to quantitatively treat. Good quality data was obtained for the samples. The minimum sample, thickness was not determined, but most of our data was obtained from the first adsorbption length in the sample. (from a surface layer about 25 um deep; we estimate a sensitivity limit of about 100 A for this technique at the Cl edge.)
- 4. The XANES region was extremely rich and worthy of detailed study. It is unfortunate that this energy region is the poorest understood from an analysis point of view, but theoretical progress in curved wave and mutiple scattering formulations is being made rapidly. This region shows major differences in structure from one sample to another, especially in the white line region which reflects the multiple scattering in the low energy (above the edge) region. For addition 1 recent

information, see references 1, pg. 573; ref. 2 and 3.

## Figure Captions

## Fig. No.

## Caption

- NSLS Site plan.
- 2. X-19A Beam line data.
- 3. Lytle detector geometry, (CWRU).
- 4a. Cl edge determination by on line computer windowing.
- 4b. Cl edge determination by differentiation. (preferred)
- 5. Chlorohydroquinone Cl XANES.
- 6. Polymer Cl XANES.
- 7. AP/binder Cl XANES.
- 8a. KCl Cl full scan showing Ar and K edges and Cl EXAFS.
- 8b. KCL K full scan showing K edge XANES and EXAFS.

#### References

- 1. X-Ray Absorption, Principles, Applications, Techniques of EXAFS, SEXAFS and XANES, Edited by D. C. Koningsberger and R. Prins, Eindhoven University, John Wiley and Sons, 1988, ISBN 0-471-87547-3 (hardcover).
- 2. X-Ray Absorption Fine Structure, Proceedings of the sixth International Conference on X-ray Absorption Fine Structures (EXAFS and XANES), York, UK 1991, (Organized by Daresbury Laboratory), Edited by S. Samar Hasnain, Daresbury Laboratory, Ellis Horwood Limited, 1991, ISBN 0-13-973199-7 (hardcover).
- 3. EXAFS and XANES studies of lead oxides and solutions of Pb(II) and Pb(IV) ions, James McBreen Department of Applied Science Brookhaven National Laboratory Upton, NY 11973 (private communication, submitted for publication 1991).

#### Future Work

Little quantitative data reduction has been carried out to date owing to the recent (13 August,1991) acquisition of the first data. It is also clear that the Xanes data is the most instructive and needs quantitative effort. It is also true that the next scheduled time is 4 days at X-19A during early October, 1991. It is suggested that those runs repeat any required data and concerntrate on the determination of buried interfacial differences by fluorescence detection and electron detection or grazing incidence fluorescence be attempted in order to gain sensitivity. Use of the polarized X-ray beam is also recommended for oriented specimens.

## 1991 AFOSR SUMMER FACULTY RESEARCH PROGRAM

Sponsored by the Air Force Office of Scientific Research

Administered by RDL, Inc.

Final Report

Polymeric Ionic Conductors - Electrolytes for Solid Polymer Batteries

I.A. Howard
Department of Physics, University of Texas at Arlington

Research Location 6/91 - 8/91, OLAC PL/STPP, Edwards AFB, CA 93523

Research Contact: Michael Powell

## Abstract

A survey has been conducted of the state of development of polymeric ionic conductors suitable as electrolytes for secondary battery applications. Criteria for suitability involve conductivity, structural stability, and anion transfer number. Although a number of modifications have been tried, it appears that a (poly(ethylene oxide) [PEO] + Li salt) complex is the best overall candidate at present. An approach to the problem that will allow predictive capability is, from a theoretical point of view, difficult since a macroscopic treatment neccessarily involves some sort of statistical averaging over chain configurations of the amorphous conducting phase. It is suggested that a series of single-chain calculations on PEO segments plus cations and anions will be useful in clarifying the positions of ions relative to the backbone, the equilibrium distortions of the PEO chain segment in the vicinity of the ions, and the activation energies for motion of ions from one backbone oxygen site to another. Substitutions on sidegroups and/or backbone can also be explored. Several possible methods are discussed.

# I. Introduction and Background

Since it was proposed by Armand<sup>1</sup> in 1980 that poly(ethylene oxide) [PEO], a polymeric ionic conductor, could be useful as a battery electrolyte, a small body of literature has grown up dealing with materials properties of PEO and closely related polymers. Polymeric electrolytes have, in principle, several advantages over more conventional liquid or solid electrolytes. There are obvious advantages in weight (leading to higher energy densities), plus ease of fabrication in any desired size or shape. Contact at interfaces, i.e., the electrode-electrolyte surfaces, should be enhanced due to the plasticity and deformability of polymeric compounds. Leakage of electrolyte should obviously not be a problem. On the negative side is the fact that polymeric ionic conductors do not have the conductivity of the conventional ionically conducting liquids or solids. Listed below are room temperature conductivities of several conventional (solid) electrolytes (from Munshi and Owens<sup>2</sup>):

<u>Material</u>	Conductivity σ, (ohm-cm)-1	
β-Ag <sub>3</sub> SI	10-2	
RbAg <sub>4</sub> I <sub>5</sub>	.26	
Rb4Cu <sub>16</sub> I <sub>7</sub> Cl <sub>13</sub>	.34	
Li <sub>3</sub> N	1.5x10 <sup>-3</sup>	
$(Li,Na)-\beta-Al_2O_3$	10-3	
$(Li,Na)-\beta-Al_2O_3$	10 <sup>-3</sup>	

By contrast, a highly conducting PEO complex such as PEO-LiClO<sub>4</sub> (ratio of PEO backbone O:Li = 8:1) has  $\sigma \simeq 10^{-5}$  (ohm-cm)<sup>-1</sup> at 30°C. Another disadvantage, to be discussed later in greater detail, is the relatively high transfer number<sup>3</sup> of the anionic species (i.e., the proportion of the total conductivity attributable to the anion) in the dopant salts in polymeric electrolytes.

Research at present focuses on improving conductivities at room temperature, or slightly elevated temperatures, and on reducing the anionic transfer number. Subsidiary concerns are optimizing conductivity versus structural stability, and ensuring that minimal degradation at electrode-electrolyte interfaces occurs during charge-discharge cycling in secondary battery applications.

Conductivity has been studied as a function of temperature, dopant salt type, level of doping (salt concentration), side group, and some backbone substituents; qualitative models have been proposed to explain some aspects of the conductivity variations.

In this report, the salient features of the physical behavior of the most-studied polymeric electrolytes are summarized. The attempt is not to provide an exhaustive review, but to highlight the similarities in conductivity mechanism, the areas of uncertainty, and the areas in which modifications could be tried.

### II. Goals of the Project

The goals of this project from 6/91 to 8/91 have been the following:

- 1) to conduct literature searches for information on the basic physical/chemical properties of PEO and related electrolytes (as opposed to, for instance, its performance in prototype cells);
- 2) to correlate this information to arrive at an overall picture of what is known on the conductivity mechanism(s) at work and how they might be optimized by variation of microscopic parameters;
- 3) to propose models, amenable to numerical or analytic solution, which allow predictions of favorable variations on existing polymeric electrolytes.

## III. Structure and Conductivity

The vast majority of the ionically-conducting polymer systems currently being studied as potential electrolytes for battery applications are modifications of the basic PEO + salt systems proposed by Armand<sup>1</sup>. The PEO chain has the structure  $(CH_2CH_2O)_n$ , where n can be very large (molecular weights of ~  $10^6$  are common). At low temperatures (below the glass transition temperature  $T_g$  of ~  $-60^{\circ}C$ ) PEO is crystalline, with a helical chain configuration<sup>1</sup>; above

T<sub>g</sub>, regions of the crystal become amorphous. When a PEO + salt complex is formed, the donor character of the oxygens on the backbone allows them to solvate the cation. (It was originally thought that upon formation of a PEO + salt complex, the cations sat within the helix, 1 although this is now thought not to be the case. 4) The anion sites are largely undetermined, although they apparently sit in the vicinity of the (O + cation) complex. Conductivity proceeds by a hopping mechanism; that is, cations (and to some extent anions) move from one O site to another "assisted" by thermally-induced local motion of the PEO backbone.<sup>5,6</sup> Table I (from Armand<sup>1</sup>) shows some of the (PEO + salt) combinations that have been attempted; as can be seen, PEO will only complex with some of the salts. In Table II<sup>3</sup> are listed the temperatures for which the conductivities of some of these solutions are 10<sup>-5</sup> and 10<sup>-4</sup>; note that with one or two exceptions, these are well above room temperature, and typically not far from 100°C. Owen<sup>6</sup> has estimated, assuming a minimum practical electrolyte thickness of .01cm and a power density of 100W/l, that the minimum acceptable conductivity for a polymeric electrolyte material would be  $2x10^{-4}(\Omega-cm)^{-1}$ . Thus improving the conductivities of polymeric electrolytes in the lower temperature range is of considerable interest.

Salts Forming (+) and Not Forming (-) Adducts with PEO

	Li+	Na+	K+, Rb+,	Cs+, NH42+	Mg2+	Ca2+	Zn2+	Cu2+
<del></del>							<del></del>	
F-	-	-		-	-	-	-	-
C1-	÷	-		-	+	-	+	+
Br-	+	+		-	+	+	+	+
I-	+	+		+	+	+	+	+
NO3-	+	-		-	+			
SCN-	+	+		+	+	+	+	+
C104-	+	+		+	+	+	+	+
CF3SO3-	+	+		+	+	+	+	+
BPh4-	+	+		+	+		+	

Table I (from Ref. 1)

Polymer	m <sup>+</sup>	x <sup>-</sup>	0/m	$T_{\sigma = 10^{-5}}$ (°C)	$T_{\sigma = 10^{-4}}$ (°C)
PEO	ri,	ī-	8	35	55
п	Ħ	C10 <sub>4</sub>	4.5	70	110
•	п	C10 <sub>4</sub> -	8	31	50
	n	CF 3503	4.5	75	120
п	1	*	8	70	100
."	n	п	14	65	85
•	Na <sup>†</sup>	ı-	10	45	50
п	κ*	CF3503	4.5	40	70

 $(\sigma \ in \ (\Omega\text{-cm})^{-1})$  Table II (from Ref.3)

There is a tradeoff between conductivity and mechanical properties, however. The complexes mentioned above are only conducting (to any significant extent) when the PEO polymer is in its amorphous phase; above T<sub>g</sub>, some domains of the polymer will still be in the crystalline phase for a sizable temperature interval.<sup>6</sup> It is advantageous, therefore, to decrease T<sub>g</sub> in order to maximize the amorphous character of the polymer at a given temperature above T<sub>g</sub>. The more amorphous the polymer, however, the greater the "creep" under stress, and the less suitable the mechanical properties. Efforts have been made to optimize both properties by, for instance, introducing crosslinks between PEO chains and attaching sidegroups to the backbone carbons to reduce the tendency toward crystalline order.<sup>7</sup> The crosslinks are intended to provide structural stability to the polymer in its amorphous phase. One promising new development is the addition of 12-crown-4 ether to PEO-based

electrolytes<sup>8</sup> to provide additional sites for ion-pair solvation without degrading the structural properties of the PEO.

An alternate polymeric system of interest is poly[bis[2-(2-methoxyethoxy)ethoxide]phosphazene], known as MEEP:

(from Ref. 9)

MEEP was first synthesized in 1984 by Blonsky, Shriver, Austin and Allcock<sup>10</sup>, who anticipated that the flexible inorganic N-P backbone would lead to high ionic conductivity. It is amenable to doping with a variety of salts; Blonsky et al. originally considered Sr(SO<sub>3</sub>CF<sub>3</sub>)<sub>2</sub>, NaSO<sub>3</sub>CF<sub>3</sub>, LiSO<sub>3</sub>CF<sub>3</sub>, and AgSO<sub>3</sub>CF<sub>3</sub>. Note that the side chains of MEEP are essentially short PEO segments; one can look at MEEP as essentially an "intrinsically amorphous" form of PEO. The conduction mechanism involves hopping between O sites on the side chains, just as in PEO. MEEP doped with LiSO<sub>3</sub>CF<sub>3</sub> in a 0.25:1 ratio of cation to polymer repeat unit was reported to have a conductivity of ~10-4 (ohm-cm)-1 at room temperature<sup>9</sup> (Li+ transfer numbers for the same complex were given as 0.32 at 70°C); conductivities of this complex between room temperature and 100°C were 1-3 orders of magnitude larger than for the analogous PEO complex<sup>10</sup>. Despite these impressive conductivities, MEEP cannot be readily used for battery applications due to its very soft, almost liquidlike consistency. Attempts have been made to stabilize the polymer by creating (MEEP + PEO) blends<sup>11</sup>, but conductivity is subsequently reduced. PEO-based electrolytes seem at present to be still the electrolyte materials of choice.

Despite the fact that motion of cations (and/or anions) involves hopping between sites in an amorphous system for which the

mediating lattice distortions are unknown, we can gain a general sense of the important parameters by considering a simple standard hopping model<sup>12</sup>. The current density j of diffusing ions in the presence of gradients (in concentration and/or electrical potential) can in general be expressed as

$$\mathbf{j} = - \underbrace{eDn}_{\mathbf{k}T} \nabla \eta$$

where e = lel is taken to be the ionic charge, n is the ion concentration, kT is Boltzmann's constant times temperature, D is a diffusion constant, and  $\nabla \eta$  is the gradient of the electrochemical potential,  $\eta = \mu + e\phi$ . The latter quantity is the sum of the zerofield chemical potential  $\mu$  and the potential energy  $e\phi$  of the ion in any applied electric field  $E = -\nabla_{\phi}$  that may exist. The quantity D/kT can be identified with the mechanical mobility B<sub>m</sub>, the ratio of particle velocity to field-applied force. Since D has units of  $(distance)^2/time$ , it can be written as D ~  $vR^2$ , with v a "hop frequency", and R the hop distance. In one dimension, a randomwalk analysis gives a proportionality constant of 1/2. The hop frequency is not a precisely known quantity but can be approximately expressed as  $v \sim (kT/h)\exp(-E_a/kT)$ , where h is Planck's constant and E<sub>a</sub> is the activation energy for a hop. This assumes, roughly speaking, that at a temperature T there is a site vibrational frequency ~ kT/h due to thermal activity; the factor exp(-E<sub>a</sub>/kT) reflects the probability that as a result of such vibration the ion that is hopping will find itself in a configuration representing the top of the potential barrier between two adjacent equilibrium ion sites.

Finally, the chemical potential  $\mu$  in zero field, as a function of temperature, is

$$\mu = \mu_0 + kT \partial \ln \left[ N! \right]$$

$$\partial n_i \quad n_i! (N-n_i)!$$

where  $n_i$  is the number of ions and N the number of hopping sites. For N and  $n_i$  large, the logarithm can be approximated by Nln N -  $n_i$ l n  $n_i - (N - n_i) ln(N-n_i)$ , so that the derivative is approximately  $ln((N-n_i)/n_i)$ . Then

$$\mu = \mu_0 - kT \ln(n/(N-n)),$$

with N the hopping site concentration and n the ion concentration as before. Now, altogether, we have

$$\mathbf{j} = \frac{\text{neR}^2}{2\text{h}} \exp(-E_a/kT) \left[ \text{eE} + kT(N/\underline{n})\underline{\nabla}\underline{\eta} \right]$$
2h (n-N)

For  $n \ll N$  (low ion concentration) the second term can be written as  $kT \nabla (\ln n)$ .

This expression for current density reflects contributions due to both an ion concentration gradient and a potential gradient, i.e., an electric field. In the absence of a concentration gradient we then have just

$$\mathbf{j} = \underline{neR^2} \exp(-E_a/kT) \mathbf{E} = \sigma \mathbf{E}$$
, or  $\sigma = \underline{neR^2} \exp(-E_a/kT)$   
2h

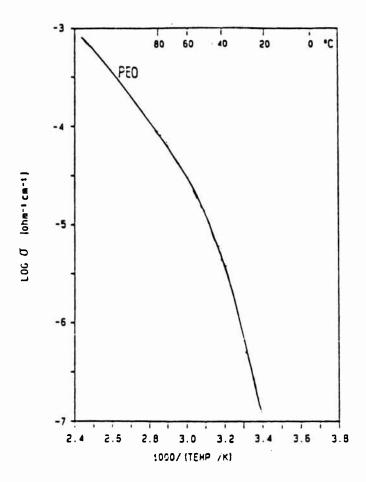
Under these circumstances the conductivity  $\sigma$  depends on three parameters of the system: ion concentration (e.g., Li<sup>+</sup> concentration in Li-salt doped PEO); hop distance R (distance between PEO oxygen sites) and hop activation energy  $E_a$  (dependent on chain distortion associated with a hop). There are many complicating factors, however. It is unclear whether PEO in its amorphous conducting state is a one-dimensional or three-dimensional conductor; i.e., do cations hop from one oxygen site to the next along a single chain of PEO, or is the hopping primarily between oxygen sites on adjacent chains? The geometrical factor 1/2 would no longer be valid for three-dimensional hopping. But, more importantly, the distance R for one-dimensional hopping would be just the on-chain distance between oxygen sites, while for three-dimensional hopping it would reflect an average distance between oxygen sites on adjacent chains.

The possible presence of concentration gradients is another factor to be considered. The ac impedance measurements usually carried out avoid the buildup of concentration gradients, but it is not clear whether significant gradients build up during operation of a SPE. battery. Influence of the anions also needs to be taken into account; these ideally do not contribute to the ionic conductivity, but are relatively immobile. In this case, motion of the cations in an applied field will set up a counter-field which must be added to the field E above. In fact, however, as discussed below, the anions in polymeric electrolytes tend to carry a large percentage of the current. It is known<sup>4</sup> that the activation energy E<sub>a</sub> is itself a function of n (and of the dopant), reaching a minimum at a mole salt fraction of ~ .05 for Li salts and increasing almost linearly at higher concentrations. Sorenson and Jacobsen<sup>13</sup> have proposed, by way of explanation, a phase diagram for a general PEO-like polymer electrolyte. They note that at a 4:1 ratio of O:Li (or other cation) the conductivity reaches a minimum and the polymer is in its crystalline phase (at low T), in which each Li+ is coordinated by four O atoms in four PEO helices. At higher salt concentrations a pure salt phase may coexist with the crystalline (or, for higher temperatures, amorphous) phase. salt phase, Li atoms are effectively removed from the conduction process, presumably by ion pairing.

Another factor affecting the suitability of a polymer electrolyte for actual secondary battery application is the transfer number for the cation and anion involved. Although the discussion above implicitly assumed that only one ionic species was hopping, this is not generally the case. The exact sites for the anions along a PEO chain are unknown, but it is assumed that they sit in the vicinity of the O + cation complex, and move between complex sites. For many of the electrolyte systems of interest, the anion transfer numbers are quite large, ~0.7.14 This presents problems in secondary battery operation, as the anode material (usually Li or Li alloy) is reversible only with respect to the cations.<sup>3</sup> During charging and recharging, a depletion/accumulation layer will form at the electrode interfaces. It is desirable therefore to develop electrolyte/ion complexes in which

the anion transfer number is near zero, i.e., the anions are relatively immobile.

The derivation above of the form of  $\sigma$  is not generally adequate for ionic conduction in polymers in the elastomeric phase (above the glass transition temperature  $T_g$ ). Small-molecule (or ion) diffusion occurs as the inter-chain vacancies are rearranged by thermally-induced local motion of chain segments. The resulting form for the conductivity  $\sigma$  contains an exponential modified in form from a Arrhenius-type expression above (the figure below shows the conductivity of PEO + LiCF<sub>3</sub>SO<sub>3</sub> in a 16:1 O:Li ratio, from Ref. 7).



The basic theory (the free-volume theory) was put forth by Cohen and Turnbull.  $^{16,17}$  The idea is that a chain segment (or other atom/ion) can move into an adjacent vacancy only if the volume of the vacancy is at or above some critical value  $v^*$ . This happens with a probability  $p = \exp(-v^*/V)$ , where V = gvf; here v is the effective volume of the chain segment and g is a geometrical overlap factor

( $\sim$ 1). The quantity f is the free volume fraction - the ratio of vacancy to total volume of the system; f is usually expressed as a linear expansion in temperature above  $T_g$ , so that

$$f(T) = f(T_g) + \alpha(T - T_g)$$

or  $f(T) = \alpha(T - T_0)$ , with  $T_0 = [T_g - f(T_g)/\alpha]$ . Here  $\alpha$ , the constant coefficient, is identified with the thermal expansion coefficient of the free volume fraction, and is generally  $\sim 10^{-4}/K.6$  Note  $T_0$  is a construct which is below  $T_g$  but not known a priori for a given system. The probability p then becomes

$$p = \exp(-v^*/gv\alpha(T - T_0)) = \exp(-B/(T - T_0)).$$

Since the final conductivity is proportional to p, we have in the end  $\sigma$   $\sim T^{-1/2} \exp(-B/(T-T_0))$  and thus a "modified Arrhenius" form. While this  $\sigma$  fits the data for most of the polymer/ion electrolytes of interest above  $T_g$ , it is not particularly useful in a predictive capacity, as it is just a matter of fitting the data to the expression for  $\sigma$  with three parameters (a prefactor, an "activation temperature" B, and  $T_0$ ). Some insight into the single-chain microscopic processes could be gained, however, by carrying out quantum-chemical calculations as described below.

## IV. Microscopic Modelling

A model of PEO (or related polymeric electrolytes) sufficiently detailed to elucidate effects of variation in microscopic parameters will need to be based, at least initially, on reliable calculations at the single-chain level. Two lines of inquiry seem worth investigation: quantum-chemical calculations to study ion-polymer backbone binding energies, electronic charge distributions, equilibrium chain configurations, and activation barriers; and molecular dynamics calculations to study the time evolution of chain configuration as a function of interatomic potentials and possibly of temperature. Let us first briefly consider the quantum-chemical approach. These calculational methods involve the approximate self-consistent

solution of the time-independent Schroedinger equation for a given cluster of atoms simulating the system of interest (in this case, for a PEO segment, with or without a complexed ion pair). Results can include the spectrum of one-electron levels of the system, the total energy as a function of configuration, the electronic charge density, and the total atomic charges. Interpretation of these results could be of great interest in understanding conductivity mechanisms in PEO.

A central question, of course, is the nature of the cation hopping sites. (Although these are generally considered to be the O sites on the PEO backbone, some authors<sup>5</sup> have suggested the anions as hopping sites.) Even if the sites are assumed to be the on-chain oxygens, the exact positions and the coordination of the cations needs to be determined. A quantum-chemical model of a finite PEO chain, cation and anion can be used to determine the most favorable locations of the cation and anion. Since the PEO backbone is flexible, a range of configurations must be tried to find the most stable sites for the ions and the local chain distortions in the vicinity of the complexed ion pair. (Most of the available quantum-chemical calculational methods are programmed to include options for finding total-energy minima as a function of atomic position.)

A subsequent question is the microscopic basis of the hopping activation energy. In "traditional" electronic hopping materials, a hop takes place when thermal fluctuations of the lattice cause local electronic energy levels to rise, while fluctuations on a nearby site cause the local level(s) there to fall. As the levels become briefly equal, an electron on the first site can "hop" to the second. A similar mechanism operates in ionic hopping conductors. The amount of energy necessary to locally distort the lattice enough to cause equality of the electronic levels is, roughly speaking, the activation energy that appears in the conductivity exponential. The situation in PEO-like materials is somewhat different because of the amount of disorder present, especially at higher temperatures (above the glass transition temperature); the distortions associated with a hop are no longer necessarily small deviations from equilibrium. There is the complicating factor of Coulomb attraction between the (somewhat electronegative) oxygens on the backbone and the cation. Within the quantum-chemical models we propose to consider, hopping activation energies can be calculated once equilibrium cation sites are known. The extent to which Coulomb attraction is important can be found by looking at the net atomic charges on the oxygen sites on the PEO chain, and by studying the total (electronic) charge density in the vicinity of a complexed cation. (Any of the quantum-chemical methods of interest can be used to produce a plot of the charge density in a planar cross-section of choice in the system.)

Single-chain modelling can also be used to "try out" various substitutions in backbone, side group, or ions. Several simple backbone substitutions could potentially be useful; if not in suggesting new materials, then in clarifying the effects of, for instance, varying the electronegativity on the oxygen site. This could be done by successive substitution of the chalcogens S and Se for O. Another possibility is substitution of one (or more) of the hydrogens in a -CH2- linkage by a group containing a halogen such as Cl. This should have the effect of withdrawing electrons from the adjacent -O- site(s) and decreasing their electronegativity. (Substitution of larger subgroups, while possible, will increase the number of degrees of freedom to be considered.) The supposition is that a decreased electronegativity will decrease the hopping activation energy for the cation - which would, all other things being equal, increase the conductivity. If at the same time the chain stiffness is increased by the substitution, however, the amorphous nature of the material will be decreased and conductivity will fall. Several variants on the PEO backbone have been synthesized, and conductivities measured. Clancy et al. 18 prepared a series of poly(alkylene sulfides) [-(CH<sub>2</sub>)<sub>n</sub>S-, n= 2 - 6] complexed with Ag salts. Results showed the highest conductivities for -((CH<sub>2</sub>)<sub>5</sub>S)- complexed with AgNO<sub>3</sub>; these reached a maximum of  $7.5 \times 10^{-6}$  (ohm-cm)<sup>-1</sup> at 63°C for S:Ag = 4:1, but did not depend strongly on salt content. The sulfur analog of PEO [PES] itself was also synthesized; its ionic conductivity when doped with Ag+ was reported to be low:  $1.5 \times 10^{-8} (\text{ohm-cm})^{-1}$  at  $70^{\circ}\text{C}$  for S:Ag = 3:1. It has been hypothesized that this is due to increased stiffness of the C-S-C linkage over the C-O-C linkage.<sup>3</sup> The melting point of PES is at 210°C, versus 65°C for -(CH<sub>2</sub>)<sub>5</sub>S-, so the suspicion of chain inflexibility would seem to be justified.

Substitution of Si for C in PEO-like structures has been investigated to some extent; it appears that the ability of these structures to from complexes, i.e., to solvate ions of interest, is less than for C-backbone structures.<sup>3</sup> This is thought to be due to the fact that the Si-O bond involves d-orbital contributions from Si which withdraw electronic charge from O, thereby reducing its donor ability. PE-imine [[PEI], -(CH<sub>2</sub>CH<sub>2</sub>NH)<sub>n</sub>-] complexes with NaI were studied by Chiang et al. 19 PEI was shown to dissolve NaI for concentrations less than 0.3mol of NaI per mol of monomer unit. At 75°C, conductivity was highest for PEI containing 0.1mol ratio NaI - 5x10<sup>-6</sup>(ohm-cm)<sup>-1</sup>. This is lower than salt-doped PEO conductivities at similar temperatures. PEO-related polymers, e.g., poly(propylene oxide)<sup>1,3,5</sup> and poly(ethylene succinate)<sup>20</sup>, with somewhat different backbones, have been investigated, but no system markedly superior to PEO-salt complexes has been identified. Quantum-chemical calculations will provide a means of quantifying the effects of various substituents. In addition, chain length effects can be studied - i.e., the number of repeat units in a chain necessary to reproduce observed behavior (for instance, the observed activation energies).

There are a number of approximation methods adapted to large clusters of atoms. At the lowest level is an extended Huckel-type calculation<sup>21</sup>, which gives a poor idea of electronic level structure but can be used to give a preliminary idea of chain configuration and requires very little computational time. At this level of treatment, electron-electron interaction is ignored. At a higher level, methods such as MNDO (Modified Neglect of Differential Overlap)<sup>22</sup> are relatively accurate in determining configurational energies and equilibrium structures. (This treatment drops elements of the Hamiltonian matrix involving integrals over functions centered on more than two sites.) A still higher level of accuracy is provided by the <u>ab initio</u> calculations carried out by the GAUSSIAN90 package; electron correlation can be included as well at several levels.<sup>23</sup> At this level the multisite integrals are retained; effects of variation in

basis set size- i.e., the degree of flexibility of the electronic wavefunction- can also be explored.

Another approach, complementary to the above, would be to carry out molecular dynamics simulations of the motions of a PEO chain segment. The basic idea of such a calculation is to specify a cluster of atoms (here, the PEO segment) and the interatomic potential to be assumed to act between each distinct type of atomic pair, e.g., C-O, C-H (pair potentials alone are sometimes not sufficient to describe large-amplitude motion). The cluster is then allowed to (computationally) "evolve" in time according to the equations of motion; that is, motion is governed by the gradients of the potentials. Total energies can be fixed so that, within the validity of the equipartition theorem, a cluster "temperature" can be assigned. Such an approach could be used to investigate characteristic chain segment motion as a function of temperature.

Ultimately, an analytical description of the conductivity in terms of Unfortunately, controllable system parameters would be desirable. as explained in Section III, the conductivity expression that best fits the data for most of the materials of interest is phrased in terms of phenomenological parameters not easily translatable into singlechain terms. Nonetheless, there may be alternate formulations for the conductivity that will be more readily useful to materials design. A model for ionic hopping conductivity, completely analogous to the approach used for electronic hopping, was developed by Flynn and Stoneham.<sup>24</sup> A knowledge of the phonon spectrum of the system in question is necessary, and so crystalline order is assumed. It is an interesting possibility that this model could be adapted to amorphous materials. As a starting point, however, the single-chain calculations discussed above will result in an improved idea of the origin of the parameter values necessary to describe PEO conductivity, and how those values might be modified to optimize conductivity. A full description of PEO, of course, will require consideration of multichain effects - ion hopping may primarily involve motion between sites associated with different chains, and the equilibrium ion sites may be formed by cooperative distortions on several adjacent chains. Nevertheless, the calculations proposed above will form a necessary basis for any consideration of multichain effects.

#### V. Conclusions and Recommendations

The literature review conducted on polymeric ionic conductors suggests that the basic goals of research directed toward developing polymeric electrolytes involve increasing the room-temperature conductivity while preserving mechanical strength of the material, and decreasing the anionic transfer number. (A subsidiary problem is ensuring the integrity of the electrolyte-electrode interface during prolonged charge-discharge cycling.) From the theoretical standpoint, the field presents many opportunities. It appears that essentially no work has been done on microscopic modelling of PEO chain segments, of possibly useful variants on the PEO structure, or on the properties of a PEO + ion-pair complex. All of these problems are amenable to consideration using a combination of moleculardynamics modelling and quantum-chemical calculation techniques. We hope to carry out some of the calculations proposed above in subsequent research.

#### VI. References

- 1. M.B. Armand, J.M. Chabagno, and M.J. Duclot, in <u>Fast Ion Transport in Solids</u>, eds. P. Vashista, J.N. Mundy and G.K. Shenoy, p.131 (Elsevier North Holland, New York, 1979).
- 2. M.Z.A. Munshi and B.B. Owens, in <u>Superionic Solids and Solid Electrolytes: Recent trends</u>, eds. A.L. Lasker and S. Chandra (Academic Press, Orlando, 1987).
- 3. M. Armand, Solid State Ionics 9 and 10, 745(1983).
- 4. M.Z.A. Munshi and B.B. Owens, preprint, 1988.
- 5. M. Watanabe, K. Nagaoka, M. Kanba and I. Shinohara, Polymer J. 14, 877(1982).
- 6. J.R. Owen, in <u>Superionic Solids and Solid Electrolytes</u>, eds. A.L. Laskar and S. Chandra, p.111(Academic Press, Boston, 1989).
- 7. D.G.H. Ballard, P. Cheshire, T.S. Mann, and J.E. Przeworski, Macromolecules 23, 1257(1990).
- 8. G. Nagasubramanian and S. Di Stefano, J. Electrochem. Soc. <u>137</u>, 3830, (1990).
- 9. P. Zurer, Chem.& Eng. News, Nov.5, 1984.
- 10. P.M. Blonsky, D.F. Shriver, P. Austin, and H.R. Allcock, J. Am. Chem. Soc. <u>106</u>, 6854 (1984).
- 11. K.M. Abraham, M. Alangir, and S.J. Perrotti, J. Electrochem. Soc., Accelerated Brief Comm. 535 (Feb. 1988).

- 12. H. Rickert, <u>Electrochemistry of Solids</u>, ch. 6 (Springer-Verlag, New York, 1982); also see Ref. 24 below.
- 13. P.R. Sorensen and T. Jacobsen, Polymer Bulletin 9, 47(1983).
- 14. Discussions with S. Surampudi, G. Nagasubramanian, E. Peled, and F. McDougall, Jet Propulsion Laboratory, Pasadena, CA, August 2, 1991.
- 15. B.L. Papke, M.A. Ratner, and D.F. Shriver, J. Electrochem. Soc. <u>129</u>, 1694 (1982).
- 16. M.H. Cohen and D. Turnbull, J. Chem. Phys. 31, 1164 (1959).
- 17. D. Turnbull and M.H. Cohen, J. Chem. Phys. <u>34</u>, 120 (1961).
- 18. S. Clancy, D.F. Shriver, and L.A. Ochrymowycz, Macromolecules 19, 606 (1986).
- 19. C.K. Chiang, G.T. Davis, C.A. Harding and T. Takahashi, Macromolecules 18, 827 (1985).
- 20. R. Dupon, B.L. Papke, M.A. Ratner, and D.F. Shriver, J. Electrochem. Soc. 131, 586 (1984).
- 21. R. Hoffman, J. Chem. Phys. <u>39</u>, 1397 (1963).
- 22. M.J.S. Dewar and W. Thiel, J. Am. Chem. Soc. <u>99</u>, 4899 (1977).
- 23. See, for example, W.J. Hehre, L. Radom, P.v.R. Schleyer, and J.A. Pople, Ab Initio Molecular Orbital Theory (J. Wiley & Sons, New York, 1986).
- 24. C.P. Flynn and A.M. Stoneham, Phys. Rev. B 1, 3966 (1970).

# MODEL REDUCTION AND CONTROL OF ASTREX

Ashok Iyer\*
Associate Professor
Department of Electrical and Computer Engineering
University of Nevada, Las Vegas
Las Vegas, NV 89154

Phone: (702) 597 4183 Email: iyer@unlv.edu

Summer 1991

#### Abstract

The Advanced Space Structures Technology Research Experiments (ASTREX) is a precision structure situated at the Phillips Laboratory, Edwards Air Force Base, CA. The structure is a testbed to develop, test and validate control strategies for large-angle, three axis slewing maneuvers and vibration suppression. The ASTREX facility consists of the test article (with primary, secondary and tertiatry substructures along with mirrors. Model Reduction using Schur decomposition and balanced truncation and control strategies using state estimation and regulator design and optimization using LQG to reduce vibrations were implemented. The controller was evaluated using the full order ASTREX model.

<sup>\*</sup>Supported by Air Force Office of Scientific Research Summer Research Program

## 1 Introduction

The Advanced Space Structures Technology Research Experiments (ASTREX) is a precision structure situated at the Phillips Laboratory, Edwards Air Force Base, CA. The structure is a testbed to develop, test and validate control strategies for large-angle, three axis slewing maneuvers and vibration suppression [2] [3]. The facility is funded by Air Force and is supported by on-site staff. Number of investigators from universities and industries have been involved in the research pertaining to the control-structure interaction.

## **ASTREX Hardware Description**

The ASTREX facility [2] [3] [7] consists of a pedestal with an air bearing system on which the test article is placed. The pedestal consists of pneumatic components, electronics, power supplies and computer at its base and an air bearing with a cable follower and electronics at the other end. The front, side, top views and the Models axes system are shown in Figures 1 to 3. The desired specification of the air bearing system are:

- Load capacity 14,500 lbs.
- ±20° Pitch and Roll, ±180° Yaw
- Measure attitude to within 1 arc second at rates up to 10°/sec and accelerations up to 10°/sec/sec.
- Cable follower to bring supply lines from "Ground" to test article: Crossover frequency at least 5 Hz.

The mirror mass simulator consists of a support truss with the primary mirror, secondary mirror and a tertiary mirror. The state space model is obtained from the finite element model of the test article and the pedestal. The ASTREX hardware is summarized below:

## **ASTREX Hardware Summary**

- Facility: 40ft by 40ft by 40ft, laboratory Overhead crane, temperature control
- Air Bearing: Spherical(3-Axis) Air Bearing, 19 inch ball, cable follower:

  Two gimbal 3 axis mechanical arrangement, Rigid Body attitude sensing 1 arc sec accuracy.
- Computer: Real time Control and Data Acquisition Computer, 32 Inputs, 32 Outputs, 1000 Hz + Sampling rate, 10-15 MFLOP Parallel Processor based system.
- Structure: 3 Mirror Beam Expander, 1/3 1/2 Dynamically scaled structure, Modular Graphite Epoxy construction
- Sensors/Actuators: Throttleable Cold Gas Thrusters, up to 200 lb force.

  The accelerometers locations are given in Figure 4.
- Proof Mass Actuators
- Reaction Wheels
- Provision for Control Moment Gyroscopes
- Accelerometers

#### • Optical Line of Sight Sensor

Section 2 contains analytical development of the control system matrices from dynamical model generated by the NASTRAN program. Section 3 discusses the model reduction schemes. Section 4 contains a simple controller design and simulation results and Section 5 the conclusions.

## 2 Analytical Development

For a detailed description of the model development please see [1]. A physical structure is often represented by its dynamical model defined by an equation

$$M\ddot{x} + E\dot{x} + Kx = f \tag{1}$$

where M, E, and K are mass, viscous damping, and stiffness matrices, respectively. x is a vector representing generalized deflections (degrees of freedom) of grid points or nodes. An overdot indicates time derivative. The vector f includes forces and moments applied to the structure. The equation can be written in a state-space form as given by

such that

$$\dot{X} = AX + F \tag{3}$$

where 
$$X = \begin{bmatrix} x \\ \dot{x} \end{bmatrix}$$
,  $A = \begin{bmatrix} 0 & I \\ -M^{-1}K & -M^{-1}E \end{bmatrix}$  and  $F = \begin{bmatrix} 0 \\ M^{-1}f \end{bmatrix}$ .

A transformation from physical degrees of freedom (n) to a modal state (m modes) can be made by defining  $x = \Phi \eta$ ; the modal state vector  $\eta$  (m  $\times$  1) includes modal amplitudes, and the column of modal matrix  $\Phi$  (n  $\times$ 

m) defines the mode shape for a particular mode. The modal matrix  $\Phi$  is normalized with respect to the mass matrix M such that  $\Phi^T M \Phi = I$  and  $\Phi^T K \Phi = \Lambda$ ; I is an identity matrix, and  $\Lambda$  is a diagonal eigenvalue matrix. Using the transformation, and multip<sub>1</sub>, ing by  $\Phi^T$ , eq.(1) is given by

$$\Phi^T M \Phi \ddot{\eta} + \Phi^T E \Phi \dot{\eta} + \Phi^T K \Phi \eta = \Phi^T f$$

which from normalization, and assuming a proportional damping, reduces to

$$\ddot{\eta} + [2\zeta_{diag}\omega]\dot{\eta} + \Lambda\eta = \Phi^T f \tag{4}$$

In the diagonal modal damping matrix  $[2\zeta_{diag}\omega]$ ,  $\zeta_{diag}$  is a diagonal modal damping factor matrix, and  $\omega$  is the square-root matrix of  $\Lambda$  representing natural frequencies of the structure. The equation (4) can be written in a state space form as follows.

$$\begin{bmatrix} \dot{\eta} \\ \ddot{\eta} \end{bmatrix} = \begin{bmatrix} 0 & I \\ -\Lambda & -(2\zeta_{diag}\omega) \end{bmatrix} \begin{bmatrix} \eta \\ \dot{\eta} \end{bmatrix} + \begin{bmatrix} 0 \\ \Phi^T f \end{bmatrix}$$
 (5)

In the compact notation.

$$\dot{X}_{\eta} = A_{\eta} X_{\eta} + F_{\eta} \tag{6}$$

where  $X_{\eta} = \begin{bmatrix} \eta \\ \dot{\eta} \end{bmatrix}$ ,  $A_{\eta} = \begin{bmatrix} 0 & I \\ -\Lambda & -\zeta_{\text{mat}} \end{bmatrix}$ , and  $F_{\eta} = \begin{bmatrix} 0 \\ \Phi^{T} f \end{bmatrix}$ . The damping matrix is written as  $\zeta_{\text{mat}} = [2\zeta_{diag}\omega]$ . Due to the fullness of the modal matrix  $\Phi$ , a force on the structure, theoretically, affects all modal states.

The participation of a force or a moment, applied in certain direction on the structure, in the modal state form can be explained as follows. Let the generalized displacement vector be written as  $\mathbf{x} = \{U, V, W, \psi, \theta, \phi\}^T$ , where U, V, W are the displacement v ctors along local x, y, z coordinates, and  $\psi, \theta, \phi$  are the slope vectors about the coordinates, respectively; each vector

has dimension equal to number of nodes (numnodes  $\times$  1). The modal matrix  $\Phi$  corresponds to this particular arrangement of the generalized displacement vector x. If a force is applied at location j in the local z direction, the force vector f is given by

$$f = \begin{bmatrix} 0 \\ 0 \\ \vdots \\ 0 \\ f_{w_j} \\ \vdots \\ 0 \\ 0 \end{bmatrix}$$
 (7)

The number of zeros in the top of eq. (7) equal to 2\*numnodes + j-1, and in the bottom equal to 6\*numnodes -  $\{2*$ numnodes +  $j\}$ . This can also be written as a unit vector with all zeros except at the location of z direction at node j, multiplied by the magnitude  $f_{w_j}$ . Symbolically, it is written as  $f_{w_j} = S_{uv_{w_j}}|f_{w_j}|$ . This representation helps in relating  $F_{\eta}$  to applied force directly.

$$F_{\eta} = \left[egin{array}{c} 0 \ \Phi^T S_{uv_{wj}} \end{array}
ight] f_{wj}$$

Thus only the  $\{wj\}$  displacement contribution of the modal matrix  $\Phi$  is effective. For multiple force and moment inputs at different location or in different direction, a summation is carried out with appropriate placement unit vector:

$$F_{\eta} = \left[egin{array}{c} 0 \ \Phi^T \sum_{j} \sum_{d} [S_{uv_{dj}}.f_{d_{j}} \end{array}
ight]$$

where d signifies the degree of freedom at node j. Effectively, a unit column-

vector matrix is created leading to equation,

$$F_{\eta} = \begin{bmatrix} 0 \\ \Phi^T S_{uvmat_{di}} \end{bmatrix} u = B_{\eta} \ u \tag{8}$$

in which u is the actual control input vector (non-zero terms in f of eq. (1)), uvmat indicates that a matrix having unit vectors as columns is generated, and  $B_{\eta}$  is the control input matrix in the modal form. The force vector

$$F = \begin{bmatrix} 0 & 0 \\ 0 & M^{-1}\Phi^{-T} \end{bmatrix} F_{\eta} = \begin{bmatrix} 0 & 0 \\ 0 & \Phi \end{bmatrix} B_{\eta}u = B u$$

$$(3)$$

where B is the influence matrix which could also be formulated from equation (2).

The output equation is given by  $y = ax + b\dot{x} + c\ddot{x}$ . The a, b, and c matrices provide the combination of displacement, velocity, and acceleration output from the sensors. The equation can be written as

$$y = \begin{bmatrix} a & b \end{bmatrix} \begin{bmatrix} x \\ \dot{x} \end{bmatrix} + \begin{bmatrix} 0 & c \end{bmatrix} \begin{bmatrix} \dot{x} \\ \ddot{x} \end{bmatrix}$$
$$y = \begin{bmatrix} a & b \end{bmatrix} X + \begin{bmatrix} 0 & c \end{bmatrix} [AX + F]$$

Using the transformation relation

$$A\left[\begin{array}{cc} \Phi & 0 \\ 0 & \Phi \end{array}\right] = \left[\begin{array}{cc} \Phi & 0 \\ 0 & \Phi \end{array}\right] A_{\eta}$$

and substituting for X, the output equation can be written in the modal form as

$$y = C_n X_n + D_n u \tag{10}$$

This equation is used to obtain response of the system.

The resulting state space model

$$\dot{x} = A_{\eta}X + B_{\eta}u$$

$$y = C_{\eta}x + D_{\eta}u \tag{11}$$

where  $A_{\eta} \in R^{50 \times 50}, B_{\eta} \in R^{50 \times 8}, C_{\eta} \in R^{9 \times 50}$  and  $D_{\eta} \in R^{9 \times 8}$ .

## 3 Model Reduction

A Schur method for balanced Model Reduction was used [9]. This reduction method overcomes the ill conditioning problems encountered in reduction procedures of most non-minimal models. The Moore reduced model [6] can be directly computed without balancing via projections defined in terms of arbitrary bases for the left and right eigenspaces associated with the "large" eigenvalues of the product PQ of the reachability and controllability grammians.

A brief discussion of the model reduction theory is presented here. Further details can be obtained from [9]. The general procedure of calculating a  $k^{th}$  order reduced model  $\hat{S}$  is given below.

#### Procedure

Input Data A, B, C, D, k

Step 1 Compute the matrices  $V_{R,BIG}, V_{L,BIG} \in R^{n \times k}$  whose columns are bases for the respective right and left eigenspaces of PQ associated with the "big" eigenvalues  $\sigma_1^2, \ldots, \sigma_k^2$ .

Step 2 Let

$$E_{BIG} := V_{L,BIG}^T V_{R,BIG}$$

and compute its singular value decomposition

$$U_{E,BIG}\Sigma_{E,BIG}V_{E,BIG}^T = E_{BIG}$$

Step 3 Let

$$S_{L,BIG} := V_{L,BIG} U_{E,BIG} \Sigma_{E,BIG}^{\frac{1}{2}} \qquad \in R^{n \times k}$$

$$S_{R,BIG} := V_{R,BIG} V_{E,BIG} \Sigma_{E,BIG}^{\frac{1}{2}} \qquad \in R^{n \times k}$$

and compute the state space realization of  $\hat{S}$ 

$$\begin{bmatrix} \hat{A} & \hat{B} \\ \hat{C} & \hat{D} \end{bmatrix} := \begin{bmatrix} S_{L,BIG}AS_{R,BIG} & S_{L,BIG}^TB \\ CS_{R,BIG} & D \end{bmatrix}$$

End of Procedure

Schur Method The numerical robustness of the procedure outlined in the previous section depends precisely how the bases  $V_{R,BIG}$  and  $V_{L,BIG}$  in Step 1 are computed and the properties of these bases. The first k columns of the matrices  $T_{BAL}^{-1}$  and  $T_{BAL}^{T}$  would be one choice for  $V_{R,BIG}$  and  $V_{L,BIG}$ , respectively. However as mentioned before, the computation of the balanced transform  $T_{BAL}$  may be numerically ill-conditioned.

To address the problem the following procedure based on the Schur decomposition of PQ computing orthonormal bases  $V_R$ ,  $V_L$  is proposed. As is well known, the use of orthonormal transformations tends to promote numerical stability in algorithms. This procedure described in detail in  $[\ ]$ , is outlined below.

#### Procedure

Step 1 Solve for P and Q via the Lyapunov equations

$$PA^T + AP + BB^T = 0$$

$$A^TQ + QA + C^TC = 0$$

- Step 2 Compute the orthogonal real matrix V such that  $VPQV^T$  is upper right triangular, i.e. put PQ in real Schur form.
- Step 3 Using orthogonal Givens rotations (e.g. [6]) compute orthogonal real transformations  $V_A$  and  $V_D$  which order the Schur forms in the ascending and descending order respectively:

$$V_A^T P Q V_A = \begin{bmatrix} \lambda_{A_n} & * & * & \cdots & * \\ 0 & \lambda_{A_{n-1}} & * & \cdots & * \\ \vdots & \cdots & \cdots & \cdots & \cdots \\ 0 & \cdots & \cdots & 0 & \lambda_{A_1} \end{bmatrix}$$

$$V_D^T P Q V_D = \begin{bmatrix} \lambda_{D_n} & * & * & \cdots & * \\ 0 & \lambda_{D_{n-1}} & * & \cdots & * \\ \vdots & \cdots & \cdots & \cdots & \cdots \\ 0 & \cdots & \cdots & 0 & \lambda_{D_1} \end{bmatrix}$$

such that

$$\{\lambda_{A_i} \mid i=1,\ldots,k\}$$

$$= \{\lambda_{D_i} \mid i=1,\ldots,k\}$$

$$= \{\sigma_i^2 \mid i=1,\ldots,k\}$$

$$egin{array}{lll} \{\lambda_{A_i} & | i = k+1, \ldots, n \} \ = & \{\lambda_{D_i} & | i = k+1, \ldots, n \} \ = & \{\sigma_i^2 & | i = k+1, \ldots, n \} \end{array}$$

Step 4 Partition  $V_A$  and  $V_D$  as

$$V_A = \left[\begin{array}{c|c} \frac{n-k}{V_{R,SMALL}} & \frac{k}{V_{L,BIG}} \end{array}\right]$$

$$V_A = \left[ \begin{array}{c|c} k & n-k \\ \hline V_{R,BIG} & V_{L,SMALL} \end{array} \right]$$

**End of Procedure** 

# 4 ASTREX Controller Design and Simulation

The Schur model reduction described in the earlier section was used. Actuator dynamics were not modeled as the actuator dynamics were very fast compared to the system dynamics. The 50th order system was reduced to an 8th order system. Using this reduced 8th order system, a Kalman Filter for state reconstruction was constructed. The 8th order system described by

$$\dot{x}_r = A_r x_r + B_r u + Gw$$

$$y = C_r x + D_r u + v \tag{12}$$

where  $A_r \in R^{8\times 8}$ ,  $B_r \in R^{8\times 8}$ ,  $C_r \in R^{9\times 8}$  and  $D_r \in R^{9\times 8}$ . Here w is the input disturbance and G is the input disturbance matrix. v is the measurement noise. The noise intensity matrices are defined as

$$E(Gw(t)w'(\tau)G') = Q_{xx}\delta(t-\tau)$$

$$E(v(t)v'(\tau)) = Q_{yy}\delta(t-\tau)$$

$$E(Gw(t)v'(\tau)) = Q_{xy}\delta(t-\tau)$$

where E is the expectation operator and  $\delta$  is the Dirac delta function. w and v were assumed to be white noise with zero mean. input and output disturbances were assumed to be uncorelated, and hence the matrix  $Q_{xy}$  was

taken to be the null matrix. For the simulation  $Q_{xx}$  and  $Q_{yy}$  were taken as identity matrices.

A linear optimal regulator was then designed under the assumption of ful! state feedback (obtained via the Kalman Filter). The quadratic cost functions was of the form

$$J(x,u) = \int_{0}^{\infty} (x'_{r}R_{xx}x_{r} + u'R_{uu}u)dt$$

The design weighting matrices  $R_{xx}$  and  $R_{uu}$  were taken as identity matrices.

Using the the estimated states and the optimal regulator a Linear Quadratic Compensator was designed. This compensator designed for the reduced order system was then used to simulate the full order system. Simulation for regulation using initial conditions  $x_i(0) = \frac{1}{w_i^2}$  results for the outputs for the secondary displacements in the x, y and z directions are shown in Figures 5 (open loop) and Figures 6 (closed loop).

## 5 Conclusion

A Schur method for balanced Model Reduction was used. This reduction method overcomes the ill conditioning problems encountered in reduction procedures of most non-minimal models. Using the reduced order model, a Kalman filter to estimate the states and a linear optimal regulator was designed. Using the the estimated states and the optimal regulator a Linear Quadratic Compensator was designed. This compensator designed for the reduced order system was then used to simulate the full order system. Simulation for regulation using initial conditions

This study is an initial attempt to control the ASTREX structure. Only the flexible modes were considered. The model needs to be improved to include the rigid modes also. Non-linear coupling may also be a major factor if large angle maneuvers are to be considered. Future work will include models that have the rigid modes. Optimal controllers will be designed along the lines described in [4] [11] [12] and [10] will be designed and implemented.

## 6 Acknowledgment

The author wishes to express his sincere thanks to Dr. Alok Das and Mr. Kevin Slimak for the opportunity which they provided and their support during the course of this research. It is also pleasure to thank Mr. Joel Berg, Dr. Nandu Abhyankar and Mr. Monty Smith for many useful discussions.

# References

- [1] Abhyankar, N. S. and Berg, J. L., "ASTREX Model Information: Supplement to astabed.mat file", AFAL, Philips Lab Report, August 1991.
- [2] Alok Das, "Large Angle Maneuver Experiments in Ground-Based Laboratories", AIAA Progress Report in Astronautics and Aeronautics: Mechanics and Control of Large Flexible Structures, Editor: John Junkins, Vol. 129, pp491-506, 1990.
- [3] Alok Das, Berg, J. L., Norris, G. A., Cossey, D. F., Strange, J. T. and Schlaegel, W. T., "ASTREX- A Unique Test Bed for CSI Research", Proceedings of the 29th. IEEE Conference on Decision and Control, Honolulu, Hawaii, pp 2018-2023, 1990.
- [4] Glover, K. and Doyle, J., "State-space formulae for all stabilizing controllers that satisfy an  $H_{\infty}$ -norm bound and relations to risk sensitivity", System and Control Letters, 11, pp 167-162, 1988.

- [5] Hu, A., Skelton, R. E., Norris, G. A. and Cossey, D. F., "Selection of Sensors and Actuators with Applications to the ASTREX Facility", 4th NASA/DOD CSI Conference, Orlando, FL, Nov. 1990.
- [6] Moore, B. C., "Principal component analysis in linear systems: controllability, observeability, and model reduction," *IEEE Transactions on Automatic Control*, AC-26, pp 17-31, 1981.
- [7] Ramakrishnan, J., Byun, K. W., and Skelton, R., "ASTREX Controller Design: OVC and OCC Approach", 4th NASA/DOD CSI Conference,, Orlando, FL, Nov. 1990.
- [8] Rao, V., Ngo, K., Berg, J. L. and Das A., "Deravation of Reduced Order Models for Large Flexible Structrures", AIAA Guidance, Navigation and Control Conference, New Orleans, LA, 1991.
- [9] Safonov, M. G. and Chiang, R. Y., "A Schur Method for Balanced Model Reduction", IEEE Conference on Decision and Control, Tampa, Florida, pp 1036-1040, 1989.
- [10] Sparks, A. G., Yeh, H. H., Banda, S. S., "Mixed  $H_2$  and  $H_{\infty}$  Optimal Robust Control Design", Optimal Control, Applications and Methods, Vol. 11, pp 307-325, 1990.
- [11] Vidyasagar, M. and Kimura, H., "Robust Controllers for Uncertain Linear Multivariable Systems", Automatica, Vol 22, No. 1, pp 85-94, 1986.
- [12] Zhou, K. and Khargonekar, P., "An algebraic Ricatti equation approach to  $H_{\infty}$  optimization", System and Control Letters, 11, pp 85-91, 1988.

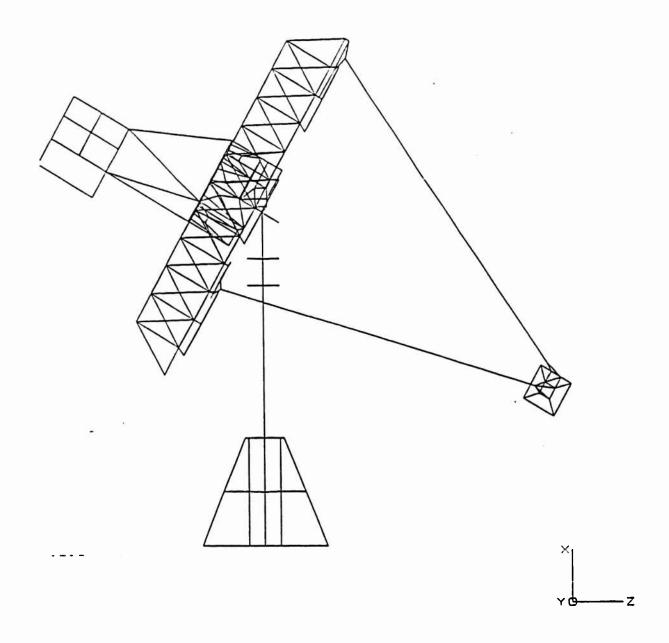


Figure 1: ASTREX Structures Side View

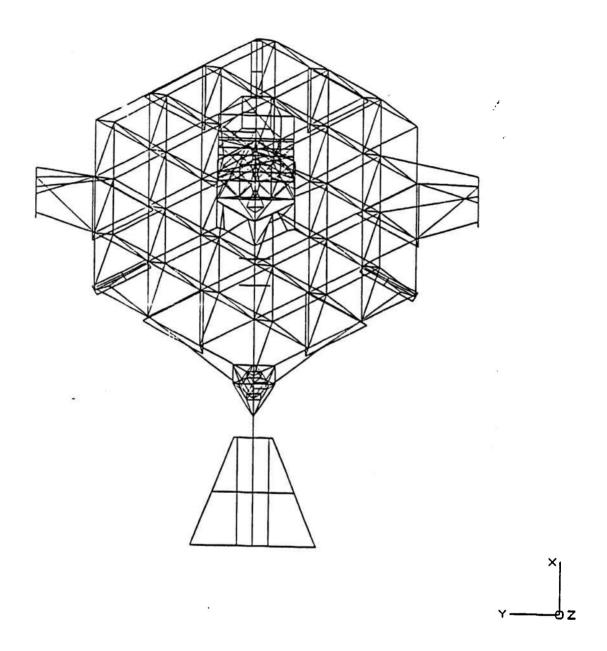


Figure 2: ASTREX Structures Front View

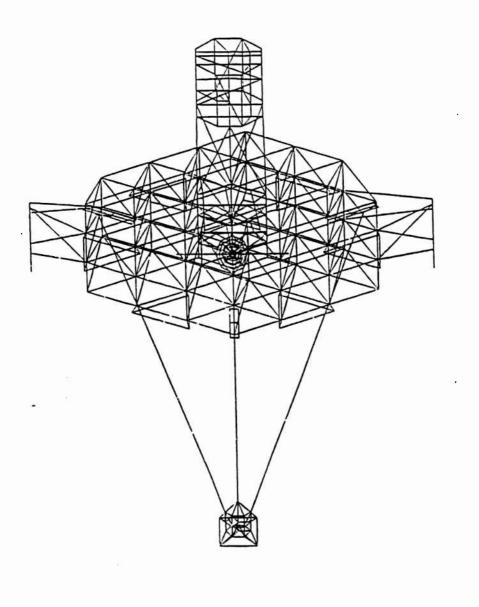


Figure 3: ASTREX Structures Top View

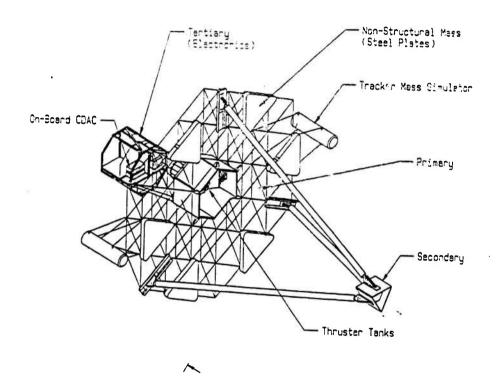


Figure 4: ASTREX Accelerometers Locations

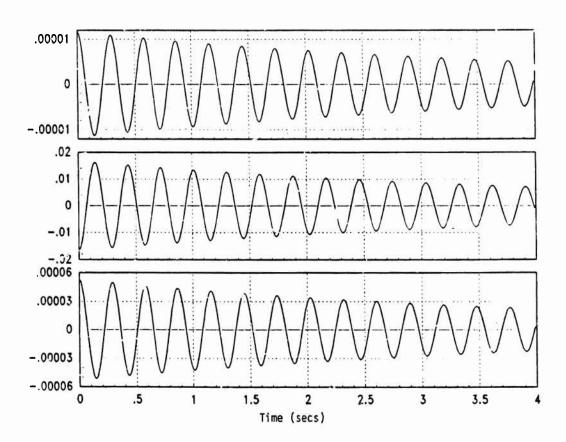


Figure 5: Secondary Deflections x, y, z directions, Openloop

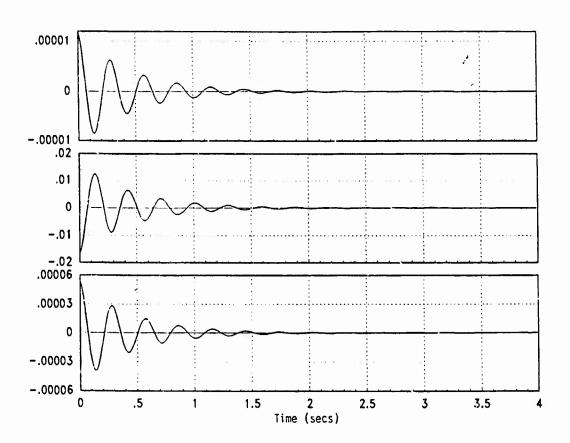


Figure 6: Secondary Deflections x, y, z directions, Closedloop

# Research in Emerging Technologies at Phillips Laboratory

P.W. Langhoff<sup>†</sup>

Department of Chemistry Indiana University Bloomington, IN 47405

### Abstract

Progress is reported in theoretical and computational studies related to the research interests of the Emerging Technology Branch at Phillips Laboratory, Edwards AFB. Topical areas under investigation include (i) photoassisted formation and detection of metal diatomic molecules, (ii) aspects of hightemperature solar absorbers for rocket propulsion systems, (iii) homopolar induction as a zero-point energy device, (iv) spectra of trapped atomic radicals, and (v) metal atom recombination dynamics in cold fluids. Individual technical reports in each topical area are in preparation and will be provided subsequently. Attention centers here on report of progress in studies of the formation and detection of metal diatomics and in related aspects of high-temperature absorbers for the solar rocket program. Specifically, calculations are performed of AlLi absorption profiles, estimates are provided of Ramanassisted formation rates of this compound, and the thermodynamics and spectral lineshapes of Li vapor in H<sub>2</sub> and buffer gases are investigated.

† AFOSR Summer Faculty Research Associate - 1991

# Outline of Report

- 1. Introduction
- 2. Photon Assisted Formation and Detection of Metal Diatomics
  - a. Gas-Phase Thermal Formation and Detection of AlLi
  - b. Gas-Phase Photon-Assisted Formation of AlLi
- 3. Solar Radiation Absorbers for Rocket Propulsion Systems
  - a. Background Information
  - b. Larson Plasma Spectroscopy Cell
  - c. Li(v)/H<sub>2</sub> Thermodynamics
  - d. Lineshape Analysis of Measured Li(v) Spectra
- 4. Concluding Remarks

## 1. Introduction

Progress is reported of studies initiated in the Emerging Technologies Branch of the Phillips Research Laboratory at Edwards Air Force Base during the summer of 1991. A number of topical areas of study were identified, related to the research interests of Branch personnel, preliminary results obtained in each case, and of continuing study devised. Specific technical areas of interest include: (i) photoassisted formation and detection of metal diatomic molecules, with particular reference to AlLi, (ii) aspects of high-temperature solar absorbers for rocket propulsion systems, (iii) homopolar induction as a zero-point energy device, (iv) spectra of trapped atomic radicals, and (v) metal atom recombination dynamics in cold fluids.

The present interim report focuses on progress made in theoretical studies of the formation and detection of AlLi molecules, and of the thermodynamics and spectra of Li(v) in H<sub>2</sub> and inert buffer gas. Specifically, calculations are reported of AlLi absorption profiles, of aspects of dynamics in the 2,3  $^{1}\Sigma^{+}$  vibrational manifold, and of estimates of Raman-assisted formation rates of this compound. These studies are in support of experimental determinations of Raman-assisted formation of AlLi employing merged-beam techniques in progress in the Branch. The Li(v) studies reported include description of statistical mechanical methods for estimates of equilibrium concentrations of  $Li_xH_y(v)$  compounds at high temperature, and of spectral lineshapes of Li(v) in absorption in H<sub>2</sub> and buffer gases. Comparisons are made vith recent concomitant experimental spectrtal studies in the Branch, which are seen to be clarified on basis of the present work.

Subsequent more technical reports dealing with each topic (i)

to (v) on an individual basis are provided separately.

2. Photon Assisted Formation and Detection of Metal Diatomics

Two distinct topical areas are studied in connection with the formation and detection of metal diatomic molecules, with particular reference to the molecule AlLi. These are:

2a. Gas-Phase Thermal Formation:

$$Al + Li + M \rightarrow AlLi + M^*$$

Vibrational Dynamics in the 2,3  $^1\Sigma^+$  Manifold of AlLi is studies as a possible detection mechanism of this compound.

2b. Gas-Phase Photon Assisted Formation:

$$Al + Li + h
u_{lpha} 
ightarrow AlLi + h
u_{eta}$$

The theory of resonance Raman-assisted molecular formation is applied to AlLi formation at high temperature and cross sectional estimates are provided.

## 2a. Gas-Phase Thermal Formation and Detection of AlLi

A number of specific tasks are identified and investigated in this topical area, including tasks to:

- Verify All 2,3  $^1\Sigma^+$  and 2  $^1\Pi$  Vibrational Energy Levels
- Study Photoabsorption into Adiabatic States
- Study Photoabsorption into Diabatic States
- Study Photoabsorption into Coupled States
- Study T Dependence of Cross Section
- Study Coherence and Interference Effects
- Consider Pulse-Probe Experiments

The relevant calculations are performed employing explicitly time-dependent computational methods for spectral studies described in the following. The first two items indicated have been largely completed, whereas the other areas are presently under study and will be reported on subsequently.

# Time-Dependent Approach to Spectra

$$(H-i\partial/\partial t)\Psi(x,t)=0;\;\Psi(x,t=0)=\Phi(x)$$

# Autocorrelation Function:

$$A(t) = <\Phi(x)|\Psi(x,t)>$$

## **Spectral Function:**

$$S(E) = (1/2\pi)^{1/2} \int_{-T}^{+T} dt A(t) e^{iEt}$$
  
=  $\sum_{n} |C_n|^2 \delta_T(E - E_n)$ 

## Eigenstates:

$$egin{aligned} ar{\Psi}_E(x) &= (1/2\pi)^{1/2} \int_{-T}^{+T} dt \Psi(x,t) e^{iEt} \ &= \sum_n C_n \Phi_n(x) \delta_T(E-E_n) \end{aligned}$$

# Lineshape Function:

$$\delta_T(E - E_n) = (1/\pi) \frac{\sin(E - E_n)T}{(E - E_n)}$$

## 2b. Photon Assisted Formation and Detection of LiAl

Experiments for the photon-assisted formation and detection of AlLi are in progress at Phillips Laboratory of Edwards AFB. Supporting theoretical studies entail calculations of cross sections for the relevant Raman process.

Raman-Assisted Molecular Formation Rate:

$$rac{d(N_{AlLi}/V)}{dt} = k_{rate}(N_{Al}/V)(N_{Li}/V)$$

$$k_{rate} = V \sum_{lpha} P_{lpha} rac{I_{lpha}}{h 
u_{lpha}} rac{1}{g_{lpha}} \sum_{eta} \sigma_{lpha 
ightarrow eta}(h 
u_{lpha})$$

$$lpha \Rightarrow \{ \vec{K}_{lpha}, \vec{k}_{lpha}, \gamma_{lpha}, g_{lpha}, I_{lpha} \}$$

$$\beta \Rightarrow \{\vec{K}_{\beta}, v_{\beta}, J_{\beta}, M_{\beta}, ^{1}\Sigma^{+}\}$$

where  $\alpha$  and  $\beta$  refer to initial and final quantum states.

## Raman Cross Section

The Raman rate constant requires values of the appropriate cross section, given as follows for unpolarized isotropic radiation:

$$\sigma_{lpha 
ightarrow eta}(h
u_lpha) = rac{128\pi^5}{9\lambda_eta^4} \sum_{m{i}} \sum_{j} ||^2$$

$$= \sum_{\gamma} igg\{ rac{<\gamma|\hat{\mu_i}|eta>}{E_{\gamma}-i\Gamma_{\gamma}/2-E_{lpha}-h
u_{lpha}}$$

$$+rac{<\gamma|\hat{\mu_j}|eta>}{E_{\gamma}-i\Gamma_{\gamma}/2-E_{eta}-h
u_{eta}} igg\}$$

$$\gamma \Rightarrow \{\vec{K}_{\gamma}, \vec{k}_{\gamma}, \gamma_{\gamma}\}$$

where  $\gamma$  refers to intermediate quantum state.

# Application to AlLi Formation at High T

Applications of the general theory to the case of AlLi formation entail a number of appropriate assumptions:

Treat Rotation Classically

Consider 2,3  $^{1}\Sigma^{+}$  and 2  $^{1}\Pi$  States Only

Neglect Non-Resonant Raman Term

Assume Broad-Band Excitation

In this case the rate constant takes the form:

$$k_{rate} 
ightarrow rac{V}{q(V,T)} \int_0^\infty d\epsilon_lpha e^{-\epsilon_lpha/kT} rac{1}{4\pi} \int_0^\pi \int_0^{2\pi} d\Omega$$

$$\int_0^\infty d(h\nu_\alpha) \frac{I_0}{h\nu_\alpha} L(h\nu_\alpha) \frac{1}{g_\alpha^{(cl)}} \sum_{\nu_\beta} \sigma_{\alpha \to \beta}(h\nu_\alpha)$$

where  $\sigma_{\alpha \to \beta}(h\nu_{\alpha})$  refers to the Raman cross section obtained under the indicated assumptions and is given further below.

# Application to AlLi Formation at High

Here, q(V,T) is the translational partition function

$$q(V,T) = V(2\pi\mu_M kT/h^2)^{3/2}$$

and

$$\sigma_{lpha
ightarroweta}(h
u_{lpha})=rac{128\pi^{5}}{9\lambda_{eta}^{4}}\sum_{m{i}}\sum_{j}||^{2}$$

is the Raman cross section, with

$$ightarrow \sum_{m{\gamma}=\Sigma}^{\Pi} \int_{0}^{\infty} d\epsilon_{m{\gamma}}$$

$$\left\{\frac{< k_{\alpha}|\hat{\mu_{j}}^{(\gamma)}(\vec{R})|k_{\gamma}>< k_{\gamma}|\hat{\mu_{i}}^{(\gamma)}(\vec{R})|v_{\beta}>}{E_{\gamma}^{(el)}(\infty) - i\Gamma/2 - E_{\alpha}^{(el)}(\infty) + \epsilon_{\gamma} - \epsilon_{\alpha} - h\nu_{\alpha}}\right\}$$

# Application to AlLi Formation at High T

Introduction of the indicated assumptions gives rise to the following final expressions:

$$egin{aligned} k_{rate} &
ightarrow \{(h^2/2\pi\mu_M kT)^{3/2}\} \left\{rac{I_0}{h
u_0}
ight\} \ & \left\{\int_0^\infty d\epsilon_lpha e^{-\epsilon_lpha/kT}rac{1}{g_lpha^{(el)}}\sum_{v_eta}ar{\sigma}_{lpha
ightarroweta} 
ight\} \ & ar{\sigma}_{lpha
ightarroweta} &= rac{128\pi^5}{9\lambda_eta^4} \ & \left\{\left|\int_0^\infty d\epsilon_\gammarac{< k_lpha|\hat{\mu}_{\parallel}^{(\Sigma)}|k_\gamma>< k_\gamma|\hat{\mu}_{\parallel}^{(\Sigma)}|v_eta>}{\epsilon_\gamma-\epsilon_lpha-i\Gamma/2}
ight|^2 \ & +2\left|\int_0^\infty d\epsilon_\gammarac{< k_lpha|\hat{\mu}_{\perp}^{(\Pi)}|k_\gamma>< k_\gamma|\hat{\mu}_{\perp}^{(\Pi)}|v_eta>}{\epsilon_\gamma-\epsilon_\gamma-i\Gamma/2}
ight|^2 
ight\} \end{aligned}$$

where the last expressions refer to body-frame quantities.

# Final Expression/Numerical Evaluation

$$k_{rate}
ightarrow \left\{rac{h^2}{2\pi\mu_M kT}
ight\}^{3/2} \left\{rac{I_0L(h
u_0)}{h
u_0/kT}
ight\} \left\{\sigma_{RR}(h
u_0)
ight\}$$

$$\sigma_{RR}(h
u_0) = rac{1}{g_{lpha^{(el)}}} \{\sigma_{\parallel}(h
u_0) + 2\sigma_{\perp}(h
u_0)\}$$

$$\sigma_{\parallel}(h
u_0) = rac{1}{\Gamma}iggl\{rac{64\pi^3}{3c^3}\sum_{m{v_eta}}rac{
u_{m{eta}}^4}{
u_{m{lpha}}}| < v_{\Sigma}^{max}|\mu_{\parallel}(R)|v_{m{eta}}>|^2iggr\}$$

$$\left\{rac{8\pi^3}{3\lambda_0}ig| < k_lpha |\mu_\parallel(R)|v_\Sigma^{max}>ig|_{lpha o 0}^2
ight\}$$

$$\sigma_{\perp}(h
u_0) = rac{2}{\Gamma}iggl\{rac{64\pi^3}{3c^3}\sum_{m{v}_m{eta}}rac{
u_m{eta}^4}{
u_lpha}| < v_\Pi^{max}|\mu_\perp(R)|v_eta>|^2iggr\}$$

$$\left\{rac{8\pi^3}{3\lambda_0}ig| < k_lpha ig|\mu_\perp(R)ig|v_\Pi^{max} > ig|_{lpha o 0}^2
ight\}$$

These results have been employed to obtain numerical values.

3. Solar Absorbers for Rocket Propulsion Systems

Attention focuses in the present studies on theoretical work in support of experiments performed in the Larson Plasma Spectroscopy Cell on Li(v) in H<sub>2</sub> and other flow gases. The following issues are addressed:

- a. Background Information
- b. The Larson Plasma Spectroscopy Cell
- c. Li(v)/H<sub>2</sub>(g) Thermodynamics
- d. Lineshape Analysis of Measured Spectra

# 3a. Background Information - Solar Rocket

Important issues associated with the solar rocket program include the concentration, absorption, and transfer of solar energy to a flowing H<sub>2</sub> gas:

- $\bullet$  Concentrate  $\approx$  kWs of Solar Radiation from  $\approx$  0.1 W/cm² to  $\approx$  50 100 W/cm²
- $\bullet$  Absorb  $\approx$  kWs of Solar Radiation at  $\approx$  50 100  $W/cm^2$
- Pass ≈ kWs of Heat Through an Apparatus
- Transfer  $\approx$  kWs of Heat Into H<sub>2</sub> Flow
- Extract  $\approx$  kWs From H<sub>2</sub> Flow for Thrust

These issues are addressed differently in the three or four classes of solar rocket devices presently under study. Possible approaches to the problem of conversion of high-flux-density solar radiation into useful thrust include:

- Radiation  $\rightarrow$  Solid  $\rightarrow$  H<sub>2</sub> Flow
- Radiation  $\rightarrow$  Fluid  $\rightarrow$  Solid  $\rightarrow$  H<sub>2</sub> Flow
- Radiation → Fluid/H<sub>2</sub> Flow

# 3b. The Larson Plasma Spectroscopy Cell

The Larson PSC is designed to study the case of radiation  $\rightarrow$  fluid/ $H_2$  flow. It has a number of additional attributes which make it suitable for study of high-temperature solar absorbers:

- Studies Radiation  $\rightarrow$  Fluid/H<sub>2</sub> Flow
- ullet Equillibrium Achieved Thru Slow Flow ( ${
  m V}_tpprox 55$  liters,  $\dot{V}pprox 3$  liters/min)
- $\bullet$  Appropriate Operating Range:  $\rightarrow$  3,000 °K,  $\rightarrow$  100 atmospheres
- Exhibits Steady Flow Mode Adequate Optical Access
- Reproducible Spectral Absorbance Profiles

In the following the thermodynamics of and spectra obtained from the PSC are considered explicitly.

3c. Li(v)/H<sub>2</sub>(g) Thermodynamics

**Basic Neutral Stoichiometry:** 

$$xLi(v) + (y/2)H_2(g) \leftrightarrow Li_xH_y(v)$$

Thermodynamics/Statistical Mechanics:

$$rac{[Li_xH_y]}{[Li]^x[H_2]^{(y/2)}}\equiv K_N(T)$$

$$K_N(T) = \frac{\{Q_{Li_xH_y}(V,T)/V\}}{\{Q_{Li}(V,T)/V\}^x\{Q_{H_2}(V,T)/V\}^{(y/2)}}$$

Molecular Partition Function:

$$Q_M^{(0)}(V,T) = \sum_{j=0}^\infty e^{-\epsilon_j/kT}$$

In the following explicit expressions are derived for the evaluation of the indicated quantitites.

## **Molecular Partition Functions**

Molecular partition functions are obtained for the defining relation:

$$Q_M^{(0)}(V,T) = \sum_{j=0}^{\infty} e^{-\epsilon_j/kT}$$

$$=Q_M^{(trans)}(V,T)Q_M^{(el)}(T)Q_M^{(vib)}(T)Q_M^{(rot-nucl)}(T)$$

evaluated in the classical limit appropriate to high temperature:

$$Q_M^{(0)}(V,T) \rightarrow \frac{g_{el}}{\gamma_M} \int_1 \cdots \int_n d\vec{r}_1 \cdots d\vec{r}_n e^{-U_n/kT}$$

$$(2\pi/h)^n \int_1 \cdots \int_n d\vec{p_1} \cdots d\vec{p_n} e^{-T_n/kT}$$

where the last (kinetic) term cancels in the rate constant expression and need not be evaluated explicitly.

## Classical Limit of the Molecular Partition Function

The partition function is evaluated in the fom:

$$Q_M^{(0)}(V,T) \rightarrow \frac{g_{el}V}{\gamma_M} \int_2 \cdots \int_n d\vec{r}_2 \cdots d\vec{r}_n e^{-U_n/kT}$$

$$\frac{Q_M^{(0)}(V,T)}{N_1(T)} \to \frac{v(T)g_{el}}{\gamma_M} \int_2 \cdots \int_n d\vec{r}_2 \cdots d\vec{r}_n e^{-U_n/kT}$$

$$ightarrow rac{v(T)g_{el}}{\gamma_M}Q_M^{(int)}(T)$$

where:

$$v(T) = (4/3 \cdot 10^3) T(^{\circ}K) (cm^{-24})$$

and

$$N_1(T) = (2.69X10^{19})(298.15/T(^{\circ}K))(cm^{-3})$$

is the volume per molecule at the indicated temperature and 1 atmosphere pressure.

# Final Result - Equilibrium Constant

The final result for the classical approximation to the equilibrium constant is obtained in the form:

$$xLi(v) + (y/2)H_2(g) \leftrightarrow Li_xH_y(v)$$

$$K_N(T) = AT^{(\frac{1}{2} - \frac{x}{2} - \frac{y}{4})} e^{-\Delta E_0^{(0)}/RT}$$

where

$$A = \frac{(g_{el}/\gamma_M) \prod_{j=1}^{x+y-1} \{4\pi R_j^2 (R/D_j)^{1/2}\}}{2^x \{2\pi R_{H_2}^2 (R/D_{H_2})^{1/2}\}^{\frac{y}{4}} \{(4/3)X10^3\}^{x+\frac{y}{2}-1}}$$

$$\Delta V_j = 4\pi R_j^2 \Delta R_j$$

$$\Delta R_j = (RT/D_j)^{1/2}$$

$$\Delta E_0^{(0)} = E_0 (Li_x H_y) - (y/2)E_0 (H_2) - xE_0 (Li)$$

$$\frac{(N_{Li_x H_y}/N_1)}{(N_{Li_z}/N_1)^x (N_{H_2}/N_1)^{(y/2)}} \equiv K_N(T)$$

# Ion Chemistry

Equilibrium constants are also require for ionic species. The basic ion stoichiometry is:

$$(x-1)Li(v) + Li^+(v) + (y/2)H_2(g) \leftrightarrow Li_xH_y(v)^+$$
 
$$Li(v) \leftrightarrow Li^+(v) + e^-$$

where the thermodynamics/statistical mechanics expressions are:

$$\frac{[(Li_xH_y)^+]}{[Li]^{(x-1)}[H_2]^{(y/2)}[Li^+]} = K_N^+(T) =$$

$$\frac{\{Q_{Li_xH_v^+}(V,T)/V\}}{\{Q_{Li}(V,T)/V\}^{x-1}\{Q_{H_2}(V,T)/V\}^{(\frac{y}{2})}Q_{Li^+}(V,T)/V}$$

$$\frac{[Li^+][e^-]}{[Li]} = \frac{\{Q_{Li^+}(V,T)/V\}\{Q_{e^-}(V,T)/V\}}{\{Q_{Li}/V\}}$$

# Ion Chemistry - Final Result

Final expressions for the ion chemistry equilibrium constants are obtained in the form:

$$(x-1)Li(v) + Li^{+}(v) + (y/2)H_{2}(g) \leftrightarrow Li_{x}H_{y}(v)^{+}$$

$$Li(v) \leftrightarrow Li^{+}(v) + e^{-}$$

$$\frac{\{Q_{Li}+(V,T)/V\}\{Q_{e^{-}}(V,T)/V\}}{\{Q_{Li}/V\}} = K_{Li}^{+}(T)$$

$$K_{Li}^{+}(T) = \left(\frac{2\pi m_{e}kT}{h^{2}}\right)^{3/2}e^{-E_{ip}/RT}$$

$$= (2.415X10^{15})T^{3/2}e^{-E_{ip}/RT}$$

$$[Li^{+}] \approx [e^{-}]$$

$$\frac{[(Li_{x}H_{y})^{+}]}{[Li]^{(x-\frac{1}{2})}[H_{2}]^{(\frac{y}{2})}} = K_{N}^{+}(T)$$

$$= (4.91X10^{7})A^{+}T^{(\frac{5}{4} - \frac{x}{2} - \frac{y}{4})}e^{-(\Delta E_{0}^{(0)} + E_{ip}/2)/RT}$$

which are in form suitable for numerical evaluation.

# 3d. Lineshape Analysis

The transmission function in the wings of an atomic or molecular absorption line can be written in the Lorentzian form:

$$T_x(h
u) = I_x(h
u)/I_0(h
u)$$
 $= exp\{-\sigma(h
u)(N_{Li}/V)x\}$ 
 $\sigma(E) = rac{f(\delta/2\pi)}{(E-E_0)^2 + (\delta/2)^2}(1.1X10^{-16}cm^2)$ 
 $T_x(E_0 \pm \Delta E/2) = 1/2$ 
 $rac{\Delta E}{E_0} = rac{2}{E_0} \left\{ rac{f(\delta/2\pi)(N_{Li}/V)x}{ln(2)} 
ight\}^{1/2} (1.1X10^{-8})$ 
 $rac{\Delta E}{E_0} pprox rac{\Delta \lambda}{\lambda_0}$ 

Corresponding measured data (see below) are:

$$\left\{\frac{\Delta\lambda}{\lambda_0}\right\}_{exp} = \{0; 1.04; 5.22; 7.45; 9.69; 19.4\}X10^{-2}$$

# Summary of Linewidth Factors

In the case of atomic Li the three dominant linewidth factors are:

1. Natural Width of Li 2p → 2s Line:

$$\delta_n = 1.95 X 10^{-4} cm^{-1}$$

2. Doppler Width  $\{T = 1,600 \text{ °K}\}$ :

$$\delta_d = rac{2}{c} 
u_0 igg(rac{2RTLn2}{M}igg)^{1/2}$$

$$=0.161cm^{-1}$$

3. Pressure Width  $\{(N/V) \approx 5X10^{18} \text{ cm}^{-3}\}$ :

$$\delta_P = C_{Li-M}(N/V)_M$$

$$C_{Li-M} \approx (0.1 - 5.0)X10^{-19} cm^{-1}/cm^{-3}$$

$$\delta_P \approx (0.05 - 2.5)cm^{-1}$$

Summary of Selected Spectral Data

The measured linewidths indicated above refer to the following experimantal conditions:

Pressure  $\approx 1$  atmosphere in all cases.

Temperature  $\approx$  1600 °K in all cases.

Number Density  $\approx 5.0 \times 10^{18}$  atoms/cm<sup>3</sup>

Li, He / Ar Data:

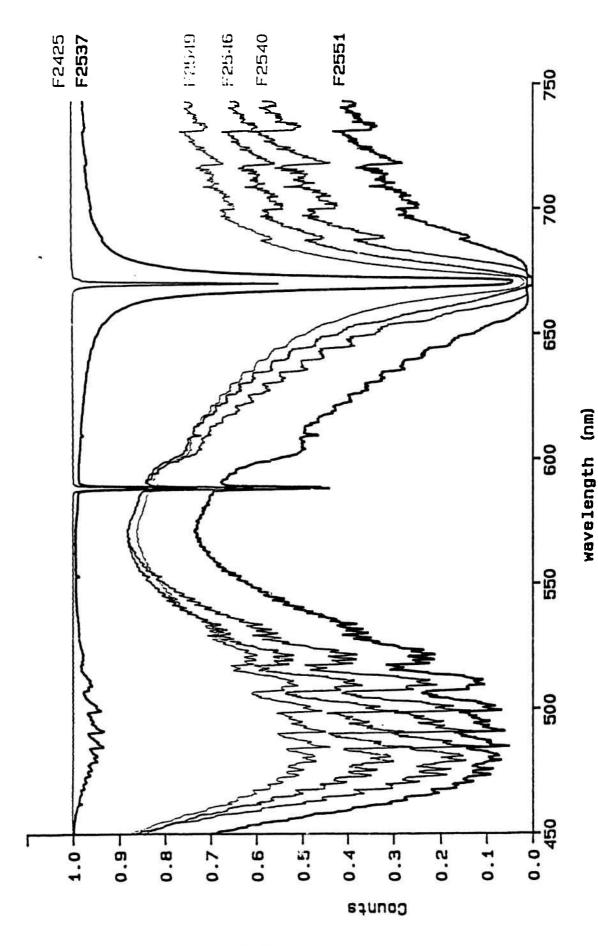
 $T_{Li} \approx 998, 1262, 1424, 1410, 1305$  °K

 $T_{Ar} \approx 1610, 1620, 1614, 1580, 1621$  °K

Li, He / H<sub>2</sub> Data:

 $T_{Li} \approx 1424$  °K

 $T_{H_2} \approx 1620$  °K



10-26

# 4. Concluding Remarks

Studies have been initiated in topical areas of interest to personnel in the Emerging Technology Branch of Phillips Laboratory at Edwards Air Force Base. Specific areas under investigation include (i) photoassisted formation and detection of metal diatomic molecules, (ii) aspects of high-temperature solar absorbers for rocket propulsion systems, (iii) homopolar induction as a zero-point energy device, (iv) spectra of trapped atomic radicals, and (v) metal atom recombination dynamics in cold fluids.

The present interim report describes progress made over the course of the summer of 1991 in selected aspects of the project. Specifically, progress is reported in studies of methods for the formation and detection of metal diatomics molecules, with particular reference to the compound LiAl, and in studies of Li(v) at high temperature and pressure in an inert or H<sub>2</sub> gas flow as a broad band solar absorber. Time-dependent methods are described for calculations of molecular absorption profiles

and for the study of vibrational dynamics relevant to possible pulse-probe experiments for detection of LiAl. Additionally, the theory is described and estimates are made of the cross section for Raman-assisted formation of LiAl relevant to a merged beam experiment in progress in the emerging Technologies Branch. Thermodynamics and spectral lineshape are studied of Li(v) transmission profiles for comparisons with and clarification of measure data.

Individual technical reports in each topical area are in preparation and will be provided subsequently.

#### MECHANICAL TESTING OF ISOGRID STRUCTURES

Dr. Christopher A. Rotz
Brigham Young University
AFOSR Summer Faculty Research Associate, Phillips Laboratory, Edwards AFB

#### Abstract

Isogrid triangles without skins were tested in compression to collect data for comparison with computer models under development at Phillips Laboratory. Descriptions of the testing system, isogrid geometry, and specimen preparation are given. Test results from six strain gages attached to the isogrid are given as a function of the applied load. Load-deflection curves were also determined.

#### 1. Introduction

Composite isogrids are strong light-weight structures which can be produced at low cost and with high quality by the highly automated filament winding process (1,2). Since they are a recent development, these structures are not as well understood as their metallic counterparts, and design innovations and new approaches to manufacturing are still being proposed (2,3). At present, the best way to evaluate and compare new isogrid concepts is through mechanical testing. Finite element computer models of isogrids are being developed at Phillips Laboratory so that proposed designs may be examined and optimized before parts are made. Mechanical testing will be used to refine, improve, and ultimately to validate the proposed models. Koury and Kim (2) have proposed that tests first be performed on triangular and hexagonal elements cut from flat isogrid panels made with and without skins, then on flat rectangular isogrid panels, and then on 2 ft (0.61 m), 4 ft (1.22 m) and larger diameter isogrid cylinders.

The purposes of this work were to (1) survey equipment that Phillips Laboratory might purchase for mechanical testing of large isogrid structures like the above mentioned cylinders, (2) put together a mechanical test system for smaller structures using equipment presently available at the lab, (3) begin testing isogrid triangles and hexagons, and (4) develop a test plan for evaluating isogrid structures and for acquiring the necessary data to verify the accuracy of proposed finite element models. The majority of time on this project was spent on the first two tasks. A survey of equipment for future purchase will not be reported in this technical paper, but will be sent directly to the lab. This report will describe

the system which was assembled for testing and the results of tests made on triangles without skins. Time constraints did not permit testing of the hexagons, and triangles and hexagons with skins were not yet available to the author by the end of the project period.

After the completion of the term of this project, tests were successfully run on isogrid hexagons with skins by Phillips Laboratory, but the results were not available for inclusion in this report.

#### 2. Experimental Work

The mechanical test system was finally assembled shortly before the end of the summer research period. At that time it was used to test tensile specimens cut from flat plate laminates of prepreg materials to measure the material properties (shear, tensile, and compression modulii and strengths and Poisson's ratios) to be used in the computer models. These tests also served to debug the testing system before the isogrid triangles were studied. These measurements were performed by a summer student from the Air Force Academy working under the direction of the author and have been reported elsewhere (4). These tests took a substantial fraction of the time available for testing

- 2.1 Isogrid Design and Materials The isogrid structure studied in this work was made from IM7 carbon fibers and 55A epoxy. The fiber volume fraction was unknown. A schematic of the design is shown in Fig. 1. Note that the ribs have been offset by 0.4 in (10 mm) at the nodes to prevent the filaments from piling up during winding. As shown in the figure, the resulting structure consists of two different types of triangles: ones with sharp corners (Type 1) and ones with the corners cut off by the offset ribs (Type 2). The experimental plan was to test both types. The lab was able to supply one unskinned rectangular isogrid panel approximately 2 x 2 ft (0.3 x 0.3 m) in size, from which two triangles (one of each type) and two hexagon-shaped specimens were cut. It was not possible to cut any additional specimens from the panel. No material was available to construct other test panels during the term of the project.
- 2.2 Specimen Preparation and Strain Gage Attachment The specimens were cut from the panel using a diamond saw. The edges were sanded smooth and flat, using care not to damage the fibers. The finished shape of the Type 2 triangle is shown in Fig. 2. Also shown is a steel block which was bonded to the top of the triangles with epoxy. The block had a 0.25 in (mm) diameter hole through it to accommodate a steel pin used to

connect the block to a clevis which in turn was mounted in a tensile test machine, as shown in Fig. 3.

Six CEA-06-250UN-350 strain gages (Measurements Group, Inc. Raleigh, NC) were attached to the triangles using MBond 200 adhesive following the manufacturer's suggested procedures for composite materials. The gage locations for the Type 2 triangle are shown in Fig. 2. The gages had a nominal resistance of 350 ohms. Gages with lower resistances are not recommended when testing carbon fiber composites. The gage locations were chosen for the following reasons.

- 1. Gages #1 and #5 measure the strains in the the legs of the triangle and provide a check on the left-right symmetry of the loading.
- 2. Gage #3, together with #5, can be used to calculate the strain due to bending,  $\varepsilon_b$ , and the strain,  $\varepsilon_a$ , due to the axial load along the right leg of the triangle:

$$\varepsilon_{a} = \frac{\varepsilon_{5} + \varepsilon_{3}}{2}$$
 and  $\varepsilon_{b} = \frac{\varepsilon_{5} - \varepsilon_{3}}{2}$  (1),(2)

where  $\varepsilon_3$  and  $\varepsilon_5$  are the strains measured by gages #3 and #5, respectively.

- 3. Gage #2 measures the strain in the base of the triangle.
- 4. Gages #4 and #6 are located as close to the top and lower right nodes as is practically possible to look for possible stress concentrations in those regions.

Wires were carefully soldered to the gages, again following the gage manufacturer's recommended procedures. The wires were connected to permit the gages to be operated in what is known as the "three-wire configuration". The wires were also taped to the legs of the triangle to prevent accidental breaking of the solder joints.

2.3 Apparatus The gages were connected in the "three-wire configuration" to six channels of a BAF-8 strain gage excitation and signal conditioning unit (Measurements Technology, Inc., Roswell, GA). The unit has a maximum capacity of 8 channels. Precision 350 ohm bridge completion resistors were added to the circuit boards within the BAF-8 so that each strain gage was part of a quarter bridge circuit. The BAF-8 has filters for each input channel, and the cut-off frequencies are set by resistor packs on the same circuit boards. In all the tests reported here the cut-off frequencies were 60 Hz. The

excitation voltage for each gage was set to  $2.000 \pm .001 \text{ v}$ . This followed the recommended practice for energizing strain gages attached to carbon fiber/epoxy composites with 2 v or less.

The conditioned signals from the BAF-8 were input to a Macintosh IIx computer through a MacAdios 2 A/D board (G. W. Instruments, Somerville, MA). This board is capable of reading 16 channels with a precision of 12 bits.

The triangles were loaded in compression on an MTS servo-hydraulic tensile test machine. The block at the top of the triangle was connected by a steel pin to a clevis clamped in the upper fixture of the machine, as shown in Fig. 3. The bottom of the specimen was supported on the two pins of an Instron three-point bending fixture, also shown in the figure. The pins had a diameter of 0.984 in (25.0 mm) and were separated by a center-to-center distance of 4.04 in (103 mm). The separation distance was chosen to place the support pins directly under the nodes of the isogrid. Voltage signals from the load cell and crosshead displacement sensor were fed into the computer through two additional channels of the previously described A-to-D board.

A program was written using LabVIEW, a commercial software package (National Instruments Corp., Austin, TX) that allows the user to write custom data acquisition programs with graphical interfaces. The program converts the voltage signals from the BAF-8, the load cell, and the crosshead displacement sensor into strain, load and displacement quantities using operator-supplied calibration factors. These quantities are displayed in real time on a video strip chart on the computer monitor during a test. The data are also automatically stored on the hard disk for later analysis. The program allows the user to select the sampling rate (software limited this to a maximum of 1 Hz per channel), to zero out any voltages in software before the start of a test, and to select which channels are to be displayed (8 maximum) and stored (16 maximum).

2.4 Procedure After the gages were attached to the triangles, they were checked with a gage installation tester (Micromeasurements Model 1300). The specimen was then mounted in the clevis clamped in the upper grip of the tensile test machine. The crosshead was carefully lowered to bring the bottom of the specimen into contact with the three-point bending fixture.

The wires were connected to the BAF-8 which in turn was connected to the A-to-D card in the computer. The signals from the load cell and the crosshead displacement sensor were

then connected to the same card. The input voltages to each bridge circuit were set, and the circuits individually balanced on the BAF-8. Next each circuit was shunt calibrated with a known resistance,  $R_s$ , and the calibration factor,  $K_s$ , calculated:

$$K = \frac{R_g}{F(R_g + R_s)v_s}$$
 (3)

where  $R_g$  and F are the nominal resistance the gage factor of the strain gage, respectively; and  $v_s$  is the voltage output from the BAF-8 when  $R_s$  is shunted across the strain gage. The calibration factor was then entered into the computer for each channel. Similarly, the calibration factors for the load cell and displacement sensor were entered. The values were obtained from the operator's manual for the MTS machine. The values were checked using a calibration procedure outlined in the manual.

The sampling rate was entered into the computer (a value of 1 Hz was used in all cases). All channels with non-zero voltages were then corrected to zero by a subroutine in the computer program. The crosshead speed was set at 0.00005 in/min (0.00127 mm/min) and the test begun. The low speed was chosen to make certain that the triangle would not fail in too short a time to get enough data to represent the load-strain and load-deflection curves well. The test was paused when the load reached 250 lbf so that photographs could be taken, and again at 285 lbf so that the speed could be increased to 0.005 in/min (0.127 mm/min).

#### 3. Results

The Type 1 triangle was accidently destroyed when the tensile test machine was mistakenly put into a fast traverse mode. The speed was so great that no data were sampled before the specimen had failed.

Experimental results for the Type 2 triangle are shown in Figs. 3 through 12. A comparison of the photographs in Figs. 3 and 4 will show that the legs of the triangle both bowed outwards, while the base bowed upwards.

Fig. 5 is a plot of the compressive load on the Type 2 triangle as a function of the vertical deflection. The load reached a maximum of about 295 lbf (1310 N) at a deflection of about 0.85 in (21.6 mm). It appears that buckling occurred at this point, but did not lead to catastrophic failure. The triangle was still able to carry a substantial load as the deflection was increased further. Catastrophic failure occurred at a deflection of 0.295 in (7.49 mm)

when the left leg of the triangle fractured near gage # 1 (see Fig. 6). At failure, the load was 215 lbf (956 N). The data from Fig. 5 are replotted in Fig. 7 in an expanded view to more fully illustrate the load-deflection behavior at smaller deflections.

The load versus strain data are plotted in Figs. 8-11. Fig. 8 shows the results for gages #1 and #5. As expected they are nearly equal throughout the entire deflection range. This indicates that the material properties, geometry and loading were symmetric, about the centerline of the triangle.

Fig. 9 is a plot of strain data for gage #3 compared with the negative of the strain measured at gage #5. If the stress in the right leg of the triangle were caused only by a bending moment, these two curves would be identical. The difference between them indicates there is an axial load present as well. The strains caused by the axial load and the bending moment,  $\varepsilon_a$  and  $\varepsilon_b$ , were calculated from Eqs. 1 and 2, and are plotted in Fig. 10. From the results it is apparent that the larger part of the strain is caused by the bending moment.

The strains near the nodes, measured by gages #4 and #6 are plotted in Fig. 11. Fig. 12 shows the strain measured at the middle of the base of the triangle. Note that these strains are much smaller than those measured at the middles of the sides. The nodes must stiffen the nearby structure considerably, resulting in the lower strains there. The small strain in the base shows that much of the load must travel from the top of the triangle, through the sides, and then into the bottom support pins. The base experiences loads when the bottom two nodes rotate and try to spread apart as the applied load is increased.

#### 4. Conclusions

#### The conclusions are:

- 1. A mechanical test system capable of monitoring 8 strain gages, a load cell, and a displacement sensor was assembled and successfully used to test an unskinned isogrid triangle. Only the lack of additional strain gage energizing and signal conditioning equipment prevent the system from monitoring 6 more gages.
- 2. The compressive load on the triangle increased with deflection, reached a maximum of 295 lbf (1310 N) at 0.085 in (2.16 mm), then decreased to 215 lbf (956 N) at 0.295 in (7.49 mm) where catastrophic failure occured. The maximum in the curve is probably the onset of buckling in the triangle

- 3. The loading and deformation were symmetric about the centerline of the triangle.
- 4. The deformation in the sides of the triangle was largely caused by bending moment. A compressive axial load was present as well, but contributed a much smaller amount to the total deformation.
- 5. The strain levels near the nodes and at the middle of the base were much lower than those measured at the mid-sides of the triangle where strains at failure were about 1.5 to 1.7%.

#### 5. References

- 1. A. D. Reddy, R. R. Valisetty, and L. W. Rehfield, "Continuous Filament Wound Composite Concepts for Aircraft Fuselage Structures", <u>Journal of Aircraft</u>, V. 22, No. 3, March 1985.
- 2. J. L. Koury and T. D. Kim, "Continuous Filament Wound Composite Concept for Space Structures", <u>SAMPE ICCM8 Proceedings</u>, July 1991.
- 3. L. J. Ashton, S. D. Huntsman, M. G. Allman, A. B. Strong, and C. A. Rotz, "Filament Winding of Composite Isogrid Fuselage Structures", in <u>Composites in Manufacturing: Case Studies</u>, ed. by A. B. Strong, Society of Manufacturing Engineers, Dearborn, MI, 1991.
- 4. M. Tenney, "Analysis of Carbon Composite Isogrids", report submitted to Phillips Laboratory, Edwards AFB, Summer 1991.

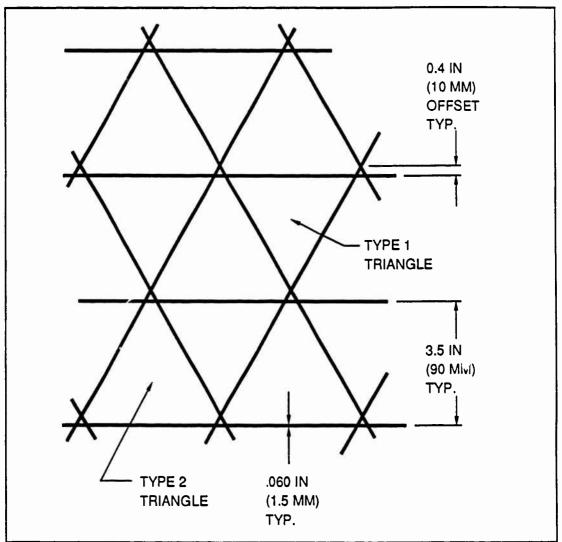


Fig. 1. Schematic diagram of the isogrid structure studied in this work. All the triangles are equilateral. Note how offsetting the ribs produces two types of triangles, one with sharp corners (Type 1) and the other with corners cut off by the offset ribs (Type 2).

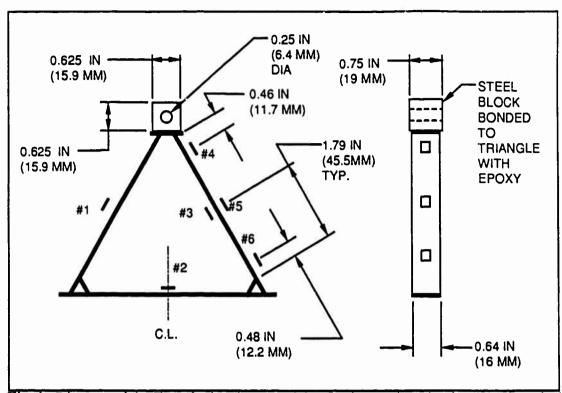


Fig. 2. Diagram of the Type 2 triangle test article. During testing, the downward vertical load was transmitted to the triangle through a 0.25 in (6.4 mm) diameter steel pin passing through a steel block bonded to the top of the triangle. The strain gages are shown schematically as short line segments. The indicated dimensions are measured to the centers of the gages

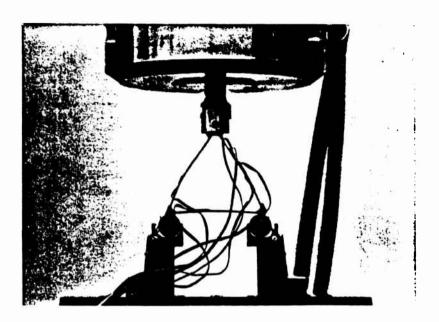


Fig. 3. Photograph of the Type 2 triangle mounted in the MTS testing machine. As shown in the picture, the steel block attached to the top of the triangle was connected to a clevis held in the upper fixture of the testing machine by a 0.25 in (6.4 mm) diameter steel pin. This made it possible to load the triangle in compression without inducing any unwanted moments about the pin axis. The bottom of the triangle was supported by an Instron three-point bending fixture, using 0.984 in (25.0 mm) diameter pins separated by a center-to-center distance of 4.04 in (103 mm). At the time the photograph was taken, the load on the triangle was in excess of 100 lbf (445 N).

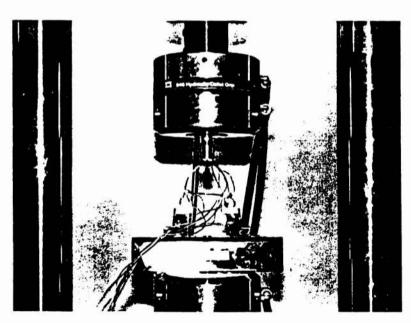


Fig. 4. Photograph of the Type 2 triangle mounted in the MTS testing machine. The load is at or near the maximum value of 295 lbf (1310 N). Note how the two legs have bowed outwards while the base has bowed upwards.

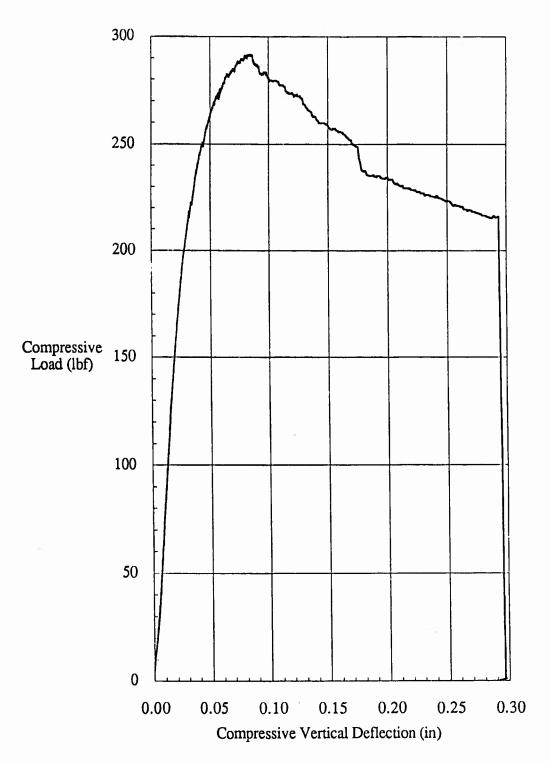


Fig. 5 Load versus deflection plot for the Type 2 triangle

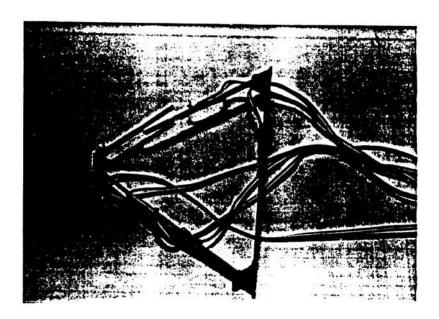


Fig. 6. Photograph of the failed Type 2 triangle. Fracture occured near gage #1.

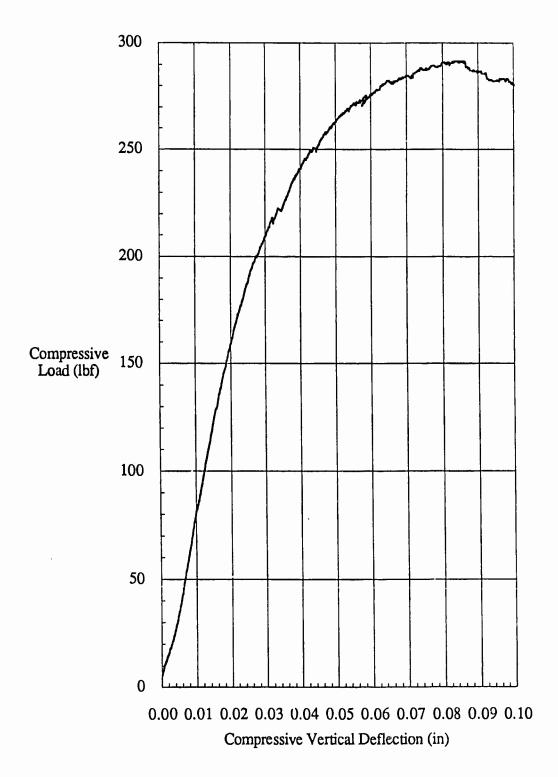


Fig. 7. Expanded view of the load versus deflection data for the Type 2 triangle.

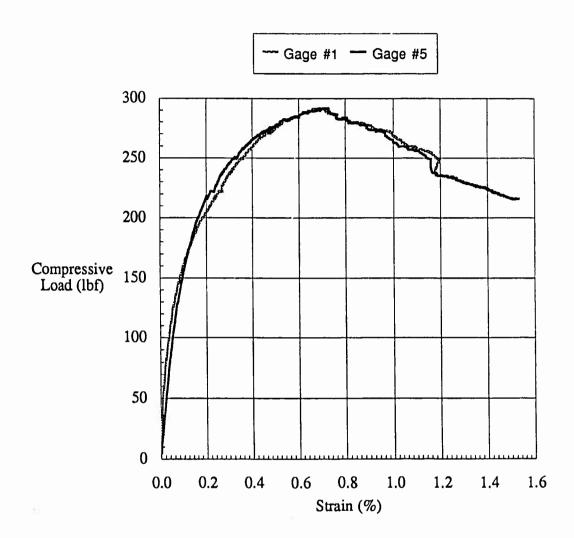


Fig. 8. Load versus strain for gages #1 and #5.

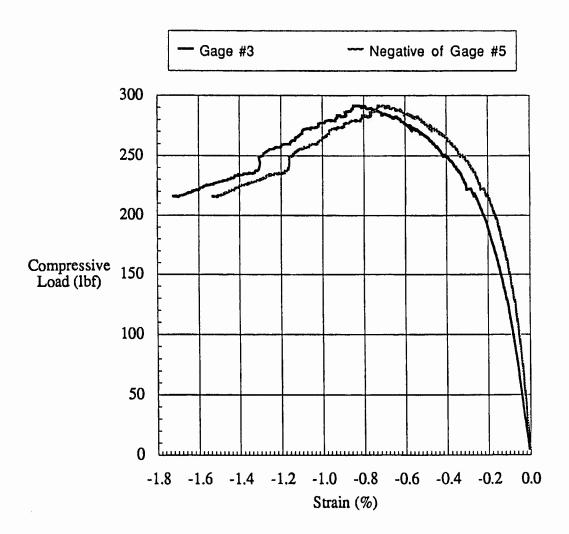


Fig. 9. Load versus strain for gage #3. The negative of the strain for gage #5 is also plotted. If all the strain were caused by a bending moment, the two curves would superimpose.

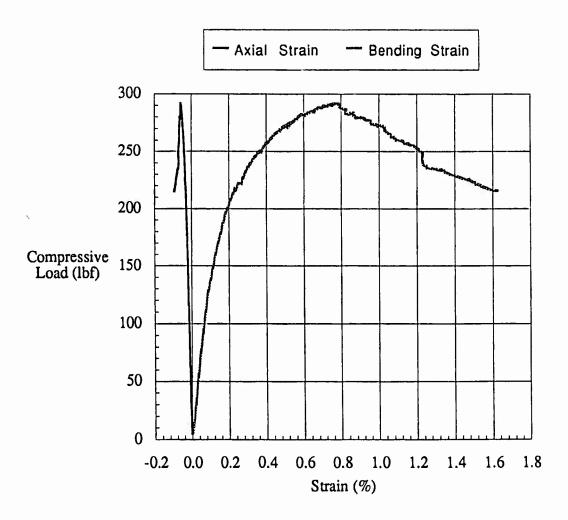


Fig. 10. Load versus the axial and bending strains in the side of the Type 2 triangle. Calculated from Eqs. 1 and 2.

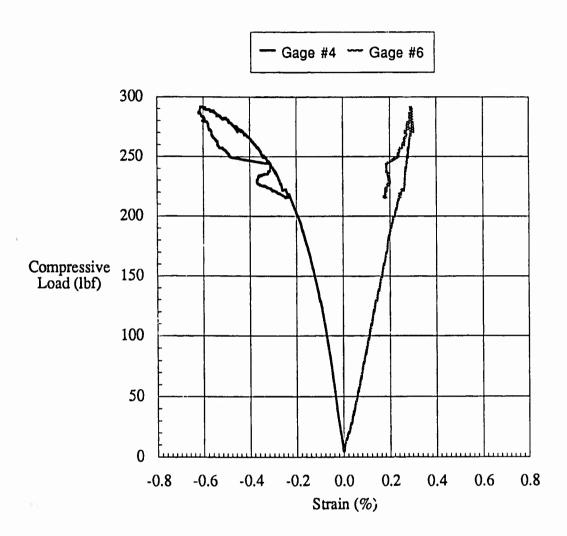


Fig. 11. Load versus strain for gages #4 and #6. The gages are near two of the nodes in the triangle. Note the strain levels are much smaller than those observed at the middle of the two sides of the triangle (gages #1 and #5).

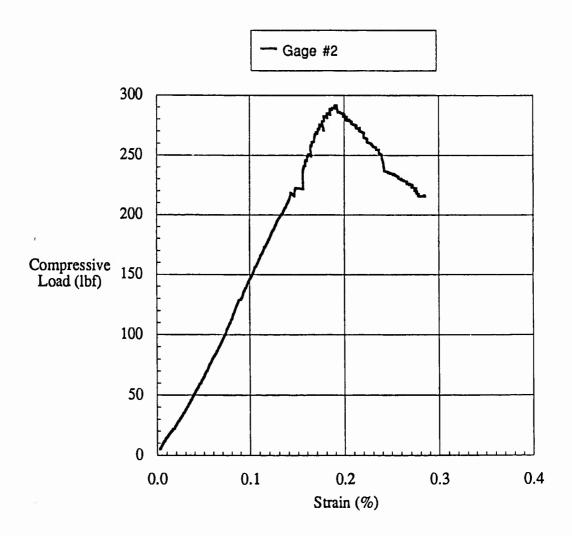


Fig. 12. Load versus strain data from gage #2 (middle of the base of the Type 2 triangle). The strain levels are much lower than those observed in the middle of the two sides of the triangle (gages #1 and #5).

# NONLINEAR ADAPTIVE CONTROL OF ASTREX SYSTEM USING GAUSSIAN AND MULTILAYER NEURAL NETWORKS

Sahjendra N. Singh\*
Professor
Department of Electrical and Computer Engineering
University of Nevada Las Vegas
Las Vegas, NEVADA 89154
Phone: (702) 597-4183

#### Abstract

This paper considers large angle rotational maneuvers and vibration damping of the Advanced Space Structures Technology Research Experiment (ASTREX) System. Multilayer neural networks (MNN3) and gaussian networks are used in the adaptive control and stabilization of the system. Large angle rotational maneuvers of the ASTREX system cause significant nonlinear coupling of the rigid and elastic modes. We derive adaptive control law for nonlinear maneuvers of the ASTREX system. Interestingly, in the closed-loop system, the elastic dynamics asymptotically decouple from the rigid dynamics. A control law is derived for the vibration suppression using the auxiliary actuators. This stabilizer includes layered neural networks in the control loop. The stabilizer is synthesized using estimated states from an observer. The observer includes a layered neural network.

<sup>\*</sup>The research is supported by AFOSR Summer Faculty Research Program

# 1 Introduction

The advanced Space Structures Technology Research Experiments (ASTREX) Laboratory has been developed at the Phillips Laboratory, Edwards Air Force Base, California. This is a versatile facility for demonstrating advanced technologies on models of high performance spacecraft [1]. Design problem has been posed for large angle rotational maneuvers and vibration suppression of this structure. ASTREX forms a testbed to test and validate control strategies developed by researchers from various institutions.

Figure 1 shows a finite element model drawing of ASTREX [2]. The front end (secondary) of the test-article is connected to the primary truss by a tripod arrangement. The rear part (tertiary) houses electronics and balances the secondary. The test article pivots on a vertical pedestal through an air-bearing system. Actuators (thurstors, proof mass actuators, reaction wheels) and sensors are mounted on the structure for control and signal measurement.

The dynamics of the ASTREX system are represented by coupled nonlinear differential equations describing its orientation and elastic deformation. Large angle rotational maneuvers introduce significant coupling among the rigid and elastic modes. The elastic motion is described by a large order system. This poses numerical difficulty in design. Furthermore, dynamics of the ASTREX system are imprecisely known. The design of controllers for a nonlinear, large order, uncertain ASTREX system is indeed a challenging task.

In the past numerous studies have been made for the design of controllers for

flexible spacecraft. Linear and nonlinear control laws have been developed (see, for example [3-7]). An adaptive control law for nonlinear maneuver of a flexible spacecraft has been presented in [8].

This research focuses on the design of nonlinear adaptive controllers using neural networks for the ASTREX system. An artificial neural network architecture has massive parallel interconnections of simple "neural" processors. The motivation for the design of such networks comes from natural neural networks which result from the interconnection of neurons in biological systems. Neural networks have been widely used in the fields of image and pattern recognition. Only recently, interest has been shown in the use of neural networks for the identification and control of nonlinear dynamical systems [9-13].

The contribution of this paper lies in the development of a nonlinear adaptive controller for the nonlinear rotational maneuvers and vibration suppression of the ASTREX system using multilayer neural networks and gaussian networks. The control system design is accomplished by treating the nonlinear rotational maneuver problem separately from the vibration suppression problem. This simplifies the design problem. A nonlinear adaptive control law is derived such that in the closed-loop system large-angle rotational maneuvers can be performed using the main thrusters. For the derivation of this control law the knowledge of system dynamics is not required, since the bound on the unknown functions in the model is generated by a gaussian network. A reference model is included to generate attitude trajectories to be followed by the spacecraft. Attitude errors are used in a dynamic feedback loop for control. Using this controller, rotational maneuvers can be performed. How-

ever, this excites the elastic modes of the system. An important advantage of the use of this controller is that the elastic dynamics of the ASTREX are asymptotically decoupled from the rigid mode dynamics. The resulting decoupled elastic dynamics are well approximated by a linear system. Based on the asymptotically decoupled elastic dynamics a stabilizer is designed for vibration suppression. Two multilayer neural networks are used in the controller for stabilization. The first MNN is used in an observer to reconstruct the state variables and the second MNN generates a control signal to compensate for uncertainty in the stabilizer.

The organization of this paper is as follows. The mathematical problem is formulated in Section 2. Section 3 presents the attitude controller and the stabilizer design is presented in Section 4.

# 2 Problem Formulation

An orthogonal coordinate system embedded in the ASTREX model is utilized to describe its orientation with respect to the inertial space. The orientation of the ASTREX model is defined by a sequence of rotations  $\theta_1, \theta_2, \theta_3$  (roll,pitch,yaw), with respect to an *inertial* coordinate system.

The orientation is completely described by the differential equation

$$\dot{\theta} = M^{-T}(\theta)\omega \tag{1}$$

where T denotes transposition and

$$\omega = (\omega_1, \omega_2, \omega_3)^T, \ \theta = (\theta_1, \theta_2, \theta_3)^T, \ M^{-T} \stackrel{\triangle}{=} (M^T)^{-1}$$

and

$$M^{T} = \begin{bmatrix} \cos \theta_{2} \cos \theta_{3} & \sin \theta_{3} & 0 \\ -\cos \theta_{2} \sin \theta_{3} & \cos \theta_{3} & 0 \\ \sin \theta_{2} & 0 & 1 \end{bmatrix}$$

Often the arguments of functions will be suppressed for simplicity.

Equation (1) relates the rotation angles and the angular velocity components  $(\omega_1, \omega_2, \omega_3)$  of the ASTREX. It is seen that  $M^T$  becomes singular at  $\theta_2 = \pm (\pi/2)$  for the stated choice of rotations of the coordinate systems. However, this singularity can be avoided by a different sequence of rotations of coordinate frames if it is required. In the following we shall be interested in the region of state space  $\Omega$  in which  $\theta_2 \neq \pm \pi/2$ . The elastic deformations of the ASTREX system are expressed as linear combinations of admissible functions and the modal deformation coordinates  $q_i(t), i = 1, ....n$ . Define  $q = (q_1, ...., q_n)^T$ , the vector of elastic modes.

The complete equations of motion describing rotational and elastic behavior of the ASTREX system can be derived using *Lagrangian* approach. In this study we shall be interested only in the rotational and elastic dynamics. The equations of motion are

$$\begin{bmatrix} I_0 & A_2 \\ A_2^T & A_3 \end{bmatrix} \begin{bmatrix} \dot{\omega} \\ \ddot{q} \end{bmatrix} = \begin{bmatrix} N_2(\theta, \dot{\theta}, \omega, \dot{q}) \\ -Kq \end{bmatrix} + \begin{bmatrix} B_1 \\ B_2 \end{bmatrix} u \tag{2}$$

where K is the stiffness matrix,  $N_2$  is a nonlinear vector function,  $B_i$  (i=1,2) are the constant input matrices,  $u = (u_m^T, u_a^T) \in \mathbb{R}^m$  is the control input vector and

$$B_1 = \begin{bmatrix} I_{3\times3} & B_{12} \end{bmatrix}$$

$$B_2 = [O_{n \times 3} \quad B_{22}]$$

Here  $u_m$  denotes the torque developed by the actuators affecting the rigid modes and  $u_a$  denotes the generalized force contribution from the actuators affecting mainly the elastic modes. I and O denote identity and null matrices of indicated dimensions. The matrix D

$$D = \left[ \begin{array}{cc} I_0 & A_2 \\ A_2^T & A_3 \end{array} \right]$$

is a positive definite symmetric matrix.

It may be pointed out that the approach of this paper can be extended to the case when the null submatrix of  $B_2$  is nonzero. Even in such a case, attitude controller and observer design remains the same. However, a new stabilizer must be designed for the simultaneous stabilization of the rigid and elastic modes following the scheme of Section 4.

We are interested in deriving control laws such that in the closed-loop system reorientation maneuvers can be performed. Let us consider the following problems.

## Angular Velocity Trajectory Control

Let a reference angular velocity trajectory  $\omega_r$ , be given such that  $\omega_r(t) \to 0$ , as  $t \to \infty$ . We are interested in deriving a control law such that in the closed-loop system  $\tilde{\omega}(t) = \omega(t) - \omega_r(t) \to 0$ , as  $t \to \infty$ .

#### Reorientation Maneuver

Let  $\theta_r(t)$  be a given reference attitude trajectory, such that  $\theta_r(t) \to \theta^*$ , a desired attitude angle, as  $t \to \infty$ . We are interested in deriving a control law such that in the closed-loop system  $\theta(t) \to \theta_r(t)$ , as  $t \to \infty$ , and elastic

modes are stabilized. The rotational maneuver to attain desired orientation will be accomplished by a judicious choice of  $\omega_r(t)$ .

# 3 Control Law for Rotational Maneuver

In this section, control laws for rotational maneuvers will be derived. First we shall consider rotational maneuver using  $u_m$ .

## 3.1 Angular Velocity Control

Here first the design of a control system for  $\omega_r$  trajectory tracking is considered. We consider the derivative of  $\omega$  from (2) which is

$$\dot{\omega} = R_{11}[N_2(\theta, \dot{\theta}, \omega, \dot{q}) + B_1 u] + R_{12}[-Kq + B_2 u] \tag{3}$$

where  $D^{-1}=(R_{ij})$ , i,j=1,2 and  $R_{ij}$  are submatrices of  $D^{-1}$  of appropriate dimensions. Then in view of the special form of matrices  $B_i$ , it follows that

$$\dot{\tilde{\omega}} = [R_{11}\{N_2(\theta, \dot{\theta}, \omega, \dot{q}) + B_{12}u_a\} + R_{12}\{-Kq + B_{22}u_a\}] - \dot{\omega_r} + R_{11}u_m$$

$$\stackrel{\triangle}{=} -\lambda \tilde{\omega} + a^*(\theta, \dot{\theta}, \dot{\omega_r}, \omega, q, \dot{q}, u_a) + R_{11}u_m$$
(4)

where

$$a^* = \lambda \tilde{\omega} + R_{11} \{ N_2 + B_{12} u_a \} + R_{12} \{ -Kq + B_{22} u_a \}$$

We treat here  $a^*$  and  $R_{11}$  as unknown functions. In the following it will be assumed that the reference attitude trajectory is such that  $q, \dot{q}, \omega_r, \dot{\omega}_r$  are bounded.

To this end, we evaluate

$$u_m^T(a^* + R_{11}u_m) \ge b_0 \parallel u_m \parallel (\parallel u_m \parallel - \Pi(c, z))$$
 (5)

where  $b_0$  is a positive real number, the function  $\Pi(c,z)$  is unknown,  $z = (\theta, \omega, \tilde{\omega}, u_a)$ , and  $c = (c_0, c_1, ..., c_k)$  is a k+1 dimensional constant vector. We assume that there exists a gaussian network such that

$$\Pi(c,z) \le \Pi_a = c_0 + c_1 g_1(||z - \xi_1||) + \dots + c_k g_k(||z - \xi_k||) \tag{6}$$

where the radial gaussian kernals are

$$g_i = \exp(-\parallel z - \xi_i \parallel)^2/r^2)$$

We note that the gaussian network generates the function  $\Pi_a$  which bounds the uncertain function  $\Pi$ . The function  $\Pi_a$  leads to the structure of the adaptive controller.

Since it is desired to track the reference trajectory  $\omega_r$ , we choose a control law  $u_m$  of the form

$$u_m = \Pi_a(\hat{c}, z) s(\hat{c}, \varepsilon, \tilde{\omega}) \tag{7}$$

$$\dot{\hat{c}} = L(\partial \Pi_a(\hat{c}, z)/\partial c) \parallel \tilde{\omega} \parallel$$
 (8)

$$\dot{\varepsilon} = -l\varepsilon \tag{9}$$

where  $\hat{c}$  denotes an estimate of  $c, \hat{c}(0) \in (0, \infty)^{k+1}, \varepsilon(0) \in (0, \infty), l > 0, L$  is a diagonal matrix with positive elements and s is given by

$$s(\tilde{\omega}, \hat{c}, \varepsilon) = sat(\Pi(\hat{c}, z)\tilde{\omega}/\varepsilon)$$

Here the sat function denotes the saturation function.

Now we can state the following result.

Theorem 1: Consider the closed-loop system (2) and (7). Suppose that the command trajectory  $\omega_r$  is such that  $q, \dot{q}, \omega_r$  and  $\dot{\omega}_r$  are bounded, and  $\theta \in \Omega$ . Then in the closed-loop system  $\tilde{\omega}$  tends to 0 as t tends to  $\infty$ .

Proof: The proof of the theorem is based on the Lyapunov stability result.

One chooses a Lyapunov function of the form

$$V(\tilde{\omega}, \hat{c}, \varepsilon) = (\tilde{\omega}^2/2) + (b_0/2)\tilde{c}^T L^{-1}\tilde{c} + (b_0 \varepsilon/l)$$
(10)

It can be shown that the derivative of V along the trajectory of the closed-loop system is given by

$$\dot{V} \le -\lambda \tilde{\omega}^2 \tag{11}$$

Since V is a positive definite function and  $\dot{V} \leq 0$ , it follows using an argument similar to that of [14-15] that  $\tilde{\omega}$  converges to 0 as t tends to  $\infty$ .

If  $\omega_r(t) \to 0$  as  $t \to \infty$ ; then  $\dot{\theta}(t) \to 0$  and  $\theta(t) \to \theta_d$ , a constant vector. In such a case, the ASTREX system attains a fixed orientation.

#### 3.2 Reorientation Maneuver

Now we shall derive a control law  $u_m$  such that  $\theta(t) \to \theta_r(t)$ , a given reference attitude trajectory, as  $t \to \infty$ , giving a desired orientation of the ASTREX system. This will be accomplished by a suitable choice of reference trajectory  $\omega_r(t)$  in the control law (7), such that the desired orientation is asymptotically attained.

Since in the closed-loop system (2) and (7),  $\omega(t) \rightarrow \omega_r(t)$ , we have that

$$M^{-1}(\theta)\omega(t) \to M^{-1}(\theta)\omega_r(t)$$
, as  $t \to \infty$ 

Thus the asymptotic relationship between  $\dot{\theta}$  and  $\omega$  obtained from (1) is

$$\dot{\theta} = M^{-T}(\theta)\omega_r \tag{12}$$

as  $t \to \infty$ . Since it is desired to track  $\theta_r(t)$ , in view of (12), it follows that a suitable choice of  $\omega_r$  is

$$\omega_r = M^T(\theta)[-\mu\tilde{\theta} + \dot{\theta}_r] \tag{13}$$

where  $\mu > 0$ , and  $\tilde{\theta} = (\theta - \theta_r)$ .

From equation (1), we have

$$\dot{\theta} = M^{-T}(\theta)(\tilde{\omega} + \omega_r)$$

$$= M^{-T}(\theta)[\tilde{\omega} + M^T(\theta)(-\mu\tilde{\theta} + \dot{\theta}_r)]$$
(14)

which yields

$$\dot{\tilde{\theta}} = -\mu \tilde{\theta} + M^{-T}(\theta) \tilde{\omega} \tag{15}$$

Since for any choice of  $\omega_r(t)$ , in the closed-loop system including the control law (7),  $\tilde{\omega} \to 0$  as  $t \to \infty$ , asymptotically (15) reduces to

$$\dot{\tilde{\theta}} = -\mu\tilde{\theta} \tag{16}$$

It is interesting to note that by a proper choice of reference trajectory  $\omega_r$  as given in (13), one obtains a first order linear differential equation asymptotically for the attitude angle tracking error. It is obvious from (16) that for any  $\omega(0)$ ,  $\omega_r(0)$ ,  $\theta(0)$ , and  $\theta_r(0)$ ;  $\tilde{\theta}(t) \to 0$ , as  $t \to \infty$ . Let  $\theta = \theta^*$  corresponds to a desired orientation of the orbiter. Thus if  $\theta_r(t) \to \theta^*$ , then  $\theta(t) \to \theta^*$ , as  $t \to \infty$ , and the desired orientation of the orbiter is attained.

# 4 Elastic Mode Stabilization

We note that in the closed-,loop system,  $\omega(t) \to 0$ , and  $\dot{\omega}(t) \to 0$ , as  $t \to \infty$  for an approxiate choice of  $\omega_r(t)$ . Also in the closed-loop system including the

reorientation controller, one can choose  $\theta_r(t)$  such that  $\theta(t) \to \theta^*$ ,  $\dot{\theta}(t) \to 0$ ,  $\omega(t) \to 0$ , and  $\dot{\omega}(t) \to 0$ , as  $t \to \infty$ . However, rotational maneuvers cause elastic deformation. Thus it becomes necessary to design a stabilizer so that the elastic modes can be damped.

In this section the design of an elastic mode stabilizer is considered. Since in the closed-loop system,  $\omega(t) \to 0$  and  $\dot{\omega}(t) \to 0$ , irrespective of the elastic oscillation of the structure; it follows from (2) that the elastic dynamics get asymptotically decoupled from the rigid dynamics as  $t \to \infty$ . Setting  $\dot{\omega}(t) = 0$  in (2), gives the decoupled elastic dynamics of the form

$$A_3\ddot{q} = -Kq + B_{22}u_r \tag{17}$$

For the damping of the vibration, it is necessary to stabilize system (17).

Define  $v=(q^T, \dot{q}^T)$ , to obtain a state variable form from (17) as

$$\dot{v} = \begin{bmatrix} 0_{n \times n} & I_{n \times n} \\ -A_3^{-1} K & 0_{n \times n} \end{bmatrix} v + \begin{bmatrix} 0 \\ A_3^{-1} B_{22} \end{bmatrix} u_a$$

$$\stackrel{\triangle}{=} A_c v + B_c u_a$$
(18)

where matrices  $A_e$ , and  $B_e$  are defined by (18). To this end, we shall consider a discrete form of representation for this system. Let T be the sampling period. Define  $F = exp(A_eT)$ , and

$$G = \int_{kT}^{(k+1)T} \{exp((k+1)T - s)\} ds B_e$$

Then the discrete-time system is

$$v(k+1) = Fv(k) + Gu_n(k)$$
(19)

where kT has been replaced by k for simplicity. Let the observation equation be

$$y(k) = Hv(k) \tag{20}$$

For the stabilization of (19), the linear quadratic optimization technique can be used. Let the performance index to be minimized be

$$J = \sum_{k=1}^{\infty} (v(k)^{T} Q v(k) + u_{a}(k)^{T} R u_{a}(k)$$
 (21)

where Q and R are positive definite matrices. Then the optimal control is given by

$$u_a(k) = Kv(k), K = -(R + G^T P G)^{-1} G^T P F v(k)$$
 (22)

K is the optimal feedback gain and the P is the solution of the algebraic Riccati equation

$$P = F^{T}PF - F^{T}PG(R + G^{T}PG)^{-1}G^{T}PF + Q$$
 (23)

We note that the system matrices are not precisely known. Thus these matrices differ from the assumed values F and G in (19). Moreover the state v(k) is not available for feedback. We shall use layered neural networks in order to compensate for the uncertainty in the observer and stabilizer design. This will be accomplished by superimposing additional loops containing neural networks around the observer and stabilizer designed for the nominal parameters.

The structure of the observer and stabilizer is shown in Fig.(2). The observer is described by

$$\hat{v}(k+1) = F\hat{v}(k) + L\tilde{y}(k) + Gu_a(k) + N_A(\tilde{y}(k), u_a(k), aw(k))$$
 (24)

$$\hat{y}(k) = H\hat{v}(k)$$

where  $\tilde{y}(k) = y_p(k) - \hat{y}k$ ,  $y_p$  denotes the actual output, aw(k) are the adjustable parameters of the network.

The adaptation law for updating the parameters is obtained by the steepest decent technique. The performance function to be minimized is chosen to be a function of the observation error

$$EM(k+1) = (y_p(k+1) - \hat{y}(k+1))^T (y_p(k+1) - \hat{y}(k+1))/2$$
 (25)

Let  $aw_i$  be an element of the parameter vector aw. Then these parameters are adjusted according to

$$aw_i(k+1) = aw_i(k) - \mu_M(\partial EM(k+1)/\partial aw_i)$$
 (26)

where  $\mu_M$  is a positive constant. Since  $y_p$  is independent of aw, it easily follows that

$$(\partial EM(k+1)/\partial aw_i) = -(y_p(k+1) - \hat{y}(k+1))^T(\partial \hat{y}(k+1)/\partial aw_i) \quad (27)$$

The partial derivatives of the neural network output is obtained by following the standard back-propagation method. This is not repeated here since one can find elsewhere [9]. Under the assumption that the system is observable, it follows that the estimated state  $\hat{v}(k)$  converges to the actual state of the system as the observation error tends to zero.

Now we consider the stabilizer design. We choose the stabilization signal of the form

$$u_a(\mathbf{k}) = K\hat{v}(\mathbf{k}) + N_C(\hat{v}(\mathbf{k}), bw(\mathbf{k}))$$
 (28)

where bw(k) are the weights of the neural network  $N_C$ . We notice that the output of a layered neural network is superimposed on the linear feedback signal in order to compensate for the uncertainty in the system dynamics. Similarly to [13], for the derivation of the stabilizer we choose a performance function

$$EC(K) = (\hat{v}^{T}(k+1)P\hat{v}(k+1) + u_{\sigma}^{T}(k)Ru_{\sigma}(k))/2$$
 (29)

Let  $bw_i$  be the *ith* element of bw. Then we update the linkweight based on the steepest decent technique according to

$$bw_i(k+1) = bw_i(k) - \mu_C(\partial EC(k)/\partial bw_i)$$
(30)

where  $\mu_C$  is a step size parameter. We have that

$$\partial EC(k)/\partial bw_i = \hat{v}(k+1)^T P(\partial \hat{v}(k+1)/\partial bw_i) + u_a^T R(\partial u_a(k)/\partial bw_i)$$
 (31)

Differentiating the observer equation gives

$$\partial \hat{v}(k+1)/\partial bw_{i} = (F - LH - (\partial N_{A}/\partial \hat{y})H)(\partial \hat{v}(k)/\partial bw(i)) +$$

$$(G + (\partial N_{A}/\partial u_{a}))(\partial u_{a}(k)/\partial bw(i)) \tag{32}$$

and one has

$$\partial u_{\alpha}(k)/\partial bw(i) = (K + (\partial N_C/\partial \hat{v}))(\partial \hat{v}(k)/\partial bw(i)) + (\partial N_C/\partial bw(i)) \quad (33)$$

Substituting (31)-(33) in (31) gives the rule for adaptation. This completes the stabilizer design.

# 5 Conclusion

The control of slewing maneuvers and vibration stabilization of the ASTREX system was considered. The design was accomplished by decomposing the slew maneuver problem from the elastic mode stabilization problem. A slewing control system including a gaussian network was used for reorientation maneuvers. An observer was designed for estimating the states. For the stabilization of elastic modes, linear quadratic optimization technique was used. In order to compensate for uncertainty in the system, layered neural networks were used for generating additional signals for the stabilizer and the observer.

Future study will include the development of digital Computer programs. Simulation study will be made to determine suitable values of the design parameters so that desired performance charecteristics can be achieved. This study will also focus on computation of bounds on the uncertainty for which the closed-loop system remains stable. Finally, objective will be to examine the control capability of the designed system for slewing and stabilization of the ASTREX in laboratory experiments.

# 6 Acknowledgment

The author wishes to express his sincere thanks to Dr. Alok Das and Mr. L. Kevin Slimak for the opportunity which they provided and their support during the course of this research. It is also pleasure to thank Mr. Joel Berg for useful discussions and for providing many references on neural networks.

This research was conducted at the Phillips Laboratory, Edwards Air Force Base, California.

## 7 References

- A. Das, "Large angle maneuver experiments in ground-based Laboratories," AIAA Progress in Astronautics and Aeronautics 'Mechanics and Control of Large Flexible Structures' Edited by J. L. Junkins, Vol. 129, pp. 491-506, 1990.
- 2. N. S. Abhyankar, and J. L. Berg, "ASTREX model information: supplement to astabed.mat file," Phillips Lab Report, 1991.
- 3. Y. P. Kakad, "Dynamics of Spacecraft Control Laboratory Experiment (SCOLE) slew maneuvers," NASA CR 4098, 1987.
- P. M. Bainum, and C. M. Diarra, "The dynamics and control of the orbiting Spacecraft Control Laboratory Experiment (SCOLE) during station keeping," *Journal of Astronautical Science*, Vol. 37, No. 4, pp. 513-527, 1989.
- S. Fisher, "Application of actuators to control beam flexure in a large space structure," Journal of Guidance, Control, and Dynamics pp. 874-879, 1989.
- 6. S. N. Singh, "Flexible spacecraft maneuver: inverse attitude control and mode stabilization," Acta Astronautica 13, pp. 507-514, 1986.
- 7. M. Azam, S. N. Singh, A. Iyer, and Y. P. Kakad, "Detumbling and reorientation maneuvers and stabilization of the NASA SCOLE system,"

٠.٠

- IEEE Trans. on Aerospace and Electronic Systems," 1991.
- S. N. Singh, "Rotational maneuvers of nonlinear uncertain elastic spacecraft," IEEE Tran. on Aerospace and Electronic Systems, pp.148-155, March 1988.
- K. S. Narendra and K. Parthsarathy, "Identification and control of dynamical systems using neural networks," IEEE Transactionson Neural Networks, 1990, pp. 4-27.
- K.S. Narendra and K. Parthsarathy, "Gradient methods for the optimization of dynamical systems containing neural networks," IEEE Transactions on Neural Networks, 1991, pp. 252-262.
- F. C. Chen and H. K. Khalil, "Adaptive control of nonlinear systems using neural networks - A dead zone approach," 1991 American Control Conference, Boston, MA.
- 12. R. M. Sanner and J. J. E. Slotine, "Gaussian Networks for direct adaptive Control," 1991 American Control Conference, Boston, MA.
- 13. Y. Iiguni, H. Sakui, and H. Tokumaru, "A nonlinear regulator design in the presence of system uncertainty using multilayered neural networks," IEEE Transactions on Neural Networks, 1991, pp. 410-417.
- 14. M. Coreless and G. Leitmann, "Adaptive control for uncertain dynamical systems," Dynamical Systems and Microphysics, Control Theory and Mechanics, Academic Press, 1984, pp. 91-158.
- 15. S. N. Singh, "Attitude Control of Three Rotor Gyrostat in Presence of Uncertainty," Journal of Astronautical Sciences, Vol. 35, pp. 329-345,

July-Sept. 1987.

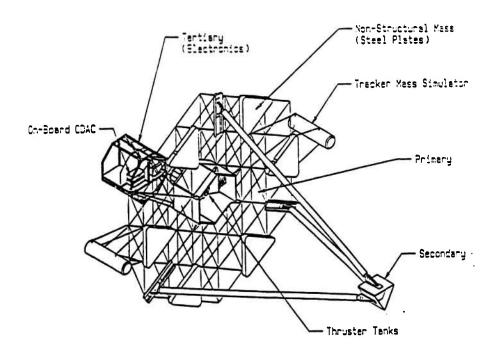


Fig. 1 ASTREX TEST ARTICLE

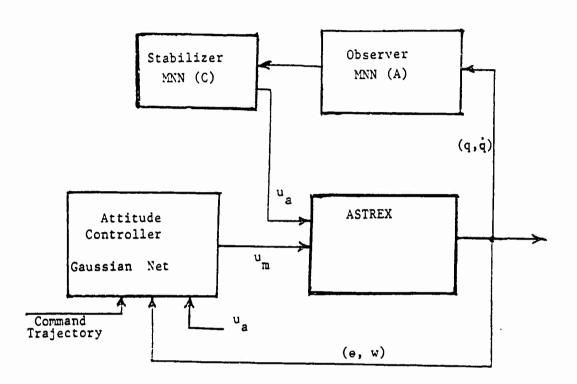


Fig. 2. The Closed-loop System including Attitude Controller, Observer and Stabilizer with Neural Networks

## SOME ASPECTS OF REMOTE SENSING

Frank P. Battles
Professor and Chairman,
Department of Basic Sciences
Massachusetts Maritime Academy

#### ABSTRACT

This report summarizes research done at the Geophysics Directorate of the Phillips Laboratory in the Optical Environment Divison of the Optical Measurements Branch under the direction of Edmund A. Murphy, focal point. This research consists of efforts along two distinct areas of remote sensing: one involving the re-analysis of stellar scintillometer derived profiles of C<sub>n</sub>, the refractive index structure parameter, the other involving the stability of the solution of certain linear systems of equations involved in the Lidar measurement of certain atmospheric properties. The re-analysis of the scintillomer data was neccesitated by the recent discovery that the originally assumed weighting functions were incorrect. We have also made comparisons to similar data obtained using an isoplanometer. These results are being prepared for publication. The Lidar work was suggested by Robert Beland of the Geophysics Directorate and involves the stability of solutions to the matrix equation  $\gamma = \mathbf{W} \mathbf{C}$  for  $\mathbf{C}$  where  $\gamma$ is a Lidar measured vector function of height and W is lower triangular matrix involving certain weighting functions. We have begun to look at the stability of solutions, C, using several types of weighting functions and measurement vectors.

# PART I

#### A. INTRODUCTION

In late April and early May 1986, Air Force Geophysics Laboratory (AFGL) personnel from the Atmospheric Optics Branch participated in a coordinated field program at Pennsylvania State University (PSU)<sup>1</sup>. The purpose of this program was, in part, to compare altitude profiles of  $C_n^2$ , the refractive index parameter<sup>2</sup>, obtained from different measuring devices and to use the acquirate for checking the reliability of certain models for  $C_n^2$ . Profiles of this parameter can be obtained using a stellar scintillometer. The one used at PSU by AFGL is a modification of that originally developed by Ochs et al<sup>3</sup>. This instrument measures the variance of stellar intensity for a first magnitude or greater star. This variance, by use of spatial filters, can be converted into a spatially and temporally averaged profile of  $C_n^2$  for 7 slant path levels where, by slant path level, we mean distance measured along the line of sight from the instrument to the chosen star. Because the elevation angle for the star used is known as a function of time, the slant path distances can be converted to obtain the corresponding altitude above ground.

The  $C_n^2$  values obtained for adjacent levels are not entirely instrument independent because there will be some overlap in the weighting functions used to separate the spatial frequencies. It is usually assumed that readings from levels 1, 4, and 7 are instrument independent. Figure 1 shows a typical scintillometer-derived profile for  $C_n^2$ . The scale shown has been chosen to show the usual altitude range of interest for this parameter and its typical variation. We see that the scintillometer does not provide information regarding  $C_n^2$  for high and low altitudes but does give a profile from about 2 km to 17 km. It should be emphasized that the "points" on this graph really represent values centered at the indicated altitude but come from averaging over distances of the order of a kilometer and a time duration of 2-3 minutes.

<sup>&</sup>lt;sup>1</sup>Markson, R. M., Anderson, B. W., Fairall, C. W., Thomson, D. W., White, A. B. and Syrett, W. J. (1989), Atmospheric Turbulence Measurements in Support of Adaptive Optics Technology, RADC-TR-89-289, ADA220445.

<sup>&</sup>lt;sup>2</sup>Hufnagel, R. E. (1978), Propagation Through Atmospheric Turbulence, in *The Infrared Handbook*, USGPO, Washington D. C., Chap. 6, 1-56.

<sup>&</sup>lt;sup>3</sup>Ochs, G. R., Wang, T., Lawrence, R. S. and Clifford, W. S. (1976), Refractive Turbulence Profiles Measured by One-Dimensional Spatial Filtering, Appl. Opt., 15: 2504-2510.

Recently<sup>4</sup> it has been found that the weighting functions originally used were incorrect and resulted in significantly lower values of C<sub>n</sub><sup>2</sup>. This has necessatated a good deal of recalculation of previous results. Also data obtained by Don Walters<sup>5</sup> of USNPGS using an isoplanometer at the PSU measurement program has become available to us. We have reanalyized the scintillometer data in light of the corrected weighting functions and made comparisons to the isoplanometer data.

### **B. ANALYSIS**

## 1. C<sub>n</sub><sup>2</sup> Analysis

Over 200 profiles of  $C_n^2$  were obtained at PSU. Those with a quality factor (which is ideally unity) of over 2.5 were rejected. This left us with 184 profiles with average quality factor of 1.5. See Table 1. For each profile the slant path values were converted into height above ground using the known azimuth angle. (See Figure 2.) In that the fluctuation about the mean height is of the order of 5% of its value we treat data from each level as if coming from the same height for the purposes of this Section.

The  $C_n^2$  values for each evening were analyized statistically. See Table 2 for some of the results. In Figures 3-9, the nightly average of  $C_n^2$  is plotted versus evening for each level. It can be seen that there is a significant difference between  $C_n^2$  values at all levels between April 30-May 3 and May 5-6 and that the behaviour on May 4 is such that at lower levels  $C_n^2$  is relatively small, but increases for higher levels.

Correlation studies done earlier<sup>6</sup> were redone in light of the corrected weighting functions and slightly different data set. In that no qualitative changes are apparent, these results will not be presented here.

## 2. $\theta_{\rm O}$ Analysis

One important measure of turbulence induced distortions on an optical beam is

<sup>&</sup>lt;sup>4</sup>Krause-Polstoff, J and Murphy, E. A., Investigation of Photomultiplier Tube Response in the Stellar Scintillometer, to be published.

<sup>&</sup>lt;sup>5</sup>Walters, D. (1991), U. S. Naval Postgraduate School, private communication.

<sup>&</sup>lt;sup>6</sup>Battles, F. P. and Murphy, E. A., Correlations Between Levels for Stellar Scintillometer Derived Profiles of  $C_n^2$ , GL-TR-90-0213, 1990.

the isoplanatic angle,  $\theta_0^{7}$ , which is the maximum angle over which an extended object can be viewed, in the absence of adaptive optics, through turbulence. For the case of vertical viewing down through the atmosphere, Loos and Hogge<sup>8</sup> have shown that, for  $\theta_0$  in  $\mu$ radians,

$$\theta_{\rm O} = 5.8 \times 10^4 \ \lambda^{1.2} \left[ \int_{0}^{\infty} z^{5/3} C_{\rm n}^2(z) \ {\rm dz} \right]^{-3/5}$$

where  $\lambda$  = wavelength (m), assumed equal to 500nm in what follows,

 $C_n^2$  = refractive structure parameter (m<sup>-2/3</sup>),

and z = altitude above ground (m).

By use of a model developed by Murphy and Battles<sup>9</sup>, it is possible to convert to each scintillometer profile into a value for  $\theta_0$ . Figures 10-11 are a graphical summary of our results and Table 3 summarizes nightly means and standard deviation.

#### 3. Comparison to isoplanometer data.

Unlike the stellar scintillometer, an isoplanometer<sup>10</sup> allows for direct measurement of  $\theta_0$  on a much finer time scale than measurements of  $C_n^2$  profiles using the scintillometer. Such a device was used at the PSU measurement program and results were recently made available to us<sup>11</sup>. In Table 4 we show comparisons for nightly means; agreement is excellent except for May 4 where the mean isoplanometer value is 80% of the scintillometer. Shown in Figure 12 is a comparison plot for May 5. Plots for other evenings are similar<sup>12</sup>.

<sup>&</sup>lt;sup>7</sup>Born, M. and Wolf, E. (1983), <u>Principles of Optics</u>, 6th ed., Pergamon Press, Oxford.

<sup>&</sup>lt;sup>8</sup>Loos, G. and Hogge, C., (1979), Turbulence of the Upper Atmosphere and Isoplanatism, Appl. Opt., 18, 2654-2661.

<sup>&</sup>lt;sup>9</sup>Murphy, E. A. and Battles F. P (1986), Isoplanatic Angle from Stellar Scintillometer Measurements at Pennsylvania State University, AFGL Technical Memorandum, No. 129.

<sup>&</sup>lt;sup>10</sup>Stevens, K. B. (1985), Remote Measurement of Atmospheric Isoplanatic Angle and Determination of Refractive Turbulence Profiles by Direct Inversion of the Scintillation Amplitude Covariance Function with Tikhonov Regularization, Ph.D. Dissertation, Naval Postgraduate School, Monterey CA; Advisor: Donald L. Walters.

<sup>&</sup>lt;sup>11</sup>Walters, D. (1991), U. S. Naval Postgraduate School, private communication.

<sup>&</sup>lt;sup>12</sup>Krause-Polstoff, J and Murphy. E. A., Investigation of Photomultiplier Tube Response in the Stellar Scintillometer, to be published.

#### 4. Jet stream effects.

During the measurement program at PSU, jet stream activity was carefully monitored. During the evenings of April 30, May 2 and May 3, the jet stream was present; on May 4 it moved out and was absent on May 5 and May 6. This suggests that we group our data in the following manner: Strong jet stream activity: April 30, May 2-3; transition period: May 4; no jet stream activity: May 5-6. The results of this grouping is found in Table 5.

#### C. CONCLUSIONS

Agreement between values of  $\theta_0$  obtained using the stellar scintillometer and the isoplanometer is quite good, not just on an average basis but as a function of time. This lends credence to both devices for measuring  $\theta_0$  and to  $C_n^2$  profiles obtained using the scintillometer and the corrected weighting functions. The jet stream's presence or absence seems to effect  $\theta_0$  by a factor of two.

# **PART II**

#### A. INTRODUCTION

Recently, it has shown<sup>13</sup> that in the Lidar approach to measurements of  $C_n^2$ , the following approximate matrix equation occurs

$$\gamma = W C$$

where  $\gamma(z_i)$  is some optical property (spot dancing, scintillation, etc.) measured by the Lidar at altitude  $z_i$  and

$$W_{ij} = \int_{z_{j-1}}^{z_j} W(z_i) dz, i \ge j$$

 $W_{ij} = 0$ , i<j (i.e. W is a lower triangular matrix<sup>14</sup>)

<sup>13</sup>Beland, R. R. and Krause-Polstroff (1991), Lidar Measurement of Optical Turbulence: Theory of the Crossed Path Technique, Phillips Laboratory Technical Report PL-TR-91-2139.

and  $W(z_i)$  is a weighting function which depends on the particular property,  $\gamma$ , being measured. We have looked at, by way of numerical simulation, some of the problems of inverting this equation.

## **B. CALCULATIONS**

## 1.Image Dancing

In this case  $W_{ij}$  takes the form (dropping constants of proportionality)

$$\mathbf{W}_{ij} = \frac{3}{8} \, \mathbf{z}_i \, \left[ \left( \, \, 1 - \frac{\mathbf{z}_{j-1}}{\mathbf{z}_i} \right)^{8/3} \, - \, \left( 1 - \frac{\mathbf{z}_j}{\mathbf{z}_i} \right)^{8/3} \right] \, , \, \mathbf{i} \! \geq \! \mathbf{j}.$$

See Table 6. We have two ways of obtaining C: We may obtain  $W^{-1}$  and use  $C = W^{-1} \gamma$  or use iteration on the system

$$C_n^2(z_i) = (W_{ii})^{-1} [\gamma(z_i) - \sum_{j=1}^{i-1} W_{ij} C_n^2(z_j)]$$

where  $C_n^2(z_0) = 0$ . We let  $z_i = i$ , i = 1, 2, 3, ...10 and for various inputs,  $\gamma$ , looked at the stability of solutions for slight changes in input. For example, for an initial  $\gamma = (.1, .2, .3, ...1)$  we obtained a numerical solution for C. We then allowed each component of  $\gamma$  to vary, at random by a factor  $\pm 1\%$ . See Table 7 for the results of this fairly small flucuation of  $\gamma$  on C.

#### 2. Variance of log-amplitude scintillation

In this case, to some approximation, we have

$$W_{ij} = (\frac{z_j^{\ 2}}{2} - \frac{z_j^{\ 3}}{3z_i}) - (\frac{z_{j-1}^{\ 2}}{2} - \frac{z_{j-1}^{\ 3}}{3z_i}) \ , \ i \ge j.$$

Results similar to that for spot-dancing were obtained for a linearly increasing  $\gamma$ .

<sup>&</sup>lt;sup>14</sup>Stewart, G. W. (1973), Introduction to Matrix Computations, Academic Press.

# 3. The crossed-path technique

In this case the specific form for  $W_{ij}$  are not given in a simple closed form. Qualitatively, they are expected to peak somewhat sharply for  $j \simeq i/2$ . To possibly see qualitatively this effect, we took

$$W_{ij} = \exp[-(j - i/2)^2], i \ge j$$

Results are extremely unstable.

# C. Conclusions

A good deal more effort is needed in this area before drawing any conclusions as to the utility of using inversion techniques on Lidar measurements.

DATE	# OF PROFILES
APR 30	11
MAY 2	39
MAY 3	51
MAY 4	32
MAY 5	27
MAY 6	24
TOTAL	184

_LEVEL	APR 30	MAY 2	MAY 3	MAY 4	MAY 5	MAY 6
1	3E-16	5E-16	5E-16	6E-17	7E-17	8E-17
2	1E-16	2E-16	2E-16	2E-17	3E-17	5E-17
3	5E-17	7E-17	4E-17	6E-18	1E-17	2E-17
4	3E-17	3E-17	2E-17	6E-18	5E-18	1E-17
5	3E-17	3E-17	2E-17	1E-17	5E-18	1E-17
6	9E-18	1E-17	1E-17	8E-18	4E-18	4E-18
7	9E-18	1E-17	7E-18	8E-18	5E-18	4E-18

Table 1: Number of profiles over the measurement period.

Table 2. Nightly averages for Cn2 by level for each night.

	Mean	Median	Std. Dev.
Apr 30	5.67	4.93	1.38
May 2	4.13	4.14	0.53
May 3	5.70	5.58	1.20
May 4	6.82	6.72	1.32
May 5	9.87	9.97	1.24
May 6	8.96	9.15	1.99

Table 3. Mean, median and standard deviation for scintillometer derived values of isoplanatic angle (microradians) by night.

	Scintillometer	Isoplanometer	%difference
Apr 30	5.67	5.36	5.5%
May 2	4.13	4.14	0.0%
May 3	5.70	5.69	0.0%
May 4	6.82	5.45	20.0%
May 5	9.87	9.08	8.0%
May 6	8.96	8.14	9.2%

Table 4. Nightly means for isoplanatic angle from scintillometer and isoplanometer over comparable time periods and % difference.

Strong Transition Absent

	TH	C1	C2	C3	C4	C5	C6	C7
ſ	5.09	4.73E-16	1.62E-16	5.23E-17	2.42E-17	2.28E-17	1.10E-17	8.93E-18
	6.82	6.00E-17	1.59E-17	5.61E-18	5.77E-18	1.03E-17	8.13E-18	7.71E-18
ſ	9.46	7.01E-17	3.61E-17	1.52E-17	7.22E-18	7.32E-18	3.70E-18	4.35E-18

Table 5. Average isoplanatic angle and average Cn2 for each level, for strong jet stream activity (April 30 and May 2–3), transition evening (May 4) and no jet stream activity (May 5–6).

	0.375	0	0	0	0	0	0	0	0	0
	0.6318	0.1181	0	0	0	0	0	0	0	0
	0.7434	0.3214	0.0600	0	0	0	0	0	0	0
	0.8034	0.4602	0.1990	0.0372	0	0	0	0	0	0
	0.8408	0.5539	0.3173	0.1372	0.0256	0	0	0	0	0
W=	0.8663	0.6205	0.4087	0.2341	0.1012	0.0189	0	0	0	0
	0.8847	0.6700	0.4799	0.3161	0.1811	0.0783	0.0146	0	0	0
	0.8987	0.7082	0.5363	0.3841	0.2530	0.1449	0.0626	0.0117	0	0
	0.9097	0.7385	0.5820	0.4407	0.3157	0.2079	0.1191	0.0515	0.0096	0
	0.9185	0.7632	0.6196	0.4882	0.3697	0.2648	0.1744	0.0999	0.0432	0.0080

Table 6. The matrix shown above was computed from the formula  $3/8zi\{[1-(zj-1/zi)]^8/3-[1-(1-zj/zi)]^8/3\}$  for z=0..10.

C(zi)	Std.Dev.	Percent
0.27	0.002	0.7407
0.262	0.013	4.9618
0.198	0.066	33.333
0.625	0.244	39.04
-0.752	0.744	-98.93
2.76	2.05	74.275
-5.72	5.41	-94.58
14.71	14.05	95.513
-36.27	36.14	-99.64
96.34	92.54	96.055

Table 7. The average and standard deviation of C(zi) gotten by letting gamma = (.1,,2,..1) and then let each component vary by +/-1%. Based on 109 simulations.

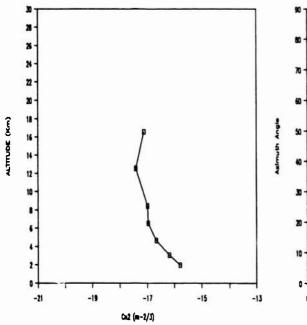


Figure 1. A typical scintillometer profile.

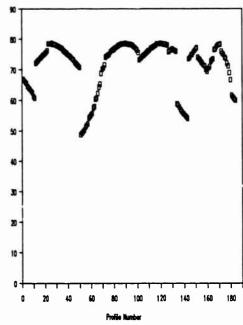


Figure 2. Azimuth angle vs profile number.

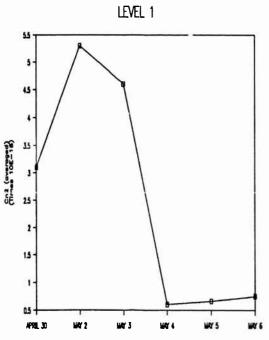


Figure 3. Cn2 at level 1.

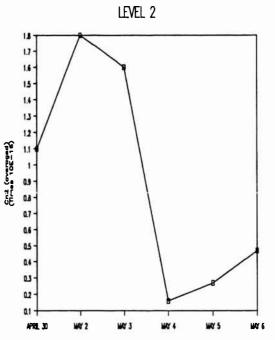
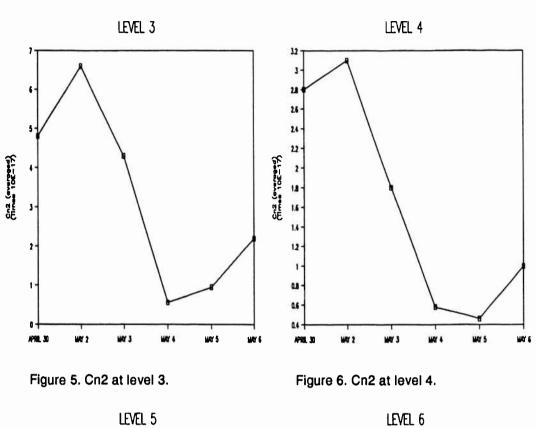
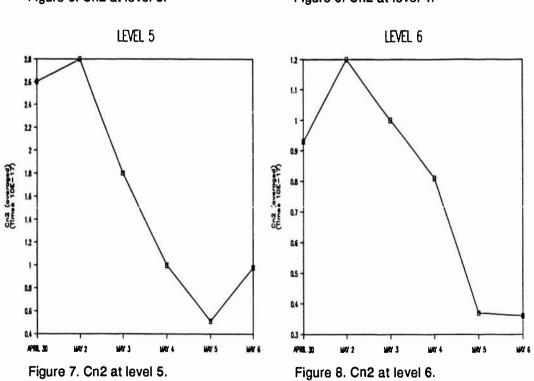


Figure 4. Cn2 at level 2.





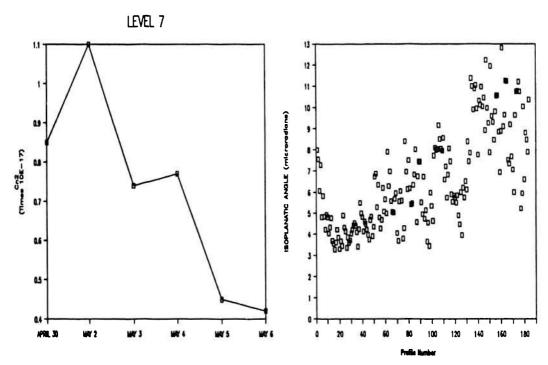


Figure 9. Cn2 at level 7.

Figure 10. Isoplanatic angle vs profile number.

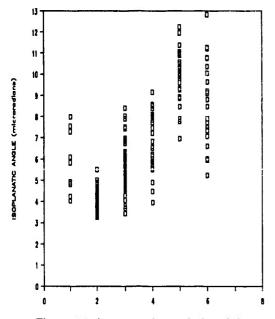


Figure 11. Isoplanatic angle by night.

Note that in Figure 11:

April 30 = 1

May 2 = 2

May 3 = 3

May 4 = 4

May 5 = 5

May 6 = 6

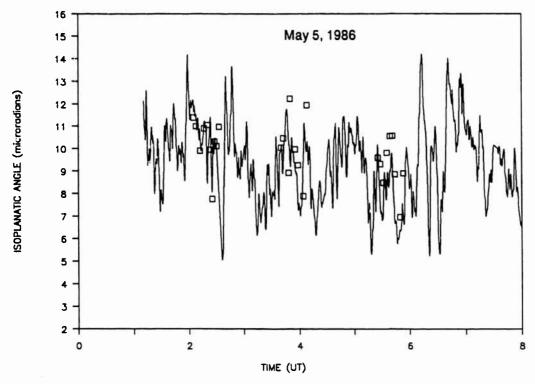


Figure 12. Comparison plot of isoplanatic angle from scintillometer (points) and isoplanometer (line).

# THEORETICAL STUDIES OF COLLISIONAL VIBRATIONAL RELAXATION OF OH Professor Ronald J. Bieniek

Experimental measurements of vibrational relaxation of OH through collisions with atmospheric constituents is an ongoing project of the LABCEDE group. Theoretical methods of computing multi-quanta transitions were required to interpret experimental data confidently. To achieve this, a method was developed to utilize T-matrix elements, based on adiabatic vibrational wavefunctions, in the exponential approximation for the scattering matrix. From quantum mechanical computations, multi-quanta transitions were found to be insignificant compared to single quanta transitions for experimental conditions and atmospheric disturbances of interest. Futhermore, a very simple scaling law was devised that readily and accurately tracks the sensitivity of relaxation rates to initial vibrational excitation. Rates for the relaxation of the nth-vibrational state were shown to be proportional to  $n \cdot (1-2x_en) \cdot [1-2x_e]^{-1} \cdot \exp[\beta(n-1)]$ , where  $x_e$  is the first-order anharmonicity constant and  $\beta$  is a constant determined from system parameters. This form successfully predicted changes in rates over several orders of magnitude.

#### INTRODUCTION

During summer of 1991, I worked on several problems in molecular collision theory that were in direct support of the long standing LABCEDE mission, in the Optical Environment Division of the Geophysics Directorate of Phillips Lab, to characterize molecular relaxation-quenching rates. The Liebe experimental group has very recently measured the vibrational relaxation rate of OH(v) through collision with typical atmospheric constituents  $(O_2 \text{ and } CO_2)$ . These rates are needed to model reaction and relaxation mechanisms in the atmosphere and in remote sensing of emissions from local atmospheric disturbances, such as exhaust plumes. Initial vibrational excitations in these circumstances are observed to occur up to vibrational quantum number v = 9.

To obtain the vibrational relaxation rates,  $K_{\rm V}$ , as a function of initial vibrational quantum number, v, the LABCEPE group had to make, in their analysis of laboratory data, the simplifying assumption that the only significant final state was  $v_{\rm f} = v - 1$ , i.e., only single quantum transitions (to the next lower vibrational level) were important. But if multi-quanta transitions (to levels below the next one down) are important in vibrational relaxation of OH, the determined rates used in atmospheric modelling and in remote-sensing become problematic. Furthermore, the group hoped that there would be a simple mathematical relationship between the relaxation rate and initial vibrational excitation. However, they found that not only was a graph of  $K_{\rm V}$  versus v non-linear, but even  $\log(K_{\rm V})$  versus  $\log(v)$  was not linear. Thus there appeared to be no simple scaling relationship to interpret or predict the rapid rise of relaxation rate with vibrational state v.

Since these issues will also arise in the further LABCEDE work on collisional vibrational relaxation of OH(v), it seemed timely to see if brute-force or simplifying analytic theories could be brought to bear on them. The LABCEDE group asked that I work on the following tasks:

(1) Apply theoretical methods to determine if, indeed, multi-quanta transitions can be ignored in the analysis of collisional relaxation of OH(v) in the experimental and atmospheric

#### conditions of interest;

- (2) Determine if there is a simple scaling rule that can be used to understand the rapid increase of relaxation rates with initial vibrational excitation;
- (3) Make some predictions about the relaxation rates of OH that would be expected with Ar as a collision partner, since it is a necessary bath gas to slow down electrons in LABCEDE experiments, whose contributions to relaxation rates must be subtracted out to obtain rates for the atmospheric colliders of interest

#### DISCUSSION OF RESULTS

# Numerical Tests and Interpretations of Approximations and Computer Codes

To determine vibrational relaxation rates in molecular collisions, it is convenient to use the breathing sphere (BS) appoximation, in which the interaction between a projectile (Ar,  $O_2$  here) and a target (OH) is averaged over the orientations of the diatomic axis.<sup>2</sup> This creates an potential in which the diatom is represented by a sphere that can vibrate radially, and can change the state of this vibration through collisions with the perturbing projectile. This approximation is based on the infinite-order sudden (IOS) approximation for rotational transitions, and has been shown to be useful in determining vibrational transitions.<sup>2,3,4</sup> Because this investigator and others have extensively investigated the HF + He system, it was used as a control system to test continuously the computer codes that were developed to handle sculti-quanta transitions in OH(v).<sup>5,6</sup> The breathing sphere potential for HF + He is accurately described by:

$$V(r,R)^{BS} = 54.372 \exp(-1.80R + 0.23718 (r-r_e))$$

$$- 33.346 \exp(-1.70R + 0.21099 (r-r_e))$$
(1)

where r is the HF stretch co-ordinate and R is the HF - He collision distance;  $r_e$  is the equilibrium separation of HF. Since the full potential hypersurface is known for this system, state-to-state cross sections were computed for rovibrational transitions  $HF(v,j) + He \rightarrow HF(v',j') + He$ , using the infinite-order sudden approximation over a wide range of collisional energies. The sum over j' of the sum ov

TABLE 1: Ratio of breatning-sphere (BS) vibrational de-excitation cross sections to infinite-order sudden (IOS) cross sections at various collisional energies  $E_{\rm c}$ .

E <sub>C</sub>	orus v=1 + 0 (E <sub>c</sub> ) (cm <sup>2</sup> )	$ \frac{\sigma_{V=1}^{BS} + 0}{\sigma_{V=1}^{IOS}} $	σ <sup>IOS</sup> v=4 + 3 <sup>(E</sup> c)	0 N N N N N N N N N N N N N N N N N N N
0.125	4.79 × 10 <sup>-25</sup>	1.65		
0.250	1.33 × 10 <sup>-23</sup>	1.67		
0.50	5.38 × 10 <sup>-22</sup>	1.69	$1.33 \times 10^{-20}$	1.75
1.0	2.11 × 10 <sup>-20</sup>	1.68	3.78 × 10 <sup>-19</sup>	1.72
2.0	5.70 × 10 <sup>-19</sup>	1.64		

As can be seen, the BS results maintain a constant factor relationship with the accurate IOS results over the entire energy range characteristic of laboratory and atmospheric conditions, even though the numerical values of cross sections have changed by many orders of magnitude. Similar results had been obtained in an earlier, more limited study of single-quantum vibrational excitation.<sup>7</sup>

This is indicative that BS results can be used to treat vibrational transitions, particularly in collisional systems for which a full potential hypersurface is not available (the usual condition). Consequently, one expects that unknown cross sections  $\sigma_{\text{V}' \to \text{V}' \pm 1}(\text{E}')$  for vibrational quenching of various levels v' in a range of energies E' may be adequately predicted from a single accurately known one  $\sigma^a_{\text{V} \to \text{V} \pm 1}(\text{E})$  at one energy E by the simple formula:

$$\sigma_{V'+V'-1}(E'_{c}) = \frac{\sigma_{V}^{B_{s}}_{V+V'-1}(E'_{c})}{\sigma_{V+V-1}^{B_{c}}(E_{c})} \quad \sigma_{V+V-1}^{Q}(E_{c})$$
(2)

This is the basic idea behind analyzing the breathing-sphere discussed in this report.

To compute cross sections,  $\sigma_{n\to j}$ , and rates,  $K_{n\to j} = \text{vel} \cdot \sigma_{n\to j}$ , for transitions from vibrational level n to level j, one employs the scattering S-matrix in the familiar equation:

$$\sigma_{n\to j} = \pi k_n^{-2} \sum_{l=0}^{\infty} (2l+1) |\delta_{nj} - S_{l,nj}|^2.$$
 (3)

To obtain the S-matrix, one can expand the total scattering wavefunction in terms of product states involving unperturbed molecular vibrational wavefunctions that depend only on the stretch coordinate r, multiplied by the corresponding continuum wavefunction for the translation motion (which depends upon the collision coordinate R). A set of coupled differential equations would result. 5 This is the technique usually employed. One of the main physical reasons that necessitate such coupled equations is the fact that a superpostion of many unperturbed vibrational wavefunctions are needed to describe the actual vibrational wavefunction as it changes during the influence of the collision. However, for the results quoted above in Table 1 for single-quantum transitions in HF + He, an adiabatic distorted-wave method was employed, in which the vibrational wavefunctions are allowed to relax adiabatically during the collision. 4 This is very similar to the standard method of using molecular electronic states to describe a collision, instead of an expansion in atomic states. But unlike the normal situation with adiabatic electronic states, d/dR terms are important coupling elements for vibrational transitions. This has been accurately handled in the numerical implementation of the cooes. net result is that one need not solve coupled equations or use perturbation theory to compute single quanta transitions. (This will be numerically demonstrated in a moment.)

However, if one is to handle multi-quanta vibrational transitions and yet avoid the cumbersome problems often associated with coupled

equations, some form of perturbation theory must be employed. One can begin with a perturbation expansion of the T-matrix. The T and S matrices are related by  $S=1-2\pi i T$ . The expansion for T is made in terms of the Green's function operator  $G^+$  and the portion V of the interation potential that is not incorporated into the Green's function. (Basically, this says that distorted-wave techniques can be used for the collisional wavefunctions.) This expansion reads:

$$T = T^{(1)} + T^{(2)} + T^{(3)} + \cdots$$

$$= V + VG^{\dagger}V + VG^{\dagger}VG^{\dagger}V + \cdots$$
(4)

In most research dealing with this approach, an unperturbed Green's function is normally employed, making V the complete perturbation potential (see Ref. 5, and citations therein). However, it was determined in this project that this restriction is not really necessary, for the derivation follows closely the complex-potential formalism this investigator established for strongly-coupled electronic processes (e.g., Penning ionization) in which distorted-wave techniques have proven very accurate. One can thus insert a unity operator between each V and G operator in the expansion above, and then write them in terms of product states of vibrational wavefunctions and energy normalized distorted-wave scattering states of the diagonal potential: 1 =  $\Sigma \int |\chi_{\Pi}(r;R)|u_{\ell}(E,R)\rangle \langle u_{\ell}(E,R)|\langle \chi_{\Pi}(r;R)|$ . The resulting spectral decomposition produces perturbation terms for the T-matrix of the sort

$$T_{nj}^{(1)} = W_{nj}(k_n, k_j) ,$$

$$T_{nj}^{(2)} = \sum_{\gamma=0}^{\infty} \int_{0}^{\infty} dE'' \frac{W_{nj}(k_n, k'')W_{\gamma j}(k'' k_j)}{-E'' + E_{\gamma} + i\epsilon}$$
(5)

where the W's represent first-order distorted-wave T-matrix elements, and the k's are asymptotic wavenumbers.

The singularity in the integral over energy can be easily evaluated by casting the integrals into the form

$$\sum_{\gamma} \int_{0}^{\infty} d\Xi \frac{f(k)}{-E + E_{\gamma} + i\epsilon} = \sum_{\gamma} \left[ P \int_{0}^{\infty} dE \frac{f(k)}{-E + E_{\gamma}} - i\pi f(k_{\gamma}) \right]$$
 (6)

and, then neglecting the principal part integral because of the approximately odd symmetry of the integrand. (This latter action essentially excludes terms that arise from channels off the energy shell.) "One can then show" that the S-matrix can be approximately written as

$$S(E) = \exp[-2\pi i t(E)] \tag{7}$$

where t(E) is the first-order T-matrix at total energy E, for all transitions. This is the adiabatic unitary exponential approximation for the S-matrix, which preserves unitarity.

There is a simple interpretation of its form. Consider a molecule in the second excited vibrational state (n=2). Assume the collisional energy is not great enough to excite the third vibrational state. the exponential approximation, for low energy collisions, the S-matrix element for the two-quanta transition to the ground state (n'=0) will have the form  $S_{20} = -2\pi i t_{20} - 2\pi^2 t_{21} t_{10}$ . The first term is the direct transition term, while the second one represents a transitional path through virtual states (2+1 then 1+0). It will turn out that the second term is dominant in this case because it involves single-quantum coupling. One might be surprised that this "perturbation expansion" does not show denominators involving the difference in energy between states. But one must remember that this process is not really between discrete states, but involves a continuum of free scattering states through the spectral decomposition arising through the unity operators inserted between the V and  $G^+$  operators. The resulting integrals over all energies had energy differences in the denominators, and the evaluation of those integrals still retains them in the small principal part correction ignored here.

This exponential approximation based on an adiabatic distorted-wave approach was numerically tested against full-close coupled results found in the literature for vibrational excitation in the HF + He system.  $^5$  The results are summarized in the graph below which displays partial cross sections as a function of collisional angular momentum  $\ell$ .

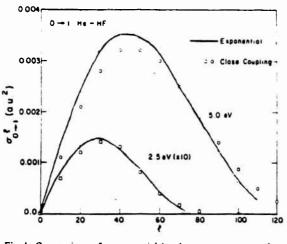


Fig. 1. Comparison of exponential ( $\longrightarrow$ ), and close-coupling (0 0) partial cross section behavior for He-HF transition (0  $\rightarrow$  1) at a collision energy of 2.5 and 5 eV. Total cross sections are given by area under curves. 2.5 eV results are multiplied by ten.

Fig. 2. Comparison of exponential ( $\longrightarrow$ ), and close-coupling ( $\circ$ ) partial cross section behavior for He-HF transition (0  $\rightarrow$  2) at 5 eV. Total cross sections are given by area under curves.

The adiabatic unitary exponential approximation compares very favorably to the close-coupled results, reinforcing an earlier, more restrictive test of the first-order adiabatic method in thermal  $SiO(v) + H_2$  collisions. (The effort to produce the computer code behind these computations comprised a major part of the summer's project. Checking for numerical consistency and tracking down bugs was time consuming, but the end product was a very useful and versatile scattering code that can run on the computers readily available to the LABCEDE group and others in the GPOS branch of the Phillips Laboratory.)

Two additional points should be noted. For the single-quantum transition  $0 \to 1$ , the first-order  $t_{01}$  elements were sufficient alone to produce accurate results because the adiabatic approach accurately describes the evolving vibrational wavefunctions, even though higher vibrational levels were energetically open. Secondly, the  $t_{01}t_{12}$  product term was by far the dominant contribution to the double-quanta excitation  $0 \to 2$ , compare to both the direct term  $t_{02}$  and paths through

other virtual states (e.g.,  $t_{01}t_{13}t_{32}$ ). This is a general result: the only significant contribution to multi-quanta transitions occurs by single-quantum steps through consecutive virtual states. From this, we can infer the reason that multi-quanta transitions are usually insignificant in comparison to single-quantum down-steps for vibrational relaxation. The strength of a single quanta transition, say  $n \to n-1$ , is related to a sum over angular momenta  $\ell$  of  $|t_{\ell,n,n-1}|^2$ :

$$\sigma_{n\rightarrow n-1}(E) \propto \Sigma |t_{\ell,n,n-1}(E)|^2$$
 (8)

However, for a two-quanta relaxation, we would have

$$\sigma_{\mathbf{n}\to\mathbf{n}-2}(\mathbf{E}) \propto \Sigma |\mathsf{t}_{\ell,\mathbf{n},\mathbf{n}-1}(\mathbf{E})|^2 \cdot |\mathsf{t}_{\ell,\mathbf{n}-1,\mathbf{n}-2}(\mathbf{E})|^2$$
 (9)

Since  $|t_{i,j}|^2 \ll 1$  generally and the sum over angular momenta is still terminated by the same centrifugal barrier in channel n, the two quanta transition should usually be much less than the single-quantum one.

# Application to Vibrational Relaxation of OH

Once the adiabatic unitary exponential approximation's efficacy was demonstrated by these computations, attention could be turned to the mission oriented problem of collisional vibrational relaxation of OH(v). Because Esposti and Werner have recently computed ab-initio information for the ground  $X^2\Pi$  potential surface of OH-Ar, it was used for representative quantal computation studies. 9 In an earlier study of this system, Thompson had simply assumed pair-wise additivity of diatomic potentials to undertake quasi-classical studies of vibrational transitions in OH + Ar collisions at elevated energies. IO Although it would have been nice to have used a breathing-sphere average of Thompson's potential for comparative adiabatic exponential computations, time was not available to do the required setup work. Fortunately, this investigator was able to acquire a copy of Esposti's and Werner's Legendre expansion of the collisional coordinate R-dependence of the interaction, for a rigid OH molecule. II The isotropic component  $V_O(R)$ 

(the  $D_0^0(R)$  Legendre-expansion coefficient) is shown below.

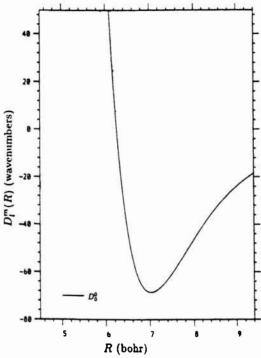


FIG. 3. Variation with R of the coefficients  $D_n^m(R)$  in the Legendre polynomial expansion of the  $Ar(^1S_0) + OH(X^2\Pi_1v^* = 0)$  interaction potential.

The problem is that the computation of vibrational relaxation requires the OH stretch dependence of the potential, for if the interaction has no r-dependence, no transitions can occur. Although Werner and his group at Bielefeld are working on the r-dependence at this moment, information is not yet available. However, preliminary studies could be undertaken this summer through the expedient of assuming a plausible r-dependence and varying its strength.

The form chosen for the "adjustable" breathing-sphere potential was  $V(r,R) = V_0(R) \exp[\gamma \cdot (r - r_e)]$ , where  $\gamma$  is a parameter that can realisticly be expected to be in the range of .02 - 2.0 (bohr)<sup>-1</sup>, from comparison with other systems such as HF + He.<sup>4,12</sup> The value of gamma definitely affected the quantal numerical values obtained for cross sections and rates, which will be discussed in more detail presently. However, one can still compare the relative strength of single-quantum transitions to multi-quanta ones. For any gamma selected in the cited range, and for all collisional energies important in the experimental

conditions of the LABCEDE project (T = 300 °K), the computed quantum mechanical rates for transitions to the next lower level (single-quantum rates) were found to be at least a factor of 100 larger than the rate to still lower levels. (The only exception was the two-quanta transition v = 9  $\rightarrow$  7, which was 2.5% of the rate single quanta 9  $\rightarrow$  8 transition.) Thus, the LABCEDE group can safely consider only single-quantum transitions in their analysis of experimental relaxation rates of vibrationally excited OH(v).

A very simple relationship was discerned between vibrational cross sections (and rates) produced by various values of  $\gamma$ , the parameter modelling the strength of the OH-stretch perturbation. It was found that cross sections produced by different values of  $\gamma$  always exhibited a simple power dependence:

$$\sigma_{i \to j}(E|\gamma') = \sigma_{i \to j}(E|\gamma) \cdot (\gamma'/\gamma)^{2|i-j|}$$
 (10)

This result can be explained by some analytic "magic" (but not slight of hand). This will also give understanding of the sensitivity of vibrational relaxation rates to anharmonicity in the OH molecule.

Changes in vibrational state through collisions is largely due to the striking of the inner core of the potential interaction, where perturbations are large. If we approximate this repulsive core with an exponential form:

$$V(r,R) = A \exp[\gamma(r-r_e) - \alpha R] - \varepsilon$$
 (11)

an analytic solution is available for the t-matrix elements:  $^{5,12}$ 

$$T_{l,nj} = \frac{1}{16} \alpha (k_n k_j)^{-1/2} \left[ (1 - \delta_{nj}) V_{nj} / V_{jj} \right] (V_{nn} / V_{jj})^{ig_n^l/2} \left[ (q_j^l)^2 - (q_n^l)^2 \right]$$

$$\times \frac{\left[ q_n^l q_j^l \sinh(\pi q_n^l) \sinh(\pi q_j^l) \right]^{1/2}}{\sinh\left[\frac{1}{2}\pi(q_j^l + q_n^l)\right] \sinh\left[\frac{1}{2}\pi(q_j^l - q_n^l)\right]} {}_{2}F_{1} (1 + \frac{1}{2}i[q_j^l + q_n^l], 1 - \frac{1}{2}i[q_j^l - q_n^l]; 2; 1 - V_{nn} / V_{jj})$$
where

$$q_n^l = 2\alpha^{-1} \left\{ k_n^2 + 2m\epsilon - \alpha^2 l(l+1) \left[ \gamma r_e + \ln(2mA/(k_n^2 + 2m\epsilon)) \right]^{-2} \right\}^{\frac{1}{2}}$$
 (12b)

and m is the collisional reduced mass, and  $V_{ij} = \langle i | \exp[\gamma(r-r_e) | j \rangle$  is

the matrix element of the vibrational wavefunctions. Although the confluent hypergeometric function  ${}_2F_1$  looks like an obstacle, its value for all collision systems examined is essentially unity, and will be dropped from further discussion. It is important to use vibrational wavefunctions  $|n\rangle$  that adequately describe anharmonicity. In this study, harmonic-oscillator wavefunctions were used, but for which the oscillator's frequency was adjusted to match the actual anharmonic energy difference  $\Delta \varepsilon_{ij}$  between the i and j levels. (This was tested against matrix elements produced by Morse-oscillator wavefunctions, with little change in results.) These approximate first-order T-matrix elements can be used in the exponential approximation to determine relaxation rates.

However, they may be more readily be used for the analysis of experimental data by some further, defensible approximations. We will concentrate solely on single-quantum transitions, since they dominate the relaxation process. We first assume that  $|t_{nj}|^2$  for all angular momenta can be replaced, on average, by the s-wave value. Then

$$\sigma_{n \rightarrow j}(E_c) \propto (\ell_{mx} + \frac{1}{2})^2 |t_{0,nj}|^2 / E_c$$
 (13)

where  $E_c$  is the collisional energy, and  $\ell_{mx}$  is the maximum angular momentum that significantly contributes to the relaxation at that energy. For the small values of  $\gamma$  that occur in the systems studied, one can show that ratio of matrix elements  $|V_{n,n\pm 1}/V_{nn}|^2$  appearing in the  $|t_{n,n\pm 1}|^2$  is proportional to  $\eta\gamma^2/\Delta\varepsilon$ , where  $\eta$  = maximum(n,n±1). This immediately explains the dependence of relaxation rates on  $\gamma$  noted above. Since  $|S_{ij}|^2$  for a multi-quanta transition can be expressed a product of |i-j| factors of single-quantum  $|t_{n,n\pm 1}|^2$ , each proportional to  $\gamma^2$ , the relaxation rates should vary as  $\gamma^2|i-j|$ , as was indeed discovered in the quantal computations. Furthermore, in most molecular collisions at thermal energies, the q's are sufficiently large that the hyperbolic sine functions can be replaced by their asymptotic exponential form. Finally, if the well depth is sufficiently small,  $\varepsilon$  can be neglected and one finds that  $(\ell_{mx} + \frac{k_1}{2}) \propto E_c$ . We these additional approximations, one can obtain a very simple scaling relation

for vibrational relaxation at different collisional energies and different states of vibrational excitation:

$$\sigma_{V \to V \pm 1}(E_c') = F(E_c', \nu, E_c, \eta) \quad \sigma_{n \to n \pm 1}(E_c)$$
 (14)

where F is a "conversion factor" between different energies and excitations, given by

$$F(E'_{C}, \nu, E_{C}, \eta) = (\nu \Delta \varepsilon_{\nu} / \eta \Delta \varepsilon_{\eta}) \exp(-2\pi [|\Delta k'_{\nu}| - |\Delta k_{\eta}|] / \alpha)$$
 (15)

 $\nu$  = max(v,v±1), and  $\Delta k_j$  is the difference in entrance and exit wavenumbers for the transition  $j \rightarrow j\pm 1$ . For a completely harmonic system, F increases linearly with vibrational quantum number  $\nu$  at a fixed collisional energy,  $[|\Delta k_{\nu}| - |\Delta k_{\eta}|] = 0$  in that case. However, real systems are not harmonic, and the anharmonic effect can be large. 12

Preliminary studies of this relationship were done on HF + He. The repulsive core of the HF-He interaction potential is adequately given by (in hartrees):

$$V^{HF-He}(r,R) = 17.5 \cdot exp(0.340r - 2.20R) - 0.000926$$
 (16)

The effect of anharmonicity on the energy difference between adjacent vibrational levels is accurately described by  $\Delta \varepsilon_{\eta} = \Delta \varepsilon_1 (1-2 x_e \eta)/(1-2 x_e)$ , where  $\Delta \varepsilon_1$  is the energy difference between ground and first excited levels (0.49 eV in HF) and  $x_e$  is the first-order anharmonicity that can be found in standard tables;  $x_e = 0.0218$  for HF. Collisional excitation of HF by He was studied thoroughly for collisional energies of 1 - 3 eV. The factor F did extremely well in predicting the behavior of cross sections. A few examples will suffice. Quantal computations using the full HF + He surface found that  $\sigma_{2\to3}(E_c-1 \text{ eV})/\sigma_{0\to1}(E-1 \text{ eV}) = 16.8$ . The value of the factor F under these conditions was 17.0 (actually produced on a hand-calculator), an error of only 1%. (it should be noted that if HF were not anharmonic, the factor would only be 3.0; the 2.2% anharmonicity changed the cross section by 17/3 or almost 600%!) The analytic factor F accurately tracked changes in cross section over many

orders of magnitude. Quantal computations on the HF + He test system showed  $\sigma_{2\to3}(3\text{ eV})/\sigma_{0\to1}(1\text{ eV})$  =  $2.55\cdot10^4$ ; the corresponding value of the conversion factor F was  $2.66\cdot10^4$ , only 4% in error even though cross sections have changed by four orders of magnitude. It seems that the simple scaling factor F can reliably indicate how vibrational cross sections and rates would change.

Under the conditions experimentally investigated by the LABCEDE effort, the collisional energies of OH and its collisional partners are small compared to the vibrational spacings in OH (0.46 eV). This allows a more transparent and utilitarian expression of F. One can show that relaxation cross sections for collisional energy E should then vary as:

$$\sigma_{n\rightarrow n-1}(E|\gamma,\alpha) \propto (\gamma/\alpha^2)^2 n \Delta \varepsilon_n (\ell_{mx} + \frac{1}{2})^2 E^{-1}$$

$$\cdot \exp(\beta' \left[ x_e n - 1 + (E/\Delta \varepsilon_1)^{\frac{1}{2}} - \frac{1}{2} E/\Delta \varepsilon_1 \right])$$
(17)

where  $\beta' = 2\pi (2m\Delta\epsilon/\hbar^2)^{\frac{1}{2}}/\alpha$ . The factor  $(\ell_{mx} + \frac{1}{2})^2/E$  appears here because the well depth can no longer be ignored at themal energies, and the maximum angular momentum is not a simple function of collisional energy E; this will not allow us, at the moment, to make accurate predictions as to the energy dependence of relaxation cross section. Still, from this information, we can arrive at a very simple expression for relating vibrational relaxation rates at different levels of initial excitation, for the scaling by vibrational quantum number n should be independent of temperature. Thus relaxation rates should follow a simple scaling relationship at thermal collisional energies:

$$K_{n\to n-1}(E_c) = f(n, x_e) K_{1\to 0}(E_c)$$
 (18a)

where

$$f(n,x_e,\alpha) = F(E,n,E,1) = n \cdot (1-2x_e) \cdot [1-2x_e]^{-1} \cdot \exp[\beta(n-1)]$$
 (18b)

where  $\beta = x_e \beta' = 2\pi (2m\Delta \varepsilon/\hbar^2)^{\frac{1}{2}} x_e/\alpha$ . (The critical dependence of f on  $\alpha$  is through the  $\beta$  parameter.)

Note that the scaling factor f is independent of collisional energy, which predicts that ratios of relaxation rates for different

initial levels, but the same collisional energy, should be independent of energy. This was tested on the breathing sphere potential for OH-Ar. Absolute rates cannot yet be determined because the potential's dependence on OH stretch is currently not available; but ratios of rates can be computed, because the  $\gamma^2$  in each one will cancel out. The ratios or ined for single-quantum transitions by quantal computations are shown in the figure below for two different collisional energies:  $E_0=0.0387$  eV (equal to 3kT/2 for the temperature of 300 K characteristic of the LABCEDE measurements) and  $E'=5E_0$  (which is toward the end of the thermal tail). For the simple scaling law  $f(n,x_0,\alpha)$ , the exponential repulsive core parameter  $\alpha$  was adjusted to give a "best eye-ball" fit. The value of  $\alpha=12.0$  produced the results in the figure.

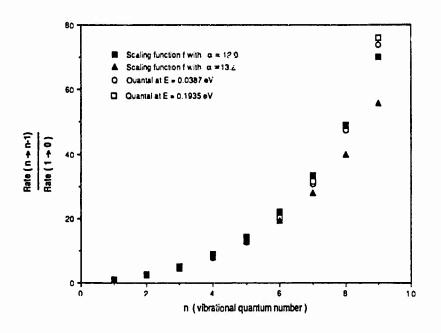


Fig. 4: Ratios of relaxation rates for OH(n) + Ar.

The simple scaling law tracked the brute-force quantal results quite well, even though the rates changed by almost two orders of magnitude. The rapid rise is a combination of exponential slope  $\alpha$  and anharmonicity  $x_e$ . Note also that the ratio rates is fairly independent of collisional energy. The value of  $\alpha$  = 12 is interesting for it does not match the actual exponential slope at high energies (1 eV). Rather it seems to be an effective slope that takes into account the attractive well of the potential. Research is needed to be able to predict the effective slope

from the shape of a known potential.

Finally, since the scaling of relaxation rates is, indeed, fairly independent of collisional energy, the simple scaling law f can be used to predict scaling of thermally averaged relaxation rates:

$$K_{\mathbf{v}}(T) = f(\mathbf{v}, \mathbf{x}_{\mathbf{e}}, \alpha) K_{1}(T)$$
(19)

The figure below displays the experimental results cotained by LABCEDE for vibrational relaxation of OH(v) due to collisions with  $O_2$  at a temperature of 300 K. The shaded circles are the experimental values, while the open circles are the values predicted by the simple scaling law from the fundamental  $K_{1\rightarrow0}$  rate, using a value of  $\alpha$  = 12.2 for the effective exponential slope (and very similar to the value of 12.0 found for OH+Ar).

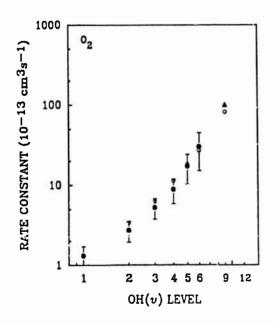


Fig. 5: Rate constants  $K_{\rm V}$  for  ${\rm OH(v)}+{\rm O}_2$  at temperature T = 300 °K. Solid circles, and accompanying error bars, are experimental data from Ref. 1. The solid triangle is an experimental point from a different research group (see Ref. 1). Open circles are those predicted from the simple scaling function  $f(n,x_a,\alpha=12.2)$ 

The rapid rise is due to the combination of  $\alpha$  = 12.2 and  $x_e$  = 0.0222 in  $\beta$ .

Again the simple scaling relation does well in predicting the trend, remaining within the experimental error bars. It is a promising tool to predict relaxation rates for transicions and, hopefully, temperatures that have not been experimentally established.

#### SUMMARY OF RESULTS

- (A) Although an OH-Ar ab-initio interaction potential has just become available, it was computed only for a rigid OH molecule. Thus it could not be used to compute vibrational transitions, which is caused by the dependence of the potential on the OH stretch distance. That is why this dependence had to modelled with an adjustable parameter, varied over a reasonable range, to do Task (1). However, the OH-stretch dependence of the potential is now being computed, and will be available in the near future. This dependence is readily insertable into the computer code developed this summer, to obtain the desired vibrational relaxation rates:
- (B) Although good OH(n) + O<sub>2</sub>(Ar) interaction potentials are not yet available, the potential parameters that strongly affect the cross sections were adjusted over a reasonable range.
  Computations based on a quantum mechanical, adiabatic unitary exponential approximation for the scattering matrix revealed that multi-quantum transitions are insignificant compared to single ones, over a realistic range of potential adjustments;
- (C) Using a analytic solution to scattering from an exponentially repulsive core, one can show that the rates should scale as  $K_n(T) = n \cdot (1 \cdot 2x_e n) \cdot [1 \cdot 2x_e]^{-1} \cdot \exp[\beta(n-1)] K_1$ , where  $x_e$  is the anharmonicity constant, and  $\beta$  is a constant that depends critically on the anharmonicity of the molecule and the effective exponential repulsion of the interaction potential.  $\beta$  is independent of temperature under thermal conditions.

#### REFERENCES

- J. A. Dodd, S. J. Lipson, and W. A. M. Blumberg, J. Chem. Phys. 95, 5752 (1991).
- 2. R. B. Bernstein (ed.), <u>Atom-Molecule Collision Theory: A Guide for the Experimentalist</u> (Plenum, New York, 1979); and references therein.
- 3. D. Rapp and T. Kassal, Chem. Rev. 69, 61 (1969).
- R. J. Bieniek, J. Chem. Phys. 73, 851 (1980); R. J. Bieniek and S. Green, Astrophys. J. Lett. 265, L29 (1983); Astrophys. J. Lett. 270, L101 (1983).
- 5. T. F. Ewing and R. W. Conn, Chem. Phys. 36, 407 (1979); and references therein.
- 6. R. J. Bieniek, J. Chem. Phys. 79, 3738 (1983).
- 7. R. J. Bieniek, XV ICPEAC, Brighton, UK, 22-28 July 1987.
- 8. R. J. Bieniek, Phys. Rev. A 18, 392 (1978).
- 9. A. D. Esposti and H.-J. Werner, J. Chem. Phys. 93, 3351 (1990).
- D. L. Thompson, Chem. Phys. Lett. 92, 383 (1982); --, J. Phys. Chem. 86, 2538 (1982).
- 11. M. I. Lester, private communication.
- 12. F. H. Mies, J. Chem. Phys. 40, 523 (1964).

# THE FORM OF CYCLONIC PRECIPITATION AND ITS THERMAL IMPACT

by

Stanley David Gedzelman

Department of Earth and Atmospheric Sciences City College of New York New York, NY 10031

and

Department of the Air Force Phillips Laboratory (AFSC) Hanscom Air Force Base, MA 01731-5000

#### THE FORM OF CYCLONIC PRECIPITATION AND ITS THERMAL IMPACT

Stanley David Gedzelman Professor of Meteorology City College of New York

#### Abstract

A two-dimensional parameterized cloud microphysics model has been developed and applied to explain the form of cyclonic precipitation and its thermal impact. A description of the model including several of the numerical techniques and physical processes is given. The model is then used to simulate three idealized case studies. The first is a strong front in which a zone of sleet separates regions of rain and snow. The second is a case of weak advection in which rain changes to snow. The third is a shallow supercooled cloud that produces freezing drizzle.

# 1. Introduction.

Forecasting the form of precipitation becomes problematic whenever the temperature at or near the surface approaches the melting point. Snow and sleet may fall even if the surface temperature is somewhat above  $0^{\circ}$ C, while sleet and freezing rain or drizzle may fall even if surface temperatures are well below  $0^{\circ}$ C.

The sounding serves as the primary data source for determining the form of precipitat on. If the melting level is far above the surface, and surface wet bulb temperatures are well above 0°C the precipitation will reach the ground as rain, while if the entire sounding is below 0°C and the cloud is deep, snow will fall.

Precipitation form is more difficult to assess in borderline situations. Snow can reach the ground even when the temperature is above freezing so long as the  $T_{\rm w}$  remains below 0°C. Freezing rain and sleet usually form when there is a cold layer of air at the surface but a melting layer aloft. Criteria for distinguishing sleet from freezing rain are more elusive. The probability of sleet increases if the warm zone is barely above 0°C and also when the layer of subfreezing air is colder and thicker.

The form of precipitation is also affected by cloud microphysical processes. Large snowflakes and ice pellets fall further without melting than smaller hydrometeors. Freezing rain or drizzle can be produced in soundings with temperatures that remain below 0°C as a result of the difficulty of producing ice in clouds whose tops are only a few degrees below 0°C. Bocchieri (1980) noted that about 30% of the cases of freezing precipitation occurred in soundings for which the temperature remained below 0°C and Huffman and Norman (1988) showed that the possibility of supercooling reduced the accuracy of statistical techniques for predicting freezing precipitation from the sounding data.

Falling precipitation may also undergo phase changes which alter the temperature structure of the sounding and even the form of subsequent precipitation. The thermal impact of evaporation and melting can thus be of paramount importance in determining the form of precipitation at the ground. The latent heat extracted from the air as the hydrometeors fall beneath the melting level cools the air column, and, if there is little

warm air advection, brings the  $0^{\circ}\mathrm{C}$  isotherm closer to ground level so that the rain can change to snow.

The amount and rate of precipitation is thus a crucial factor in determining whether cooling is adequate to produce the changeover from rain to snow. McQuire and Penn (1953) and Wexler, et. al. (1954) first identified this process in their analyses of a surprise snowstorm that struck New England in April, 1953. Wexler, et. al, showed that snow did not reach the surface until about 2 cm of rain had fallen and cooled the air sufficiently by melting. Gedzelman and Lewis (1990) have shown that evaporation and rising of the cooled air can also alter the precipitation form and the thermal structure of such self-cooled storms (see Fig. 1).

The latent heat absorbed by the melting precipitation may also cool a warm layer aloft enough to change freezing rain or sleet to snow. Ivens (1987) examined such cases and established criteria for determining the form of precipitation based both on predicted soundings and precipitation totals. Ivens also exhibited some success at discriminating between cases of sleet and freezing rain. He found that almost all sleet forms when the melting layer is so thin that the snow falling through it does not completely melt.

The thermal changes caused by the melting and evaporating snow or rain can also alter storm structure and dynamics. An example of how evaporating rain affected a front was first documented by Oliver and Holtzworth (1953). Atlas et al. (1969) showed how melting snow can alter storm

dynamics and change the mesoscale wind field, with a thermally direct circulation developing along the rain-snow line. This has been studied further by Stewart and King (1987) who pointed out that it is responsible for an advance of the snow boundary. More recently, Huang and Emanuel (1991) have shown that evaporation beneath a developing cold front shortens the time needed for frontal collapse by several hours and increases the intensity of the self-induced frontal circulations.

Correctly determining the form of precipitation has other implications of direct importance to the Air Force. Freezing rain or drizzle presents potentially hazardous icing situations while ice pellets are not so dangerous. The form of precipitation also affects the interpretation of microwave signals from clouds obtained by radar and satellite. The different dielectric properties of ice and water, the varying air bubble content of ice pellets or hailstones and the different possible crystal forms of snow seriously alter the backscattering and transmission properties of microwaves (see e. g. Ludlam, 1980).

The important roles of thermodynamics and microphysics in determining precipitation form, the feedback of precipitation form on storm structure and development, and its impact on icing and on remote sensing efforts all demonstrate the importance of developing models that can determine the form of cyclonic precipitation and its thermal impact. Although the literature is full of studies that treat the problem of hydrometeor formation, relatively little attention has been devoted to understanding the form that precipitation will take when it approaches the ground.

Models with parameterized microphysics have been developed and applied to convective clouds (Lin, et. al., 1983) and to hurricanes (Lord et. al., 1984). Similar parameterized microphysical models (see e. g., Rutledge and Hobbs, 1983, and Rutledge, 1989) have also been used to explain some of the banded and frontal features of active mesoscale structures in winter storms.

In this study we have adapted these microphysical models for more typical stratiform winter storm situations. The model is two-dimensional and uses prescribed velocity fields with an advection scheme based on Crowley (1968). Idealized test cases have been run which show the model distinguishes different forms of precipitation and captures its thermal impact, but flaws have also been revealed which show further improvements are needed before the model can be used as a quantitative forecasting tool in real situations.

In the following section an overview of the model and its various modules is presented. Results of idealized test cases are then shown and discussed. Finally, the merits and shortcomings of the work are summarized, and suggestions for future work are made.

#### 2. Model Overview.

The model diagnoses the temperature, humidity and hydrometeor fields in two-dimensional, vertical cross-sections. Velocity fields are prescribed

since there is currently no dynamics in the model. The water substance is divided into 6 categories - vapor, cloud water, cloud ice, rain, snow and graupel or ice pellets - and all of these can interact by a variety of processes. Cloud water and cloud ice are considered to consist of small particles and, along with vapor, do not precipitate. The precipitating fields are all assumed to have Marshall-Palmer size distributions and their interactions are expressed in terms of integrals over the entire range of radii.

The code for the model is written in C because it can be readily transported to different computer systems. The model consists of several modules which are illustrated schematically in Fig. 2. All modules are coordinated and called by MAIN. Initial and boundary conditions as well as prescribed velocity fields for the cross-section are specified in SPECS. Since vertical and horizontal advections must be calculated separately to avoid computational instability, the vertical advection and dry adiabatic temperature changes are calculated first in CONV, and the horizontal advection is calculated immediately afterward in ADV. The moist adiabatic process including growth or evaporation of cloud droplets or crystals is then calculated in MOIST. Finally, the microphysical transformations between different water species are calculated in MICRO. A dynamics module could be added at a later stage.

Both CONV and ADV use the fourth order difference approximation to the advection equation of Crowley (1968). Because this high order scheme introduces spurious high frequency oscillations of all fields at frontal

boundaries and at the edges of clouds which are further compounded by phase changes (Grabowski and Smolarkiewicz, 1990) we have found it necessary to introduce three modifications. The first eliminates all negative values of mixing ratios and all spurious jumping of quantities away from the cloud. The second forbids negative diffusion of any quantity in the presence of asymmetric minima or sharp gradients and actually reverses its sign. The third smooths any unphysical minima of water substance within clouds. An example of a physically acceptable minimum is the mixing ratio of snow in the lowest gridbox of a layer with T > 0°C.

All three of these modifications have been used in CONV and even though they violate strict conservation, have produced significant improvement in model realism. The internal smoothing routine is not used in ADV because it causes instabilities. This allows spurious stationary oscillations in the horizontal fields which sometimes impair the accuracy of the output. For most runs the spurious oscillations are small, but in the worst cases, precipitation rates can vary by as much as 30% from one grid point to the next and temperatures at a few isolated grid points may deviate by up to 2°C from physically expected values.

The second modification deserves further discussion. Around sharp gradients, the fourth order scheme creates a smooth curve for the values of the functions between gridpoints and thereby introduces spurious minima and maxima. If the wind has the proper sign the scheme then advects the fictive extrema toward the gridpoint and renders the value of the function

even more extreme (see Fig. 3). The second model is keyed to deny and reverse such a refrigerator effect, just as would a lower order advection scheme, but it does so without simultaneously introducing the adverse effects of diffusion characteristic of lower order schemes. The magnitude of the corrections are no doubt incorrect.

The module, MOIST calculates the amount of condensation or evaporation of cloud water and cloud ice needed as a result of the vertical and horizontal advection. This must be done iteratively and also involves assumptions regarding the division of condensate between cloud ice and cloud water at temperatures below 0°C. The scheme used by Lin et. al., (1983) was altered in two major ways. First, a nonlinear function of temperature is used for the disposition of water substance to more realistically simulate the relative inactivity of ice nuclei at temperatures above about -15°C. However, once the mixing ratios of snow and rain in the cloud exceed a critical value, the excess vapor is assigned to water and ice in proportion to existing ratio of rain and snow. Clearly, this ad hoc approach must be replaced by a more physically compelling scheme such as used by Rutledge and Hobbs (1983).

After the moist adiabatic adjustments, the various microphysical interactions are treated in the module MICRO and in MAIN. These interactions include freezing, melting, evaporation, sublimation and deposition, coalescence and accretion, as well as autoconversion and the Wegener-Bergeron-Findeisen process. An diagram of the processes involving graupel is shown in Fig. 4.

Because the models of Lin (1983) and Rutledge and Hobbs (1983) were developed for use in cases with much larger vertical velocities than typically observed in stratiform precipiation, we introduced several new terms and changed several others. The critical values for autoconversion were reduced to values more appropriate for the more slowly growing, but longer lasting stratiform cloud fields. This allowed formation of freezing drizzle in shallow cold clouds. More accurate representation was given for raindrop freezing below 0°C and snowflake melting above 0°C and for evaporation and sublimation. Furthermore, since ice pellets are often smaller than snowflakes, larger snow was allowed to collect smaller graupel. The collision of smaller snowflakes with larger raindrops was allowed to result in freezing to graupel at a rate determined by the turbulent heat diffusion equation.

# 3. Results of Idealized Case Studies.

Three fundamentally different idealized situations are now presented and discussed. In all cases the time step is  $\delta t=20$  s and the horizontal distance between gridpoints is  $\delta y=2(10)^4$  m. There are 20 gridpoints in the horizontal. In the first two cases the vertical distance between gridpoints is  $\delta z=250$  m and there are 30 vertical levels, while in the third case, which only requires a shallow cloud,  $\delta z=200$  m and there are only 15 vertical levels.

The first situation represents a strong front with a pronounced frontal

inversion aloft. The horizontal temperature difference across the grid is 15°C, with surface temperatures run from 10°C at the ground on the warm (left) side. The velocity and initial temperature fields are shown in Fig. 5. Since the wind field is confluent and therefore in the vicinity of the front and since the model does not allow diffusion, the temperature gradient increases with time. Rising air on the cool side leads to the formation of a cold core aloft, as is so often observed in mature extratropical cyclones.

Fig. 6 shows the temperature and precipitating fields after 1500 time steps. The front has been sharpened and there is a distinct inversion aloft. The mixing ratio of rain is confined to the warm air at the lower left where snow has melted, but rain extends down beneath the front into subfreezing air where it will be recorded as freezing rain. The snow field occupies the bulk of the cloud and extends to the ground undiminished where temperatures remain below 0°C throughout the sounding. One interesting feature of this case is that it captures the narrow band where sleet is the dominant form of precipitation. This occurs where the air above the front is only slightly above 0°C and thus where snow has only partially melted. Where the snow has melted completely, the concentration of ice pellets is very low, even in a relatively thick layer of sub zero air near the surface.

The second case shows how melting and evaporating precipitation can cool the air column and change rain to snow. Since such situations occur mainly when there is little or no warm air advection all runs were

initialized with a horizontally uniform temperature field and a surface temperature of 5°C. The magnitude of the horizontal and vertical velocities at all gridpoints and the relative humidity of the air entering from the right (RH<sub>4</sub>) were chosen at the beginning of each run.

Model output from the various runs produced physically reasonable results. Because falling precipitation invariably cooled the air near the surface, the smaller the ratio of horizontal to vertical velocity, the sooner or the more likely the change from rain to snow. Snow also occurred sooner and was more likely when the relative humidity of the air entering from the right was lower.

Three different values of  $RH_i$  (50%, 70% and 99%) were chosen. Precipitation began as snow in the run with  $RH_i$ =50% because the wet bulb temperature is 0°C, while the change from rain to snow began sooner and occurred over a wider area in the run with  $RH_i$ =70% than in the run with  $RH_i$ =99%. A comparison of rainfall and snowfall rates for the two latter runs is shown at gridpoint y=5 in Fig. 7. For  $RH_i$ =70% snow began mixing with rain after only 2.5 mm of rain had fallen while for  $RH_i$ =99% snow did not begin mixing with rain until 11 mm of rain had fallen.

One interesting feature of these runs is that the region of snow is surrounded by rain. Since the cooling due to precipitation is cumulative the coldest air should be found in the core of the precipitation shield. This is seen in both Fig. 8 and Fig. 1, and is a characteristic feature of the type of warm snowstorms analyzed by Wexler, et. al., (1954) and by

Gedzelman and Lewis (1990).

The third case was designed to see if the model would produce freezing drizzle in shallow, supercooled clouds with weak vertical velocities. Fig. 9 shows that the model produced all three forms of precipitation in the supercooled regions of the cross section. In order to obtain freezing rain it was necessary to reduce the model's minimum value of cloud water mixing ratio required for autoconversion to rain. Clearly the model must incorporate a more physically compelling expression for autoconversion.

# 4. Summary and Suggestions for Further Work.

During this project I developed a 2-dimensional parameterized cloud microphysics model so it can convincingly simulate the form of precipitation and its thermal impact for a variety of classical winter storm situations. The model generated distinct regions of rain, sleet and snow; it simulated the cooling due to melting and evaporating precipitation and the subsequent changeover from rain to snow. Finally, it produced freezing drizzle in shallow, slightly supercooled clouds.

Future work includes applying the model to actual cases. The model will also be generalized to include the equations for stable isotopes of water to explain the climate signal recorded in these isotopes. However, before this is done there are problems in the model that must be corrected. These are listed below.

- 1. Spurious oscillations appear in the horizontal fields.
- 2. Mass is not conserved when precipitation form changes.
- 3. Parameterizations of autoconversions lack firm physical basis.
- 4. Condensing vapor is not properly divided between liquid and ice.
- 5. Bergeron Process produces too much snow at low mixing ratios.
- 6. Too much graupel or snow is produced at some boundary points.

Despite these shortcomings the model represents just about the only physically based tool for simulating and predicting precipitation form and its thermal impact in winter storms.

# Acknowlegdments.

The progress I made this summer would not have been possible without the assistance of many at the Phillips Lab. Joe Doherty and Chuck Ivari got me on the computer system. Gary Gustavson, Mike Griffin, Vincent Falconi and George Modica helped with many programming aspects. Ken Yang and Sam Yee helped on matters of numerical analysis. Stuart Muench and Rosemary Dyer provided meteorological and cloud microphysical insights. Don Chisholm helped with the project overview. All these and more have made it a wonderful professional experience for me.

#### References.

Atlas, D., R. Tatehira, R. C. Srivastava, W. Marker and R. E. Carbone, 1969: Precipitation-induced mesoscale wind perturbations in the melting layer. Quart. J. Roy. Meteor. Soc., 95, 544-560.

Bocchieri, J. R., 1980: The objective use of upper air soundings to

specify precipitation type. Mon. Wea. Rev., 108, 596-603.

Crowley, W. P., 1968: Numerical advection experiments. Mon. Wea. Rev., 96, 1-11.

Gedzelman, S. D., and E. Lewis, 1990: Warm snowstorms. <u>Weatherwise</u>, 43, 265-270.

Gedzelman, S. D. and L. R. Lawrence, 1990: The isotopic composition of precipitation from two extratropical cyclones. <u>Mon. Wea. Rev.</u>, 118, 495-508.

Grabowski, W., and P Smolarkiewicz, 1990: Monotone finite difference approximations to the advection-condensation problem. Mon. Wea. Rev., 118, 2082-2097.

Hoskins. B. J., I Draghici and H. C. Davies, 1978: A new look at the Omega equation. Quart. J. Roy. Meteor. Soc., 104, 31-38.

Huang, H. and K. A. Emanuel, 1991: The effects of evaporation on frontal circulations. J. Atmos. Sci., 48, 619-628.

Huffman, G. L., and G. A. Norman, Jr., 1988: The supercooled warm rain process and the specification of freezing precipitation. <u>Mon. Wea. Rev.</u>, 116, 2172-2182.

Ivens, R., 1987: Forecasting the kind of precipitation in winter. <u>Proc. Symp. Mesoscale Analysis & Forecasting</u>, Vancouver, Canada, 17-19 August 1987, ESA SP-282.

Lin, Y, R. D. Farley, and H. D. Orville, 1983: Bulk parameterization of the snow field in a cloud model. J. Clim. Appl. Meteor., 22, 1065-1092.

Lord, S. J., H. E. Willoughby, and J. M. Pietrowicz, 1984: Role of a parameterized ice-phase microphysics in an axisymmetric, nonhydrostatic tropical cyclone model. J. Atmos. Sci., 41, 2836-2848.

Ludlam, F. H., 1980: <u>Clouds and Storms</u>. The Pennsylvania State University Press, University Park, PA, 28-33.

McGuire, J., and S. Penn, 1953: Why did it snow at Boston in April? Weatherwise, 6, 78-81.

Oliver, V. J., and G. C. Holzworth, 1953: Some effects of the evaporation of widespread precipitation on the production of fronts and on changes in frontal slopes and motions. <u>Mon. Wea. Rev.</u>, 81, 141-151.

Rutledge, S. A., 1989: A severe frontal rainband. Part IV: Precipitation mechanisms, diabatic processes and rainband maintenance. <u>J. Atmos. Sci.</u>, 46, 3570-3594.

Rutledge, S. A., and P. V. Hobbs, 1983: The mesoscale and microscale

structure and organization of clouds and precipitation in midlatitude cyclones. VIII: A model for the "seeder-feeder" process in warm-frontal rainbands. <u>J. Atmos. Sci.</u>, 40, 1185-1206.

Stewart, R. and P. King, 1987: Rain-snow boundaries over southern Ontario. Mon. Wea. Rev., 115, 1894-1907.

Wexler, R., R. J. Peed, and J. Honig, 1954: Atmospheric cooling by melting snow. <u>Bull. Amer. Meteor. Soc.</u>, 35, 48-51.

# Figure Legends

- Fig. 1. Four storms with cold cores produced by melting precipitation. Hatched regions show snow.
- .Fig. 2. Schematic flow chart of the modules in MAIN.
- Fig. 3. Effect of 4th order scheme. Dashed curve is the best fit to data at gridpoints. Arrow shows motion and computed change.
- Fig. 4. Microphysical interactions between graupel and other water species.
- Fig. 5. Imposed velocity field and initial temperature field for strong front.
- Fig. 6. Temperature and mixing ratios of rain, snow and graupel after 1500 time steps for initial conditions of Fig. 5.
- Fig. 7. Rain and snow totals as a function of time and initial relatve humidity for weak advection situation.
- Fig. 8. Temperature and mixing ratios of rain and snow after 1000 time steps for initial conditions of weak advection situation.
- Fig. 9. Temperature and mixing ratios of rain, snow and graupel after 2000 time steps for shallow, supercooled cloud.

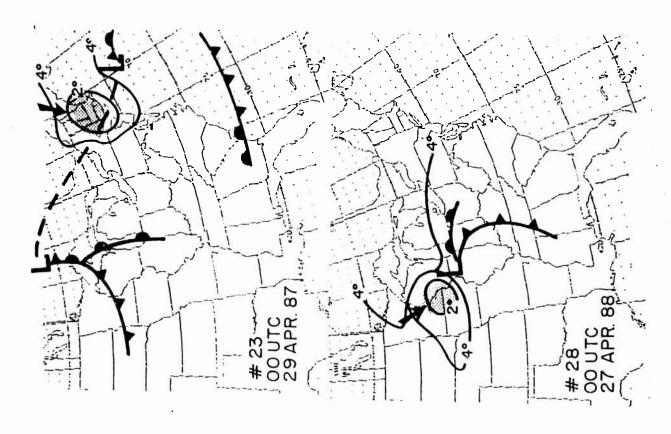
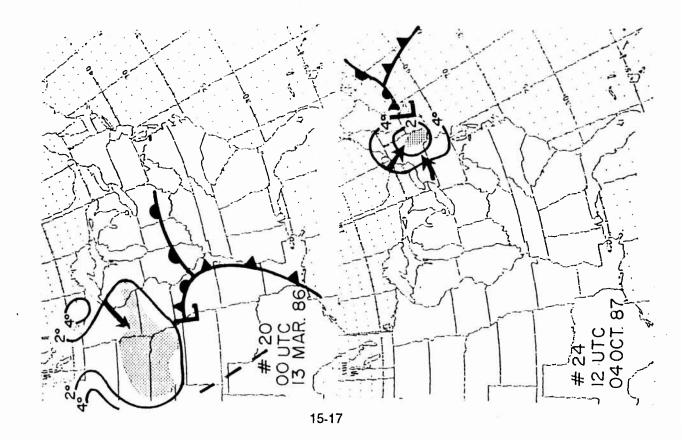
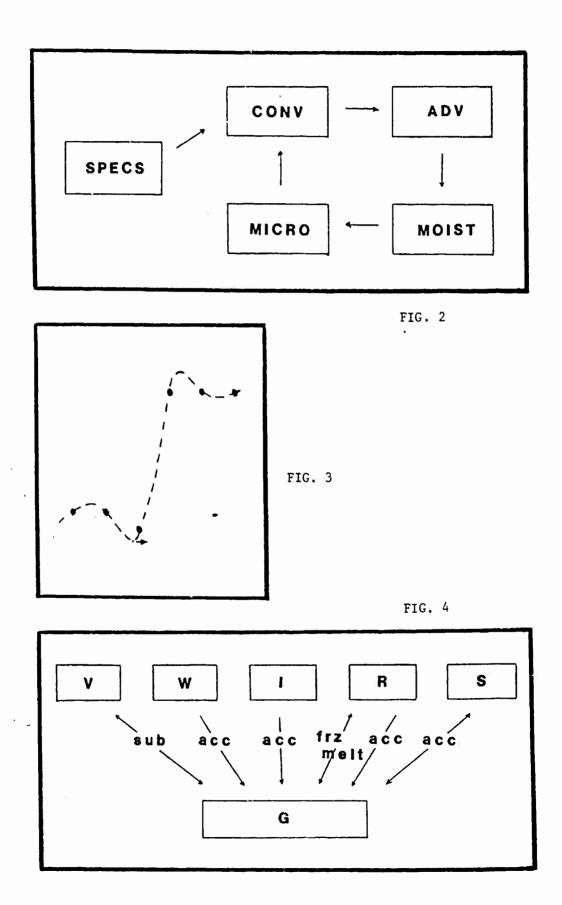


FIG. 1





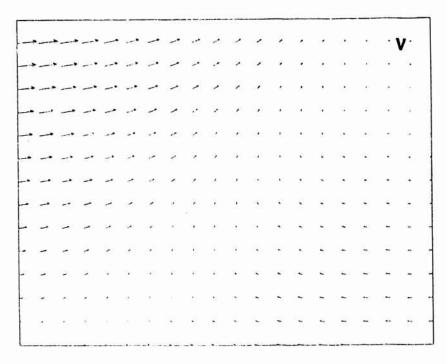
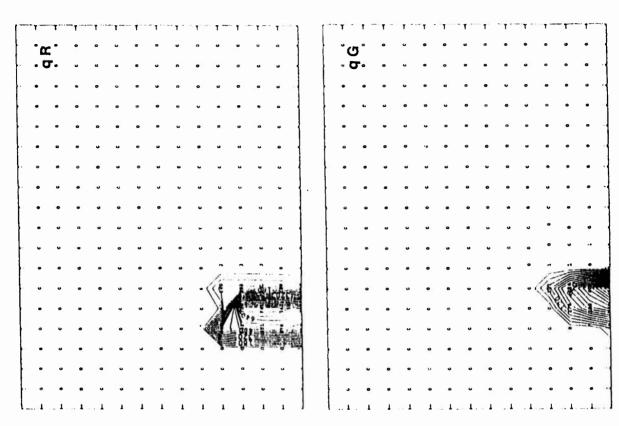
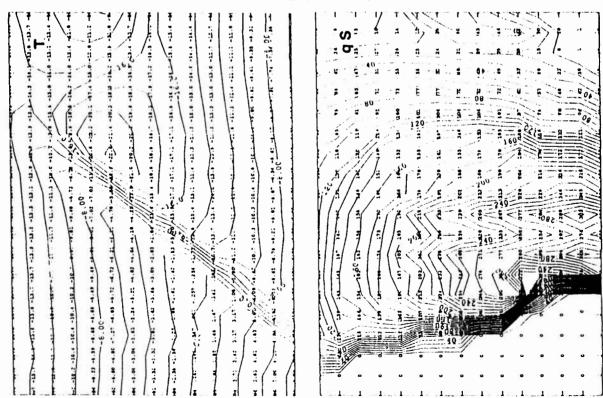
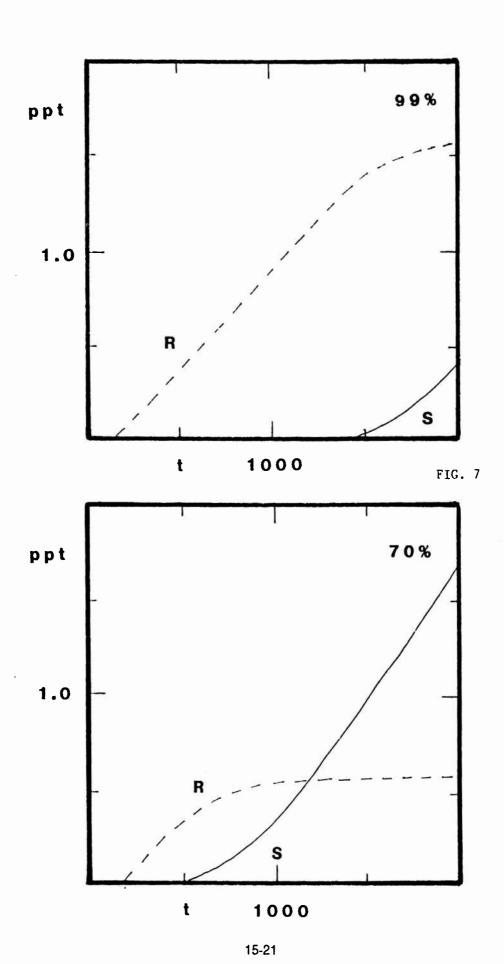


FIG. 5









o S 221 18 .58 m m m

FIG. 8

480 TIV

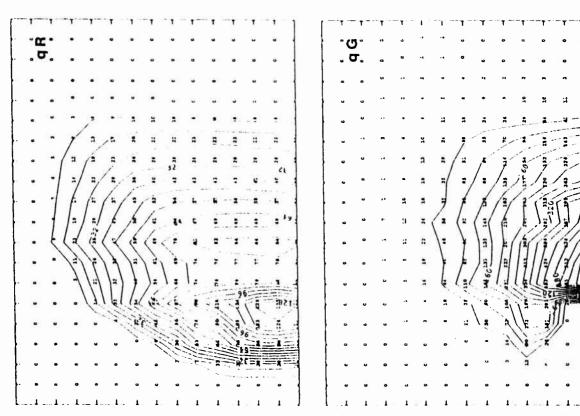
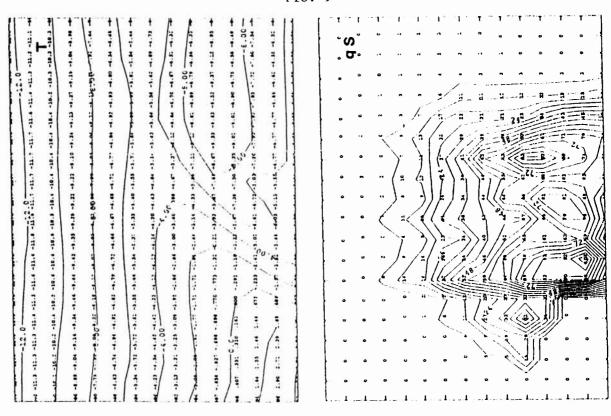


FIG. 9



# A GEOGRAPHIC INFORMATION SYSTEMS IMPLEMENTATION ANALYSIS FOR THE GEOPHYSICS DIRECTORATE/ATMOSPHERIC STRUCTURE BRANCH PHILLIPS LABORATORY

William L. Hamilton, Ph.D. Phillips Lab/Geophysics Directorate/Atmospheric Structure Branch

Abstract: The purpose of this document is to present an analysis for Geographic Information Systems (GIS) implementation within the USAF Phillips Lab/Geophysics Directorate/Atmospheric Structure Branch (GL/LYA). Methodology included three analysis partitions; GIS needs and functions identification, spatial data dictionary design recommendations, and hardware and software platform review and recommendations. Results indicated possible GIS applications within tactical cartography and modeling, cloud climatology, and mesoscale meteorologic modeling with common functional use of digital elevation models and associated first and second order derivative information. GIS hardware and software recommendations utilize existing computer platforms and public domain software to reduce integration cost and speed GIS implementation.

# 1 INTRODUCTION

Establishment of geo-information processing is essential for those using geo-science data as, if properly deployed, it allows access to previously unattainable and/or unintelligible information sources. GIS is a relatively new form of geo information processing which uses space-time coordinates as information indices and employs analytic cartography as a communicative medium. This unique style of reference and display can engage large multi-discipline geophysical data sets enabling a more efficient tactical and strategic decision making process. Thus, the purpose of this document is to present an analysis for Geographic

Information Systems (GIS) implementation within the USAF Phillips Lab/Geophysics Directorate/Atmospheric Structure Branch (GL/LYA).

The primary problem with initiating a GIS in a research institution is the identification of proper uses and common GIS functionalities. If GIS applications and functions can be determined then implementation becomes more efficient and successful. Further, GIS use and function identification enables proper spatial database design and development. This design process is necessary to maintain efficient, viable, and reliable use of the spatial data as well preserve GIS end product integrity. Indeed, if the GIS spatial data structure is properly deployed the following benefits accrue:

- Reduction of data redundancy
- Standardized data format
- Efficient use of data through shared resources
- Standardization of data content
- · Capability of identifying and tracking data uncertainty
- Capability of communicating error is GIS products
- Capability of locating information in a timely fashion

These benefits are amplified when the spatial data structure is designed to allow easy and logical access to requisite information. Such, access helps defuse potential problems of spatial data and map misuse in GIS applications. As stated by the National Center for Geographic Information and Analysis (NCGIA) "The best insurance [against misuse of spatial data] at this point is surely to sensitize the GIS user community to the accuracy issue, and to develop tools which allow spatial data handling systems to be used in ways which are sensitive to error" (Goodchild, 1989). The same organization issued a summary objective with respect to accuracy of spatial data bases which states that "The objective should be a measure of uncertainty on every GIS product" and that "ideally, the

result of describing error in the database and its propagation through the GIS processes would be a set of confidence limits on GIS products...The main motivation for interest in the accuracy of spatial databases comes from an applied perspective—the problem is real and we need better methods for addressing it." (Goodchild, 1989). Thus a properly implemented GIS is a tool which enables the end user to determine and engage the correct spatial analysis methods while utilizing the existing institutional knowledge base and facilities. Further, a GIS should serve as a map librarian and guide to knowledge base approaches for spatial analysis.

Given the purpose of this document the following sections detail analyses, results, and recommendations relevant to GL/LY GIS implementation.

#### 2 GIS IMPLEMENTATION ANALYSES

The GIS implementation analyses was divided into three partitions: literature review and personnel interview for identification of GIS application, common GIS functions, and GIS prototype delineation; spatial data dictionary (SDD) design recommendations; and hardware and software platform analysis and recommendations.

#### 2.1 Literature Review

database Computerized on-line searches referencing GIS implementation with USAF tactical and atmospheric projects were conducted. Use of GIS with military or defense descriptors generated six references from publication dates 1969 to present inclusive. Searches employing GIS and climatology and/or descriptors produced thirteen references from publication dates 1969 to present inclusive (see appendix). The low number of cited references indicate use of GIS technologies in tactical mapping and/or meteorology/climatology is still a emerging

field of research.

#### 2.2 Interviews

Interviews were conducted with LY personnel from the branches of atmospheric structure, atmospheric prediction, and remote sensing (see appendix). Three main implementation initiatives were addressed throughout the interview process. The first initiative was to determine if GIS is a viable tool for GL/LY personnel and, if so, what current applications could benefit by the use of the technology. The second initiative was to ascertain if certain GIS functions were common to the applications derived from the previous initiative. The final initiative was to have GL/LY personnel identify GIS prototype implementation projects relevant to their own research interests.

- 2.2.1 <u>Initiative One Identified GIS Application</u>
  At the conclusion of the interview process three primary GIS applications had been identified.
- GIS may be an effective technology for use with Cloud Impacts on DOD Operations And Systems (CIDOS) research.
- GIS may be a viable tool for tactical mapping and modeling applications.
- GIS may be a useful technology for mesoscale weather forecasting and modeling.

# 2.2.2 <u>Initiative Two - Common GIS Functions</u>

Data reduction from the interview process generated the following GIS functions common to applications identified in section 2.2.1.

- Development and use of digital elevation models (DEM) and associated first order derivatives (slope, etc., etc.,) and second order derivatives (concavity, surface roughness, etc.) of terrain features would be valuable for cloud climatology, atmospheric model development, and tactical display.
- Accessing terrain and associated geographic information by space time indices in an integrated database environment would be beneficial to basic research and the dispersion of information to other USAF installations.

## 2.2.3 Initiative Three - Possible GIS Prototypes

Given the identified GIS application and common functions three possible prototypes were identified to aid GL/LY GIS implementation process into GL/LY.

• Prototype One - GIS technologies would be used to aid in cloud identification studies using shape, size, and inter and intra distance indices. Such indices would be stored in databases allowing researchers access to the cloud geography. Requisite cloud data would be attained from the Whole Sky Imaging network presently under analysis at GL/LYA.

- Prototype Two GIS technologies would be used to develop terrain derivative information from digital elevation models (DEMs). This information would be integrated into fog prediction models currently under development at GL/LYP. Additional lithospheric and hydrospheric information including relative and absolute topologic relations would be generated by the GIS and maintained in the related database structure.
- Prototype Three GIS technologies would be used to enhance Tactical Decision Aids (TDAs) currently under development at GL/LYA. This prototype would integrate Rome Labs Digital Cartographic Applications (DCA) into an object oriented GIS allowing access to spatial data necessary to improve target resolution and tactical decisions.

Initiation of one or more prototypes is essential to the GL/LY GIS implementation process for the following reasons:

- Prototypes establish operational procedures for data capture, data analysis, and data display in an applied setting.
- Prototypes are used to identity and correct errors in the operational analytic sequence.
- Prototypes allow the system integrators to perceive previously unidentified operations necessary to the success of the GIS.

- Prototypes allow for the establishment of baseline data regarding system performance and task/time expenditures necessary to quantify cost/benefit analyses.
- Prototypes, when fully implemented, demonstrate GIS technologies as a viable management, planning, and analyses tool to the user community.

Upon review of the above stated applications, functions, and prototypes the following section details a spatial data dictionary structure requisite for successful GIS implementation.

#### 2.3 LOGICAL DATA STRUCTURE AND SPATIAL DATA DICTIONARY

The proposed spatial data dictionary (SDD) structure was developed by decomposition of a hypothetical GIS analysis. The resulting logical data structure is based upon an object oriented relational data architecture (figures 1). The primary assumption for the data structure is that GIS analyses require multiple input maps features. As such each map feature may exist in one moment of space and time and is given the name of feature instance. A feature instance is equivalent to the subject or the main thesis of the map and can be spatially subdivided into facets. Each facet, in turn, can be subdivided in various spatial strata. The various spatial strata are comprised of a number of spatial objects. requirements of GL/LY, it is recommended that three spatial object be employed for each spatial strata; source, model, and accuracy. Each of the spatial objects have related informational attributes and associated sub attributes.

Non spatial information about each spatial strata is contained in an item table. Each item is comprised of feature objects which can encompass any number of attributes and sub attributes. The many to many join between the strata is essential as it enables the user to obtain spatial information about non spatial items or inversely, non-spatial information about spatial strata (figure 1).

# 2.4 Spatial Information - Sources, Models, and Accuracies

Including spatial source, model, and accuracy information in the SDD enables the researcher to quantitatively evaluate the quality of GIS output. When such information is absent from the SDD, GIS output is of little value as accuracy, reliability, and validity factors cannot be developed. The following describes the aforementioned information categories:

- Spatial source attributes allow the researcher to attain information about materials from which the digital GIS products were derived. This information also permits the GIS to function as a digital map librarian by maintaining location and access information (as well as other attributes) of source materials. When implemented correctly, the map librarian function is cost effective as end users can quickly determine cartographic source status necessary to efficient project planning.
- <u>Spatial model</u> (any digital spatial strata) attributes include information on the actual GIS product. For example, DEM spatial model attributes yield information about that coverage as it is virtually held in the GIS.

• <u>Spatial accuracy</u> attributes contain information about the accuracy of the spatial model NOT THE SPATIAL SOURCE.

Positional, vertical, and thematic accuracies would be addressed in this section of the SDD.

#### 2.5 Attribute Accuracy

Information about non-spatial items are stored as related feature objects. For example, given a feature instance of soils it is feasible the related items contain a variety of feature objects (porosity, compaction, etc., etc.). It is critical that end users have access to non-spatial attribute accuracy descriptors (as stated in NCDCDS, 1988) as these aid selection of analysis methods and map type.

## 3 SPATIAL OBJECTS AND ATTRIBUTES

This section contains suggested data dictionary elements for the GL/LY GIS. Each SDD element is defined by meaning, values, and units. Codes found at the end of each element define data type, width, representation, and give an example when necessary. Code definitions are located in the appendix.

#### 3.1 Source Attributes

The following lists recommended attributes to be included under the source spatial object.

- <u>Source Accuracy</u> = Listing of stated source accuracy or lack thereof. C|128|AN|Horizontal, Vertical, Thematic.
- Source Comments = C|128|AN|\*
- <u>Source Condition</u> = Physical condition of source document. C|128|AN|\*

- <u>Source Coordinate Systems</u> = List of all coordinate systems shown on source document (UTM, Long-Lat, State Plane, etc., etc.). C|128|AN|\*
- <u>Source Created By</u> = Individual(s)/Agency(s) who created source document. C|128|AN|\*
- <u>Source Date</u> = Date of origin for source document exclusive of editorial or revision updates C|12|MDY|\*
- Source Datum = Year and name of plane from which elevations are measured. C|64|AN|1927 NORTH AMERICAN
- Source From = Used when the source is a secondary or tertiary document compiled from multiple sources. For example, calculated surface (trend surface, overlay analysis, etc.,etc.,) are commonly comprised of two or more sources. The original sources (titles if possible) should be noted. C|256|AN|\*
- <u>Source Index Number</u> = Index number of the source document, if one exists, as stated on the source item. These indices permit the map user to find an original source document should the title be changed over a period of time. C|64|AN|\*
- <u>Source Location</u> = Physical address of source documents and access policy and/or procedures. C|256|AN|\*
- <u>Source Media</u> = Type of media on which source is plotted or printed. C¦64|AN|VELUM
- <u>Source Projection</u> = Type and name of map projection. C|128|AN|CYLINDRICAL = UTM
- <u>Source Revision Date</u> = Date of latest source revision. C!12!MDY!\*
- <u>Source Revision Type</u> = Form of latest source revision (field survey, photogrammetric, etc.). C|64|AN|\*
- <u>Source Scale</u> = Scale of document stated as a representative fraction. F|15.5|N|
- <u>Source Title</u> = Title of the source document as it appears on the document. Where the source document is known by more than one title a convention must be established to select one title C|256|AN|\*.
- Strata Name = Name of the coverage as it resides on the GIS system C|256|AN|\*.

# 3.2 Model Attributes

The following lists suggested attributes to be included under the models spatial object.

- <u>Date Last Altered and Type</u> = Date the model was last altered and type of alteration. C|256|AN|\*
- Model Comments C|256 AN \*
- Model Coordinate Systems = coordinate system(s) used to encode digital positions. C|128|AN|\*
- Movel Created By = Individual(s)/Agency(s) who
  created the model. C|128|AN|\*
- Model Date = Date the model was created. C|12|MDY|\*
- Model Location = system address of model C|256|AN|\*
- Model Method = Mathematical and/or statistical method to convert source data to model (ie. trend, interpolation, etc.,etc.). C|256|AN|\*
- Model Projection = Map projection type and name C|128|AN|CYLINDRICAL = UTM
- Model Scale = Scale of model stated as a representative fraction. F|15.5|N|
- Model Spatial Level = Level of spatial data of coverage (i.e. point, line, area, volume). C|1|A|P,L,A,V
- <u>Model System</u> = System used to convert source material to model (i.e. Gestalt Stereoplotter). C|128|AN|\*
- Number of Control Points = Number of control prints used in establishing the model. I | 5 | N | 0=10000
- <u>RMS Error</u> = root mean square error of source to model conversion. F|15.5!N|\*
- Strata Name = Name of coverage as it resides on the GIS system. C|256|AN|\*
- <u>Verification Process</u> = process and/or procedures used to verify source to model conversions. C|256|AN|\*

#### 3.3 ACCURACY ATTRIBUTES

The following lists suggested attributes to be included under the accuracy spatial object.

- Horizontal Positional Accuracy = plus or minus units of horizontal accuracy. F|15.5|N|\*
- Horizontal Positional Accuracy Assessment Method = method employed to develop accuracy (ie. RMSE). C|128|AN|\*
- <u>Horizontal Positional Number Of Samples</u> = number of samples used to establish accuracy. I|5|N|0=99999
- Thematic Accuracy = plus or minus accuracy of thematic classification accuracy. F|15.5|N|\*
- Thematic Accuracy Assessment Method = method used to determine thematic accuracy. C|128|AN|\*
- Thematic Confidence = confidence limit of thematic accuracy classification F|4.2|N|95.
- Thematic Number Of Samples = number of sample used to determine the thematic accuracy value. I 15 N 0=99999
- <u>Vertical positional accuracy</u> = plus or minus units of vertical accuracy. F|15.5|N|\*
- <u>Vertical Positional Accuracy Assessment Method</u> = method used to determine vertical accuracy (ie. RMSE) C|128|AN|\*
- Vertical Positional Number Of Samples = number of samples used to determine vertical accuracy I 15 N 0=99999
- Comments C|256|AN|\*

## 3.4 Suggested Feature Object Attributes

The following is a list of generic attributes which are are necessary to ensure valid GIS analysis. While not all of the suggested attributes may apply in all situations it has been recommended by both the National Center for Geographic Information and Analysis and the National Committee for Digital Cartographic Standards that attribute data (non-spatial) be encrypted with the level of data value.

- <u>Level Of Data</u> = Defines the data level associated with the feature object (ie. nominal, ordinal, interval, or ratio). C|1|A|N,O,I,R
- Accuracy of Data = Defines the data accuracy of the value associated with the feature object. F|15.5|N|\*
- <u>Accuracy Assessment Method</u> = Defines method used to determine the accuracy of the data. C|128|N|\*
- <u>Acquisition Date</u> = Date when feature object data was acquired. C|8|MDY|\*
- Comments C|256|AN|\*

#### 4 DIGITAL MAP LIBRARIAN FUNCTION

The recommended SDD structure enables the database to serve as a digital map librarian. Indexing GIS data by physical spatial location and system location allows the end user to logically determine the system location of digital map products and the physical location of associated source information. Implementation of the map librarian function provides the following benefits:

- · logical GIS navigation and data access
- aids organization of data maintenance functions
- · enables effective project planning and analysis.

The recommended map librarian implementation method is to employ facets as a vehicle for spatial indexing. Facets allow for the effective "packaging" of spatial information by user defined spatial area.

#### 4.1 Spatial Indexing

A commonly applied and successful spatial indexing system for those using large area databases is the USGS quad base facet scheme. This system can accommodate the 1:25000, 1:100000, 1:250000 and 1:1000000 map scales and allows facets to be subdivided into nested quadrants for efficient data storage. File names are encrypted with spatial index information thereby giving the end user knowledge of both file

contents and spatial coverage.

# 4.2 Map Librarian Access Scheme

Use of the map librarian function reduces those tasks associated with data maintenance while providing a minimal level of data security. The following is a suggested library organization under which GIS users could be subdivided.

- <u>Library Director(s)</u> Those users who manage spatial strata acquisition and updates and are responsible for quality assurance and quality control.
- <u>Library Coordinator(s)</u> Those users that perform updates and maintenance on spatial strata.
- <u>General Users</u> the GIS end user having read only privileges to the library database.

Implementation the map librarian functions are more effectively achieved using relational database architecture. While the map librarian system can operate in a non relational database environ it is cumbersome and probably not cost effective. Thus, it is recommended that GL/LY develop their GIS SDD within a relational database system.

## 5 GIS HARDWARE AND SOFTWARE RECOMMENDATIONS

Given applications, functions, and prototypes identified is section 2 and current cost constraints within GL/LY the subsequent sections detail hardware and software recommendations for GIS implementation. These recommendations provide the following benefits.

 Maximize use of existing hardware and software at GL/LY thereby substantially reducing GIS implementation costs.

- Reduces training overhead by employing existing hardware platforms with which end user are already familiar.
- Distributes the GIS implementation architecture over several GL systems thereby eliminating the problem of an individual knowledge based system.
- Uses public domain software to reduce acquisition costs and allows GL/LY personnel access to source code enabling modification for specific needs.

#### 5.1 Hardware

GL already possess a wide array of computer hardware capable of running large scale GIS projects. It is suggested that GIS software be utilized on the NEXT computers already present in GY/LYA and that database operations be housed on the GL VAX system. This configuration has the benefits of a no cost solution for GIS hardware, distributes operational overhead throughout the GL computer system, and will expedite the development of the GIS database NEXT - VAX interface. Other required peripherals such as digitizers and plotters are present in GL and may be utilized for GIS purposes or such services may be acquired from local academic institutions.

# 5.2 Software

Selection and implementation of GIS software is predicated upon a double tier approach. Initially GL/LY should acquire the Geographical Resources Analysis Support System (GRASS) which is an inexpensive GIS used by many federal, academic, and private agencies. Like many public domain software products GRASS presumes

the end user has the programming sophistication to develop necessary modules to customize the GIS to project requirements. This limitation should not be a problem for GL/LY. GRASS in a UNIX based system and should be functional on the NEXT system with little modification.

The database of choice for most large scale GIS work is ORACLE. Unfortunately, this software package is not available to GL/LY for GIS purposes and it is suggested that Digital Equipment Corporations RDB product, which is available, be utilized. Additionally SYBASE is available on the NEXT computer and may also be utilized on that platform.

Should GIS become more firmly ingrained within GL/LY and expand throughout the other GL division it is suggested that a second tier of GIS technology be implemented. This level would include the purchase of GDS GIS software from McDonald Douglas Corporation and access to the ORACLE database system. It should be noted that this second tier of software architecture will not be needed until the GIS user community grows substantially within GL.

# 6 FUTURE DIRECTIONS FOR GIS AT GL/LY

This report has detailed GIS applications, functions, and prototypes which can be enabled within GL/LY. In order to continue the GIS implementation process it will be necessary to select and integrate prototype(s). This process accrues those benefits detailed in section 2.2.3 and allows for greater refinement of GIS within GL/LY while generating other spatial research initiatives. Additionally, subsequent investigations into the integration of GL/LY remote sensing capabilities with GIS should be explored as this technology shows great promise for acquiring large area data sets in a timely and systematic manner.

#### 7 SUMMARY AND RECOMMENDATIONS

Results from literature review and interview have indicated that GIS is a viable, necessary, and desired technology at GL/LY. Of interest, is the GL/LY spatial data resolution requirements are relatively low and can use existing data for the identified prototypes. This is in direct contrast to the majority of GIS users who require high resolution spatial data which are either to expensive or technologically impossible to acquire. Another unique spatial data requirement of GL/LY is for large area coverage at global scale. Fortunately the Defense Mapping Agency (DMA) is in the process of generating this data but GL/LY must take care to coordinate its spatial research requirements with availability of DMA products.

GIS technologies are prevalent in many private geophysical enterprises and are used to a very large extent by the U.S. Army. Given the nature of the work performed by GL/LY, the expressed desire to use GIS by GL/LY personnel, and the need for the technology in current GL/LY research, it is recommended that the Geophysics Directorate begin the process of GIS integration into the Phillips Laboratory as soon as feasible.

#### BIBLIOGRAPHY & REFERENCES

- Abler, R. F. (1987), The National Science Foundation Center for Geographic Information and Analysis. <u>International Journal of Geographic Information Systems</u>, 1, pp. 303-326.
- Brusegard, D. and Menger, G. (1989) Real data and real problems: dealing with large spatial databases. In: <u>Accuracy Of Spatial Databases:</u> Goodchild & Gopal (eds.)
- Burrough, P.A., 1986, <u>Principles of Geographical Information</u>
  Systems for Land Resource Assessment. (Oxford: Clarendon Press).
- Crowell, M.L. (1989) Application of a GIS to a water regulatory permit inventory. <u>Proceedings GIS/LIS '89</u>, Orlando, 1989, pp.
- Daratech, (1989) As reported in <u>Computer World</u>, August 28, pp.10 & 30.
- Fisher, P.F. (1989) Knowledge-based approaches to determining and correcting areas of unreliability in geographic databases. In:
  <u>Accuracy Of Spatial Databases:</u> Goodchild & Gopal (eds.)
- Goodchild, M. F., (1988), Stepping over the line: technological constraints and the new cartography. <u>American Cartographer</u> 15, pp. 311-320.
- Goodchild, M. F., and Gopal, S. (eds) (1989). Accuracy Of Spatial Databases. (New York: Taylor & Francis)
- Guptill, S. C. (1989) Inclusion of accuracy data in a feature based, object-oriented data model. In: <u>Accuracy Of Spatial Databases:</u> Goodchild & Gopal (eds.)
- Guptill, S. C., and Fegeas, R. G., (1988) Feature based spatial data models-the choice for global databases in the 1990s? In: <u>Building Databases for Global Science</u>, Mounsey, H., and Tomlinson, R., (eds.), pp. 279-295. (london: Taylor & Francis)
- Kennedy, S. (1989) The small number problem and the accuracy of spatial databases. In: <u>Accuracy Of Spatial Databases:</u> Goodchild & Gopal (eds.)
- National Committee for Digital Cartographic Data Standards (NCDCDS), 1988, The proposed standard for digital cartographic data.

  The American Cartographer, 15.
- Rhind, D. and Clark, P. (1988). Cartographic data inputs to global databases. In: <u>Building Databases for Global Science</u>, Mounsey, H. and Tomlinson, R., (eds.), pp. 79-104. (London: Taylor & Francis)
- Samet, Hanan (1990) <u>Application of spatial data structures</u>. (Reading, MA: Addison-Wesley)
- Samet, Hanan (1990) The design of spatial data structures. (Reading, MA: Addison-Wesley)

# APPENDIX

# GL/LY PERSONNEL INTERVIEWS

Jeffery Yapez
Rosemary Dyer
Captain John Pickle
Major James Hancock
Steve Hnat (Rome Labs, Griffiss AFB)
Frank Ruggeriero
Julia Steves (STX Corp.)
Joan Ward
Gary Gustevson

# BIBLIOGRAPHIC ENTRIES GIS and MILITARY or DEFENSE and Tactics

- Buening, U. "Tactical mapping in combat aircraft." <u>IEEE 1988</u>

  <u>National Aerospace and Electronics Conference: NAECON</u>
  (1988): 74-78.
- Disdero, M.C. "The airborne synthetic cartographic display." Navigation 38 (July 1990): 332-338.
- Fatale, L.A. and Messmore, J.A. "The Army's evaluation of tactical terrain data." <u>GIS/LIS '89 Proceedings</u> (1988): 791-799.
- Felleman, J. "There's a GIS in your future." Government Information Quarterly 7 (1990): 262-267.
- Meitzler, W.D. and Millard, W.D. "The airland battlefield environment integrated software environment."

  <u>GIS/LIS '89 Proceedings</u> (1989): 733-742.
- Tschudi, M.K. "A technique for viewing a large digital map background." GIS/LIS '88 Proceedings (1988): 91-99.

# BIBLIOGRAPHIC ENTRIES Meteorology or Climatology and GIS or Terrain

- Rabin, R.M. et. al. "Observed effects of landscape variability on convective clouds." <u>Bulletin of the American Meteorologic Society</u>. 71 (March, 1990): 272-280.
- Eichhorn, J. et. al. "Three-dimensional numerical simulations of the urban climate." <u>Contributions to Atmospheric Physics</u>. 61 (August, 1988): 187-203.
- Giorgi, F. and Bates, G.T. "The climatological skill of a regional model over complex terrain." <u>Monthly Weather Review.</u> 117 (November, 1989): 2325-2347.
- Gross, G. "Some effects of deforestation on nocturnal drainage flow and local climate-a numerical study." Boundary-Layer Meteorology. 38 (March, 1987): 315-337.
- Kelly, J.G. et. al. "Mesoscale forecasts generated from operations numerical weather prediction model output."

  <u>Bulletin of the American Meteorological Society</u>. 69
  (January, 1988): 7-15.
- Lalas, D.P. "Wind energy estimation and siting in complex terrain."

  <u>International Journal of Solar Energy</u> 3 (1985): 43-71.
- Mass, C.Rr., et. al. "The onshore surge of marine air into the Pacific Northwest: a coastal region of complex terrain."

  <u>Monthly Weather Review</u>. 114 (December, 1986): 2602-2627.

- Segal, M. et. al. "Application of a numerical mesoscale model for the evaluation of seasonal persistent regional climatological patterns." <u>Journal of Applied Meteorology</u>. 21 (November 1982) 1754-1762.
- Wieringa, J. "Roughness-dependent geographical interpolation of surface winds speed averages." <u>Quarterly Journal of the Royal Meteorological Society</u>. 112 (July, 1986): 867-889.

# Code Definition For Spatial Dictionary Elements

#### Code Format:

Data Type | Width | Representation | Suggested Units and/or Example

# Data Type:

C = Character

I = Integer

F = Floating

## Width:

Given as number of character places.

For an floating data type the number to the right of the decimal indicates the number of decimal places and the number to the left of the decimal indicates the total field with.

## Representation:

A = Alpha only

N = Numeric only

AN = Alpha - Numeric

MDY = Month Day Year

## Suggested Units and/or Example:

\* = Self defining or not deemed necessary

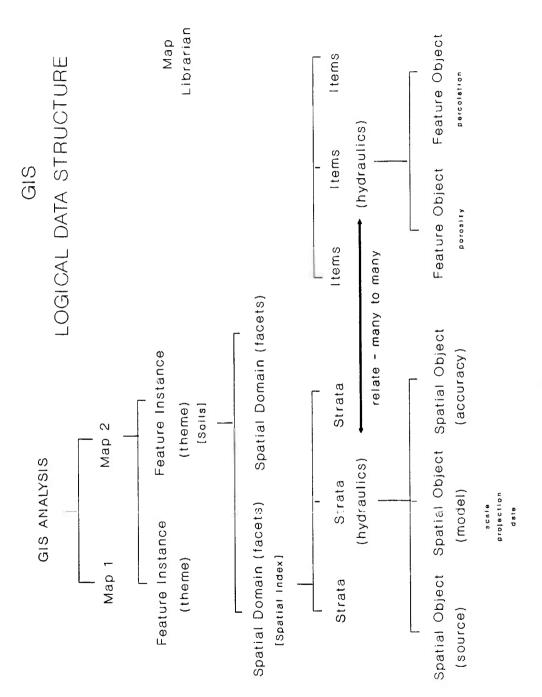


Figure 1

# 1991 US AFOSR SUMMER FACULTY RESEARCH PROGRAM AIR FORCE OFFICE OF SCIENTIFIC RESEARCH AIR FORCE SYSTEMS COMMAND

#### FINAL REPORT

## E. CARTAN MOMENT OF ROTATION IN ASHTEKAR'S THEORY OF GRAVITATION

Prepared by:

Arkady Kheyfets, Ph. D.

Academic Rank:

Assistant Professor

Department and

University:

Department of Mathematics

North Carolina State University

Raleigh, NC 27695-8205

**USAF** Researcher:

Dr. Warner A. Miller

PL/AWX

Kirtland AFB, NM 87117-6008

Date:

July 30, 1991

## E. CARTAN MOMENT OF ROTATION IN ASHTEKAR'S THEORY OF GRAVITATION

by Arkady Kheyfets

#### Abstract

The geometric construction of the E. Cartan moment of rotation associated to the spacetime curvature provides a geometric interpretation of the gravitational field sources and describes geometrically how the sources are "wired" to the field in standard geometrodynamics. E. Cartan moment of rotation yields an alternate way (as opposed to using variational principles) to obtain Einstein equations. The E. Cartan construction uses in an essential way the soldering structure of the frame bundle underlying the geometry of the gravitational field of general relativity. The geometry of Ashtekar's connection formulation of gravitation theory is based on a complex-valued self-dual connection that is not defined on the frame bundle of spacetime. We show how to transfer the construction of the E. Cartan moment of rotation to Ashtekar's theory of gravity and demonstrate that no spurious equations are produced via this procedure.

#### Acknowledgments

I wish to thank the Air Force Systems Command and the Air Force Office of Scientific Research for sponsorship of this research. The Office of the Chief Scientist at the Phillips Laboratory, Kirtland AFB, and the Research & Development Laboratories, Culver City, CA must be mentioned for their concern and help to me in all administrative and directional aspects of this program.

I am grateful to Colonel J. Periso of the Air Force Office of Scientific Research for his encouragement and support in the course of my research.

I want to express my gratitude to Mr. R. Keppler of the Office of the Chief Scientist at the Phillips Laboratory, Kirtland AFB for his advice and assistance in administrative matters.

I am grateful to my colleagues Dr. S. Colgate, Mr. D. Holtz, Dr. B. Shumacher, Dr. W. H. Zurek of the Los Alamos National Laboratory, Prof. J. A. Wheeler of the Princeton University, and Prof. J. York Jr. of the University of North Carolina at Chapel Hill for very useful discussions, suggestions, and encouragement.

I am especially thankful to Capt Warner A. Miller. All my work was performed in close cooperation with him. This report contains the results of our joint efforts.

#### I. Introduction.

The geometric construction of the moment of rotation associated to the spacetime curvature was introduced originally by E. Cartan. The meaning of this construction, as well as its importance for clear understanding of the geometric structure of general relativity was further investigated by C. W. Misner and J. A. Wheeler<sup>2</sup>. It was Wheeler<sup>1</sup> that first linked E. Cartan moment of rotation to the deeper foundational aspects of general relativity. Wheeler has also conjectured that such a relation can be extended to other basic field theories such as electrodynamics and Yang-Mills theory. His conjecture has been proven recently<sup>2,4,5</sup>. The difficulties of extending the E. Cartan construction to the field theories other than general relativity are related to the fact that this construction in general relativity uses, in an essential way, the soldering structure of the spacetime geometry. This structure appears to be absent in the geometry of electrodynamics and Yang-Mills theory. Nevertheless, the geometry of all basic field theories, when properly understood and reinterpreted, admits the E. Cartan construction. Furthermore, exactly as in general relativity, such an extension of the E. Cartan construction to other field theories describes geometrically how the sources of the fields are "wired" to the fields themselves and provides an alternate way (as opposed to the variational approach) to deduce the field equations in a way quite similar to that of obtaining Einstein equations in general relativity.

Ashtekar's theory of gravity introduces a new set of variables in the Hamiltonian (ADM) formulation of general relativity. Such a reformulation leads to a significant simplification<sup>6,7,8,9</sup> of both the evolution equations and constraints. It provides (1) a revolutionary new look at the whole structure of geometrodynamics, and (2) an opportunity of achieving considerable progress in many important problems of classical and quantum geometrodynamics. At this time Ashtekar's theory is viewed as a rapidly developing field of classical and

quantum geometrodynamics.

Originally Ashtekar's theory was introduced in its Hamiltonian formulation. However, a Lagrangian formulation of Ashtekar's theory also exists<sup>8,9</sup>. This is fortunate because the results we obtain via an application of the E. Cartan construction can be compared much easier with the Lagrange formulation than with the Hamilton formulation.

The geometry of Ashtekar's formulation (sometimes also called the connection formulation) of general relativity is based on a complex valued self-dual connection that is, strictly speaking, not defined on the frame bundle of the real spacetime. The curvature of this connection is complex valued. The soldering form of Ashtekar's theory is, in general, complex valued (complex vector or spinor valued), and is defined on the complexified tangent spaces. In its variational formulation, the action of Ashtekar's theory is also complex valued. The usual worry in Ashtekar's theory is that the imaginary part of the curvature, and the imaginary part of the action in a variational approach, might lead to spurious equations; thus, making the theory different from general relativity even when the reality conditions are imposed. Fortunately, this does not occur when variational principles are used<sup>6,9</sup>.

In this report we extend the E. Cartan moment of rotation construction to Ashtekar's theory and demonstrate that no spurious equation are produced via this procedure. Although the self-dual Riemann curvature is complex even in the case of real relativity, the E. Cartan moment of rotation turns out to be real in this case.

In Sec. II we describe the E. Cartan moment of rotation in standard general relativity. Here we introduce the terminology and our notations. Sec. III contains the translation of this construction in the language of the tetrad formulation, which is used frequently as a transitional step from standard general

relativity to Ashtekar's theory<sup>6</sup>. Sec. IV considers the E. Cartan moment of rotation of the self-dual Riemann curvature and demonstrates that in real relativity it is real. The imaginary part of the E. Cartan moment of rotation vanishes due to the cyclic symmetries of the Riemann tensor. Sec. V provides a formulation of the results in the language of two-spinors. It contains the expression of the spinor components of the E. Cartan moment of rotation in terms of the unprimed spinor connection curvature.

#### II. E. Cartan Moment of Rotation in General Relativity.

The geometry underlying the spacetime formulation of general relativity can be defined on an orthonormal frame bundle with the Lorentz group as its structure group and spacetime as its base. The structure group is represented as the group of automorphisms of a four dimensional vector space – the space of values – isomorphic to the to the tangent space of spacetime at a point. The space of values at a point of spacetime can be considered as a copy of the tangent space to spacetime at this point.

The tangent space to spacetime at each point of spacetime is assumed to be endowed with a basis  $\{e_{\mu}\}_{\mu=0}^{3}$ . In most cases we will assume that this basis is a coordinate basis  $(e_{\mu} = \partial/\partial x^{\mu})$  with the dual 1-form basis  $\{dx^{\mu}\}_{\mu=0}^{3}$ . The space of values, considered as a copy of the tangent space, is assumed to be spanned by the same basis  $\{e_{\mu}\}_{\mu=0}^{3}$ . Spacetime has a pseudoriemannian metric  $g_{\mu\nu}(x) dx^{\mu} \otimes dx^{\nu}$  on it such that

$$g_{\mu\nu}(x) = \mathbf{e}_{\mu}(x) \cdot \mathbf{e}_{\nu}(x). \tag{1}$$

Although the tangent space and the space of values are described as two copies of the same space they should be treated quite differently in the description of the geometric structure of general relativity. Fasticularly, the Lie algebra of the

structure group can be identified, as a vector space, with the space of bivectors (or 2-forms) of the space of values. All the geometric quantities (such as the connection form, the curvature form, etc.) are defined as linear maps from the tangent space (or its tensor products with itself and its dual) to the space of values (or its tensor products with itself and its dual).

The principal bundle of general relativity, being a frame bundle, admits the canonical soldering structure given by the canonical soldering form

$$\theta = \mathbf{e}_{\mu} \, \delta^{\mu}_{\nu} \, dx^{\nu} = \mathbf{e}_{\mu} \, dx^{\mu}. \tag{2}$$

In this formula  $e_{\mu}$  that stands to the left of the component expression  $\delta^{\mu}_{\nu}$  is a vector in the space of values and  $dx^{\nu}$  that stands to the right of the  $\delta^{\mu}_{\nu}$  is a 1-form in the tangent space. From now on we are going to stick with the agreement that in all the expressions the vectors (multivectors, forms, etc.) standing to the left of the component expression are those of the space of values whereas the vectors (multivectors, forms, etc.) standing to the right of the component expression are those of the tangent space. It is clear that the canonical soldering form, in fact, is nothing but an isomorphism between the tangent space and the space of values.

The geometry itself is defined by a connection form on the principal bundle described above. Its pulldown to spacetime (a bivector valued 1-form) is

$$\Gamma = \mathbf{e}_{\mu} \wedge \mathbf{e}_{\nu} \Gamma^{\mu\nu}{}_{\lambda} dx^{\lambda}. \tag{3}$$

Here, just as in expression (2), the bivector  $\mathbf{e}_{\mu} \wedge \mathbf{e}_{\nu}$  standing to the left of the  $\Gamma^{\mu\nu}_{\lambda}$  is a bivector of the values space, and the form  $dx^{\lambda}$  standing to the right of  $\Gamma^{\mu\nu}_{\lambda}$  acts on the vectors of the tangent space. This connection form determines the exterior covariant derivative. We use the symbol  $\nabla$  for its pulldown to spacetime. By pulldown to spacetime we mean the pullback of the form via a section of the frame bundle. When performing practical calculations at a point of spacetime it is often convenient to pick up a section horizontal at this point (such a choice of the section implies  $\Gamma^{\mu\nu}_{\lambda} = 0$  at the point).

The curvature form of the geometry determined by (3) is defined as the exterior covariant derivative of the connection form. The pulldown of this curvature form to spacetime is expressed locally as

$$R = \mathbf{e}_{\alpha} \wedge \mathbf{e}_{\beta} R^{\alpha\beta}{}_{\mu\nu} dx^{\mu} \wedge dx^{\nu} = \nabla \Gamma. \tag{4}$$

In general relativity physicists call R determined by the expression (4) the curvature of spacetime. This curvature satisfies the Bianchi identities

$$\nabla R = 0. ag{5}$$

The connection in general relativity is restricted by the demand that it is compatible with the metric structure and the canonical soldering structure

$$\nabla g = 0$$

$$\nabla \theta = 0.$$
(6)

Such a connection is called the Levi-Civita connection.

In the standard formulation of general relativity<sup>2</sup> that we are considering here the space of values and the tangent space are closely related in the sense that the choice of the local coordinate system on spacetime fixes both the coordinate basis of the tangent space and the local section of the principal bundle (a basis of the space of values). However, they are treated very differently in operations involving derivatives which is of a crucial importance in considering the construction of E. Cartan moment of rotation and, particularly, when the operators of dualization and exterior covariant derivative are used in the same expression. Indeed, if we use the notations \* for the duality operator on the tangent space and \* for the duality operator on the values space, then<sup>2</sup>

$$\nabla^* \neq {}^*\nabla$$

$$\nabla^* = {}^*\nabla.$$
(7)

The E. Cartan moment of rotation is defined as the values space dual of the exterior product of the canonical soldering form and the curvature form

$$M = {}^{\star} (\theta \wedge R), \tag{8}$$

which can be rewritten using equations (2) and (4) in the following way

$$M = {}^{\star} \left( \mathbf{e}_{\mu} \wedge \mathbf{e}_{\alpha} \wedge \mathbf{e}_{\beta} R^{\alpha \beta}{}_{\nu \lambda} dx^{\mu} \wedge dx^{\nu} \wedge dx^{\lambda} \right)$$

$$= \mathbf{e}_{\gamma} \epsilon^{\gamma}{}_{\mu \alpha \beta} R^{\alpha \beta}{}_{\nu \lambda} dx^{\mu} \wedge dx^{\nu} \wedge dx^{\lambda}$$

$$= \mathbf{e}_{\gamma} \epsilon^{\gamma}{}_{\mu \alpha \beta} R^{\alpha \beta}{}_{\nu \lambda} \epsilon^{\mu \nu \lambda \tau} d^{3} \Sigma_{\tau}$$

$$= \mathbf{e}_{\gamma} G^{\gamma \tau} d^{3} \Sigma_{\tau} = \mathbf{e}_{\alpha} G^{\alpha \tau} \epsilon_{\tau \mu \nu \lambda} dx^{\mu} \wedge dx^{\nu} \wedge dx^{\lambda} = G,$$

$$(9)$$

where G is the Einstein form (a vector valued 3-form) and  $G^{\mu\tau}$  is the Einstein tensor.

Taking into account equations (7) (compatibility of the connection  $\Gamma$  with the canonical soldering structure), (5) (Bianchi identities), and the fact that the exterior covariant derivative operation  $\Gamma$  commutes with the internal space duality operator  $\star$  we can write down the conservation equation for the Einstein form

$$\nabla G = \nabla [^{\star} (\theta \wedge R)] = 0, \tag{10}$$

which suggests the standard form of the Einstein equation

$$G = T, (11)$$

and provides a geometric interpretation of the source of gravitational field as the E. Cartan moment of rotation in the tetrad formulation of general relativity.

#### III. E. Cartan Moment of Rotation in Tetrad Formulationl.

The tetrad formalism uses instead of the metric four linearly independent covariant vector fields  $e^{I}_{\mu}$  related to the metric by the equation

$$g_{\mu\nu}(x) = e^i_{\mu}(x) \, e^j_{\nu}(x) \, \eta_{ij}, \tag{12}$$

where  $\mu, \nu, \ldots$  are spacetime indices running from 0 to 3, and  $i, j, \ldots$  are internal indices also running from 0 to 3. The internal indices are raised and lowered with the Minkowski metric  $\eta_{ij} = \text{diag}[-1, 1, 1, 1]$ .

The geometry underlying the tetrad formalism is defined on a SO(3,1) principal bundle with the Lorentz group as its structure group and spacetime as its base. The structure group is represented as the group of automorphisms of a four dimensional vector space (internal space) with a basis  $\{e_i\}_{i=0}^3$ . The tangent space to spacetime at each point of spacetime is assumed to be endowed with a basis  $\{e_{\mu}\}_{\mu=0}^3$ . In most cases we will assume that this basis is a coordinate basis  $\{e_{\mu} = \partial/\partial x^{\mu}\}$  with the dual 1-form basis  $\{dx^{\mu}\}_{\mu=0}^3$ . The described frame bundle has the canonical soldering structure determined by the canonical soldering form

$$\theta = \mathbf{e}_i \, e_\mu^i \, dx^\mu. \tag{13}$$

The form  $\theta$  is a vector valued 1-form and defines a one to one map from the tangent space of spacetime at a point to the internal space.

The geometry itself is defined by a connection form. Its pulldown to spacetime is a bivector valued 1-form

$$\omega = \mathbf{e}_i \wedge \mathbf{e}_j \,\omega^{ij}_{\ \mu} \,dx^{\mu}. \tag{14}$$

The connection determined by (14) frequently called the spin connection<sup>6</sup> is defined to be compatible with the canonical soldering structure

$$\nabla_{\omega}\theta = 0,\tag{15}$$

where  $\nabla_{\omega}$  denotes the pulldown to spacetime of the exterior covariant derivative determined by the connection  $\omega$ . In components, equation (15) takes the form

$$\partial_{[\mu}e^{i}_{\nu]} + \omega^{i}_{[\mu|j]}e^{j}_{\nu]} = 0. \tag{16}$$

The curvature bivector valued 2-form R (more precisely R is the pulldown of the curvature form to spacetime) is defined in a standard way as the covariant exterior derivative of the connection form  $\omega$ 

$$R = \mathbf{e}_i \wedge \mathbf{e}_j R^{ij}_{\mu\nu} dx^{\mu} \wedge dx^{\nu} = \nabla_{\omega} \omega, \tag{17}$$

so that it satisfies the Bianchi identities

$$\nabla_{\omega} R = 0. \tag{18}$$

The tetrad components  $R^{ij}_{\mu\nu}$  of the curvature are related to the standard spacetime components  $R^{\alpha\beta}_{\mu\nu}$  in a simple fashion

$$R^{ij}_{\mu\nu} = e^i_{\alpha} e^j_{\beta} R^{\alpha\beta}_{\mu\nu}. \tag{19}$$

The E. Cartan moment of rotation is defined as the internal space dual of the exterior product of the canonical soldering form and the curvature form

$$M_C = {}^{\star} (\theta \wedge R) \,, \tag{20}$$

which can be rewritten using equations (13) and (17) in the following way

$$M_{C} = {}^{\star} \left( \mathbf{e}_{i} \wedge \mathbf{e}_{j} \wedge \mathbf{e}_{k} \ e_{\mu}^{i} R^{jk}_{\nu\lambda} \ dx^{\mu} \wedge dx^{\nu} \wedge dx^{\lambda} \right)$$

$$= \mathbf{e}_{m} \ \epsilon^{m}_{ijk} e_{\mu}^{i} R^{jk}_{\nu\lambda} \ dx^{\mu} \wedge dx^{\nu} \wedge dx^{\lambda}$$

$$= \mathbf{e}_{m} \ \epsilon^{m}_{ijk} e_{\mu}^{i} R^{jk}_{\nu\lambda} \ \epsilon^{\mu\nu\lambda\tau} \ d^{3}\Sigma_{\tau}$$

$$= \mathbf{e}_{m} \ G^{m\tau} \ d^{3}\Sigma_{\tau} = \mathbf{e}_{m} \ G^{m\tau} \ \epsilon_{\tau\mu\nu\lambda} \ dx^{\mu} \wedge dx^{\nu} \wedge dx^{\lambda} = G,$$

$$(21)$$

where G is the Einstein form (a vector valued 3-form) and  $G^{m\tau} = e^m_{\mu} G^{\mu\tau}$  is the Einstein tensor expressed a half in internal components and a half in spacetime components.

Taking into account equations (15) (compatibility of the connection  $\omega$  with the canonical soldering structure), (18) (Bianchi identities), and the fact

that the exterior covariant derivative operation  $\nabla_{\omega}$  commutes with the internal space duality operator \* we can write down the conservation equation for the Einstein form

$$\nabla_{\omega}G = \nabla_{\omega} \left[ {}^{\star} (\theta \wedge R) \right] = 0, \tag{22}$$

which suggests the standard form of the Einstein equation

$$G = T, (23)$$

and provides a geometric interpretation of the source of gravitational field as the E. Cartan moment of rotation in the tetrad formulation of general relativity.

#### IV. E. Cartan Moment of Rotation in Ashtekar's Theory.

Geometry of Ashtekar's theory is quite different from that of general relativity in both spacetime and tetrad formulations. The principal bundle of Ashtekar's theory is an  $SO(3,1;\mathbb{C})$  bundle over spacetime. Its structure group is the complex Lorentz group represented as the automorphisms group of a complex four dimensional vector space (internal space) obtained via a complexification of the internal space of the tetrad formalism.

Geometry on this principal bundle is determined by Ashtekar connection<sup>6</sup>

$${}^{+}A = \mathbf{e}_{i} \wedge \mathbf{e}_{j} {}^{+}A^{ij}_{\mu} dx^{\mu}, \tag{24}$$

which is fixed to be the self-dual spin connection\*

$${}^{+}A^{ij}_{\mu} = \omega^{ij}_{\mu} + i \,\epsilon^{ij}_{mn} \,\omega^{mn}_{\mu}. \tag{25}$$

<sup>\*</sup> We wish to point out the difference between the Rovelli's self-dual spin connection<sup>6</sup> and the self-dual connection used in some other references<sup>9</sup>. The difference is not important for our results. It would cause trivial changes in some expressions (factors 2 and  $\frac{1}{2}$ ).

The curvature  ${}^+F$  of the Ashtekar connection  ${}^+A$  is defined in a standard fashion as the exterior covariant derivative  $\nabla_{+A}$  of  ${}^+A$ 

$${}^{+}F = \mathbf{e}_{i} \wedge \mathbf{e}_{j} {}^{+}F^{ij}_{\mu\nu} dx^{\mu} \wedge dx^{\nu} = \nabla_{+A} {}^{+}A.$$
 (26)

The components  ${}^+F^{ij}_{\mu\nu}$  are related to the components  $R^{ij}\mu\nu$  as follows<sup>6</sup>

$${}^{+}F^{ij}_{\ \mu\nu} = R^{ij}\mu\nu + i\,\epsilon^{ij}_{\ mn}\,R^{mn}_{\ \mu\nu}.\tag{27}$$

We recall here that in both spacetime and tetrad formulations of general relativity the E. Cartan moment of rotation  $M_C$  is defined to be the left dual (the internal space dual in case of the tetrad formulation) of the exterior product of the canonical soldering form  $\theta$  and the curvature form R.

The principal bundle of Ashtekar's theory is not a frame bundle in the strict sense of the word and, consequently, does not have the canonical soldering structure, very much like electrodynamics or Yang-Mills theory (although  $\theta$  can be considered as an isomorphism between the complexified tangent space and the complex internal space). A more detailed analysis<sup>3,5</sup> has shown that in electrodynamics as well as in Yang-Mills fields it is possible to express the source of any of these fields in terms of E. Cartan moment of rotation, and that the soldering form taking a part in the E. Cartan construction in both cases is just the canonical soldering form of the frame bundle over spacetime. Following the same pattern, we form the E. Cartan moment of rotation in Ashtekar's theory using the expression (13) for the canonical soldering form in the tetrad basis

$$M_C^A = {}^{\star} (\theta \wedge {}^{+}F). \tag{28}$$

From the definition of the Ashtekar connection (25), the compatibility of the connection with the spacetime soldering, commutativity of the exterior covariant differentiation with the duality operator on the internal space, and Bianchi identities

$$\nabla_{+A}{}^+F = 0 \tag{29}$$

it is easy to see that the E. Cartan moment of rotation (28) in Ashtekar's theory is conserved

$$\nabla_{+A} M_C^A = \nabla_{+A} \left[ {}^* \left( \theta \wedge {}^+ F \right) \right] = 0, \tag{30}$$

just as in both spacetime and tetrad formulations of general relativity. In expressions (29) and (30)  $^{+}A$  stands for the pulldown of the Ashtekar connection to spacetime and  $^{+}F$  for the pulldown of the Ashtekar curvature form to spacetime.

However, the curvature form of Ashtekar's theory contains, in addition to the standard tetrad curvature, an imaginary part proportional to the internal space dual of the tetrad curvature form. The usual worry in Ashtekar's theory<sup>6,7,9</sup> is that such an imaginary part might produce spurious equations and in this way lead to the theory different from general relativity. As it is well known<sup>8,9</sup> this does not occur when variational principles are used. To see whether it happens or not in our case we inspect closer the expression (28) for the E. Cartan moment of rotation via substituting expressions (13) for  $\theta$  and (26), (27) for  $^+F$ . It is convenient to rewrite equations (26), (27) in the form

$$^{+}F = R + i \,^{\star}R. \tag{31}$$

Thus, the expression (28) for  $M_C^A$  yields

$$M_C^A = {}^{\star}(\theta \wedge R) + i {}^{\star}(\theta \wedge {}^{\star}R). \tag{32}$$

The first term of this expression yields the standard expression for the Einstein form (an internal vector valued 3-form) G as we have already shown in Sec. III of this report (cf. equation (21) and the related discussion). The second term can be calculated by means of straightforward performing all the operations of dualization and exterior multiplication listed in its expression, and using the standard identity for  $e^{ijmn}$ 

$$\epsilon^{mi}_{np} \, \epsilon_{jq}^{np} = -2(\delta^m_j \delta^i_q - \delta^m_q \delta^i_j). \tag{33}$$

The result is

$$^{\star}(\theta \wedge {}^{\star}R) = \mathbf{e}_{m} \ e_{i\nu} R^{mi}_{\ \mu\lambda} dx^{\nu} \wedge dx^{\mu} \wedge dx^{\lambda}. \tag{34}$$

Using the relations

$$R^{mi}_{\mu\lambda} = e^{m}_{\alpha} e^{i}_{\beta} R^{\alpha\beta}_{\mu\lambda}$$

$$e^{i}_{\beta} e_{i\nu} = g_{\beta\nu}$$

$$e^{m}_{\alpha} e_{m} = e_{\alpha}$$
(35)

between the tetrad and spacetime variables (34) can be reduced to

$$^{\star}(\theta \wedge {}^{\star}R) = \mathbf{e}_{m} \ e_{\alpha}^{m} \ e_{\beta}^{i} \ e_{i\nu} R^{mi}_{\ \mu\lambda} dx^{\nu} \wedge dx^{\mu} \wedge dx^{\lambda}$$

$$= \mathbf{e}_{\alpha} \ g_{\beta\nu} \ R^{\alpha\beta}_{\ \mu\lambda} dx^{\nu} \wedge dx^{\mu} \wedge dx^{\lambda}$$

$$= \mathbf{e}_{\alpha} \ R^{\alpha}_{\ \nu\mu\lambda} dx^{\nu} \wedge dx^{\mu} \wedge dx^{\lambda} = 0.$$
(36)

The last equality in (36) follows from the identity satisfied by the Riemann tensor

$$R^{\alpha}{}_{\nu\mu\lambda} + R^{\alpha}{}_{\mu\lambda\nu} + R^{\alpha}{}_{\lambda\nu\mu} = 0. \tag{37}$$

We can summarize our analysis by the statement that the E. Cartan moment of rotation in Ashtekar's theory is real and, just as in standard relativity, is equal to the Einstein form

$$^{\star}(\theta \wedge {}^{+}F) = {}^{\star}(\theta \wedge R) = G. \tag{38}$$

#### V. Two-Component Spinor Language.

As it has been noted above, in Ashtekar's theory of gravity we deal only with the self-dual part of of a frame bundle connection. Therefore, in this theory it is convenient to use a two-component spinor language<sup>10</sup>, as it is done in most of the literature on the subject<sup>7,8,9</sup>. In most of this section we use common index notations that can be interpreted by a reader either as abstract indices or as

the components of spinors in a basis. When the two-component spinor language is used the internal tetrad indices  $i, j, \ldots$  are replaced by the pairs of unprimed and primed indices  $AA', AB', \ldots$  referring to the internal two dimensional vector space (over complex numbers) of spinors and its complex conjugate. The internal space of spinors is assumed to be endowed with a fixed non-degenerate 2-form  $\varepsilon_{AB}$ , its inverse  $\varepsilon^{AB}$ , and the conjugates  $\varepsilon_{A'B'}$  and  $\varepsilon^{A'B'}$  which are used to raise and lower the spinor indices<sup>10</sup>.

Just as it is the case for all other formulations of general relativity the tangent space to spacetime is soldered to the internal space. This time the soldering form  $\sigma^{AA'\mu}$  is an isomorphism (over the field of complex numbers) between the complexified tangent space and the four dimensional space of (1,1) spinors. The soldering form  $\sigma^{AA'\mu}$  is a vector of the (complexified) tangent space and a (1,1) spinor of the internal space. Using the tetrad field we can transform it into a 1-form on the complexified tetrad internal space  $\sigma^{AA'}{}_{i}$  via the relation

$$\sigma^{AA'\mu} = e^{i\mu} \, \sigma^{AA'}{}_i. \tag{39}$$

In the case of real relativity  $\sigma^{AA'\mu}$  is required to be such that  $\overline{\sigma^{AA'\mu}} = \sigma^{AA'\mu}$ . In such a case  $\sigma^{AA'\mu}$  is related to the spacetime metric in a simple way

$$g^{\mu\nu} = \sigma^{AA'\mu} \,\sigma_{AA'}{}^{\nu}. \tag{40}$$

An SL(2,C) connection  $A_{BC\mu}$  and the related covariant derivative  $\mathcal{D}_{\mu}$  is defined on the unprimed spinors bundle in such a way that

$$\mathcal{D}_{\mu}\,\varepsilon_{AB} = 0. \tag{41}$$

The action of the covariant derivative  $\mathcal{D}_{\mu}$  on an unprimed spinor  $\lambda_B$  is expressed in terms of the connection 1-form  $A_{BC\mu}$  by

$$\mathcal{D}_{\mu}\lambda_{B} = \partial_{\mu}\lambda_{B} + A_{B}{}^{C}{}_{\mu}\lambda_{C}. \tag{42}$$

It follows from (41) that  $A_B{}^C{}_{\mu}$  is traceless, or equivalently  $A_{BC\mu} = -A_{CB\mu}$ . It is clear that  $A_{BC\mu}$  has  $4 \times 3 = 12$  independent complex components. It is equivalent to a self-dual connection of Sec. IV via the one to one correspondence between  ${}^+A^{ij}_{\mu}$  and  $A_{BC\mu}\,\varepsilon_{B'C'}$  when the pair of indices BB' is identified with the tetrad index i. The identification is given by a fixed map  $\sigma^{BB'}{}_{i}$  between the internal tetrad space and the internal space of (1,1) spinors

$$\sigma^{BB'i} \sigma^{CC'j} A_{BC\mu} \varepsilon_{B'C'} = {}^{+}A^{ij}_{\mu}. \tag{43}$$

Likewise, the relation between the curvature  $F_{BC\mu\nu}$  of the connection  $A_{BC\mu}$  defined by

$$\frac{1}{2}F_{BC\mu\nu} = \partial_{[\mu}A_{|BC|\nu]} + A_B^{P}_{[\mu}A_{|PN|\nu]}$$
 (44)

and the self-dual Riemann curvature  ${}^+F^{ij}_{\mu\nu}$  is given by

$$\sigma^{BB'i}\sigma^{CC'j}F_{BC\mu\nu}\varepsilon_{B'C'} = {}^{+}F^{ij}_{\mu\nu}. \tag{45}$$

As we already know (cf. equation (38)) the E.Cartan moment of rotation does not change (and, in particular, remains to be real) when the Riemann curvature R in it is replaced with the self-dual curvature +F

$$M = M_C^A = {}^{\star} (\theta \wedge R) = {}^{\star} (\theta \wedge {}^{+}F) = G$$
$$= e_i G^{i\mu} d^3 \Sigma_{\mu} = e_{\nu} G^{\nu\mu} d^3 \Sigma_{\mu}, \tag{46}$$

where  $G^{i\mu}$  and  $G^{\nu\mu}$  are the tetrad and spacetime components of the Einstein tensor respectively. Equivalently,  $G^{i\mu}$  and  $G^{\nu\mu}$  can be called the tetrad and spacetime components of the E. Cartan moment of rotation. It follows from the expression (46) that the spacetime components of the E. Cartan moment of rotation can be expressed in terms of the self-dual Riemann curvature as follows

$$G^{\mu\nu} = {}^{+}F^{\mu\nu} - \frac{1}{2}g^{\mu\nu} + F, \tag{47}$$

where  ${}^+F^{\mu\nu}$  and  ${}^+F$  are the Ricci part and the scalar part of the self-dual Riemann curvature

$$^{+}F^{\mu\nu} = ^{+}F^{\alpha\mu}{}_{\alpha}{}^{\nu}$$

$$^{+}F = ^{+}F^{\alpha}{}_{\alpha}.$$

$$(48)$$

In expressions (47) and (48) we have switched from the internal space indices of the Sec. IV to all spacetime indices. To avoid an ambiguity we should point out that the self-duality in these expressions means the self-duality with respect to the first pair of indices of  ${}^+F^{\mu\nu\alpha\beta}$ .

The expressions for the spinor components  $G^{AB'\mu}$  of the E. Cartan moment of rotation can be obtained easily based on the equation (47)

$$G^{AB'\mu} = \sigma^{AB'}{}_{i} G^{i\mu} = \sigma^{AB'}{}_{\nu} G^{\nu\mu} = \sigma^{AB'}{}_{\nu} \left( {}^{+}F^{\nu\mu} - \frac{1}{2} {}^{+}F \right)$$
 (49)

via a substitution into it the expressions

$$+F^{\alpha\beta}{}_{\mu\nu} = \sigma^{BB'\alpha} \sigma^{CC'\beta} F_{BC\mu\nu} \varepsilon_{B'C'}$$

$$+F^{\alpha}{}_{\nu} = \sigma^{BB'\mu} \sigma^{CC'\beta} F_{BC\mu\nu} \varepsilon_{B'C'}$$

$$+F = \sigma^{BB'\mu} \sigma^{CC'\nu} F_{BC\mu\nu} \varepsilon_{B'C'}$$

$$(50)$$

together with the expression (40) for  $g^{\mu\nu}$ .

The resulting expression for the spinor components  $G^{B'}_{\ C}{}^{\mu}$  of the E. Cartan moment of rotation is

$$G_{C}^{B'\mu} = \sigma^{BB'\nu} F_{BC}^{\mu}{}_{\nu} - \frac{1}{2} \sigma_{C}^{B'\mu} \left( \sigma^{MM'\alpha} \sigma_{M'}^{N}{}^{\beta} F_{MN\alpha\beta} \right). \tag{51}$$

This expression is not manifestly real. However, in the case of real relativity it is, indeed real, which is clear from the considerations of the Sec. IV and reality of the  $\sigma^{AA'\mu}$ . Comparing the equation (51) with the gravitational field equation

$$\sigma^{BB'\nu} F_{BC}^{\mu}{}_{\nu} - \frac{1}{2} \sigma^{B'\mu}_{C} \left( \sigma^{MM'\alpha} \sigma^{N}_{M'}{}^{\beta} F_{MN\alpha\beta} \right) = 0, \tag{52}$$

obtained by Jacobson and Smolin<sup>9</sup> from the Lagrangian variational principle we conclude that this equation is the statement in spinor language of the fact that

in vacuum the E. Cartan moment of rotation is equal to zero, as it is supposed to be.

#### VI. Conclusion.

We have demonstrated that the construction of the E. Cartan moment of rotation can be extended to the Ashtekar's theory of gravity. Despite the fact that the self-dual curvature is complex even in real relativity the E. Cartan moment of rotation in this case is real. The imaginary part of the E. Cartan moment of rotation vanishes due to the cyclic symmetries of the Riemann tensor. We have also shown that the two-spinor components of the E. Cartan moment of rotation can be expressed in terms of the curvature of the unprimed spinor connection. Such an expression coincides with the left hand side of the Lagrangian equation obtained by Jacobson and Smolin from variational principles. This leads us to an elegant geometric interpretation of their result.

Our next goal would be to extend this construction to the loop variables formulation of the theory of gravitation. The loop variables formulation is one of the most promising approaches in quantizing gravity. If a 3 + 1 ADM split of spacetime is performed in loop variables, the constraint equations are satisfied automatically, which removes one of the main difficulties in solving the quantization problem for gravity.

E. Cartan construction allows one to retain a clear and deep geometric picture when dynamics of the gravity theory is analyzed. However, to be able to extend this construction to loop variables it is necessary to develop the machinery for comparing the E. Cartan contruction to the Familtonian formulation and to clarify its relation to the Hamilton-Jacobi equation of general relativity.

This will be the main goal of our future research.

#### References.

- Wheeler J. A.: Physics and Austerity, Anhui Science and Technology Publications, China, Anhui (1982)
- <sup>2</sup> Misner C. W., Thorne K. S., Wheeler J. A. Gravitation. W. H. Freeman and Co., New York (1973)
- 3 Kheyfets A.: Foundations of Physics, 16, 463 (1986)
- <sup>4</sup> Kheyfets A. & Wheeler J. A.: Int. J. Theor. Phys., 25, 573 (1986)
- <sup>5</sup> Kheyfets A. & Miller W. A.: J. Math. Phys., to appear in November, 1991
- <sup>6</sup> Rovelli C.: Ashtekar Formulation of General Relativity and Loop-Space Non-Perturbative Quantum Gravity: a Report (1991)
- Ashtekar A.: Old Problems in the Light of New Variables, to appear in the Proceedings of the Osgood-Hills conference on Conceptual Problems of Quantum Gravity (1990)
- <sup>8</sup> Ashtekar A.: *Phys. Rev.* **D40**, 2572 (1989)
- <sup>9</sup> Jacobson T. & Smolin L.: Class. Quantum Grav., 5, 583 (1988)
- Penrose R. & Rindler W.: Spinors and Space-Time, V.1, Cambridge University Press, Cambridge (1984)

### Criteria for Excitation of Parametric Instability in the Ionosphere by Obliquely Incident HF Heater

S.P. Kuo
Weber Research Institute
Polytechnic University
Route 110
Farmingdale, NY 11735

#### Abstract

Parametric excitation of lower hybrid decay mode together with upper hybrid sideband in the ionosphere by an Obliquely HF pump is studied. The conditions for the instability, including the frequency range, the elevation angle, and the threshold field intensity of the pump, are determined.

#### I. Introduction

Heating and modification of the ionosphere by high power radio waves transmitted from various ground heating facilities have been actively pursued during the past 30 years. A large number of unexpected phenomena have been observed in addition to the originally anticipated electron temperature and density change. These phenomena including sideband attenuation of the ionosonde signal, artificially induced Spread-F<sup>1</sup>, large and samil-scale irregularities<sup>1</sup>, generation of geometric pulsation<sup>2,3</sup>, enhancement of fluxes of suprathermal electrons<sup>4</sup>, stimulated electromagnetic emission<sup>5</sup>, plasma line overshoot<sup>6,7</sup> and the expansion of its originating altitude interval<sup>8</sup>, height difference between the natural line and HFPLs<sup>9</sup>, and asymmetric plasma lines having anomalously upshifted frequencies 10, etc. Most of these phenomena are believed to be attributed to the plasma turbulence excited by the HF heater via parametric instabilities directly or indirectly 11-17. In other words, parametric instabilities plays a primary role in the HF heating of the ionosphere 18,19. they provide effective channels to convert EM wave energy into electrostatic plasma waves of high and low frequencies which are trapped inside the plasma and cause much more significant perturbation to the plasma than the perturbation caused directly by the original EM heater.

So far these phenomena have been observed while the heater waves are transmitted vertically and polarized at O-mode. It is consistent with the theoretical analyses which show that the frequency and wavevector matching condition as well as the threshold condition of various parametric instabilities can be satisfies near the reflection height of the vertically

incident O-mode heater. By contract, it was thought that the matching conditions for similar parametric instabilities could not be satisfied in the oblique ionospheric heating processes.

The ionospheric heating by obliquely incident heaters has also been investigated experimentally during the past<sup>20-23</sup>, however, so far there is no report about the observation of any drastic effect. On the other hand, oblique heating has the advantage of potentially enlarging the modification region of the ionosphere. Moreover, high power radar and communication systems, in general, operate at oblique incidence. In this aspect, it is still of great interest in examining the potential effects of an obliquely incident heater<sup>24</sup> which, even though, was believed not being able to produce the same effects as a vertically incident one. Especially, it is noted that near the reflection height, the obliquely transmitted 0-mode heater still has a finite wave number. Thus, the wave field of the 0-mode pump does not orientate to align with the geomagnetic field and exists a perpendicular wave field component even in the region near the reflection height. This wave field component which does not exist in the vertical incidence case could potentially become a driving force to excite hybrid plasma modes via parametric instabilities<sup>25</sup> and result with distinctively different modification effects to the ionosphere.

In this work, the conditions for the excitation of parametric instability of hybrid waves are examined for the oblique ionospheric heating. These include the frequency range, the elevation angle, and the threshold field intensity of the pump. The threshold field is expected to be a function of the wave frequency, the elevation angle, the magnetic dip

angle, the wavenumber of the decay mode, and the collision and plasma frequency. Following these conditions, one can selectively modify the ionospheric region with the obliquely transmitted heater, or estimate the perturbations caused by the feedback of the ionosphere to some radar and communication systems.

#### II. Theory

Different from the vertically transmitting case, the wavenumber of the obliquely incident heater always has a finite component in the horizontal direction. Thus, the wave field of the O-mode (vertical polarization) heater does not orientate toward the direction of geomagnetic field and exists a perpendicular wave field component near the reflection height. Choosing the coordinate system as shown in Fig. 1, the wave vector  $\mathbf{k}_0$  of the heater near the reflection height can be expressed to be

$$\mathbf{k}_0 = (\widehat{\mathbf{x}} \sin \theta_0 - \widehat{\mathbf{z}} \cos \theta_0) \ \mathbf{k}_0 \cos \theta_i \tag{1}$$

where  $\theta_0$  and  $\theta_i$  are the magnetic dip angle and the incident elevation angle of the heater respectively;  $k_0 = \omega_0/c = (\omega_p^2 + \omega_0^2 \cos^2\theta_i)^{1/2}/c$  is the wavenumber of the heater on the ground;  $\omega_p$  is the plasma frequency at the reflection height of the heater.

Since  $\omega_0 > \omega_p >> \Omega_e$ , heater can be considered still being a transverse wave near the reflection height. Its wave field is then given by

$$\mathbf{E}_{\mathbf{p}} = [-(\widehat{\mathbf{x}} \cos \theta_0 + \widehat{\mathbf{z}} \sin \theta_0) \mathbf{E}_0 + \widehat{\mathbf{y}} \mathbf{E}_{0\mathbf{y}}] \exp[i(\mathbf{k}_0 \cdot \mathbf{r} - \omega_0 \mathbf{t})] + c.c. \tag{2}$$

where the horizontally polarizated wave field component  $(\widehat{y} \ E_{oy})$  is included for generality.

We now study parametric instability excited by a pump (heater) featured with (1) and (2) in a region slightly below the reflection height of

the pump. The process under condition is the decay of the pump wave  $(\mathbf{k}_0, \omega_0)$  into upper hybrid wave  $(\mathbf{k}, \omega)$  and lower hybrid wave  $(\mathbf{k}_3, \omega_3)$  pair through the nonlinearity of the plasma. It is represented by the following wavevector and frequency matching relations

$$\mathbf{k}_0 = \mathbf{k} + \mathbf{k}_3$$

$$\omega_0 = \omega + \omega_3^*$$
(3)

In the following analysis,  $\mathbf{k} = \widehat{\mathbf{x}} \mathbf{k}$  is assumed to simplify the analysis. However the extension of the analysis to the more general case that  $\mathbf{k} = \widehat{\mathbf{x}} \mathbf{k}_x + \widehat{\mathbf{y}} \mathbf{k}_y$  is straightforward.

## III. Upper hybrid wave excited by an EM pump coupling with a lower hybrid wave

The coupled mode equation for the potential function  $\phi$  of the upper hybrid sideband  $(\mathbf{k}, \omega)$  in terms of the obliquely incident pump  $(\mathbf{k}_0, \omega_0)$  and lower hybrid decay wave  $(\mathbf{k}_3, \omega_3)$  is derived from the electron continuity equation and momentum equation as

$$\begin{split} &(\frac{\partial}{\partial t} + v_{e})[\frac{\partial^{2}}{\partial t^{2}} + v_{e}\frac{\partial}{\partial t}\omega_{p}^{2} - v_{te}^{2}\nabla_{\perp}^{2}]\nabla_{\perp}^{2}\phi + \Omega_{e}^{2}\frac{\partial}{\partial t}\nabla_{\perp}^{2}\phi \\ &= \omega_{p}^{2}[(\frac{\partial}{\partial t} + v_{e})\nabla_{\perp} \cdot \mathbf{E}_{p}(\delta n_{e3}^{*}/n_{0}) - \Omega_{e}\nabla_{\perp} \cdot (\mathbf{E}_{p} \times \widehat{\mathbf{z}})(\delta n_{e3}^{*}/n_{0})] \end{split} \tag{4}$$

where  $v_e$  is the electron collision frequency;  $v_{te} = (3T_e/m_e)^{1/2}$  is the electron thermal speed;  $\omega_p$  and  $\Omega_e$  are the electron plasma and cycltron frequency respectively;  $\delta n_{e3}$  is the electron density perturbation associated with the lower hybrid decay wave..

We assume that the perturbations take the form  $\phi = \phi \exp[i(kx - \omega t)] + c.c.$  and  $\delta n_{e3} = \delta n_{e3} \exp[i(k_3 \cdot r - \omega_3 t)] + c.c.$ 

Substituting them into (4) and using the matching relation (3) to cancel out the common exponential phase factor, the coupled mode equation (4) is then reduced to

$$\widetilde{\Phi} = -(\omega_p^2/k)\delta\widetilde{n}_{e3}^*[(\omega + i\nu_e)E_0\cos\theta_0 + i\Omega_eE_{0y}]/[i\omega\Gamma + \nu_e(\omega^2 + \Omega_e^2)]$$
(5)

where  $\Gamma = \omega_k^2 + \Omega_e^2 + n_e^2 - \omega^2$  and  $\omega_k^2 = \omega_p^2 + k^2 V_{te}^2$ .

Eq.(5) gives the potential perturbation of the upper hybrid sideband as a function of the pump field and the density fluctuation of the lower hybrid decay mode.

#### IV. Coupled Mode Equation for the Lower Hybrid Decay Mode

The governing equations describing the lower hybrid wave include the continuity equations and momentum equations of electrons and ions, and the Possion Equation:

$$\delta n_{e3}/n_0 = k_3 \cdot \delta v_{e3}/\omega_3 + k_3 \cdot (\delta n_e^*/n_0) v_{pe}/\omega_3$$
 (6)

$$\delta n_{i3}/n_0 = k_3.\delta v_{i3}/\omega_3 \tag{7}$$

$$\omega_3 \delta \mathbf{v}_{e3} + i \Omega_e \delta \mathbf{v}_{e3} \mathbf{x} \hat{\mathbf{z}} = -i \mathbf{A} + \mathbf{k}_3 \mathbf{D}_e$$
 (8)

$$\omega_{3i}\delta \mathbf{v}_{i3} - i\Omega_{i}\delta \mathbf{v}_{e3}\mathbf{x}\hat{\mathbf{z}} - \mathbf{k}_{3}D_{i}$$
(9)

and

$$k_3^2 \phi_3 = 4\pi e (\delta n_{i3} - \delta n_{e3})$$
 (10)

where  $\delta n_e$  is the electron density perturbation associated with the upper hybrid sideband;  $\mathbf{v_{pe}}$  is the electron velocity introduced by the pump field;  $\mathbf{A} = \langle \mathbf{v_e} \cdot \nabla \mathbf{v_e} \rangle$  and  $\langle \rangle$  stands for average over the period of the pump;  $D_{i,e} = \pm e \phi_3 / m_{i,e} + v_{ti,e} = \delta n_{i,e3} / n_0$ ;  $\omega_{3e} = \omega_3 + i v_e$ , and  $\omega_{3i} = \omega_3 + i v_{in}$ .

Using (8) and (9) to determine  $\delta v_{e3}$  and  $\delta v_{i3}$  explicitly and substituting the results into (6) and (7), yield

$$\delta n_{e3}/n_0 = (\omega_{3e}/\omega_3)(k_{3x}^2/\Omega_e^2 - k_{3z}^2/\omega_{3e}^2)(e\phi_3/m_e) + \{(k_3 \cdot v_{pe}/\omega_3)(\delta n_e^*/n_0) + (k_{3x}^2/\Omega_e^2)[iA_x + (\Omega_e/\omega_3)A_y - i((k_{3z}/k_{3x})(\Omega_e^2/\omega_3^2A_z)]\}$$
(11)

and

$$\delta n_{i3}/n_0 = k_3^2 (e \phi_3/m_i \omega_3^2)$$
 (12)

Substitute (11) and (12) into (10), the coupled mode equation for the lower hybrid decay mode is derived to be

$$[\omega_{3}^{2}+i(2-1/\xi)v_{e}\omega_{3}-\omega_{Lk3}^{2}]\phi_{3}=-[4\pi n_{0}e\omega_{3}/k_{3}^{2}(1+\omega_{p}^{2}/\Omega_{e}^{2})]$$

$$\{(k_{3}\cdot v_{pe})(\delta n_{e}^{*}/n_{0})+(k_{3x}/\Omega_{e}^{2})[i\omega_{3}A_{x}+\Omega_{e}A_{y}]-ik_{3z}A_{z}/\omega_{3}\}$$
(13)

where 
$$\xi=1+(m_i/m_e)(k_{3z}^2/k_3^2)$$
,  $\omega_{Lk3}^2=\omega_{LH}^2\xi$ , and  $\omega_{LH}^2=\omega_{pi}^2/(1+\omega_p^2/\Omega_e^2)$ .

The RHS of (13) shows that the decay mode is produced by the net effect of the nonlinear beating current and the radiation pressure force introduced by the coupling of the pump to the sideband through the nonlinearity of the plasma.

Using the electron momentum equation to determine the linear velocity responses to the high frequency wave field, thus, A can be expressed explicitly in terms of the product of the pump and sideband wave field. Similarly,  $\delta n_e$  can be expressed explicitly in terms of the sideband wave field via the Possion equation. Substituting these explicit expression for A and  $\delta n_e$  into (3), results to

$$\begin{split} [\omega_{3}{}^{2} + \mathrm{i}(2 - 1/\xi)\nu_{e}\omega_{3} - \omega_{Lk3}{}^{2}] \widetilde{\varphi}_{3} &= -\mathrm{i}(e/m_{e})[\omega_{Lk3}{}^{2}k_{3x}k\omega^{*}\omega_{0}/k_{3}{}^{2}(1 + \omega_{p}{}^{2}/\Omega_{e}{}^{2})\Omega_{e}{}^{2}(\omega_{0}{}^{2} - \Omega_{e}{}^{2})] \\ & \{ [k_{3x} + (\Omega_{e}{}^{2}/\omega_{0}\omega_{3})k_{0x}]E_{0}cos\theta_{0} + \mathrm{i}(\Omega_{e}/\omega_{0})(k_{3x} + k_{0x}\omega_{0}/\omega_{3})E_{0y} - (k_{3z}/k_{3x})(\Omega_{e}{}^{2}/\omega_{3}{}^{2}\omega_{0}{}^{2})(\omega_{0}{}^{2} - \Omega_{e}{}^{2})(k_{0x} + k\omega_{3}/\omega^{*})E_{0}sin\theta_{0}\} \widetilde{\varphi}^{*} \end{split}$$

Equs. (5) and (14) form a complete coupled set of equations describing the parametric instability process considered in the present work.

#### V. Dispersion Relation

Substituting (5) into (14) and with the aid of (11), a dispersion relation for the proposed instability process is derived to be

$$\begin{split} [\omega_{3}{}^{2}+\mathrm{i}(2\text{-}1/\xi)\nu_{e}\omega_{3}\text{-}\omega_{Lk3}{}^{2}][-\mathrm{i}\omega^{*}\Gamma^{*}+\nu_{e}(\omega^{*2}+\Omega_{e}{}^{2})]\xi \\ =&\mathrm{i}(e/m)^{2}[\omega_{Lk3}{}^{2}\omega^{*}\omega_{0}k_{3x}{}^{3}/k_{3}{}^{2}(\omega_{0}{}^{2}-\Omega_{e}{}^{2})\Omega_{e}{}^{2}]\{k_{3x}+(\Omega_{e}{}^{2}/\omega_{0}\omega_{3})k_{0x}]E_{0}cos\theta_{0} \\ +&\mathrm{i}(\Omega_{e}/\omega_{0})(k_{3x}+k_{0x}\omega_{0}/\omega_{3})E_{0y}-(k_{3z}/k_{3x})(\Omega_{e}{}^{2}/\omega_{3}{}^{2})(1-\Omega_{e}{}^{2}/\omega_{0}{}^{2})(k_{0x}+k\omega_{3}/\omega^{*})E_{0}sin\theta_{0}\} \\ &[(\omega^{*}\mathrm{-i}\nu_{e})E_{0}cos\theta_{0}\mathrm{-i}\Omega_{e}E_{0y}{}^{*}] \end{split} \tag{15}$$

where the higher order terms proportional to  $|Ep|^4$  arising from the second term on the RHS of (11) are neglected.

This is the general expression of the dispersion relation for parametric excitation of lower hybrid decay mode together with an upper hybrid sideband by an EM pump of elliptical polarization.

In order to minimize the instability threshold field, it is preferred that the excited waves are the natural modes of the medium, i.e. satisfying the dispersion relation. Thus, we set  $\omega=\omega_{UH}+i\gamma$  and  $\omega_3=\omega_{LK3}+i\gamma$  in (15), where  $\omega_{UH}=(\omega_k^2+\Omega_e^2+\nu_e^2)^{1/2}$  is the upper hybrid resonance frequency and  $\gamma$  is the growth rate of the instability, an equation for the growth rate  $\gamma$  is obtained to be

$$\begin{split} & [\gamma + (1 - 1/2\xi)v_e][\gamma + v_e(1 + \Omega_e^2/\omega_{UH}^2)/2] \\ = & \frac{1}{4}(e/m)^2[\omega_0k_{3x}^3\omega_{Lk3}/k_3^2(\omega_0^2 - \Omega_e^2)\xi\Omega_e^2]\{[k_{3x} + (\Omega_e^2/\omega_0\omega_{Lk3})k_{0x}]E_0\cos\theta_0 \\ & + i(\Omega_e/\omega_0)(k_{3x} + k_{0x}\omega_0/\omega_{Lk3})E_{0y} - (k_{3z}/k_{3x})(\Omega_e^2/\omega_{Lk3}^2)(1 - \Omega_e^2/\omega_0^2) \end{split}$$

$$(k_{0x}+k\omega_{Lk3}/\omega_{UH})E_0\sin\theta_0\}[E_0^*\cos\theta_0-i(\Omega_e/\omega_{UH})E_{0y}^*]$$
 (16)

This equation is analyized in the following for two cases of independently polarized pumps:

#### A. Horizontal point ization, i.e. $E_p = \widehat{y}E_{0y}$

Eq.(16) is then reduced to

$$(\gamma + \nu_e)(\gamma + \nu_e/2) = \frac{1}{4} (e/m)^2 (k_{3x}^2 k_{0x}/k_3^2 \omega_0^2 \xi) |E_{0y}|^2$$
 (17)

where  $\Omega_e^2 << \omega_{UH}^2 < \omega_0^2$  and  $k_{0x}\omega_0/k_{3x}\omega_{Lk3}>>1$  are assumed.

Setting  $\gamma$ =0 in (17), the threshold field of the instability is determined to be

$$|eE_{th}/m\omega_0| = (2\xi/k_{3x}k_{0x})^{1/2}v_e(k_3/k_{3x})$$
 (18)

In terms of the threshold field, the growth rate  $\gamma$  of the instability is given by

$$\gamma = (v_e/2)\{[2(E_{0v}/E_{th})^2 + 1/4]^{1/2} - 3/2\}$$
 (19)

B. Vertical polarization, i.e.,  $E_p = -(\widehat{\mathbf{x}} \cos \theta_0 + \widehat{\mathbf{z}} \sin \theta_0) E_0$ 

One can reduce (16) to

$$(\gamma + v_e)(\gamma + v_e/2) = \frac{1}{4} (e/m)^2 (k_{3x}^2 k_{0x}/k_3^2 \omega_0^2 \xi) E_0^2 \cos^2 \theta_0 [1 - (k_{3z} \omega_0/k_{3x} \omega_{Lk3}) \tan \theta_0]$$
 (20)

The threshold field and the growth rate are derived in a similar way to be

$$|eE_{tb}/m\omega_0| = \sqrt{2\xi} \left[ v_e k_3 / k_{3x} (k_{3x} k_{0x})^{1/2} \right] / \cos\theta_0 \left[ 1 - (k_{3z} \omega_0 / k_{3x} \omega_{Lk3}) \tan\theta_0 \right]$$
 (21)

and

$$\gamma = (v_e/2)\{[2(E_0/E_{th})^2 + 1/4]^{1/2} - 3/2\}$$
 (22)

So far, the threshold conditions of the instability for two cases of independently polarized pumps have been derived. However, the instability process also requires that the frequency and wavevector matching conditions be satisfied. They impose additional instability criteria for obliquely incident pumps.

#### VI. Additional Criteria for the Instability

In order to satisfy the matching conditions (3), the pump's frequency  $\omega_0$  and the incident angle  $\theta_i$  can not be chosen arbitrarily. Their applicable regions are determined in the following.

Using the relations  $\omega + \omega_3^* = \omega_{UH} + \omega_{Lk3}$ , and  $\omega_{UH}^2 = \omega_k^2 + \Omega_e^2 + V_e^2$ ,  $\omega_{Lk3}^2 = \omega_{LH}^2 \xi$ , and  $\omega_0^2 = k_0^2 c^2 = \omega_p^2 + k_0^2 c^2 \cos^2\theta_i$ , (3) leads to

$$\cos^2\theta_i = (\Omega_e^2 + v_e^2 + 2\omega_0\omega_{Lk3})/\omega_0^2(1 + \Omega_e^2\cos^2\theta_0/k_{3x}^2c^2)$$

Thus,  $\theta_i \ge \pi/2 - \sin^{-1}[(\Omega_e^2 + \nu_e^2 + 2\omega_0\omega_{3m})^{1/2}/\omega_0]$  is required, where  $\omega_{3m}$  is the maximum possible value of  $\omega_{Lk3}$ , and  $|k_{3x}c| > \Omega_e \cos\theta_0$  is assumed.

Let  $\omega_{pf}$  be the F-peak plasma frequency, hence, the [lasma frequency at the reflection height of the incident wave,  $\omega_p^2 = k_0^2 c^2 \sin^2 \theta_i$ , has to be less than  $\omega_{pf}^2$ , thus,

$$\sin^2\theta_i \le \omega_{pf}^2/\omega_0^2$$
, or  $\theta_i \le \sin^{-1}(\omega_{pf}/\omega_0)$ .

One then has

$$\pi/2-\sin^{-1}[(\Omega_e^2+v_e^2+2\omega_0\omega_{3m})^{1/2}/\omega_0] \le \sin^{-1}(\omega_{pf}/\omega_0)$$

It leads to the condition

$$\omega_0 \le \omega_{3m} + (\omega_{3m}^2 + \omega_{Um}^2)^{1/2}$$

where  $\omega_{Um} = (\omega_{pf}^2 + \Omega_e^2 + v_e^2)^{1/2}$  is the maximum upper hybrid resonance frequency.

In summary, it is shown that the frequency  $\omega_0$  and the elevation angle  $\theta_i$  of the heater must satisfy these conditions

$$\omega_{0} \leq \omega_{3m} + (\omega_{3m}^{2} + \omega_{Um}^{2})^{1/2}$$

$$\theta_{i} \geq \pi/2 - \sin^{-1}[(\Omega_{e}^{2} + v_{e}^{2} + 2\omega_{0}\omega_{3m}^{2})^{1/2}/\omega_{0}]$$
(23)

So that the necessary frequency and wavevector matching conditions for the parametric coupling process considered in the present work, i.e. pump decays into a lower hybrid decay mode together with an upper hybrid sideband, can be satisfied.

Considering a case that the heater is operated at a frequency  $\omega_0/2\pi=6$  MHz, and an incident angle  $\theta_i=75^\circ$ . In order to satisfy (23), it requires that  $\omega_{3m}/2\pi\cong 110$  KHz and  $\xi\cong240$ , i.e.  $k_{3z}/k_{3x}\sim0.09$ . These are reasonable values for the lower hybrid wave in the ionosphere. Using the parameters  $v_e=130$  sec<sup>-1</sup>,  $k_0=2\pi/50$  m<sup>-1</sup>, and  $\theta_0=60^\circ$ , the threshold field of the instability excited by horizontally polarized heater is calculated from (18) to be

$$E_{th} \sim 10(k_0/k_3)^{1/2} (V/m) \sim 0.7 V/m$$
, for  $k_0/k_3 \sim 5 \times 10^{-3}$  (24)

For vertically polarized heater the threshold field obtained from (21) is given by

$$E_{th}\sim 20(k_0/k_3)^{1/2} (V/m) \sim 1.4 V/m$$
, for  $k_0/k_3 \sim 5\times 10^{-3}$  (25)

## VII. Summary

The condition for parametric excitation of lower hybrid wave together with upper hybrid wave by obliquely incident HF heater in the ionosphere are examined. The source of the upper hybrid sideband of the parametric instability is the induced nonlinear beating current driven by the pump field in the density perturbation of the lower hybrid decay mode. On the other hand, the upper hybrid sideband is also coupled simultaneously with the pump wave in the plasma to generate radiation pressure force and nonlinear beating current oscillating at the frequency of the lower hybrid decay mode. These nonlinear products then become the driving source of the lower hybrid decay mode. When the pump field exceeds a threshold field, the coupling leads to a positive feedback for instability.

It is shown that the elevation angle and the frequency of the heater are related in order to satisfy the necessary frequency and wavevector matching conditions for the considered parametric coupling process. In other words, the elevation angle has to increase with the pump's frequency. For lowest possible operation frequency 6MHz of the existing OTH radars, the elevation angle of the pump has to be larger than 75°. However, the elevation angle can be smaller, if the frequency of the heater considered in the example in the previous section is made lower than 6MHz.

the threshold field of the instability is calculated for both horizontally and vertically polarized pump. In either case, the threshold field (0.7 V/m and 1.4 V/m respectively) is quite high. It may not be exceeded with the output power of the current OTH radar facility. However, it is quite possible to be exceeded by the plasma upgraded facilities such as AOTH and the Arecibo's HF heater.

#### Acknowledgements

This work was performed at the Air Force Geophysics Laboratory, Hanscom, Massachusetts. The hospitality of the Air Force Geophysics Laboratory is appreciated. I also wish to acknowledge frequent and useful discussions with Paul Kossey and John Heakscher of the Air Force Geophysics Laboratory, and M.C.Lee of the Massachusetts Institute of Technology.

This work was supported by the summer faculty research program of the Air Force Office of Scientific Research.

#### References

- 1. Special Issues, "ionospheric Modification by High Power Transmitters." J. Geophys. Res., 75, Nov. 1970, and Radio Science, 9 (11), Nov. 1974.
- 2. Stubbe, P., H. Kopka, "Generations of PC5 Pulsations by Polar Electrojet Modulations: First Experimental Evidence," J. Geophys. Res., 86, 1606, 1981.
- 3. Stubbe, P., H. Kopka and R.L. Dowden, "Generation of ELF and VLF Waves by Polar Electrojet Modulation: Experimental Results," J. Geophys. Res., 86, 9073, 1981.
- 4. Carlson, H.C., V.B. Wickwar and G. Mantas, "Observations of Fluxes of Suprathermal Electrons Accelerated by HF Excited Instabilities," JATP, 44, 1089,1982.
- 5. Thide, E. et al., "Observations of Stimulated Electromagnetic Emmissions in Ionospheric Heating Experiments," Radio Science, 18, 851,1983.
- 6. Showen, R.L. and R.A. Behnke, "The Effect of HF-Induced Plasma Instabilities on Ionospheric Electron Temperatures," J.Geophys. Res. 82, 1839, 1977.
- 7. Showen, R.L. and D.M. Kim, "Time Variations of HF-Induced Plasma Waves," J. Geophys. Res. 83, 623, 1978.

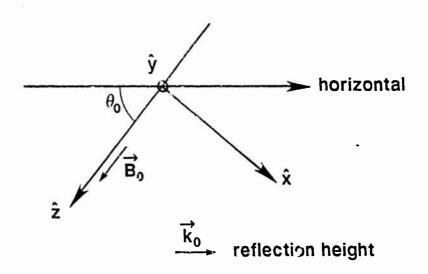
- 8. Djuth, F.T., M.P. Sulzer and J.H.Elder High Resolution Observations of HF-Induced Plasma Waves in the Ionosphere," Geophys. Res. Lett., 17, 1893, 1990.
- 9. Muldrew, D.B., and R.L. Showen, "Height of the HF-Enhanced Plasma Line in Arecibo, J. Geophys. Res. 82, 4783, 1977.
- 10. Isham, B., W. Kofman, T. Hagfors, J. Nordlang, B. Thide, C. LaHoz and P.Stubbe, "New Phenomena Observed by EISCAT During an RF Ionospheric Modification Experiment," Radio Science, 25, 251, 1990
- 11. Kuo, S.P., B.R. Cheo and M.C. Lee, "The Role of Parametric Decay Instabilities in Generating Ionospheric Irregularities," Geophys. Res., 88 (A1), 417, 1983.
- 12. Kuo, S.P. and G. Schmidt, "Filementation Instability in Magneto Plasma," Phys. Fluids, 26, 2529, 1983.
- 13. Kuo, S.P. and M.C. Lee, "Earth Magnetic Field Fluctuations Produced by Filementation Instabilities of Electromagnetic Heater Waves," Geophys. Res. Lett., 10,979,1983.
- 14 Kuo, S.P., M.C. Lee and F.T. Djuth, "A New Interpretation of Plasma-Line Overshoot Phenomena," Geophys. Res. Lett., 14, 961, 1987.
- 15 Kuo, S.P., and F.T. Djuth, "A Thermal Instability For the Spread\_F Echoes from HF-Heated Ionosphere," Geophys. Res. Lett., 15, 1345, 1988.

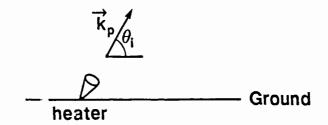
- 16. Kuo, S.P., and M.C. Lee, "Intensity Modulation of HF Heater-Induced Plasma Lines," J. Geophys. Res. 85, 2063, 1990.
- 17. Kuo, S. P., A.Y. Ho, and M.C. Lee, "Temporal Evaluation of HF-Enhanced Plasma Lines Echoes," Geophys. Res. Lett. 17, 2209, 1990.
- 18. Perkins, F.W., C. Oberman and E.J. Valeo, "Parametric Instabilities and Ionospheric Modification," J. Geophys. Res. 79, 1678, 1974.
- 19. Fejer, J.A., "Ionosphere Modification and Plasma Instabilities," Rev. Geophys. Space Phys., 17, 135, 1979.
- 20. Bochkarev, G.S., et at., "Effect of Artificial Perturbations of the Ionosphere on the Propagation of Short-Wave Signals," Radiofizika, 20, 158,1979.
- 21. Bochkarev, G.S., et at., "Interaction of Decametric Radio Waves on Frequencies Close to the MUF of F2 During Oblique Propagation," Geomagnet. Aeron., 19, 557, 1979.
- 22. Bochkarev, G.S., et at., "Nonlinear Interaction of Decametric Radio Waves at Close Frequencies in Oblique Propagation," J.Atmos. Terr. Phys., 44, 1137, 1982.
- 23. Bochkarev, G.S., et at, "Simulation of the Action of a Strong Obliquely Incident Waves," Geophys. Res. Lett., 12, 761,1985.

25. Kuo, S.P. and B.R. Cheo, "Parametric Excitation of Coupled Plasma Waves," Phys. Fluids, 21, 1753, 1978.

# Figure Caption:

Fig.1 Coordinate system and the orientation of the wavevector of the heater wave on the ground and at the reflection height.





RDL Summer Research Report: June-August 1991

Associate Faculty Program: A. S. Marathay, Optical Sciences Center, University of Arizona,

Tucson, Arizona 85721

Focal Point: Dr. R. H. Picard, GL/OPS, Hanscom, AFB, Bedford, MA 01731

1. Introduction

Atmospheric dynamics is a very broad topic of research. There is a lot of activity at Hanscom. The group headed by Dr. Richard H. Picard is involved with multidiscipl...ery areas such as: atmospheric gravity waves, airgiow and auroral phenomena, radiative transfer calculation, to mention a few. I found my involvement with the group highly educational and intellectually stimulating. Of all these projects, I was mainly involved with the radiative transfer calculation.

The radiative transfer equation (RTE) has been used in the study of planetary atmospheres for several decades. It describes what happens to a pencil of radiation travelling in a medium that can absorb and emit radiation. It does so by providing a formula for the space rate of change of specific intensity by appropriate accounting of the absorption (loss) and emission (gain) processes. The loss term contains the absorption coefficient and the specific intensity. The gain mechanism is best described by a generalized source term that includes spontaneous emission and scattering. In any problem of practical interest the RTE is coupled to the rate equations of populations which are governed by collisional processes and photochemical reactions in the atmosphere.

Atmospheric dynamics is complicated by the numerous small and large scale complex processes continually going on in the atmosphere. The chemical species and their interactions, the temperature profile, the atmospheric waves etc., in one form or another affect the radiative energy transfer. The atmospheric waves are mainly of three types: the gravity waves (vertical and transverse to the direction of propagation) acoustic waves (longitudinal to the direction of propagation) and Rossby waves (horizontal and transverse to the direction of propagation). The absorption of incoming and reradiated solar radiation is responsible for a majority of things going on in the atmosphere.

In this report we focus our attention on radiative transfer. In Section 2 the radiative transfer equation is discussed. In Section 2.1 we give some examples from applications. In Section 2.2 a formal solution is given and is applied to plane-parallel atmosphere in Section 2.2.1. Armed with this background material we look at some modifications of the equation of radiative transfer in Section 3.

#### 2. Radiative Transfer

The equation of transfer in its generic form is,

$$\pm \frac{dI_{\nu}}{d\tau_{\nu}} = I_{\nu} - S_{\nu} \tag{1}$$

where  $S_{\nu}$  is the source function,  $\tau_{\nu}$  is the monochromatic optical depth calculated along an outgoing ray.

Following Scharmer (1974) we may distinguish between two limiting cases. In the first  $I_{\nu} \approx S_{\nu}$ , the specific intensity is related to the source function in a local way and the Planck function may be used to describe the source function,  $S_{\nu}$ . In this situation the photon is absorbed almost at the same point it was emitted and each layer in the atmosphere may be treated independent of other layers. The other limiting case is where the specific intensity is related to the source function in a nonlocal way. In this case photons can travel over large distances before getting absorbed and the Planck function is no longer a good representation of the source function.

#### 2.1 Some Examples

For an example of a source function in terms of level populations we turn to Rybicki (1984) and write the radiative transfer equation in the form,

$$\frac{dI^{t}(\nu)}{d\ell} = -\kappa(\nu)I^{t}(\nu) + j(\nu) \tag{2}$$

where for the spectral line between the lower level i and the upper level j we have the line emission coefficient defined by

$$j(\nu) = \frac{h\nu}{4\pi} n_j A_{ji} \varphi_{ji}(\nu) , \qquad (3)$$

and the absorption coefficient defined by

$$\kappa(\nu) = \frac{h\nu}{4\pi} (n_i B_{ij} - n_j B_{ji}) \varphi_{ij}(\nu) \quad . \tag{4}$$

At this stage one makes the reasonable assumption that the absorption and emission lines are the same,  $\varphi_{ji} = \varphi_{ij} = \varphi$ . With this assumption the line source function  $S(\nu)$ ,

$$S(\nu) = \frac{j(\nu)}{\kappa(\nu)} = \frac{n_j A_{ji}}{n_i B_{ij} - n_j B_{ji}}$$
 (5)

becomes independent of frequency. In these definitions the Einstein coefficients are:

 $B_{ij}I(\nu)=$  probability per unit time for the system in the field,  $I(\nu)d\nu$  will absorb a quantum  $h\nu$  and go to the upper level j from the lower level i;

 $A_{ji}$  = probability per unit time that a system in the upper level j will spontaneously go to the lower level i and emit a photon  $h\nu$ ; and

 $B_{ji}I(\nu)$  = probability per unit time that the system will be induced to emit a photon  $h\nu$  by making a transition from j to the lower level i.

Finally the differential element  $d\ell$  in depth is related to the monochromatic optical depth by  $d\tau_{\nu} = -\kappa(\nu)d\ell$ .

As special subexamples we note that the emission coefficient in the case of a scattering atmosphere (but not perfect scattering i.e. albedo,  $\varpi \neq 1$ ) is written as,

$$j_{\nu}^{s}(\theta,\phi) = \frac{\kappa_{\nu}}{4\pi} \int_{0}^{\pi} \int_{0}^{2\pi} p(\theta,\phi;\theta',\phi') I_{\nu}(\theta',\phi') \sin\theta' d\theta' d\phi' \quad . \tag{6}$$

As a second subexample we state an atmosphere in local thermal equilibrium (LTE) for which a local temperature T can be defined. Here, emission equals absorption of radiation, and by Kirchhoff's law we have

$$j_{\nu} = \kappa_{\nu} B_{\nu}(T) = \kappa_{\nu} \frac{2h\nu^3}{c^2} \frac{1}{e^{h\nu/k_BT} - 1}$$
, (7)

where the right-hand side is the Planck function. This ends our special cases that we may refer to later on in this report.

#### 2.2 Formal Solution of the Equation of Radiative Transfer

Consider a simplified version of the radiative transfer equation

$$-\frac{dI}{\kappa o ds} = I - S , \qquad (8)$$

where  $\kappa$  is the absorption coefficient,  $\rho$  is the density, ds is the element of length, I is the specific intensity and S is the source function. We define the optical thickness  $\tau(s,s')$  between points s and s' along the path by

$$\tau(s,s') = \int_{s'}^{s} \kappa \rho(s'') ds'' \qquad . \tag{9}$$

In terms of Eq. (9), a formal solution can be written in the form

$$I(s) = I(0)e^{-\tau(s,0)} + \int_0^s S(s_1)e^{-\tau(s,s_1)} \kappa \rho(s_1) ds_1$$
 (10)

where the value s = 0 is some convenient initial point on the path. For the limiting case of an "optically thin atmosphere,"  $\tau(s,s') < < 1$  which leads to

$$I(s) = I(0) + \int j(s_1) \varrho(s_1) ds_1 . {11}$$

The  $j(s_1)$  in the integrand appears because S is defined by  $S = j/\kappa$ .

#### 2.2.1 Plane parallel atmosphere

A simple but interesting application of the formal solution is found in the plane parallel atmosphere model (Chandrasekhar, 1960). Take the z axis vertical from the ground up. First the length element ds must be expressed in terms of the length element dz by

$$ds = \frac{dz}{\cos\theta} = \frac{dz}{\mu} \quad . \tag{12}$$

Suppose we wish to study the slab bounded between  $z=z_0$  to  $z=z_1>z_0$  (see Fig. 1). Radiation is incident in the -z direction down the z axis onto  $z=z_1$  in the direction  $(-\theta_0,\phi_0)$ . We are interested in finding the sum total "reflected" from the surface,  $z=z_1$ , in the direction  $(+\theta,\phi)$ , and the sum total "transmitted" along (-z) from the surface,  $z=z_0$ , in the direction  $(-\theta,\phi)$ .

In this situation it is more convenient to define the "normal optical thickness,"  $\tau$ , by

$$\tau = \int_{z}^{\infty} \kappa \rho(z') dz' \quad . \tag{13}$$

For propagation in the +z direction from  $z_0$ , with  $0 \le \mu \le 1$ , we have

$$I(\tau,\mu,\phi) = I(\tau_0,\mu,\phi)e^{-\frac{\tau_0-\tau}{\mu}} + \int_{\tau}^{\tau_0} S(\tau'',\mu,\phi)e^{-\frac{\tau''-\tau}{\mu}} \frac{d\tau''}{\mu} , \qquad (14)$$

and for propagation in the -z direction from  $z_1$ , with  $0 \le \mu \le 1$ , we have

$$I(\tau, -\mu, \phi) = I(\tau_1, -\mu, \phi)^{\sigma} \frac{-\frac{\tau_1 - \tau}{\mu}}{\mu} + \int_{\tau_1}^{\tau} S(\tau'', -\mu, \phi) e^{\frac{\tau'' - \tau}{\mu}} \frac{d\tau''}{\mu} . \tag{15}$$

Equations (14) and (15) supply the specific intensity I for the two respective cases, provided we know the value of I on the boundary. Therefore, for the "reflected" case,  $I(\tau_1,\mu,\phi)$  is obtained from Eq.(14) by substituting  $\tau=\tau_1$ , and for the "transmitted" case,  $I(\tau_0,-\mu,\phi)$  is obtained by replacing  $\tau$  of Eq.(15) by  $\tau_0$ .

In next sections some modifications of the radiative transfer equation and the possibility of deriving it from the wave equation are discussed.

#### 3. Energy Transfer in Wave Theory

In this section we discuss ways in which diffraction effects may be important. The possibility of deriving the radiative transfer equation in the wave theoretic frame work will be considered in a later section. The procedure is not straightforward. However, we bring out the approaches made to date toward that goal.

The purpose of this research is to give a wave-theoretic basis to the radiative transfer equation and, on the way, increase the scope of the research and its applicability. The work will indicate conditions under which diffraction effects are important, the properties of radiation and energy in the direction transverse to the direction of propagation and permit us to study spatial, angular and temporal frequency correlations.

#### 3.1 Diffraction Effects

Light waves propagate through free space. They exhibit the phenomenon of diffraction with every obstacle they encounter. Consider light of wavelength  $\lambda$  diffracted from a circular aperture of diameter d in an otherwise opaque screen. For an observing screen at some distance L from the aperture we have two main types of diffraction: when  $L < < d^2/\lambda$  Fresnel and for  $L > > d^2/\lambda$ , Fraunhofer diffraction.

Fresnel diffraction is characterized by numerous edge fringes but shows almost no spreading of the beam. Frounhofer diffraction exhibits a characteristic angular spread,  $\lambda/d$ . The diffraction pattern is characteristic of the entire object and as the distance of the observing screen is increased from the diffracting object, the pattern increases in size according to the angular spread given above.

For small particles [diameter d on the order of a wavelength] such as aerosols the angular spread can be large. For a random distribution of aerosols in a region of the atmosphere the diffraction from

each is noncoherently added to the contribution of others, unless of course there is some mechanism that causes phase correlation.

A different aspect of diffraction can be seen for example in airglow where a relatively thin layer of the atmosphere is involved. Here diffraction is important at distances large compared to the square of the thickness of the layer divided by the wavelength. If the wavelength considered is on the order of  $[10^{-3}\text{cm}]$  and the satellite making measurements is about  $L = [10^{+8}\text{cm}]$  then diffraction effects will be important for layer thickness larger than 3 meters.

It will be interesting to see how these considerations compare with the findings from a properly formulated wave-theoretic radiative transfer equation.

#### 3.2 Intensity Correlations

Before going into the wave formulation we can look for intensity correlations as derived from the existing radiative transfer equation. For the purposes of this discussion, let us consider the optically thin case and the equation for the return beam case

$$I(z,\mu,\phi) = I(z_L,\mu,\phi) + \int_z^{z_L} j(z'',\mu,\phi) \frac{dz''}{\mu}$$
 (16)

We have changed the variable  $\tau$  to z which is more suitable for the optically thin case. The subscript 0 corresponds to the z value of the lower most boundary of the slab and the z variable corresponds to any layer of the slab, see Fig. 1. Before proceeding we list some definitions of correlation functions by using the ensemble average:

$$R_{II}(z_{1},\mu_{1},\phi_{1};z_{2},\mu_{2},\phi_{2}) = \mathcal{E}\{I(z_{1},\mu_{1},\phi_{1})I(z_{2},\mu_{2},\phi_{2})\}$$

$$R_{Ij}(z_{1},\mu_{1},\phi_{1};z_{2},\mu_{2},\phi_{2}) = \mathcal{E}\{I(z_{1},\mu_{1},\phi_{1})j(z_{2},\mu_{2},\phi_{2})\}$$

$$R_{II}(z_{1},\mu_{1},\phi_{1};z_{2},\mu_{2},\phi_{2}) = \mathcal{E}\{j(z_{1},\mu_{1},\phi_{1})j(z_{2},\mu_{2},\phi_{2})\}$$
(17)

With these definitions we go back to Eq.(16) and use subscripts 1 and 2 to refer to separate layers. Multiply the equation with itself, and take ensemble average, to get

$$R_{II}(z_{1},\mu_{1},\phi_{1};z_{2},\mu_{2},\phi_{2}) = R_{II}(z_{01},\mu_{1},\phi_{1};z_{02},\mu_{2},\phi_{2})$$

$$+ \int_{z_{02}}^{z_{2}} \frac{dz_{2}'}{\mu_{2}} R_{IJ}(z_{01},\mu_{1},\phi_{1};z_{2}',\mu_{2},\phi_{2})$$

$$+ \int_{z_{01}}^{z_{1}} \frac{dz_{1}'}{\mu_{1}} R_{JI}(z_{1}',\mu_{1},\phi_{1};z_{02},\mu_{2},\phi_{2})$$

$$+ \int_{z_{01}}^{z_{1}} \frac{dz_{1}'}{\mu_{1}} \int_{z_{02}}^{z_{2}} \frac{dz_{2}'}{\mu_{2}} R_{JJ}(z_{1}',\mu_{1},\phi_{1};z_{2}',\mu_{2},\phi_{2})$$

$$(18)$$

This equation provides a relationship between mixed correlation functions of two layers labelled  $z_1$  and  $z_2$ , in terms of the correlation function of two initial layers labelled  $z_{01}$  and  $z_{02}$ . However, going back to Eq.(16) and multiplying it with the source function, j, with ensemble averaging leads to

$$R_{lj}(z_{3},\mu_{3},\phi_{3};z_{4}',\mu_{4},\phi_{4}) = R_{lj}(z_{03},\mu_{3},\phi_{3};z_{4}',\mu_{4},\phi_{4})$$

$$+ \int_{z_{03}}^{z_{3}} \frac{dz_{3}'}{\mu_{3}} R_{jj}(z_{3}',\mu_{3},\phi_{3};z_{4}',\mu_{4},\phi_{4})$$
(19)

It connects the cross correlation with the source autocorrelation which can be used in Eq. (18) to eliminate the cross terms

$$R_{II}(z_{1},\mu_{1},\phi_{1};z_{2},\mu_{2},\phi_{2}) = -R_{II}(z_{01},\mu_{1},\phi_{1};z_{02},\mu_{2},\phi_{2})$$

$$+ R_{II}(z_{01},\mu_{1},\phi_{1};z_{2},\mu_{2},\phi_{2})$$

$$+ R_{II}(z_{1},\mu_{1},\phi_{1};z_{02},\mu_{2},\phi_{2})$$

$$+ \int_{z_{01}}^{z_{1}} \frac{dz_{1}'}{\mu_{1}} \int_{z_{02}}^{z_{2}} \frac{dz_{2}'}{\mu_{2}} R_{IJ}(z_{1}',\mu_{1},\phi_{1};z_{2}',\mu_{2},\phi_{2})$$

$$(20)$$

On the other hand if we form a difference function

$$i(z,\mu,\phi) = I(z,\mu,\phi) - I(z_0,\mu,\phi) , \qquad (21)$$

between the specific intensity at level z from that at level z<sub>0</sub> then,

$$R_{ii}(z_1,\mu_1,\phi_1;z_2,\mu_2,\phi_2) = + \int_{z_{01}}^{z_1} \frac{dz_1'}{\mu_1} \int_{z_{02}}^{z_2} \frac{dz_2'}{\mu_2} R_{jj}(z_1',\mu_1,\phi_1;z_2',\mu_2,\phi_2) . \tag{22}$$

These relationships, and Eq. (16), indicate that specific intensities correlated between different levels contain no angular correlations! It appears to be a basic property of the radiative transfer equation, that the angle variables involved are not directly operated on as the pencil of rays proceeds from one point

to the next in the field. It is perhaps related to the rectilinear propagation of light rays. This is unlike wave optics, wherein the amplitude at a point in the field is determined by the amplitude at all points of the earlier Huygens wave. In the next section we begin with the wave equation approach.

#### 3.3 Scalar Waves

Light waves are transverse and not scalar. However, using a scalar wave amplitude is a convenient artifice, for it brings out the essential properties without the added complication of dealing with vectors. The vector approach will be discussed in Section 3.3.2. To grasp the picture one may identify the scalar with one of the components of the vector field when the other two are absent.

The scalar wave amplitude.  $\psi$ , obeys the wave equation

$$\nabla^2 \psi - \frac{1}{c^2} \frac{\partial^2 \psi}{\partial t^2} = 0 \quad . \tag{23}$$

Its Fourier decomposition,

$$\psi(\mathbf{r},t) = \int_0^\infty \hat{\psi}(\mathbf{r},\nu)e^{-i2\pi\nu t}d\nu \tag{24}$$

leads to the Helmholtz equation for the Fourier amplitude,

$$\nabla^2 \hat{\psi} + k^2 \hat{\psi} = 0 \tag{25}$$

where  $k=2\pi\nu/c$ . Anticipating comparison with radiative transfer we cast the formulation in the parabolic approximation valid for relatively small angles off the forward direction. In this approximation the Fourier amplitude is assumed to have the form

$$\hat{\varphi}(\mathbf{r},\nu) = \varrho(\mathbf{r}_{\mathbf{T}},z,\nu)e^{ikz}$$
 (26)

where  $\hat{\mathbf{u}}$  is a slowly varying function of z,  $\mathbf{r}_T$  is a (2d) vector transverse to the assumed direction of propagation z. With this form the Helmholtz equation can be approximated to,

$$\nabla_T^2 \hat{u} + i2k \frac{\partial \hat{u}}{\partial z} = 0 \quad , \tag{27}$$

where the condition

$$|\partial a/\partial z| \ll 2k|a| \tag{28}$$

for the slowly varying envelope û was used. In the above work the Laplacian was expressed as a transverse part separate from the z part:

$$\nabla^2 = \nabla_T^2 + \frac{\partial^2}{\partial \tau^2} \quad . \tag{29}$$

Equation (27) is the parabolic approximation for the Helmholtz equation. It describes the wave but does not include the effects of absorption (loss) and/or sources (gain). These effects may be included phenomenologically by making k complex to include absorption and adding a source term to the right-hand side as done in

$$\nabla_T^2 \hat{a} + 2(ik - \alpha) \frac{\partial \hat{a}}{\partial z} = -\hat{Q} \quad . \tag{30}$$

We momentarily leave the wave amplitude to define the mutual coherence function. This function is defined as the cross correlation of the fields at two space-time points:

$$\Gamma(\mathbf{r}_1, \mathbf{r}_2, \tau) = \mathcal{E}\{\psi(\mathbf{r}_1, t+\tau)\psi * (\mathbf{r}_2, t)\} \quad . \tag{31}$$

It is a function of two space points and is a function of the time delay  $\tau$ . Its temporal Fourier transform defines the mutual spectral density function or also called cross spectral density,

$$\hat{\Gamma}(\mathbf{r}_1, \mathbf{r}_2, \nu) = \mathcal{E}\{\hat{\psi}(\mathbf{r}_1, \nu)\hat{\psi} * (\mathbf{r}_2, \nu)\} . \tag{32}$$

It is this function that has the dual properties, namely, it propagates like a Huygens wave and as we shall see it is related to the spectral radiance of radiometry. The equation obeyed by this function can be derived by using the parabolic equation of the wave amplitude given in Eq. (27). To briefly describe the derivation, we use the short-hand notation

$$\begin{aligned}
\hat{a}_1 &= \hat{u}(\mathbf{r}_{T1}, z, \nu) \\
\hat{a}_2 &= \hat{u}(\mathbf{r}_{T2}, z, \nu) \\
\hat{\Gamma}_{12} &= \hat{\Gamma}(\mathbf{r}_{T1}, \mathbf{r}_{T2}, z, \nu) &= \mathcal{E}\{\hat{a}_1 \hat{a}_2 *\} \\
\hat{Q}_1 &= \hat{Q}(\mathbf{r}_{T1}, z, \nu) \\
\hat{Q}_2 &= \hat{Q}(\mathbf{r}_{T2}, z, \nu)
\end{aligned} (33)$$

The governing equation of û may be written in the form

$$\nabla_{TI}^2 \hat{u}_1 + 2(ik - \alpha) \frac{\partial \hat{u}_1}{\partial z} = -\hat{Q}_1 \quad . \tag{34}$$

Multiply this equation from the right by  $\hat{u}_2^*$ . A similar equation can be written for  $\hat{u}_2^*$  which can be multiplied from the left by  $\hat{u}_1$ . Observe that the differential operators with their appropriate subscripts operate on only one of the functions  $\hat{u}$ . The next step is to add these two equations and take the ensemble average; the result is

$$(k_{\alpha}^{*} \nabla_{TI}^{2} + k_{\alpha} \nabla_{T2}^{2}) \hat{\Gamma}_{12} + 2|k_{\alpha}|^{2} \frac{\partial \hat{\Gamma}_{12}}{\partial z} = -k_{\alpha}^{*} \hat{S}_{12} - k_{\alpha} \hat{S}_{21}^{*} . \tag{35}$$

In this equation the following relations have been used:

$$k_{\alpha} \equiv ik - \alpha$$

$$|k_{\alpha}|^{2} \equiv k_{\alpha}^{2} + \alpha^{2}$$

$$\frac{\partial \hat{\Gamma}_{12}}{\partial z} = \mathcal{E}\left\{\frac{\partial a_{1}}{\partial z}a_{2}^{*} + a_{1}\frac{\partial a_{2}^{*}}{\partial z}\right\}$$

$$S_{12} \equiv \mathcal{E}\left\{\hat{Q}_{1}a_{2}^{*}\right\}$$
(36)

Although not the answer we are looking for, this equation is important. It is the parabolic equation for  $\hat{\Gamma}$ , it has the first partial on z and includes the transverse behavior of the field. Now  $\hat{\Gamma}$  can be used to make contact with the radiometric quantity called spectral radiance. Equation for  $\hat{\Gamma}$  in (35) is used to derive the corresponding equation for the spectral radiance, which is the one of interest to us to compare with radiative transfer. This project is the subject of Section 3.3.1.

#### 3.3.1 Scalar version of the equation of spectral radiance:

In the wave-theoretic framework, the definition of spectral radiance,  $B_{\omega}$ , as proposed by Walther (1968) may be written as

$$B_{\omega}(\mathbf{r_a}, \hat{s}_a) = 2c^3k^2m_a \int \hat{\Gamma}(\mathbf{r_{Ta}} + \frac{1}{2}\mathbf{r_{Td}}, \mathbf{r_{Ta}} - \frac{1}{2}\mathbf{r_{Td}}, z, \nu)\exp(-i2\pi\kappa s_{Ta} \cdot \mathbf{r_{Td}})d^{(2)}\mathbf{r_{Td}} . \tag{37}$$

The various symbols used above are defined as follows:

$$\mathbf{r} = \hat{i}x + \hat{j}y + kz, \quad \mathbf{r_{T}} = \hat{i}x + \hat{j}y,$$

$$\hat{s} = \hat{i}p + \hat{j}q + \hat{k}m, \quad \overrightarrow{s_{T}} = \hat{i}p + \hat{j}q,$$

$$\hat{s} \cdot \hat{s} = p^{2} + q^{2} + m^{2} = 1,$$

$$\mathbf{r_{Ta}} = \frac{1}{2}(\mathbf{r_{T1}} + \mathbf{r_{T2}}), \quad \mathbf{r_{Td}} = \mathbf{r_{T1}} - \mathbf{r_{T2}}$$

$$\mathbf{s_{Ta}} = \frac{1}{2}(\mathbf{s_{T1}} + \mathbf{s_{T2}}), \quad \mathbf{s_{Td}} = \mathbf{s_{T1}} - \mathbf{s_{T2}}$$
(38)

It defines  $B_{\omega}$  proportional to a partial Fourier transform on  $\hat{\Gamma}$  which makes it a mixed function of the space variable  $\mathbf{r_a}$  and the angle variables through the unit vector  $\hat{\mathbf{s}_a}$ . The unit vector is defined in terms of the direction cosines p,q, and m. However, recall that  $\Gamma^{\wedge}$  is a function of two space variables:  $\mathbf{r_{T1}}$  and  $\mathbf{r_{T2}}$ . These are replaced by their average  $\mathbf{r_{Ta}}$  and difference  $\mathbf{r_{Td}}$  variables as given in Eq.(38). Likewise, the direction cosine variables are replaced by their average and difference variables:  $\mathbf{s_{Ta}}$  and  $\mathbf{s_{Td}}$ . Observe that the arguments of the mixed function are not Fourier conjugate variables. The pairs (shown in square brackets:[]) of Fourier conjugate variables are as follows:

Fourier conjugate variable pairs:

$$[x_{1}, \kappa p_{1}]; [y_{1}, \kappa q_{1}]; \quad \kappa = \frac{1}{\lambda}$$

$$[\mathbf{r}_{Ti}, \kappa \mathbf{s}_{Ti}], \quad i=1,2 \qquad . \tag{39}$$

$$[\mathbf{r}_{Ta}, \kappa \mathbf{s}_{Td}]$$

$$[\mathbf{r}_{Td}, \kappa \mathbf{s}_{Ta}]$$

In Eq. (37) c is the speed of light,  $k = 1/\lambda$  is the propagation constant and  $m_a$  is the average:  $m_a = \frac{1}{2}(m_1 + m_2)$ . The superscript (2) on the differential is a reminder that the integration is in two dimensions.

Equation (37) is our bridge from wave theory to radiometry. Since we know the differential equation that governs  $\Gamma^{\wedge}$ , we are in a position to obtain one for  $B_{\omega}$ . The procedure although straight forward, is very labor intensive. To outline the procedure we begin with the conversion of Eq. (35) from variables  $\mathbf{r}_1$  and  $\mathbf{r}_2$  to the average and difference variables. Equation (37) is then inverted to express  $\Gamma^{\wedge}$  in terms of the spectral radiance  $B_{\omega}$ . The differentials on the difference variables are carried out. The equation fulfilled by  $B_{\omega}$  is then found to be,

$$\frac{\partial B_{\omega}}{\partial z} + \frac{k^2}{k^2 + \alpha^2} (\overline{s_T} \bullet \overline{\nabla}_T) B_{\omega}$$

$$= -\frac{\alpha}{k^2 + \alpha^2} [ \frac{1}{4} \nabla_T^2 B_{\omega} - k^2 (s_T \cdot s_T) B_{\omega} + k^2 c^3 m (\overline{S}_{QU} + \overline{S}_{UQ}^{\bullet}) ]$$

$$- \frac{i k^3 c^3 m}{k^2 + \alpha^2} (\overline{S}_{QU} - \overline{S}_{UQ}^{\bullet})$$
(40)

where for this equation we have defined

$$\overline{\nabla}_{T} = \hat{i} \frac{\partial}{\partial x} + \hat{j} \frac{\partial}{\partial y}$$

$$\overline{S}_{QU}(\mathbf{r}_{T}, \kappa \mathbf{s}_{T}, z, \nu) = \int d^{(2)} \mathbf{r}_{Td} \mathcal{E} \{ \hat{Q}(\mathbf{r}_{T} + \frac{1}{2} \mathbf{r}_{Td}, z, \nu) \hat{U} \cdot (\mathbf{r}_{T} - \frac{1}{2} \mathbf{r}_{Td}, z, \nu) \}$$

$$\exp(-i2\pi \kappa \mathbf{s}_{T} \cdot \mathbf{r}_{Td})$$

$$\overline{S}_{UQ}(\mathbf{r}_{T}, \kappa \mathbf{s}_{T}, z, \nu) = \int d^{(2)} \mathbf{r}_{Td} \mathcal{E} \{ \hat{U}(\mathbf{r}_{T} + \frac{1}{2} \mathbf{r}_{Td}, z, \nu) \hat{Q} \cdot (\mathbf{r}_{T} - \frac{1}{2} \mathbf{r}_{Td}, z, \nu) \}$$

$$\exp(+i2\pi \kappa \mathbf{s}_{T} \cdot \mathbf{r}_{Td})$$

$$\exp(+i2\pi \kappa \mathbf{s}_{T} \cdot \mathbf{r}_{Td})$$
(41)

In Eq. (40) the extra subscript (a) used in describing the average variable has been dropped, since it has no purpose here. The first term on the right-hand side of Eq. (40) vanishes if there is no absorption,  $\alpha$  = 0; while the second term is absent if there is no source. Thus the equation of propagation of the spectral radiance,  $B_{\omega}$ , in free space is

$$\frac{\partial B_{\omega}(\mathbf{r},\hat{s})}{\partial z} + (\mathbf{s}_{\mathsf{T}} \bullet \overrightarrow{\nabla}_{T}) B_{\omega} = 0 \quad . \tag{42}$$

It contains the effect of the transverse behavior of the field.

Recall that the absorption and the source terms were introduced into the theory phenomenologically. Although we have an equation for spectral radiance, it contains terms that involve cross correlations of the source and field, namely the "S" terms. This is an undesirable feature, since these are both difficult to specify and to measure. Next we observe that if the source and field are statistically independent, then the cross correlation term factors into the mean value of the source times the mean value of the field. But the mean value of the field is zero, and hence the source contribution vanishes from the right-hand side.

Some more work is needed to look for different forms of the radiance equation. Instead of proceeding further on these lines, we turn our attention to the vector aspects of the problem in the next section.

### 3.3.2 Vector analog of the scalar version of Eq. (35) for $\hat{\Gamma}_{12}$

In this section we start with the wave equation as derived from Maxwell's equations

$$\nabla^2 \mathbf{E} - \overline{\nabla} (\overline{\nabla} \bullet \mathbf{E}) - \mu_0 \epsilon_0 \frac{\partial^2 \mathbf{E}}{\partial t^2} = \mu_0 \frac{\partial^2 \mathbf{P}}{\partial t^2} . \tag{43}$$

The second partial on time of polarization, **P** (dipole moment per unit volume) plays the role of a "source" term. The absorption enters the calculation with a complex propagation constant, k. This equation is derived from first principles and it is of interest to see how it develops in the desired radiative energy-transfer relationship. The necessary modifications to make it suitable for atmospheric problems can be studied later. Here we have a possibility of developing a full vector theory.

We summarize the approach and the procedure of calculation followed to date. The middle term on the left-hand side indicates that the E field in the medium is not transverse, it has a longitudinal component. Assume that the fields have the Fourier decomposition,

$$\mathbf{E}(\mathbf{r},t) = \int \mathbf{E}(\mathbf{r},\nu) \exp(-i2\pi\nu t) d\nu$$

$$\mathbf{P}(\mathbf{r},t) = \int \mathbf{P}(\mathbf{r},\nu) \exp(-i2\pi\nu t) d\nu$$
(44)

We further assume that the direction of propagation is in the z direction and that the Fourier-component fields have a slowly varying envelope function in z with the form

$$\mathbf{E}(\mathbf{r},\nu) = \mathcal{E}(\mathbf{r},\nu)e^{ikz} = (\hat{e}_{T}\mathcal{E}_{T} + \hat{e}_{z}\mathcal{E}_{z})e^{ikz}$$

$$\mathbf{P}(\mathbf{r},\nu) = \mathcal{O}(\mathbf{r},\nu)e^{ikz} = (\hat{e}_{T}\mathcal{O}_{T} + \hat{e}_{z}\mathcal{O}_{z})e^{ikz}$$

$$\hat{e}_{T}\mathcal{E}_{T} = \hat{i}\mathcal{E}_{x} + \hat{j}\mathcal{E}_{y}$$

$$\hat{e}_{T}\hat{\mathcal{O}}_{T} = \hat{i}\mathcal{O}_{x} + \hat{j}\mathcal{O}_{y}$$

$$(45)$$

We can shorten the notation by setting

$$\mathcal{E}_{1i} \equiv \mathcal{E}_{i}(x_{1}, y_{1}, z, \nu),$$

$$\mathcal{O}_{1i} \equiv \mathcal{O}_{i}(x_{1}, y_{1}, z, \nu), \qquad (46)$$
where,  $i=x,y,z$ 

As before we make the parabolic approximation to yield the following set of equations:

$$\left[i2k\frac{\partial}{\partial z} + \frac{\partial^{2}}{\partial y_{1}^{2}}\right] \mathcal{E}_{1x} - \frac{\partial^{2}}{\partial x_{1}\partial y_{1}} \mathcal{E}_{1y} - \frac{\partial}{\partial x_{1}} \left[ik + \frac{\partial}{\partial z}\right] \mathcal{E}_{1z} = -\mu_{0}\omega^{2} \mathcal{O}_{1x} 
- \frac{\partial^{2}}{\partial x_{1}\partial y_{1}} \mathcal{E}_{1x} + \left[i2k\frac{\partial}{\partial z} + \frac{\partial^{2}}{\partial x_{1}^{2}}\right] \mathcal{E}_{1y} - \frac{\partial}{\partial y_{1}} \left[ik + \frac{\partial}{\partial z}\right] \mathcal{E}_{1z} = -\mu_{0}\omega^{2} \mathcal{O}_{1y} 
- \frac{\partial}{\partial x_{1}} \left[ik + \frac{\partial}{\partial z}\right] \mathcal{E}_{1x} - \frac{\partial}{\partial y_{1}} \left[ik + \frac{\partial}{\partial z}\right] \mathcal{E}_{1y} + \left[\frac{\partial^{2}}{\partial x_{1}^{2}} + \frac{\partial^{2}}{\partial y_{1}^{2}} + k^{2}\right] \mathcal{E}_{1z} = -\mu_{0}\omega^{2} \mathcal{O}_{1z}$$

$$(47)$$

The operator operating on the vector with components  $\mathcal{E}_{1x}$ ,  $\mathcal{E}_{1y}$  and  $\mathcal{E}_{1z}$  is symmetric about the main diagonal.

Without going through the details, following the procedure used in deriving Eq. (35) of Section 3.3 we obtain the equations for the cross correlations of the fields at two space points  $x_1$ ,  $y_1$ , z and  $x_2$ ,  $y_2$ , z:  $\Gamma_{ij}^{(12)}$ , where i,j = x,y,z for the three polarization components of the field. We show, for example, the equation of  $\Gamma_{xx}^{(12)}$ ,

$$2|k|^{2} \frac{\partial}{\partial z} \hat{\Gamma}_{xx}^{12} + \left[ ik \frac{\partial^{2}}{\partial y_{2}^{2}} - ik * \frac{\partial^{2}}{\partial y_{1}^{2}} \right] \hat{\Gamma}_{xx}^{12}$$

$$+ \left[ -ik \frac{\partial^{2}}{\partial x_{2} \partial y_{2}} \hat{\Gamma}_{xy}^{12} + ik * \frac{\partial^{2}}{\partial x_{1} \partial y_{1}} \hat{\Gamma}_{yx}^{12} \right] - ik \frac{\partial}{\partial x_{2}} \left[ \frac{\partial}{\partial z} - ik * \right] \hat{\Gamma}_{xz}^{12} + ik * \frac{\partial}{\partial x_{1}} \left[ \frac{\partial}{\partial z} + ik \right] \hat{\Gamma}_{zx}^{12}$$

$$= -\frac{|k|^{2}}{\epsilon_{0}} \left[ ik * E\{\mathcal{E}_{1x}\mathcal{O}_{2x}^{*}\} - ikE\{\mathcal{O}_{1x}\mathcal{E}_{2x}^{*}\} \right]$$

$$(48)$$

If only the x component of polarization is nonzero, we get the simpler relation,

$$2|k|^{2} \frac{\partial}{\partial z} \hat{\Gamma}_{xx}^{12} + \left[ ik \frac{\partial^{2}}{\partial y_{2}^{2}} - ik * \frac{\partial^{2}}{\partial y_{1}^{2}} \right] \hat{\Gamma}_{xx}^{12}$$

$$= -\frac{|k|^{2}}{\epsilon_{0}} [ik * E\{\mathscr{E}_{1x}\mathcal{O}_{2x}^{*}\} - ikE\{\mathcal{O}_{1x}\mathscr{E}_{2x}^{*}\}]$$

$$(49)$$

#### References

- Beer, Tom. (1974). Atmospheric Waves, Wiley, New York.
- Chandrasekhar, S. (1960). Radiative Transfer, Dover, New York, New York.
- Goody, R. M. and Y. L. Yung, (1989). Atmospheric Radiation: Theoretical Basis, Oxford University Press, Oxford, United Kingdom.
- Houghton, J. T. (1977). The Physics of Atmospheres, Cambridge University Press, Cambridge, United Kingdom.
- Kelley, M. C. and R. A. Heelis, (1989). The Earth's Ionosphere, Academic, New York, New York.
- Marathay, A. S. (1982). Elements of Optical Coherence Theory, Wiley, New York, New York.
- Panofsky, W. K. H. and M. Phillips, (1956). Classical Electricity and Magnetism, Addison-Wesley, Reading, Massachusetts
- Rybicki, G. B. (1984). "Escape probability methods," in *Methods in Radiative Transfer*, ed. Kalkofen, W. Cambridge University Press, Cambridge, United Kingdom.
- Scharmer, (1984). "Accurate solutions to the non-LTE problems using approximate lambda operators," in *Methods in Radiative Transfer*, ed. Kalkofen, W. Cambridge University Press, Cambridge, UK.
- Walther, A. (1968). "Radiometry and coherence," J. Opt. Soc. Am. 58, (9):1256-1259.

# PRELIMINARY ANALYSIS OF THE WESTERN NORILSK - LAKE BAIKAL DEEP SEISMIC SOUNDING PROFILE

Keith F. Priestley, Seismological Laboratory, University of Nevada,
Reno, Nevada 89557

John Cipar, Phillips Laboratory, Hanscom AFB, Ma 01731

A.V Egorkin, N.I. Pavlenkova, and V. Martynov, Soviet Academy of Sciences

Moscow, U.S.S.R.

#### INTRODUCTION

At the present there is a great deal of interest in the velocity structure of the upper mantle. Many of the important, unresolved questions concerning upper mantle dynamics will only be answered when a more detailed picture of the upper mantle velocity structure and its lateral variations is attained. For example, some studies (Lerner-Lam and Jordan, 1987) indicate that the structure of the continents extends to upper mantle depths ( $\sim 400 \text{ km}$ ) suggesting that the continental lithosphere does not passively drift on the low-velocity asthenosphere. Variations in upper mantle velocity structure also have important implications in a nuclear discrimination/verification context. Regional seismic phases will play a major role in monitoring any future Comprehensive Test Ban Treaty (CTBT) or Low Yield Threshold Test Ban Treaty (LYTTBT). Regional waveforms are more complicated than teleseismic waveforms and can vary greatly between different geologic provinces. Before source contributions (e.g., spall, tectonic release, etc.) to P-wave complexity can be understood, seismic waveform complexities arising from propagation effects must be explained. A knowledge of the seismic velocity and attenuation structure is critical to comprehending regional seismic wave propagation characteristics. For example,  $P_n$  amplitude behavior as a function of range is strongly influenced by both upper mantle attenuation and by the sub-Moho velocity gradient (Hill, 1971; 1973). The  $P_n$  frequency content is also affected by the upper mantle lid thickness (Mellman and Helmberger, 1974). In the stable regions of the Soviet Union where the upper mantle attenuation might be expected to be low, the velocity structure may well be the dominant influence on  $P_n$  and  $S_n$  propagation. Variations in the lithospheric velocity structure may cause significant variations in the mode of  $P_n$ ,  $P_g$  and  $L_g$  propagation resulting in major differences in the  $P_n/P_g$  or  $P_n/L_g$  amplitude behavior within the various geological provinces. Thus a seismic discriminant developed in one geologic province may not necessarily be transportable to another geologic province.

During the past 30 years the Soviet Ministry of Geology has conducted an extensive seismic exploration program of the Eurasian crust and upper mantle. Several of these lines use nuclear explosions as seismic sources for recording at large offsets (up to 3000 km) and conventional explosives for shorter offsets. Scheimer and Borg (1984) reviewed the Soviet nuclear DSS program. The energetic sources used on several DSS profiles have permitted recording of significantly longer profiles than typically recorded in U.S. refraction experiments. This has permitted interpretation of velocity structure (from refraction) to upper mantle depths (150-200 km) and of velocity contrasts (from reflections) at much deeper depths. The Soviet analysis of the data has been performed using a method analogous to forward raytracing methods. Yegorkin et al, (1977) describe a forward modelling procedure by which travel times are computed for successively deeper penetrating rays and the theoretical travel times for a proposed structure are compared with the observed travel time until they fit to within prescribed error limits (about 0.3-0.5 sec). Soviet seismologists consider wave amplitudes only by comparing observed seismic amplitudes with the density of computed rays. Results for only a few of these profiles are discussed in the western literature (Yegorkin and Pavlenkova, 1981; Pavlenkova and Yergorkin, 1983; Egorkin et al, 1984).

During the 1991 summer, we began a more comprehensive study of the Western Norilsk - Lake Baikal deep seismic sounding profile (Fig. 1.). The purpose of our investigation is to improve our understanding of the Eurasian crust and up-

per mantle velocity structure. A better comprehension of these factors in these areas will help in evaluating the significant factors controlling the propagation of regional seismic phases; in "calibrating" the IRIS seismographs and the Scandinavian arrays in terms of the seismic wavefield resulting from Kazakh Test Site (KTS) explosions; and in assessing the efficiency of high frequency propagation, and its use in elucidating source characteristics of Central Asian seismic events. An improved understanding of the propagating characteristics of regional seismic phases will facilitate interpretation of source characteristics from regional seismograms.

#### DATA ANALYSIS

In spring 1991 we obtained a copy of data for a 2400 km long seismic profile recorded in 1982 which extends across the Siberian Platform from Norilsk to Lake Baikal (Fig. 1). Data from two shot points are being studied. The first shot point is in western Norilsk within the West Siberian rift on the northwest edge of the Siberian Platform. This failed rift developed in Triassic time (235-215 my) during the initial breakup of Pangea. Following the extinction of extension, the rift was buried beneath approximately 15 km of sediment. Geochemical analysis of the basalts within the rift indicate they have a chemical composition similar to ocean tholeites. This profile extends southeast across the Tunguss Basin, a region of Late Paleozoic extension and widespread intraplate flood basalts  $(1.2 \times 10^6 km^3)$ in 10 Ma), to the presently active Baikal rift. The second shot point is in western Tura within the Tunguss Basin, approximately 700 km southeast of the first shot point. Data from this shot extends 560 km northwest reversing a section of the profile from the first shot point and 1700 km southeast across the Baikal rift. Data for these profiles were obtained in the form of large paper copies (25 mm/sec X 2.5 mm/km) with station locations accurate to 0.1 km. The traces were commercially digitized and corrected for amplitude scaling to produce a true amplitude record section.

Arrival times of first and prominent later arrivals have been measured. Much of the summer was spent in digitizing and preparing the data for analysis.

A portion of the data from the distance range 1600 - 2000 km is shown in record section format in Figures 2a and 2b. The first arrival travels through the lithospheric lid while the prominent second arrival is a reflection from the 670 km discontinuity. The lower figure is a blowup of the upper record section illustrating the structure in the wavefield in the 1700 - 1800 km distance range. First arrival times were read from the digitized seismograms for the West Norilsk shot point (DSS Shot Point 245) and are shown in Figures 3 and 4. The data are compared to two published models for the Eurasian upper mantle. Model K8 was derived using long-period seismograms of Soviet nuclear explosions recorded in Europe (Fig. 3) while Section I of Egorkin et al (1984) was inferred from DSS profiles in central Siberia (Fig. 4). Models K\* and EZC01 have similar structures below 400 km depth. In general, the agreement between K8 and the observed data is fair. Model EZC01 is in good agreement with the data in the 1500 - 2400 km range, but is distinctly poorer than K8 at closer ranges. There appears to be no evidence for the alternating high and low velocities in the EZC01 model between 100 and 250 km depth. The data suggest that the low velocity zone is weak or absent in central Siberia. Further discussion of each model is given in the figure caption.

Results of the summer research will be reported at the 1991 Fall meeting of the American Geophysical Union in San Francisco, California. In addition, we are preparing a manuscript for submission to the journal Geophysical Research Letters.

#### CONTINUING RESEARCH PLANS

Modelling of this important data set has just begun. We are assembling information on the variations in geology and crustal structure along the profile to correct the travel times for receiver structure beneath each recording site. This will allow us to better isolate upper mantle travel time information. Once the travel times are corrected for local structure, the  $\tau(p)$  bounds from the travel time data will be inverted for extremal velocity bounds using the computer code developed by Stark et al (1988). Once we have established realistic bounds on the velocity-depth function, we intend to forward model the waveforms using the reflectivity method.

This will allow us to constrain specific velocity-depth models within the range of the extremal velocity depth bounds.

#### REFERENCES

Egorkin (Yegrokin), A. V., S. K. Ziuganov, and N. M. Chernyshev (1984), The upper mantle of Siberia, *Proceeding of the 27th International Geological Congress*, 8, 29-56.

Given, J. W. and D. V. Helmberger (1980), Upper mantle structure of Northwestern Eurasia, J. Geophys. Res., 85, 7183-7194.

Hill, D. P. (1971), Velocity gradients and anelasticity from crustal body wave amplitudes, J. Geophys. Res., 76, 3309-3325.

Hill, D. P. (1973), Critically refracted waves in a spherically symmetric radially heterogeneous earth model, Geophys. J. R. astr. Soc., 34, 149-177.

Lerner-Lam, Arthur L. and Thomas H. Jordan (1987). How thick are the continents?, J. Geophys. Res., 92, 14007-14026.

Mellman, G.R., and D.V. Helmberger (1974), High-frequency attenuation by a thin high-velocity layer, Bull. Seis. Soc. Am., 64, 1383-1388.

Pavlenkova, N.I. and A.V. Yegorkin (1983), Upper mantle heterogeneity in the northern part of Eurasia, *Phys. Earth Planet. Int.*, 33, 180-193.

Priestley, K.F., G. Zandt, and G.E. Randall (1988), Crustal structure in eastern Kazakh, U.S.S.R. from teleseismic receiver functions, Geophys. Res. Lett., 15, 613-616.

Scheimer, J.F. and I.Y. Borg (1984), Deep seismic sounding with nuclear explosives in the Soviet Untion, Science, 226, 787-792.

Stark, P.B., R.L. Parker, G. Masters, and J.A. Orcutt (1988), Strict bounds on seismic velocity in the spherical Earth, J. Geophys. Res., 91, 13892-13902.

Yergorkin, A.V., V.Z. Ryaboy, L.P. Starobinets, and V.S. Druzhinin (1977), Velocity cross sections of the upper mantle from DSS data on land, *Izvestiya*, *Earth Physics*, 13, 467-477.

Yegorkin, A.V. and N.I. Pavlenkova (1981), Studies of mantle structure of U.S.S.R. territory on long-range seismic profiles, *Phys. Earth Planet. Int.*, 25, 12-26.

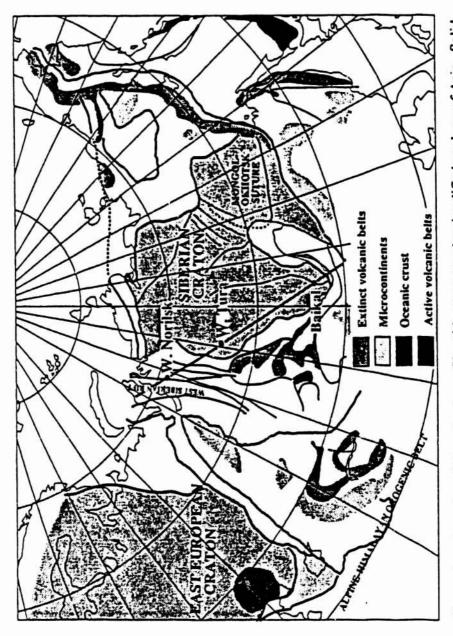
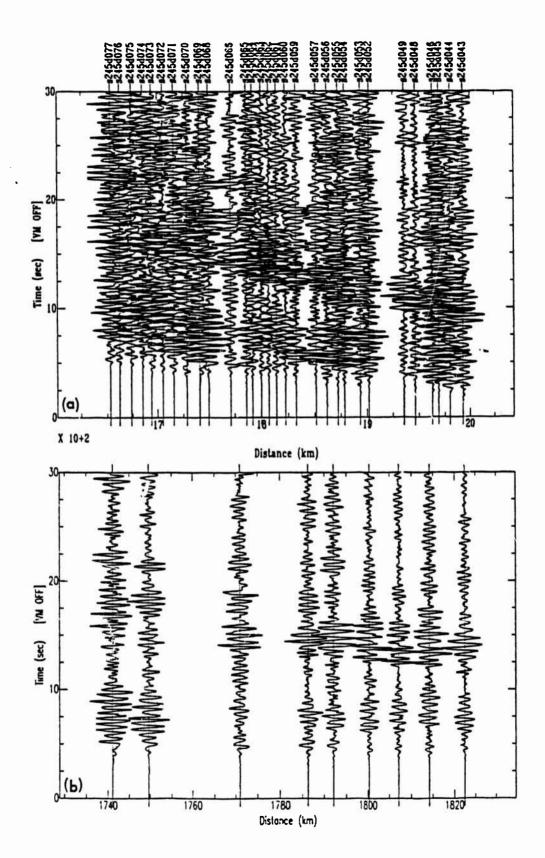


Figure 1. Location of the seismic profile with respect to the simplified geology of Asia. Solid circles denote the W. Norilsk, W. Tura, and Baikal shot points



Figures 2a,b. Seismograms from the DSS shot point at West Norilsk (SP 245) shown in record section format at a reduction velocity of 8.2 km/sec. Note the clear first arrival and the prominent secondary arrival.

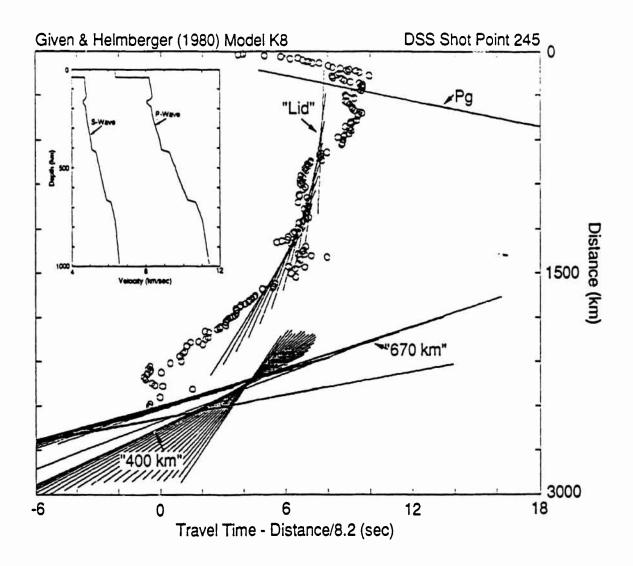


Figure 3. Observed arrival times for DSS shot point 245 (open circles) compared to travel times predicted by Model K8 (Given and Helmberger, 1980). The inset shows the P and S wave velocity model. The model is parameterized by a stack of homogeneous layers in which velocity gradients are approximated by a series of thin layers. The travel time curves are computed as refractions along the tops of these layers. No reflection computations are included. Regions of high gradient such as just above the 400 km discontinuity produce a series of widely spaced travel time curves. Portions of the velocity-depth function with low gradient produce nearly coincident curves (the 670 km arrival). In general, the agreement between K8 and the observed data is fair. The data suggest that the low velocity zone is very weak or absent in central Siberia.

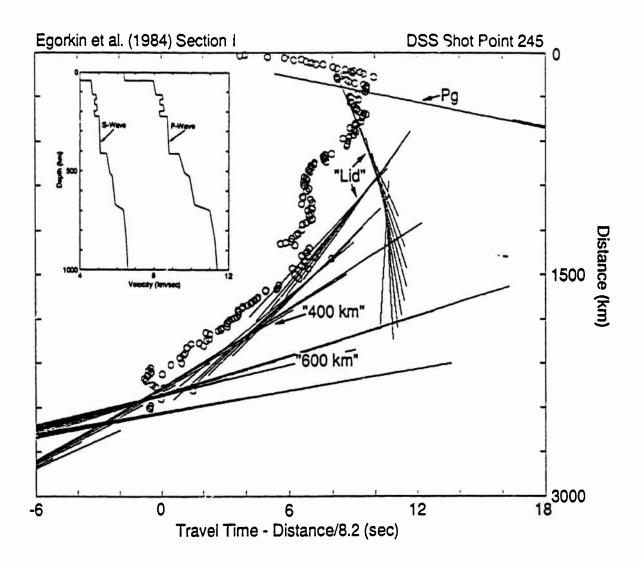


Figure 4. Observed arrival times for DSS shot point 245 (open circles) compared to travel times predicted for model EZC01 (Section I of Table 1 in Egorkin et al. (1984). Same format and computations as in Fig. 3. The complex structure in the upper mantle produces several branches to the travel time curve as well as arrivals from the 400 and 670 km discontinuities. Models K8 and EZC01 have similar structures below 400 km depth. The model is in good agreement with the data in the 1500-2400 km range, but is distinctly poorer than K8 at closer ranges. There appears to be no evidence for the alternating high and low velocities between 100 and 250 km.

## 1991 SUMMER RESEARCH PROGRAM FOR FACULTY AND GRADUATE STUDENTS

# Sponsored by the UNITED STATES AIR FORCE OFFICE OF SCIENTIFIC RESEARCH

# Conducted by the RESEARCH & DEVELOPMENT LABORATORIES

#### **FINAL REPORT**

# STRUCTURAL AND VIBRATIONAL ANALYSES OF THE WAKE SIDE PLASMA SENSOR FOR THE WAKE SHIELD FACILITY

Prepared by: Dr. Joseph J. Rencis, Associate Professor, P.E.

Timothy J. Urekew, Ph.D. Candidate Christopher Scarpino, M.S. Student

Academic Department: Mechanical Engineering

University: Worcester Polytechnic Institute

100 Institute Road

Worcester, Massachusetts 01609

Research Location: Phillips Laboratory

Geophysics Directorate

Space Systems Technology Branch

Hanscom Air Force Base, Massachusetts 01731

USAF Research Contact: Dr. David Hardy

Date: August 31, 1991

# **ACKNOWLEDGEMENT**

The authors would like to thank the USAF Office of Scientific Research, and the Research and Development Laboratories for extending them the opportunity to participate in the 1991 Summer Research Program at the Phillips Laboratory, Geophysics Directorate, Hanscom Air Force Base, Massachusetts. The authors would also like to acknowledge the contribution of Dr. David Hardy, Dr. Lon Enloe, Al Locker, Paul Hartnett, Martha Woodward and the staff of the Space Systems Technology Branch. In addition, the authors would like to thank Dr. Adolph Jursa for his efforts during the course of the project.

# I. SCOPE

This report serves as supporting documentation in certifying the Wake Side Plasma Sensor (WSPS) for flight as a secondary structure on the Wake Shield Facility. The WSPS is an experiment package that mounts on the free-flying Wake Shield Facility (WSF). A sectional view of the WSPS is shown in Fig. 1.

### II. APPLICABLE DOCUMENTS

The following documents were used in defining the scope and analysis procedure used in this report.

### **NASA**

JSC-20545 (July 1985)

Simplified Design Options for STS Payloads

(November 1990)

SED Engineering Handbook EHB-2 Systems Engineering Division Bolted Joint Handbook

# III. ANALYSIS METHODOLOGY

A static, margin-of-safety based analysis was carried out for critical areas of the WSPS structure. The analysis was performed using the IMAGES-3D personal computer based finite element package [1]. The numerical results were checked against hand calculations when possible. In the Finite Element analyses, inertial loadings are distributed uniformly, throughout the model. In the hand calculations, inertial loadings are applied as point loads acting at the center of gravity of the WSPS. Reactions in critical areas of the structure were determined using Newton's Laws for static equilibrium. Stresses are calculated from the reactions and the structural response is reported as a margin of safety. A finite element modal analysis was also performed to obtain the first three natural frequencies and corresponding mode shapes.

### 3.1 Applied Loads

The WSPS is an experiment package which is attached to the Wake Shield Facility and is therefore classified as a secondary structure. The approximate weight of the WSPS is 25.0 lbs. This is the weight of the mass simulator used in dynamic testing of the Wake Shield Facility at Space Industries Incorporated (SII). The actual weight of the WSPS is not expected to deviate significantly from 25.0 lbs. In

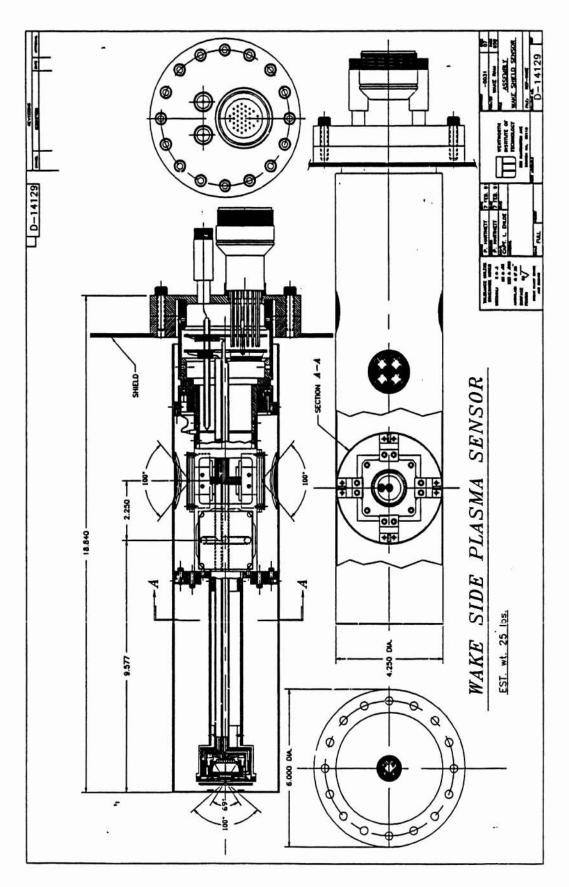


Figure 1 - Sectional View of WSPS

accordance with p.6 of NASA document JSC-20545, a load factor of 31.0 g was applied to the WSPS since its weight is in the 20-50 lb. range. This load factor is intended to represent mechanically and acoustically induced random vibration as well as excitation from low frequency transients. A primary load factor of 31.0 g is applied along each of three coordinate axes with a load factor of 25% of the primary load applied to each of the remaining two orthogonal axes. The three resulting load cases, as required in JSC-20545, are listed in Table 3.1.1. The coordinate system used for applying the required load factors is shown in Fig. 3.1.1 and is parallel to the coordinate system for the WSF. All analyses are carried out relative to the coordinate system shown in Fig. 3.1.1.

Table 3.1.1 - Load Cases for Secondary Structure

	Load Factors, g		
Load Case	X	Y	Z
1	31.0	7.75	7.75
2	7.75	31.0	7.75
3	7.75	7.75	31.0

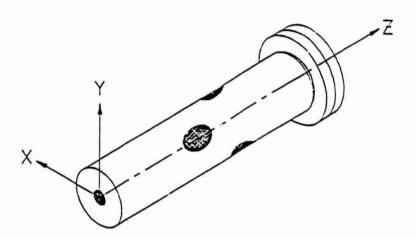


Figure 3.1.1 - WSPS Coordinate System

### 3.2 Critical Structures.

The critical structural items on the WSPS are labeled in Fig. 3.2.1 and are listed in Table 3.2.1. The critical structures are fabricated from AISI 304 stainless steel, A-286 alloy, and from 99% aluminum oxide ceramic. Material properties for the AISI 304 stainless steel and A-286 alloy are taken from [2] and [3], respectively.

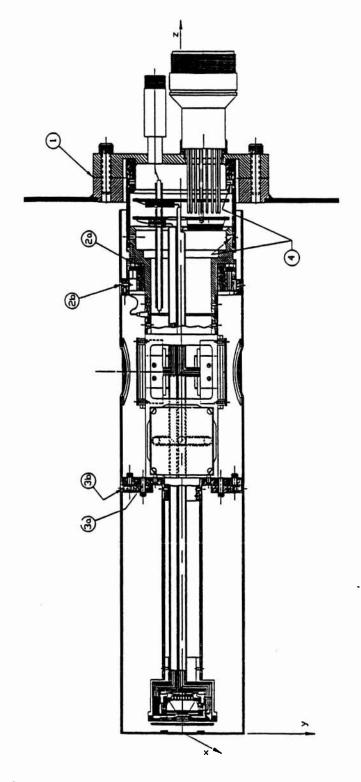


Figure 3.2.1. - Safety Critical Structures

Material properties for the ceramic are taken from [4] and are included in Appendix A.

Table 3.2.1 - Critical Structural Items on WSPS

Item No.	Description	
1	Joint between conflat flange.	
2a	Joint between ceramic ring, probe, and cover	
2b	Joint between sensor cover and stainless steel ring	
3a	Joint between ceramic tab, stainless steel bracket and cover	
3b	Joint between sensor cover and stainless steel ring	
4	Inner cylinder probe joints	

Critical items 1, 2b, 3b, and 4 are analyzed for ductile failures modes since these items are constructed of stainless steel. Items 2a and 3a are analyzed for fracture and ductile failures since these items are constructed of ceramic and stainless steel. The ceramic material in items 2a and 3a is used as an electrical insulator between the WSPS cover and probe.

# 3.3 Analysis Steps.

The critical structural items of the Wake Side Plasma Sensor are the parts and hardware found in the six joints described in Table 3.2.1. The general procedure used to analyze these joints are listed below:

- 1. Determine fastener forces reacting secondary structure load factors.
- 2. Determine the minimum required fastener preload for the joint.
- 3. Determine the maximum allowable fastener preload for the joint.
- 4. Determine the margin of safety for the joint fasteners using minimum preload.
- 5. Determine the margins of safety for applicable failure modes of the joint components.
- 6. Perform a fail-safe analysis by removing the most severely stressed fastener and repeating steps 1 through 5.
- 7. Determine the minimum and maximum torque values for the joint fasteners using the minimum and maximum preload values from steps 2. and 3., respectively.

The above analysis procedure is based upon theory presented in the Systems Engineering Division Bolted Joint Handbook, NASA Langley Research Center, and in Mechanical Engineering Design by Joseph Shigley [5]. A detailed description of the analysis procedure can be found in Appendix B. A description of the

finite element model used for the inertial loading and vibration analyses is included in Appendix C. The detailed analyses for critical items 1, 2a, 2b, 3a, 3b, and 4 can be found in Appendices D, E, F, G, H, and I, respectively.

A vibration analysis of the Wake Side Plasma Sensor is performed using the finite element model to obtain the first three natural frequencies and corresponding mode shapes. Details of the vibration analysis are included in Appendix J.

### IV. ANALYSIS SUMMARY

The results are presented as margins of safety for the structural analysis and as natural frequencies for the vibrational analysis.

### 4.1 Structural Analysis

The parts and hardware associated with each critical structural item listed in Table 3.2.1 were analyzed for appropriate modes of failure (i.e. ductile failure, fracture). Factors of safety of 2.0 and 4.0 were applied on the margin of safety for ductile and fracture critical items, respectively, as required for non-tested structures in JSC-20545. A fail-safe analysis was performed for each critical structural item by removing the most severely stressed fastener in the joint and reanalyzing the WSPS subjected to the load cases shown in Table 3.1.1. A summary of the structural and fail-safe analyses results are included in Table 4.1.1. In addition, assembly torques were calculated for the minimum required and maximum allowable preloads, and are listed in Table 4.1.2. All of the critical structural items satisfy the non-negative margin of safety requirement in JSC-20545. Detailed structural analyses are included in Appendices D, E, F, G, H, and I for critical structural items 1, 2a, 2b, 3a, 3b, and 4, respectively.

Table 4.1.1 - Structural Analysis Results

				_	
-					- Safe
Critical Item No.	WODG D	Margins of Safety		Margins of Safety	
	WSPS Part	Yield	Ultimate	Yield	Ultimate
1	5/16-24 A-286 Soc. Head Cap Scr.	5.6	8.3	5.3	7.9
	AISI 304 SS Conflat Flange	1.9	6.3	2.2	7.0
	AISI 304 SS Flange Weldment	2.9	3.7	2.9	3.7
2a	#8-32 A-286 Soc. Head Cap Scr.	2.7	3.3	2.6	3.3
	AP35 99% Al <sub>2</sub> O <sub>3</sub> Ceramic Ring	-	7.4	-	7.8
	AISI 304 SS Receiving Cylinder	7.9	21.2	8.9	23.7
2b	#8-32 A-286 Flat Head Soc. Scr.	3.4	4.5	4.9	6.5
	AISI 304 SS Ring Screwed to Cover	13.1	34.2	19.9	51.3
	AISI 304 SS Cover	0.8	3.5	0.3	2.2
	AISI 304 SS Spacer Ring	21.7	55.8	5.2	14.4
3a	#8-32 A-286 Flat Head Soc. Scr.	4.5	6.1	0.4	0.8
	AP 35 99% Al <sub>2</sub> O <sub>3</sub> Ceramic Tabs	-	20.6	_	5.4
	AISI 304 SS Tab on Sensor Housing	6.1	16.9	1.0	4.1
3b	#8-32 A-286 Flat Head Soc. Scr.	6.6	7.6	5.3	6.3
	AISI 304 SS Steel Ring	40.2	102.1	20.2	52.0
	AISI 304 SS Steel Cover	0.8	3.5	0.3	2.2
4	#10-24 A-286 Flat Head Soc. Scr.	0.5	0.9	0.1	0.4
	AISI 304 SS Quarter Panels	1.4	5.1	2.1	6.8
	AISI 304 SS Conflat Flg. Weldment	1.5	5.1	1.6	5.6
	AISI 304 SS Cyl. to Qrt. Panels	8.5	22.8	9.0	24.0

Table 4.1.2 - Assembly Torque Specifications

Critical Item No.		Assembly Torques (in-lbf)		
	WSPS Fasteners	Minimum	Maximum	
1	5/16-24 A-286 Socket Head Cap Screw	23	224	
2a	#8-32 A-286 Socket Head Cap Screw	8	36	
2b	#8-32 A-286 Flat Head Socket Screw	4	36	
3a	#8-32 A-286 Flat Head Socket Screw	7	20	
3b	#8-32 A-286 Flat Head Socket Screw	2	20	
4	#10-24 A-286 Flat head Socket Screw	24	52	

# 4.2 Vibrational Analysis

A modal analysis of the WSPS was performed using the finite element model to obtain the first three natural frequencies. These frequencies are listed in Table 4.2.1. The fundamental frequency of 85.3 Hz is more than fourteen times the 6.0 Hz limit specified in JSC-20545. Detailed vibrational results are included in Appendix J.

Table 4.2.1 - Vibrational Analysis Results

Mode	Frequency (Hz)	
1	85.3	
2	85.3	
3	155.0	

# V. REFERENCES

- 1. IMAGES-3D User's Manual, Version 2.0, Celestial Software, Inc., 125 University Ave., Berkeley, CA 94710, 1990.
- 2. MIL-HDBK-5E, "Metallic Materials and Elements for Aerospace Vehicle Structures."
- 3. Unbrako Socket Screws, (Personal Communication: John Buda), Highland Avenue, Jenkintown, PA, 1991.
- 4. McDanel Refractory Co., "Catalog of Standard Products", 1991, 510 Ninth Avenue, P.O. Box 560-s, Beaver Falls, PA 15010.
- 5. Shigley J. E., Mechanical Engineering Design, 3rd edition, McGraw-Hill, 1977.

# A PRELIMINARY INVESTIGATION OF HIGH RESOLUTION INTERFEROMETRY OF THE SOLAR DISK

E. J. Seykora
Professor of Physics
East Carolina University
Greenville, North Carolina 27834

### ABSTRACT

Spatial interferometry was investigated as a high resolution method for the measurement of the solar angular diameter as well as short term variations in the solar angular diameter as a result of 5-min. oscillations. The interferometer used in this investigation was based on the Talbot self-imaging effect and its application in a lensless mode and telescopic exit pupil mode where investigated. Potential applications of spatial interferometry toward the measurements of the solar diameter, sunspots and their motion, and the solar angular position at the fraction of an arcsec level are discussed.

### INTRODUCTION

The concept of spatial interferometry as a measurement method in astronomy began with the suggestion by H. L. Fizau in 1868 to J. Stefan, that the angular diameter of stars might be measured utilizing the visibility of fringes from star light in an arrangement similar to that of Young's double slit experiment. An early attempt by Stefan failed because of the small telescope aperture and thus the small separation distance between the objective slits. Also, at the suggestion of Fizau, the experiment was attempted by A. A. Michelson with a 36-in. telescope in 1890. Although the angular diameter of a star was not determined, he did measure the angular diameter of Jupiter's moons. In order to increase the distance between the objective slits and thus the angular resolution, two plain mirrors were placed on a long girder in front of the objective of the 100-in. reflector at Mt. Wilson. The two widely spaced mirrors were used to reflect the light to two other mirrors and direct two beams of light through the apertures of a double slit at the telescope objective. Using this method, Michelson measured the angular diameter of the star Betelgeuse (0.042 arcsec) in 1920. Since that time spatial interferometry has been

used to measure the angular diameter of a number of stars using the basic principles of the Michelson stellar interferometer. The application of these methods to large angular diameter objects and their precision measure has not, in general, been utilized because of the low degree of spatial or lateral coherence expected from such objects. In this paper it will be shown that precision spatial interferometry of large angular diameter objects is attainable at the present time.

#### THEORY

In Young's double slit or Michelson's stellar interferometry arrangement, shown schematically in Figure 1, the visibility of the fringes which result may be defined by

$$V = 2 \frac{\left(I_{\text{max}} - I_{\text{min}}\right)}{I_{\text{max}} + I_{\text{min}}} = \frac{\Delta I}{I_0}. \tag{1}$$

The fringe visibility is also a measure of the degree of lateral coherence of the light entering the slits. For a distant circular source this visibility can be shown to be given by

$$V = 2 \left| \begin{array}{c} J_1 \overline{\Lambda} d\Theta \\ \overline{\Lambda} \end{array} \right|, \qquad (2)$$

where J is a Bessel function (of the first kind) of the order 1,  $\Theta$  is the source angular diameter, d is the separation between slits and  $\lambda$  is the average wavelength of the light used.

Now, provided that the fringe visibility can be measured for a given source, the angular diameter of the source may be determined from Eq. (2). In the case of small angular diameter objects, stars for example, d must be made very large in order that the product of d\*0 is large and Eq. (2) has a measurable value less than two. It is important to note at this point that the case for large angular diameter sources represents the reverse situation from the stellar interferometer with large d.

For large angular diameter sources,  $\Theta$  is large and d must be made small in order that Eq. (2) has a measurable value of less than two. Precision measurements of  $\Theta$ , require sensitive measurements of V because of the small amplitude of the Bessel Function for large arguments. Nevertheless, within the context of the van Cittert-Zernike Theorem the resolution depends only on the measuramental accuracy of the visibility of the fringes. Estimates indicate that in order to measure the lateral coherence for source diameters of  $\sim 0.5^{\circ}$ , d must be of order  $10^{-2}$ cm. Clearly, this would represent a problem in a standard double slit interferometer because of the very low degree of light transmission. Such a low transmission would ultimately affect the accuracy of the measurement of fringe visibility. In 1986 an interferometer was proposed which circumvents the low transmission problems of a double slit, and a pro-type<sup>2</sup> was tested in 1989 at the National Solar Observatory, Sunspot, N.M.

This interferometer was based on the Talbot self-imaging effect<sup>3-5</sup> and represents a diffraction-free solution to the Helmholts Equation. The Talbot self-imaging effect occurs within a region of overlapping orders behind a ruling at distances of

$$r_n = \frac{nd^2}{\lambda},\tag{3}$$

where n is an integer. For even n the self—images of the ruling are aligned with the ruling, and for odd n the images are shifted by half of the periodicity of the ruling. The range of the images as a result of the overlapping orders is

$$r_{\max} = \frac{\mathrm{Dd}}{2\lambda},\tag{4}$$

where D is the width of the ruling aperture. For each image position  $r_n$ , the image results from diffraction from object slit pairs which are  $n^*d$  units apart. For a distant uniform circular source illuminating the ruling the visibility or degree of lateral coherence in the Talbot self—image is

$$V = 2 \left| \frac{J_1 \left( \frac{\pi n d\Theta}{\lambda} \right)}{\frac{\pi n d\Theta}{\lambda}} \right|. \tag{5}$$

This visibility function is identical to that of Young's double slit arrangement or Michelson's stellar interferometer, where n\*d represents the separation of two slits or mirrors in the case of the stellar interferometer. Precision determinations of the solar angular diameter may be accomplished by measurements of the Talbot self—image visibility at different interferometer orders. Ratios of the measured visibilities,

$$\frac{V_1}{V_2} = \frac{\Delta I_1}{\Delta I_2} = \frac{n_2}{n_1} \left| \frac{J_1}{J_1} \frac{\left[\frac{\pi n_1 d\Theta}{\lambda}\right]}{\left[\frac{\pi n_2 d\Theta}{\lambda}\right]} \right|, \tag{6}$$

are related to Bessel functions with arguments dependent on  $\Theta$ , the solar angular diameter. Solutions of Eq. (6) for  $\Theta$  are multivalued, and the proper value may be isolated using estimates of the acceptable range of  $\Theta$ .

#### INSTRUMENT

Shown in Fig. 2 is a diagram of the optical and electronic configuration of the interferometer used in this investigation to measure the visibility of the grating self-images. The optical arrangement, which was similar to the previously tested pro-type model, consisted of two  $(2.54-x\ 2.54-cm)$  precision Ronchi rulings (118 lines/cm), which had a linewidth equal to the space width between lines. The aperture ruling which generates the self-images was attached to a speaker voice coil such that it could be translated sinusolidally with a total excursion of one-half of the ruling period in a direction perpendicular to the ruling. The detector assembly, as shown in Fig. 2, consisted of a field stop, F; ruling, G2; and detector, D; which could be positioned at various distances from ruling G1 while keeping both rulings collinear. Field stop F was set so that grating orders  $m = \pm 1$ , and m = 0 entered its aperture from an extended source object. Rulings G2 acted as an optical gate such that as ruling G1 was translated, as well as its self images at G2, light exiting G2 was modulated at the frequency of the drive oscillator. Detector D was a low

noise Si photovoltaic cell which produced a current which was proportional to  $\Delta ISin(\omega t + \phi)$ , where  $\omega$  is the frequency of the drive oscillator,  $\phi$  is the phase angle between the self-image of G1 and G2, and  $\Delta I$  is the intensity variation of the self-image. Here the intensity variation  $\Delta I$  is proportional to the visibility, Eq. (1), of the self-image of ruling G1 at position  $r_n$ . In order to detect accurately the very small intensity variations with a known angular frequency,  $\omega$ , and unknown phase angle,  $\phi$ , a lock-in amplifier system was used to form a high gain low noise amplifier system. The detector input signal,  $\Delta ISin(\omega t + \phi)$ , was converted to a voltage signal by a current to voltage converter and detector coherently with the drive oscillator of angular frequency  $\omega$ . The amplifier output was then proportional to  $\Delta ISin\phi$ . The signal representing  $\Delta ISin\phi$  was digitized with a 12 bit analog to digital converter and recorded. During all measurements and observations a narrow band filter was used with a central pass band wavelength of 6328Å, and a FWHB = 50Å.

This interferometer may be used in a lensless mode in the arrangement shown in Fig. 2 and operated in the solar tracking mode using a coelostat or in the non-tracking mode. In the non-tracking mode the output signal  $\phi$  is time dependent and depends on the apparent angular motion of the sun. The amplitude in this mode is proportional to the visibility of the fringes.

### **OBSERVATIONS**

In order to investigate the definition of the extreme solar limb, the interferometer was arranged in the telescopic exit pupil mode as shown in Fig. 3. In this arrangement approximately 100 arcsec of the limb was observed using an image stop at the prime focus of the coelostat lens. Although in this arrangement the visibility function is not defined by Eq. (5), because the source is not a uniform circular source, the variation of  $\Delta I$  is nevertheless proportional to the mutual coherence of the limb. Any variation in the highest spatial frequencies of the limb would produce a variation in the visibility of the fringes. During all observations of the limb, limb guiders were used to stabilize the solar tracking.

Shown in Fig. 4 is a 110 min time sequence of the variations in the visibility of the fringes, AI, recorded on June 17, 1991. This time sequence is similar to that recorded on several other days when the atmospheric seeing was good for several

hours. Apparent in the time sequence of June 17 is a low frequency oscillation with periods in the 5-min range. A power spectrum of this time sequence is shown in Fig. 5. Here it can be noted that there is an excess of power in the 3 mHz range, probably resulting from the 5-min p-mode solar oscillations. From the spacing of the peaks in this power spectrum it was determined that the predominate mode of angular degree  $1 \approx 27$ . Shown in Fig. 6 is a theoretical k-w diagram for p-mode solar oscillations with angular degrees of 0 to 200 vs. oscillation frequency. The power spectra of Fig. 5 has been inserted for comparison at vertical slice 1 = 27. The excess power at low frequencies, 0 - 0.75 mHz may have resulted from the short duration of the data set. In general there is a rather good agreement between the detected coherence variations of the solar limb and the expected p-mode oscillations.

Observations of the entire solar disk are carried out using the coelostat tracking system with the coelostat lens removed. In this arrangement the interferometer was used in the lensless mode. Limb guiding was achieved using a portion of the light reflected from the coelostat mirrors to form an image of the sun. Under these conditions, tracked full disk observations, the lateral coherence would be dependent on the solar angular diameter. In addition, any sunspots may be expected to change the coherence in a time dependent manner because of the solar rotation.

A typical time sequence of the maximum visibility taken at interferometer order n=20, pre-set for  $\sin\phi=1$ , for June 25, 1991, is shown in Fig. 7. In this data set, as with all other full disk observation, no oscillations appeared. Under these condition the sensitivity is expected to be reduced by 10X compared to the telescopic exit pupil mode previously discussed. What is apparent is the low noise of the output signal even under poor seeing conditions. Also, it should be noted that the downward trend in the fringe visibility was real and not a result of guiding errors or a time dependent change in  $\phi$ . Calibration checks before and after this run indicated that  $\phi$  had not changed during this observation. This variation in the visibility appears to be rather typical of the variation expected from the net motion of sunspots due to solar rotation as well as their proper motions.

Measurements of the absolute solar angular diameter were attempted on a number of occasions during June and July of 1991. During this interval of time the solar activity was high and a large number of sunspots were visible on the solar disk. The angular diameter measurements are most easily accomplished in the non-tracking mode with a small heliostat mirror arranged such that the solar diameter horizontal to the earth's horizon is perpendicular to the interferometer This method of observation reduces any errors due to atmospheric rulings. distortion of the solar disk. In this non-tracking mode the resultant recordings at a given interferometer order are given by  $\Delta I \sin(\phi t)$ . That is, the resultant oscillation period depends on the position of the sun and its angular motion due to the earth's The amplitude, AI, was recorded and averaged from a number of rotation. oscillation periods at each interferometer order and the angular diameter was determined from the ratio of the visibilities using Eq. (6) and tables for the Bessel functions.

Because of the large number of spot groups on the sun during the observation period precision angular diameter measurements were not possible. The added coherence and its time variation due to the solar rotation, as well as the rotation of the solar image from the heliostat, indicate that precision measurements of the solar angular diameter are only possible during times with a minimum number of sunspots.

#### CCNCLUSIONS

The application of spatial interferometry to the measurement of the solar angular diameter at the 10 milli arcsec level appears possible at the present state of development. Such measurements are only possible when there are no sunspots. When the interferometer is operated in the telescope exit pupil mode on the solar limb, it shows potential as a new method for the observation of solar oscillations. The oscillations which have been observed most probably result from variations in the shape of the extreme limb profile which modulate the coherence of the light from the limb and not a true variation in the solar angular diameter. The application of spatial interferometry to the measurement of the lower frequency g-mode oscillations remain a distant possibility, although such measurements are not attempted during this investigation.

Sunspot motion has been recorded interferometrically, and this opens the possibility of a new method of detecting changes in sunspot motion, especially in the exit pupil mode. This may have important application in relation to sunspot groups which have larger shear motions in a pre-flare phase and warrants further investigation.

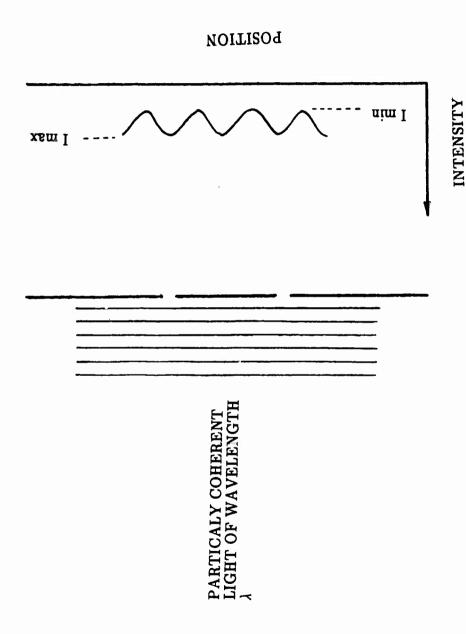
Finally, it should be noted that spatial interferometers may be used as a new method for precision tracking or telescope guiding using the solar limb. In the exit pupil mode, angular position resolutions of 0.05 arcsec have been achieved during these observations.

# **ACKNOWLEDGEMENTS**

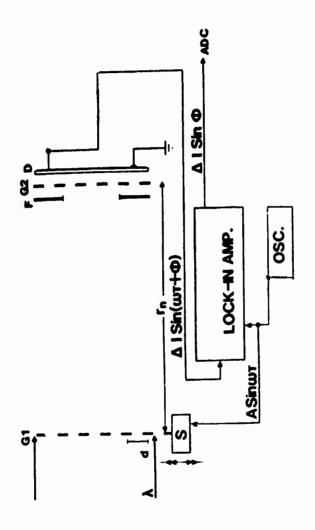
The author wishes to thank R. N. Smartt for his helpful discussions and S. L. Keil, and L. B. Gilliam, J. Elrod and B. Armstrong for their assistance. RDL and AFOSR are gratefully acknowledged for the support of the AFOSR Summer Research Program.

### REFERENCES

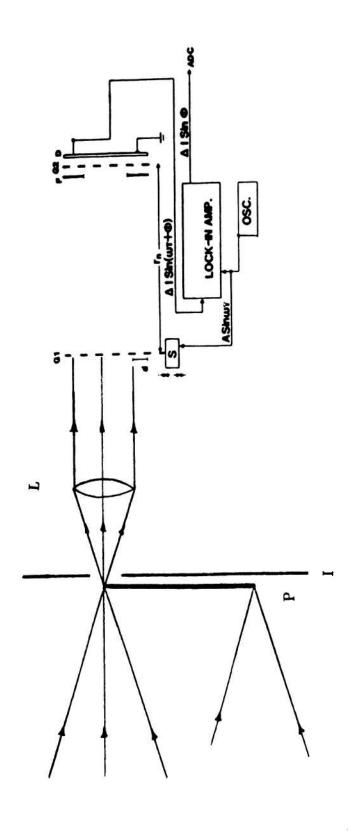
- 1. E. J. Seykora, "A Spectral Coherence Interferometer Utilizing a Grating and Its Possible Use for Solar Limb Investigations," *Bull. Am. Astron. Soc.* 18, No. 2, 703 (1986).
- 2. E. J. Seykora, "Solar Interferometry Utilizing the Visibility of Diffraction-Free Images," *Applied Optics* 29, No. 34, 5039-5041 (1990).
- 3. F. Talbot, "Facts Relating to Optical Science," Philos. Mag. 9, 401-407 (1836).
- 4. J. M. Crowley and A. F. Moodie, "Fourier Images IV: The Phase Grating," Proc. Phys. Soc. 76, 378-384 (1960).
- 5. J. M. Crowley, Diffraction Physics (North-Holland, New York 1984).
- 6. Global Oscillations Network Group, a Proposal to Study the Solar Interior by Measuring Global Oscillations with a World-Wide Network of Instruments (National Solar Observatory, NOAO 1984).



Experimental arrangement for Young's double slit experiment. For partially coherent light I min is greater than zero and the visibility may be defined by Eq. (1). Fig. 1



at 100 Hz by speaker drive S. The visibility of self-images of ruling G1 at field stop F and ruling G2 were detected at detector D using a lock-in amplifier system which operated coherently with the speaker drive Optical and electronic configuration used to measure the visibility of the Talbot self-image as a function of rn, the distance between rulings G1 and G2. Light of wavelength illuminated ruling G1, which was vibrated frequency.



Exit pupil interferometer arrangement where P is the image of the solar disk at the prime focus of the coelostat, I is the image stop and L is the collimating lens with a focal length of 78.6 cm. The focal length of the coelostat lens was 1053.1 cm. Fig. 3

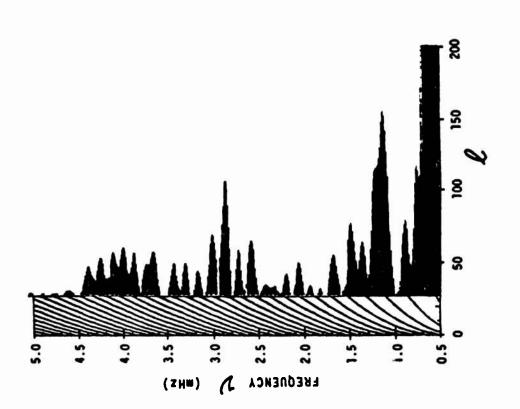


Amplitude of visibility variations vs. time measured at the solar limb on June 17, 1991. The total time span is 110 min. Fig.4

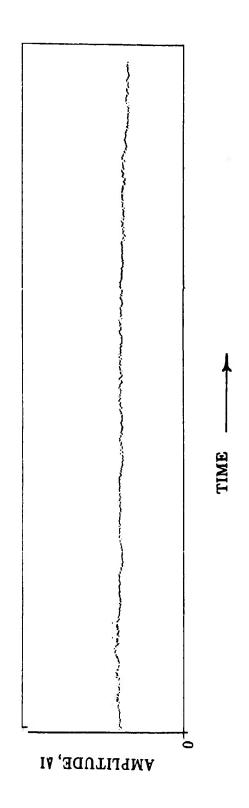


Power spectra of the data recorded on June 17, 1991 at the solar limb. Fig. 5

FREQUENCY mHz



Power spectra of June 17, 1991 plotted as a vertical slice with l=27 on the theoretical K-W diagram for solar p-mode oscillations. Fig. 6



Amplitude of visibility variations of the entire solar disk taken at interferometer order n = 20 and pre-set for  $Sin\phi = 1$  on June 25, 1991. The total time span is 3 hours. Fig. 7

### IMPROVED HITRAN DATA FOR MOLECULAR OXYGEN

R. H. Tipping

Department of Physics

University of Alabama

Tuscaloosa, AL 35487

### **ABSTRACT**

Improved molecular parameters including transition frequencies, strengths, transition moments, and halfwidths for the ground electronic state magnetic dipole and electric quadrupole transitions and two electronic transitions (the  $a^I \Delta_g$  <-  $X^3 \Sigma_g^-$  and  $b^I \Sigma_g^+$  <-  $X^3 \Sigma_g^-$ ) of molecular oxygen have been calculated. These results have been assembled in the HITRAN 1986 format and will supplant the current values in a forthcoming edition.

#### I.INTRODUCTION

For many years the Air Force through the Air Force Geophysics Laboratory (AFGL), now called the Phillips Laboratory (PL), has compiled a high-resolution transmission molecular absorption database known under the acronym HITRAN.1 This data is very useful for many applications and its scope has increased dramatically in recent years, both in the number of transitions for each molecule and in the number of molecular species.<sup>2</sup> Periodically, when new experimental data become available or when theoretical methods improve, the molecular parameters contained in the database (transition frequencies, strengths, transition moments, self- and airbroadened halfwidths, ground state energy levels, coefficient of the temperature dependence of air-broadened halfwidths, line shifts, identifying quantum numbers, and error codes) are The work discussed in the present paper describes the improvements made in the parameters for molecular oxygen, giving the sources for the improved data.

In the next section, we first describe the improvements in the ground electronic state magnetic dipole transitions, in the corresponding electric quadrupole transitions, and finally in the  $a^1\Delta_g < - X^3\Sigma_g^{\cdot}$  and  $b^1\Sigma_g^{+} < - X^1\Sigma_g^{\cdot}$  electronic transitions. The accuracy and completeness of the available data is reviewed. Transitions associated with other electronic states and with atomic oxygen that are important for atmospheric applications are discussed in the final section.

#### II. THE OXYGEN DATABASE

### A. Magnetic Dipole Transitions

Because the ground electronic state arising from two unpaired electrons is  $X^3\Sigma^+$ , the  $O_2$  molecule has an electronic magnetic dipole moment. The electron spin also leads to a splitting of the vibration-rotational levels due to spinrotation and spin-spin splittings. The theory of these effects is well known following the work of Steinbach and Gordy.3 Using the improved molecular Dunham coefficients,4 abundances. fundamental isotopic constants for the Bohr magneton, 6 the ratio and molecular gyromagnetic parameters for the v = 0 level<sup>7</sup> and the v = 1 level<sup>8</sup> of the <sup>16</sup>O<sub>2</sub> isotope, for the v = 0 levels of the  $^{16}O^{17}O$  isotope<sup>9</sup> and  $^{16}O^{18}O$ isotope, 10 respectively,

we have recalculated the HITRAN parameters for the magnetic dipole transitions. Because of the weakness of the magnetic dipole transitions, very little experimental work has been reported for the halfwidths or for their temperature dependence; consequently, we have not modified substantially the values of the halfwidths in the present compilation, although we have adopted the constant value for the temperature coefficient 0.83 which is an average value for a few transitions discussed by Chance et al.<sup>11</sup>

### B. Quadrupole Transitions

Because none of the O<sub>2</sub> isotopes has a permanent dipole moment within the Born-Oppenheimer approximation, the leading

electric moment is the quadrupole moment. Like the magnetic dipole transitions discussed above, the strengths of these transitions are also weak, but have been observed both in the laboratory<sup>12</sup> and in atmospheric spectra.<sup>13</sup> Using the same molecular data mentioned above, improved frequencies and ground state energies have been calculated. The largest changes result, however, in the strengths and transition moments of the pure rotational transitions arising from a more accurate value of the quadrupole moment (0.34 x 10-26 versus an older value of 0.82 x 10<sup>-26</sup> esu cm<sup>2</sup>). The strengths of the fundamental transitions that are based on the laboratory measurements have not been changed, nor have the halfwidths or the temperature coefficients. Just as in the case of the magnetic dipole transitions, it would be desirable to have accurate laboratory data for the self- and air-broadened halfwidths.

#### C. Electronic Transitions

There are two electronic transitions presently on the HITRAN database: the  $a^1\Delta_g$  <-  $X^3\Sigma_g^-$  and the  $b^1\Sigma_g^+$  <-  $X^3\Sigma_g^-$ .

For the v'=0 level of the  $a^1\Delta_g$  state of  $^{16}O_2$ , we use the improved rotational constants of Hillig et al.  $^{15}$  determined from the pure rotational spectrum; the constants for the other levels and isotopes are not modified. However, adopting the recently reported absolute band strength of Lin et al.  $^{16}$  [A(0,0) = 1.3 x  $10^4$  sec-1 versus the older value of 2.68 x  $10^4$  sec-1, together with the same relative values of A(1,0) and

A(0,1), the intensities of all the transitions are reduced by approximately a factor of 2. No new data on halfwidths or their temperature dependence have been reported, so that these parameters remain unchanged.

For the  $b^1\Sigma^+_g <- X^3\Sigma^-_g$  transitions in  $^{16}O_2$ , new intensities and self- and a few air-broadened halfwidths for the A-band (v' = 0 <- v = 0),  $^{17}$  and intensities and self-broadened halfwidths for the  $\gamma$ -band (v' = 2 <- v = 0),  $^{18}$  have been reported and are incorporated in the compilation. The other parameters remain unchanged. It would be desirable to have similar data on the less abundant isotopes, as well as more extensive measurements of air-broadened halfwidths and their temperature dependence.

## III. DISCUSSION AND CONCLUSIONS

In addition to the data discussed above, there are several other molecular bands, atomic lines, and other phenomena associated with oxygen that are useful to atmospheric scientists and which could eventually be included in the HITRAN database. These include: 1. The Schumann-Runge and Herzberg bands; 2. The fundamental band of the magnetic dipole transitions in the ground electronic state; 19 3. The quadrupole branches of the A band (the  $\mathbf{v'}=0$  <-  $\mathbf{v}=0$  rotational lines in the  $\mathbf{b}^1\Sigma^+_g <- \mathbf{x}^3\Sigma^-_g$  electronic transition); 20 4. The  $\mathbf{b}^1\Sigma^+_g <- \mathbf{a}^1\Delta_g$  transitions; 21 and 5. The fine structure transitions in atomic oxygen in the 161 and 226 cm<sup>-1</sup> spectral regions. 22

In addition to the transitions discussed above that can be incorporated within the current format of the HITRAN database, there are two other effects involving molecular oxygen that are important for atmospheric calculations, but which cannot be easily incorporated. These are: interference due to overlapping of spectral lines, and collision-induced absorption. The effects of interference in the millimeter spectrum of O2 are well known, and along with Zeeman effects, affect the propagation and absorption of radiation.<sup>23</sup> collision-induced fundamental of O2 plays a significant role in transmission through the upper atmosphere24 and is included approximately in the LOWTRAN codes.25 A more accurate theoretical treatment including the absorption induced by other species (e.g., N2, H2O, etc.) and an improved temperature dependence would be useful. We note in passing that similar effects in N2 are even more important, especially in the spectral region beyond the band head in CO2 near 4.3 microns.

Finally, we would like to mention another set of possible transitions that could easily be included in the HITRAN database (although this would constitute an expansion of the original scope of HITRAN to encompass only neutral species) and which may play a significant role in the upper atmosphere. These are due to the  ${\rm O_2}^+$  ions whose spectroscopy and concentration in the upper atmosphere are well known. Because of symmetry, the homonuclear species (e.g., 16-16, 18-18, etc.) do not have a permanent dipole moment. However, the

isotopically heteronuclear species (e.g., 16-17, 16-18, etc.) do; this is due to the separation between the centers of mass and charge. For instance, to a good approximation, the dipole moment of the most abundant isotopically heteronuclear species (16-18) has a dipole moment function (in Debye) of the form

$$M(R) = 8.276 \times 10^{-2} R$$
 (1)

where R is the internuclear separation. Therefore, approximately 0.4% of oxygen molecules undergo reasonably strong dipole pure rotational and vibration-rotational Because electric dipole transitions are much transitions. stronger than magnetic dipole or electric quadrupole transitions, the lower concentration of the isotopically heteronuclear species can to a large extent be more than compensated for by the stronger transition moment. The dipole nature of the isotopically heteronuclear ions may also play a role in the observed differences in isotope abundances at different heights in the atmosphere. More work on this problem should be done, and if the effects described above are significant, the molecular parameters of the oxygen ion should be incorporated into HITRAN. Similar comments obviously also apply to  $N_2$ .

#### **ACKNOWLEDGMENT**

The author would like to acknowledge many useful discussions with and the helpful support of Dr. L. S. Rothman of the Phillips Laboratory, and the Air Force Office of Scientific Research for their financial support.

#### REFERENCES

- L. S. Rothman et al., Appl. Optics, 22, 2247 (1983); L. S.
   Rothman et al., Appl. Optics 26, 4058 (1987).
- 2. L. S. Rothman et al., J. Quant. Spectrosc. Rad. Transfer, to be published (1992).
- 3. W. Steinbach and W. Gordy, Phys. Rev. 8, 1753 (1973).
- 4. R. R. Laher and F. R. Gilmore, J. Chem. Phys. Ref. Data 20, 685 (1991).
- 5. P. De Bievre, M. Gallet, N. E. Holden, and I. L. Barnes, J. Phys. Chem. Ref. Data 13, 809 (1984).
- 6. E. R. Cohen and B. N. Taylor, Phys. Today, BG9, Aug. (1990).
- 7. L. R. Zink and M. Mizushima, J. Mol. Spectrosc. 125, 154 (1987).
- 8. M. Mizushima, K. M. Evenson, J. A. Mucha, D. A. Jennings, and J. M. Brown, J. Mol. Spectrosc. 100, 303 (1983).
- M. Mizushima, L. R. Zink, and K. M. Evenson, J. Mol. Spectrosc. 107, 395 (1984).
- 10. M. Mizushima and S. Yamamoto, J. Mol. Spectrosc. 148, 447 (1991).
- 11. K. V. Chance, W. A. Traub, K. W. Jucks, and D. G. Johnson, Int. J. of Infrared and Millimeter Waves, 12, 581 (1991).
- 12. J. Reid, R. L. Sinclair, A. M. Robinson, and A. R. W. McKellar, Phys. Rev. A24, 1944 (1981).

- 13. A. Goldman, J. Reid, and L. S. Rothman, Geophys. Res.

  Lett. 8, 77 (1981); L. S. Rothman and A. Goldman, Appl.

  Optics, 20, 2182 (1981).
- 14. E. R. Cohen and G. Birnbaum, J. Chem. Phys. 66, 2443 (1977).
- 15. K. W. Hillig, C. C. W. Chiu, W. G. Read, and E. A. Cohen, J. Mol. Spectrosc. 109, 205 (1985).
- 16. L.-B. Lin, Y.-P. Lee, and J. F. Ogilvie, Q. Quant. Spectrosc. Rad. Transfer 39, 375 (1988).
- 17. K. J. Ritter and T. D. Wilkerson, J. Mol. Spectrosc. 121, 1 (1987).
- 18. M. A. Melieres, M. Chenevier, and F. Stoeckel, J. Quant. Spectrosc. Rad. Transfer 33, 337 1985).
- 19. M. Dang-Nhu, R. Zander, A. Goldman, and C. P. Rinsland, J. Mol. Spectrosc. 144, 366 (1990).
- 20. J. W. Brault, J. Mol. Spectrosc. 80, 384 (1980).
- 21. E. H. Fink, H. Kruse, K. D. Setzer, D. A. Ramsay, and M. Vervloet, Acta Phys. Hung. 67, 67 (1990).
- 22. T. G. Kyle, Atmospheric Transmission, Emission and Scattering, Pergamon Press, New York (1991).
- 23. P. W. Rosenkranz, J. Quant. Spectrosc. Rad. Transfer 39, 287 (1988).
- 24. C. P. Rinsland, R. Zander, J. S. Namkung, C. B. Farmer, and R. H. Norton, J. Geophys. Res. 94, 16303 (1989).
- 25. F. X. Kneizys et al., AFGL-TR-88-0177, Hanscom AFB, MA.

#### COHERENT LASER RADAR AND ARRAY IMAGING

Richard Anderson

Professor of Physics

University of MO-Rolla, Department of Physics Rolla, MO 65401

#### Abstract

Coherent heterodyne laser radar detector array imaging has been suggested. This paper is a theoretical study for laboratory measurements. The heterodyne signal measured is averaged over N different target perspectives to reduce speckle. This yields a signal proportional to the square root of the target intensity distribution. In theory this signal should yield the line of sight velocity component. The averaged autocorrelation of the heterodyne signal yields a quantity proportional to the target intensity distribution. The average cross correlation of the signals from different target positions of different samplings allows the transverse velocity to be determined.

#### I. Introduction

Several assumptions are made about the target. The target is a rough, diffuse, Lambertian scatterer. It completely depolarizes the incident light. Only the random

scattering from the microstructure of the surface is considered. It will be assumed that there are no deterministic surface variations. The target is a circular complex Gaussian surface whose ensemble averaged reflection coefficient has the properties,

$$\langle \rho(u_i) \rangle = 0$$

$$\langle \rho(\mathbf{u}_1) \rho(\mathbf{u}_1) \rangle = 0$$

and (1)

$$\langle \rho(\mathbf{u_i}) \rho^*(\mathbf{u_j}) \rangle = \lambda^2 R_d / \pi \delta(\mathbf{u_i} - \mathbf{u_j})$$

where Rd is the target reflectance or transmittance depending on the type of target. The target is a Lambertian scatterer and is an idealized surface which does not exist in reality. There are no ideal scatterers and in reality in backscatter there is an effect called the "opposition effect". The backscattered light from most targets exhibits a high degree of polarization in the same direction as the incident light. The light in backscatter retains the incident polarization similar to a retroreflector. Most targets at all angles retain a degree of polarization coherence with the incident light. means in heterodyne detection the reflection coefficient is a 2x2 Jones matrix and polarized laser light is represented by a 2x1 Jones vector. Each component of the reflectance matrix consists of an amplitude and a phase term or it is  $\rho_{ij} \exp(j\phi_{ij})$  so,

$$\hat{\rho} = \begin{cases} \rho_{11} \exp(j\phi_{11}) & \rho_{12} \exp(j\phi_{12}) \\ \rho_{21} \exp(j\phi_{21}) & \rho_{22} \exp(j\phi_{22}) \end{cases}$$
(2)

If a vertical polarized beam of light is scattered by the target the resultant field has horizontal and vertical components,

$$\bar{E}_{S} = E_{i} \begin{bmatrix} \rho_{11} \exp(j\phi_{11}) & \rho_{12} \exp(j\phi_{12}) \\ \rho_{21} \exp(j\phi_{21}) & \rho_{22} \exp(j\phi_{22}) \end{bmatrix} \begin{bmatrix} 0 \\ 1 \end{bmatrix} = E_{i} \begin{bmatrix} \rho_{12} \exp(j\phi_{12}) \\ \rho_{22} \exp(j\phi_{22}) \end{bmatrix}$$
(3)

If the local oscillator field which is mixed with this signal is vertically polarized, the intermediate frequency heterodyne signal occurs between vertical components of the field and the horizontal signal would be a very small noise term. Then

$$E_{S} = \rho_{22}E_{1}exp(j\phi_{22}) + E_{LO}$$
and
(4)

 $s_{\rm IF}=2\rho_{22}E_{\rm i}E_{\rm LO}Cos(\omega_{\rm IF}t+\phi_{22})+{\rm LO}$  shot noise The backscatter signal from most targets exhibits a high degree of polarization correlation with the incident beam and the Mueller matrix in backscatter can be approximated by a constant times the unit matrix. This means the diagonal components of the reflection coefficients in the Jones matrix above will be largest.

Since the reflection coefficient depends on the microstructure of the surface, both the amplitude and phase

depend on the angles of incidence of the light, the incident position, the emergent position, and the angles of emergence  $(\theta_i, \phi_i, u_{xi}, u_{vi}; u_{xe}, u_{ve}\theta_e, \phi_e)$  where  $u_x$  and  $u_v$  are the target x and y position coordinates. The reflection coefficient is called the bidirectional reflection coefficient. For the backscatter reflection coefficient  $\rho_{ij}$  and  $\phi_{ij}$  depend only on the incident angles and the incident position point. Since \( \rho \) depends on the incident angles of the light on the target, it will change considerably if the target moves a large distance during the total observation time T. If the motion is large, this means the perspective of the microstructure surface has changed considerably and large changes in the appearance will lead to speckle patterns of different appearance which will make correlation difficult. The motion of the target should be small so the reflection coefficient is only a function of the incident target position and not the incident angles. Equation (4) resembles the signal scattered in the scalar theory of diffraction and the scalar theory of diffraction is valid with the lose of some information.

When an acousto-optic modulator, AOM, is used as a frequency shifter, there are fundamental and harmonic acoustic signals generated at decreasing power levels. The modulator crystal is driven by a piezoelectric quartz crystal which is driven by an applied voltage whose frequency is accurately controlled. Any acoustic wave set

up in the medium will oscillate at the fundamental frequency and at harmonic frequencies at greatly reduced amplitude. In certain experiments these harmonic oscillations must be considered and give rise to secondary effects. Also the AOM driver will have a definite line half width and this leads to a frequency spread in the optical diffracted signal and in the intermediate frequency heterodyne signal.

In many laser radars these effects are overcome by using a slightly detuned laser local oscillator. The local oscillator is a laser amplifier pumped by the master oscillator. It has piezoelectric controlled mirrors which vary the cavity length and detune the amplifier. A small portion of the master oscillator signal drives the amplifier and a small portion of this master oscillator signal is mixed with a small portion of the amplifier output to produce an intermediate frequency which drives a phase locked loop. The output voltage of the phase locked loop is used to supply a reference voltage to adjust the mirror separation using the piezoelectric drivers. technique eliminates the problem of heterodyne harmonic signals, the phase difference between the LO and MO fields, and the heterodyne signal has a much narrower half width for it is effected by the line width of the LO laser.

## II. Theory

# (a) Laboratory Target at Rest

The target is a rough, diffuse, Lambertian, depolarizing surface which may be transmittive or reflective and its transmission or reflection coefficient is a circular complex Gaussian function. In this discussion it is assumed a reflective target is used and it has a definite shape. The target is located in a plane perpendicular to the direction of propagation of the incident beam and a position vector of a point in the target plane is the vector  $\bar{\mathbf{u}}$ . A plane, monochromatic laser beam of wavelength  $\lambda$  is incident on the target and its magnitude is a constant value  $\mathbf{E}_{\mathbf{O}}$ . The  $\rho(\bar{\mathbf{u}})$  reflection coefficient has a different value at each point of the target and defines the target shape. This means outside the target geometric shape the reflection coefficient is zero or

$$\rho(\bar{\mathbf{u}}) = \begin{cases} \rho(\bar{\mathbf{u}}) & \text{Inside the target area} \\ 0 & \text{Elsewhere} \end{cases}$$
 (5)

The reflection coefficient is wavelength and positional dependent and is of the form  $\rho(\bar{u}) = \rho'(\bar{u}) \exp[j\phi(\bar{u})]$ .

The target is at the first focal point of an ideal lens and is irradiated with this expanded monochromatic laser field. It is beam expanded to assure uniform illumination of the target. The local oscillator is frequency shifted

using a AOM or AOMs and it is also initially a plane expanded wavefront which enters a spatial filter. The LO beam originates from the pin hole of a spatial filter and is also at the first focal point of the lens. The two beams travel initially at right angles to each other but are combined by a beamsplitter placed in front of the lens. The emergent beam from the target and the LO beam are of the form

$$E_{S}(\overline{u},t) = \rho'(\overline{u})E_{O}\exp[j\phi(\overline{u})]\exp(j\omega_{O}t)$$

$$= k\sqrt{I(\overline{u})}\exp[j\phi(\overline{u})]\exp(j\omega_{O}t)$$
(6)

$$E_{LO}(\bar{u},t) = E_{LO} cyl(\bar{u}) exp[j(\omega_O t + \phi_{LO})]$$

and

where  $\sqrt{I(\bar{u})} \simeq \rho^{+}(\bar{u})E_{0}$  is the magnitude of the square root of the incident intensity, k is a constant, and  $\phi_{L0}$  is the phase difference between the LO beam and incident laser beam at the target. The detector is placed at the second focal point of the lens and a point (pixel) in the detector pupil is designated by the position vector  $\bar{r}$ . The fields in the detector pupil at position  $\bar{r}$  are

$$E_{DS}(\bar{r},t) = k/2\pi j f \exp(jkf) \sqrt{J(\bar{r}/\lambda f)} ** \exp[j\Phi(\bar{r}/\lambda f)] \exp(j\omega_0 t)$$
 and (7)

$$E_{\text{DLO}}(\bar{r},t) = \pi/j\lambda f \ E_{\text{LO}}(jkf) Somb(\bar{r}/\lambda f) exp[j(\omega_{\text{LO}}t + \phi_{\text{LO}})]$$

When the pin hole is very small, the sombero function is very broad and its central maximum has dropped only a small amount over the total entrance pupil of the detector array. As a result,  $Somb(\bar{r}/\lambda f) \simeq 1$  over the entrance pupil and the LO field can be considered of the form

$$E_{DLO}(r,t) = \pi/4j\lambda f E_{LO}(jkf) \exp[j(\omega_{LO}t + \phi_{LO})]$$
 (8)

The mixed field at the detector is

$$E_{\text{Total}}(\bar{r},t) = E_{\text{DS}}(\bar{r},t) + E_{\text{LO}}(\bar{r},t)$$
 (9)

and the heterodyne signal, neglecting any contribution from the small signal intensity, is

$$s(\bar{r},t) = E_{DS}E_{DLO}exp[j(\omega_{IF}t-\phi_{LO})]+E*_{DS}E_{DLO}exp[-j(\omega_{IF}t-\phi_{LO})]$$
+ LO shot noise (10)

Since the scattered field is complex and a convolution, the IF signal does not reduce to the usual cosine relation and the signal must be analyzed at either the upper or lower side band. The temporal Fourier transform can be taken and yields the initial phase shift between the LO and incident fields. The modulus of the positive side band is

$$m_{+}(\bar{r}) = k E_{LO} \sqrt{\varrho(\bar{r}/\lambda f)} ** \exp[j\varphi(\bar{r}/\lambda f)]$$

$$= k' \sqrt{I_{LO}} \sqrt{\varrho(\bar{r}/\lambda f)} ** \exp[j\varphi(\bar{r}/\lambda f)]$$
(11)

The intensity term  $\mathcal{L}(\bar{r}/\lambda f)$  is the diffraction pattern in the Fourier transform plane produced by the physical shape

of the target but it is speckled by the convolution with the transformed variable phase term. The spatial Fourier transform can be taken of this signal and yields

$$M_{+}(\bar{\mathbf{u}}) = k' \sqrt{I_{LO}} \sqrt{I(\bar{\mathbf{u}})} \exp[j\phi(\bar{\mathbf{u}})]$$
 (12)

The important result of this experiment is the determination of  $\phi_{\text{LO}}$ .

# (b) Laboratory Target in Motion

The same target is placed in motion. The motion is small and the rate of change is slow. The motion occurs over a period of time T with N samplings taken at all detector points (pixels) and the samplings are separated by a time  $\tau$ . The samplings take a small finite amount of time and there is some target motion during each sampling but the samplings are assumed taken at a fixed target position  $\bar{u}$ . At each sampling enough data is gathered at each point (pixel) to determine the phase and modulus. The image recorded in each sampling exhibits speckle but as the target moves the speckle pattern is moved across the detector array and a slightly different speckle distribution is measured at each point (pixel) in each sampling.

The motion must be small and slow so the reflection coefficient remains a function of position and the speckle shape is not radically different in different samplings. A

large angular variation makes the reflection coefficient a function of the incident angles and position and this means the target microstructure perspective has changed and the correlation between speckle patterns from one sampling to the next is destroyed. In the scalar Rayleigh-Sommerfeld diffraction equation the area eleret  $d^2\bar{u}$  is the projected area whose normal is along the lime of sight. In the time period T the surface normal and the line of sight direction should remain nearly fixed so an average set of projection angles may be used in the elemental area element or  $d^2\bar{u} = \cos\bar{\theta}\cos\bar{\theta}du_xdu_y$  where  $du_x$  and  $du_y$  are the differential displacements in the target plane. The velocity of the target in 3-D space has a component  $\mathbf{v}_{\mu}$  in the line of sight and v\_ perpendicular to the line of sight. In the reduction of the diffraction equation f will be replaced by f ±  $\mathbf{v}_{ii}$  t in the phase term in the line of sight direction but since the motion is slow the two terms do not differ appreciably and this replacement is not required in the other terms. At a sampling at time t the field at position r in the detector pupil is

$$\begin{split} \mathbb{E}_{\mathrm{DS}}(\bar{\mathbf{r}}) &= k/2\pi \mathrm{j} f \; \exp\{\mathrm{j} [kf + \omega_0 \pm kv_{||})t]\} \\ &\int_{\bar{\mathbf{u}}} \rho^{\,!}(\bar{\mathbf{u}}) \mathbb{E}_0 \exp[\mathrm{j} \phi(\bar{\mathbf{u}})] \exp[-\mathrm{j} k/f(\bar{\mathbf{u}} \cdot \bar{\mathbf{r}})] \mathrm{d}^2\bar{\mathbf{u}} \end{split}$$

= 
$$k/2\pi jf \exp\{j[kf + (\omega_0 \pm kv_{||})t]\}\sqrt{J(\bar{r}/\lambda f)^{**}\exp[j\Phi(\bar{r}/\lambda f)]}$$
(13)

The local oscillator field is the same as in equation (8). The IF signal measured at time t in position (pixel)  $\bar{r}$  is

$$s(\bar{r},t) = E_{DS}(\bar{r})E_{LO}exp\{j[(\omega_{IF} \pm kv )t - \phi_{LO} - \phi(\bar{r})]\}$$

$$+E*_{DS}(\bar{r})E_{LO}exp\{-j[(\omega_{IF} \pm kv )t - \phi_{LO} - \phi(\bar{r})]\}$$

$$+ LO \text{ shot noise}$$
(14)

The phase term  $\phi(\bar{r})$  is included because each sampling at a point  $\bar{r}$  requires a finite time and this is represented by an average phase change produced by path length variations to this point from various points of the target during the measurement time. This term will lead to a broadening of the IF line and will make it difficult to measure v even though  $\phi_{LO}$  is known. Again this signal cannot be reduced to a simple cosine term for  $E_{DS}(\bar{r})$  is a complex convoluted function. The temporal Fourier transform of either signal will give the phase difference of the signal from the intermediate frequency and the modulus of the signal. The modulus of the positive sideband is

$$m_{+}(r) = K \sqrt{I_{LO}} \sqrt{\mathcal{G}(\bar{r}/\lambda f)} **exp[j\phi(\bar{r}/\lambda f)]$$
 (15)

This is the heterodyne intensity measured at a point (pixel) at position  $\bar{r}$  at time t. There are N samplings of this point as the target moves slowly over a time T. The point (pixel) shall be designated by two subscripts i and k where i is the point (pixel) examined and i=1,2,3, ,n where n is the total number of points or pixels in the

array. The subscript k indicates the sampling or target perspective observed and k = 1,2,3, N where N is the total number of samplings in the time T. At each point (pixel) in each samplings the inverse spatial Fourier transform is performed

$$M_{+}(\bar{\mathbf{u}}_{ik}) = K \sqrt{I_{LO}} \sqrt{I(\bar{\mathbf{u}}_{ik})} \exp[j\phi(\bar{\mathbf{u}}_{ik})]$$
 (16)

where  $\bar{u}_{ik}$  is a target point in the kth sampling corresponding to the detector pupil point  $\bar{r}_i$ . The modulus at each target point  $\bar{u}_{ik}$  is summed and averaged over all N samplings and gives the averaged modulus at point  $\bar{u}_i$  or

$$M_{\text{sum}}(\bar{\mathbf{u}}_{i}) = K \sqrt{I_{\text{LO}}/N} \sum_{k=1}^{N} \sqrt{I(\bar{\mathbf{u}}_{ik})} \exp[j\phi(\bar{\mathbf{u}}_{ik})]$$
 (17)

If the total target motion is small, the intensity at each target point is nearly constant so

$$M_{sum}(\bar{u}_i) = K \sqrt{I_{I,O}} \sqrt{I(\bar{u}_i)} \sum_{k=1}^{N} \exp[j\phi(\bar{u}_{ik})]/N$$
(18)

The heterodyne signal sensed is the real part of this signal so

$$Rl[M_{sum}(\bar{u}_i)] = K \sqrt{I_{LO}} \sqrt{I(\bar{u}_i)} \sum_{k=1}^{N} Cos[\phi(\bar{u}_{ik})]/N$$
(19)

The sum may in some cases be zero, unity, or any value between 0 and 1. This leaves an image after the summing which is an improved heterodyne image but it is still a speckled image for the sum is not unity everywhere. The image is improved if the number of samplings are increased and N should be a large number. The interesting fact is

the heterodyne image which is proportional to the square root of the product of the local oscillator intensity and the target intensity. This is a 2-D representation of the square root of the target intensity.

## (c) Autocorrelation and Cross Correlation

The true 2-D intensity distribution can be realized by taking the autocorrelation of the modulus at each position  $\bar{u}_i$  in all N of the samplings and then summing these autocorrelation functions over all N samplings. This will represent a quantity proportional to  $I(\bar{u}_i)$  when and only when N is a very large number or

$$I(\bar{u}_{i}) = \lim_{N \to \infty} \frac{1/N \sum_{m} (\bar{u}_{ik}) m^{*}(\bar{u}_{jk})}{k=1}$$
(20)

In this discussion an aperture function  $A(\bar u)$  is introduced which has a value of unity in the geometric shape of the object and is zero elsewhere and  $E_0A(\bar u)=E_0(\bar u)$ . The reflection coefficient  $\rho(\bar u)$  represents the reflective properties of the surface and may have a different value at every point of the target and does not represent the target shape. The reduction in equation (20) is obvious for if N is very large, then in the diffraction integral representation of the autocorrelation the sum is nearly continuous and the sum can be replaced by an integral over the period T. The signal field is

$$E_{DS}(\vec{r}) = k/2\pi j f \exp(jkf) \int_{\vec{u}} \rho'(\vec{u}) E_{O}(\vec{u}) \exp[j\phi(\vec{u})]$$

$$\exp[-jk/f(\vec{u} \cdot \vec{r})] d^{2}\vec{u}$$

The cross correlation of the signals at two image points i and j in the kth sampling at time t is

$$\Gamma(\bar{r}_{ik},\bar{r}_{jk}) = s_{IF}(\bar{r}_{ik})s*_{IF}(\bar{r}_{jk})$$

$$= K I_{LO} \int_{\vec{u}_{jk}} \int_{\vec{u}_{ik}} [E_O(\vec{u}_{ik})E_O^*(\vec{u}_{jk}) \rho(\vec{u}_{ik})\rho^*(\vec{u}_{jk})]/T$$

$$x \exp[-jk/f(\bar{u}_{ik}\cdot\bar{r}_{ik}-\bar{u}_{jk}\cdot\bar{r}_{jk}] d^2\bar{u}_{ik}d^2\bar{u}_{jk}$$
 (21)

This cross correlation of each sample is summed and averaged over a large number of target representations N which change little in perspective and which are separated by a very short time  $\tau$  and extend over a time T. If N is very large, the sum is virtually continuous and the sum can be replaced by a time integral of equation (21) over the period T

$$\bar{\Gamma}(\bar{\mathbf{r}}_{ik}, \bar{\mathbf{r}}_{jk}) = K \mathbf{I}_{LO} \int_{0}^{T} \left\{ \int_{\bar{\mathbf{u}}_{jk}} \int_{\bar{\mathbf{u}}_{ik}} \mathbf{I}_{ik} \right\}$$
$$[E_{O}(\bar{\mathbf{u}}_{ik})E_{O}^{*}(\bar{\mathbf{u}}_{jk}) \rho(\bar{\mathbf{u}}_{ik})\rho^{*}(\bar{\mathbf{u}}_{jk})]/T$$

$$\times \exp[-jk/f(\bar{u}_{ik}\cdot\bar{r}_{ik} - \bar{u}_{jk}\cdot\bar{r}_{jk})] d^2\bar{u}_{ik}d^2\bar{u}_{jk} d^2$$
 (22)

If N is a large number, the time integral of  $[E_0)\bar{u}_{ik})E_0^*(\bar{u}_{jk}) \ \rho(\bar{u}_{ik})\rho^*(u_{jk})]/T \ \text{is the ensemble average}$  product of  $\langle E_0(\bar{u}_i)E_0^*(\bar{u}_j)\rangle \ \text{and} \ \langle \rho(\bar{u}_i)\rho^*(\bar{u}_j)\rangle. \ \text{The value of}$  the product  $\langle \rho(\bar{u}_i)\rho^*(\bar{u}_j)\rangle \ \text{which is a circular complex}$ 

Gaussian function is given in equation (1). Then

$$\vec{\Gamma}(\mathbf{r_i}, \mathbf{r_j}) = K' I_{LO} \int_{\bar{\mathbf{u}}_j} \int_{\bar{\mathbf{u}}_i} R_d \langle E_O(\bar{\mathbf{u}}_i) E_O^*(\bar{\mathbf{u}}_j) \rangle \delta(\bar{\mathbf{u}}_i - \bar{\mathbf{u}}_j)$$

$$\times \exp[-jk/f(\bar{u}_i \cdot \bar{r}_i - \bar{u}_j \cdot \bar{r}_j)] d^2\bar{u}_i d^2\bar{u}_j$$
 (23)

where the index k is deleted for the same sampling is understood.

Now  $R_d < E_O(\overline{u}_1)E_O^*(\overline{u}_1) > = <I(\overline{u}_1) >$ so

$$\vec{\Gamma}(\vec{r}_{i}, \vec{r}_{j}) = K' I_{LO} \int_{\vec{u}_{i}} \langle I(\vec{u}_{i}) \rangle \exp[-jk/f(u_{i} \cdot (\vec{r}_{i} - \vec{r}_{j})] d^{2}\vec{u}_{i}$$

$$= K' I_{LO} \vec{g} \{ [(\vec{r}_{i} - \vec{r}_{j})]/\lambda f \}$$
(24)

where  $\sqrt[3]{(r_i - r_j)/\lambda f}$  is the average spatial Fourier transform of the target intensity. The autocorrelation function is

$$\vec{\Gamma}(\vec{r}_1, \vec{r}_1) = K' I_{LO} \vec{Q} (\vec{r}_1/\lambda f)$$
 (25)

If the motion is small and slow, the average intensity is nearly constant and can be written as an intensity  $(\bar{r}_1/\lambda f)$  so

$$\vec{\Gamma}(\vec{r}_1, \vec{r}_1) = K' I_{LO} \mathcal{J}(\vec{r}_1/\lambda f)$$
 (26)

The inverse spatial Fourier transform is proportional to the intensity at the point  $\bar{u}_i$  in the target or

$$\vec{\Gamma}(\vec{u}_1, \vec{u}_1) = K' I_{LO} I(\vec{u}_1)$$
 (27)

This proves that the speckle in the image can be reduced if the number of samplings are very large and the autocorrelation of the modulii of the same position is averaged over many perspectives N.

The averaged cross correlation of signals obtained at the same point in different samplings separated by a time  $\tau$  will yield information about the target speed perpendicular to the line of sight. In the time  $\tau$  the point  $\bar{u}_i$  in one sampling moves to  $\bar{u}_j$  in another sampling so  $\bar{u}_j = \bar{u}_i \pm \bar{v}_\perp \tau$  where  $v_\perp$  is the transverse speed. The cross correlation between point  $\bar{u}_i$  and  $\bar{u}_j$  in different samplings, employing the exact Rayleigh Sommerfeld theory, is

$$\Gamma(\bar{r}_{i}, \bar{r}_{j}, \tau) = K' I_{LO} \int_{\bar{u}_{j}} \int_{\bar{u}_{i}} E_{O}(\bar{u}_{i}) E_{O}^{*}(\bar{u}_{j}) \rho(\bar{u}_{i}) \rho^{*}(\bar{u}_{j})$$

$$\times \exp[jk/2f(|\bar{u}_{i} - \bar{r}_{i}|^{2} - |\bar{u}_{j} - \bar{r}_{j}|^{2})] d^{2}\bar{u}_{i}d^{2}\bar{u}_{j} \qquad (28)$$

Now using the fact  $\bar{u}_j=\bar{u}_i\pm\bar{v}_\perp$   $\tau$  and the fact that  $\tau$  and  $\bar{v}_\perp$  are small then

$$(|\bar{u}_{i} - \bar{r}_{i}|^{2} - |\bar{u}_{j} - \bar{r}_{j}|^{2}) = r_{i}^{2} - r_{j}^{2} + u_{i}^{2} - u_{j}^{2} - 2\bar{u}_{i} \cdot (\bar{r}_{i} - \bar{r}_{j} \pm \bar{v}_{\perp}\tau)$$
(29)

Now

$$\Gamma(\bar{r}_{i}, \bar{r}_{j}, \tau) = K' I_{LO} \exp[jk/2f(r_{i}^{2} - r_{j}^{2})]$$

$$\int_{\bar{u}_{j}} \int_{\bar{u}_{i}} E_{o}(\bar{u}_{i}) E_{o}^{*}(\bar{u}_{j}) \rho(\bar{u}_{i}) \rho^{*}(\bar{u}_{j}) \exp[jk/2f(u_{i}^{2} - u_{j}^{2})]$$

$$\times \exp\{-jk/f[\bar{u}_{i} \cdot (\bar{r}_{i} - \bar{r}_{j} \pm \bar{v}_{\perp}\tau)]\} d^{2}\bar{u}_{i} d^{2}\bar{u}_{j}$$
(30)

If this equation is averaged over a large number of samplings N over a time period T, the sum is replaced by an integral over t,

$$\vec{\Gamma}(\vec{r}_i, \vec{r}_j, \tau) = K' I_{LO} \exp[jk/2f(r_i^2 - r_j^2)]$$

$$\int_{0}^{T} \left\{ \int_{\bar{u}_{j}} \int_{\bar{u}_{i}} [E_{0}(\bar{u}_{i})E_{0}^{*}(\bar{u}_{j}) \rho(\bar{u}_{i})\rho^{*}(\bar{u}_{j})]/T \exp[jk/2f(u_{i}^{2}-u_{j}^{2})] \right\}$$

$$\times \exp\{-jk/f[\bar{u}_i\cdot(\bar{r}_i - \bar{r}_j \pm v_{\perp}\tau)]\} d^2u_id^2u_j \} dt$$

= K' 
$$I_{LO} \exp[jk/2f(r^2_i - r^2_j)] \int_{\bar{u}_1} \int_{\bar{u}_1}$$
  
 $\langle E_O(\bar{u}_i)E_O^*(\bar{u}_j) \rangle \langle \rho(\bar{u}_i)\rho^*(\bar{u}_j) \rangle$ 

$$x \exp(-jk/f[\bar{u}_i \cdot (\bar{r}_i - \bar{r}_j \pm \bar{v}_{\perp}\tau)]) d^2\bar{u}_i d^2\bar{u}_j$$
 (31)

Since the motion is small,  $\langle \rho(\bar{u}_i) \rho^*(\bar{u}_j) \rangle = \lambda^2 R_d / \pi \ \delta(\bar{u}_i - \bar{u}_j)$ , then

$$\Gamma(\bar{r}_i, \bar{r}_j, \tau) = K'' I_{LO} \exp[jk/2f(r^2_i - r^2_j)]$$

$$\int_{\bar{\mathbf{u}}_{\mathbf{j}}} \int_{\bar{\mathbf{u}}_{\mathbf{i}}} R_{\mathbf{d}} \langle \mathbf{E}_{\mathbf{0}}(\bar{\mathbf{u}}_{\mathbf{i}}) \mathbf{E}_{\mathbf{0}}^{*}(\bar{\mathbf{u}}_{\mathbf{j}}) \rangle \delta(\bar{\mathbf{u}}_{\mathbf{i}} - \bar{\mathbf{u}}_{\mathbf{j}}) \exp[jk/2f(\mathbf{u}_{\mathbf{i}}^{2} - \mathbf{u}_{\mathbf{j}}^{2})]$$

$$\times \exp\{-jk/f[\bar{u}_{i}\cdot(\bar{r}_{i}-\bar{r}_{j}\pm\bar{v}_{\perp}\tau)]\} \ d^{2}\bar{u}_{i}d^{2}\bar{u}_{j}$$

= K" 
$$I_{LO} \exp[jk/2f(r^2_i - r^2_j)]$$

$$\int_{\bar{\mathbf{u}}_{\mathbf{i}}} \mathbf{I}(\bar{\mathbf{u}}_{\mathbf{i}}) \exp(-j\mathbf{k}/\mathbf{f}[\bar{\mathbf{u}}_{\mathbf{i}} \cdot (\bar{\mathbf{r}}_{\mathbf{i}} - \bar{\mathbf{r}}_{\mathbf{j}} \pm \bar{\mathbf{v}}_{\perp}\tau)]) d^{2}\bar{\mathbf{u}}_{\mathbf{i}}$$

= K" 
$$I_{LO} = [(\bar{r}_i - \bar{r}_j \pm v_{\perp}\tau)/\lambda f] \exp[jk/2f(r_i^2 - r_j^2)]$$
 (32)

Since the motion is small and slow,

$$\bar{\Gamma}(\bar{\mathbf{r}}_{i},\bar{\mathbf{r}}_{j},\tau) = K \operatorname{ILO} \mathcal{J} [(\bar{\mathbf{r}}_{i} - \bar{\mathbf{r}}_{j} \pm \bar{\mathbf{v}}_{\perp}\tau)/\lambda f] \exp[jk/2f(\mathbf{r}^{2}_{i} - \mathbf{r}^{2}_{j})]$$
(33)

Theoretically from the normalized cross correlation function it is possible to determine the targets velocity component perpendicular to the line of sight.

#### III. Conclusions

The sample averaging of the heterodyne signal will yield a quantity proportional to the square root of the 2-D intensity distribution of the target. The intensity can be calculated from the average of the sum over N samplings of the autocorrelation. Information can be obtained about the target perpendicular component of velocity to the line of sight by averaging the cross correlation from different samples.

## IV. References

- 1. J. H. Shapiro, B. A. Capron, and R. C. Harney, Imaging and target detection with a heterodyne-reception optical radar, Appl. Opt. 20, 3292-3313 (1981).
- D. A. Haner and R. T. Menzies, Reflectance characteristics of reference materials used in the lidar hard target calibration, Appl. Opt. 28, 857-864 (1989).

- J. D. Gaskill, Linear Systems, Fourier Transforms, and
   Optics, John Wiley and Sons, New York, N. Y. (1978).
- 4. J. W. Goodman, Statistical Optics, John Wiley and Sons, New York, N.Y. (1985).

The author wishes to thank RDL for awarding an appointment at the Phillips Laboratory, Kirtland, AFB and the laboratory for making their facilities available.

# EXPERIMENTAL TECHNIQUES FOR HETERODYNE LASER SPECKLE IMAGING

J.K. Boger,
Oregon Institute of Technology
3201 Campus Drive
Klamath Falls, OR 97601
(503) 885-1572

#### **ABSTRACT**

Targets in the laboratory have been successfully imaged using a coherent illumination/heterodyne detection scheme. In principle the technique allows both spatial and temporal Doppler target information to be recovered. Speckled images where averaged to approximate an incoherent image.

#### INTRODUCTION

Experiments in heterodyne laser speckle imaging have been conducted in the laboratory. The heterodyne method of imaging offers the advantages of direct phase measurement and allows the recovery of information related to the radial velocity of the target. The experiment discussed in this paper successfully reconstructed and averaged images of reflective and transmissive targets.

The basic system consisted of an argon laser operating at 488 nm illuminating a target to be imaged. The speckle from the target is captured by an area array element which effectively acts as the pupil of the system. Phase and modulus of the speckle function is recovered by mixing a local oscillator with the target beam. Two dimensional data on modulus and phase is inverse transformed to recover a speckled image. A sequence of data was then taken and a technique for averaging out speckle effects was developed and used. The averaging technique may also help to average out atmospheric effects in ground-based imaging problems.

A method for determining the velocity components of the object using data obtained by the heterodyne method is discused. It has also been found that the misalignment between the local oscillator and the target signal produces a shift in the image with little detectable degradation in the final image.

This report covers the basic theoretical concepts behind the experiment, covers the actual arrangement used and presents the results obtained. No attempt is made to include mathematical rigor. This was investigated by Dr. Richard Anderson from the University of Missouri and a report on theoretical concepts was written. The intent of the discussion here is to convey a solid physical understanding of the concepts behind the experiment and the experiment itself. Theoretical concepts are covered first followed by an experimental description and concluded with the results obtained.

### THEORETICAL BACKGROUND

#### REASON FOR SPECKLE

The primary goal of this experiment is to develop techniques for obtaining the maximum amount of information on a satellite target illuminated with coherent radiation which has propagated through the atmosphere. An incoherent image of that target and its velocity is the goal of this work. Because of the atmosphere, a single snapshot of the target will not produce a good image. From a very simple point of view, we need more data to construct a better image. Recording multiple speckle patterns from the target is one way of obtaining more data.

Speckle is generally thought of as noise in a signal resulting from microstructure in the target creating random phase in the field. Random phase in the field can also be introduced by atmospheric turbulence. The concept behind this experiment is to treat speckle as a tool. Simply put, speckle distributes the data giving us the ability to record many different speckled images of a target and then average these images to reconstruct an unspeckled image. The effect of averaging is to remove the speckle resulting from the microstructure and more importantly remove the effect of atmospheric turbulence. Let us briefly go on to consider the reason the speckle has more information on a target than an unspeckled pattern has.

All of the speckles contain the information on the macroscopic features of the target. This results from the convolution of the random microscopic height function with the function describing the macroscopic features of interest to us. In frequency space, this is a multiplication of the transforms for each function. This multiplication is the reason the speckles contain the information we seek. A simple analogy would be the double slit of finite width. The transform of the double slit is the familiar interference fringes enveloped by the diffractive sinc pattern. In other words, in this analogy the separation of the slits represent the macroscopic information and width of the slits represent the microscopic information. Consequently, in frequency space, macroscopic information is contained within the microscopic information.

#### HETERODYNING

The first objective in the process of constructing an image from speckle data is to determine the modulus and phase of the target field at all points in the pupil plane. This is accomplished by an optical heterodyne process. Heterodyning is done by mixing a local oscillator with the target field. The two fields are separated in frequency by several hertz allowing for a beat signal to emerge from the mixing. The beating actually occurs as an approximately sinusoidal variation in the intensity at the detector. To recover the modulus and phase it is most convenient to Fourier transform the signal in time. Because of the importance of this step in the experiment, a basic description is in order.

Equations 1 and 2 can be used as two fields in the pupil plane to be added together.

$$\mathbf{E}_{T}(\mathbf{x}_{1}, \mathbf{y}_{1}, t) = \mathbf{E}_{0T} \exp[j2\pi f_{1}t + j\phi_{T}(\mathbf{x}_{0}, \mathbf{y}_{0}) + j\vec{\mathbf{k}}\cdot\vec{\mathbf{r}}_{T}]$$
(1)

$$\mathbf{E}_{L}(\mathbf{x}_{1},\mathbf{y}_{1},t) = \mathbf{E}_{0L} \exp[j2\pi f_{2}t + j\phi + j\vec{\mathbf{k}}\cdot\vec{\mathbf{r}}_{L}]$$
(2)

Equation 1 represents the field from the target and equation 2 represents the field from the local oscillator at a given point. Note that the phase factor in 1 carries the information from the target and the amplitude is probably complex. The complex nature in the amplitude results from the fact that there is an arbitrary phase in the field due to the microstructure of the target. Additional phase can be introduced as a result of atmospheric turbulence. Arbitrary phase will carry though all of the calculations and eventually result in the speckling of the image. Equation 2 also carries an arbitrary

constant phase. This phase could be nullified in the experimental arrangement but it has little effect on the results and will be neglected. The amplitude of the local oscillator is a small sampled portion of a large sombero function resulting from the transform of a spatial filter. Consequently the amplitude of this field is considered constant.

At the detector equations 1 and 2 are added together and the result squared as given by equation 3.

$$I \alpha |E_{0T}|^2 + |E_{0T}|^2 + E_{0T}^* E_{0L} \exp[j2\pi\Delta ft + \phi_T] + E_{0T} E_{0L} \exp[-j2\pi\Delta ft - \phi_T]$$
(3)

The phase term from equation 2 has been set to zero and the complex nature of E<sub>T</sub> is evident. Also, f represents the difference in the two frequencies which is detected in the experiment as the beat frequency. The explanation of the data processing is facilitated, albeit unrealistic, if we assume the target field to be purely real. With this simplification equation 3 reduces to equation 4.

$$I \alpha |E_{0T}|^2 + |E_{0L}|^2 + 2E_{0T}E_{0L}\cos[j2\pi\Delta ft + \phi_T]$$
(4)

This cosine function with an added constant term has a particularly simple Fourier transform in time. Figure 1 is the plot of the transform of equation 4.

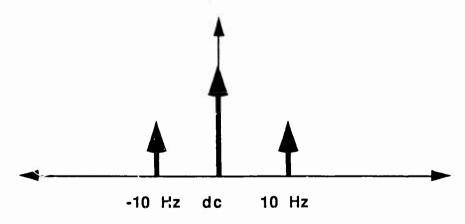


Figure 1. Fourier Transform of equation 4.

Both the modulus and the phase are recovered from the Fourier transform of the heterodyned signal. Phase is determined by taking the arctangent of the imaginary part

of the first frequency component divided by its real part. The modulus is a relative function of the strength of the first frequency component.

There are two factors which can contribute to erroneous results using the algorithm describe. The first concerns an incorrect estimate of the modulus. This is an obvious error which is easily seen in equation 3 where the amplitude is a mix of the local oscillator and the target field. It is possible to improve the estimate of the modulus simply by multiplying the function by its complex conjugate. Doing this gives the square of the target field multiplied by a constant term which is the local oscillator. The second problem encountered with the algorithm in the determination of the phase. In the computer program used the phase is calculated from data taken at the beat frequency. If there is a shift or broadening of this component, it will change the resultant phase. The phase problem was not addressed in this work.

The local oscillator is not considered a problem as might be perceived from the previous discussion. Instead, the local oscillator offers the advantage of increasing the signal to noise ratio. This is because the amplitude we seek has been enhance I by a constant value which is proportional to the square root of the power in the local oscillator. This boost in power is an important advantage of the heterodyne imaging technique over other methods such as correlography.

#### **IMAGING**

The purpose of the heterodyning technique is to construct a two dimensional function of the target in frequency space. To do this an array of detectors in the form of a CCD camera was used. The array elements had a finite size which must be taken into account when adjusting parameters which control the speckle size. The idea is have the smallest individual speckle cover approximately 16 (a 4 by 4 square) elements in the array. This allows for each speckle to be sampled a number of times which provides a much better estimate of the speckle as a smoothly varying function. In other words, multiple sampling kept us above the Nyquist limit.

Speckle size in the lower limit is governed by the macroscopic dimensions of the target. Equation 5 was used to estimate maximum target dimensions.

$$w = \lambda f/x \tag{5}$$

Here x represents the width of the speckle which is taken as four times the CCD element width, f is the focal length of the transform lens and w is maximum target dimension. This equation is easily derived from the interference of two waves originating from opposite points on the target.

At this point, the heterodyned speckle data has been collect. And manipulated to produce a two dimensional frequency space function. To produce an image from this data it is necessary to inverse spatially Fourier transform. With this done, a speckled image of the original target is obtained. It is important to emphasize the idea that the image is speckled. A speckled image will always be obtained with the heterodyne imaging method because there is no way to remove the arbitrary phase. This is also true of other imaging methods [1]. Atmospheric disturbances will add to this problem. The only way to remove the speckle from the image is to average many images together. Averaging washes out the speckle effect since the actual speckles in the image occur at random positions.

Image averaging is used to produce an unspeckled or incoherent image. To average images, the final speckled images were added togetherand then divided by the appropriate number. In order to make averaging work effectively, it is important to obtain new speckle data for each speckled image. This is simply done since the target is in motion and consequently the speckle is constantly being scanned across the pupil. Clearly the rate at which the speckle scans will dictate the timing for the heterodyne signal. The speckle scan also can give information on the transverse velocity of the target.

#### VELOCITY OF THE TARGET

In addition to the image, it is also desirable to determine the velocity of the target. There are two basic parts to determining the velocity. The first is the radial velocity which will effect the frequency function obtained in the heterodyne process. The second is the transverse velocity which is determined by tracking the rate of the speckle motion. Consider each in turn.

Radial velocity will produce Doppler shifts in the frequency of the target field. The Doppler equation governing the change in frequency is given by equation 6.

$$f = f (1 \pm v_r/c)\gamma$$
where
$$\gamma = (1 - (v/c)^2)^{1/2}$$
(6)

Here the  $v_r$  is the radial velocity of the target. Rearranging this equation and solving for velocity gives equation 7 which relates the radial velocity to the change in frequency.

$$Vr \cong \Delta f \lambda \tag{7}$$

Here  $\Delta f$  is the change in frequency resulting from the Doppler shift. If the radial velocity is uniform, the frequency function will be shifted. If the velocity is not uniform, the function will be broadened. This equation shows that small velocities will produce large changes in the frequency. This can be a problem because the shift is seen in the heterodyne signal which may be running at a low frequency due to speed of detection. According to this equation a shift of one hertz is produced by a uniform velocity of one wavelength per second! Increasing the speed of detection by two orders of magnitude would still restrict detectable velocities to incredibly small values.

Before leaving the topic of radial velocity it should be pointed out that this motion causes an optical path change in the interferometer of which the target is a part of. Phase change in the target field is a function of the radial velocity and time. Equations 8 expresses the phase term and equation 9 is the resulting fringe frequency, for the phase term and equation 9 is the resulting fringe frequency, for the phase term and equation 9 is the resulting fringe frequency.

$$\phi = (\vec{k} \cdot \vec{v})t \tag{8}$$

$$f_{OPD} = v/\lambda$$
 (9)

Equation 9 yields the same value for fringe frequency as the Doppler effect.

Consequently the frequency shift produced by a moving target is double the Doppler effect.

Transverse velocity is related to speckle motion in the pupil plane by the geometry shown in figure 2.

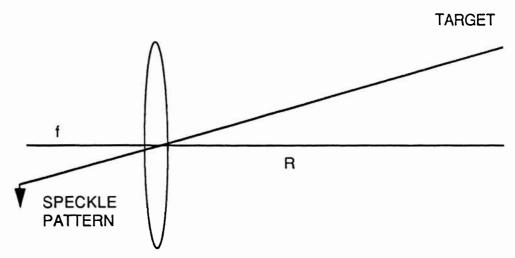


Figure 2. Geometry relating target motion to speckle motion.

The principal ray through the lens sets up a very simple relationship between speckle velocity and the target's velocity.

$$v_{target} = v_{speckle}(R/f)$$
 (10)

It is clear from this relationship that the real challenge is found in tracking speckle motion in time.

Speckle data is taken at discrete intervals in time which produces moduli which are effectively shifting in the pupil plane. Determining the the shift in the speckle and knowing the time interval between moduli leads to the velocity of the speckle. By cross correlating two moduli functions and then normalizing the result, the position shift of the centroid is obtained. In other words, the of the autocorrelation of either moduli would be at the center of a two dimensional map. The cross correlation produces a shift in the centroid because the functions match only when one is shifted relative to the other. To actually calculate the shift accurately it is necessary to normalize the cross correlation by the product of the autocorrelations of each moduli function. Equation 11 is the expression used to preform normalized cross correlation.

$$1/Q \int \int dx \, dy \, M_1(x,y) \, M_2(x+u,y+v)$$

$$Q = \left\{ \int \int dx \, dy \, [M_1(x,y)]^2 \int \int dx \, dy \, [M_2(x,y)]^2 \, \right\}^{1/2}$$
(11)

The actual calculations are facilitated by transforming the moduli and the multipling the transforms. This avoids the tedious integration.

## **EXPERIMENTAL ARRANGEMENTS**

#### TRANSMISSIVE TARGETS

Basic experimental methods used to record and interpret data have been successfully demonstrated in earlier work on imaging correlography [2]. The following two figures contain the basic outline of the experimental arrangement used in the transmissive portion of the experiment.

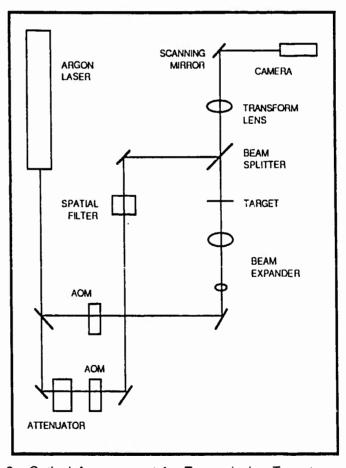


Figure 3. Optical Arrangement for Transmissive Targets.

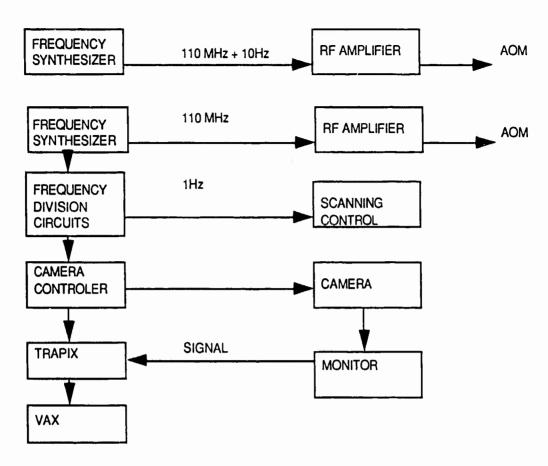


Figure 4. Electronic and data acquisition arrangement.

The laser was operated at 488 nm in the TEM<sub>00</sub> mode at 100 mW with an intracavity etalon. The etalon was used to increase the coherence length making the construction of the basic interferometer easier. The Isomet acousto optic modulators where run at 110 MHz. The modulators along with the frequency synthesizers were of a very high quality as has been documented [3]. Later in the experiment the stability of the modulators was lost. The problem appeared to be in the RF amplifiers. The beam expander in the target arm of the interferometer created a collimated beam 1 in diameter. The local oscillator ran through a spatial filter containing a 20x microscope objective and a 15 micron pinhole. The intensity of the local oscillator was controlled with a variable attenuator as shown in figure 3. The target used was a masked off NRC RES-1 exposing the 0.1 group. In order to obtain a scattering effect, a piece of 3M clear plastic tape covered the target. Several different size targets were tested. The half millimeter bar target was the primary target used while optimizing the system.

The transform lens used was a 50 cm focal length lens with a 2 inch aperture. The focal length was chosen based on the size of the pixel elements in the camera. Equation 12 was used to estimate the focal length need for the experiment.

$$f = 4dw/\lambda \tag{12}$$

Here d represents the maximum width of the target, w is the element size of the camera and  $\lambda$  is the wavelength. The constant factor of four was included to allow the smallest speckle to cover four pixels in the camera. Assuming a maximum target dimension of 4 mm and a pixel element size of 15  $\mu$ m, a focal length of 50 cm was calculated. This focal length was not exact but simply the closest value to those available.

The scanning mirror was used to simulate the transverse motion of the satellite. The scanning mirror is triggered by a 1 Hz signal obtained from the master oscillator so that the scan begins when the camera starts to take data. The scan is very slow because a fast scan would reduce the data from the heterodyne signal. The scan rate could be increased by increasing the rate at which the camera takes data. In a real system this may require using a parallel data acquisition scheme unlike the camera used in this experiment. The purpose of the scan is to average the speckled images with new speckle data as discussed in the previous section. The actual device used was a scanning mirror from General Scanning controlled with an external input from a function generator. The function controlling the scan was a triangular wave operating at a very low frequency (f=.004 Hz).

The camera used to record the data was a Cidtec CID 2250. The camera was triggered by a 100 Hz signal which limited the data to 64 rows of elements. The trigger signal was obtained from the 10 MHz square wave off of the master oscillator in the frequency synthesizers. This trigger was divided down to 100 Hz by five divide by 10 integrated circuits(SP8504). The trigger used for the scanning mirror was the camera trigger divide by 100. With the camera running at 100 Hz and the acousto-optic modulators separated by 10 Hz, it is clear that the heterodyne optical signal would be sampled 10 times during one optical beat cycle.

The electronic portion of the experiment really started with the camera passing data to the computer for collecting and processing. In order to align the system and set the scanning mirror amplitude, the camera was connected to a real time monitor. This allowed for direct viewing of the speckle and its motion. The speckle data was record in dynamic memory by a hardware device called a Trapix 5500 made by Recognition Concepts Inc.. This device was also synchronized by the 100 Hz signal triggering the camera. Data was stored and processed on a micro VAX. The main program controlling the experiment was called IMAGE, written by Applied Technology Associates for the Air Force Weapons Laboratory. Several manuals on the operations of the image program and the Trapix were referenced [4-6]. A subtask was written in the IMAGE environment called HETERODYNE which directly controlled data acquisition and processing.

The HETERODYNE program will acquire data, review this data by displaying the captured frames on the monitor, and process the data. In the process mode, the program displays as many frames on the screen to be used in the calculation as the operator chooses. One frame is a single snapshot of the speckle pattern. The operator is limited to choosing from 10 to 250 frames in increments of 10. The program then does a fast Fourier transform with respect to time on the data element by element. In order to develop a two dimensional plot of modulus and phase, all of the elements are transformed and then plotted. The result is a two dimensional plot of modulus and a separate plot for phase. Both modulus and phase plots are displayed on the screen side by side. Using modulus and phase data, an inverse Fourier transform in space is performed to reconstruct a speckled image. This image is displayed next to the phase map. As long as the operator chooses more than ten frames to process, a frequency plot will also be displayed. This plot is useful for observing the Doppler shifts or broadening which may have occurred.

The HETERODYNE program was also capable of averaging images. The purpose of averaging is to remove the speckle effect in the final image. To do this, the operator instructs the computer to average as many or as few speckled images as desired. Care had to be taken here to insure that the scanning mirror did not change direction during the period of data collection. Each speckled image used in the average is obtained from ten or more frames of data. The number of frames to process for a single speckled image was chosen by the operator. Twenty frames of data became the standard choice because it was relatively fast to process, provided a rough frequency plot and had a more consistent modulus when compared to that obtained from ten frames. Finally, the operator could choose the time delay between speckled images. The time delay option was included to allow the operator to adjust the data collection rate such that each new speckled image was obtained from new speckle data. Figure 5 pictorially represents how the speckle function has changed from time zero to time one.

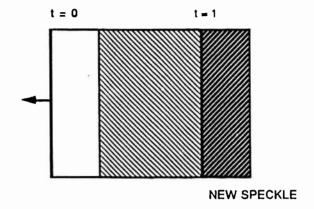


Figure 5. Effect of speckle scanning off the pupil.

In this figure, the box represents the pupil of the camera and the arrow indicates the motion of the speckle pattern. The first box on the left represents data taken at time zero and the shaded box on the right is data taken at the later time. The heavily shaded area indicates new speckle data which allows for a new speckled image significantly different from the first. In general delays where chosen such that approximately one quarter of the pupil had new speckle data in it. This allowed us to track the speckle in an attempt to determine transverse velocity. Typically, the experiment worked well with delays of approximately 15 seconds.

#### REFLECTIVE TARGETS

Figure 6 shows the optical arrangement used to record images of reflective targets. The basic Mach-Zender interferometer remains unchanged from the transmissive case except for the deflection of the target beam. The modification was made simple due to the long coherence length of the laser.

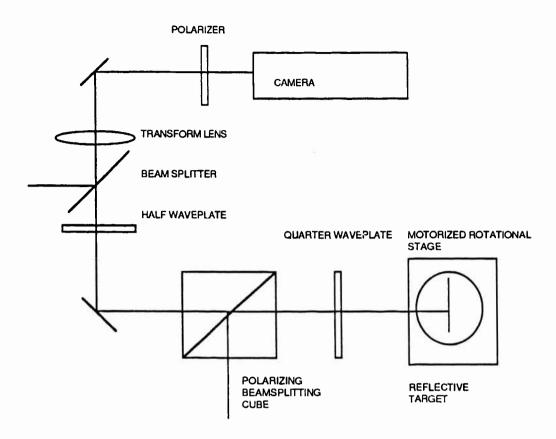


Figure 6. Optical arrangement for reflective targets.

The primary change in the arrangement is the deflection of the beam through a retroreflective system. The retroreflective system used polarization of the beam to direct the full intensity of the illuminating laser to the target. The target was painted with retroreflective scotchlite paint to boost the signal. The target was also placed on a Klinger programmable motorized translational stage used to produce radial motion. However, this stage proved to be unusable due to the extremely low velocities required for a detectable change in the frequency. To scan the speckle pattern the target was mounted on a NRC 471 rotational stage driven by a motorized Oriel micrometer. Clearly increasing the speed of detection is the solution to velocity detection problems.

The reflective target was a piece of sheet metal cut into the shape of a sharks tooth. It was necessary to use this material and to run the laser at 200 mW in order to get enough signal to the camera for detection. The physical dimensions of the target are shown in figure 7. Only one target was made and tested due to the relative difficulty producing accurate small targets by hand.

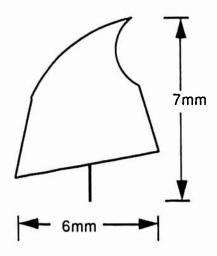


Figure 7. Reflective target geometry.

#### **RESULTS**

The experiment was successful at obtaining speckled images of both reflective and transmissive targets. The images were averaged to estimate the incoherent image desired. The experiment was also successful at cross correlating moduli for the purpose of determining velocity. Some Doppler effects where also observed with the experiment, but the effects where small and no quantitative data was gathered. The results of the experiment are most easily presented in a series of figures which were obtained directly from the screen of the Trapix monitor using a Sieko CH-5504 printer.

The first output to consider is shown in figure 8 and is the result of 40 snapshots of the speckle pattern processed into an image. The target in this case was the NRC RES-1 1/2 mm bars. This output contains 21 individual snapshots of the speckle pattern in 64 by 64 pixel blocks. Discontinuities in the patterns help to distinguish the blocks. Located four blocks from the top left of the figure is the calculated modulus map. To the right of the modulus map is the phase map and constructed image. The phase map varies from 0 phase in the dark areas to  $\pi$  phase in the light areas. On the far right of the figure there is a gray chart indicating the strength of the speckle. At the bottom of the figure is the plot of the Fourier transform in time of the original heterodyned signal. Notice that at

Fo (10 Hz) there is a large peak while much smaller peaks appear at 2Fo and 3Fc. These smaller peaks arise from harmonics in the acousto optic modulators.

Results from averaging speckled images are seen in figures 9 and 10. Figure 9 is the result of averaging 70 speckle images of the 1/2 mm bars. Each speckle image was calculated from 20 frames of data. Shown are the last calculated modulus map, phase map and speckled image along with the resulting averaged image. Figure 10 displays the results obtained for the reflective target. As in figure 9, the last speckled image is shown along with the final average. Notice the pin at the top of the image which was the support pin holding the target in place. This averaged image was produced from 100 independent speckle images. Each speckle image was calculated from 10 frames of speckle data. The reason for using fewer frames of data for the reflective target was the instability experienced with the equipment.

Figure 11 shows the results of the cross correlation. The image was doubled to allow for easy interpretation. In order to produce good results from the cross correlation it was necessary to filter out the lower level signals in the maps and then square the elements making up the map. The two moduli were separated by 2.8 seconds and are displayed along with the normalized cross correlation. Notice that the shift in the centroid matches the shift in the speckle pattern. The centroid was found to have shifted by 13 pixels in one direction only, giving a speckle velocity of 69  $\mu$ m/s. In general this method for finding transverse velocity works well provided the data used is clean.

The final result obtained concerned the stability of the alignment between the target beam and the local oscillator. Initially it was assumed that this alignment would be critical. Experience proved that this was not the case. Instead, it was found that a slight misalignment produced a linear phase shift in the Fourier transform of the target at the pupil. This linear phase inverse transfroms as a lateral shift in the image[7]. This final result can be seen in figure 10. In the figure, it can be seen that the sharks tooth image is shifted downward from the center. This effect was produced by inducing an intentional misalignment before taking data.

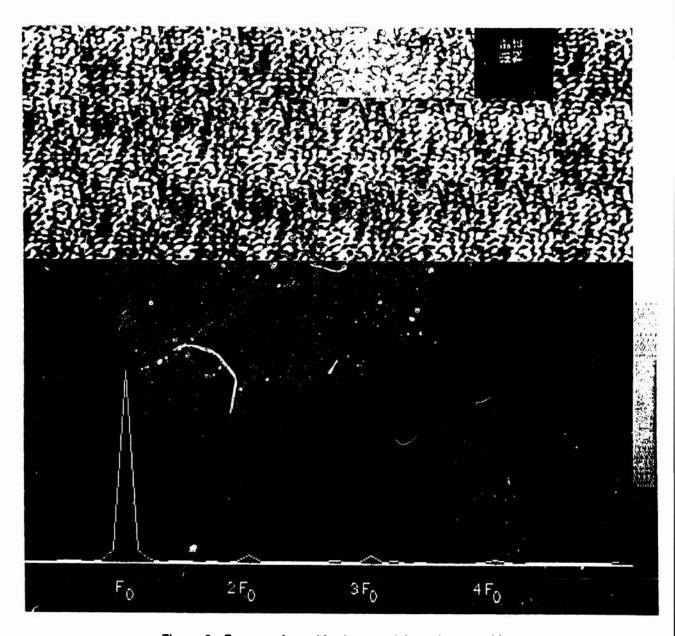


Figure 8. Frames of speckle data, modulus, phase and image.



Figure 9. Averaged image from a transmissive target.



Figure 10. Averaged image from a reflective target.



Figure 11. Cross correlation of speckle.

# **ACKNOWLEDGMENTS**

This work was supported through a summer contract with AFSOR. Special recognition should go to D.G. Voelz and J.D. Gonglewski initiating and guiding the project. Additionally, I would like to recognize B. Pierson and B. Speilbush for their excellent work in data acquisition and code development for the heterodyne experiment. Many others at the Phillips laboratory, too numerous to mention, have contributed to help make this project a success.

### REFERENCES

- 1 P.S. Idell, J.R. Fienup and R.S. Goodman, "Image synthesis from non imaged laser-speckle patterns", Opt. Lett. Vol. 12, p. 858, (1987).
- J.D. Gonglewski, D.G. Voelz, P.S. Idell and J. Knopp, "Image synthesis from nonimaged laser-speckle patterns: experimental verification", Opt. Lett. Vol. 14, No. 3 p. 154, (1989).
- 3 S. Hanes, "Characterization of acousto-optic modulators", Internal letter to the Phillips Laboratory Imaging branch, (1990).
- Applied Technology Associates, Inc., "Image user functions coded in support of ARBB Trapix", Revision 2, (1990).
- 5 Applied Technology Associates, Inc., "Image users guide", Volume 1, (1987).
- Applied Technology Associates, Inc., "Appendices to image users guide", Volume 2, (1987).
- J.D. Gaskill, Linear Systems, Fourier Transforms and Optics", (John Wiley and Sons, New York 1978), p. 199.

#### FIBEROPTIC INTERFEROME FER STUDIES

#### Douglas A. Christensen, Professor University of Utah

#### Abstract

Work was accomplished in the following three areas: 1) white light fringes were obtained through a prototype 2 x 60m fiberoptic interferometer by first utilizing a variable coherence length laser diode source to balance the arms; 2) the interferometer was characterized with regard to temperature sensitivity, tringe contrast and polarization properties; and 3) the effect of fiber dispersion in an interferometer with unequal fiber lengths was experimentally and theoretically explored.

#### I. INTRODUCTION

Long baseline optical interferometry accomplishes high spatial resolution images of distant objects by separating two (or more) receivers tens or hundreds of meters apart, then recombining their signals to obtain phase and amplitude imformation from the target. The signals must be recombined with minimal phase distortion. One current technique, though complex, is to use long temperature-controlled evacuated tubes to propagate the light from each receiver to a central location for recombination.

This summer's project investigated the use of single-mode optical fibers to replace the evacuated tubes in a long baseline interferometer. Fibers have the potential advantages of being less costly, more flexible in path arrangement, possessing no diffraction widening of the beam, and needing procise alignment only at the two fiber ends. Disadvantages include limited light collection efficiency into the single-mode fiber, some loss (though small), and dispersion effects over the finite source bandwidth. Some convenient means for the control and modulation of the optical path length difference (OPD) between the two arms must also be developed and tested.

A prototype fiber system had already been bench assembled at Phillips Laboratory (using some parts and fibers from an earlier system developed by OPTRA Corp.), but white light fringes had not been initially obtained. Figure 1 shows a schematic diagram of the overall

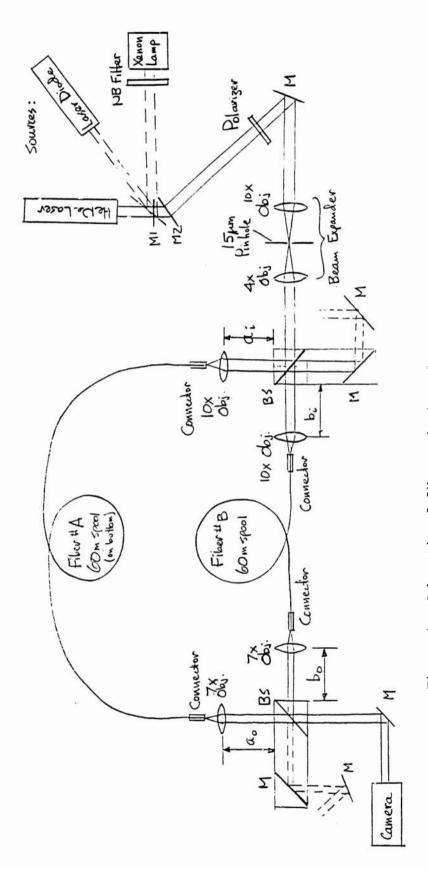


Figure 1 - Schematic of fiberoptic interferometer.

system. In each of the two arms was a 60m long spool of single-mode polarization-preserving fiber, apparently physically matched to each other in length to less than 1mm. The source was a xenon lamp with a 10nm-wide bandpass filter.

During the course of the summer, the following goals were undertaken: 1) To obtain fringes with the 10nm-wide "white light" source. This was accomplished by first using a variable coherence length laser diode to match optical path lengths. 2) To characterize the system with regard to drift, coherence length, etc. 3) To predict and measure the effects of fiber dispersion on phase fidelity.

#### II. USE OF LASER DIODE TO MATCH OPTICAL PATH LENGTHS

In order to obtain fringes from the broadband source, the optical path lengths of the two interferometer arms must be matched to within the source's coherence length, which, for a 10nm-wide source centered at 656nm is:

$$l_c = \frac{\lambda^2}{\Lambda\lambda} = 43 \mu m$$

This is difficult since this close match must be obtained over paths of longer than 60m, including the spools of fiber, which (although supposedly matched to within 1mm in length) may possess slight refractive index differences resulting in much greater optical path (OPD) mismatch. Balancing the paths often becomes a difficult trial-and-error search.

A more systematic approach was developed here. We used a 675nm laser diode (Toshiba TOLD 9200) whose coherence length (inversely related to spectral width) can be varied in a quasi-continuous manner by changing its dc drive current and, correspondingly, its stimulated emission gain. This is used to balance the paths in the following steps:

- 1. Start with maximum drive current to the diode (approximately 61mA). This gives the narrowest spectrum for a course path adjustm. Int. Find fringes and adjust one path for maximum fringe contrast.
- Reduce drive current in steps (near the lasing threshold), adjusting path length for maximum fringe contrast in each step. For intermediate currents, multiple fringe envelopes will be found; lock on to the one with the maximum contrast.

- 3. Continue reducing the drive current until the laser diode is clearly below threshold (less than 40mA) and the spectrum is widening. Continue to adjust the path for maximum fringe contrast.
- 4. Replace the laser diode source with the 10nm filtered xenon source. White light fringes should be obtained with only slight path adjustment.

A key element of this technique is the changing laser diode spectrum versus drive current. It was important, then, to measure the output power spectra from the laser diode. A SPEX 3/4 meter Czerny-Turner spectrometer was used. Some representative spectra for variuos drive currents are shown in Fig. 2. Clearly noticable is the broadening of the spectra (with resulting decrease in overall power) as the drive current is lowered.

At high currents (Fig. 2a), the laser spectrum is a narrow peak (with perhaps two modes) leading to a relatively long coherence length:

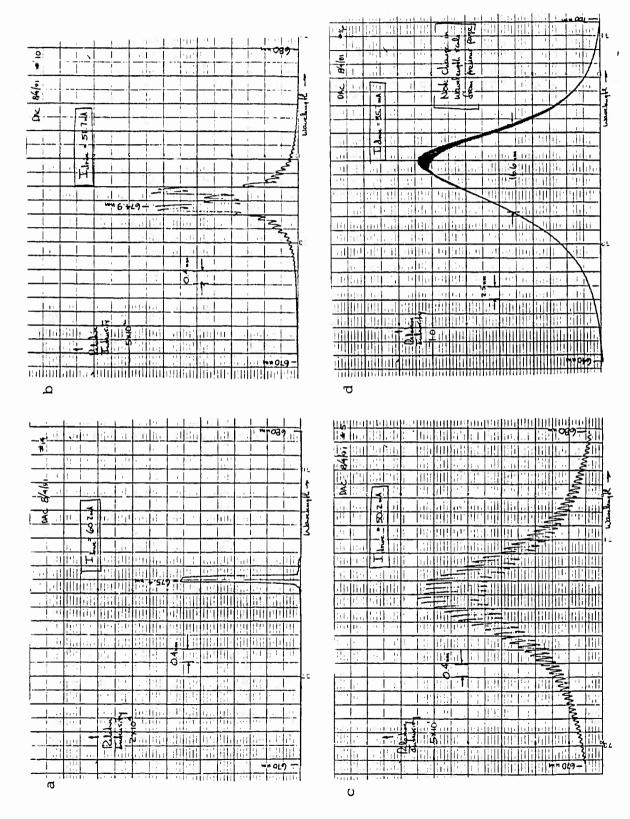
$$l_c = \frac{\lambda^2}{\Delta \lambda} = 2.3 \text{mm}$$

making initial alignment relatively easy. Then, as current is reduced, less stimulated gain in the laser results in more longitudinal modes present and a relatively larger percentage of the smooth spontaneous emission floor (Figs. 2b and 2c).[1] As current is reduced further below threshold, the output becomes predominantly broadband spontaneous emission (>10nm) when the laser is operating essentially as an LED (Fig. 2d). For the 16.6nm spectral width of Fig. 2d, the coherence length is:

$$l_c = \frac{\lambda^2}{\Delta \lambda} = 27.4 \mu m.$$

At this point, if the interferometer alignment has been tuned to stay at maximum fringe contrast as the current is reduced, the laser source can then be replaced with the filtered xenon source, and the interferometer should still be balanced to a sufficiently small OPD to obtain fringes.

It is informative to calculate the interference fringe pattern versus OPD for the spectrum shown in Fig. 2c, typical of an intermediate drive current near threshold. The spectrum can be approximately modeled as the sum of two parts, a lorentzian-shaped curve representing the spontaneous emission background and a smaller periodic portion (conveniently modeled as the product of a cosine function with a gaussian envelope) representing the longitudinal modes of



stimulated emission:

$$S(v) = aL(v) + bG(v) \cdot \cos(2\pi v / \Delta v')$$

where S(v) is the power spectral density, L(v) is a lorentzian function with FWHM linewidth of  $\Delta v_L$ , G(v) is a gaussian function with FWHM linewidth of  $\Delta v_G$ , and a and b are relative spectral strengths. Figure 3 shows the total power spectral density modeled as a sum of these functions.

The fringe visibility V(x) in the interferogram resulting from this source can then be obtained from the following relationships [2]:

$$V(x) = K_1 \gamma(x/c)$$

$$\gamma(\tau) = \left| \frac{\int_0^\infty 4S(v)e^{-j2\pi v\tau} dv}{\int_0^\infty 4S(v)dv} \right|$$

$$= K_2 \left| \int_0^\infty S(v)e^{-j2\pi v\tau} dv \right| \equiv K_2 \left| \Im^+ \{S(v)\} \right|$$

where V(x) is the fringe visibility,  $\gamma(\tau)$  is the modulus of the complex degree of coherence,  $K_1$  and  $K_2$  are constants, and  $S^+$  represents the Fourier transform for positive frequencies only.

The Fourier transformation can be performed on each component of S(v), then the modulus combined as indicated in the lower part of Fig. 3. The transform of the lorentzian part leads to an exponential term in the fringe visibility with a FWHM width of:

$$\nabla \iota_{\mathbf{L}} = 0.44 / \Delta \nu_{\mathbf{L}}$$

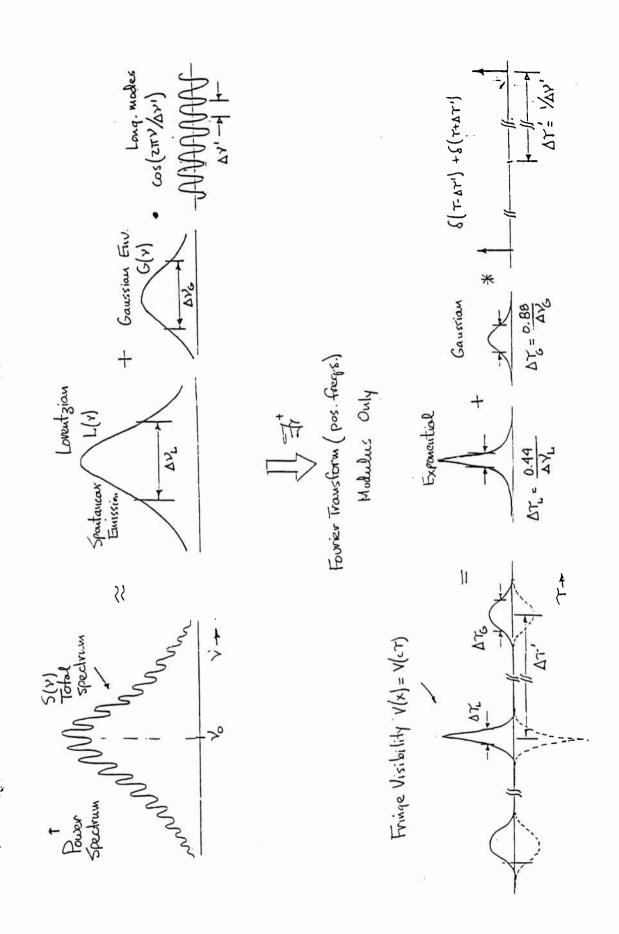
while the cosine with gaussian envelope results in two gaussians positioned on either side of the exponential by a displacement of:

$$\nabla \tau' = 1 / \Delta \nu'$$

with each gaussian having a FWHM width of:

$$\nabla \tau_{\rm G} = 0.88 / \Delta v_{\rm G}$$
.

An experimental verification of this predicted fringe visibility was obtained by using the laser diode as a source in the fiber interferometer at a drive current (49.6mA) near the conditions for which Fig. 2c applies. The experimental setup for recording the fringes is



with theoretical prediction of its resulting fringe visibilty envelope. Figure 3 - Model of power spectrum of laser diode at intermediate drive current,

shown in Fig. 4. Figure 5 shows the resulting interferogram. Note that the fringe visibility follows the same general form as predicted by the above transformation results and as shown in the lower left of Fig. 3. In particular, using Fig. 2c,  $\Delta\lambda_L \approx \Delta\lambda_G \approx 3.2$ nm, so  $\Delta\nu_L \approx \Delta\nu_G \approx 2.11 \times 10^{12}$  Hz. Thus  $\Delta x_G = c\Delta \tau_G = 0.88c/\Delta\nu_G = 125\mu\text{m}$ , which closely corresponds to the experimental FWHM in Fig. 5. Similarly,  $\Delta x_L = c\Delta \tau_L = 63\mu\text{m}$ . Also, again from Fig 2c,  $\Delta\lambda' \approx 0.133$ nm, so  $\Delta\nu' \approx 8.76 \times 10^{10}$  Hz. Thus  $\Delta x' = c\Delta\tau' = c/\Delta\nu' = 3.42$ mm, which again corresponds well to the experimental value in Fig. 5.

Note incidentally that the coherence length of the central fringe envelope shown in Fig. 5 when the laser is driven at an intermediate drive current is about  $60\mu m$ , which falls between the extremes at high drive current (2.3mm) and at low drive current (27.4 $\mu m$ ), as expected.

#### III. WHITE LIGHT FRINGES AND INTERFEROMETER CHARACTERIZATION

Using the technique described in the previous section, fringes were then obtained through the 2 x 60m fiber interferometer with a white light (xenon lamp) source filtered by a 10nm-wide bandpass filter centered at 565nm (subsequently changed to other center wavelengths with results described later). Using the setup of Fig. 4, the interferogram in Fig. 6 was obtained. The fringe contrast was suprisingly good, indicating good polarization holding capabilities of the single-mode fibers. The FWHM width of the fringe visibility in Fig. 6 is approximately 45 $\mu$ m compared to a predicted width of  $0.88\lambda^2/\Delta\lambda \approx 28 \mu$ m for a 10nm-wide gaussian spectrum centered at 565nm. The difference between the experimental value and the theoretical prediction may be possibly due to the filter being narrower than 10nm and of a more rectangular shape than gaussian. (Later measurements on the filter showed its center wavelength to be 576nm and its FWHM to be 9.1nm.)

Once white light fringes were obtained, some characterization of the fiberoptic interferometer was done. First, the difference in air paths outside each of the fiber spools was measured at maximum fringe contrast. The difference was:

Path B - Fath A = 236.5mm - 230.5mm = 6.0mm.

Thus Fiber A appears optically to be 6.0mm longer (in optical length) than Fiber B, even

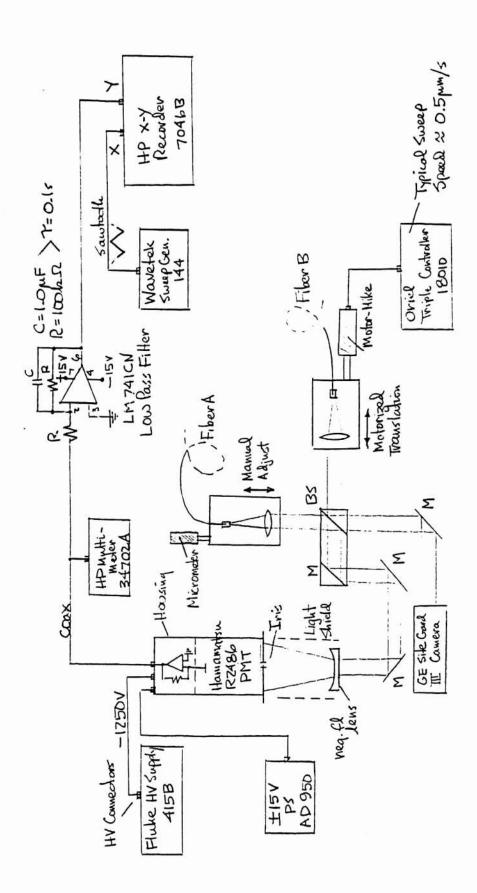


Figure 4 - Experimental setup for recording the fringes as OPD is varied ("interferogram")

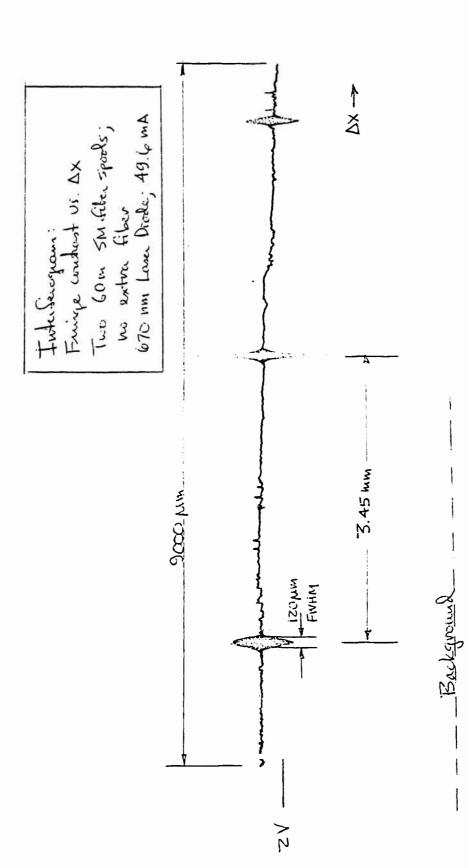
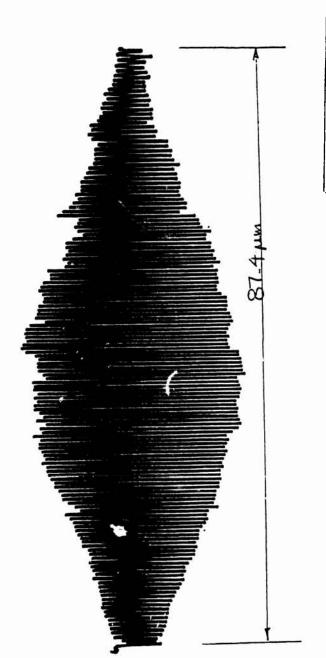


Figure 5 - Interferogram using laser diode at an intermediated drive current of 49.6mA. Thus the laser's power spectrum is approximately that shown in Fig. 2c. Compare the fringe visibility to the predicted pattern in the lower left of Fig. 3.



<u>و</u>ا کِ

Fruge Condust FOSI 60 m SM fibers xenon W/NB filler 505 nm; DN=10 nm

2 my Buckground

0

Figure 6 - Interferogram for xenon source through 10nm wide bandpass filter.

though they are supposed to be physically within 1mm in length. This finding shows that: 1) they are actually unequal in physical length by greater than 1mm; 2) they have a net difference in the mode refractive index; or 3) a combination of these two effects.

The performance of the interferometer was also tested for different orientations of the input polarization. The results are shown in Fig. 7 for three orientations. The optical path length setting for maximum fringe contrast changed by a slight amount, 250µm, between horizontal and vertical polarization, indicating that the optical path length difference between the fibers for these two orientations was only 250µm over 60m of fiber (4 ppm).

The temperature drift in the interferometer was also tested by slowly varying the room temperature and recording the setting of the OPD which gives maximum fringe contrast. These data are shown in Fig. 8. Fiber B appears to increase its refractive index (or length, or both) more than Fiber A as temperature is increased.

Finally, the dispersion <u>difference</u> between the two fibers was tested by varying the center wavelength of the narrowband filter and adjusting OPD for maximum fringe contrast. As Fig. 9 shows, the path length setting changed only a very small amount (approximately twice the experimental reading error) as the center wavelength was changed over almost the entire visible wavelength range. Thus, it can be concluded that the dispersion difference between the fibers is very small.

#### IV. EFFECT OF FIBER DISPERSION ON FRINGES

One feature of concern that is present in silica fibers but not in air paths is intramodal dispersion (changes in mode effective refractive index as a function of wavelength).[3] Dispersion will be a problem whenever the two paths in the interferometer are unbalanced with regard to the length of fiber which is in each path. For example, if a long baseline interferometer is configured with the two telescopes at ground level, some additional delay line must be added to one of the paths to compensate for the longer air path when the system is aimed away from the normal. If a fiber is used for this additional delay line, the two paths will contain grossly unequal fiber lengths. Due to unbalanced fiber dispersion, the optical path length difference will be different for the various wavelength components in the source spectrum. For wideband sources, this will significantly reduce the ability to detect fringes.

A. SIMPLE THEORY OF DISPERSION - Let  $\sigma_{\lambda}$  be the spectral width of the light into a single

# FRINGE CONTRAST US. AIR PATH LEWSTH FOR DIFFERENT POLARIZATIONS

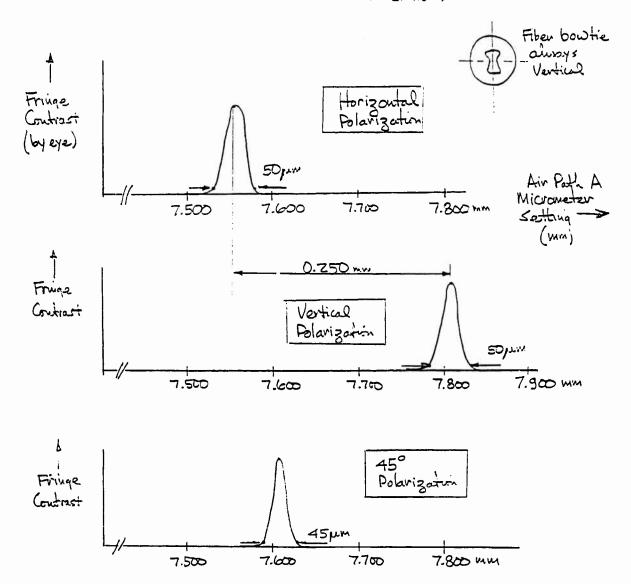


Figure 7 - Interferograms for three input polarizations.

The slight shift in center path length setting (0.250mm) shows that the variation in refractive index differences between the .wo fibers is small as polarization is rotated.

DRIFT OF AIR PATH LENGTH VS. ROOM TEMPERATURE

(60m Fikers on Spools; Path length adjusted

Manually to give wax. Stringe contrast)

Air Path A (Fiber A)

Micrometer

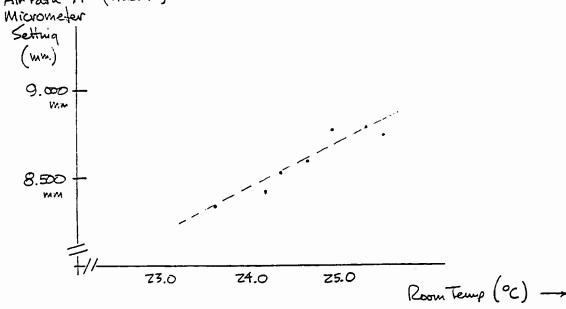


Figure 8 - Effect of room temperature on OPD of fiberoptic interferometer.

## DISPERSION DIFFERENTIAL BETWEEN TWO SPOOLS OF 60 m SM FIBER

Experiment: Place 4 different NB filters at 4 center unveloughes in front of xeuon source, and adjust air path length for max. Fringe contrast at each wavelength.

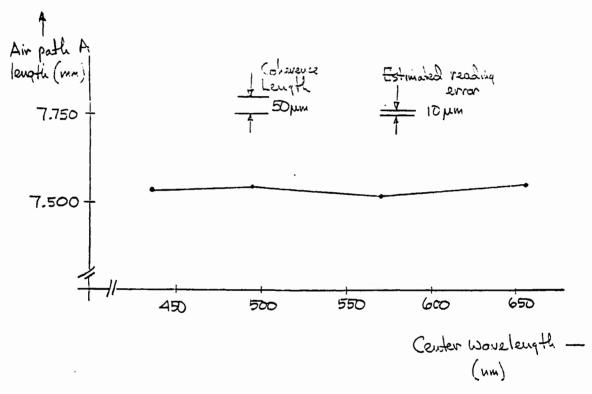


Figure 9 - The variation in OPD at maximum fringe contrast as a function of the filter center wavelength.

mode fiber of length L. Due to dispersion, the optical length of the fiber will appear longer for the shorter wavelengths of the source's spectrum than for the longer wavelengths. Let  $\Delta L'$  be the effective difference in optical length as seen at the two extreme wavelengths of the spectrum. There will be two contributions to  $\Delta L'$ :

1. Material Dispersion - Since the index of refraction n varies with wavelength, the optical path length through the fiber also varies. This effect gives

$$\Delta L'_{matl} = L \sigma_{\lambda}(dn/d\lambda).$$

For a silica core fiber in the 600-1000nm region,  $dn/d\lambda \approx -1.52 \times 10^{-5}/nm$  [3]. Thus, for typical  $\sigma_{\lambda} = 10nm$ ,

 $\Delta L'_{matl} = -152 \mu m$  per meter of fiber.

2. Waveguide Dispersion - The effective propagation constant of the lowest mode varies slightly with wavelength, leading to

$$\Delta L'_{Wg} = Ln_2\Delta \sigma_{\lambda}[b - d(Vb)/dV] /\lambda$$

where  $n_2$  is the clad index,  $\Delta$  is the normalized index difference between core and clad, b is the normalized propagation constant, and V is the normalized frequency. For a typical operation of a single-mode fiber, V = 2.2,  $b \approx 0.47$ , d(Vb)/dV = 0.98,  $n_2 = 1.45$ ,  $\Delta = 0.01$ , and  $\lambda = 1000$ nm. Then, again for  $\sigma_{\lambda} = 10$ nm,

$$\Delta L'_{Wg} = -74 \mu m$$
 per meter of fiber.

Putting these two factors together,

$$\Delta L' = \Delta L'_{matl} + \Delta L'_{wg} = -226 \mu m$$
 per meter of fiber.

The following points should be noted regarding the above analysis:

- a) The analysis is based upon changes in <u>phase</u> velocity with wavelength, not <u>group</u> velocity. Phase velocity appears to be more appropriate for the quasi-continuous waves which form the interferometer fringes, while group velocity is more appropriate for pulse propagation analysis.
- b)  $\Delta L'_{matl}$  is negative for all wavelengths of interest (and is a minimum in the 600-1500nm range).

- c)  $\Delta L'_{Wg}$  is also always negative for a SM fiber, and thus there is <u>no</u> wavelength for which the two phase velocity variations cancel (as opposed to the group velocity variations, which can cancel near 1300nm).
- d)  $\Delta L'_{wg}$  is usually smaller than  $\Delta L'_{matl}$ . In fact, as  $V \rightarrow 0$ ,  $\Delta L'_{wg} \rightarrow 0$  and dispersion is caused entirely by material effects.
- e) To cancel the above dispersion, an anomolous dispersion element would have to be placed in series with the longer fiber, or a compensating dispersion element placed in series with the shorter path.

Overall, the effect of dispersion is to "blur" out the path lengths over the source spectrum. An interesting calculation is to determine the length of fiber L for which  $\Delta L'$  is approximately equal to the coherence length, say 40 $\mu$ m. Let  $\sigma_{\lambda}=10$ nm. Then

|L| = 40/226 = 18cm

which is short compared to the expected additional fiber length needed to steer an all-fiber, long baseline interferometer.

B. EXPERIMENTAL EFFECTS OF DISPERSION - In order to test the effect of unbalanced fiber lengths in the interferometer, an additional short length of single-mode polarization-preserving fiber (Newport F-SPA) was placed in Path B of the interferometer (see Fig. 1 for location of Path B). Path A, of course, was then lengthened in air by an amount to compensate for the additional time delay now present in Path B. Balancing to zero OPD was accomplished by the technique employing the variable coherence length laser diode, as described in Sec. II. Polarization orientation of the new piece of fiber was aligned to the vertical by rotating the fiber while checking the output beam with a polarization-analyzer film. The extinction ratio was better than 10:1 (by eye).

Figure 10 shows the interferogram which results when a 26cm length of additional fiber is inserted. The laser diode is driven at 50.0mA; thus the source spectrum is very similar to Fig. 2c, and the interferogram of Fig. 10 (for the case of an additional piece of fiber) can be compared to the center of the pattern shown in Fig. 5 (for the case of approximately equal fiber lengths) since the source spectra are similar. (Note, however, that the horizontal scales are

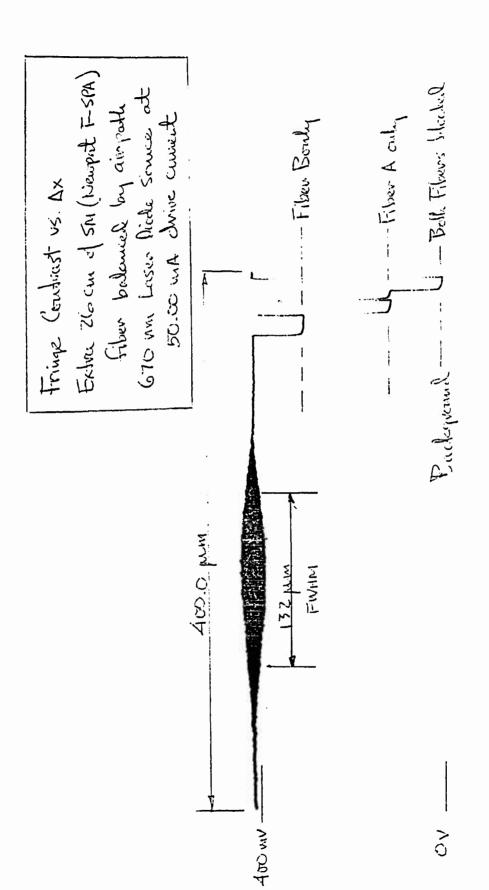


Figure 10 - Interferogram for an additional 26cm length of fiber in one arm of interferometer. The coherence length is still approximately 132 µm, while the fringe visibility is significantly reduced.

different in the two figures.) It can be seen by this comparison that the coherence length does not seem to be affected by the addition of the fiber, but the fringe visibility is significantly reduced.

#### V. CONCLUSIONS AND SUGGESTIONS FOR FUTURE RESEARCH

Several goals of the project were met during the summer, including the obtaining of white light fringes, development of the laser diode source technique, some characterization of the interferometer, and studies of the effects of fiber dispersion.

Many questions remain, however, before the practicality of an all-fiber interferometer can be determined. These include the key questions of the effects of fiber dispersion (theoretical and experimental) on fringe visibility and whether this dispersion can be balanced by the addition of some cleverly designed dispersion cancellation elements. Also to be studied are low-light level effects, the use of low-noise amplifiers (fiber amplifiers or semiconductor amplifiers), phase modulation elements to lock finges, such as piezoelectric stress or temperature stress devices, and the tradeoffs involved with the use of multimode fibers.

#### ACKNOWLEDGMENTS

This work was supported by the AFOSR Summer Faculty Program. The help of Phillips Lab and Rockwell Power Systems personnel is gratefully appreciated, including Gary Loos, Andrew Klemas, Jim Rotge, Dave Merriman, and Bruce Crawford.

#### REFERENCES

- 1. Siegman, A.E., Lasers, University Science Books, Mill Valley, CA, 1986.
- 2. Goodman, J.W., Statistical Optics, John Wiley & Sons, New York, 1985.
- 3. Keiser, G., Optical Fiber Communications, Second Edition, McGraw-Hill, New York, 1991.

### CONSTRUCTION AND INITIAL OPERATION OF THE WORKING FLUID EXPERIMENT

John Gahl, Assistant Professor, The University of New Mexico

#### Abstract

A working fluid experiment was successfully constructed, operated, and initial data characterizing its performance collected. The experiment was designed to generate a cold (~1 eV), high density (~10<sup>19</sup> cm<sup>-3</sup>) plasma that would be useful as a medium for shockless compression. This report describes the construction of the experiment and the initial data collected from it.

#### Introduction

In an application such as projectile acceleration, it is useful to have a medium, a working fluid, that has an extremely high speed of sound. Since the speed of a projectile is limited to the sound speed of the medium pushing it, the development of a source of high density, low temperature plasma could be useful for this and other applications.

In this report we describe the construction, operation and initial results of a plasma source intended to provide such a plasma. This initial work was conducted largely by my graduate student J. F. Crawford with help from myself and a variety of personnel at Phillips Laboratory.

Discussion of the Problem (Experiment)

The working fluid experiment (WFX) is essentially a coaxial plasma gun which is operated in the snowplow mode (see for example [1,2]). The WFX is operated at relatively high fill pressures. Whereas coaxial plasma guns operated in the snowplow mode are typically prefilled to a few torr in pressure, the WFX has been operated with fill pressures above 50 torr. This high fill pressure is used with the intent to achieve a resulting high density plasma.

Figure 1 is a schematic diagram of the WFX and Figs. 2 and 3 are photographs of the WFX taken from different angles. The inner conductor of the WFX terminates in a "doorknob" and is approximately 30 cm in length. At the inner conductor feedthrough, or breech of the gun, the inner conductor is insulated from the grounded outer vacuum vessel by a glass sleeve. The outer gun conductor near the breach (which is inside a larger diameter vacuum vessel) is composed of rods.

To fire the experiment, the WFX is prefilled with gas and a power pulse is impressed between the inner and outer conductors. The outer conductor is at ground potential with the rest of the vacuum vessel. When a power pulse is impressed between the conductors, a discharge tracks down the glass sleeve insulating the inner conductor. The outer conductor is composed of rods at this

location to allow any contamination from the insulator or any potentially damaging pressure pulse to escape the gun region.

The power pulse is delivered to the experiment by a 55 kilojoule, 60 kV capacitor bank.

Once a discharge has been initiated across the insulating sleeve, J x B forces cause the discharge to lift off the sleeve and travel down the gun, enveloping gas as it travels, turning it into plasma. The discharge travels to the "doorknob" region where the moving plasma is forced into the confined region at the end of the WFX opposite the breech. Here, in this "bucket" at the end of the WFX, the desired "working fluid" should be created.

The particular geometry, material composition and configuration of the WFX is in large part due to the availability of existing components from other preexisting experiments. The driving capacitor bank, trigger system, and capacitor bank charging system all came as well from a preexisting experiment.

The WFX can be configured to fire in two distinct modes of operation. In the first mode of operation, the inner and outer conductors are electrically isolated throughout their entire length. It was speculated that this configuration would allow both magnetic flux and plasma to enter the "bucket" region of the experiment. In the second mode of operation, a plate is placed between the inner and outer conductors in the "doorknob" region. This plate, which has many holes drilled into it to allow plasma to

flow through it (which I will call the "mixing plate"), electrically shorts the inner and outer conductors at the "doorknob", effectively excluding flux from the "bucket" region. Though somewhat counterintuitive, it was expected that the driving circuit would see enough inductance to still allow for the initiation of a discharge across the insulating glass sleeve around the inner conductor. It was hoped that this configuration would allow for the injection of plasma into the "bucket" while excluding the injection of magnetic flux.

The diagnostics conducted in the initial stage of operation of the WFX were rather rudimentary but were nevertheless quite informative. Simple voltage monitors and Rogowski current monitors were utilized to determine the performance of the driving capacitor bank. The metal endplate of the "bucket" was removed and replaced with Lexan to allow for open shutter photography and hence a determination of plasma fill of the bucket region.

And finally, B dot probes were placed in the WFX to give sheath velocity, flux intensity, plasma pulse duration, and plasma sheath symmetry. Three probes were used (all located near the edge of the outer conductor), one in approximately the middle of the "bucket" region, the other two located respectively, approximately 6 cm and 10 cm closer to the breach.

#### Results

What follows is the variation in performance of the WFX under different experimental configurations (with or without the "mixing plate"), with different fill gases (Hydrogen/Helium) and with different fill pressures (20 Torr, 50 Torr, and higher pressures). The discharge always rang quite severely, which limited us in operating our old 60 kV capacitor bank. All data discussed was taken with a discharge voltage of only 40 kV. Though in some cases there were restrikes, the primary plasma pulse was typically 5 us in length.

Our first case for comparison will be between Hydrogen fill shots and Helium fill shots conducted with a fill pressure of 20 Torr and with no "mixing plate" present. The Hydrogen fill shots had a much more symmetric current sheath, particularly away from the breach. The Hydrogen fill shots resulted in approximately 30% of the magnetic flux present in the gun reaching the "bucket" compared to only 5% of the magnetic flux reaching the "bucket" in the Helium fill case. Two sheaths were produced in both gases, the second sheath occurring on the third half cycle of the current feed. The second sheath did not reach the "bucket" in the Hydrogen fill case. For both gases the first two B dot probes from the breach, which are separated by 4 cm, have simultaneous signals, while there is a 2 us delay between the signal these probes see and the signal from the "bucket" B dot probe. The separation between the

second B dot probe in the gun and the "bucket" B dot is approximately 6 cm. Plasma reaches the "bucket" for both gas fills, while the Helium fill seems to result in a more symmetric plasma fill.

The next comparison is again between shots with Hydrogen fill and Helium fill, again with all shots taken at 20 Torr, but now with the "mixing plate" in the experiment. Hydrogen fill shots have one current sheath, which is very symmetric. Helium fill shots have two current sheaths which are nonsymmetric. No magnetic flux enters the "bucket" region for either gas. The magnitude of the B dot probes in the Helium fill shots is approximately three times that in the Hydrogen fill cases, even though the Rogowski current signal at the coaxial gun feed is approximately the same. In both gases, again the first two B dot probes have apparently simultaneous signals. Hydrogen plasma did not reach the "bucket", and in the case of Helium (though later questioned by different diagnostics) open shutter photography suggests that Helium plasma did reach the "bucket" and that the resulting plasma was more uniform than the case with no "mixing plate".

I will now discuss briefly Helium fill shots at pressures of 50 Torr and above. At higher fill pressures in Helium, B dot probe signals were seen to decrease dramatically. Open shutter photography suggested that at higher pressures, the Helium discharge was having difficulty "lifting off" the glass insulator

surrounding the inner conductor. Therefore, no plasma was being driven down the WFX under these experimental conditions.

Finally, I will now discuss Hydrogen fill shots taken at pressures of 50 Torr and above. At higher fill pressures in Hydrogen there was essentially one current sheath followed by a very small second. At 50 Torr and utilizing a "mixing plate", a very symmetric current sheath was seen in the WFX everywhere except in the "bucket", where no plasma or magnetic flux was seen. At 50 Torr and utilizing no "mixing plate", a symmetric current sheath was seen everywhere in the WFX except in the "bucket", where a large but very noisy B dot signal was observed. The B dot magnitude was approximately 30% less than when utilizing a "mixing plate", and plasma was observed filling the "bucket", but it was very nonsymmetric. At 75 Torr and utilizing the "mixing plate", again the current sheath was symmetric and no flux or plasma was observed in the "bucket". However, the B dot signal did elongate (to approximately 10 us) and became more of a "flat top" pulse. At 75 Torr and using no "mixing plate" the WFX shorted. At 100 Torr and using a "mixing plate" the WFX shorted.

#### Conclusions

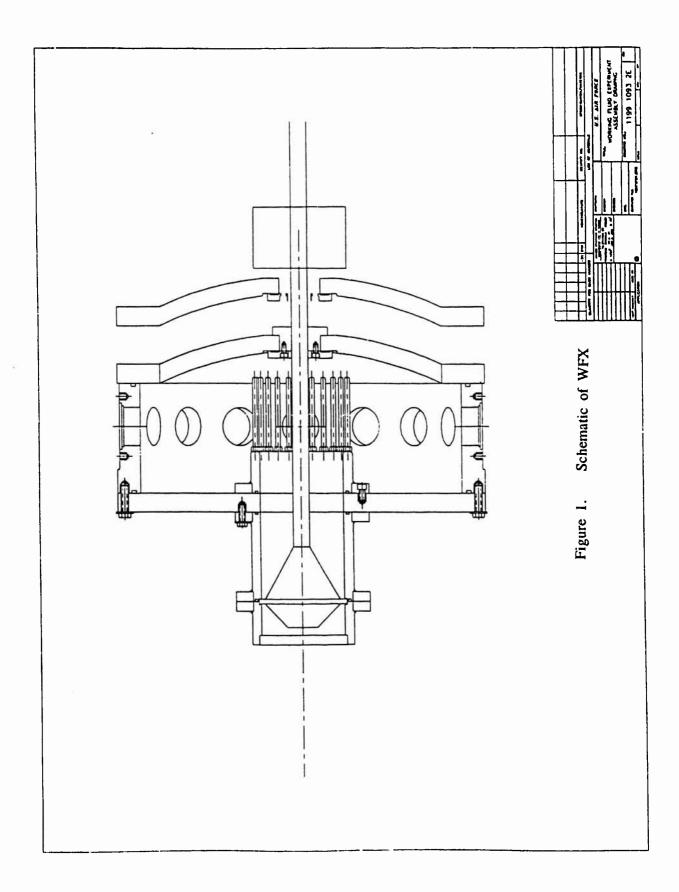
Clearly, there is a great need to implement move sophisticated diagnostics on this experiment to come to a better understanding of the underlying physics. Fortunately, improved diagnostics have been implemented on this experiment since our

leaving. Spectroscopy is being conducted to determine the density and temperature of the plasma, fast framing cameras are being utilized to show the time dependent evolution of the plasma, and many other diagnostics are possible.

What is particularly satisfing about the work we completed is that we were able to construct, operate, and take initial measurements on a relatively complicated experiment in a extremely short period of time. Though we did not have the time to complete this experiment, I feel we established a firm foundation for others to build on.

#### References

- 1. Cheng, D. Y., "Plasma Deflagration and the Properties of a Coaxial Plasma Gun," Nuclear Fusion, 10, 305, (1970).
- 2. Len, L. K., The Snowplow and Deflagration Modes of Operation in Coaxial Plasma Guns, Ph.D. Thesis, The University of New Mexico, (1984).



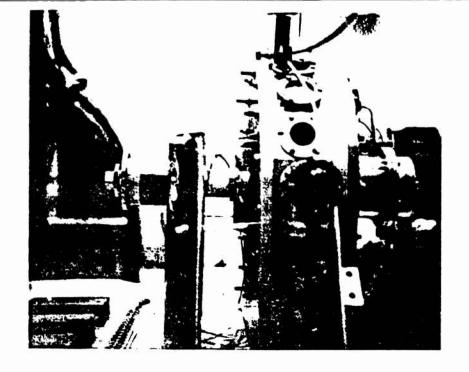


Figure 2. Photograph of WFX

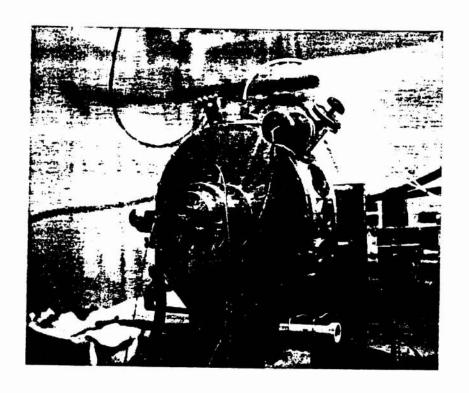


Figure 3. Photograph of WFX

## FINITE ELEMENT ANALYSIS OF HARDENED AIRCRAFT SHELTERS Walter Gerstle, Assistant Professor

#### Abstract

The Shock Physics Division is presently involved in a multi-million dollar effort to upgrade existing US and NATO reinforced concrete protective shelters. The finite element analysis of such structures subject to blast loading is currently an art, not a science, because it can give the engineer only a rough approximation of the actual behavior of the structure. The purpose of my AFOSR-sponsored summer research was to develop better numerical analysis tools for simulation and visualization of structures subject to dynamic loading.

#### Introduction

The Shock Physics Division is presently using the finite element codes DYNA2D [HALL87], DYNA3D [HALL82B], and DELTA2D [LIU91] for the purpose of modeling the response of hardened reinforced concrete aircraft shelters to blast loadings. My goal this summer was to link CoMeT [PANT90] (Computational Mechanics Toolkit) to these finite element codes. DYNA2D and DYNA3D are explicit, nonlinear dynamic Lagrangean finite element codes developed at Lawrence Livermore National Laboratories. DELTA2D is an Eulerian extension of DYNA2D, in which after each time step the mesh is returned to its original configuration, while material is

allowed to flux through the mesh. Thus, DELTA2D is appropriate for modeling phenomena in which very large strains and deformations occur (such as air and soil under blast loading), while the DYNA codes are more appropriate for modeling the response of structures which exhibit up to twenty percent strain.

The modeling of a hardened cylindrical shell aircraft shelter, as shown in Fig. 1, to an accidental bomb detonation inside the shelter involves both the response of air to the detonation, and the response of the shelter to the pressurized air inside. This type of analysis is called a fluid-structure interaction problem. To model such problems, it is desirable to model the air, using an Eulerian code, as one domain and the structure, using a Lagrangean code, as another. It is therefore desired to couple an Eulerian code, such as DELTA2D, to a Lagrangean code, such as DYNA2D. The interaction between the air and the structure can then be accurately simulated. Current finite element modeling of such problems takes into account only the first-order effect of the air pressure upon the structure.

CoMeT, with its dynamic computational mechanics database, was designed as a platform for coupling dissimilar finite element codes. My objective was to use domain decomposition methods to link the codes DELTA2D and DYNA2D together for the purpose of modeling fluid-structure interaction problems. This goal has not been accomplished, for reasons which will be explained. However, CoMeT has been

successfully linked to DYNA2D, and we were able to perform finite element analyses of the aircraft shelter. These results will be presented and discussed in the body of this report.

#### Coupled Domain Analysis

In traditional structural analysis approaches, the loading on a structure is considered to be independent of the structural response. In the case of blast loadings, however, the loading and the response may be coupled, as the blast pressures may depend upon the response of the structure and vice versa. For this reason, I decided to try to couple the DELTA2D and DYNA2D codes.

The approach is to define two separate domains (A and B) in the CoMeT finite element database. The domains are coupled along an interface (I). The displacements of the nodes on the interface (I) are assigned as prescribed displacement boundary conditions to the domains (A) and (B) during each time step. DELTA2D and DYNA2D then perform an analysis of a single (or possibly several) time steps, with the prescribed displacement boundary conditions. At the end of each time step, the forces from (A) and (B) acting on (I) are returned to the CoMeT database, and are then summed, to get the unbalanced forces acting on (I). The displacements of the nodes on (I) are then updated in accordance with the finite difference equations derived from the coupled differential equations of motion,  $M\ddot{x} + C\dot{x} + Kx = F(t)$ . The process is repeated for each time step.

This approach assumes that each of the finite element codes can accept prescribed displacement boundary conditions, and also that each code can calculate and return the reactive forces at each of the interface degrees of freedom to the CoMeT database. DYNA2D can accept specified displacement boundary conditions, and with minor modification could return reactive forces at fixed degrees of freedom. DELTA2D, however, cannot currently accept arbitrary displacement (or velocity) boundary conditions. It was therefore decided, that, as a more modest goal, for research purposes, I would work only on linking DYNA2D to CoMeT, and use DYNA2D to model both domains (A) and (B). As a side note, this approach is an interesting way to do distributed computing, with separate processors modeling each of the domains.

#### Linking CoMeT with DYNA2D

Before attempting to perform coupled-domain analysis, CoMeT was linked to DYNA2D. This took longer than expected because of the time necessary to learn how to use the DBXTOOL debugger on the SUN SPARC station and to find some bugs in CoMeT. The DBXTOOL debugger has some bugs in it, and work-around methods were required.

COMET is now linked to DYNA2D, and can be used as both an interactive graphical pre- and postprocessor for DYNA2D, replacing the codes MAZE [HALL83] and ORION [HALL82A]. It is possible to interactively generate geometries and meshes using CoMeT. Velocity, displacement,

and pressure boundary and initial conditions are attached to nodes and edges once the mesh is defined. Fig. 2 shows the Boundary/Initial Conditions menu page of CoMeT, with pressures and velocities attached to the appropriate nodes and edges. Time-history curves can be interactively defined. Two of the many material models (elastic and elastic-plastic) in DYNA2D have been implemented in CoMeT; others can be added by editing an environment file as the need arises. The user can interactively define and attach these material models to elements or domains. Fig. 3 shows the Elastic-Plastic material model menu page, which was added to CoMeT. Once the user has defined the problem geometry and boundary conditions, he can specify problem control parameters, and write an input file for DYNA2D. Fig. 4 shows the ANALYSIS TOOLS menu page, with the DYNA2D analysis options. After DYNA2D has been run, the response information at various time steps is read back into the CoMeT database (using the dyna2d output menu option in Fig. 4), and the results can be viewed.

Several of the features which DYNA2D accepts have not yet been implemented in CoMeT. For instance, body accelerations cannot currently be specified in CoMeT; instead the input file to DYNA2D must be edited to specify non-zero accelerations. Also, stone-walls, slidelines, and equation-of-state models need to be implemented to have a complete link to DYNA2D. This should not be difficult; but more time is needed than was available this summer.

Because DYNA3D, DELTA2D, NIKE2D, and NIKE3D have very similar input formats, linking CoMeT to these programs should be straight-forward, but again, requires more time than was available during my 10 week stay at the Phillips Laboratory.

#### Aircraft Shelter Analysis

One of the goals was to perform an analysis of a one-third scale model of a Norwegian aircraft shelter subject to accidental internal blast loading from the detonation of a scaled-down 500 pound general purpose bomb. The scale model test will be conducted this fall at the Utah Test and Training Range, so it will be interesting to compare the results of our finite element analyses to the test results.

Fig. 1 shows the plans for the aircraft shelter. The scaled 500 lb bomb is located on the floor at the center of the shelter. Doug Seemann gave us the spatial and temporal pressure distribution acting on the interior of the shelter due to the detonation. This complicated temporal and spatially distributed pressure was generated using the program GUSH [NEWE87], and is given in Fig. 5. As an approximation, the pressure time-history associated with station number 5 was assumed to be applied along the entire inner surface of the shelter shell.

Linear-elastic and elastic-plastic plane-strain analyses of the aircraft shelters were performed. First, a linear-elastic dynamic analysis was performed to determine whether the stresses would be sufficient to cause damage to

the concrete shell, and to determine the general structural behavior in response to the blast. Young's modulus was assumed as 30 gPa, Poisson's Ratio was 0.2, and the density of the concrete was assumed as 2403 kg/m³. Fig. 6 shows the maximum principal stresses plotted on the deformed shape at several key time steps during the analysis. Fig. 7 shows the vertical displacement and velocity of the bottom node at the centerline of the shelter as a function of time. The peak displacement was only about 1 cm. It was found that the maximum principal stress (61.4 mPa) was significantly in excess of the cracking strength of the concrete (3.7 mPa). Clearly, a nonlinear analysis was required.

Subsequently, the reinforced concrete shelter was modeled as an elastic-plastic material. The assumed material properties are given in Fig. 8. The yield strength was determined by assuming a steel ratio of .009, and assuming a yield strength of the reinforcing bars and steel liner of 60000 psi. Fig. 1(b) shows a schematic of the assumed cross section of the shell.

These results show that the shelter will sustain a permanent deformation of about 1.8 cm, and will sustain significant cracking of the concrete. Fig. 9 shows a plot of maximum principal stresses at several time steps, superimposed upon the deformed shape of the structure at these time steps. The maximum principal stress was found to be 4.8 mPa, somewhat higher than, but of the same order of magnitude as, the yield strength of the material. Fig. 10

shows a time-history of the vertical displacement at the bottom surface of the center of the shell.

Realizing that a weak link in the aircraft shelter might exist at the connection between the footing and the shell, we then released the fixity at the bottom of the shell. Also, in this analysis, we modeled the soil which covers the shelter and included the effect of gravity. This provided the interesting result that the tensile hoop stresses in the barrel vault disappear almost entirely, but that the entire shelter moves upward almost as a rigid body, as shown in Fig. 11. Including the effects of gravity, the shelter is predicted to jump off the ground by about 9.1 cm. The maximum principal stress, however, is only 0.12 mPa, an order of magnitude lower than if the shell is rigidly attached to the ground.

A three-dimensional linear elastic static analysis was performed to determine whether the assumption of plane strain behavior was justified. Fig. 12 shows the deformed shape of the shelter assuming that the entire load is applied to the faces of the elements labeled A,B, and C. The three-dimensional behavior is evident. In comparison, the plane strain analysis gives a maximum displacement about 20% higher.

### Conclusions

This has been an interesting and educational summer experience. In linking CoMeT and DYNA2D, several valuable things were learned:

- (1) I learned how to use the SUN SparcStation. In particular, I became proficient with UNIX, and also learned how to use the VI editor, the DBX debugger, the MAKE facility, the F77 compiler and the SCCS facility.
- (2) I learned more about the use of dynamic codes such as DYNA2D and DYNA3D.
- (3) CoMeT and DYNA2D were linked together. CoMeT provides a consistent pre- and postprocessing environment which is considerably easier to use and more flexible than MAZE and ORION.
- (4) The two-dimensional plane-strain analysis of the one-third scale aircraft shelter was accomplished using the CoMeT user interface to DYNA2D. Considerable insight was reached in the response of the shelter to internal blast loading. A separate report may result from our analysis of the aircraft shelter.
- (5) Directions for future development of CoMeT were determined. Particularly, some new techniques for treating generalized boundary conditions and responses were developed.
- (6) The CoMeT approach appears to be reasonable for this type of analysis environment.

The structural zooming approach was investigated. The most recent results from the University of New Mexico show that the method works well for static problems (using a conjugate gradient approach). As a direction for future

research, the structural zooming approach should be tried for dynamic problems.

### Acknowledgements

The help of Gene Fosness in performing the analyses of the concrete shelter are appreciated. Doug Seemann provided the loading curves shown in Fig. 5, and provided insight into the physical behavior of the structure. Dr. Rod Galloway gave valuable advice in the use of DYNA2D. Dr. John Higgins provided expertise on the code DELTA2D. Aaron Perea helped in obtaining the color images which are contained within this report.

### References

- [BROW92] Brown, B.E., and Hallquist, J.O., "TAURUS: An Interactive Post-Processor for the Analysis Codes NIKE3D, DYNA3D, TACO3D, GEMINI", LLNL Report UCID-19392, July, 1982.
- [HALL81] Hallquist, J.O., "NIKE3D: An Implicit, Finite-Deformation, Finite Element Code for Analyzing the Static and Dynamic Response of Three-Dimensional Solids", LLNL Report UCID-18822, Jan. 1981.
- [HALL82A] Hallquist, J.O. and Levatin, J.L., "ORION- An Interactive Color Post-Processor for Two-Dimensional Finite Element Codes", LLNL Report UCID-19310, Jan. 1982.
- [HALL82B] Hallquist, J.O., and Benson, D.J., "DYNA3D User's Manual", LLNL Report UCID-19592, Nov. 1982.
- [HALL83] Hallquist, J.O., "MAZE- An Input Generator for DYNA2D and NIKE2D", LLNL Report UCID-19029, 1983.
- [HALL86] Hallquist, J.O., "NIKE2D- A Vectorized Implicit, Finite Deformation Finite Element Code for Analyzing the Static and Dynamic Response of Two-Dimensional

- Solids with Interactive Rezoning and Graphics", LLNL Report UCID-19677, Dec., 1986.
- [HALL87] Hallquist, J.O., "User's Manual for DYNA2D An Explicit Two-Dimensional Hydrodynamic Finite Element Code with Interactive Rezoning and Graphical Display", LLNL Report UCID-18756, Feb., 1987.
- [LIU91] Liu, J.Y., "DELTA2D User's Manual", Intellisys Corporation, 3801 Eubank NE, Suite 201, Albuquerque, NM, 87111, July, 1991.
- [PANT88] Panthaki, M.J. and Gerstle, W.H., "CoMeT: A Computational Mechanics Toolkit User's Manual", RE/SPEC Inc., 4775 Indian School Rd. NE, Suite 300, Albuquerque, NM 87110, August, 1990.
- [STIL81] Stillman, D.W., and Hallquist, J.O., "A Three-Dimensional Mesh Generator for Modelling Nonlinear Systems", LLNL Report UCID-20506, Dec., 1981.
- [NEWE87] Newell, R.T., "NMERI GUSH Program", New Mexico Engineering Research Institute, Univ. of New Mexico, P.O. Box 25, University Station, Albuquerque, NM, 87131, 1987.

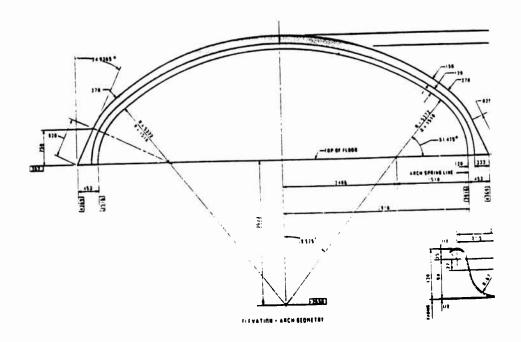


Fig. 1(a) - Design Drawing of One-Third Scale Hardened Aircraft Shelter.

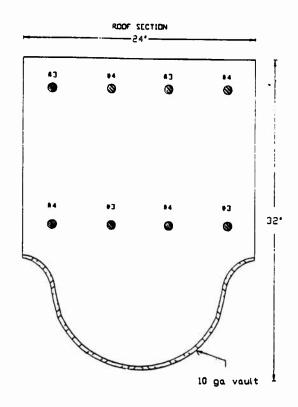


Fig. 1(b) - Typical Cross-Section of Reinforced Shelter Shell.

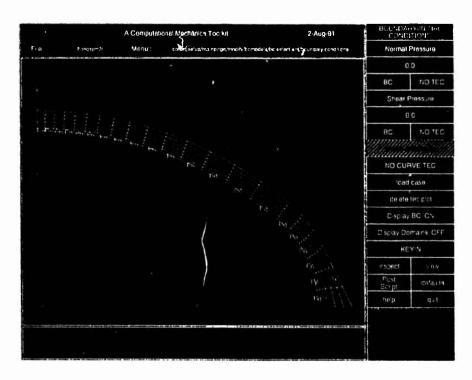


Fig. 2- BOUNDARY/INITIAL CONDITIONS Menu Page of CoMeT.

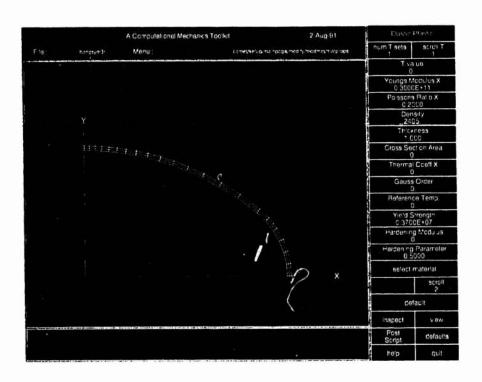


Fig. 3- Elastic-Plastic Material Model Menu Page of CoMeT.

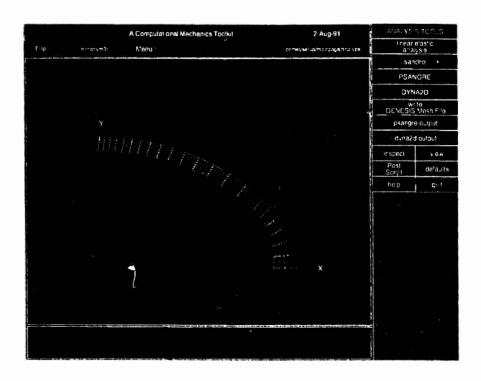


Fig. 4- ANALYSIS TOOLS Menu Page of CoMeT.

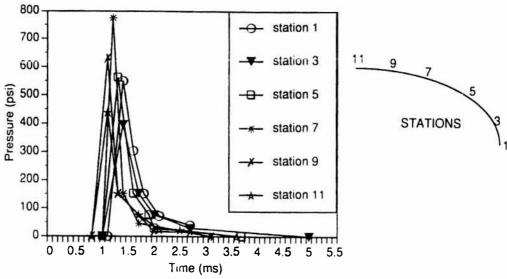


Fig. 5- Temporally and Spatially Distributed Pressure Generated using the Program GUSH.

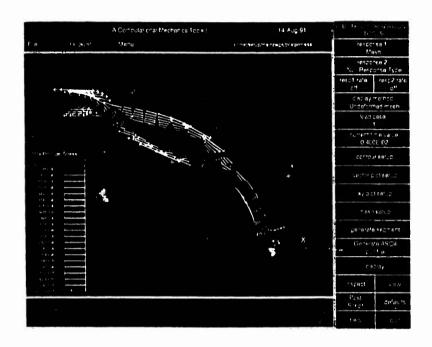


Fig. 6- Maximum Principal Stresses Plotted on the Deformed Shape at Several Key Time Steps During the Analysis (Elastic Analysis).

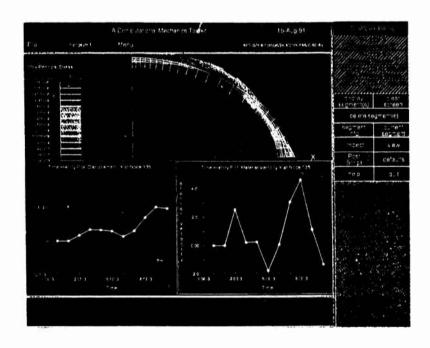


Fig. 7- Vertical Displacement and Velocity of the Bottom Node at the Centerline of the Shelter as a Function of Time (Elastic Analysis).

Assumed Material Properties		
Parameter	Reinforced Concrete	Soil
Young's Modulus (gPa)	30.	1.0
Poisson's Ratio	0.2	0.2
Density (kg/cu.m.)	2403.	1800.
Yield Strength (mPa)	3.7	0.1
Hardening Modulus	0.0	0.0
Hardening Parameter	0.5	0.5

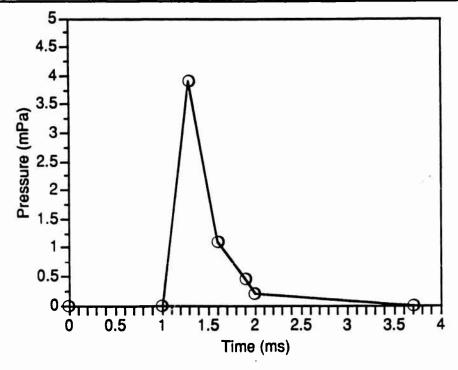


Fig. 8- Assumed Material Properties and Pressure Loading.

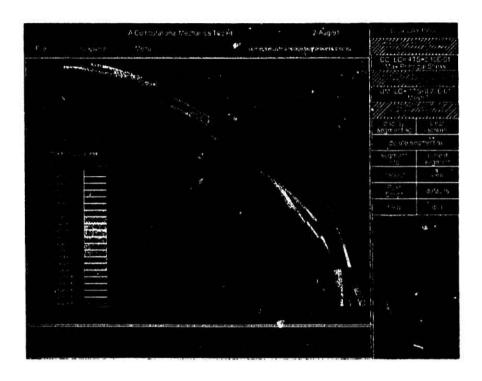


Fig. 9- Maximum Principal Stresses at Several Time Steps (Elastic-Plastic Analysis).

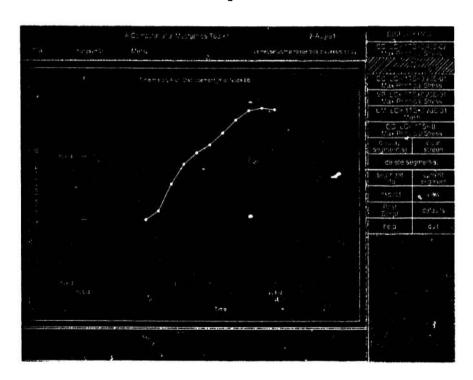


Fig. 10- Time-History of the Vertical Displacement at the Bottom Surface of the Center of the Shell (Elastic-Plastic Analysis).

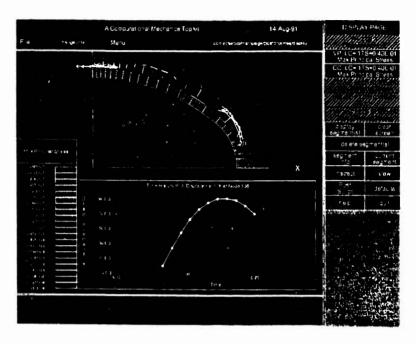


Fig. 11- Vertical Displacement Time-History Plot and Maximum Principal Stresses Plotted on the Deformed Shape at Time Step 0.004 During the Analysis (Elastic-Plastic Analysis, with Gravity and Soil; no Attachment to Foundation).

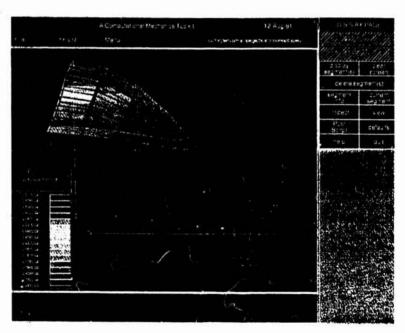


Fig. 12- Three-Dimensional Response of Shelter due to Internal Pressure applied to Elements along Centerline (Static Elastic Analysis).

## ALTERNATING DIRECTIONS OPTIMIZATION AN APPROACH TO LINEAR EQUATION SOLVING

### Dr. Jerald A. Kabell

#### Abstract

In this paper we explore a new iterative method for the solution of systems of linear equations proposed by Arman. We first show that the method converges for all non-singular systems. We then establish some bounds on the rate of convergence and identify the features of a system which may have a negative impact on that rate. Coupled with these are some issues of computational precision which can in some cases render the method unsuitable. A geometric interpretation leads to some enhancements of the method which can in some cases improve its performance. After exploring several serial implementations, we investigate the potential for parallel implementation of the method.

### 1. Introduction

In [1], Arman proposed the following new iterative approach to the solution of systems of linear equations, which he terms the Alternating Directions Optimization (ADO) method. Given the equation Ax = b, the method begins by selecting an arbitrary starting vector  $\mathbf{x}_{.1}$ , determining the value of  $\lambda$  which will minimize  $\|\mathbf{b} - \mathbf{A}(\mathbf{x}_{.1} + \lambda \mathbf{e}_0)\|$ , and then setting  $\mathbf{x}_0^0 = \mathbf{x}_{.1} + \lambda \mathbf{e}_0$ . This process is repeated for each of the remaining unit coordinate vectors, and the cycle iterated until the approximation is sufficiently accurate.

In the analysis of the ADO method, it will be convenient to establish certain notational conventions. We shall number our coordinates 0 thru n - 1, with unit coordinate vectors  $\mathbf{e_0}$  through  $\mathbf{e_{n-1}}$ . The approximation to  $\mathbf{x}$  after i complete iterations and the adjustment of coordinates 0 through  $\mathbf{j}$  in the current iteration will be designated by  $\mathbf{x_j}^i = (\mathbf{x_{j,0}}^i, \ \mathbf{x_{j,1}}^i, \ ..., \ \mathbf{x_{j,n-1}}^i)$ . We will also require the following additional definitions:

$$\mathbf{b_j}^i = \mathbf{A}\mathbf{x_j}^i;$$

$$s_{j}^{i} = b_{j}^{i} - b_{j-1}^{i};$$

$$\mathbf{d}_{j}^{1} = \mathbf{b}_{j}^{1} - \mathbf{b};$$

$$\mathbf{r}_{j}^{i} = \mathbf{b}_{j}^{i} - \mathbf{b}_{j}^{i-1};$$

 $\alpha_i^i$  = the angle between  $\mathbf{d}_{i}^i$  and  $\mathbf{d}_i^i$ ;

 $\beta_i$  = the angle between the line of  $b_{i-1}$  and the line of  $b_i$ 

$$(0 \leq \beta_i \leq \pi/2);$$

 $b_i = Ae_i$ ;

 $\mathbf{b_i}^{\perp}$  = the flat (n - 1 hyperplane) perpendicular to  $\mathbf{b_i}$  and containing b;

All matrices will be assumed non-singular unless specifically noted, and when performing arithmetic on indices, we shall interpret  $x_{j+1}^i$  as shorthand for  $x_{(j+1)mod}$ , and similarly for other quantities and operations.

### 2. Analysis of the basic ADO method

Much of the behaviour of the method can be best understood in geometric terms, so we shall begin with several observations. First we note that the basic step of the algorithm, a correction in one component (the  $i^{th}$ ) of the current approximation to x,

consists of adding to the current approximation to **b** the multiple of **b**<sub>i</sub> which will bring the resultant to  $\mathbf{b}_{i}^{\perp}$ , i.e., to the point of closest approach to **b**. The corresponding multiple of  $\mathbf{e}_{i}$  is then used as the correction factor for **x**. Figure 1 illustrates this process in the two dimensional case. We observe that for each choice of i and j,  $\mathbf{d}_{j}^{\perp}$ ,  $\mathbf{d}_{j+1}^{\perp}$ , and  $\mathbf{s}_{j+1}^{\perp}$  forms a right triangle with  $\mathbf{d}_{j}^{\perp}$  as the hypotenuse, and furthermore, these are all similar since they share the angle  $\alpha_{j}^{\perp} = \beta_{j}$ . Consequently, we can compute  $\|\mathbf{d}_{j}^{\perp}\|_{1}^{\perp} = \cos^{2k}\beta_{j}\|\mathbf{d}_{j}^{\perp}\|_{1}^{\perp}$ , which goes to 0 with increasing k, thus guaranteeing convergence and specifying the convergence rate.

In the general (n dimensional) case, the situation becomes more complex, but the geometry can still be exploited to yield some of the desired results. In the two dimensional case, each of the lines  $\mathbf{b_0}^{\perp}$  and  $\mathbf{b_1}^{\perp}$  divides the plane into two half-planes, and their intersections yield a partition of the plane into four parts, which we shall refer to as wedges, all meeting at  $\mathbf{b}$  and with opposite wedges congruent. After the initial step, all further corrections take place within one of the two wedges having the smaller central angle. In the general case, each of the flats  $\mathbf{b_1}^{\perp}$  divides the n dimensional space into two half-spaces, and the intersections of the half-spaces partition the space into  $2^n$  wedges, all meeting at  $\mathbf{b}$  and with opposite wedges either congruent or symmetric, depending upon whether n is even or odd. Again, after the initial step, all further corrections take place within one of the wedges with the smallest central angle. As in the two dimensional case,  $\mathbf{d_j}^i$ ,  $\mathbf{d_{j+1}}^i$  and  $\mathbf{s_{j+1}}^i$  form a right triangle with  $\mathbf{d_j}^i$  as the hypotenuse. While it is no longer true in general that  $\alpha_j^i = \beta_j$  (in fact, it is not even the case generally that  $\alpha_j^i = \alpha_j^{i+1}$ ), we can still observe that  $\mathbf{d_j}^{i+1} = \Pi \cos \alpha_j^{i} \mathbf{d_j}^i$ , where the product is taken over the full cycle of corrections between the two vectors.

Although the angles  $\alpha_j^i$ , and thus the product of their cosines, vary from cycle to cycle, it is always the case that  $\sum \alpha_j^i \ge 2(\min \beta_j)$ . Consequently there exists some fixed  $\varepsilon > 0$  such that for every i,  $\prod \cos \alpha_j^i < 1 - \varepsilon$ , and convergence is guaranteed. Unfortunately, this gives us only a very weak lower bound on the convergence rate.

In establishing the convergence of the ADO method, we have also determined the convergence rate, when n = 2, and a lower bound for that rate for larger values of n. There are some additional observations on convergence to be made, however. If there is an i such that  $\mathbf{b_i} \perp \mathbf{b_j}$ ,  $\mathbf{j} \neq \mathbf{i}$ , then after the first correction in the direction of  $\mathbf{b_i}$ , all further corrections will lie in  $\mathbf{b_i}^{\perp}$ , and all further adjustments of the  $i^{th}$  coordinate will have zero magnitude. As a consequence, if the  $\mathbf{b_i}$  are mutually orthogonal, then the process will converge in one iteration. A complete analysis of the convergence rate in the general case is difficult, but it is clear that small angles among the  $\mathbf{b_i}$  quickly come to dominate (and hence slow) the convergence process.

While we have shown that the ADO method will converge for any non-singular A, this is a theoretical result, and in the practical computational arena there are some additional problems. One of these is the rate of convergence, noted above. The other is the effect of the limited precision to which computerized calculations are of necessity performed. Again we may gain some insight by considering first the case of two dimensions. We have shown that  $\|\mathbf{s}_j\|$  approaches 0 with increasing i, so at some point it will be smaller in magnitude than the estimated precision of our computations. Unfortunately, if  $\beta_j$  is small,  $\|\mathbf{d}_j\|$  may still be relatively large and our approximation correspondingly poor. Thinking in terms of Figure 1, we reach the position where the

error in our computation of  $\mathbf{s_i}^1$  carries us outside the wedge of convergence, and while the next correction will bring us back in, it does so without improving the approximation. This basic problem remains unchanged in the general case. The other major problem arises from the need to relate  $\|\mathbf{d_i}^1\|$  to  $\|\mathbf{x_i}^1 - \mathbf{x}\|$ . While it is certainly true that  $\|\mathbf{d_i}^1\| \le \|\mathbf{A}\| \cdot \|\mathbf{x_i}^1 - \mathbf{x}\|$ , the actual ratio of the two quantities may vary dramatically, depending upon the orientation of  $\mathbf{x_i}^1 - \mathbf{x}$  and the condition number  $\kappa(\mathbf{A})$ .

### 3. Improving the basic method

It is natural to turn next to the problem of circumventing these practical difficulties. Since the convergence rate and, to a lesser extent, the precision problems are both bound up with the angles between the b<sub>i</sub>, we turn again to the geometry of the situation. Starting as before with the two dimensional case, we note that the controlling angle is fixed because the successive similar triangles are confined within the wedge of convergence. By allowing them to expand outside of that wedge, we may increase the central angle and thus accelerate the convergence. This idea is illustrated in Figure 2.

The question is, of course, how to accomplish this without compromising the convergence. One approach is to multiply the correction vectors  $(s_i^1)$  by some preselected relaxation factor. If this is done for every correction, however, the fixed ratios of the similar triangles are lost and convergence becomes problematic at best. By relaxing only alternate corrections, the similar triangles remain with fixed ratios and as long as the limit point is not overshot, convergence is guaranteed just as in the case of the basic ADO method (the figure shows a factor of 1.5). The determination of the

optimum relaxation factor is clearly the key to this approach, as a choice which is too large will move the process past the desired limit point and cause it to diverge, while one which is too small will not improve the convergence rate sufficiently.

In the two dimensional case, geometry again provides the solution, and we can exploit the triangles shown in Figure 3. Since the triangles ( $\mathbf{b}$ ,  $\mathbf{b}_1^0$ ,  $\mathbf{b}_0^1$ ) and ( $\mathbf{b}$ ,  $\mathbf{b}_0^0$ ,  $\mathbf{c}$ ) are similar and the lengths  $\mathbf{p}$ ,  $\mathbf{q}$  and  $\mathbf{r}$  have already been calculated, the necessary additional correction  $\mathbf{x}$  is easily obtained. The subsequent correction in the direction of  $\mathbf{b}_1$  then results in an exact solution. Unfortunately, this precise geometric fudge factor can be easily calculated only in the two dimensional case. In the more general case the line of the correction from  $\mathbf{b}_1^0$  to  $\mathbf{b}_0^1$  will be skew to the line  $\mathbf{b}_1$ , i.e., they will not intersect, and thus the subsequent correction in the direction of  $\mathbf{b}_1$  will be parallel to that line rather than precisely along it. The resulting approximation to  $\mathbf{b}$  will be such that the error vector is orthogonal to the plane determined by the last two correction vectors. This process can be repeated with other coordinate pairs, either mutually disjoint or overlapping. Clearly, if at some point one of the  $\mathbf{b}_1^1$  lies on  $\mathbf{b}_k$ , and this can be either detected or predicted, then a single correction in the  $\mathbf{k}^{th}$  coordinate will suffice to complete the solution.

Another approach involves treating the coordinates independently. This is illustrated in Figure 4. Here we begin by calculating the initial corrections independently in each of the n coordinates. The results are averaged and then used to correct the initial approximation, **b**<sub>.1</sub>, thus guaranteeing that the next approximation, **b**<sup>0</sup>, lies within the wedge of convergence. Subsequently corrections to **b**<sup>0</sup> are calculated independently in

all coordinates and then added simultaneously, so that b<sup>1</sup> is the diagonally opposite corner of the resulting parallelipiped. There is no guarantee that this point will always be within the wedge of convergence, but should it not be, averaging one set of correction vectors, as was done for the very first approximation, guarantees that its successor will be. In this approach, too, the use of a relaxation factor can effectively enlarge the central angle and improve the rate of convergence.

### 4. Implementing ADO and its variations

At the heart of the ADO method and all of the variations discussed above is the computation of the correction factor  $\lambda$  which will minimize  $\|\mathbf{b} - (\mathbf{b_j}^i + \lambda \mathbf{b_{j+1}})\|$ . This length will be minimized when the vector is orthogonal to  $\mathbf{b_{j+1}}$ , so we need only solve the equation

$$(\mathbf{b} - (\mathbf{b}_{i}^{1} + \lambda \mathbf{b}_{i+1})) \cdot \mathbf{b}_{i+1} = 0$$

Remembering that  $d_j^i = b_j^i - b$ , this is easily solved to yield

$$\lambda \ = \ -(d_j^{\ i} \cdot b_{j+1})/||b_{j+1}||^2 \ .$$

The basic algorithm is then obtained by enclosing this in a loop which calculates the correction for each coordinate in turn, applies it to the current approximations for x and b, and updates the error vector. This is in turn imbedded in an outer loop which repeats the process until the approximation is sufficiently close or until a preset number of iterations is reached. The algorithm skeleton is thus as follows:

while (error exceeds tolerance and i does not exceed iteration limit)

for 
$$(0 \le j \le n - 1)$$
  

$$\lambda = -(\mathbf{d}_{j-1}^i \cdot \mathbf{b}_j) / \|\mathbf{b}_j\|^2$$

$$\mathbf{x}_j^i = \mathbf{x}_{j-1}^i + \lambda \mathbf{e}_j$$

$$\mathbf{b}_j^i = \mathbf{b}_{j-1}^i + \lambda \mathbf{b}_j$$

$$\mathbf{d}_j^i = \mathbf{b}_j^i - \mathbf{b}$$
error = norm $(\mathbf{d}_j^i)$ 

Since the (euclidean) norms of the vectors  $\mathbf{b_j}$  can be precomputed and stored, the only computationally expensive operation which must be repeated for every iteration of the inner loop is the dot product in the computation of  $\lambda$ . The norm of the error vector which is taken in the outer loop need not be the euclidean norm, but can be one which is computationally less expensive (our test programs have used the 1-norm, or sum of the absolute values of the components). All of the enhancements to the method discussed in previous sections may be obtain by straight-forward modifications of this basic algorithm.

We have implemented the standard ADO method and several of these suggested enhancements on a single node of an iPSC/860. Preliminary and as yet incomplete and unverified tests using a collection of 512x512 matrices indicate that standard ADO compares very unfavorably with the standard LINPACK direct solver, except in the cases where the matrix columns are mutually orthogonal. In those instances, ADO converges exactly in one iteration and represents a modest improvement over

LINPACK. The enhanced versions of ADO all show improvements over the standard, and in some cases over the LINPACK solver. The ones involving relaxation, however, require careful tuning of the relaxation factor to achieve optimum performance. Further testing is in progress in this area.

### 5. Parallelizing the ADO method

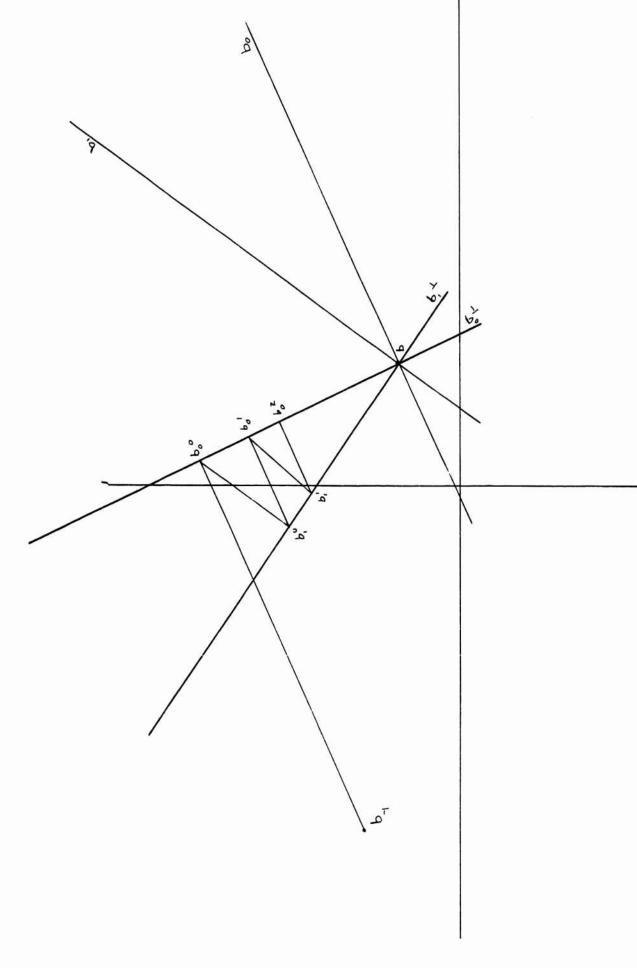
Several approaches were taken to parallelizing the ADO method both on the shared memory Sequent Balance 21000 and the distributed memory Intel iPSC/860 (both machines having 16 processors). The most notable success has been with the independent coordinates version with relaxation on the iPSC/860, where preliminary testing seems to indicate slightly sublinear speedup. Further testing is also underway in this area.

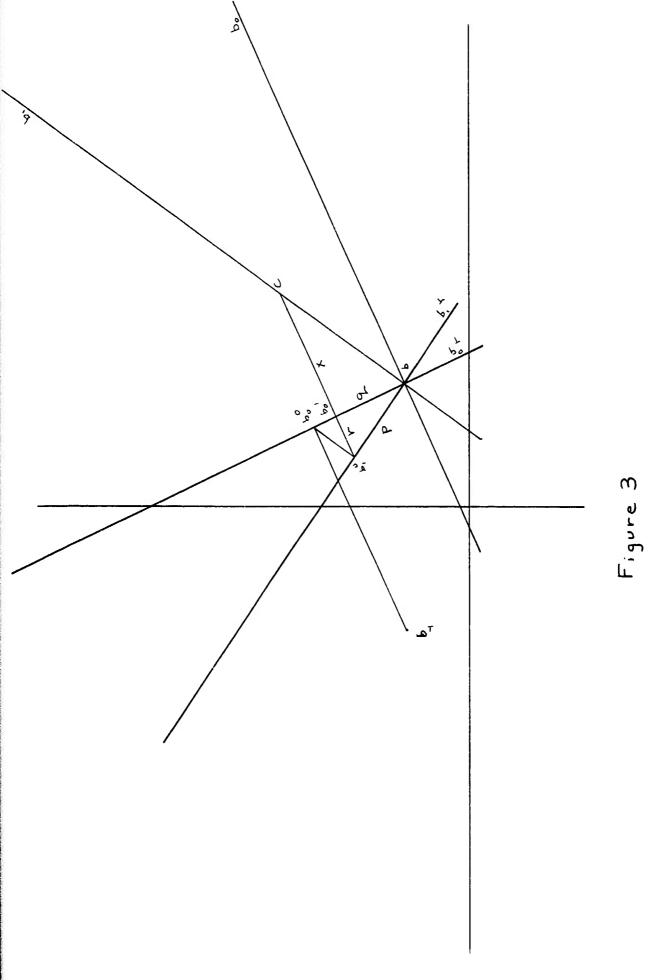
### 6. Conclusions

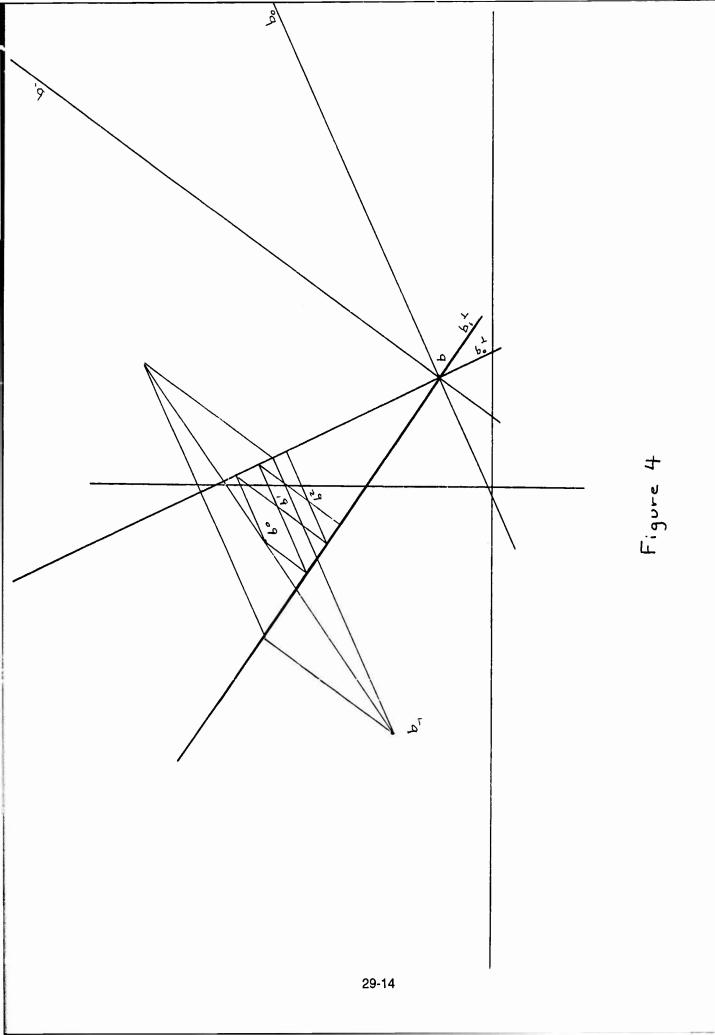
It is evident that the standard ADO method is not a viable general purpose solver for either sparse or dense systems. It may well have potential, however, as a niche method for cases in which the matrices are known in advance to be orthogonal or nearly so. Some of the enhanced methods may prove to be useful for larger classes of matrices, particularly if ways can be found to choose the relaxation factor either analytically or adaptively. In the parallel arena, the relaxed independent coordinate version appears to have some potential. Further testing is indicated in all of these areas, as well as theoretical studies of the choice of relaxation factors and the identification of specific obstructions to effective solution by these methods.

### 7. References

 Arman, Moossa, "Alternating Directions Optimization: A new method for solving large linear systems." seminar presentation, Phillips Laboratory, Albuquerque, NM, 28 May 1991.







# FINAL REPORT

### SUMMER FACULTY RESEARCH PROGRAM

AT

PHILLIPS LABORATORY

KIRTLAND AIR FORCE BASE

ALBUQUERQUE NEW MEXICO

September 30, 1991

SPACE DEBRIS IMPACT EFFECTS ON SPACECRAFT MATERIALS

by

Jon H. Shively
School of Engineering
California State University at Northridge

### INTRODUCTION

Space debris arise from many scurces; spent motor cases, deorbiting satellites, exploded satellites, space shuttle discards are a few examples. The disintegration of major components produces hunks of materials which continue to orbit the earth. The size distribution ranges from whole components to parts only a millimeter in diameter. Space debris are not particularly a problem unless they happen to collide with spacecraft. If this occurs the resulting damage can be very serious with the possible loss of mission. Some debris particles are estimated to be travelling at hypervelocities of 3-15 km/sec. It is estimated that the energy in the collision of a piece of aluminum only one centimeter in diameter is equivalent to that of a car travelling sixty miles per hour. No wonder spacecraft designers worry about survivability of a spacecraft facing collision with this energy.

The project supported by RDL lasted ten weeks during June, July, and part of August of 1991. The project was aimed at developing an approach to studying damage from the collisions of space debris with spacecraft materials. Originally, studies were planned using a hypervelocity accelerator to simulate the space collisions. The accelerator is located at Sandia in Albuquerque. However, due to funding adjustments, a new project was defined which is aimed at identifying the chemical species that form after the collisions with hypervelocity particles. This involves the use of a time-of-flight mass spectrometer located at Los Alamos National Laboratory. The summer at Phillips Laboratory was spent planning and designing an experiment to be conducted at LANL. In addition, time was also spent working on current Phillips Laboratory projects. A description of the tasks performed this summer and the results are summarized below.

### TASK 1 LONG DURATION EXPOSURE FACILITY SPECIMENS

About 6 years ago NASA launched an earth satellite called the Long Duration Exposure Facility, LDEF. The Phillips Laboratory participated in that program and supplied several specimens for long term exposure to the space environment. The

materials included metals and composite materials. The specimens were exposed to the trailing and leading edges of LDEF. Post-mortem studies of the specimens revealed several salient features, craters from the impact of small space objects, erosion on surfaces, and surface deposits. The presence of the deposits on originally clean surfaces suggests that chemical reactions are taking place in outer space on surfaces as the result of the migration of chemical species around the satellite. As a result an experiment was conceived to study the production of chemical compounds from impacts of space debris.

The LDEF specimens of polysulfone were of particular interest because the crystalline deposits found on the aluminum surface contained sulphur. Therefore a detailed program was implemented to characterize the polysulfone matrix material used in the composite and to characterize the effects of exposure in low-earth orbit. One difficulty that arose was the fabrication data on the polysulfone was lost and the nature of the chemical species used to make up the composite needed to be determined. Post exposure mechanical tests on the polysulfone material were also planned which included tensile and bend tests on the archive and the exposed polysulfone composite.

The surface characterizations and fabrications histories were completed. However, the mechanical tests were not completed due to an equipment failure. During the time set aside for testing, construction projects on the base reduced the water pressure so low that it was not possible to adequately cool the pumps for the mechanical tester. Prior to the water system problem, the instrumentation was developed to conduct the tests on polysulfone using aluminum samples of the same dimensions. This work will continue because NASA reported a loss of stiffness in samples exposed in LDEF that they have tested. Phillips will need to confirm the NASA results. The possibility of using the Dynatup Impact Test Machine was examined and found to be impractical for the size specimens used in LDEF.

### TASK 2 REVIEW OF HYPERVELOCITY IMPACT PHENOMENA

A significant portion of the time was spent in a careful review of the literature

on the phenomena associated with hypervelocity impacts such as those produced by space debris. A major portion of the research in this area was carried out during the 1960's and 70's. About 50 references were reviewed. Unfortunately, the spacecraft materials used in LDEF were to modern for the test on impact performed during the 60's and 70's. However much of the theory and technology are applicable

In investigating the literature and comparing materials, a interesting discovery was made. It was found that all the data from hypervelocity impacts could be place on a single master curve of shock Hugoniots. The result for a few materials are presented in Figure 1. As can be seen shock data for materials with major differences in density, strength, atomic weight fit one graph when the data are normalized by correcting for differences in density and the velocity of sound. At present no theoretical basis for this is evident, but if verified by additional experiments and/or theory the chart will be of great value to the designer of spacecraft. The master chart of Hugoniots would enable data to be extrapolated from other materials and add confidence to interpolating data. Since the shock Hugoniots are a vital part of survivability calculations from spacecraft, the Hugoniot master chart could reduce errors in estimating shock pressures.

While damage was carefully characterized during the impact process, no research was revealed on chemical changes that result from impact process, especially in the ejecta from the impacts themselves. The absence of data lead to the project conducted this summer.

### TASK 3 POLYSULFONE CHARACTERIZATION

The use of polysulfone as a matrix material in a composite was popular at the time LDEF was conceived. Since then other matrix materials have become favored for aerospace applications. Nevertheless, polysulfone was exposed to the space environment and survived very well. Therefore, it was decided to continue the studies of space debris effects on this material. As mentioned previously, background on the polysulfone composite was scant. Therefore a task was undertaken to develop a way of characterizing the matrix to identify the chemical species inside. The use of infrared

spectroscopy was selected to verify the chemistry. New polysulfone was acquired which met the original specification for LDEF. Sample were analyzed at University of New Mexico using Fourier Transforms of the IR Spectra. A complete match was made between the MIL Handbook data on polysultone and the new material. Samples of the matrix material in the composite were not tested by IR because a suitable solvent was not available. The UNM FTIR results are shown in Figure 2. Subsequent discussions with McDonald-Douglas management who supplied the polysulfone composite material revealed that it was purchased to the same specification as the MIL Handbook IR spectra. If a suitable solvent were acquired, the matrix material could be dissolved and analyzed using IR at UNM.

### TASK 4 SHOCK CHEMISTRY OF POLYSULFONE

Through the contact at the Phillips Laboratory, Dr. Charles Stein, an experiment was conceived which is aimed at determining the chemical species that form in the ejecta from space debris collisions with polysulfone. The hypervelocity collisions produce a very rapid heating of the material directly under the impacting particle. This effect is due to the pressure wave which is propagated into the material after contact with the speeding particle. The pressure rises so rapidly and the process is adiabatic. A peak pressure in a shock wave of a million atmospheres produces temperature increases in hundreds of degrees in the span of a nanosecond. Under these conditions the temperature rises quickly and can produce a liquid or vapor state under the impact particle. If changes of state occur, it is possible that polymerization and other chemical processes will occur. In fact, Los Alamos has observed the polymerization of pure sulphur and the formation of diamonds from soot in their work in shock chemistry. Since hypervelocity impacts produce shock waves in the material, the chemistry of shock process need to be explored for the space debris collisions.

The principle of the shock wave chemistry experiment jointly with Phillips
Laboratory and LANL is shown in Figure 3. Briefly, a shock wave is generated by a
collision which is caused by an exploding pellet of HMX. The explosion causes a shock

wave in the polysulfone which vaporizes and travels out into large vacuum chamber. The moving front is rapidly quenched which freezes in the chemical species formed during the shock wave propagation. The chemical species travel to the opposite side of the chamber where they encounter a molecular skimmer which funnels a molecular steam down a tube into a time-of-flight mass spectrometer. The spectrometer measure the mass of the species as the arrive at its detector and from the masses, the chemical species are identified. Arrival of species looks backward in time at the chemical process which occurred in the few nanoseconds of the shock.

Specimens of polysulfone were prepared for exposure to shock waves generated by the HMX pellet. Specimens of varying thickness were prepared by mechanical lapping equipment at Phillips. The thicknesses ranged from 0.1 to 0.5 mm. The specimens were cleaned with acetone and rinsed with distilled water. They were place in airtight containers and transported to LANL, to Dr. Roy Greiner. They have not been tested as of this date, but it expected that they will be shocked this month.

### **FUTURE PLANS**

The future plans include expanding this research area of shock chemistry at Los Alamos and at Phillips Laboratories in the next two years. While reasons from continuing the studies differ at the two laboratories, the cooperative effort demonstrates the benefits to both DCD and DOE of collaboration. Shock wave chemistry is new and little is known because the techniques for studying it were not available until LANL began its work.

The plans also include a continuation of research at California State University at Northridge, (CSUN). Two areas of collaboration with LANL and Phillips have been identified. CSUN will prepare other specimens for shock studies at LANL and will seek to provide a better method of producing shock waves in advance spacecraft materials. It is hoped that the excellent cooperative arrangement between Phillips, LANL, and CSUN can be continued using a Research Initiation Grant as part of this contract.

### CONCLUSIONS AND RECOMMENDATIONS

The Faculty Summer Research Program funded by AFOSR through RDL is an excellent example of a win-win program. From both the host laboratory and the educational institution perspectives, the faculty research is immensely beneficial. The laboratory gets an opportunity to move into a new research area without diverting valuable personnel away from the main thrust of the missic — he faculty research associate can bring new ideas and expertise to laboratory problems. The educational institution gains by having one of its faculty members exposed to new and innovative technologies without expense and has the opportunity to initiate research on the campus in new areas. The faculty member also gains through experience and has a chance to meet and work closely with other researchers. It is hoped that the AFOSR will continue to support this very worthwhile program.

It is the authors conclusion that this was a prime example of how the RDL Program should work. It has been very rewarding experience. It is hoped that RDL and Phillips agree. The author acknowledges the support of Dr. Charles Stein at Phillips for his patience and guidance this summer. Also from Phillips the close support of Mr. Robert Roybal and Charles Maglionico are gratefully appreciated. Finally, the recommendations of Dr, Roy Greiner at LANL are also appreciated.

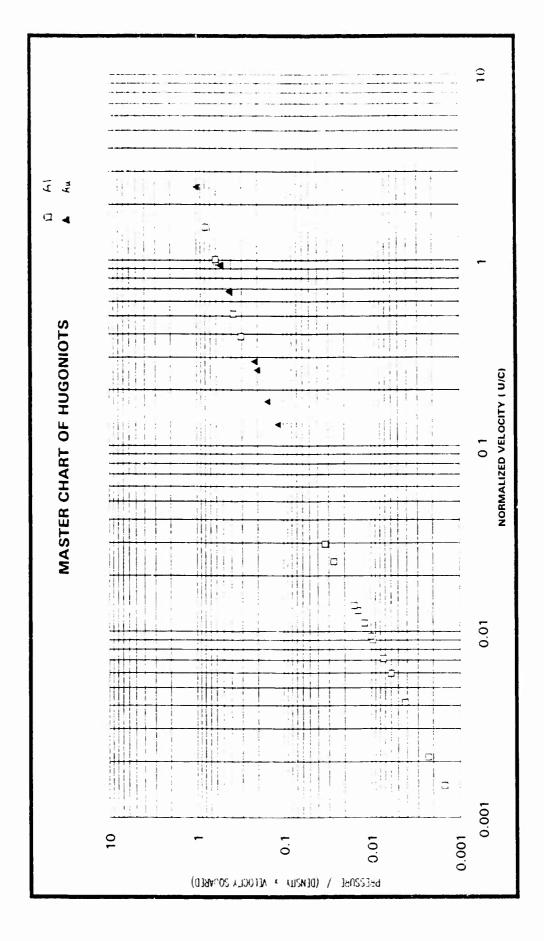
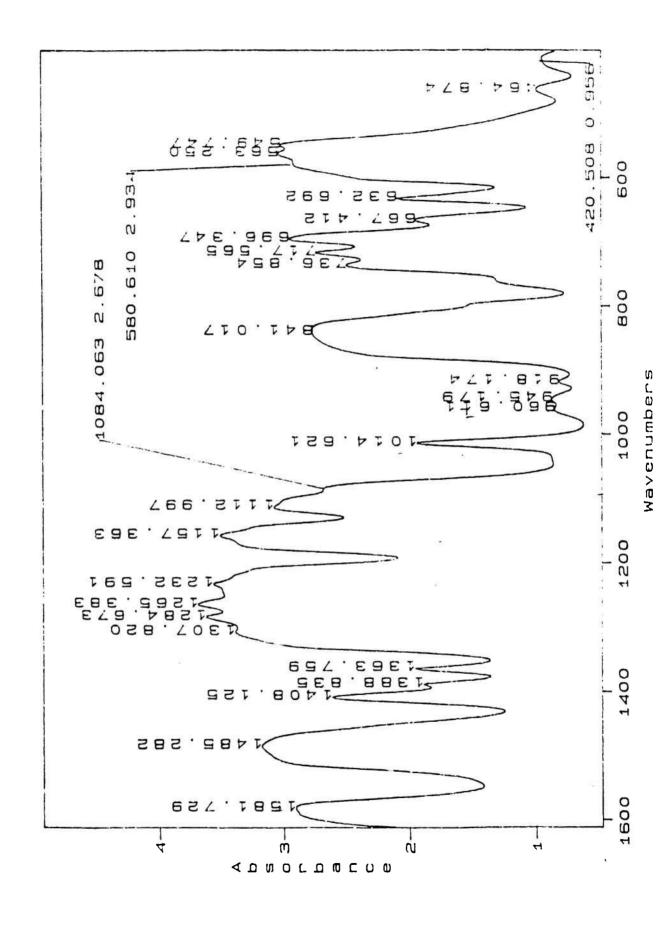
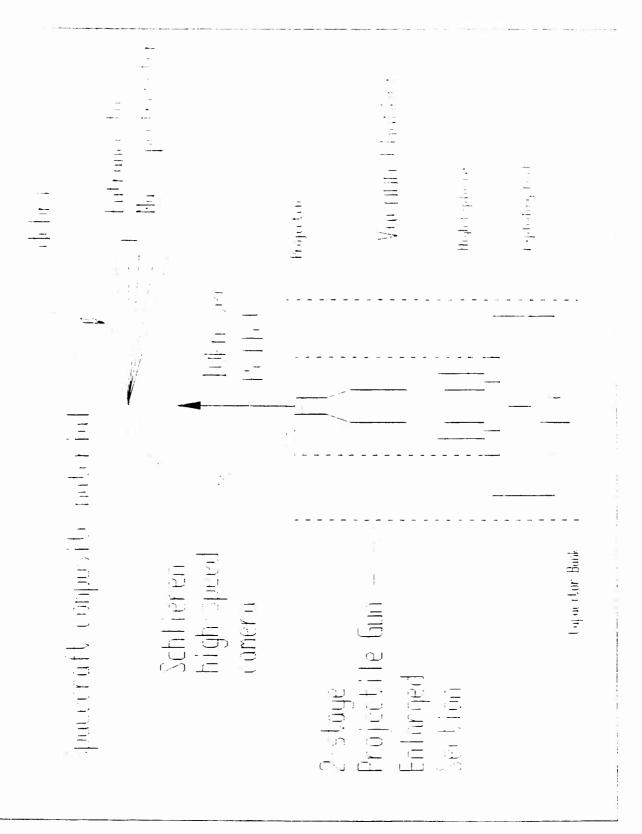


FIGURE 1 HUGONIOTS FOR ALUMINUM AND GOLD

FIGURE 2 INFRARED SPECTRA FOR POLYSULFONE





## NUCLEAR AND PLASMA PHYSICS WITH ANTIPROTONS AT SHIVA STAR

PROF. GERALD. A SMITH
DEPT. OF PHYSICS
PENNSYLVANIA STATE UNIVERSITY
Sept. 30, 1991

#### ABSTRACT

Prof. Gerald A. Smith spent the 10 week period July 22-September 29, 1991 as an AFOSR Summer Faculty Awardee in residence at the Phillips Laboratory, Kirtland AFB, Albuquerque, NM. An important purpose of the visit was to become more familiar with the operation and properties of SHIVA Star, an electromagnetic solid liner imploder operated by the High Energy Plasma Branch. SHIVA Star will be used to compress fissile targets which will be exposed to short bursts of antiprotons. This work is being sponsored by AFOSR under a joint proposal from the Phillips Laboratory and Penn State University. The goal of this program is to test features of subcritical microfission in small targets. This concept has been proposed by Prof. Smith and colleagues at Penn State University as a potential source of propulsion power for missions requiring large thrust and Isn. During the visit Prof. Smith refined and extended calculations on yields of neutrons in the device, including using external magnetic fields. In addition, he presented several seminars and lectures on the subject, internal to the Phillips Laboratory and external to professional groups. All prior objectives of the visit were addressed. Considerably more work is anticipated before experiments on SHIVA Star will be ready for execution. Prof. Smith and his group will continue their active collaboration with the Phillips Laboratory for the next several years until the objectives of the program are met.

### I. INTRODUCTION

On March 29, 1991 at the AFOSR Spring Initiatives Review, Bolling AFB, Washington, DC, the proposal "Nuclear and Plasma Physics with Antiprotons," submitted jointly by the Phillips Laboratory, Kirtland AFB and Penn State University, was approved for funding. In addition to \$215K of seed money for FY92, an additional \$593K was approved for each of FY93, 94 and 95 (\$1994K total). The following sections of this report review the concepts of the proposal. At approximately the same time, Prof. Smith was approved for a 1991 AFOSR Summer Faculty Award, which was spent at the Phillips Laboratory from July 22-Sept. 29 of this year. This report reviews fully that 10 week activity, including progress achieved toward implementing the approved experimental program.

The goal of this program is to demonstrate subcritical fission initiated by low energy antiprotons in a microtarget of uranium. The problem was identified by Prof. Smith following the discovery of antiproton-induced fission by the Penn State group under AFOSR sponsorship in experiments at CERN in Geneva, Switzerland in 1989. It was observed that the yields of neutrons from the antiproton-uranium interaction were very large. This led to the notion that intense beams of locally directed, low energy antiprotons could be used to "jump-start" the chain reaction, thereby decreasing the time required to completely consume a target. Since the burn propagates at a finite velocity, decreased times

correspond to reduced size of the target. Reasonable physical assumptions suggest that targets as small as one gram could be ignited.

The first logical step in the demonstration of these concepts is to show neutron multiplication in a target under modest compression, resulting in subcritical gain and low neutron yield. This led to the proposal with the Phillips Laboratory, which operates the electromagnetic imploder SHIVA Star. A successful set of experiments at this facility could lead to more ambitious experiments, which are potentially important to interplanetary space propulsion technologies and national defense. The next section describes the physics and technical issues briefly sketched above in much more detail.

### II. DISCUSSION OF PROBLEM

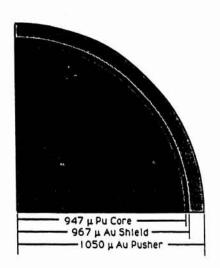
The goal of microfission is to initiate self-propagating fission reactions in the smallest possible amount of material. The material is compressed to high density, and its inertia maintains this density while the fission reactions are occurring. The challenge is to find practical methods of speeding up the fission reactions, so that the fuel is burned before the material dissipates. We propose using antiprotons to initiate fission reactions, by-passing the time-consuming early stages of the chain reaction.

The microfission concept was proposed in 1973 by Askar'Yan et all and Winterberg.<sup>2</sup> The concept was a natural extension of inertial confinement fusion (ICF) research. These authors reasoned that the same techniques could be used to produce a microexplosion of a fissionable target. The required compression work has been estimated by several

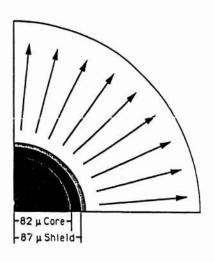
authors, with values ranging from kilojoules to tens of megajoules. Similarly, yield estimates have varied considerably.

### a) Antiproton-Induced Fission

In recent experiments at the Low Energy Antiproton Ring (LEAR) at CERN located in Geneva, Switzerland, antiproton-induced fission in a U(238) target was observed for the first time.<sup>3-5</sup> Based on the number



(a) Before Compression



(b) Peak Compression

Figure 1

of low energy neutrons observed,<sup>3</sup> as well as heavy charged fission fragments,<sup>5</sup> it was concluded that fission occurs nearly 100% of the time. It was found that 13.7 neutrons are produced per antiproton<sup>6</sup>; these include neutrons resulting from fission, evaporation and direct knock—out processes occurring within the nucleus. In addition, 2.47 charged pions are produced,<sup>7</sup> giving sixteen particles total which can induce subsequent fissions in a highly compressed target.

### b) Structure and Dynamics of Target

In Figure 1 we show a quadrant of the proposed target. A core of plutonium is surrounded by a spherical shell of gold. The gold pusher is heated by a driver, which compresses the core as the outer shell ablates. A thin shell of gold is left unheated, which acts as a radiation shield to reduce preheating of the core. When the

core is compresed to its maximum density, a pulse of antiprotons from a storage ring or trap is introduced to initiate a fission chain reaction.

To illustrate the dynamics of the system, we have chosen three targets with output energies in the 1-50 Gjoule range. The targets are compressed to 3,000 or 30,000 g/cm³ to illustrate effects over a large dynamic range in density. The largest pressure discussed in the literature on target compression is 50 Tbar, 8 which motivates our upper limit value. We then calculate the number of antiprotons required to achieve a 100% burn of each target. The results are shown in Table I.

Table I - Examples of Burn Dynamics

(A)	30,000 g/cm <sup>3</sup> 1 Gjoule	(B) 30,000 g/cm <sup>3</sup> 5 Gjoule	(C) 3,000 g/cm <sup>3</sup> 50 Gjoule
Mass of plutonium	13.9 mg	70 mg	700 mg
Initial radius	554 microns	947 microns	2041 microns
Initial density	19.5 g/cm <sup>3</sup>	19.5 g/cm <sup>3</sup>	19.5 g/cm <sup>3</sup>
Final density	30,000 g/cm <sup>3</sup>	30,000 g/cm <sup>3</sup>	3000 g/cm <sup>3</sup>
Pressure	52 Tbar	52 Tbar	485 Gbar
Final radius	48 microns	82 microns	381 microns
Confinement time	90 psec	153 psec	2.3 nsec
Compression work No. antiprotons Output energy	3.6 Mjoules	18 Mjoules	17 Mjoules
	2.5×10 <sup>14</sup>	2.1×10 <sup>8</sup>	1.26×10 <sup>13</sup>
	1 Gjoule	5 Gjoules	50 Gjoules

To illustrate with case (B) of Table I, a burst of  $2.1\times10^8$  antiprotons initiates  $2.3\times10^9$  secondary fissions chains, consuming the target in 153 psec. For comparison, we note that a single initial fission requires 5 psec/generation  $\times \log_{2.2} (1.8\times10^{20} \text{ atoms}) = 296 \text{ psec}$ , where 2.2 is the neutron gain/generation. Therefore, the burst of antiprotons reduces the burn time by a factor of 1.93 and consequently the target mass by  $(1.93)^3$ , or 7.2. Furthermore, since the antiproton beam can be

delivered in short bursts with precision (~ lmm), it is unique in its ability to initiate a burn of such small targets.

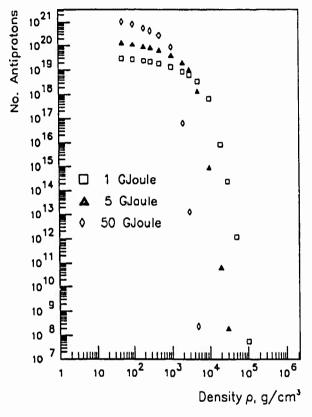


Figure 2

### c) Results

Figure 2 shows the number of antiprotons required to achieve 100% fuel consumption as a function of target density, computed for energy outputs of 1, 5 and 50 Gjoules. At low densities, the product of density times radius ( $\rho$ R) of the target is too small to yield appreciable fission gain. The demand for antiprotons drops precipitously for densities large enough to create a super-critical core. For example, at a density of 30,000 g/cm³ the 5 Gjoule target requires only 2.1×108 antiprotons, well within the production rate of  $10^{10}$  antiprotons per hour at CERN or Fermilab. The extraction of subnanosecond pulses of  $10^8$  anti-

protons from storage devices is within the present state-of-the art.

### d) Application of Antiproton-Boosted Microfission

In this section we discuss possible applications of antiproton-boosted microfission. One of these applications is space propulsion, where power and specific mass are critical parameters. For case (B) of Table I, we see that the explosion of one pellet per second would produce 5GW of power, assuming 100% efficiency. A recent study finds that a complete system, including an antiproton-boosted microfission target which ignites a fusion burn, e.g. D-He<sup>3</sup>, could result in multi-gigawatt jet power and a specific mass of as little as 0.07 kg/kW.<sup>10</sup> Both parameters are competitive with previously considered fission and fusion propulsion systems.<sup>11</sup> An especially attractive feature for space propulsion is the antiproton source, which is a light weight (few metric tons), portable system, consisting of traps filled with up to 108-10 antiprotons each and a small, low energy accelerator (1-2 MeV) for precision (1mm) delivery of antiprotons to the pellet.

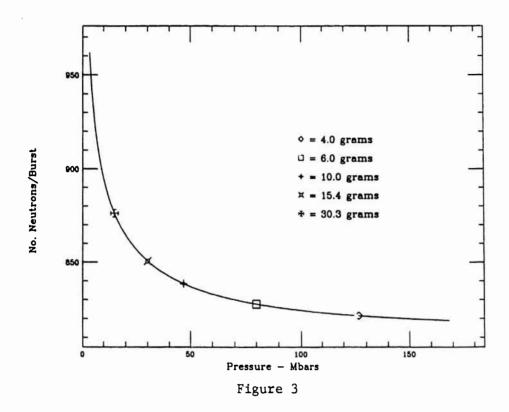
A second application of antiproton-boosted microfission is its use as an intense source of pulsed neutrons. Again illustrating with case (B) of Table I, a single initial fission produces a chain reaction with  $4\times10^{10}$  fissions occurring during the last 5 psec. It follows that the peak rate at which neutrons are produced is ~ 3 neutrons/fission ×  $4\times10^{10}$  fissions/5 psec ~  $2.4\times10^{22}$  neutrons/sec. The rate increases with the number of antiprotons to a maximum of ~  $10^{31}$  neutrons/sec, which corresponds to 100% fuel consumption. As noted above, realistically one may expect 10% fuel consumption before dilution effects dampen the reaction. By comparison, we note that alternate sources of fast bursts of

neutrons are vastly inferior in terms of realizable fluxes, e.g. from a fast burst reactor with a 200  $\mu$ s pulse and a peak rate of  $\sim 10^{24}$  neutrons/sec<sup>12</sup> or from a proposed dense plasma focus yielding up to  $5\times10^{23}$  neutrons/sec in a 100 ns burst.<sup>13</sup> An obvious application of such an intense, pulse neutron source is as a driver for a nuclear-pumped laser, which would far exceed in light intensity presently conceived systems.<sup>14</sup>

Finally, it should be noted that the target provides an intense source of X-rays. The energy release corresponds to ~ 180 MeV/94 electrons, or ~ 2 MeV/electron. At this density, most of the energy is in the form of electromagnetic radiation, with the temperature reaching ~ 100 KeV and X-rays radiated at a rate near the black body limit. 15

### e) Antiproton Experiments at SHIVA Star

In previous sections we describe conditions under which a complete burn of a fissile microtarget can be achieved. The requirements on numbers of antiprotons are within present delivery capabilities of antiproton sources. However, the requirements on compression work and pressure cannot be met with today's technology. It is important to find conditions under which the concept of antiproton-boosted microfission can be tested. This can be done under relaxed conditions of compression work and pressure (typically 200-2000KJ and 10-40Mbar respectively), provided the target mass is increased to the tens of gram range. Calculations show that, with one-thousand antiprotons injected into such a target in a short burst, significant subcritical neutron multiplication (30-50%) can be observed (Fig. 3). We assume a U(235) target, 250KJ compression work, a neutron detector with 5% net efficiency, and a 10 ns



pulse of antiprotons. The test would be considered a success if multiplication relative to thin target yields (660) were observed, and scaled in proportion to the number of antiprotons. It is important to note that these numbers constitute a ten standard deviation effect.

SHIVA Star is a solid liner imploder operated at the Phillips Laboratory, Kirtland AFB, Albuquerque, NM. Energy is provided from a 9.45MJ capacitor bank, which is inductively discharged through an anodecathode structure. The resultant multi-megamp current which flows down the liner (Fig. 4) forces it to collapse inwardly. For the antiproton-boosted microfission application, the liner will be used to compress a working fluid, such as hydrogen, with a large speed of sound.

The basic properties and application of the working fluid are: (1) forms hot (1-5 eV), dense  $(10^{19} \text{ atom/cc})$  hydrogen working fluid for

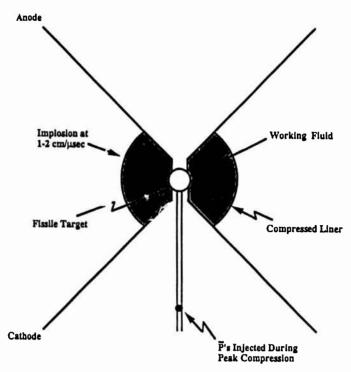


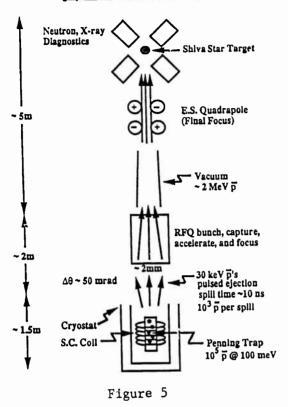
Figure 4

staged solid liner implosions; and (2) avoids shock formation and achieves uniform drive pressure in a spherical geometry. This produces a spherically symmetric pressure field around the fissile target which is positioned at the center of the liner. The resultant acceleration of the working fluid avoids shock formation, leading to a fast (several hundred ns) uniform pressure on the spherical target.

The apparatus consists of a portable Penning trap, a radiofrequency quadruple for accelerating and focusing protons(antiprotons) released from the trap onto the target, and the target arrangement situated inside SHIVA Star (Fig. 5). Particles are injected along the symmetry axis of the anode-cathode system to avoid transverse magnetic fields.

The experiment will be staged. First, implosion tests will be made on an inner gold target to test the working fluid concept. Then, the

## π ufission at Shiva Star



trap will be filled with deuterons, which will be injected into the gold target. The resultant compression inside the target will cause DD fusion reactions to occur, giving off 2.45 MeV neutrons. This will test injection and plasma conditions, as well as the sensitivity of the neutron counters. Finally, the trap will be filled with roughly 100 million antiprotons and transported to SHIVA Star. This will provide many shots of 1000-100,000 antiprotons each for

subsequent injections into a uranium (235) target under compression.

### III. RESULTS

The previous discussion, especially that of section e), outlines the problem and goals of the experimental program at SHIVA Star. During the 10 week visit this summer, Prof. Smith carried out many activities which bear on the ability of the experiment to meet these goals. Among those are:

1) Previous work has shown that the fission chain can be started using 13.7 neutrons per antiproton. The visit to SHIVA Star alerted Prof. Smith to the fact that the solid liner operation involves a very large (up to 10 megamp) current flowing through the liner (see Fig. 4). The current, nearly axial, creates a large B(theta) magnetic field around

the target. Within a few millimeters of the target the field reaches 10 megagauss. It therefore seemed apparent that one should consider magnetic trapping of charged pions, and subsequent recirculation of the pions through the target, as a complementary source of neutrons. The mechanisms involved are pion-induced fission, as well a other inelastic capture reactions induced by pions on uranium nuclei. A detailed Monte Carlo calculation produced images of pions making many turns through the target (Fig. 6). A detailed numerical analysis of the interactions indicated that an additional 15.8 neutrons could be produced by these mechanisms.

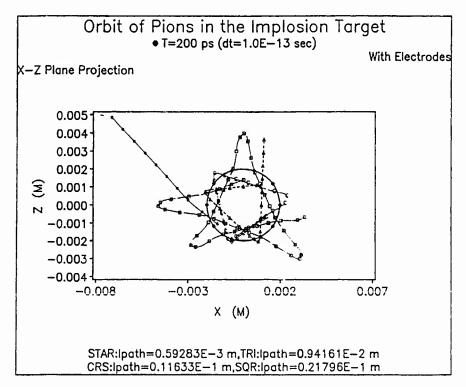


Figure 6

The magnetic field described above is contained solely outside the target. It was pointed out by Dr. James Degnan of the High Energy Plasma Branch that it is possible to inject additional field inside the

target, either axially using a Helmholtz coil pair outside the electrodes, or azimuthally by driving a current down a filament in the direction of the target. Further modeling of these fields, in addition to the external field, is presently underway. Preliminary indications are that it can further enhance the neutron yield.

- 2) A collaboration with Dr. Tom Hussey of the High Energy Plasma Branch was started. Dr. Hussey is an expert theoretical plasma physicist who agreed to look in detail at the working fluid concept, and produce calculations of adiabatic compression of the target. Dr. Hussey produced a series of graphics, which are reproduced here to illustrate progress to The rationale for the working fluid technique leading to adiadate. batic compression is illustrated in Figs. 7 and 8. The computational methodology using the code CALE is outlined briefly in Fig. 9. Results showing pre-compression and peak-compression geometries, as well as pressure flow, are shown in Figs. 10-12. We note in Fig. 12 the apparent isotropic compression pattern at the target. Prof. Smith and Dr. Hussey spent considerable time discussing the significance of this work This interaction will continue for the to the upcoming experiments. foreseeable future. Working fluid experiments are presently underway at the Phillips Laboratory, and Dr. Degnan has recently reported results that appear to be in agreement with CALE predictions.
- 3) Time was spent looking at the details of extracting a small fraction of the antiprotons from the Penning trap in fast bursts. A visit to Los Alamos National Laboratory (LANL) was made for discussions with Dr. Michael Holzscheiter on this subject.

# We choose compression of a cold, dense plasma working fluid in our initial attempts to achieve high pressure

- because direct collision of the liner with the target will generate shock waves in the target, leading to higher temperature, but lower density.
- because B-fields of sufficient initial intensity will be difficult to inject.
- because the plasma working fluid can supply symmetric compression to an on-axis spherical target.
- because appropriate plasma initial conditions appear possible:

$$- n_0 \sim 10^{19} \text{ cm}^{-3}$$

Figure 7

There is a trade-off between the requirement that thermal losses be minimized and the requirement that compression be adiabatic.

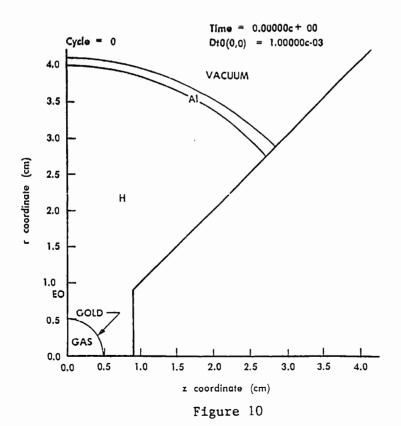
- Thermal losses from the working fluid to the electrode walls must be minimized.
  - The implosion must be as fast as possible.
  - The fluid temperature must be as <u>low</u> as possible.
- The compression of the working fluid must be ablabatic (i.e. no shocks). This requires that the implosion velocity be slower than the fluid sound speed.
  - The implosion must be as slow as possible.
  - The fluid temperature must be as <u>high</u> as possible ( $C_a \sim T^{1/2}$ ).
- Since, for adiabatic compression, PV<sup>r</sup> = const, we want as high an initial pressure as possible, consistent with the above.

Figure 8

# Sophisticated, two-dimensional (2-D) magnetohydrodynamic (MHD) calculations verify shockless compression of a central target.

- The 2-D MHD code, CALE, developed at LLNL (B-division) was utilized.
- Cale is ideally suited for this problem with:
  - arbitrary Lagrangean-Eulerian hydrodynamics.
  - strength of materials.
  - a sophisticated low-temperature equation-of-state package.

Figure 9



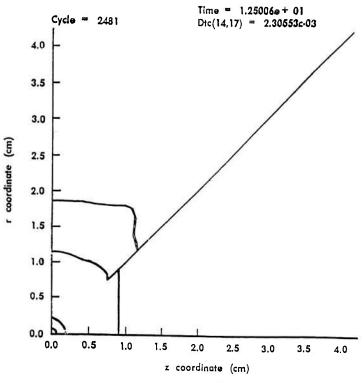
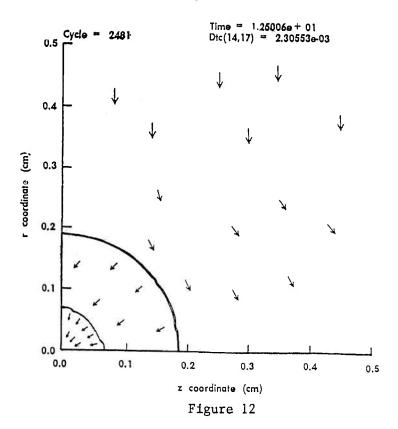


Figure 11



31-16

- 4) Prof. Smith received a SECRET DOD clearance during his visit to Phillips. This enabled several trips to LANL to consult with experts in X4-Division with access to sophisticated computer codes on the subject of target compression and nucleonics. Dr. Bruce Wienke has started computations on the microfission/fusion models put forth by Prof. Smith and his colleagues at Penn State. An ongoing dialogue on these subjects will continue.
- 5) Prof. Smith delivered the Advanced Concepts Seminar sponsored by T-Division, LANL, on Aug. 23. During this seminar he outlined the SHIVA Star experiment.
- 6) Prof. Smith presented a seminar in the High Energy Plasma Branch, Phillips Laboratory, on Aug. 6. The purpose of the seminar was to inform the staff of the meaning of the upcoming experiments, and to enlist their assistance when possible. This led to several informal discussions with staff members.
- 7) Prof. Smith traveled to Cleveland, Ohio on Sept. 6 to deliver an invited paper on propulsion applications of microfission/fusion at the AIAA Conference on Advanced SEI Technologies.
- 8) At the suggestion of the Jet Propulsion Laboratory, Pasadena, California, a visit of four NASA officials to the Phillips Laboratory on Sept. 24 was arranged. The Jet Propulsion Laboratory supports work of Prof. Smith's group at Penn State on propulsion applications of the microfission/fusion concept. Included in that visit were Mr. Earl Van-Landingham, Director, Propulsion Power and Energy, NASA Headquarters, Washington, DC; Mr. James Kelley, Manager, Power and Propulsion Office, Jet Propulsion Laboratory; Mr. Joel Sercel, Technical Group Leader,

Advanced Propulsion Technology, Jet Propulsion Laboratory; and Dr. Michael LaPointe, NASA Lewis, Cleveland, Ohio. The meeting lasted the full day, with presentations from Major Bill Mullins, Chief, High Energy Plasma Branch, Dr. Degnan, Dr. Hussey and Prof. Smith. The NASA officials also met with Dr. Brendan Godfrey, Phillips Laboratory Associate Laboratory Director for Advanced Weapons and Vulnerability, and Major Douglas Beason, Deputy to Dr. Godfrey. Discussions were held on the subject of the joint interest of the Air Force and NASA in the project, and future cooperation in this area.

### IV. CONCLUSIONS

The 10 week visit of Prof. Smith to the Phillips Laboratory led to important refinements and improvements to the upcoming experiment on subcritical microfission using the SHIVA Star facility. New contacts and initiatives were started between Prof. Smith and the staff of the High Energy Plasma Branch. Talks were given, both internal to the Phillips Laboratory and external to professional groups, on the subject of the experiments. The visit was extremely stimulating and informative, and in closing Prof. Smith expresses his sincere thanks to the Phillips Laboratory, and especially Majs. Mullins and Beason, and Drs. Degnan, Hussey and Godfrey, for their considerable hospitality during the visit.

### References

 G.A. ASKAR'YAN, V.A. NAMIOT and M.S. RABINOVICH, "Supercompression of Matter by Reaction Pressure to Obtain Microcritical Masses of Fissioning Matter, to Obtain Ultrastrong Magnetic Fields, and to

- Accelerate Particles, JETP Letters 17, 424 (1973).
- 2. F. Winterberg, "The Possibility of Micro-Fission Chain-reactions and Their Application to the Controlled Release of Thermonuclear Energy," Z. Naturforsch. <u>28a</u>, 900 (1973); "The Possibility of Microfission Explosions by Laser or Relativistic Electron-Beam High-Density Compression," <u>Lettere al Nuovo Cimento 6</u>, 407 (1973); "Micro-fission Explosion and Controlled Release of Thermonuclear Energy," <u>Nature 241</u>, 449 (1973).
- 3. A. ANGELOPOULOS et al, "Neutron Emission from Antiproton Annihilation at Rest in Uranium," Phys. Lett. B205, 590 (1988).
- 4. T.A. ARMSTRONG et al, "Nuclear Gamma-Ray Emission from Antiproton Annihilation at Rest in Uranium," Z. Phys. A 331, 519 (1988).
- 5. J.P. BOCQUET et al, "Antiproton Induced Fission in <sup>238</sup>U and <sup>209</sup>Bi,"

  Physics at LEAR With Low Energy Antiprotons, Proceedings of the

  Fourth LEAR Workshop, Villars-sur-Ollon, Switzerland, 6-13 Septem
  ber 1987, eds. C. Amsler, G. Backenstoss, R. Klapisch, C. Leluc, D.

  Simon and L. Tauscher, Harwood Academic Publishers (Switzerland, 1988), p. 793.
- 6. B. CHEN et al, "Fission Neutron Yields and Angular Distributions
  Produced by Antiproton Annihilation at Rest in Uranium," Pennsylvania State University, 1991 (unpublished).
- 7. E.D. MINOR et al, "Charged Pion Spectra and Energy Transfer Following Antiproton Annihilation at Rest in Carbon and Uranium," Z. Phys. A 336, 461 (1990).

- 8. N.A. TAHIR and K.A. LONG, "Inertial Confinement Fusion Target Design for a Reactor System Using Light Ions," <u>Nucl. Fusion</u> 29, 295 (1989).
- 9. D.C. PEASLEE, "Potential Low Energy p Sources in the U.S.," <u>Anti-proton Science and Technology</u>, Proceedings of the RAND Workshop on Antiproton Science and Technology, The RAND Corporation, October 6-9, 1987, ed. B.W. Augenstein, B.E. Bonner, F.E. Mills and M.M. Nieto, World Scientific Pub. Co. (Singapore, 1988), p. 16.
- 10. T. NUGENT, "A Performance Evaluation of the Ion Compressed Antiproton Catalyzed Nuclear (ICAN) Propulsion System," Jet Propulsion Laboratory Internal Document <u>D-8572</u> (1991).
- J.R. ROTH, "Space Applications of Fusion Energy," <u>Fusion Tech.</u> <u>15</u>,
   1375 (1989).
- 12. R.J. DEYOUNG et al, "Fission-fragment Nuclear Lasing of Ar(He)-Xe,"

  Appl. Phys. Lett. 37, 679 (1980).
- 13. H. CONRADS, "Dense Plasma Focus as a Neutron Source for Fusion Research," Nucl. Sci. and Eng. 106, 299 (1990).
- 14. M.A. PRELAS et al, "Nuclear Driven Flashlamps," <u>Laser and Particle</u>

  <u>Beams</u> 6, 25 (1988).
- 15. Y.B. ZEL'DOVICH and Y.P. RAISER, <u>Physics of Shock Waves and High</u>

  <u>Temperature Hydrodynamic Phenomena</u>, Vol. <u>1</u>, Chapter 2, Academic

  Press (New York and London, 1966).
- J.H. Degnan et al, IEEE Trans. on Plasma Sci., PS-15, No.6, 760 (1987); Megagauss Technology and Pulsed Power Applications, ed.
   C.M. Fowler, R.S. Caird and D.J. Erickson, Plenum Pub. Corp. (New York, 1987), p. 699.

## CONSTITUTIVE MODELING OF SLURRY INFILTRATED FIBER CONCRETE (SIFCON)

David J. Stevens, Assistant Professor Department of Civil and Env. Eng. Clarkson University Potsdam, NY 13676

### ABSTRACT

Slurry Infiltrated Fiber CONcrete (SIFCON) is a unique material, containing 5 to 20 percent, by volume, of steel fibers; in contrast, Fiber Reinforced Concrete (FRC) contains only 0.5 to 2 percent fibers. SIFCON exhibits high compressive and tensile strengths (up to 35 ksi and 5.5 ksi, respectively), and it is extremely "tough", capable of carrying a compressive stress of 10 ksi to a strain in excess of 10%. Thus, SIFCON has great potential for energy absorbent components in civilian and military structures. SIFCON also typically exhibits a low modulus of elasticity (usually less then half of plain concrete), and it's response strongly depends upon the orientation distribution of the fibers. In order to represent these unique characteristics of SIFCON, a new constitutive model was developed this summer, for the Shock Physics Division of the Phillips Laboratory, Albuquerque, New Mexico. The terminal goal of this model is implementation into a Finite Element code, which would be used to analyze SIFCON structures. The Finite Element application of the model will be proposed in a follow-on study.

The SIFCON model was developed within the theory of mixtures. An anisotropic, continuum damage/plasticity model, previously developed by the author for concrete, was modified to represent the slurry. A simple model that accounts for the resistance of the fibers and the enhanced resistance of the plain slurry was developed. The predictions of the model are compared to data from a number of laboratory tests.

### INTRODUCTION

The introduction of short, stiff, deformed, randomly oriented, steel fibers with high aspect ratios into a cementitious material results in a composite that is significantly superior to the plain material; improvements in strength, ductility, failure toughness, postcracking strength, and impact resistance are often observed as well as a reduction in the number of cracks and the mean crack width. SIFCON, unlike conventional FRC, is composed of much higher volume percentages of fibers, in the range of 5 to 20 percent. SIFCON is formed by placing the fibers in the mold and then pouring a liquid slurry onto the fibers; the slurry "infiltrates" the fibers.

A previous mixture model for FRC by the author (Stevens and Liu '91) showed that the response of the plain concrete could be taken as independent of the fibers; thus, with a volume of 0% fibers, the model predicts the behavior of plain concrete quite well. While SIFCON contains much higher percentages of fibers (usually ~12%), it was assumed that the same type of mixture approach would be effective, since the majority of SIFCON is still ~90% slurry. As the preliminary results from the model show, this assumption is adequate for SIFCON but it does hold better for conventional FRC.

The model was developed with two main objectives: 1) to match the observed responses of SIFCON adequately and 2) to minimize the complexity of the model and the number of material constants. Both objectives were met in the course of this research, as shown in this report. The following section describes the model and a later section presents the predictions of the model versus laboratory test results. These comparisons show that the model does an adequate job in representing the complex, nonlinear behavior of SIFCON.

### APPROACH

In this model, the theory of mixtures is modified and applied to SIFCON, which consists of two phases: slurry and fiber. It is assumed that the strain in the slurry  $e^t$  and the fiber "mat"  $e^t$  are equal to the overall strain e (a Voigt estimate). In addition, in classic

mixture theory, the stresses of the constituents are assumed to be independent of each other; this is certainly not true for SIFCON in either the pre- or post-peak regions. Therefore, a modified mixture approach is taken:

$$c = \sigma^s + \sigma^f \tag{1}$$

where  $\sigma^s$  and  $\sigma^f$  are the stresses in the slurry and fibers, respectively. Unlike typical mixture approaches, the sum of the stresses is not weighted by the volume percentage, since the fiber contribution reflects both the fiber and (fiber-enhanced) slurry response.

### Slurry Model

The contribution of the sturry is represented by a continuum damage/plasticity model, previously proposed by Stevens and Liu '92 for plain concrete. It is assumed that the response of the sturry is determined by two small scale phenomena: the initiation, growth and coalescence of microcracks and the pressure-dependent (frictional) tangential movement of the microcrack surfaces. A kinematic inelastic surface is used to account for the strong anisotropy of the damage created by the microcrack growth and coalescence; in conjunction, an isotropic surface is used for the frictional movement of the microcrack surfaces. The inelastic surfaces are taken as functions of the elastic strain, due to it's strong relationship to damage growth, stiffness recovery, permanent deformation, and the current stress level (Stevens and Liu '91). To preserve consistency and retain simplicity, the same surfaces are used to define both the elastic degradation and the permanent deformations.

The slurry stress is decomposed as

$$\sigma = \sigma^e - \sigma^p \tag{2}$$

where  $\sigma^p$  is the plastic stress of the slurry,  $\sigma^c = \mathbf{C}$ :  $\varepsilon$  is the elastic stress, and the superscript s has been dropped.  $\mathbf{C}$  is the 4th order anisotropic stiffness. Ortiz '85 proposed that  $\mathbf{C}$  be decomposed as:

$$C = C^{\circ} - C^{*} - C^{-} \tag{3}$$

Co is the original elastic stiffness, and, Co are the changes in the positive and negative

effective stiffness. Unlike the previous model for concrete, C is taken as zero for the slurry, i.e., due to the small size of the sand particles in the slurry, the contribution of compression softening is assumed to be negligible.

For the compressive mode, an isotropic "inelastic" surface, g' is used and, for tension, a kinematically hardening "inelastic" surface, g<sup>+</sup>, is employed. These surfaces are used for evolution of both damage and permanent deformation.

$$g^*(e^e, \alpha^*) = \tau^* - r_o^* = 0, \qquad g^-(e^e) = \tau^- - r^- = 0$$
 (4)

where

$$\tau^* = \sqrt{\langle e^{\epsilon^*} - \alpha^* \rangle : C^\circ : \langle e^{\epsilon^*} - \alpha^* \rangle}, \qquad \tau^- = \sqrt{e^{\epsilon^-} : C^\circ : e^{\epsilon^-}}$$
 (5)

$$e^{\epsilon \cdot \cdot} = \sum_{a=1}^{3} \langle e_{(a)}^{\epsilon} \rangle \underline{e}_{(a)}^{\epsilon} \otimes \underline{e}_{(a)}^{\epsilon}, \qquad e^{\epsilon \cdot \cdot} = e^{\epsilon} - e^{\epsilon \cdot \cdot}$$
 (6)

$$\langle e^{\epsilon^*} - \alpha^* \rangle_{ij} = \langle e^{\epsilon^*}_{ij} - \alpha^*_{ij} \rangle$$
 (7)

 $\tau^-$  and  $\tau^+$  are the energy norms of the negative strain tensor and the shifted positive strain tensor, respectively.  $r_o^+$  and  $r_o^-$  are the thresholds for further damage/permanent deformation;  $r_o^+$  is a constant while  $r_o^-$  evolves from an initial value of  $r_o^-$ . The values of  $r_o^+$  and  $r_o^-$  can be chosen by identifying the first deviation from linearity in the stress-strain curve (not always an easy task).  $\alpha^+$  is a kinematic "back strain" that defines the current origin of  $g^+$ .  $e_{(a)}^-$  and  $e_{(a)}^-$  are the eigenvalues and normalized eigenvectors of  $e^-$ , respectively and  $e_{(a)}^-$  is the Macaulay bracket. These surfaces are shown in Figure 1, for a plane strain state and with  $e_{(a)}^-$  is identity tensor), for plotting purposes.

The positive surface in Eq. 4 is used to define the rate of change of the tensile elastic degradation:

$$\dot{C}_{t}^{*} = \dot{\mu}^{*} \frac{\partial g^{*}}{\partial e^{\epsilon} \otimes e^{\epsilon}}$$
 (8)

where  $\dot{C}_{t}^{+}$  is the positive <u>total</u> stiffness rate, which is related to the effective stiffness,  $C^{+}$ , later.  $\dot{\mu}^{+}$  is the consistency parameter.

The kinematic translation of the tensile surface is governed by an associated flow rule:

$$\dot{\alpha}^* = \dot{\mu}^* \frac{c_1}{H^*} \frac{\partial g^*}{\partial e^c}$$
 (9)

$$H^* = \gamma_1 e^{-\gamma_2 r_v^*} [e_v^* + \gamma_1 \hat{H}(\lambda_{\max} - e_v^*)]$$
 (10)

where  $e_v^+ = tr(e^{e^+})$ ,  $e_v^- = tr(e^{e^+})$ , and  $\lambda_{max}$  is the maximum eigenvalue of  $e^e$ .  $\gamma_1$ ,  $\gamma_2$ ,  $\gamma_3$  are material constants. The tensile rurface and the associated kinematic hardening allows elastic degradation to occur in one direction without degrading the strength in the orthogonal directions. The hardening function in Eq. 10 is different than that used for concrete, requiring only 3 material constants.  $\gamma_1$  defines the magnitude of the stiffness degradation,  $\gamma_2$  determines the rate at which the stiffness degradation is damped out, and  $\gamma_3$  is used to define the stiffness degradation in situations when the total tensile strain exceeds the compressive strain (e.g. under uniaxial tension).  $\gamma_1$ ,  $\gamma_2$ ,  $\gamma_3$  are unique for any given slurry mix; in this model, the constants were chosen by trial and error.

The isotropic hardening for the compressive surface is:

$$\dot{r}^- = \frac{\dot{\mu}^-}{2\tau^- H^-} \tag{11}$$

$$H^- = A^- \tag{12}$$

where H is the hardening function which is equal to A, a material constant. A defines the ductility of the slurry and is fitted by trial and error. Again, this function is different from that for concrete.

Kuhn-Tucker relations are used to define the loading/unloading conditions for the plastic stress and elastic degradation. In applying these relations, the following operator is identified

$$P^* = \sum_{a=1}^{3} \hat{H}(\varepsilon_{(a)}^{\epsilon}) \underline{e}_{(a)}^{\epsilon} \otimes \underline{e}_{(a)}^{\epsilon} \otimes \underline{e}_{(a)}^{\epsilon} \otimes \underline{e}_{(a)}^{\epsilon}$$
(13)

P<sup>+</sup> is called the positive orthogonal projection operator (Orti<sub>2</sub> '85).

In the development of the elastic degradation, it is assumed that all of the cracks are

active and the evolution equation defines the change in the <u>total</u> elastic stiffness. To capture stiffness recovery under reversed loading, Ortiz (1985) proposed that the effective stiffness,  $C_1^+$ , be related to the total stiffness,  $C_1^+$ , as follows:

$$C^* = P^* : C^* : P^* \tag{14}$$

The development of permanent deformation is also signaled by the inelastic surfaces; associated flow rules are used with <u>both</u> surfaces:

$$\dot{\sigma}^{p} = \dot{\mu}^{+} \frac{\partial g^{+}}{\partial e^{e}} + \dot{\mu}^{-} \frac{\partial g^{-}}{\partial e^{e}}$$
 (15)

The Kuhn-Tucker loading conditions and consistency condition are then used to define the rate of change in plastic stress.

### Fiber Model

A strong synergistic relation exists between a cementitious matrix and the fibers, which act as crack arrestors, resisting the microcracks through debonding, frictional pullout, dowel action, fiber interlock and mechanical anchorage. In the proposed approach, the fiber model represents both the direct load-carrying contribution of the fibers and the enhancement of the matrix response due to the reduced stress concentration. The effects of the complex, small scale mechanisms (debond, pullout, interlock, etc.) are smeared into a macroscopic model in which the overall response is taken as uniaxial in any tensile strain direction; experiments show that the fibers contribute little under direct compression (Schneider '91).

Before the model is presented, the effects of fiber orientation must be discussed. In FRC, the orientation and spatial distribution of fibers can be taken as uniformly random; however, the strong dependence of SIFCON response on alignment of the fibers must be considered. Typically, in SIFCON fabrication, the fibers are sprinkled by hand into the mold; thus the fibers tend to align perpendicular to the gravity vector and, if the mold is small, the edges can affect the density and orientation of the fibers. In a large form, the fibers create a transversely isotropic fabric--the response is isotropic in the plane of the fibers but is different in the out-of-plane direction. As Figure 2 shows, a cylindrical specimens with its axis

perpendicular to the fiber plane is defined as a "vertical" specimen. If it's axis is in the fiber plane, it is a "horizontal" specimen. The effect of this alignment can be seen in Figure 5; a horizontal specimen has lower stiffness, peak strength and plateau strength, compared to a vertical specimen.

To account for fiber orientation, a second order "orientation tensor", a, is used, as suggested by Advani and Tucker '87. With the coordinate system shown in Figure 3, a is defined as:

$$a = \oint \underline{p} \otimes \underline{p} \ \psi(\underline{p}) \ d\underline{p} \tag{16}$$

where  $\underline{p}$  is the unit vector associated with the fiber,  $\psi(\underline{p}) = \psi(\theta, \varphi)$  is the probability distribution function, and integration is over the surface of a unit sphere (all possible directions of  $\underline{p}$ ). The distribution function must satisfy two conditions: 1) it must be periodic with respect to  $\theta$  and  $\varphi$  [ $\psi(\theta, \varphi) = \psi(\pi - \theta, \varphi + \pi)$ ] and 2) it must be normalized [ $f \psi(\underline{p}) d\underline{p} = 1$ ].

For the case of large molds, from which the specimens are cored out, the fiber orientation is almost uniformly random in the plane normal to gravity (the 1-2 plane in Figure 3) and the distribution function can be taken as independent of  $\phi$ . Thus, to determine the orientation tensor a, we need to perform stereological experiments to determine the orientation of the fibers as a function of  $\theta$ . This information is not available and  $\psi$  was taken as

$$\psi(\theta, \phi) = \psi(\theta) = e^{-a\cos^2\theta} \left(1 - b\cos^2\theta\right) \tag{17}$$

a and b are constants that must be assumed. With this form of  $\psi$ , the only nonzero terms of a are on the diagonal.

The orientation tensor is combined with the assumption that the fibers act only to restrain tensile strain. The total strain tensor is decomposed as follows

$$\varepsilon = \sum_{N=1}^{3} e_{(N)}^{\star} \underline{e}_{(N)} \underline{\otimes} \underline{e}_{(N)}$$
(18)

Each positive eigenvalue e\* and the associated eigenvector e are used to define the active tensile planes. On each of the tensile planes, a simple uniaxial hypoelastic model is used to define the fiber stress normal to the plane. The loading criteria on plane N is given by

$$f(e^*, \alpha^*) = e^* - \alpha^* = 0$$
 (19)

where  $\alpha^*$  is the "hardening" variable and it is defined as the magnitude of a second order tensor  $\alpha$  that is resolved on tensile plane N, i.e.,

$$\alpha^{\bullet} = \underline{e}_{(N)} \cdot \alpha \cdot \underline{e}_{(N)} \tag{20}$$

By enforcing consistency on the loading criteria,

$$\dot{\alpha}^{\bullet} = \dot{e}^{\bullet} \tag{21}$$

and the increment in the second order tensor  $\alpha$  is given by

$$\dot{\alpha} = \sum_{N=1}^{3} \dot{\alpha}_{(N)}^{*} \underline{e}_{(N)} \otimes \underline{e}_{(N)}$$
(22)

The summation is taken over all tensile planes.

The governing stress-strain law on the tensile plane is shown in Figure 4; an earlier model for conventional FRC used an elastic-perfectly plastic law but it was determined during development of this model that a degrading tangent stiffness performed better. For a strain less than the critical strain,  $\epsilon_c$ , the rate equations for the stress are given by:

$$\dot{\sigma}^{f*} = a^* \sigma_y \overline{e} e^{\overline{c} c^*} e^* \qquad f = 0$$

$$\dot{\sigma}^{f*} = Ra^* \sigma_y \overline{e} e^{-\overline{e} c^*} e^* \qquad f < 0$$
(23)

where  $a^*$  is the resolved component on the tensile plane of a, the second order orientation distribution tensor defined in Eq. 16 ( $a^* = \underline{e} \cdot \underline{a} \cdot \underline{e}$ ).  $a^*$  then accounts for the distribution of fibers that cross the tensile plane.  $\sigma_y$  defines the maximum obtainable stress,  $\overline{e}$  defines the rate  $a^*$  which  $\sigma_y$  is reached, and R determines the unloading stiffness ( $R \ge 1$ ). At some point, the fibers pull out of the matrix and the fiber stress reduces to zero. As Figure 4 shows, the

stress decreases linearly between  $\epsilon_c$  and  $\epsilon_f$ . Since a confining stress in the slurry will increase the resistance to pullout,  $\epsilon_{co}$  and  $\epsilon_{fo}$  are taken as functions of the confining stress:

$$\epsilon_c = \epsilon_{co}(1. + m\sigma_v^s), \qquad \epsilon_f = \epsilon_{fo}(1. + m\sigma_v^s)$$
 (24)

where m is a frictional coefficient and  $\sigma_v^s = tr(\alpha^s)$  is the confining stress. Five of the fiber material constants  $(\sigma_y, \bar{e}, R, \epsilon_e, \text{ and } \epsilon_f)$  can be found easily from a uniaxial tension test and the sixth constant, m, can be determined from a uniaxial compression test.

The incremental fiber stress on the tensile plane is converted to the second order incremental fiber stress tensor as follows

$$\dot{\sigma}^f = \sum_{N=1}^3 \dot{\sigma}^{f^*}_{(N)} \, \underline{e}_{(N)} \otimes \underline{e}_{(N)} \tag{25}$$

The numerical evaluation of the constitutive equations was performed with an explicit Forward Euler integration. For the particular loading path chosen, an increment in elastic strain(s) is input to the model and the new slurry stiffness tensor and the increment in inelastic slurry strain are calculated, using the values of variables at the end of the previous increment. The stiffness and inelastic strain of the slurry are then "frozen." The fiber model is then called and an iterative approach is used to balance the fiber stresses and the unknown elastic strains in the slurry.

Lastly, as with plain concrete, SIFCON exhibits strain-softening in tension and in compression. Due to the heterogeneity created by coalesced microcracks, strain softening is a "structural" phenomenon, not a material characteristic. Since strain-softening is size dependent, the post-peak region must be considered within the framework of boundary value problems, not as an aspect of the material model. For strain-softening problems, either the constitutive model or the numerical technique must be modified to remove the mesh sensitivity and to predict the correct energy dissipation. Examples of such methods include a nonlocal approach or a fracture energy equivalence technique. Within the context of the present model, strain-softening will be addressed later when boundary value problem solutions are attempted.

### RESULTS

The model's predictions are compared with the stress-strain data from a number of laboratory tests on SIFCON. While there is data available that describes the strength surface in stress space, time did not allow for those calculations to be performed; the follow-on proposal will include an effort to compare the model's results to the strength surface.

The first set of comparisons are shown in Figure 5, where axial stress vs. axial strain data from uniaxial compression tests on cored vertical and horizontal specimens are shown (no radial strains were measured). The compression data comes from Mondragon '86. Also shown are the model's predictions for uniaxial tension compared to data from a different test program by Homrich and Naaman '87. The material constants are given in Table 1.

As Figure 5 shows, the model predicts the peak stress and the plateau stress quite well. The strains at peak stress aren't as close but are considered acceptable by concrete modeling standards, considering the typical scatter in data. What is particularly pleasing is the close prediction of the horizontal specimen response, since such specimens have different fiber orientations in the two radial directions of the cylinder. During the loading process, the SIFCON stiffness degrades quickly in the lightly reinforced direction while in the highly reinforced direction, the slurry is confined. It should also be noted that this confinement "effect" (in either direction) is not constant but increases nonlinearly with strain. The predictions of the tensile response are quite good also, showing good agreement with the stress and strain at peak.

A comment concerning the post-peak plateau of the model and data should be made. Experimentally, uniaxial SIFCON specimens will typically develop a shear band mode of deformation after the peak stress is reached; the remaining resistance is due to frictional sliding across the inclined crack. Thus, since the model is based on continuum theories, it cannot, by definition, reproduce such discontinuous behavior and agreement between model and experiment in the post-peak range does not contain a lot of significance. However, it should be considered as very positive that the model does show a constant resistance after the

peak stress occurs since this will be important when boundary value problems are addressed.

As mentioned earlier, it was assumed that the model will predict the behavior of the slurry when the fibers aren't present ( $\sigma_y = 0$ ). Figures 6 and 7 show the model's predictions for SIFCON and the slurry. Unfortunately the only data available for the plain slurry is the strength measured from 3" cubes (= 7354 psi). The model predicts peak compressive and tensile strengths of 5475 psi and 865 psi, respectively, which are reasonable. The strain at peak tensile stress is 0.00036 which is also reasonable; however, in compression, the strain at peak is 0.0083, about three times that of plain concrete at peak. While there is no data available, this strain appears high and points out that the slurry properties in the mixture model may have to be chosen to match the SIFCON response, not just the plain slurry. The material values for this test were chosen by trying to get good predictions for both the plain slurry and the SIFCON; however, the best predictions for SIFCON did not yield good slurry predictions. A better set of material values or hardening rules may correct this and further exploration should be performed.

Figure 8 presents data from Mondragon '86 for a uniaxial vertical specimen loaded in compression and undergoing two cycles of unloading and loading. Since this is a different mix from the SIFCON shown in Figure 5, new material constants were chosen, as shown in Table 1. The model gives a good overall prediction stress-strain envelope. It also predicts the slope of the unloading leg very well. The model doesn't show the hysteretic loop that the data indicates, but the energy dissipated in the loop is small compared to the total energy dissipated so this is not of great concern.

Figures 9 and 10 show experimental data from Homrich and Naaman '87 for uniaxial compression and tension testing of horizontal and vertical molded specimens with different slurgy mixes. Their specimens were cast in relatively small forms; for the vertical specimens, edge effects will be significant but the fiber distribution normal to the gravity vector should be close to uniformly random. The fibers for the horizontal specimens were sprinkled through a slot in the long side of the mold. Hence the fiber axis would be strongly aligned with the long

dimension of the mold and there would also be some edge effects. To account for this, different values for a and b in the probability distribution function were used and the values for the diagonal terms of the a tensor are shown in Table 2. Also, since different slurry mixes were used (but with the same fiber type and volume), different material constants were used, as given in Table 1.

As Figures 9 and 10 show, the model's results are in fairly good agreement with the data. In compression, the comparisons of stiffness, peak strengths, and strains at peak strength agree well. The plateau strength is not predicted as well but it is not unreasonable, considering the typical scatter in post-peak data. In tension, the model predicts the peak strength, strain at peak and the strain-softening quite well.

The last comparisons are shown in Figure 11 where the confined compression test data on vertical specimens (from Schneider '88) are presented. The confinement pressures were 0, 600, and 10000 psi. As this figure shows, very good agreement is seen between the prediction and experiment, particularly for the 10000 psi confinement. It is not clear if the unloading portion of the experimental curves were deliberately created by unloading the specimen or if this indicates complete deterioration of the specimen. The termination of the model simulations for 600 and 10000 psi occurred due to complete failure of the model as indicated by a lack of convergence of the iterative procedure. In any event, the model does a nice job of capturing the pressure dependency of SIFCON.

### CONCLUSIONS

The proposed constitutive model for SIFCON satisfactorily reproduces the stress-strain curves of SIFCON under uniaxial compression and tension and confined compression. The number of material constants is 14, which is not large, compared to phenomenological models of plain concrete. Six of the constants are required by the fiber model and may be easily determined from uniaxial tension and compression tests. The remaining 8 constants are related to the slurry model, and, as discussed above, they cannot, in general, be chosen by

considering the slurry only; the SIFCON response should also be used. Improvements in the material constants or the hardening rules may improve this, however. In addition to the material constants, two parameters are needed to find the orientation tensor; these values are related to the geometry and preparation of the specimen and can either be assumed or fitted, since stereological data are not available. The fiber model appears to be a simple but efficient method for reproducing the contribution of the fibers to the enhanced response of the composite and the continuum damage/plasticity model for the slurry appears to represent the stiffness degradation of the SIFCON quite well.

### RECOMMENDATIONS FOR FURTHER RESEARCH

The proposed SIFCON model adequately reproduces the stress-strain curves of specimens undergoing simple uniaxial and confined loadings. Additional data regarding the failure surface of SIFCON is available and the model should be evaluated against this data. In addition, the material constants and the hardening laws should be further refined to determine if the slurry portion of the model can yield better results in predicting plain slurry behavior.

The next step, after refinement of the model, is implementation into a Finite Element code. In this step, the problem of strain softening/localization problem must be addressed. Previous experience of the author with a nonlocal approach for plain concrete has been quite positive and such a technique should be modified and implemented for SIFCON. If the nonlocal approach is not successful, then alternative methods such as fracture energy equivalence techniques or enhanced finite elements should be evaluated.

Lastly, providing that the Finite Element implementation is successful, numerical analyses of full-scale specimens containing SIFCON should be performed. There have been a number of experimental studies on beam tests, beam column tests, and deep beam shear tests, as well as blast load tests of SIFCON components. Agreement between the Finite Element model and the full-scale experimental results will provide the strongest verification of the effectiveness of the SIFCON model.

### **ACKNOWLEDGEMENTS**

I would like to thank the Air Force Office of Scientific Research for providing financial support over the summer, the Shock Physics Division (Major Clarence Fennell, Captain Tim Boone, and Dr. Rod Galloway) for their guidance and assistance, and Serri Doorn and Gary Leichting for their help in preparing the figures.

#### REFERENCES

Advani, S.G., and Tucker, C.L., 1987. "The use of tensors to describe and predict fiber orientation in short fiber composites," J. of Rheology, 31(8), p. 751-784.

Homrich, J., and Naaman, A., 1987. "Stress-strain properties of SIFCON in compression," ACI SP 105, p. 283-304.

Homrich, J., and Naaman, A., 1987. "Stress-strain properties of SIFCON in uniaxial compression and tension," AFWL-TR-87-115, Phillips Laboratory, Kirtland Air Force Base, Albuquerque, New Mexico.

Mondragon, R., 1987. "Development of material properties for slurry infiltrated fiber concrete (SIFCON)--Compressive strength," AFWL-TR-86-43, Volumes I and II, Phillips Laboratory, Kirtland Air Force Base, Albuquerque, New Mexico.

Naaman, A.E., 1991. "SIFCON: Tailored properties for structural performance," Pre-Proceedings, International Workshop on High Performance Fiber Reinforced Cement Composites, Mainz, Germany, p. 3-24.

Naaman, A.E., and Homrich, J.R., 1989. "Tensile stress-strain properties of SIFCON," ACI Materials J., 86(3), p. 244-251.

Schneider, B., Mondragon, R., Kirst, J., and Berglund, J., 1988. "ISST structure with SIFCON--HFC-2 test," AFWL-TR-87-101, Phillips Laboratory, Kirtland Air Force Base, Albuquerque, New Mexico.

Stevens, D.J., and Liu, D., 1991. "Constitutive modeling of fiber reinforced concrete," Tentatively Accepted for Publication in "Symposium for New Developments in Fiber Reinforced Concrete for the 21st Century", ACI.

Stevens, D.J., and Liu, D., 1992. "Strain-based continuum damage/plasticity model with mixed evolution rules for concrete," Accepted for Publication in the Journal of Engineering Mechanics, ASCE.

	E (psi)	ν	r + (psi) 1/2	r <sub>o</sub> (psi) <sup>1/2</sup>	A' (psi) 1/2	Υ <sub>1</sub> (psi)	Y <sub>2</sub> (psi)
Mondragon '86, Fig. 5	2.4x10 <sup>6</sup>	0.22	0.6	3.0	0.6	3.3x10 <sup>9</sup>	250.
Mondragon '86, Fig. 8	2.8x10 <sup>6</sup>	0.22	0.6	3.0	0.55	3.3x10 <sup>9</sup>	250.
Homrich '87, Fig. 9	2.4x10 <sup>6</sup>	0.22	1.0	6.0	0.2	1.3x10 <sup>9</sup>	100.
Homrich '87, Fig. 10	2.4x10 <sup>6</sup>	0.22	1.0	6.0	0.3	1.1x10°	50.
Schneider '88, Fig.	2.8x10 <sup>6</sup>	0.22	1.3	6.0	0.2	1.7x10 <sup>9</sup>	150.
4							
	Y <sub>3</sub> (psi)	σ <sub>y</sub> (psi)	ē	R	m	€ <sub>co</sub>	€ <sub>fo</sub>
Mondragon '86, Fig. 5			ē 950.	R 3.	m 3.3x10 <sup>-4</sup>	e <sub>co</sub> 2.x10 <sup>-2</sup>	e <sub>fo</sub> 4.x10 <sup>-2</sup>
Mondragon '86, Fig. 5  Mondragon '86, Fig. 8	(psi)	(psi)					
5	(psi) 32.x10 <sup>-4</sup>	(psi) 4300.	950.	3.	3.3x10 <sup>-4</sup>	2.x10 <sup>-2</sup>	4.x10 <sup>-2</sup>
5 Mondragon '86, Fig. 8	(psi) 32.x10 <sup>-4</sup> 32.x10 <sup>-4</sup>	(psi) 4300. 6500.	950. 650.	3.	3.3x10 <sup>-4</sup> 3.3x10 <sup>-4</sup>	2.x10 <sup>-2</sup> 2.x10 <sup>-2</sup>	4.x10 <sup>-2</sup> 4.x10 <sup>-2</sup>

Table 1. SIFCON Material Values

	Vertical			Horizontal			Tension		
	a <sub>11</sub>	a <sub>22</sub>	a <sub>33</sub>	a <sub>11</sub>	a <sub>22</sub>	a <sub>33</sub>	a <sub>!1</sub>	a <sub>22</sub>	a <sub>33</sub>
Mondragon '86, Fig. 5	0.48	0.48	0.04	0.48	0.04	0.48	0.48	0.04	0.48
Mondragon '86, Fig. 8	0.48	0.48	0.04	NA	NA	NA	NA	NA	NA
Homrich '87, Fig. 9	0.47	0.47	0.06	0.2	0.2	0.6	0.2	0.2	0.6
Homrich '87, Fig. 10	0.47	0.47	0.06	0.2	0.2	0.6	0.2	0.2	0.6
Schneider '88, Fig. 11	0.47	0.47	0.06	NA	NA	NA	NA	NA	NA

Table 2. Diagonal Terms of the Orientation Tensor (axis 3 is parallel to the long axis of the cylinder)

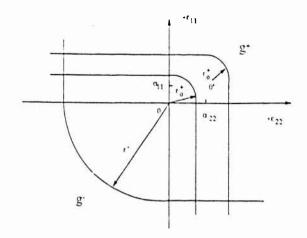


Figure 1. Inelastic Surfaces for a Plane Strain Condition, with C = I (for plotting purposes).

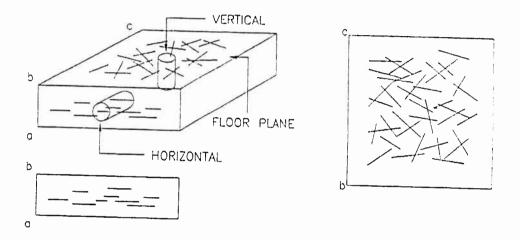


Figure 2. Transverse Isotropy of Fiber "Mat": Definition of "Vertical" and "Horizontal" Specimens

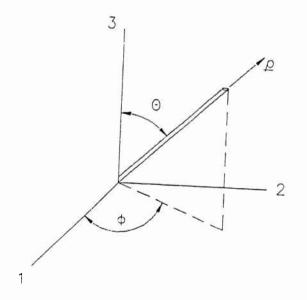


Figure 3. Definition of Fiber Orientation

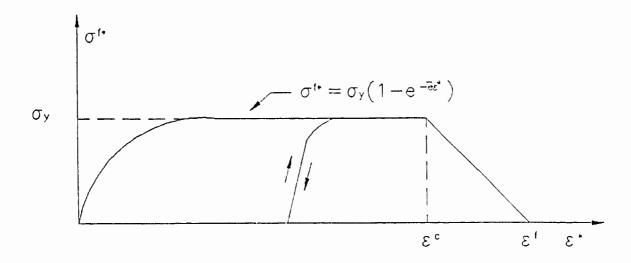


Figure 4. Uniaxial Model of Fiber Stress vs. Tensile Strain

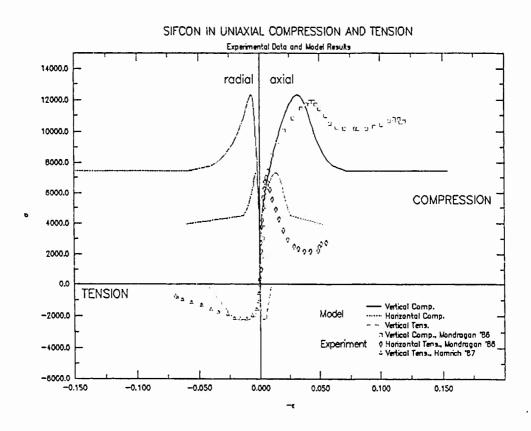


Figure 5. Model and Experimental Results for Uniaxial Compression Tests of Cored Vertical and Horizontal Specimens (Mondragon '86) and a Tensile Test of a Molded Horizontal Specimen (Homrich and Naaman '87).

## SIFCON IN UNIAXIAL COMPRESSION

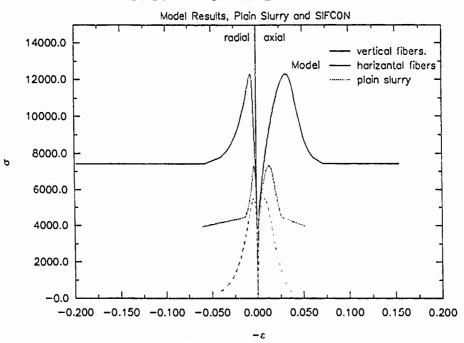


Figure 6. Model Predictions for Uniaxial Compression of Vertical and Horizontal SIFCON Specimens and a Plain Slurry Specimen

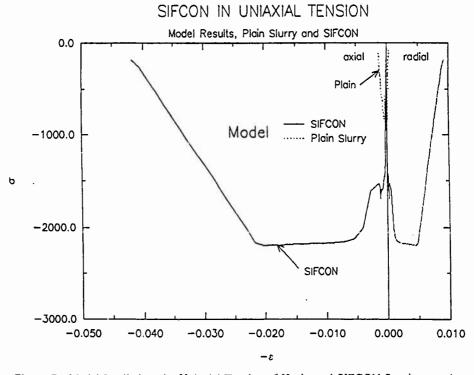


Figure 7. Model Predictions for Uniaxial Tension of Horizontal SIFCON Specimen and a Plain Slurry Specimen

## SIFCON IN UNIAXIAL COMPRESSION W/ UNLOADING

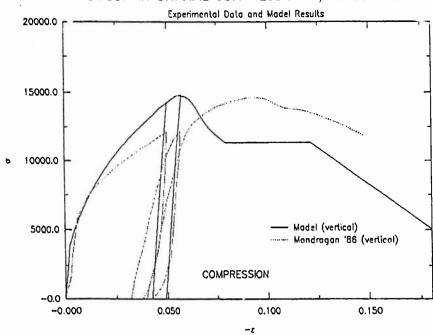


Figure 8. Model and Experimental Results for Reversed Uniaxial Compression Loading of a Vertical Specimen (Mondragon '86)

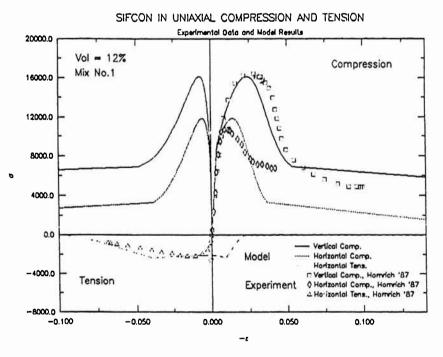


Figure 9. Model and Experimental Results for Uniaxial Compression Tests of Molded Vertical and Horizontal Specimens and a Molded Tensile Test of Horizontal Specimen, Mix 1. (Homrich and Naaman '87).

## SIFCON IN UNIAXIAL COMPRESSION AND TENSION

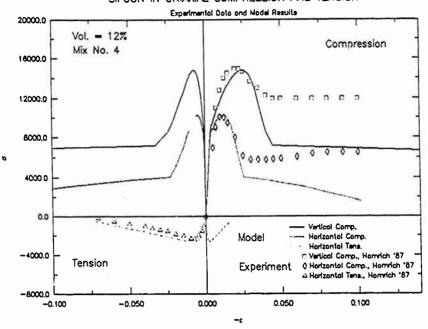


Figure 10. Model and Experimental Results for Uniaxial Compression Tests of Molded Vertical and Horizontal Specimens and a Molded Tensile Test of Horizontal Specimen, Mix 4. (Homrich and Naaman '87).

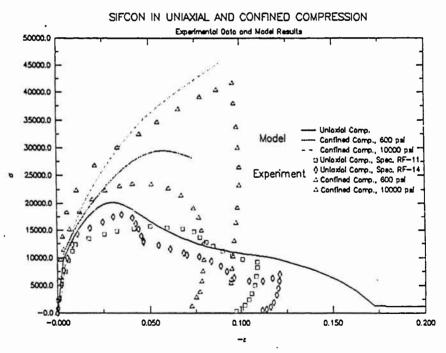


Figure 11. Model and Experimental Results for Confined Compression Tests of Cored Vertical Specimens (Schneider '88).

# SURFACE DEACTIVATION EFFICIENCIES FOR $O_2(^1\Delta)_{(a)}$ QUENCHING ON A RANGE OF COIL RELATED MATERIALS\*.

P.D. Whitefield,

Cloud and Aerosol Science Laboratory,

University of Missouri - Rolla,

Rolla, MO 65401

#### Abstract

A kinetic model is presented that describes both homogeneous  $(k_q)$  and heterogeneous  $(\gamma)$  deactivation of  $O_2(^1\Delta)_{(g)}$  in a flow reactor experiment. The model is validated through measurements made on pyrex surfaces where  $k_q$  and  $\gamma$  were found to be  $(1.64 \pm 0.04) \times 10^{-18} \text{cm}^3 \text{ s}^{-1}$  and  $(7.7 \pm 0.4) \times 10^4$  respectively. The model has been used to interpret data recorded for the aged surfaces of the following metals: Nickel  $\gamma = (3.5 \pm 0.1) \times 10^4$ , Copper  $\gamma = (2.8 \pm 0.3) \times 10^4$ , Nickel - Copper alloy  $\gamma = (4.0 \pm 0.1) \times 10^4$  and Inconel  $\gamma = (0.11 \pm 0.05) \times 10^4$ . Results obtained on fresh, non-oxidized metal surfaces are also discussed.

(\*A manuscript similar in content to this research paper, with several coauthors from the Phillips Laboratory, has also been prepared and will be submitted to the Journal of Physical Chemistry in September 1991).

#### Introduction

The generation and quenching of the lowest lying electronically excited state of molecular oxygen  $(O_2(^1\Delta)_{(g)})$  has received considerable attention in recent years<sup>1-4</sup>, in particular the application of  $O_2(^1\Delta)_{(g)}$  as the energy transfer partner in the Chemical Oxygen Iodine Laser  $(COIL)^{5-7}$ . Several researchers have reported surface deactivation efficiencies on Pyrex<sup>8-12</sup> and on other surfaces<sup>13-18</sup>. Most of these studies have concentrated on Pyrex, quartz and glass and good agreement is found between these studies, particularly in the case of Pyrex.

The work presented in this paper has focussed on:

- (1) the development and validation of a kinetic model that describes both homogeneous and heterogeneous deactivation processes for  $O_2(^1\Delta)_{(g)}$ , occurring in a flowing reactor. The validation is achieved through a detailed study on Pyrex deactivation;
- (2) the application of this model to deactivation on metal surfaces. This work is motivated by a desire to advance the fundamental understanding of  $O_2({}^1\Delta)_{(g)}$  quenching on surfaces, and to enhance the reliability and accuracy of the database upon which COIL performance models draw.

#### Experimental

A schematic diagram of the experimental apparatus is shown in figure (1). It consists of a high purity oxygen supply (Grade 5 (99.994%), AIRCO Industrial gases), a discharge/bypass system<sup>19,20</sup>, an observation region with detector and p.c. for data acquisition and analysis and a high capacity vacuum pump facility. The oxygen flows into the two arms of the discharge/bypass system were independently regulated by two mass flow controllers (Unit Instruments model no. UFC 1500A) operating over the flow rate ranges 0-100 SCCM and 0-2000 SCCM. These controllers afforded independent control of both the total ground state oxygen  $(O_2(^3\Sigma)_{\mathfrak{G}})$  and

excited  $O_2(^1\Delta)_{\mathfrak{Q}}$  concentrations entering the observation region.  $O_2(^1\Delta)_{\mathfrak{Q}}$  was a generated by a microwave discharge (generator and cavity, Opthos Instruments Inc., operational frequency 2.45GHz, operational power typically 30 watts) through the ground state oxygen flow in the discharge arm of the discharge and bypass system. The inner wall of the discharge arm was coated with mercury exide (HgO) to scavenge any atomic oxygen produced by the microwave discharge<sup>2</sup>. Downstream of the discharge bypass system the remixed oxygen flows passed through a woods horn en-route to the observation region.

The observation region consisted of upstream and downstream observation ports coupled by de-mountable reactor tubes constructed of elements or materials whose surfaces were to be examined. The observation ports were machined Teflon blocks with couplings, internally taped with teflon, to connect the discharge/bypass system to the reactor tube (upstream) and the reactor tube to the vacuum system (downstream). Pressure and temperature measurements were made at each observation port using a pressure transducer ( MKS Baratron No.390-HA00010) over the range 0-10 torr and thermocouples (Omega Corp.) respectively. Each observation port has a plexiglas window (90% transmitting) and an aluminum coated mirror mounted on the opposite side. A fiber optic holder is mounted over the plexiglas window. The flow region within the blocks is a 1.9cm ID smooth cylindrical bore common in 1.0 inch OD pipe.

The fiber optic, (Oriel Corp.), terminated at each end with a collimating beam probe, provided a convenient low light loss conduit through which light from either observation port could be transmitted to the remotely located detector along an identical path. The detector, a liquid nitrogen cooled intrinsic germanium detector (Applied Detector Corp., model no. 403LL) was a custom modified device optimized for slowly changing near i.r. radiation detection with extra high responsivity of 7 x 10<sup>10</sup>V/W and best noise equivalent power of 8.6 x 10<sup>-17</sup>. A light chopper (EG&G Parc 194A) operating at 24.9 2 and a narrow band pass filter

centered at 12680nm with 48% peak transmission and a FWHM of 80nm, were mounted close to the entrance port of the detector, thus permitting phase sensitive detection of  $\{O_2(^i\Delta)_{(g)} \rightarrow O_2(^3\Sigma)_{(g)}\}$  emission at the amplifier (Stanford Research Systems Lock-in, model no. SR510, typically operated with a square wave signal at 2mv and time constant of 0.03 sec.).

The detector was calibrated against an EPR spectrometer using the technique similar to that described by Benard and Pchelkin<sup>21</sup> for absolute concentrations of  $O_2(^1\Delta)_{(g)}$  in the range  $10^{13} - 10^{14}$  molecule cm<sup>-3</sup>.

The signals from the lock-in amplifier were sent to a lab p.c. (Zenith 248) for data acquisition and analysis. The data acquisition and analysis process can be summarized as follows. The upstream and downstream signals were sampled 2000 times over 15 seconds in alternating order. Each run was averaged and the variance calculated. The data were reviewed for intermittent noise interference. Large short-lived noise spikes were often recorded. Spikes greater than 2σ from the mean were cut off at 2σ and the average was recalculated. This process was repeated several times and the results for each block averaged. pressure was changed and the acquisition process was repeated. From these data the observed decay rate was plotted as a function of the total pressure (see kinetic model section below). A detailed description of the data acquisition and analysis software is given in a recent report by Workema et al.22 .

## Kinetic Model.

A nine reaction kinetic model, describing a non-reactive gas stream containing the electronically excited species  $O_2(^1\Delta)_{(p)}$  and  $O_2(^1\Sigma)_{(p)}$ , certain quenching gases including  $O_2(^3\Sigma)_{(p)}$ , and allowing for wall losses, has been proposed by Heidner<sup>23</sup> This model and its inherent assumptions has been employed to analyze  $O_2(^1\Delta)_{(p)}$  loss in the surface quenching studies described in this paper. In order to develop the mathematical analysis for this model, Heidner made two major assumptions. The first was that  $O_2(^1\Sigma)_{(p)}$  was

quenched both in the gas phase and on the walls of the reactor to  $O_2(^1\Delta)_{(g)}$ . This assumption is justified in terms of spin conservancy. The second assumption was that the  $O_2(^1\Sigma)_{(g)}$  concentration is in steady-state, with respect to  $O_2(^1\Delta)_{(g)}$  concentration throughout the reactor tube test section. This assumption can be justified by comparing the rate constants for reactions (1) and (2)<sup>10,24-26</sup>:

$$O_2(^1\Delta)_{(e)} + O_2(^1\Delta)_{(e)} -> O_2(^1\Sigma)_{(e)} + O_2(^3\Sigma)_{(e)}$$
 (1)

$$k_1 = 2 \times 10^{-17} \text{ cm}^3 \text{ s}^{-1}$$
.

$$O_2(^{1}\Sigma)_{(a)} + O_2(^{3}\Sigma)_{(a)} -> O_2(^{1}\Delta)_{(a)} + O_2(^{1}\Delta)_{(a)}$$
 (2)

$$k_2 = 4 \times 10^{-17} \text{ cm}^3 \text{ s}^{-1}$$
.

and appreciating that under experimental conditions the ratio  $[O_2(^1\Delta)_{(g)}]/[O_2(^3\Sigma)_{(g)}]$  was always <0.005; and that the wall deactivation efficiency  $(\gamma)$  for  $O_2(^1\Sigma)_{(g)}$  lies within the range  $\gamma=10^{-2}$  to  $10^{-3}$  <sup>27,28</sup>.

Under all experimental conditions  $\{O_2(^1\Delta)_{\mathfrak{Q}}\}$  >>  $\{O_2(^1\Sigma)_{\mathfrak{Q}}\}$  and  $\{O_2(^1\Delta)_{\mathfrak{Q}}\}$  was very small. With the above assumptions and conditions, two reactions predominate in Heidners model, they are the collisional quenching of  $O_2(^1\Delta)_{\mathfrak{Q}}$  by  $O_2(^3\Sigma)_{\mathfrak{Q}}$  and the flow tube wall.

$$O_2(^1\Delta)_{(g)} + O_2(^3\Sigma)_{(g)} --> O_2(^3\Sigma)_{(g)} + O_2(^3\Sigma)_{(g)}$$
 (3)

$$O_2(^1\Delta)_{(g)}$$
 + wall  $\longrightarrow O_2(^3\Sigma)_{(g)}$  + wall (4)

Reactions (3) and (4) serve as the basis for the differential equation

describing the decay of  $O_2(^1\Delta)_{(g)}$ . Such a differential equation depends on both radial and axial diffusion. The strength of the radial dependence terms will depend on the magnitude of the wall quenching rate. If the wall quenching rate is small, the rapid radial diffusion, typically found in such flow reactors, will minimize any radial concentration gradients that form. Under these circumstances, the resulting differential equation, (equation 5) can be solved in terms of axial position alone.

$$D \{d^{2}[O_{2}(^{1}\Delta)_{(g)}]/dx^{2}\} - v\{d[O_{2}(^{1}\Delta)_{(g)}]/dx\} - k_{obs}[O_{2}(^{1}\Delta)_{(g)}] = 0$$
 (5)

where D is the diffusion coefficient, v is the axial velocity of the flow stream, and  $k_{obs}$ , is the total quenching rate constant. The parameters D, v and  $k_{obs}$ , all depend on pressure and therefore, depend on axial position. The experiments described here, were designed to minimize any pressure gradients along the flow tube and thus any changes in D, v, and  $k_{obs}$  were also minimized. With these parameters constrained to be independent of pressure, the differential equation (5) can be integrated and rearranged to solve for  $k_{obs}$ :

$$k_{obs} = D/x. \ln([O_2(^1\Delta)_{(g)}]/[O_2(^1\Delta)_{(g)}]_0)$$

$$\{\ln([O_2(^1\Delta)_{(g)}]/[O_2(^1\Delta)_{(g)}]_0) + vx/D\}$$
(6)

In virtue of the simplicity of these experimental conditions,  $k_{obs}$ , the rate constant for total loss of  $O_2(^1\Delta)_{(g)}$ , can be expressed in terms of the wall loss rate constant,  $k_w$ , the gas phase quenching rate constant,  $k_q$  and the total concentration of  $O_2(^3\Sigma)_{(g)}$ , thus:

$$k_{obs} = k_w + k_q [O_2(^3\Sigma)_{(g)}]$$
 (7)

Small radial diffusion effects were accounted for by using an approach described by Wayne<sup>1</sup>. This approach uses a random walk approximation to derive the equation:

$$k_{rr} = \{ (r^2/8D) + (2r/(\gamma)c) \}^{-1}$$
 (8)

where c is the gas kinetic mean speed of the oxygen molecules.

In all experiments the total pressure, which is, to a good approximation, equal to the  $O_2(^3\Sigma)_{(g)}$  partial pressure, was used as the independent variable. The experiments were run with a constant initial  $O_2(^1\Delta)_{(g)}$  concentration and a varied total pressure. Optical signals upstream and downstream of the flow tube were recorded as described above.  $k_w$ ,  $k_q$ , and  $\gamma$  were obtained by performing a linear least square fit to the resulting data plotted as  $k_{obs}$  versus total pressure. The fit provided a gas quenching rate from the slope and a wall quenching rate from the intercept at zero pressure.

## Results and Discussion

Deactivation on pyrex and kinetic model validation - There have been a significant number of measurements of  $\gamma$ , between which there is reasonable agreement, see table 1. Pyrex, was chosen, therefore, as the reference material with which the model could be validated, prior to the model's application to other material surfaces. Since the model addresses both heterogeneous and homogeneous  $C_2(^1\Delta)_{(e)}$  deactivation, the model was also validated by comparing the value for ka determined using the model analysis with the recommended literature value for this rate constant  $(k_a(rec) =$  $1.56 \times 10^{-18} \text{cm}^3 \text{s}^{-1}$ ). Two physical corrections had to be made to the signal ratio measurements in order to obtain a good fit between the modelled and experimentally determined values of k and y. The first correction adjusted the ratio by subtracting the effects due to the non-identicalness of the two observation blocks. This correction factor was

experimentally determined by removing the flow tube and connecting the blocks together with a 5cm long pyrex tube. The signal upstream and downstream were measured at  $P_{total}=2$  torr, and the predicted loss between the two observation ports was calculated using the accepted literature value for  $k_q$  on pyrex<sup>1,12</sup> and a preliminary experimental value for  $k_w$  of 0.6 s<sup>-1</sup>. The resulting correction factor of 0.958 was incorporated into the data by multiplying the downstream signal by this factor.

The second correction factor is the loss between the observation port in each block and the edge of the sample tube. The factor was calculated for all pressures from the predicted loss of  $O_2(^1\Delta)_{(a)}$  in these regions using equation (6) and employing the same rate constants used to determine the first correction factor. The resulting concentration loss was added to the downstrsam signal measurement. Table 2 presents typical data from the pyrex model validation studies. These data were chosen specifically to demonstrate the reproducibility of the experiment. The sample tested in each case was a 2.264 m tube (pyrex 2.134 m and teflon 0.13 m), 1.84cm ID. Prior to the 9 Nov 90 test, the tube was rinsed with methanol, scrubbed with lint free cloth and re-rinsed with methanol. After the test it was stored in air for 18 weeks after which it was tested again without any The agreement between the k values is within experimental error. The increase in  $\gamma$  between the tests is thought to be real and is attributed to surface contamination during storage. The sensitivity of the value of  $\gamma$  to the exact nature of the surface, which in most cases is not well defined is a real problem in analyses of this nature and limits the accuracy with which is reasonable to quote \( \gamma \). Without adequate surface definition, values of  $\gamma$  quoted with high accuracy should be treated with skepticism.

(b) Deactivation on aged Nickel and Inconel - Table 3. lists the values of  $k_w$ ,  $k_q$  and  $\gamma$  measured for quenching on aged nickel and inconel surfaces. By the term aged it is the author's intent to describe metals whose

surfaces have been cleaned ultrasonically, and rinsed with methanol, to remove grease etc. but not etched or abraded in any way to disturb the metals oxide surface. Figure 2. is a typical plot of  $k_{obs}$  versus  $P_{total}$  for a nickel surface. Reproducibility was good. The magnitude of k, indicates that in every case wall deactivation was slight and  $\gamma$  was found to be, typically, an order of magnitude greater than that of pyrex. Values for  $k_a$  were found to be within experimental error of the recommended value. The accuracy of k, measured in these metal surface experiments would be expected to be less than that in the case of pyrex. These measurements are based on two competing rate processes. The metal surface experiments have smaller reaction zones, compared to those for pyrex. This constraint is required to limit the wall deactivation process. This constraint dictates that k can only be determined in the metal surface experiments for very small changes in  $O_2({}^1\Delta)_{(e)}$  concentration and therefore will be determined with only limited accuracy. The mean values for: Y (aged nickel) =  $(3.5 \pm 0.1) \times 10^4$  and  $\gamma$  (aged inconel) =  $(0.11 \pm 0.05) \times 10^4$ .

- (c) <u>Deactivation on aged copper and copper nickel alloy</u> Table 4. lists the values of  $k_w$ ,  $k_q$  and  $\gamma$  measured for quenching on aged copper and copper-nickel alloy surfaces. In all cases wall deactivation was small and any radial concentration gradients that occurred were well handled by the model. Values for  $k_q$  were found to be within experimental error of the recommended value. The mean values for  $\gamma$  (aged copper) =  $(2.8 \pm 0.3) \times 10^4$  and  $\gamma$  (aged copper-nickel alloy) =  $(4.0 \pm 0.1) \times 10^4$ .
- (d) <u>Deactivation on deoxidized surfaces</u> Thus far, the experiments described have measured surface deactivation efficiencies on "aged" metal surfaces. Experiments were also performed on metal surfaces that were cleaned with a wire brush or sandblasted. Such treatment removes some of the oxide layer at the metal surface. In all cases the model failed to account for the data (see figure 3.) and plots of  $k_{obs}$  versus  $P_{total}$  had extremely high intercepts at zero pressure and negative curvature. The

failure of the model can be attributed to the creation of significant radial concentration gradients that invalidate the essential assumption of the model that such gradients should be small or negligible. The gradients arise from the substantial wall deactivation efficiencies of the deoxidized metal surfaces.29 In the case of nickel, copper-nickel alloy and inconel, continued exposure to the oxygen flow caused a gradual and continuous decline in the wall deactivation efficiency as manifested by the zero pressure intercepts of the plots of  $k_{obs}$  versus  $P_{total}$ . In the case of nickel, for example,  $k_w$  fell from an initial value of 23.7s<sup>-1</sup> to 8.8s<sup>-1</sup> during a continuous exposure to oxygen period of 10 days, (see figure 4.). In the case of deoxidized copper, both the initial large radial concentration gradients and the long term time dependence were observed, but the interpretation of the data was further complicated by an anomalous short-lived and distinct time dependence that manifested itself as an increase in k, over the time period of a typical single days experiments (i.e. ~4hours). This effect was clearly observed in data sets where k, fell between 10 and 20 s<sup>-1</sup>. This result was reproducible, but declined in magnitude as a function of aging (or long term exposure to oxygen). short term time dependence was essentially linear and could be subtracted from k, to yield data that fit the model. Furthermore, the associated increase in wall deactivation efficiency, generated during a given days experiments, would persist for significant time periods after the microwave discharge was shut down (at least 3-4 hours) before eventually, succumbing to the fate of aging, see figure 5. An explanation for this anomalous behavior is not apparent to the authors at the time of writing. This effect, apparently unique to copper obviously warrants further investigation. Studies, however, are currently underway to modify the model to account for the large radial concentration gradients observed for newly deoxidized metal surfaces and will be the topic of a forthcoming publication.

Table 5. is a compilation of currently available data for the metal surfaces examined in this study. There is relatively good agreement between the deactivation efficiencies reported in this work and similar studies by Ryskin and Shub18 and Blauer10, especially considering the comments in the preceding discussion concerning how closely defined the surfaces are and how readily they can be directly compared. The work of Sharpless and Slanger differed in general approach and absolute  $O_1(^1\Delta)_{(a)}$ concentration detection technique. It was also far less sensitive, y's < 10<sup>3</sup> could not be observed in their experiments. Their deactivation efficiency calculations depended on estimates of  $O_2(^1\Delta)_{(a)}$  deactivation on pyrex reactor walls between their detector and metal sample and although they employ much greater concentrations of  $O_2(^1\Delta)_{(a)}$  they do not appear to have accounted for homogeneous deactivation within the test zone. Therefore, considering the aforementioned agreement between 3 independent studies and the limitations of the Sharpless and Slanger study the authors suggest that Sharpless and Slangers results should be considered as an upper bound for estimates of the deactivation efficiencies for nickel and copper.

## Conclusions

These studies were motivated by the need to enhance the reliability and accuracy of the database upon which COIL performance models draw. The model dealt successfully with the deactivation processes associated with aged metal surfaces and these are the surfaces most likely to be employed in a device. The validated approach employed in these studies is the most detailed and accurate to date. With further work to resolve the large radial concentration gradient problems associated with deoxidized surfaces this approach will be ideal to address the problems of temperature dependent deactivation and deactivation on water liquid salt solution, ice surfaces and surfaces contaminated by exposure to iodine and chlorine.

#### Acknowledgements

The author would like to thank K Truesdell for assigning the project, R Crannage and E Dorko for initiating the project and performing the experiments, and E. Workema and D.E. Johnson for much appreciated assistance in the design and documentation of this facility. This work was supported in part under Air Force Office of Scientific Research (AFOSR) contract No. 2303Y205 and in part through the AFOSR summer research program.

## References

- R.P. Wayne "Reactions of Singlet Molecular Oxygen in the Gas Phase,"Ch. 4 in <u>Singlet Oxygen Vol 1: Physical-chemical Aspects</u>, A.A. Frimer, ed, CRC Press, Inc., Boca Raton, FLa., 1985.
- E.A. Ogryzlo, "Gaseous Singlet Oxygen,"Ch. 2 in <u>Singlet Oxygen</u>, H.H.
   Wasserman and R.W. Murray, ed., Academic Press, New York, 1979.
- 3. P.D. Whitefield, J. Photochem., 25, 465 (1984).
- 4. H.V. Lilenfeld, AFWL TR 84-145, 30 November 1984.
- M.H. Van Bentham and S.J. Davis, J. Phys. Chem., 90, 902 (1986).
- 6. H.V. Lilenfeld, J.D. Kelley and C. Wiswall, J. Appl. Phys., <u>52</u>, 4962 (1981).
- J.P. Singh, J. Bachar, D.W. Setser ans S. Rosenwaks, J. Phys. Chem., 89, 5347 (1985).
- 8. A.M. Winer and K.D. Bayes, J. Phys. Chem. 70, 302 (1966).
- 9. I.D. Clark and R.P. Wayne, Chem. Phys. Letts., 3, 93 (1969).
- 10. R.G. Derwent and B.A. Thrush, Trans. Faraday Soc. 67,2036, (1971).
- 11. T-B Kh. Nugaev, M.P. Popovich and Yu V. Filippov, Russian J. Phys. Chem., E.T. <u>59</u>, 965 (1985).
- 12. P. Borrell, P.M. Borrell and M.D. Pedley, Chem. Phys. Letts., <u>51</u>, 300 (1977).
- 13. A.A. Leiss, U. Schurath, K.H. Becker and E.H. Fink, J. Photochem., 8, 211 (1978).

- 14. G.A. Fisk and G.N. Hays, J. Chem. Soc., 77, 4965 (1982).
- 15. R.G.O. Thomas and B.A. Thrush, Proc. Roy. Soc. London, 356, 287, (1977).
- E.I. Grigor'ev, I.A. Myasnikov and V.I. Tsivenko, Russian J. Phys. Chem., E.T. <u>57</u>, 312 (1983); <u>55</u>, 1652 (1981).
- 17. R.P. Steer, R.A. Ackerman and J.N. Pitts, Jr., J. Chem. Phys., <u>51</u>, 813 (1969).
- M.E. Ryskin and B.R. Schub, Reaction Kinetics Catalysis Letts., <u>17</u>,
   41 (1981).
- 19. M.A.A. Clyne and P.D. Whitefield, J.C.S. Faraday II, <u>75</u>, 1327 (1979).
- 20. M.A.A. Clyne and H.W. Cruse, J.C.S. Faraday II, 68, 1603 (1972).
- 21. D.J. Benard and N.R. Pchelkin, Rev. Sci. Instrum., 49, 794 (1978).
- 22. E. Workema, P. Whitefield and R. Crannage, Laser Digest, Submitted
  August 1991.
- 23. R.F. Heidner III, J. Photochem., 25, 449 (1984).
- 24. R.F. Heidner III, C.E. Gardner, T.M. El-Sayed, G.I. Segal and J.V.V. Kasper, J. Chem. Phys., 74, 5618 (1981).
- 25. L.R. Martin, R.B. Cohen and J.F. Schatz, Chem. Phys. Letts., <u>41</u>, 394 (1976).
- 26. S.A. Lawton, S.E. Novick, H.P. Broida and A.V. Phelps, J. Chem. Phys., <u>66</u>, 1381 (1977).
- 27. T.P.J. Izod and R.P. Wayne, Proc. R. Soc. London, A 308, 81 (1968).
- 28. W.H. Breckenridge and T.A. Miller, J. Chem. Phys., <u>56</u>, 465 (1972).
- 29. F. Kaufman, Prog. React. Kin. 1, 1 (1961).
- 30. J. Blauer, Private communication 1990.
- 31. R.L. Sharpless and T.G. Slanger, J. Chem. Phys., 91, 7947 (1989).

Table 1: Comparative listing of deactivation efficiencies for pyrex and pyrex-like materials

Material	γ (×10 <sup>5</sup> )	Pressure (torr)	Reference
Pyrex	(1.7±0.4)	0.5-	this work
_ н	2.9	2.0- 8.0	8
ų)	1.2-2.3	0.2- 5.0	9
	5.0	0.8- 5.6	10
н	1.5	1.0-10.0	11
Quartz	1.4	0.0- 5.0	16
Pyrex	(1.23±0.14)		12
- 11	1.3		30
Glass	4.4		18

Table 2: Typical pyrex data demonstrating model validation.

Source	k <sub>q</sub> cm³s-¹	k <sub>w</sub>	Υ	
	(x10 <sup>-18</sup> )		(×10 <sup>-5</sup> )	
This work(110990)	1.9±0.2	0.60±0.02	2.5±0.1	
This work(032791)	1.6±0.4	0.75±0.04	3.1±0.2	
Rec. lit. value"	1.56		1.2 - 5.0	

Table 3: Typical data for aged nickel and inconel surfaces.

Metal	k <sub>q</sub> cm³s-	ı	k <sub>w</sub> s <sup>-1</sup>		Υ	
	(x10 <sup>-11</sup>	<sup>3</sup> )			(x10 <sup>-4</sup> )	
Nickel	5.4 ±	2.6	6.0 ±	: 0.3	3.0 ±	0.1
н	6.5	1.2	4.9	0.1	2.3	0.1
••	3.9	3.6	11.5	4.5	5.4	0.2
	5.2	2.0	8.7	2.8	4.0	0.1
tt	5.4	2.6	6.5	2.8	3.0	0.1
Inconel	0.14	0.08	0.3	0.1	1.2	0.4
u	0.20	0.06	0.2	0.1	1.0	0.3

Table 4: Typical data for aged copper and copper-nickel alloy surfaces.

Metal	$k_{q}$ $cm^{3}s^{-1}$ $(x10^{-18})$	k <sub>w</sub> s <sup>·l</sup>		Y (×10 <sup>-4</sup> )	
	(XIO )				
Copper		7.5 ±	0.3	3.4 ±	0.2
**		5.6	0.2	2.6	0.5
**		5.4	0.4	2.5	0.1
Cu/Ni Alloy		8.6	0.5	4.0	0.1

Table 5: Comparative listing of deactivation efficiencies for metal surfaces studied in this work.

	Reference →	This	work	Ref. 18	Ref. 30	Ref. 31
1	Metal	<u>.</u>	<u></u>			<u> · </u>
	Nickel	3.5 ±	0.1	27.0	6.1 - 8.7	110
	Copper	2.8	0.3	8.5	7.0 - 11.0	140
	Cu/Ni	4.0	0.1			
	Inconel	0.11	0.05			

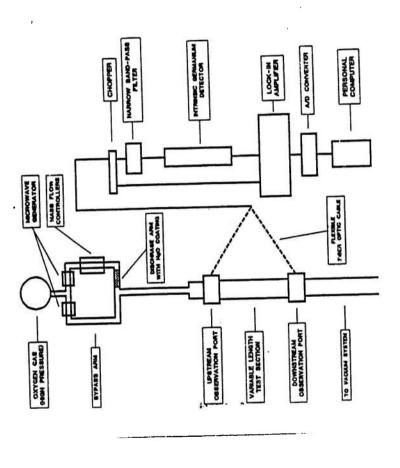


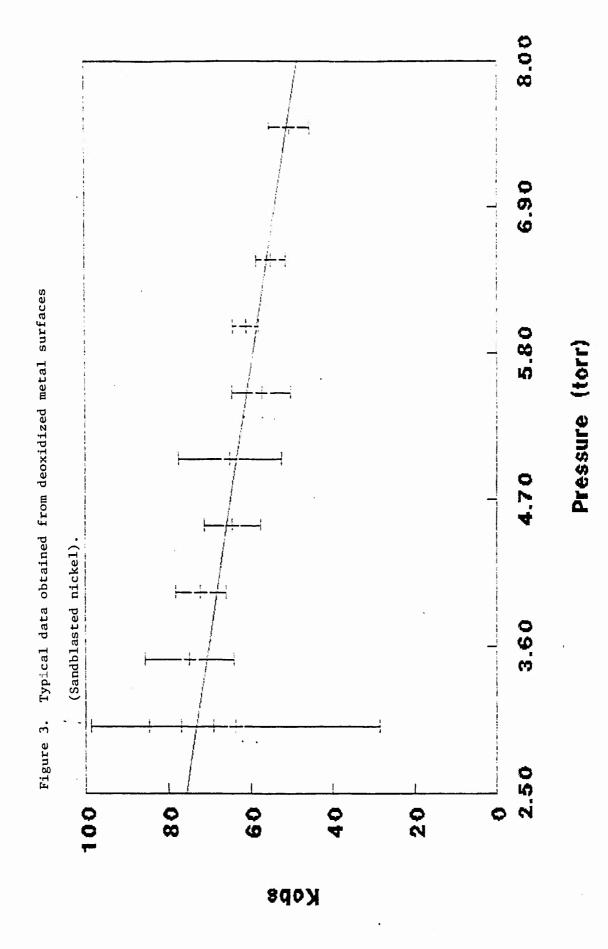
Figure 1. Schematic diagram of the flow reactor and diagnostics.

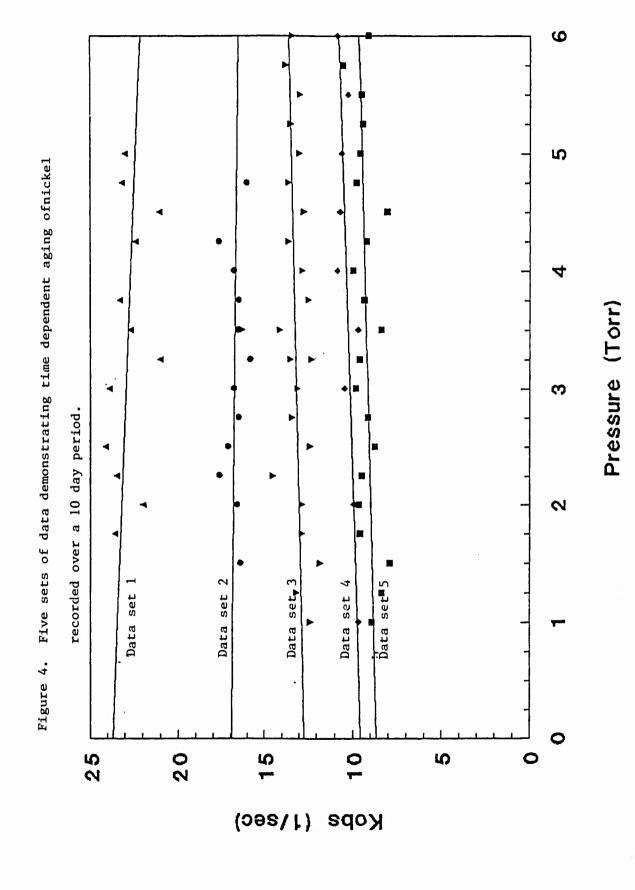
2 œ 9 2 Kobs (1/sec)

9

Pressure (Torr)

Figure 2. Typical data for aged nickel.





100 80 Signal ratio as a function of time for sandblasted copper with Microwave power off crowave power on 9 microwave power on and off. 20 Figure 5. Ø ന (nwob)gi2/(qu)gi2

Time (arb units)

33-20

# ESTIMATION OF CONTAMINANT TRANSPORT PARAMETERS FROM LABORATORY STUDIES: BATCH AND COLUMN TECHNIQUES WITH SORBING ORGANIC SOLUTES

William P. Ball
Assistant Professor
Dept. of Civil and Environmental Engineering
Duke University
Durham, NC 27706

Dirk F. Young
Graduate Student
Dept. of Civil and Environmental Engineering
Duke University
Durham, NC 27706

#### ABSTRACT

Batch and column experiments were performed with halogenated organ's solutes and sandy aquifer solids. Column results were analyzed with two solute transport models that incorporated nonequilibrium sorption as a) first-order mass transfer and b) Fickian spherical diffusion. The diffusion model was able to predict the column results using input parameters from prior independent batch tests. On the other hand, the first-order model required 3 to 4 parameters to be varied for good simulation, and fitted parameters were often not in good agreement with the batch results.

## INTRODUCTION

Laboratory batch and column experiments are frequently used to predict pollutant transport at the field scale. Batch experiments are able to isolate fundamental grain-scale processes, but are unable to asses flow-dependent processes. Columns can better replicate flow-dependent processes and will provide some measure of the effects of heterogeneity on transport.

However, with columns, isolation of grain-scale properties is more difficult. Comparison of these two laboratory processes using the same sorbent material and solutes may provide useful insight into the most appropriate means of establishing the correct input parameters for groundwater models. Such comparison was a major motivation for the research described here. More specific objectives of this research follow:

- Determine the extent to which contaminant fate parameters (sorption equilibrium and rate) measured in batch experiments can predict behavior in a flowing column.
- Determine the extent to which appropriate transport parameters can be "backed out" by model fitting of column experiments.
- 3. Long-term goal: Determine which types of experiment are most useful in field-scale modeling efforts.

#### BACKGROUND

Solute Transport With Sorption.

The transport equation for one-dimensional flow and linear equilibrium between the sorbed and aqueous phase can be expressed as follows:

$$R dC/dt = D d^2C/dx^2 - v dC/dx$$
 (1a)

$$R = (1 + pK_a/\theta) \tag{1b}$$

where R = retardation factor, [--]

C =solute concentration in aqueous phase,  $[kg/m^3]$ 

D = dispersion coefficient [m<sup>2</sup>/s]

t = time, [s]

x = position, [m]

p = bulk density of solids, [kg/m<sup>3</sup>]

K<sub>d</sub>= partitioning coefficient, [m<sup>3</sup>/kg]

 $\theta = \text{porosity}, [--]$ 

v = velocity, [m/s]

Recent work has suggested that sorption and desorption can be slow

processes, thus putting the equilibrium assumption into question. For example, batch work on Borden aquifer solid by Ball and Roberts (1991a,b) showed that equilibrium may require months to years to be attained. In such cases, modeling solute transport with the local equilibrium assumption would be invalid, and a transport model which includes mass transfer should be used.

## Modeling Transport and Mass Transfer.

Current models which account for mass transfer assume the existence of two regions—a mobile and an immobile region. Convection and dispersion are assumed to occur only in the mobile region, whereas transport into the immobile region is by diffusion only. Sorption sites are distributed throughout the mobile and immobile regions (though not necessarily evenly), with sites in the mobile region being at equilibrium with the mobile water. The governing equation for this model follows (Goltz and Roberts, 1986):

$$R_{m}\theta_{m} dC_{m}/dt = \theta_{m}D_{m} d^{2}C_{m}/dx^{2} - \theta_{m}v_{m} dC_{m}/dx - \theta_{im}R_{im} dC_{im}/dt$$
 (2a)

$$R_{n} = 1 + \frac{fpK_{d}}{\theta_{n}} \tag{2b}$$

$$R_{im} = 1 + \frac{(1-f)pK_d}{\theta_{im}}$$
 (2c)

where

 $C_{\rm i}$ ,  $C_{\rm im}$  - average concentrations in mobile and immobile zones, [kg/m³]  $\theta_{\rm m}$ ,  $\theta_{\rm im}$  - pore volumes of mobile and immobile water,  $(\theta_{\rm m} + \theta_{\rm im} - \theta)$ 

f = fraction of sites in direct contact with mobile water

 $D_m$  - dispersion coefficient for the mobile zone,  $[m^2/s]$ 

The last term in Equation 2a represents the mass transfer into the

immobile region and has been accounted for in several ways. The two most common models are a first-order model which uses an empirical first-order mass transfer coefficient and a mechanistic model which assumes Fickian diffusion.

First-order model. The first-order model assumes that rate of solute mass transfer is a linear function of the concentration difference between the mobile and immobile regions, and thus uses a first-order mass transfer coefficient to approximate solute mass transfer. Since concentration gradients are assumed to be nonexistent in the immobile region, an average immobile concentration is used. Under these conditions, the last term in Equation 2a, which represents mass transfer to the immobile region, would be replaced with the following:

$$\theta_{im}R_{im} dC_{im}/dt = \alpha(C_m - C_{im})$$
 (3)

where  $\alpha = \text{first-order rate constant, } [s^{-1}].$ 

As shown by Parker and van Genuchten (1984), the two-region model is mathematically equivalent to a two-site model in which all sorption sites are in contact with mobile water, but a fraction of these sites are kinetically limited. In this conceptualization,  $S_1$  and  $S_2$  are the sorbed-phase concentrations [kg/kg] in the equilibrium and rate-limited region, respectively, and F is the fraction of sites in the equilibrium region. The sorption rate equations for each type of site follow:

$$dS_1/dt = FK_0dC/dt$$
 (4)

$$dS_2/dt = \alpha[(1-F)K_dC - S_2]$$
 (5)

Under these conditions, the transport equation becomes

$$(1 + \frac{\text{FpK}_d}{a})dC/dt + \frac{\alpha p}{a} [(1-F)K_dC - S_2]$$
 (6)

This equation can be represented in nondimensional terms as follows (Parker and van Genuchten 1984):

$$\delta R \ dC^*/dT = 1/Pe \ d^2C^*/dz^2 + (1-\delta)R \ dS/dT$$
 (7a)

$$(1-\beta)R dS/dT = w(C^*-S)$$
 (7b)

where

$$B = \frac{\theta + FpK_d}{\theta + pK_d}$$
 Fraction of retardation due to instantaneous equilibrium

$$w = \alpha(1-8)RL/v$$
 Dimensionless Rate Constant

$$S = S_2/[(1-F)K_dC_o] \qquad \qquad \text{Dimensionless sorbed concentration in the rate-limited region}$$

$$C^* = C/C_o$$
 Dimensionless Concentration

Parker and van Genuchten (1984) and van Genuchten (1980) developed a computer program (CXTFIT) which employs such a first-order model and fits transport models to experimental data. In the research described subsequently, CXTFIT is used to interpret column breakthrough curves generated in the laboratory.

Diffusion model. The diffusion model assumes that the regions of immobile water are spherical, and solute mass transfer into these spherical zones occurs by Fickian diffusion, with the concentration at the outer radius of the immobile water equal to the concentration of the mobile water. Such a model may be applicable, for example, to intraparticle diffusion in sand grains, as assumed by Ball and Roberts (1991a,b). The immobile region concentration is described as follows (Rao et al., 1980):

$$C_{im}(x,t) = 3/a^3 \int_0^a r^2 C_{im}(x,r,t) dr$$
 (8a)

$$C_{im}(x,a,t) = C_{m}(x,t)$$
 (8b)

$$R_{im}dC_{im}/dt - D_{e}/r^{2} d(r^{2} dC_{im}/dr)$$
 (8c)

where

 $C_{im}(x,r,t)$  concentration at position r within each sphere,  $[kg/m^3]$ 

 $D_e$  - the effective diffusion coefficient within the immobile zone,  $[m^2/s]$ 

r - radial coordinate within sphere, [m]

a - radius of sphere, [m]

Combining the above equations with the transport equation (Equation 2) gives the diffusion model as described by Goltz and Roberts (1986), Rao et al. (1980), and Nkedi-Kizza et al. (1982). A solute transport code incorporating this model, identical to that used by Goltz (1986), was used in this research to predict column behavior for the Borden 40-60 material, using diffusion rate parameters previously published by Ball and Roberts (1991b).

## BATCH EXPERIMENTS

Sorbents and Solutes.

The aquifer materials used in these experiments were a 40-60 mesh size fraction of Borden aquifer material from the same batch of material as that used several years prior by Ball and Roberts (1991a,b) and bulk Borden material from the same batch as that used by Burris and Goltz (1991). Both pulverized (<200 mesh) and unpulverized samples of both materials were used. Pulverization was accomplished with a mortar and pestal.

Solutes used were 1,2,4-trichlorobenzene (TCB) and tetrachloroethene

(PCE). Unlabeled TCB was HPLC grade from Fisher Scientific Co. (Fairlawn, NJ). Radio-labeled TCB came from Sigma Chemical Co. (St. Louis, MO). Unlabeled PCE was Ultrapure grade from Alfa Products (Danvers, MA). Radio-labeled PCE came from Dupont Biomedical Products Dept. (Boston, MA).

Aquifer material (Borden 40-60 or Box material) was added to flame-sealable ampules, and the quantity was determined gravimetrically. A solution comprising de-ionized water, 0.005M CaSO<sub>4</sub>, and 0.02% NaN<sub>3</sub> was added to the ampules to a level so as to minimize headspace; the exact amount was determined gravimetrically. Each ampule was spiked with the appropriate radio-labeled compound (TCB or PCE) and immediately flame sealed. Sealed ampules were rotated at 5 rpm in a temperature-controlled chamber until they were ready to be analyzed. Quantitative analysis was performed by a scintillation counter. Losses to headspace were accounted for by the use of blanks (ampules without solids).

#### Results for Box Material with TCB.

The isotherm for TCB on pulverized Borden box material equilibrated for 7 days is shown in Figure 1. The figure presents both a Freundlich isotherm and a linear isotherm fit to the experimental data. The Freundlich and linear fit parameters are summarized in Table 1. The linear fit coefficient ( $K_d$ ) was obtained by averaging the  $K_d$ s from all the data with  $C_e$  < 1000 ug/l. As Figure 1 shows, the data are quite nonlinear (1/n = 0.81), but are fit well by the Freundlich isotherm. The differences can be seen more dramatically in Figure 2, where the data are shown on a linear plot. Here the low concentration linear fit can be seen to diverge greatly from the data obtained at higher concentrations.

Figure 3 shows isotherms obtained from batch experiments for both pulverized and unpulverized Borden box material at various equilibration times as well as individual points obtained from column studies (discussed later), box studies (Burris, 1991), and batch rate studies (Burris, 1991). This graph shows that, as expected, sorption to unpulverized solids increases with time. It also indicates that if the ultimate  $\mathbf{K_d}$  for pulverized and unpulverized material is the same, as shown by Ball and Roberts (1991b) using a different solute and different Borden aquifer material, then equilibrium with TCB and unpulverized material still has not been obtained after 46 days. This figure also shows that the uptake capacity as determined from Box experiments (Burris, 1991) tend to be much lower than the capacities determined by batch methods. Long-term (4 to 6 week) column-derived  $\mathbf{K_d}$ s were greater than batch-derived  $\mathbf{K_d}$ s using unpulverized material, but were still lower than the  $\mathbf{K_d}$ s derived from the pulverized material.

## Results for Borden 40-60 with PCE.

Figure 4 shows the isotherms for both pulverized and unpulverized Borden 40-60 equilibrated with PCE and fitted with both linear and Freundlich fits. This graph reveals the data to be fairly linear, and thus use of a linear model is justified. (Freundlich and linear fit parameters are summarized in Table 1.)

The average linear  $K_d$  for the unpulverized material was found to be 0.35 ml/g which differs greatly from the value determined by Ball and Roberts (1991), who determined the  $K_d$  to be 1.2 ml/g. The Borden 40-60 aquifer material used in this study, although from the same batch as that used by Ball and Roberts (1991a), had been exposed to the atmosphere about

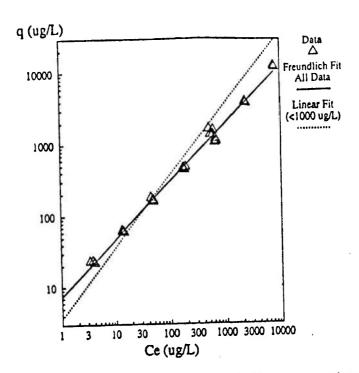


Figure 1. Isotherms (log-log scale) for pulverized Borden box material equilibrated for 7 days with TCB.

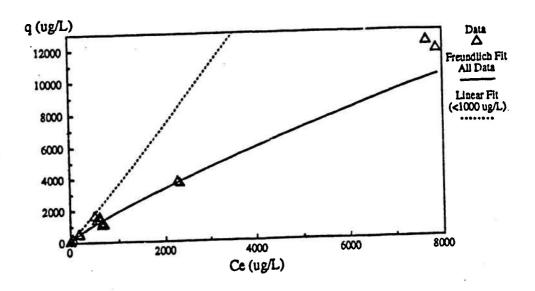


Figure 2. Isotherms (linear scale) for pulverized Borden box material equilibrated for 7 days with TCB.

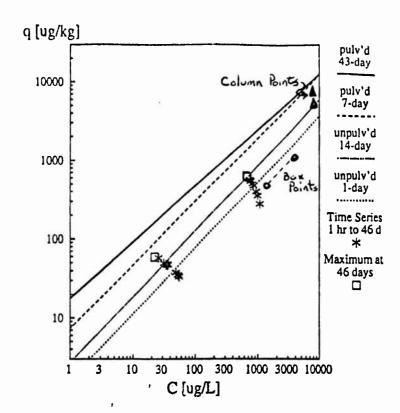


Figure 3. Isotherms for pulverized and unpulverized Borden box material equilibrated with TCB for various times. Data points not shown for clarity. "Column point" was determined from column experiment. "Box points" were determined from box experiment.

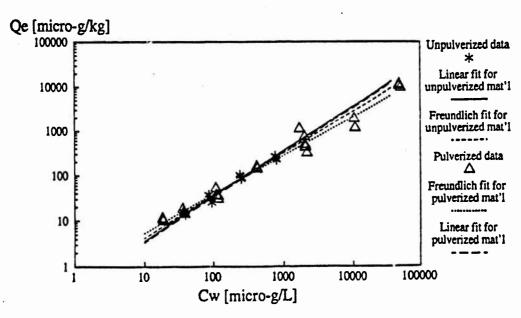


Figure 4. Freundlich and linear isotherms for Borden 40-60 equilibrated with PCE.

Table 1. Summary of the linear and Freundlich parameters as determined from batch experiments.

Material	Compound	Equilibration Time (days)	Linear K <sub>d</sub> (ml/g)	K <sub>f*</sub>	1/n
Borden 40-60	PCE	28	0.359	0.476	0.941
Pulverized Borden 40-60	PCE	6	0.333	0.723	0.863
Pulverized Borden box	TCB	7	2.94	7.35	0.806
Pulverized Borden box	TCB	43	5.92	17.9	0.713

<sup>\*</sup> C in ug/l, S in ug/kg

three years longer and may have been altered, perhaps by oxidation of the organic matter. Also, some contamination was present in the radio-labeled PCE; however, even in the extreme case (if the contaminants were completely non-sorbing), the contamination could only count for part of the observed difference.

## COLUMN EXPERIMENTS

## Sorbents and Solutes.

Sorbents used for column experiments were the same as those used in the batch studies. As before, Borden box material was used with TCB as the sorbing solute, while Borden 40-60 was studied using PCE. In addition to the sorbing solutes, tritiated water was used as a conservative tracer for the column work.

#### Methods.

The aquifer material was packed into stainless steel columns (2.1 cm ID, 25 cm long). To insure complete saturation, packed columns were purged

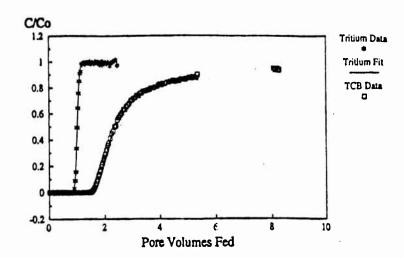


Figure 5. TCB and tritium with Borden box material (v = 3 cm/hr).

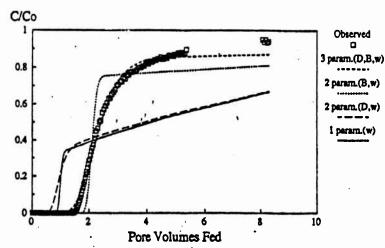


Figure 6. First-order fits for TCB and Borden box material (v = 3 cm/hr).

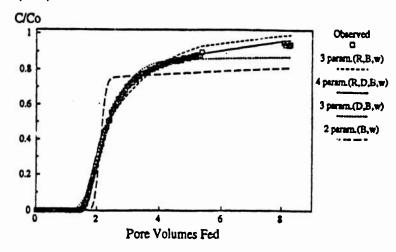


Figure 7. First-order fits for TCB and Borden box material (v = 3 cm/hr).

equilibrium. However, at the 6-week interval, the  $K_d$  decreased, which may reflect the initially incomplete breakthrough, with higher aqueous concentrations near the inlet of the column. Note that the results should not be affected by TCB diffusing back toward the column clean water at the inlet, since this effect was minor for tritium (Table 4), and back diffusion of tritium should be much more rapid.

Table 4. TCB intermittent uptake by Borden box material.

	Effluent Conc. (C/C <sub>o</sub> )		Implied	
Time	3 <sub>H</sub>	14C	K <sub>d</sub> (ml/g)	
3 days	1.0	0.96	0.46	
2 weeks	0.95	0.81	0.84	
4 weeks	0.93	0.69	1.0	
6 weeks	0.90	0.76	0.91	

## Results for Borden 40-60 with PCE.

Figure 8 shows the PCE and tritium breakthrough data for the column run with a pore water velocity of 2.98 cm/hr. Also shown is the tritium fit (CXTFIT), from which the dispersion coefficient (D) was determined.

With the batch data from this research, two predictions of column breakthrough were made using the spherical diffusion model—one using the batch data from this work and one using the batch data from Ball and Roberts (1991a). Both predictions used rate data from Ball and Roberts (1991b). As shown by Figure 9, the prediction using the batch data from this experiment  $(K_d = 0.35)$  exhibits excellent agreement with the column data, whereas the prediction using the data of Ball and Roberts (1991a)  $(K_d = 1.2)$  does not. Thus, the column data appear to reflect the equilibrium uptake exhibited in the current batch work. Possible reasons for the discrepancy with the results of Ball and Roberts (1991a) have been previously discussed.

Fits using the first-order model are shown in Figure 10, and parameter values are given in Table 5. For the two parameter fit ( $\beta$  and w varied), the fitted w is within 33 percent of that implied by  $D/a^2$  determined by Ball and Roberts ( $D/a^2$ =0.026 s<sup>-1</sup>, w=22.5D/a<sup>2</sup> = 0.59), but the model did not fit the data very well. A better fit was obtained by allowing R to vary, as the 3-parameter fit shows. To obtain an excellent fit, however, four parameters ( $\beta$ , w, R, D) had to be allowed to vary.

Figure 11 shows the data for the high velocity column (30.9 cm/hr) along with the diffusion model prediction using the batch equilibrium data from this work. As the figure shows, the diffusion model prediction is again in generally good agreement with the data.

The first order model simulations of the high velocity column using 2and 3-parameter fits are shown in Figure 12. The first-order fits all
required that w be much higher than the value determined by Ball and Roberts
(1991b), from which w was estimated to be 0.056. The 2-parameter fit also
was not in good agreement with the data, but a reasonable fit was obtained
by also allowing R to vary (3-parameter fit); however, the value of w is
then off by an order of magnitude. Also shown in Figure 12 is a prediction
using the first-order model and parameters derived from the low velocity
column. The prediction from the low velocity data, which used w = 0.79,
also gives a poor fit. These results suggest that for high velocity
experiments differences of breakthrough shape with diffusion and first-order
models are sufficiently severe to make the first-order models act as poor
means of estimating diffusion-based rate constants.

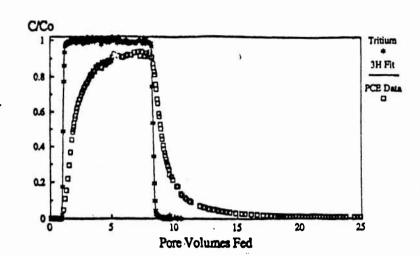


Figure 8. PCE and tritium with Borden 40-60 (v = 3 cm/hr).

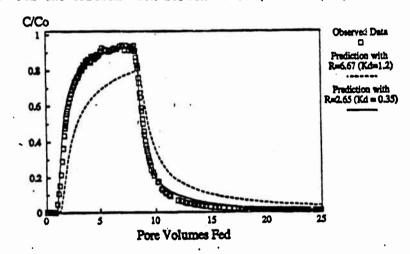
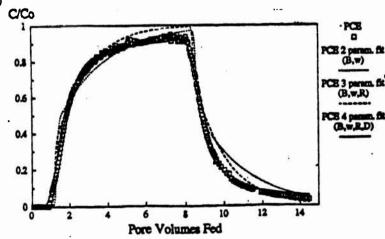


Figure 9. Diffusion model predictions for PCE and Borden 40-60 (v = 3 cm/hr)



Pigure 10. Pirst-order fits for PCE and Borden 40-60
(v = 3 cm/hr)

egggymiel ↓ .v.n.e.d.

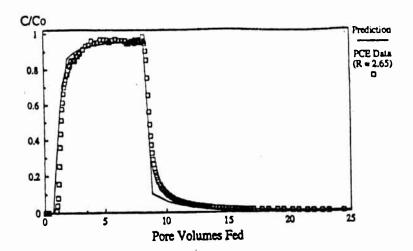


Figure 11. Diffusion model prediction for PCE and Borden 40-60 (v = 30.9 cm/hr).

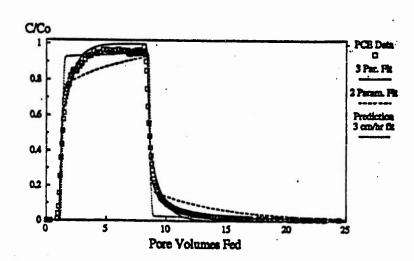


Figure 12. First-order fits for PCE and Borden 40-60 (v = 30.9 cm/hr).

Table 5. Fitting parameters for simulations in Figures 10 and 12.

	v	۲۲	D	ß	w
Figure 10:	-				
4 par fit (ß, w, R, D)	0.0496	3.0	0.0932	0.591	0.202
3 par fit (R, B, w)	0.0496	2.3	0.00218	0.520	1.13
2 par fit (B, w)	0.0496	2.7	0.00218	0.502	0.787
Figure 12:					
Prediction from col4	0.515	2.65	0.229	0.506	0.79
3 par fit (R, B, w)	0.515	1.56	0.229	0,724	0.772
3 par fit (D, B, w)	0.515	2.65	0.229	0.474	0.251

### CONCLUSIONS

From this study the following conclusions were drawn:

- The Borden box material exhibits very slow uptake of TCB. At least four weeks is required to attain equilibrium, and batch studies with pulverized material suggest that an even longer equilibration time may be required.
- The diffusion model describes the breakthrough data quite well for Borden 40-60 with PCE, and batch-based rate and equilibrium data served as good predictors of column results.
- The first-order fit was sufficiently inappropriate as to lead to misestimation of the sorption rate coefficient w, especially at higher velocities.
- The simultaneous fitting of & and R gives better data matches but is physically meaningless and leads to greater error in the estimation of w.

## **ACKNOWLEDGEMENTS**

This work was conducted in the laboratories of the Environics Division of the Engineering and Services Center, Tyndall AFB, FL as part of a 10-week summer research program. Dr. Thomas Stauffer was the focal contact for the research. Dr. David Burris provided valuable assistance with the

experimental aspects, and Dr. Kirk Hatfield (University of Florida) assisted with the application of the CXTFIT computer program. We would like to thank Dr. Stauffer and his staff for their considerable efforts toward making our visit enjoyable and productive.

## REFERENCES

Ball, W. P., and P. V. Roberts, 1991a. "Long-Term Sorption of Halogenated Organic Chemicals -- Part 1. Equilibrium Studies", <u>Environ. Sci. Technol.</u> 25(7), 1223-1237.

Ball, W. P., and P. V. Roberts, 1991b. "Long-Term Sorption of Halogenated Organic Chemicals -- Part 2. Rate Studies", <u>Environ. Sci. Technol.</u> 25(7), 1237-1249.

Burris, D.B., 1991. Personal communication, Air Force Engineering and Services Center, Tyndall Air Force Base, Panama City, FL.

Burris, D.B. and Goltz, M.N., 1991. "Use of a Physical Box Model to Examine the Role or Rate-Limited Sorption on Aquifer Remediation" <u>AGU-MSA 1991</u>

<u>Spring Meeting</u>, Baltimore, MD., American Geophysical Union and the Mineralogical Society of America.

Goltz, M.N. 1986. "Three-Dimensional Analytical Modeling of Diffusion-Limited Solute Transport", Ph.D. Dissertation, Stanford University, Stanford CA, 172pp.

Goltz, M.N. and Roberts P.V., 1986. "Interpreting Organic Solute Transport Data from a Field Experiment Using Physical Nonequilibrium Models", J. Contaminant Hydrology, 1(1), 77-93.

Nkedi-Kizza, P, Rao, P.S.C., Jessup, R.E., and Davidson, J.M., 1982. "Ion Exchange and Diffusive Mass Transfer during Miscible Displacement Through an Aggregated Oxisol" Soil Sci. Soc. Am. J., 46, 471-476.

Parker, J.C. and van Genuchten, M. Th., 1984. "Determining Transport Parameters from Laboratory and Field Tracer Experiments", <u>Bulletin 84-3</u>, Virginia Ag. Exp. Stn., Virginia Polytechnic Institute and State University, Blacksburg, VA.

van Gemuchten, 1980. "Determining Transport Parameters from Solute Displacement Experiments" Research Report No. 118, U.S. Salinity Lab., Riverside, CA.

Rao, P.S.C., Ralston, D.E., Jessup, R.E. and Davidson, J.M., 1980. "Solute Transport in Aggregated Porous Media: Theoretical and Experimental Evaluation" Soil Sci. Soc. Am. J. 44, 1139-1146.

# 1991 USAF-RDL SUMMER FACULTY RESEARCH PROGRAM

Sponsored by the

AIR FORCE OFFICE OF SCIENTIFIC RESEARCH

Conducted by the

RESEARCH AND DEVELOPMENT LABORATORIES

5800 UPLANDER WAY

CULVER CITY, CA 90230-6608

## FINAL REPORT

# MICROBIAL DEGRADATION OF 4-NITROPHENOL

Prepared by:

Joseph H. Dreisbach, PhD

Department and

University:

Chemistry Department University of Scranton

Research Location:

USAF Engineering and Services Center

Tyndall Air Force Base, FL 32403-6001

USAF Researcher:

(Lab Focal Point)

Jim C. Spain, PhD

Date:

September 20, 1991

## MICROBIAL DEGRADATION OF 4-NITROPHENOL

Joseph H. Dreisbach, PhD

#### ABSTRACT

Several gram positive bacterial isolates (designated 443, 428 and 402) have previously been isolated and demonstrated to actively degrade 4-nitrophenol. Previous research revealed these isolates convert 4-nitrophenol to 1,2,4-benzenetriol prior to ring fission and mineralization. The purpose of this project was to characterize the biochemical pathway of 4-nitrophenol conversion to 1,2,4-benzenetriol by these isolates.

Circumstantial evidence supports the hypothesis that 4-nitroresorcinol is an intermediate on this pathway. This compound induces full oxygenase activity against 4-nitrophenol and 1,2,4-benzenetriol. Evidence of an active monooxygenase enzyme was obtained by observing the conversion of 3-nitrophenol to 3-nitrohydroquinone by 443. It is unclear from the 0-18 atmosphere studies as to how the intermediates may be formed.

## INTRODUCTION

Nitroaromatic compounds are found in the manufacturing process of many substances including explosives, certain

pesticides, dyes, pharmaceuticals, and industrial solvents. The accumulation of nitroaromatic compounds in the environment is a problem which is being addressed by military, industrial and agricultural institutions.

One way of addressing the environmental damage caused by these and other chemical agents involves the use of bioremediation. Bioremediation utilizes biological agents such as bacteria in the reclamation of contaminated soil and water. The occurrence of microbes with diverse metabolic capabilities along with the potential to use these microbial agents on site renders bioremediation techniques widely applicable and cost effective.

The microbiology laboratory at Tyndall Air Force Base, Florida is headed by Jim C. Spain, PhD. Dr. Spain's research group is studying the use of microbes in the degradation of substituted aromatic compounds and other substances. A major effort is being focused on characterizing the degradation pathways of these compounds by a number of microbial isolates. Identification of the intermediates on these degradation pathways is essential in order to utilize the microbes in field remediation applications.

## BACKGROUND TO THE RESEARCH

The widespread use of nitroaromatic derived compounds, especially in the manufacture of explosives and pesticides, and the occurrence of these compounds and their derivatives in

the environment, make them major targets for bioremediation applications. The compound 4-nitrophenol (paranitrophenol) is of special interest since it is derived from hydrolysis of parathion which is a common insecticide. Even more important, from a military perspective, is the fact that 4-nitrophenol is an excellent model compound for investigations of biodegradation of nitrotoluenes major components of explosives.

Previous studies on the bacterial degradation of 4nitrophenol show that some pseudomonads convert 4-nitrophenol to hydroquinone with concomitant release of nitrite (1,2). More recently a species of Moraxella was shown to degrade 4nitrophenol to hydroguinone (3). Hydroguinone is then converted to gamma-hydroxymuconic semialdehyde through a dioxygenase catalyzed ring fission reaction (4). Investigations 4-nitrophenol catabolism of by other pseudomonad isolates suggest that 4-nitrocatechol may be an intermediate in some pathways (5,6).

A number of bacterial isolates which are able to utilize 4-nitrophenol as the sole carbon source were isolated by Jim Spain and his research group at Tyndall Air Force Base, Florida. Results from studies with these isolates indicate that 1,2,4-benzenetriol is produced as an intermediate during degradation. The compound 1,2,4-benzenetriol subsequently undergoes a dioxygenase-catalyzed ring fission reaction to yield maleylacetate (7). This is the first report which shows

that 4-nitrophenol is converted to 1,2,4-benzenetriol during degradation.

## STATEMENT OF THE RESEARCH PROBLEM

Degradation of 4-nitrophenol through 1,2,4-benzenetriol has been demonstrated for the first time with the gram positive bacterial isolates designated 443, 428 and 402 (7). A mutant of the 402 wild type organism was obtained through methane sulfonic acid ethyl ester (EMS) treatment. This mutant, designated 1490, accumulates 1,2,4-benzenetriol when 4-nitrophenol is provided as the sole carbon source and is additional evidence that 1,2,4-benzenetriol is an intermediate on this pathway.

Although 1,2,4-benzenetriol has been shown to be an intermediate on this degradation pathway, the reactions which lead to its formation from 4-nitrophenol remain to be characterized. The objectives of this research were to determine the pathway by which 4-nitrophenol is converted to 1,2,4-benzenetriol.

Three pathways can be proposed for this reaction sequence. In one route a single, dioxygenase catalyzed reaction results in the elimination of nitrite ion from substrate to yield 1,2,4-benzenetriol. In another hypothesis, the triol intermediate is formed and the incorporation of hydroxyl groups and the elimination of nitrite ion occur through two separate reactions. The intermediates in the

proposed two step sequence are dihydroxynitrobenzenes and might be 4-nitrocatechol (1,2-dihydroxy-4-nitrobenzene) or 4-nitroresorcinol (1,3-dihydroxy-4-nitrobenzene). The pathway where nitrite is first eliminated to yield hydroquinone and the hydroquinone is subsequently hydroxylated to yield 1,2,4-benzenetriol is not supported by evidence acquired from previous research. It has been shown that these isolates produce hydroquinone in small amounts from 4-nitrophenol and that the hydroquinone accumulates in the reaction media (7).

#### RESULTS

Attempts to Identify Intermediates During 4-Nitrophenol Catabolism. A number of experiments were performed to identify reaction intermediates. Cells which were induced to degrade 4-nitrophenol as well as cells which were uninduced were incubated with the substrate at normal and low oxygen tensions. No intermediates could be identified using reversed phase HPLC to monitor the reaction. Experiments using iron chelating agents such as o-phenanthroline and radiolabel trapping experiments with authentic 4-nitrocatechol and 4-nitroresorcinol also yielded negative results.

Growth of the isolates with potential intermediates.

A number of potential intermediates were used in experiments where the compound of interest was used as the sole carbon source for the organism. The compound 4-nitroresorcinol was synthesized (8) and 4-nitrophenol, 4-nitrocatechol, and 1,2,4-

benzenetriol were obtained from commercial sources. Uninduced (yeast-extract grown) cells were cultured overnight on a minimal salts-agar medium and then a crystal of the compound of interest was added. Alternatively uninduced cells were added to a broth of minimal salts media containing 5 ppm of the compound. Both experiments yielded the same results. The isolates (443) utilized 4-nitrophenol and 4-nitroresorcinol as growth substrates. Experiments in which 4-nitrocatechol or 1,2,4-benzenetriol were used did not yield cell growth. In the latter case, the rapid oxidation of the triol to hydroxylquinone complicates the experiment and one cannot conclude that the triol itself is unable to support growth.

Utilization of potential intermediates by the isolates. Utilization of potential intermediates by the 443 isolate was measured using a Clark type oxygen selective electrode. Cells grown on 4-nitrophenol rapidly oxidized 4-nitrophenol, 4-nitroresorcinol, 4-nitrocatechol and 1,2,4-benzenetriol. Cells grown on 4-nitroresorcinol demonstrated the same proportional rates of utilization for each of the substrates. Hydroquinone oxidation was not observed in either case and, as stated previously, 4-nitrocatechol did not induce the activities.

Accumulation of 1,2,4-benzenetriol from reaction of 1490 with potential intermediates. An EMS mutant of 402 which accumulates 1,2,4-benzenetriol from 4-nitrophenol was prepared as reported previously (7). The compound 1,2,4-benzenetriol

also accumulated in the medium when 4-nitroresorcinol or 4-nitrocatechol were used as substrates.

## Cell-free oxygenase activities with 4-nitrophenol.

Cell free extracts of 443, 428, and 402 with 1,2,4-benzenetriol oxygenase activity have been obtained (7). A number of attempts to prepare cell free extracts with activity using 4-nitrophenol as substrate met with limited success. Cell free extracts incubated with 4-nitrophenol and 4-nitroresorcinol for 18 hours yielded some nitrite release. It is unclear as to whether this is due to slight oxygenase activity, some hydrolase activity or a nonenzymic process. Further effort must be directed to preparing a cell free extract active against 4-nitrophenol.

# Reaction of 4-nitrophenol in an oxygen-18 atmosphere.

Uninduced 1490 cells were incubated with 4-nitrophenol in an atmosphere containing O<sub>2</sub>-18 (46% O-18, 54% O-36). The compound hydroxylquinone accumulated in the reaction media. The quinone was reduced to 1,2,4-benzenetriol and extracted. GC-MS analysis of the triol showed that the accumulated product was comprised of 57% mass 126; 36% mass 128; and 7% mass 130. These results are consistent with neither a single dioxygenase conversion of substrate to triol (theoretical product: 54% 126 and 46% 130) nor with pathway in which two monooxygenase steps yield triol (theoretical product: 21% 126; 50% 128; 21% 130).

Reaction of 4-nitroresorcinol in an 0-18 atmosphere.

The experiment described above was repeated with 4-nitroresorcinol substrate. The atmosphere contained 30% O-18 and 70% O-16. No O-18 was incorporated into the 1,2,4-benzenetriol product.

Exchange of 1,2,4-benzenetriol hydroxyl groups with water. The data from the 0-18 atmosphere experiments suggest that some exchange of oxygen atoms may be occurring between 1,2,4-benzenetriol and water. An experiment was designed in which commercially obtained triol was incubated in 0-18 water under conditions similar to those of the 0-18 atmosphere experiments. No significant oxygen exchange was observed over a period of 21 hours.

Reaction of 443 with 3-nitrophenol. When induced 443 cells were incubated with 3-nitrophenol a slow reaction occurred to yield a bright yellow intermediate. The intermediate was identified as 3-nitrohydroquinone using wet chemical analysis and GC-MS data. The 3-nitrohydroquinone was slowly degraded and after 24 hours none of the intermediate was present in the reaction medium.

#### DISCUSSION

Monooxygenase activity in 443. The conversion of 3-nitrophenol to 3-nitrohydroquinone by 443 demonstrates an active monooxygenase system in this organism. Further evidence in support of this monooxygenase activity was made previously with the observation that some (>10%) 4-nitrophenol

is converted to 1,4-hydroquinone.

4-Nitroresorcinol as an intermediate on the pathway. Circumstantial evidence supports the hypothesis that 4-nitroresorcinol is an intermediate in the conversion of 4-nitrophenol to 1,2,4-benzenetriol by the gram positive bacterial isolates designated 443 and 402. Both 4-nitrophenol and 4-nitroresorcinol support growth of 443 as the sole carbon source. Furthermore, both compounds induce the same degree of oxygenase uptake by 443 when using 4-nitrophenol, 4-nitroresorcinol, 4-nitrocatechol and 1,2,4-benzenetriol as substrates. The compound 4-nitrocatechol is unable to support growth as the sole carbons source or induce oxygen uptake by 443 with these substrates. In addition, 4-nitrocatechol is significantly more toxic to the organism that are 4-nitrophenol or 4-nitroresorcinol.

Reactions of 4-nitrophenol conversion to 1,2,4-benzenetriol. Experiments using a mutant strain of 402 which accumulates 1,2,4-benzenetriol were performed. These experiments were performed in an 0-18 atmosphere in order to determine how the hydroxyl groups are inserted into the substrate. The data from these experiments are unclear in that they do not correlate with either a diox/genase or two monooxygenase reactions.

The observation that no 0-18 from the atmosphere is present in the 1,2,4-benzenetriol when 4-nitroresorcinol is used as substrate indicates that there may exist rapid oxygen

exchange between the substrate and water. No evidence of oxygen exchange between pure 1,2,4-benzenetriol and water was observed when a control experiment was performed. There remains the possibility, however, that exchange of oxygen may take place between an enzyme-substrate intermediate and water. Another explanation is that the nitrite from 4-nitroresorcinol is released using an enzyme system other that an oxygenase. This enzyme system may involve hydrolase activity. Hydrolase catalyzed release of chloride ion has been demonstrated in other systems.

Clarification of the pathway. Further clarification of the pathway will best be obtained by using a cell-free extract preparation with activity against the substrates. Such a system will provide for controlled experiments and will eliminate many of the side reactions which might be occurring in the cell systems.

## **ACKNOWLEDGEMENTS**

An opportunity to perform research in Jim Spain's laboratory is an exciting and rewarding occasion. His offer to return to the laboratory for a second summer research period is truly an honor. I sincerely thank Dr. Spain and his colleagues at Tyndall Air Force Base for their generous invitation for me to participate in the Summer Faculty Research Program in 1991.

Jim Spain manages his research group in the most

professional and productive manner that I have ever encountered. He is surrounded by excellent scientists but they are also outstanding persons. I've learned as much about coordinating a research group as I have about biodegradation and I thank him for giving me this opportunity. Shirley Nishina's assistance was well beyond that which one can justifiably expect and I thank here for her patience.

Thanks also to Billy Haigler who seems to have answers to every question I ask. He also has infinite patience. Jeff Robertson's advice was generously given whenever I sought it and many times when I did not seek it but needed it. Thanks also to Wen-Chen Suen for his expertise which he so kindly provided.

Sergeant Don Volnoff and Bob Donne provided assistance in the day-to-day operations of the facilities. Dr. Howard Mayfield ran some GC-mass spectrum experiments at Tyndall AFB and Andrea Dreisbach performed some NMR experiments at Syracuse University. The results from these studies were very important in allowing the research to progress and I thank them both for donating their time.

Thanks also to Captain Catherine Vogel, Dr. Hubert Attaway and Dr. Hiltrud Lemke for their conversations and suggestions throughout the project.

#### REFERENCES

- 1. Munneke, D. M., D. P. H. Hsieh. (1974). Microbial decontamination of parathion and p-nitrophenol in aqueous media. Appl. Microbiol. 28: 212-217.
- 2. Simpson, J. R. and W. C. Evans. (1953). The metabolism of nitrophenols by certain bacteria. <u>Biochem. J.</u>
  55: xxiv.
- 3. Spain, J. C., O. Wyss, and D. T. Gibson. (1979). Enzymatic oxidation of p-nitrophenol. <u>Biochem. Biophys. Res.</u>

  <u>Commun.</u> 88: 634-641.
- 4. Spain, J. C. and D. T. Gibson. (1991). Pathway for biodegradation of p-nitrophenol in a Moraxella sp.. Appl. Environ. Microbiol. 57: 812-819.
- 5. Raymond, D. G. M. and M. Alexander. (1971). Microbial metabolism and cometabolism of nitrophenols. Pesticide Biochem. Physiol. 1: 123-130.
- 6. Sudhakar-Barik, R. Siddaramappa, P. A. Wahid, and N. Sethunathan. (1978). Conversion of p-nitrophenol to 4-nitrocatechol by a <u>Pseudomonas</u> sp.. <u>Antonie von Leeuwenhoek</u> 44: 171-176.
- 7. Dreisbach, J. H. (1990). USAF-UES Summer Faculty Research Program Final Report. "Pathways of 4-Nitrophenol Degradation".

8. Dreisbach, J. H. (1991). USAF-UES Research Initiation Program Final Report. "Synthesis of Potential Intermediates of Microbial Biodegradation Pathways of Nitroaromatic Compounds".

# EXTRACTION OF AROMATIC POLYMERS FROM MONTMORILLONITE CLAY USING SUPERCRITICAL FLUIDS

Larry E. Gerdom, Ph.D., Research Associate
Headquarters Air Force Engineering and Services Center
Environics Division, Site Restoration Branch
(HQ AFESC/RDVC)
Tyndall AFB, Panama City, FL 32403-6001

#### **ABSTRACT**

The extraction by supercritical fluids of aromatic polymers formed during reflux on the surface of montmorillonite clay has been investigated. The supercritical fluid used was carbon dioxide with methanol as a solvent modifier. These materials have been partially characterized by gas chromatography with a mass spectrometer detector, GC/MS.

#### INTRODUCTION

A wide variety of reactions are known to take place on clays which act as either supports or catalysts[1]. Specifically, aromatic molecules are known to undergo polymerization reactions when heated in the presence of a metal cation supported on a high surface area clay [2, 3,4,5,6]. Metal cations include Cu<sup>2+</sup>, Fe<sup>3+</sup>, or Ru<sup>+3</sup>[7] and the clay most often is montmorillonite[8]. These polymerization reactions are thought to be similar to those that take place in the presence of an

<sup>1.</sup> P. Laszlo, Science, 235, 1473(1987).

<sup>2.</sup> M.M. Mortland and T.J. Pinnavia, Nature(London), Phys. Sci., 229, 75(1971).

<sup>3. 3.</sup> T.J. Pinnavia and M.M. Mortland, J. Phys. Chem., 75, 3957(1971).

<sup>4.</sup> Y. Soma, M. Soma, and I. Harada, Chem. Phys. Lett., 99, 153(1983).

<sup>5.</sup> M.P. Eastman, D.E. Patterson, and K.H. Pannell, <u>Clays Clay Miner.</u>, <u>32</u>, 327(1984).

<sup>6.</sup> Y. Soma, M. Soma, and I. Harada, J. Phys. Chem., 88, 3034(1984).

<sup>7.</sup> Y. Soma, M. Soma, and I. Harada, J. Phys. Chem., 89, 738(1985).

<sup>8.</sup> J.P. Rupert, <u>J. Phys. Chem.</u>, <u>77</u>, 784(1973).

aluminum chloride-cupric chloride catalyst [9,10,11,12].

Montmorillonite is a layered clay mineral of the general group known as smectites. These clays consist of an octahedral arrangement of  $A10_6^{-3}$  units sandwiched between two layers of tetrahedral  $Si0_2^{-2}$  units in the primary structure. There is a secondary structure of interstitial cations (such as Na<sup>+</sup>, K<sup>+</sup>, and Ca<sup>+2</sup>) held between the negatively charged planes. A tertiary structure exists because water or other small organic molecules can be absorbed between layers due to an attraction for the interlamellar cations. This absorption process actually causes the clay to expand and contract with wetting and drying. With overall dimensions below 2 µm, montmorillonite clay particles have specific areas on the order of 500 to 760  $m^2/g$ . In contrast, alumina has a specific area in the range of  $70-200 \text{ m}^2/\text{g}[1]$ . Water molecules are easily replaced by small organic molecules upon dehydration of the clays. When transition metal ions are exchanged for the interlayer cations these clays have catalytic properties. In particular, dry Cu(II)-montmorillonite clays will catalyze the polymerization of benzene or toluene to form several products which are polymers of the starting compound[3].

This type of reaction has been actively investigated and it is generally believed that a single electron transfer takes place from the aromatic ring to the copper(II) cation producing a carbocation[13]. The existence of organic radical cations is substantiated by (1)loss of the ESR signal associated with the paramagnetic metal cation(reduction of Cu<sup>2+</sup> to Cu<sup>+</sup>)[8], (2)the appearance of a "new" ESR signal assigned to an organic radical cation[5], and (3)changes in the infrared[2] and

<sup>9.</sup> P. Kovacic and A. Kyriakis, J. Am. Chem. Soc., 85, 454(1963).

<sup>10.</sup> P. Kovacic and R.M. Lange, J. Org. Chem., 29, 2416(1964).

<sup>11.</sup> P. Kovacic and F.W. Koch, <u>J. Org. Chem.</u>, <u>30</u>, 3176(1965).

<sup>12.</sup> P. Kovacic and J.S. Ramsey, <u>J. Polm. Soc.</u>, <u>A-1</u>, <u>7</u>, 111(1969).

<sup>13.</sup> C.T. Johnson, T. Tipton, D.A. Stone, C. Erickson, and S.L. Trabue, Langmuir, 7, 289(1991).

Raman[6,7] spectra. In the case of either benzene or toluene these radical cations can react with other cations or neutral molecules to form a variety of polyaromatic hydrocarbons[13].

A supercritical fluid results when a substance is under high pressure above its critical temperature. Supercritical fluids are characterized as having low viscosities and high solute diffusivities which enhances mass transfer as compared to HPLC or GC methods. The critical temperature of CO, is 31 °C and typical pressures are 100 to 360 atmospheres(atm). The solvent strength of a supercritical fluid is directly related to its density which is a function of its pressure and to a lesser extent its temperature. The polarity of a supercritical fluid can be controlled by adding solvent modifiers such as methanol. In a method developed for the extraction of polycyclic aromatic hydrocarbons (PAH) from environmental solids the supercritical fluids composed of ethane, CO2, N2O, CO2 with 5% methanol, or N2O with 5% methanol were compared[14]. The best results were found using the N<sub>2</sub>O with 5% methanol; however, CO2 with 5% methanol was also found to be significantly more effective than the pure supercritical fluids. Nitrous oxide is a strong oxidant and extractions of large amounts of easily oxidized materials may present an explosion hazard at higher temperatures. Also, the gas coming out of the restrictor tube would need to vented to a hood if N<sub>2</sub>O is used. For these reasons carbon dioxide was used in this study.

## DISCUSSION OF THE PROBLEM

The number of products for this reaction and their chemical identities has not been fully determined. As in most analytical procedures the first step to identification is separation. In the present study the feasibility of removing the products from the clay surface by supercritical fluid extraction will be explored. Supercritical fluid extraction methods will be optimized for the analytes in

<sup>14.</sup> S.B. Hawthorne and D.J. Miller, Anal. Chem., 59, 1705(1987).

question. Finally, some attempt will be made to chemically identify each component of the extract.

#### RESULTS SECTION

- I. Preparation of copper(II) clay.
  - A. Particle size exclusion.
    - 1. 5.0 g of clay were placed into a 250 mL centrifuge bottle with 150 mL of 0.5 M NaCl solution. The bottles were adjusted to a constant weight by the addition of a small amount of distilled water.
    - 2. The contents were mixed by placing the containers on a mechanical shaker for 10 minutes.
    - 3. The containers were centrifuged at 3000 RPM for 10 minutes.
    - 4. The liquid was decanted and discarded. The bottles were filled with 150 mL of distilled water.
    - 5. Steps 2-4 were repeated until the decanted liquid did not give a positive test for Cl using 0.1 M silver nitrate.
    - 6. 150 mL of distilled water was added to each bottle and then the bottles were shaken for 10 minutes.
    - 7. The contents of each bottle were allowed to settle undisturbed for about 30 minutes. The suspension was poured off and saved and the remaining solid was discarded.
    - 8. The suspensions were centrifuged and the liquid was discarded.

## B. Copper(II) ion exchange

- 1. 150 mL of 0.05 M copper(II) chloride dihydrate were added to each bottle.
- The contents were mixed by placing the containers on a mechanical shaker for 10 minutes.

- The containers were centrifuged at 3000 RPM for 10 minutes.
- 4. Steps 1-3 were repeated until the decanted liquid did not give a positive response for either Ca<sup>2+</sup> or Na<sup>+</sup> ion by atomic absorption spectroscopy, AA.

## C. Washing of Cu(II)-clay

- 150 mL of distilled water were added to each bottle.
   The contents were mixed by shaking.
- The bottles were centrifuged and the liquid was decanted and tested for Cl<sup>-</sup> ion.
- 3. Steps 1 and 2 were repeated until their was no positive test for Cl<sup>-</sup> ion using silver nitrate or Cu<sup>2+</sup> ion by AA.
- 4. Finally, distilled water is added to make a clay suspension. This suspension is freeze dried overnight. The solid was collected, weighed, and placed into two vials. Total weight of the solid was 13.8715 grams, 46.2% yield based on starting clay.

## II. Reaction of Cu(II)-clay with aromatics.

About 0.5 grams of the clay is refluxed with 30-50 mL of an aromatic compound such as toluene. The mixture is kept under an argon atmosphere and heated to reflux. The reflux is sustained for about 1.5 hours. During this time the blue colored clay will undergo a color change to a dark color. For toluene the clay appears to be very dark brown. With benzene the color is more of a dark reddish brown. The solvent is then allowed to boil off and the remaining solid is placed into a sealed tube for future analysis.

## III. Extraction by supercritical CO2

#### A. General Method

A Suprex SFE/50 extractor was programmed to start at 150 atm

at 50 °C and to maintain these conditions for 10.00 minutes. The temperature was then be changed to 60 °C and the pressure would ramp to 200 atm over a 10.00 minute period. Finally, the temperature was increased to 70 °C and the pressure was ramped to 250 atm over a 10.00 minute period. These conditions were used for the extraction of PAH's from sand[15]. The extraction was monitored by HPLC analysis.

## B. Extraction results

- 1. Material was extracted by using supercritical fluid CO<sub>2</sub> by this method. It requires three extraction runs to get all of the material out of a 0.500 g sample using the parameters above.
- Even more material and more products can be removed from the clay if the CO<sub>2</sub> is modified with either acetone or methanol.
- 3. 200 μL of methanol was added to the clay in the extractor. Even though the clay had already been extracted by pure CO<sub>2</sub>, several more milligrams of product could be extracted. It took two more additional extractions of this type to remove the maximum amount of material from the clay as determined by HPLC analysis.
- 4. GC/MS analysis revealed that there are no products removed by CO<sub>2</sub> extraction that are not removed by the methanol modified extraction. However, methanol modified CO<sub>2</sub> removes compounds from the clay not extracted by the pure CO<sub>2</sub>.
- 5. It would seem reasonable that a SFE grade CO<sub>2</sub> modified

<sup>15.</sup> V. Lopez-Avila and R.C. Phutela, "Extraction of Trace Organics from Soils and Sediments using Supercritical Fluid Extraction Technique," Acurex Corporation. EPA Contract 68-03-3511, Las Vegas, Nevada. 1989.

with 1 to 5 percent methanol under these conditions with 30.00 minutes for each step instead of 10.00 minutes should effectively remove all the products from the clay. The total extraction time would be 90 minutes which might be reduced considerably if methanol is used throughout the extraction process.

6. As a side note. At one point two extractors were used in tandem with the first extractor in line with the  $CO_2$  filled with silicon and about 0.5 mL of solvent. This method was abandoned because too much modifier went through the sample at one time and the restrictor tended to clog. This might also be a problem if modified  $CO_2$  is used with a high percentage of methanol.

## IV. HPLC analysis

- A. A C-18 column with an length of 250 mm and an ID of 4.5 mm with a 5  $\mu$ m particle size was employed.
- B. HPLC model HP 1050 instrument parameters
  - 1. 1.00 mL flow rate
  - back pressure was -145 bar with 80% methanol and 20% water
  - 3. 20 µL sample loop
  - 4. gradient program
    - a. 80% methanol and 20% water for five minutes
    - b. 100% methanol in a gradient increase over the next 20 minutes
    - c. 100% methanol for 5 additional minutes
    - d. 80% methanol and 20 % water at this point
    - e. total run time is 31 minutes
- C. The Waters model 450 UV/Vis variable wavelength detector was set at 264 nm based on a Cary-219 spectra for the initial

sample which had a broad shoulder at this wavelength.

- V. Analysis by Gas Chromatography with Mass Spectrometry, GC/MS
  - A. Samples were submitted for analysis. The HP 5890 GC was set for splitless injection. The injection port temperature was 250 °C, the column temperature was initially 40 °C for four minutes. The temperature was then ramped to 350 °C at 10 degrees/minute. The temperature was then held constant for 10 additional minutes.
  - B. The HP 5970 mass spectrometer was set to monitor ions in the mass range from 35 to 350 and the interface temperature was 225 °C.
  - C. The flow from the gas chromatograph was split to allow detection by a flame ionization detector and the mass spectrometer.
  - D. Peaks were identified by a computer program that automatically does a qualitative analysis of each mass spectra
  - E. To identify some of the lower molecular weight ions a known sample was prepared with methanol as the solvent so that retention times from the gas chromatography could be compared with the results of the mass spectral analysis.

    Only benzene and toluene were positively identified as being components in the samples. Other minor components suggested by mass spectral matching were not be identified.
- VI. Analysis by Fourier transform infrared spectrometry, FTIR
  - A. KBr pellets were prepared with a 150:1 salt to sample ratio.
  - B. Samples were mixed for ten minutes.
  - C. A blank KBr pellet was used to zero the instrument.
  - D. 0.0400 g was used to prepare each pellet.

#### CONCLUSION

Although the polymerization of aromatic molecules by clays has been studied by several researchers, the use of supercritical fluid extraction(SFE) to remove the products from the clay and the subsequent analysis by GC/MS is unique to this study. Previous mass spectra analysis of the reaction products did not utilize GC separation and was used only to show that polymerization does take place in the reaction of aromatic compounds with transition metal ion clays[16].

The extraction by SFE as compared to soxhlet extraction is less prone to interferences. This is obvious in comparing the number of peaks in total ion chromatograms (Fig. 1). Several of the peaks for the acetone extraction are absent from the SFE extractions. The analysis of these extra peaks identifies compounds that are not realistic for this reaction and that are poorly identified by their mass spectra(probabilities below 50%). These peaks probably result from either the acetone reacting with the products in the clay or interferences such as from the extraction thimble. It is also interesting to note that in the case of toluene the reaction products could not be extracted by soxhlet techniques with methanol as the solvent. This is why acetone was used for soxhlet extraction and as the initial modifier for the SFE process. However, methanol is a better solvent modifier than acetone in SFE because it removes more products than acetone and all products to a greater extent. This evidenced by the CC/MS data which show several compounds in the methanol SFE extraction not found in the acetone SFE extraction(see Tables 1-2) and from the UV absorbance of the samples. Furthermore, methanol is a common modifier for SFE grade CO, and gas cylinders can be purchased with a set composition of methanol.

The efficiency of the extraction was followed by both FTIR and HPLC. FTIR of the original clay, the extracted clay, and the clay

M.M. Mortland and L.J. Halloran, <u>Soil Sci. Soc. Am. J.</u>, <u>40</u>, 367(1976).

before extraction clearly show that reaction products are being removed from the clay(Fig. 2). Even after one extraction run with CO<sub>2</sub> and three extractions with methanol modified CO<sub>2</sub> some material still remains on the clay. It may be necessary to consider a second solvent modifier if it is important to remove all of this material since HPLC analysis suggested that the maximum amount of product had been removed from the clay.

HPLC analysis was performed after each extraction run. When the UV absorbance of the major compounds in the extract did not increase after an SFE extraction it was concluded that all of the material that could be removed had been removed. Figure 3 illustrates typical chromatograms for this analysis.

The gas chromatography retention times of compounds in the extract are consistent between different extractions. The mass spectra of compounds with the same retention time are nearly identical. Extracted samples appear to differ only in the amount and number of products extracted from the clay.

Table 1 lists retention times for GC peaks that are identified as dimers of toluene. The first three peaks have average retention times of 22.30, 22.45, and 22.51 minutes. These compounds are believed to have the chemical formula  $C_{14}H_{14}$  and are probably the ortho, meta, and para isomers of (methylphenyl)phenylmethane(Fig. 4). The mass spectra of the peaks are nearly identical to each other and to the reported mass spectra for this type of compound[17](Fig. 5). The formation of meta isomers as well as ortho/para isomers has already been reported for these types of reactions[18,19].

V.A. Elder, B.L. Proctor, and R.A. Hites, <u>Envir. Sci. Tech.</u>, <u>15</u>, 1237(1981).

<sup>18.</sup> S. Chalais, A. Cornelis, A. Gerstmans, W. Kolodziejski, P. Laslo, A. Mathy, and P. Metra, <u>Helv. Chim. Acta</u>, <u>68</u>, 1196(1985).

<sup>19.</sup> P. Laslo and A. Mathy, Helv. Chim. Acta, 70, 577(1987).

The remaining peaks in table one were determined to have the general chemical formula  $C_{15}H_{16}$ . These compounds are believed to be isomers of benzyl toluene(Fig. 6). This would mean that an additional methyl group is added to one of the rings in comparison to the previous compounds. The boiling point of benzene is 80.1 °C and that of toluene is 109.6 °C. In the actual reaction of toluene with the Cu(II)-clay the toluene is boiled off at the end of the reaction and it seems reasonable that even if benzene were a product in this reaction(toluene minus a methyl group) it would be boiled off as well. Fortuitously, in one of the syntheses not all of the toluene was removed at the end of the reaction. This sample did show benzene present in the SFE extract based on GC retention times and the best match of the mass spectrum for this peak. In reactions involving carbocations it is not unusual that such products as these would form[20].

Table 2 lists retention times for compounds with the chemical formula  $C_{21}H_{20}$ . There are two general types of compounds with average retention times of 29.61 and 31.22 minutes. All of these compounds have a major ion peak at 272. The key to differentiation is the peak at 257. Only the compounds of type A(see Figure 4) would be expected to have this as a major peak in the mass spectrum. The first group of compounds in table 2(rows 1-5) are isomers of methylbis(phenylmethylbenzene) and the second group of compounds are isomers of bis(methylphenyl)phenylmethane(Fig. 7). The mass spectra of these compounds are closely matched to those reported in the literature[17].

The exact assignment of isomers to individual peaks in the GC/MS analysis has not been possible because reference compounds were not available. Positive chemical identification should be based on retention times for the GC as well as spectral matching of the MS data.

<sup>20.</sup> J. March, "Advanced Organic Chemistry: Reactions, Mechanisms, and Structure", McGraw-Hill, New York, 1968.

TABLE 1

ACETONE <sup>21</sup>	CO <sup>2</sup> 22	METHANOL <sup>23</sup>	CO <sub>2</sub> 24	METHANOL <sup>25</sup>	
22.31	22.32	22.28	22.30	22.31	
22.45	22.47	22.41	22.46	22.45	
22.52	22.53	22.47	22.51	22.52	
·			23.19		
23.52			23.51	23.52	
23.64	23.65		23.64	23.64	
23.70	23.72		23.71	23.71	
23.77	23.78		23.78	23.78	
23.85	23.86		23.85	23.85	

<sup>21.</sup> Two extractors in tandem were used. Only one extraction with about 0.5 mL of acetone.

<sup>22.</sup> Three extractions were performed to remove as much material as possible.

<sup>23.</sup> Two extractors were used. Only one extraction with about 0.5  $\,\mathrm{mL}$  of methanol was performed.

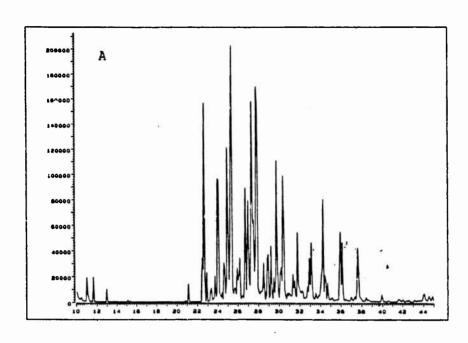
<sup>24.</sup> Only one extraction was performed.

<sup>25.</sup> Three extractions were performed. 200  $\mu L$  of methanol was added to the material in the extraction vessel.

TABLE 2<sup>26</sup>

ACETONE	co²	METHANOL	CO2	METHANOL
29.17		29.18		29.19
29.28		29.29		29.30
		29.35		29.35
29.71	29.71	29.71	29.70	29.73
30.13	30.13	30.13	30.12	30.15
		30.42		30.43
R				30.57
30.62		30.67		30.68
		30.84		30.84
				30.89
		31.05		31.06
31.16		31.14		31.17
31.29		31.30		31.30
31.60		31.59		31.59
				32.40
				32.53
				32.64
32.74				

<sup>26.</sup> Same conditions as in table one.



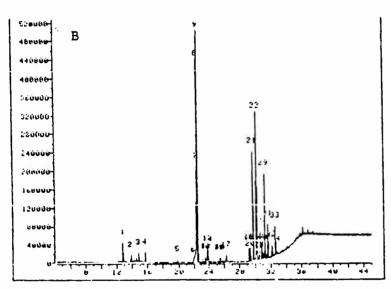
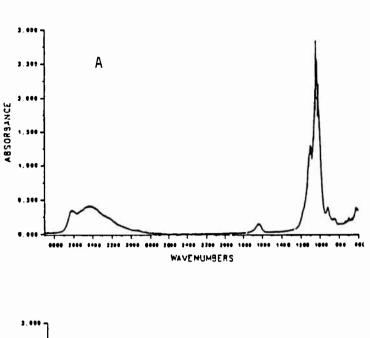


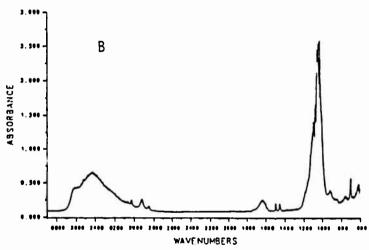
Figure 1. Total Ion Chromatograms of SFE and Soxhlet Extractions.

- A) Soxhlet extract prepared by Dr. T. Tipton
  B) SFE extract with methanol

Original Cu(II)-clay B) Clay after refluxing with toluene Clay after extraction with  ${\rm CO_2}$  and methanol modified  ${\rm CO_2}$ FTIR of Clay Samples FIGURE 2.

G G





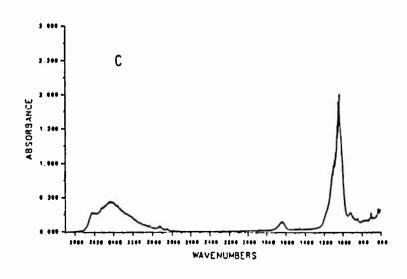


FIGURE 3. Typical Chromatograms for HPLC Analysis

A) Methanol modified extract B) Pure CO<sub>2</sub> extraction

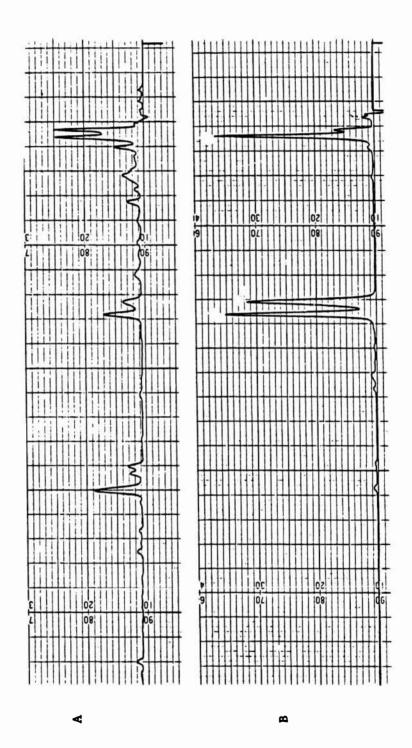
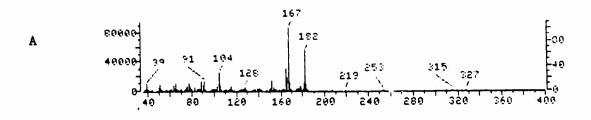
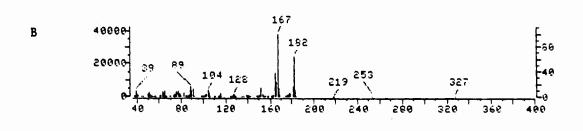
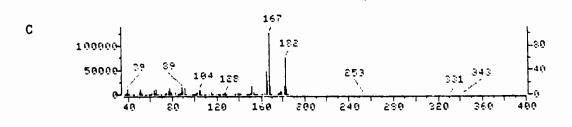


Figure 4. Compounds Partially Identified as Reaction Products







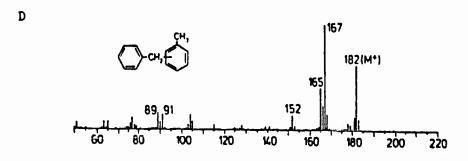
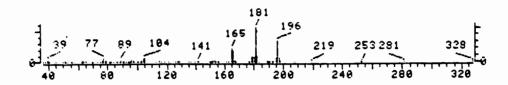


Figure 5. Mass Spectra of (methylphenyl)phenylmethane.

A-C) This work

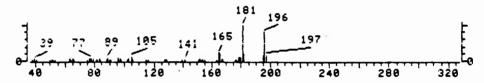
D) reference 17

A



В

Benzene, 1-methy1-3-[(4-methylpheny1)methy1]-



C

Benzene, 1-methyl-2-[(4-methylphenyl;methyl]-

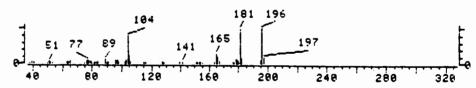
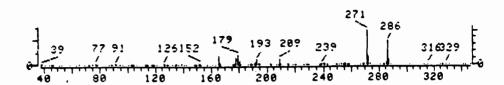


Figure 6. Mass Spectra of bis(methylphenyl)methane.

A) This work B-C) mass spectral reference library



91 165 100 120 140 160 180 200 200 220 240 260

165<sub>179</sub> 195 229 284 328 165<sub>179</sub> 195 229 284 328

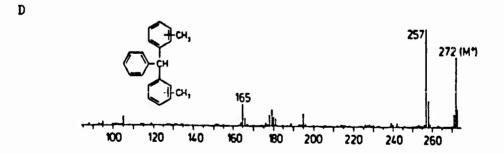


# Figure 7. Mass Spectra

A

В

С

- A) methylbis(phenylmethyl)benzene
  C) bis(methylphenyl)phenylmethane
- B) reference 17D) reference 17

# DATA ACQUISITION AND INSTRUMENTATION INTEGRATION FOR THE TYNDALL AFB ANTI-PENETRATION LABORATORY

Bobby Green
Assistant Professor
Department of Technology
Texas Tech University
Lubbock, TX

## Introduction

The Anti-Penetration Laboratory received an array of electronic parts to install in a PC to make the PC capable of performing as a data acquisition and control system. Their former data acquisition system was a single storage oscilloscope with two channels. All of the parts were purchased from CyberResearch inc., of New Haven, CT. CyberResearch surveys the market for computer peripherals. Our catalog was concerned primarily with the data acquisition and control type peripheral equipment to enable a PC, Macintosh, or PC compatible computer, capable of data acquisition and process control, either digital or analog, or both. CyberResearch has also taken the hardware and software from several manufactures and assigned catalog part numbers of their own to each set of software they sell.

To fully utilize the various Data acquisition systems purchased it will be necessary to purchase additional PC's, preferably rack mounted or portable 386 or 486 type machines, so the several data acquisition systems can be operated separately in parallel. It is possible to reprogram the separate data acquisition systems to work together from a single PC by rewriting and combining the control programs of the several data acquisition systems, but the data acquisition systems would then work serially in a

single PC rather than in parallel in several PC's. Serial operation of the several data acquisition systems would reduce the through-put of all the data acquisition systems and reduce the resolution of each of the data acquisition systems because of operation and execution times. Since reducing the resolution of a data acquisition system is counterproductive and separating the data acquisition and control systems into several discrete parallel data acquisition and control systems is productive, and provides peak operation of all components. Then Anti-Penetration Laboratory should install all the separate data acquisition system components into separate PC's for peak performance of all the data acquisition systems.

Table 1 lists the primary components of the several data acquisition systems, first with the CyberResearch catalog number then the manufacturers designation and manufacturers address.

INST 601 1 MHz data acquisition system with software

INST 292
signal generator base board
INST 293
Arbitrary wave form generator module
INST 294
pulse generator module
with software

ACPC 1616
16-channel, 16-bit
Analog input board
STT 11
Thermocouple measurement
terminal panel
with software

ACAP 128
8-channel 12-bit
Analog output board
STT 31
General purpose terminal panel
for ACJR and ACAO
with software

COMPUTERSCOPE ISC-16 RC Electronics 6464 Hollister Ave. Goleta, CA 93117-3110 Ph 805-685-7770

RC-200 Series Programmable Stimulator and Control System RC Electronics 6464 Hollister Ave. Goleta, CA 93117-3110 Ph 805-685-7770

Analog Connection ACPC Strawberry Tree Inc. Computer Instrumentation and Controls 160 South Wolfe Rd Sunnyvale, CA 94086 Ph 408-736-8800

Analog Connection ACAO Strawberry Tree Inc. Computer Instrumentation and Controls 160 South Wolfe Rd Sunnyvale, CA 94086 Ph 408-736-8800 DIO 32 F 32-channel high speed Digital I/O Board INST 347 50-pin screw terminal block with cable

CYCTM 05
5-channel
Counter/timer board
STA 02
Low cost miniature 37-pin
screw terminal panel
CBL 3702
37-pin flat ribbon cable, 2'
with software

INST 140
2-channel 40 MHz
digital oscilloscope board
2 ea. oscilloscope leads
with software

DAP 2405
Data Acquisition processor
235 KHz, 512K RAM, DSP
MSX 00102
Analog input multiplexing panel
with overvoltage
INST 346
40-pin screw terminal block
with cable
with software

CYDAS 16F
16-channel 100 KHz
Analog I/O
INST 432
16-position mounting board
for High-Perf Modules
INST 465
Isolated Thermocouple input
signal conditioning module
INST 451
Isolated voltage input
signal conditioning module

AT-DIO-32F National Instruments Corp. 6504 Bridge Point Parkway Austin, TX 78730-5039 Ph 512-794-0100

CIO-CTR
Digital input/output device
Computer Boards, Inc.
44 Wood Ave.
Mansfield, MA 02040
Ph 508-26I-1123

Compuscope 220
digital sampling oscilloscope
Gage Applied Sciences Inc.
5465 Vanden Abeele
Monteral, PQ, Canada H4S1S1

DAPL
Data Acquisition processor
Microstar Laboratories, Inc.
2863 152nd Ave. NE
Redmond, WA 98052
Ph 206-881-4286

mfg unknown at this time

Signal conditioning Input/Output Subsystems

Analog Devices Inc.
One Technology Way
PO Box 9106
Norwood, MA 02062-9106

Table 1 Data Acquisition System Catalog Part Numbers and Manufacture

## Abstract

The goals of this project were to bring several data acquisition systems on line and perform data acquisition and reduction at the Anti-Penetration Laboratory, integrate the new data acquisition systems with the instruments on site and with future instrumentation requirements of the HQ AFESC/RCDS Anti-Penetration Laboratory. The work required subsystem assembly, system testing, calibration, and operational testing to insure system reliability and accuracy of the data acquisition systems and associated instruments. After the data acquisition systems and instruments were operational, acquisition and reduction of test data and preparation of a user manual for the instrumentation systems began. As time permitted some electronics was redesigned and assistance to the RCDS group with instrument selection, design, and operation was accomplished.

# **INST 601**

The RC Electronics' Computerscope [1,2] is capable of 1 megasample per second (MSPS) 16-channel, 12-bit per channel, data acquisition. The channels are operated most efficiently if used in powers of 2. That is, one may operate any 1, 2, 4, 8, or 16 channels with maximum use of the data acquisition systems data gathering capability. Using and odd number of channels, 3 or 5 channels or a number of channels other than powers of 2 will result in less than optimum channel utilization because the data acquisition system will take extra samples of the lowest channel to compensate for missing "power of 2" channels. For example, with one channel and the maximum sample rate selected the single channel will sample data once every microsecond and store the data. The data acquisition system has an on board 64Kbyte memory buffer, since each sample fills about one byte so the buffer is full after about 65,000 data points or about 65,000 microseconds. With two channels selected the maximum sample rate is one sample every microsecond but the sample period for a channel is one sample every 2 microseconds for a total of about 32K data points per channel. The buffer will still last for about 65,000 data points or 65,000 microseconds. If 4 channels are chosen each channel is sampled once every 4 microseconds for a total of 16K data points. If 3 channels are chosen channels 2 and 3 are sampled once every 4 microseconds and channel 1 is sampled once every 2 microseconds for a total of 64K data points per channel. Channel 1 will have 32K data points and channels 2 and 3 will have 16K data points each, channel one is sampled twice each cycle. The maximum sample rate per channel is limited by the number of channels being sampled and the total number of samples is currently limited by the Computerscope's data buffer size to the 64K bytes. With additional software from CyberResearch the buffer size may be enhanced using PC RAM, hard disk, or floppy drive but the maximum sample rate is always limited to 1 sample per microsecond.

The sample rate is fixed but the sample period may be increased to a maximum sample period of 100 seconds, so each channel is sampled in 1

microsecond and the channels are sampled 1 microsecond apart, then each channel will be sampled again after the 100 second sample period has elapsed. At the shortest sample period, 1 microsecond, the Computerscope buffer will operate for about 64 milliseconds, at the longest sample period, 100 seconds, the buffer will operate for about 100 hours with 16 channels or 1700 hours with 1 channel. When the Computerscope is operating it is continuously gathering data in either a default mode or a user specified mode with oldest data being discarded when new data is input, after the data buffer is full.

The Computerscope has a pretrigger mode in which the data acquisition saves data already in the buffer after a data gathering trigger signal has been received. The pretrigger mode works as follows: the buffer always holds 64K data points. As new data points above the 64K are added to the buffer, the oldest data is written over and lost. When a trigger signal is received data acquisition and storage begins, but by limiting the number of data points stored after the trigger has occurred one may save data already in the buffer. So if only 44K data points are stored after a trigger signal there will be 20K old data points prior to the trigger event stored in the memory buffer. So events that occurred before the trigger event began data acquisition have been stored and if anything interesting happened just prior to the trigger event it will be available for analysis.

The Computerscope is limited to a 64K memory on the board but there is a software mass storage upgrade that may be obtained with the hardware. The mass storage upgrade allows data to be stored directly to other storage media off the Computerscope board. The mass storage upgrade is useful if the signals the data acquisition system is gathering are low frequency because data in the Computerscope may be transfered to other storage media if permits. For example, as table 2 shows, to transfer 1024 data points from Computerscope to another medium takes,

Hard disk	RAM	
34.0 ms	10.2 ms	data transfer time
40.0 ms	0.0 ms	disk access time
15.0 res	15.0 ms	display counter update time
89.0 ms	25.2 ms	total operation times
		-

Table 2 Transfer time for 1024 data points

The 1024 samples represent a single channel sampled 1024 times or 16 channels sampled 64 times each at some sample rate. If the period between samples is greater than the sample transfer times, then no data will be lost when data is transfered. However if the sample rate is smaller than the transfer rate, the data transfer will degrade data acquisition and higher frequency resolution of the data acquisition system will begin to suffer.

With the 64K buffer the Computerscope, using only 1 channel and sampling every microsecond, it will have 500 KHz as the highest resolvable frequency and the buffer will operate for 64 ms. Using 8 channels and sampling every microsecond each channel will be sampled once every 8 microseconds and the buffer will store 64K data points or 8K data points per channel. With one data point every 8 microseconds the highest resolvable frequency for each channel is 62 KHz. Using all 16 channels of the data acquisition system 4K data points will be taken for each channel to fill the 64K buffer, each channel will have a data point every 16 microseconds with a frequency resolution of 32 KHz. In each case the data buffer will last only 64 ms.

A few things need to be considered when using the Computerscope. What is the highest frequency it will be called upon to resolve, how much data must be gathered during a single event and how long will the event

last? Our events lasted 20 ms to 40 ms so the 64 ms Buffer was long enough. Our events had a 2 microsecond or shorter pulse rise times so ve were limited to using 1 or 2 channels. Using 4 channels would have provided resolution too poor to record the short rise time.

The Computerscope is programmed to store Jata to disk in one of two modes either in an ASCII format, so that the data may be reduced by other data reduction software or in two image files labeled ".PRM" and ".DAT". The Parameter file is named ".PRM", the Data file is named ".DAT", and the ASCII file is named ".ASC", the user specified a prefix of up to eight characters then selects the storage mode either ASCII or image files. The ".PRM" and ".DAT" image files may only be opened by the Computerscope software only if the Computerscope hardware is on the PC buss and operational. If the Computerscope hardware is not installed on the PC buss the data files will not be opened, read or operated on. The ASCII file may be opened and operated on by a variety of software packages. The ASCII file does not depend on the Computerscope hardware the ".PRM" and ".DAT" does.

With the Mass Storage upgrade the software can be enhanced to analyze captured data using Data Conditioning Software, Wave shape Recognition Software, Real Time Signal Averaging Software, Histogram Software, Power Spectrum Analysis Software is capable of directly addressing 640K of Ram Ram memory, but this software still works only with the ".PRM" and ".DAT" data files and only if there is a Computerscope on the PC buss.

## **INST 292**

The RC-200 series Programmable Stimulator and Control System [1,3] manufactured by R.C. Electronics, it is made up of a control board, an optional pulse generator board and/or a analog a waveform generator card, an instrument interface unit and the RC-200 or RC-200A software. The system was used with an IBM compatible and the RC-200 software.

The instrument interface has screw terminal connections and BNC connectors for analog and digital inputs and outputs. The RC-200 can automatically output analog or digital signals and record and update data inputs. If the RC-200 is used with other R.C. compatible equipment, the Computerscope, the programming automatically updated information across menus and checked for potential conflicts or out of tolerance conditions. The basic system contains four analog voltage outputs, eight digital inputs and eight digital outputs. A four-channel pulse generator and arbitrary wave form generators are available in addition to the basic system. There is currently an arbitrary wave form generator in use and a pulse generator has been ordered for future use. RC-200A software has also been ordered to replace the RC-200 software so the RC-200 and the RC Computerscope may be used simultaneously. RC-200A software must be used when the Computerscope and the RC-200 are used together. Both the RC-200 and the Computerscope are menu driven. Single key commands are used to control both the Computerscope and the RC-200. The main menu for the RC-200 is divided into 10 sections. Seven of the sections provide access to further supmenus.

The analog output submenu allows selection of voltage level for Digital to Analog conversion (DAC). Analog outputs choose the voltage level for the states of the pulse generator channels and print out acquired data on a Chart Recorder or dot matrix printer.

The digital output submenu allows logic levels for the digital outputs. A logic high or a logic low may be selected from the submenu for each of the digital outputs. The pulse generator submenu selects pulse train characteristics and can be synchronized by either internal or external pulses.

The analog wave form generator has standard predetermined wave forms programmed for direct use, or arbitrary wave shapes may be generated by the user. Arbitrary wave forms may be generated in three ways. The first is loading a previously saved file from the Computerscope or some other input. The second method allows voltage levels to be added point by point to a data file to create a data file and generate a wave form.

The third method is by user programming; writing a program to generate the wave form necessary for a particular application. The number of data points the file will contain can be adjusted from 1K to 8M data points in the waveform, but like the Computerscope, only 64K of the data points will be cycled in any single interval. The output is a series of pulses which may be filtered to generate an analog signal.

A state table for the RC-200 allows execution of up to twelve user defined test states. The test states may be executed in any order and may be terminated in one of four ways: the selected buffer size is filled, it is terminated after a fixed time, it is terminated at a random time selected by the RC-200, or when digital inputs are the same as some predetermined digital state in the state table.

With the RC-200A software and the Computerscope installed, the data acquisition submenu allows control of the Computerscope from the RC-200A software. The RC-200A software allows creation of up to 12 individual data acquisition buffers. Data acquisition may also be initiated by the state table. When used together, the Computerscope can gather and store data, then the RC-200's waveform generator can replay the data in real time, compressed time or expanded time.

## ACPC 1616

Strawberry Tree's, Analog Connection ACPC [1,4] data acquisition and control system was designed for process monitoring and process control. The ACPC can measure temperature, pressure, flow, or other analog inputs of interest and can be used to turn peripheral equipment on or off based on setpoints installed in the ACPC. The ACPC will measure temperature using any of the ten different Thermocouple types or many RTD's. Cold junction compensation and linearization are handled internally and the Terminal Block used with the ACPC has a large isothermal plate for connection of Thermocouple leads or RTD leads.

The ACPC software is menu driven with screen icons used as a programming tool for icon driven software. Since the software is icon driven, the PC requires the use of a mouse to program the ACPC. Data may be displayed in charts or as meter type readings on the PC screen. Data may be written to disk in a format compatible with several data analysis programs.

The ACPC card used here by the Acci-Penetration Laboratory has 16 differential analog inputs and 16 digital input/output lines. The system uses from one card up to fifteen cards. The 15 cards are capable of monitoring 240 analog inputs and 240 digital input/output lines. The analog inputs may range from 25 mV to 10 volts or 1 mA to 50 mA and the inputs are protected to 50 VDC and pulse to 150 V for a short period of time. The resolution of each differential input is from 12 bits to 16 bits selectable by the user and an acquisition speed of from 225 Hz to 2.5 KHz.

The Strawberry Tree hardware is not as fast as the R.C. Electronics; 225 Hz to 2.5 KHz for the Strawberry Tree v.s. 60 KHz to 1 MHz for the R.C. Electronics. However, for measuring temperatures, pressures and flow rates and performing process controls, the Strawberry Tree equipment is more than adequate. Temperatures, pressures and flow rates change slowly for most process controls, they change in seconds or minutes so the sample rate is adequate.

The Anti penetration Lab group will use the ACPC to initiate events and for monitoring thermal couples and other low frequency events. Higher frequency events will be observed by the 1 MHz device.

# **ACAO 128**

Strawberry Tree's Analog Connection Analog Output Card [1,5] is an analog proportional controller with eight analog outputs 8 digital I/O lines individually selectable as input or output signals. Like the ACPC card, the ACAO can be extended to up to 15 cards for a total of 120 analog output lines and 120 digital I/O lines. When the ACPC and ACAO are used together, the maximum number of cards is still a combined total of 15 cards in the data acquisition and control system. The data output rate is up to 130 KHz with ranges selected from 4-20 mA, 0-10 V, 0-5 V, or  $\pm$  5 V, which are the normal range of control equipment.

When configuring the ACPC and ACAO cards together it is necessary to address ACPC card as card 1 and ACAO card as card 2 if the cards are not addressed in proper sequence the software will not operate the hardware. The instruction manuals failed to mention the configuration conflicts in its literature. Phone conversations with the CyberResearch personnel eventually corrected the configuration oversight in the instruction manual and the data acquisition was configured energized. After configuring, addressing and installing the Strawberry Tree software and equipment, a hardware failure was discovered in the ACPC Board. The ACPC Board was returned to the manufacturer for repair. At the time of this writing, the Board is still under repair and laboratory is awaiting return shipment of the ACPC board.

When the ACPC and ACAO Boards are installed and operational, a basic data acquisition and control configuration is input into the menu driven software and saved. Now when the Data acquisition and control system is turned on, the Control system is on line, configured properly and ready to operate. If changes are necessary, they may be added to the basic configuration and saved, or for a temporary change, they may be added to the basic system configuration while the system is on line but not saved to the permanent file when the system is shut down.

# **INST 140**

Gage Applied Scier Les' Compuscope 220 [1,6] digital sampling oscilloscope is a 2 channel device capable of sampling up to 40 megasamples per second (MSPS). The Compuscope 220 has four BNC

connections for channel A, channel B, an external trigger, and a test output signal. The Compuscope is a two channel storage oscilloscope with computing capabilities allowing signal sampling, waveform display, and data storage for future analysis or display. The sampling rate for the Compuscope is from 1 Hz to 40 MHz. The scope is triggered in one of three ways: with an internal trigger, an external trigger or the PC keyboard and with optional software is capable of reducing and analyzing data gathered by the Compuscope. Channels A and B both have  $1 \text{ M}\Omega$ , 20 pf inputs and will gather signals from 100 mV to 10 V with gains selectable over several orders of magnitude. Channel A has an maximum sampling rate of 40 MSPS and a memory buffer of 256 Kbytes, channel B has a maximum sample rate of 20 MSPS and a memory buffer of 128 Kbytes. So channel A will resolve frequencies up to 20 MHz for 6.4 ms and channel B will resolve frequencies of up to 10 MHz for 6.4 ms. The external trigger will trigger on an amplitude or a slope and will pretrigger using the pretrigger mode in the menu driven software. The test output can provide a 100 KHz 5 V peak to peak square wave output for calibration purposes. The Compuscope is menu driven and may be configured in much the same way as the Computerscope. The Compuscope has a higher frequency response than the Computerscope, 20 MHz vs 500 KHz and it has two channels where the Computerscope has 16.

## CYCTM 05

Computer boards' CIO-CTR [7] is a digital input/output device having 8 digital inputs, for an 8-bit digital input port and 8 digital outputs, for and 8-bit digital output port and an on board frequency of 1 MHz. The CIO-CTR is a digital communications device to communicate between the PC and peripheral digital feedback control equipment.

1

# **DIO 32F**

National Instruments', AT-DIO-32F [8] is a high speed, 32-bit, parallel, digital interface and is designed for high-performance data acquisition and control. The 32 lines of digital I/O are organized into four 8-bit ports. The AT-DIO-32F is compatible with a range of peripheral devices and other computers. Both the DIO 32F and the CYCTM 05 require programming to use these devices as digital I/O communication and control links, for to operating peripheral equipment or to communicate with other computers as a data link.

# **DAP 2504**

Microstar Laboratories', Data Acquisition Processor [9] like the other data acquisition system equipment will perform in many data acquisition and control applications. Each analog input has a gain factor variable from 1 to 1000 and each is independently specified for the individual channel with 16-bit accuracy. The DAP performs analog data acquisition with a 16-bit microprocessor, an 80186, freeing the PC for file management or user interaction. The digital and analog inputs and outputs are connected through a 40-pin connector on the DAP board to a ribbon cable to a screw terminal panel, to the outside world. The DAP has a digital filtering program available with its software. The filter is inexpensive, easy to use, and produces consistent results with no analog type filter drift. To modify the digital filter parameters one enters new program parameters into the DAP software and operates on data stored in memory. Modifying the program parameters to process input data rather than changing the electronics in an analog circuit simplifies data processing considerably. Stored data may be digitally filtered many times as opposed to an analog filter for each frequency of interest making several analog filters necessary to do the task of one programmable digital filter.

The DAP is supplied with its own on board software in ROM and an on board operating system, called DAPL, which will perform many

standard data acquisition tasks and when an application is running, DAPL controls the analog sampling and scheduled DAPL tasks.

The DAP 2400 series can receive 16 single ended analog inputs or 8 differential analog inputs, and with the use of an external multiplexer the DAP will accept up to 512 single ended analog inputs or 256 differential analog inputs. The digital inputs of the DAP 2400 has 16 digital inputs and the 16 are sampled simultaneously. The input pins are labeled S, D, or B single ended, differential, or binary. The DAP can sample and process between 25K and 100K samples per second with most of the data being processed by the DAP faster than it can be transmitter to the PC and processed by the PC.

## CYDAS 16F

The CYDAS 16F had not been received at the time of this writing so an evaluation of that DAS and its peripheral equipment could not be made at this time.

# Cannon Firing System

The Tyndall Anti-Penetration Laboratory uses a 155 mm cannon to simulate a scale model of a penetration bomb. The firing mechanism is adapted to remotely operate a solenoid to hit the firing pin of the cannon and set of the charge in the cannon. The solenoid had operated for several shots when the project was first started but had failed to set off the charge recently. After studying the electro-mechanical firing mechanism it was found that the designer was using a 1:1 isolation transformer and a full wave bridge rectifier to charge 35,000 microfarads of capacitance from a nominal power-line voltage of 120 VAC. When the firing mechanism failed to fire the cannon another 10,000 microfarad of capacitance was added, but the new 45,000 microfarads was still not adequate to fire the cannon. The problem with the firing mechanism was the line voltage, not

the capacitance. When the project started there was very little instrumentation, only a small electrical power load at the test site and the site line voltage was high, as more equipment was added at the site the line voltage was pulled down due to the new load. Typically, the voltage on a power line will fluctuate between 115 and 128 VAC depending on line loads. When the line voltage was 115 VAC or 128 VAC, the rectifier charged the capacitors from 100 VDC or 115 VDC depending on the conditions on the power lines during charging. With 100 VDC the solenoid did not produce enough energy to operate the firing mechanism. With 110-115 VDC the solenoid would produce just enough energy to fire the cannon but was unreliable and the 35,000 to 45,000 microfarad capacitance also took from 25 to 40 seconds to charge.

To fix the cannon firing problem, a voltage doubler network was designed and built in place of the full-wave rectifier and the capacitance was reduced from 45,000 to 2500 microfarads. The full charge voltage of the voltage doubler is always between 200 and 250 VDC; more than enough to positively fire the cannon every time and the extra capacitance was removed because in was not necessary. Even the 2500 microfarads are more than necessary but it was readily available. The new design now charges in 2 to 5 seconds and will not misfire due to low line voltage on the power-line.

# Grounding and Shielding

The Anti-Penetration Laboratory uses two 300 KV marx banks to operate four x-ray flash tubes. Grounding and shielding electronics instruments and electronic measuring devices from the marx bank pulse was an initial problem at the site causing instrumentation trouble. To limit the effect of the pulse on the instrumentation several ferrite cores were order and instructions on their instillation were given to site personal.

# Conclusion

The Anti-Penetration Laboratory events occur in less than 30 ms to 1 s so the data will have frequency components from megahertz to hertz and the laboratory needed data acquisition systems that operate in a broad range of frequencies to capture both low and high frequency components of their test data. The Anti-Penetration Laboratory acquired five separate data acquisition and control systems capable of digital or analog control and at two DI/O systems specifically for digital communication and control. The INST 601 has 16 available channels and will operate for 64 ms at it highest acquisition rate. It will also resolve up to 500 KHz for a single channel, up to 32 KHz for 16 channels and any frequency below 32 KHz. The INST 140 will resolve higher frequencies than the INST 601, 20 MHz and 10 MHz for channel A and channel B respectively and will operate for 6.4 ms at its highest acquisition rate adequate for accelerometers. The ACPC and ACAO are good data acquisition and control systems for events from 200 to 2000 Hz. Thermocouple, RTD's and similar devices work very well with ACPC and ACAO hardware. The DAP like the ACPC and ACAO is also for lower frequency events and has a multiplexing capability making it useful for gathering data points from hundreds of separate instruments. Each of these data acquisition systems have a niche in Anti-Penetration Laboratory work, but they all need to be operated in parallel from separate PC's rather in series form a single PC controller. Serial operation of all the systems from a single PS controller would slow down all the individual systems and serial operation would require significant reprogramming to operate the systems as a single unite.

The DIO 32F and the CYCTM 05 are digital output and communication devices used to communicate between digital devices. The communication Gear needs user specific programming to fully utilize the communication links to control peripheral digital control devices.

The Anti-Penetration in particular and the civil engineering research branch in general are in need of electronic instrumentation specialists, engineers and technicians, to design and deploy electronic instrumentation tailored to their needs. There is work to be done in assisting the Anti-

Penetration Laboratory in configuring all the gear, matching their instrumentation to their data acquisition and control systems, and training operators on site to operate and use their electronics gear.

# Refrences

- [1] CyberResearch Inc., "PC Systems Handbook for Scientists & Engineers", CyberResearch, New Haven, CT, Vol 7, No 2., fall 1990.
- [2] RC Electronics, "Computerscope ISC-16 Reference Manual", RC Electronics, Goleta, GA, December 1991.
- [3] RC Electronics, "RC-200 Programmable Stimulator and Control System User's Manual Version 1.3", RC Electronics, Goleta, GA, December 1990.
- [4] Strawberry Tree Inc., "Analog Connection ACPC Data Acquisition & Control System for the IBM PC and Compatible Computers", Strawberry Tree Inc. Computer Instrumentation and Controls, Sunnyvale CA, October 1988.
- [5] Strawberry Tree Inc., "Analog Connection ACAO Data Acquisition & Control System for the IBM PC and Compatible Computers", Strawberry Tree Inc. Computer Instrumentation and Controls, Sunnyvale CA, June 1988.
- [6] Gage Applied Sciences, "Compuscope 220 Digital Sampling Oscilloscope Installation & Users Guide", Gage Applied Science, Monteral Canada, February 1988.
- [7] ComputerBoards Inc., "CIO-CTR User's Manual Revision 1.1 March 1990 & CIO-CTR Utility Disk Revision 1.1", ComputerBoards Inc., Mansfield, MA, March 1990.
- [8] National Instruments Corporation, "AT-DIO-32F Users Manual, January 1991 Edition Part Number 320147-01", National Instruments Corporation, Austin, TX, January 1991.
- [9] Microstar Laboratories Inc., "DAPL Manual Data Acquisition Processor Analog Accelerator Series Version 3.3A", Microstar Laboratories Inc., Redmond, WA, 1991.

# THE COMPARISON OF COMPLEXATION-ULTRAFILTRATION TO CHELATION ION EXCHANGE IN THE TREATMENT OF SPENT ELECTROLESS NICKEL PLATING BATHS

Dr. Douglas Klarup Assistant Professor Department of Chemistry University of Montana Missoula, MT 59812

#### ABSTRACT

Chelation ion exchange has proved problematical for recycling electroless metal plating baths, so currently the Air Force uses hydroxide precipitation and disposal to treat spent baths. This is expensive and produces a large amount of hazardous waste. An alternative technology, complexation-ultrafiltration, may be a more appropriate method to treat spent plating baths, but quantitative information is required. The project reported here compares complexation-ultrafiltration using polyethylenimine with chelation ion exchange using Duolite ES-467 in the treatment of contaminated electroless nickel plating baths. A simple model is developed to understand the chemistry in each process. The results show that Duolite ES-467 is selective toward the zinc contaminant over nickel, but to remove all of the zinc will require removing much of the nickel as well. The polyethylenimine is more selective toward nickel, so to remove the zinc contaminant virtually all of the nickel must be removed. However, complexation-ultrafiltration may prove to be more efficient then hydroxide precipitation in removing all of the metals from the waste stream.

## INTRODUCTION

Metal plating baths are used in many Air Force installations to modify various parts to desired specifications. The baths function in different ways, but in general consist of large vessels containing the primary plating metal as well as supporting chemicals. The electroless nickel bath uses a reducing agent, usually sodium hypophosphite, to reduce nickel(II) to nickel(0) at the surface of the piece being plated. The advantage of the bath is that uniform coverage of the nickel plate is possible (assuming the solution can easily reach the desired surfaces) since no current density dependence exists as is found in electrolysis. One disadvantage is that the baths etch the metal parts while plating the nickel, and subsequently become contaminated with other metal ions, the nature of which are dependent on the parts being plated. In addition, pieces to be plated often have been previously plated with other material, particularly zinc, which carries contamination into the bath.

These problems require that nickel electroless plating baths be replaced periodically. Replacement of the baths is expensive (several thousand dollars per bath) and disposing of the old bath--which must be treated as hazardous waste--is also expensive.

For these reasons it is desirable to either recycle metal plating baths or find efficient means of removing these metals from the waste stream. In order to recycle electroless nickel baths, the contaminant metals must be removed while, ideally, leaving the nickel ions and other supporting chemicals behind. Traditional methods such as pH control, in

order to precipitate the metal hydroxides, are not suitable for bath recycling since 1) the bath pH is 4.4 and should remain at this pH to simplify solution chemistry control and 2) a large portion of nickel hydroxide also would precipitate. Even when used as a final treatment precipitation via pH control results in a relatively large volume of waste requiring extensive de-watering. Another traditional method such as simple ion exchange is another possibility. However, because the contaminants are copper(II), lead(II), and zinc(II), whose electrical charge is the same as nickel(II), and there is a very large amount of sodium(I) present, this technology is not suitable to bath recycling.

One of the most promising technologies which has been applied to Air Force electroless nickel baths is chelate ion exchange. this technique employs a chelating ion exchange material which, theoretically, can preferentially bind contaminant metal ions over nickel ions, leading to contaminant removal. A pilot plant using the chelation ion exchange resin Duolite ES-467 was constructed and tested with spent electroless nickel plating bath solution. The method removed most of the contaminants, but removed much of the nickel as well. Regeneration of the resin also is difficult.

Since the construction of the pilot plant, other technologies and resins have been developed. A new resin, Duolite C-73, is now marketed by Rohm and Haas and supposedly will perform the separation required. Regeneration of this resin may be easier. A relatively new technology, complexation-ultrafiltration, has emerged which may complete with column chelate ion exchange. In complexation-ultrafiltration a large polymer or macromolecule is present in a flow-through ultrafiltration cell. The

filter at the exit end of the cell is fine enough to prevent the transmission of the polymer. The contaminated solution is pumped through the cell where the metals form a complex with the polymer. Those metal ions complexed are retained in the cell, of course, and effectively separated from the bulk solution. Complexation-ultrafiltration has the potential to be very selective in what is complexed, although the appropriate polymer or macromolecule must be found. Short of this, the technique provides a possible alternative to hydroxide precipitation in the removal of heavy metals from the waste stream.

When considering either chelation ion exchange or complexationultrafiltration, there is a need to understand how the large number of
variables and chemical reactions which are present in the bath interact
with each other and affect the ability of the complexant to treat the
bath. In other words, an effective model which takes as many of these
factors into account can allow for an understanding of the
bath/complexant chemistry, which in turn allows predictions to made
considering the effectiveness of various treatment procedures in
treating spent bath solution. The project reported here develops a
simple equilibrium model to gauge and compare the effectiveness of
complexation-ultrafiltration with chelation ion exchange in treating
spent electroless nickel baths for recycling or waste reduction.

## ELECTROLESS NICKEL PLATING BATH DESCRIPTION

The electroless nickel bath used by the Air Force consists of the following reagents and their amounts:

$$NiSO_4$$
 24 g/L  $Na_3C_6H_5O_7$  85 g/L  $NaH_2PO_2$  10 g/L  $NH_4C1$  50 g/L

and the chemical reaction responsible for the plating action is: $^{1}$ 

$$NiSO_4 + 3H_2O + 3NaH_2PO_2 --- Ni(0) + 3NaH_2PO_3 + 2H_2 + H_2SO_4$$

The bath is a high ionic strength, buffered bath with a pH of 4.4-4.6. Because the effect of this high ion concentration is difficult to predict, all measurements and experiments were carried out in solutions which included all of the non-metal constituents at the appropriate concentrations found in the bath.

## BATH MODEL

In order to understand the interaction between nickel, zinc contamination, and a sorbent or complexant, the nickel electroless bath was modeled using the following chemical equilibrium expressions and constants:

Citric Acid Dissociation Constants:

$$K_1 = [H_2Cit^-][H^+]/[H_3Cit] = 7.1 \times 10^{-4}$$
  
 $K_2 = [HCit^{2-}][H^+]/[H_2Cit^-] = 1.7 \times 10^{-5}$   
 $K_3 = [Cit^{3-}][H^+]/[HCit^{2-}] = 8.4 \times 10^{-6}$ 

Metal Citrate Formation Constants:

$$K_{m_1} = [MHCit]/[M^{2+}][HCit^{2-}]$$
Ni: 1990 Zn: 955

$$K_{m_2} = [MH_2Cit^+]/[M^{2^+}][H_2Cit^-]$$
Ni: 56 Zn: 17.8

Metal Sorption/Complexation:

$$K_{s_m} - S_m/[M^{2+}]S_f$$

where  $S_{m}$  is the concentration of metal bound or complexed in moles/gm, and  $S_{f}$  is the remaining free binding sites in moles/gm.

This model is better than a simple isotherm because it takes into account the competition between nickel, zinc, metal citrates, and the complexant sites. However, it is unlikely that the value of  $K_{\rm Sm}$  is actually a constant—it is more likely that it varies as sorption or complexation continues. Never-the-less the model can account for trends in the data.

## **EXPERIMENTAL**

Due to time constraints the project focused only on nickel and zinc, since zinc is the limiting contaminant in these baths. Experiments were designed to quantitatively test the affinity of nickel and zinc for each complexant. This was accomplished by using two separate stock solutions, one containing 9000 ppm nickel and the other containing 1000 ppm zinc along with all of the other supporting chemicals found in the plating baths. Each of these solutions was tested with Duolite ES-467 (Rohm and Haas), polyphosphate (Aldrich), polyhistidine (Sigma), and polyethylenimine (Aldrich). From these experiments values of  $K_{\rm S_m}$  for each metal-complexant were determined. These  $K_{\rm S_m}$  values were plugged into the equilibrium bath model described above and the model results compared with experimental results.

Both the chelating ion-exchange resin Duolite ES-467 and the complexing polymers were tested in a 10 mL stirred flow-through ultrafiltration cell (Amicon). However, each type of complexing material required different procedures in order to measure K<sub>sm</sub>. The chelation ion-exchange resin (Duolite ES-467 from Rohm and Haas) was placed in the cell with a 0.2 micron filter (Spectrum) in the bottom of the cell. A syringe pump filled with the appropriate metal solution was connected to the cell, and the solution pumped through the cell. This provided a "breakthrough curve" which when compared to the theoretical dilution breakthrough provided a continuous measure of the metal ion in solution and, via mass balance calculations, the amount of metal sorbed on the resin; a continuous isotherm was calculated. Care was taken to pump slowly to ensure that equilibrium was maintained. All concentrations were determined using atomic absorption spectroscopy.

The complexing polymers required a different approach than the chelating ion exchange resin. A 1000 nominal molecular weight cutoff (NMWCO) filter (Millipore) was used to prevent the polymers from leaving the ultrafiltration cell. This meant a backpressure in the cell of 75 psi., beyond the tolerance of a syringe pump. Therefore nitrogen pressure was used to pressurize the cell. Initially, a dynamic pressure reservoir was pressurized, which forced metal solution through the cell in a procedure similar to using a syringe pump. This is an appropriate technique when simply carrying out filtrations, but is not appropriate when trying to measure complexation parameters. The reason for this is that the compression of air in the cell and lines from the reservoir to the cell prevent accurate knowledge of when solution actually begins to

enter the cell. To some extent this problem could be circumvented through more elaborate plumbing, but it is difficult to see how it could be avoided completely. Therefore, to measure complexation parameters the cell was periodically opened up, a known amount of metal solution added, mixed until equilibrium was achieved, and then the cell was repressurized.

One complication in measuring the complexation parameter of the polymers using this method was that the 1000 NMWCO filters also inhibited the passage of nickel and zinc. This occurs because the filters are heterogeneous in nature, with a range of size openings. This results in a portion of the fluid flowing through the membrane to pass through openings too small for the hydrated metal-citrate complex to pass. The relationship is expressed mathematically as:

$$R_x = 1-[M]_f/[M]_c = \sigma/(1+\Delta x/J_w)$$

where  $\Delta x$  is the membrane thickness,  $J_w$  is the solution flux,  $\sigma$  is the fraction of openings in the membrane through which the solute cannot pass,  $[M]_f$  and  $[M]_c$  are the solute concentrations in the filtrate and the cell, respectively, and  $R_x$  is the retention coefficient.

### RESULTS

The isotherms derived from the breakthrough curves of nickel and zinc after mixing with Duolite ES-467 are shown in figures 1 and 2. Each solution was buffered with the NH<sub>4</sub>Cl/Citrate system described above. Hypophosphite was also present to ensure that true nickel bath conditions existed. It is clear that the Duolite ES-467 does have a clear preference for zinc. The results show that the relative amount of

zinc removed from solution, as compared to nickel is much greater. On the other hand, there is a significant amount of nickel removed as well. This is particularly important since the concentration of the nickel solution was so much higher than that of the zinc solution.

The values of  $K_{S_m}$  for nickel and zinc with the Duolite ES-467 are shown in Table I. These are average values taken from points along the metal/resin isotherm for which analytical data were available. The data were substituted in the appropriate points in the model, and  $K_{S_m}$  calculated. The relative values of these constants demonstrate the preference zinc holds over nickel with Duolite ES-467.

When these  $K_{S_m}$  values are plugged into a model describing a nickel electroless plating bath contaminated with zinc, the results do not describe the experimental results too well. Table I shows that predicted results from the theory compared to the experimental results from a synthetic contaminated nickel bath mixed with Duolite ES-467. The inaccuracy of the model is most likely due to the fact that an average  $K_{S_m}$  value was used, when in fact the value of the equilibrium constant changes upon addition of metal ions. Also the model ignores ionic strength effects, and for such a high ionic strength bath this may cause sever deviations from the conditions under which the citric acid dissociation constants and metal-citrate formation constants were measured.

Both the model and experimental results indicate, however, that in order to remove all of the zinc from the contaminated bath, a significant amount of nickel also will be removed. This is what has been found in practice, and is what the model predicts--at least in a

qualitative way. Therefore, using Duolite ES-467 it is theoretically possible to remove all of the zinc, just as it is theoretically predictable that a fair amount of nickel also will be removed. The reason for this result is that, although the Duolite ES-467 prefers zinc over nickel, the nickel concentration in a plating bath is 9000 ppm, while the zinc contaminant concentration is 200 ppm. Therefore the equilibrium shifts in response to the large amount of nickel in solution.

Table I also shows the calculated values of  $K_{S_m}$  for polyethylenimine. The other polymers tested, polyphosphate and polyhistidine, showed no apparent zinc complexation, either because they did not bind at this pH, or because the filter was permeable to a large portion of the polymer. Polyethylenimine, however, binds strongly to both metals, although greatly favors ackel. Polyethylenimine consists of the  $-C_2$ -N- unit, and metal binding occurs at the nitrogen atom. The  $K_{S_m}$  values for metal-polyethylenimine reported in Table I are average values of several different points.

The model and experimental results for mixing polyethylenimine with the synthetic contaminated plating bath solution also are shown in Table I. Again the model does not predict the experimental results exactly, but most of the inaccuracy is in the zinc value. Considering the magnitude of the zinc concentration compared to the nickel concentration, it appears this simple model does a better job of explaining the polyethylenimine/bath system that the Duolite Es-467/bath system. Both the model and experimental results show that in order to remove all of the zinc from the solution using polyethylenimine,

virtually all of the nickel would also be removed.

## CONCLUSIONS

It is clear from experience, experiment, and theory that Duolite ES-467 will remove zinc from the electroless nickel plating bath, but also will remove a large amount of the nickel. To better predict exactly how much nickel would be lost from a typical plating bath, a more accurate model, one which takes into account a varying  $K_{\rm Sm}$  value, needs development. In addition, the use of a larger NMWCO filter, perhaps 20,000, would reduce the error in the  $K_{\rm Sm}$  values calculated for the polyethylenimine complexes.

It is also clear that polyethylenimine alone will not remove just the contaminants from solution, but most if not all of the nickel as well. Therefore, it alone cannot be used for the most attractive metal bath treatment: recycling. On the other hand, the polyethylenimine would provide a very efficient means of removing all of the heavy metals from the waste stream, leaving a relatively low volume of hazardous waste. In addition, the results suggest that polyethylenimine competes very effectively against citrate form metal complexation. This is significant since ligands like citrate have been shown to reduce the efficiency of hydroxide precipitation for metal removal.

## FUTURE WORK

There are other problems associated with chelation ion exchange which were not addressed in this project but which make the technique awkward to used in bath treatment. Primary among these is regeneration

problems. The metal ions chelate with Duolite ES-467 resin so effectively that it is very difficult to remove them. An alternative resin, C-73, also marketed by Rohm and Haas, may prove to be more easily regenerated, although probably at the expense of metal removal efficiency. This should be tested, however, before abandoning chelation ion exchange as a treatment method. The C-73 was not available during the project time due to manufacturing changes being made at Rohm and Haas, but will be available in December, 1991.

Complexation-ultrafiltration has some interesting possibilities which require exploration. Two major ones come to mind. First, to explore the feasibility of using this technique to reduce the amount of hazardous waste associated with a spent bath. In other words, to compare this alternative to the currently used hydroxide precipitation. The second possibility involves determining the regeneration ability of polyethylenimine. If the complexed metal can be removed easily, then it may be possible to use complexation-ultrafiltration to recycle spent electroless plating bath solutions using a two step process.

#### REFERENCES

- 1. Murphy, James A., ed., <u>Surface Preparation and Finishes for Metals</u>, Society of Manufacturing Engineers, Maple Press Company, Caledonia, 1971.
- 2. Molyneux, Philip. <u>Water Soluble Synthetic Polymers: Properties and Behavior, Vol I.</u>, CRC Press, Inc., Boca Raton, Florida, 1984.

Table I

Duoli	te ES-467	•	Polyeth	ylenimine
$^{K_{\mathbf{s}_{Ni}}}$	<b>-</b> 3729		$\kappa_{\mathtt{s}_{\mathtt{Ni}}}$	<b>-</b> 7873
$^{\mathrm{K}}\mathbf{s}_{\mathbf{Z}\mathbf{n}}$	<b>-</b> 18576		K <sub>s</sub> Zn	<b>-</b> 611
s <sub>t</sub> -	2.4e-4 mol/gm .		s <sub>t</sub> -	1.2e-2 mol/gm
<u>Model</u>	Experimental		<u>Model</u>	Experimental

Ni-soln/Ni-total: 0.91 0.77 . 0.068 0.078

Zn-soln/Zn-total: 0.48 0.24 . 0.308 0.624

Table I. Model and experimental results for nickel and zinc concentrations when a synthetic contaminated electroless nickel plating bath is mixed with Duolite ES-467 and polyethylenimine. Concentrations are expressed as the fraction of metal remaining in solution. The initial concentrations of nickel and zinc are 9725 and 266 ppm, respectively. The mass of complexant and solution used in each experiment is 0.94 and 10.9 gms, respectively, for the Duolite ES-467 and 0.64 gm and 5.32 gm, respectively, for the polyethylenimine.

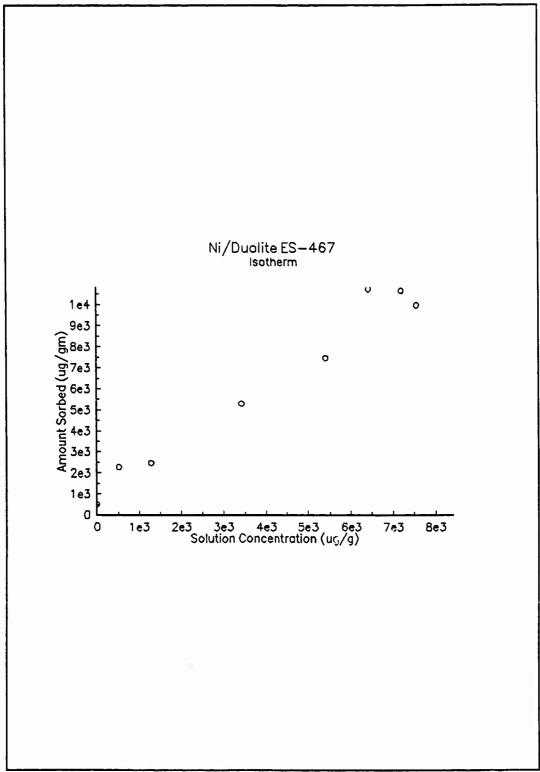


Figure 1. Isotherm derived from the breakthrough of nickel from a flow through cell containing Duolite ES-467.

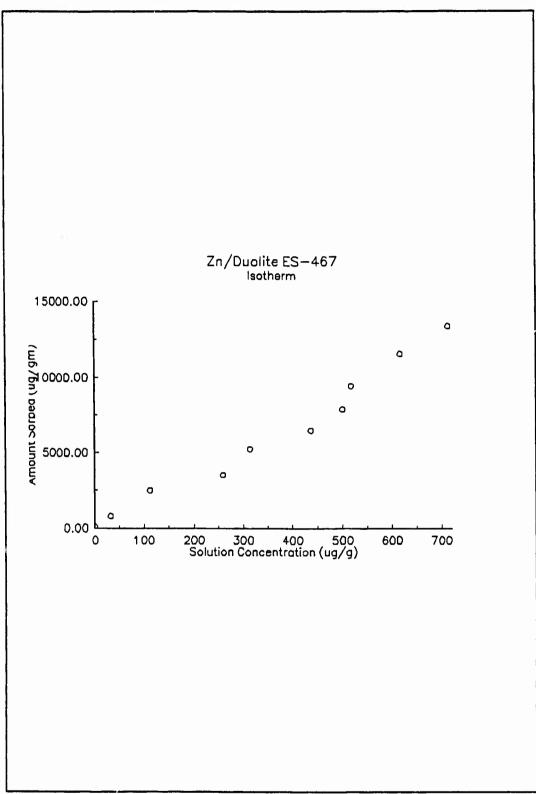


Figure 2. Isotherm derived from the breakthrough of zinc from a flow cell containing Duolite ES-467.

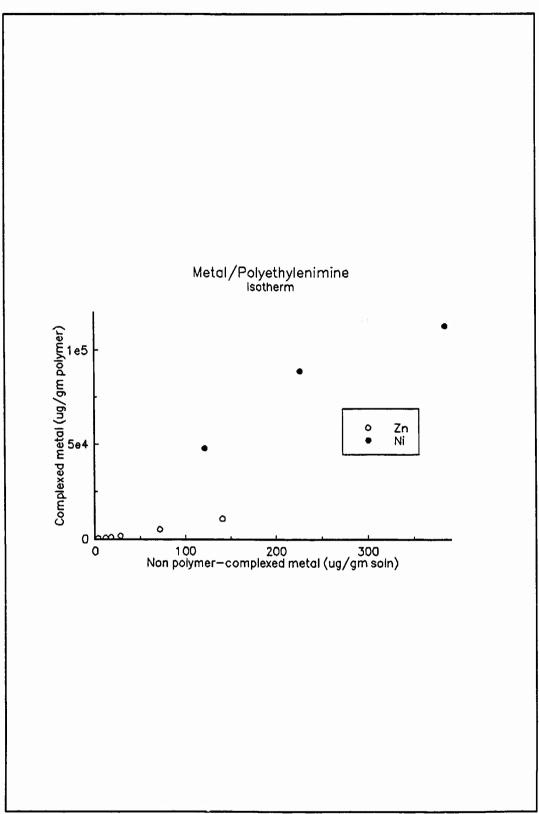


Figure 3. Points used in calculating  $K_{s_m}$  values.

# FEASIBILITY STUDY TO USE THE GYRATORY TESTING MACHINE FOR FIELD COMPACTION CONTROL OF AGGREGATE BASE COURSE IN FLEXIBLE AIRFIELD PAVEMENTS

Cheng Liu

Professor

The University of North Carolina of Charlotte

#### ABSTRACT

The purpose of this study was to evaluate the feasibility of using the Gyratory Testing Machine (GTM) to determine density requirements for aggregate base course in flexible airfield pavements trafficked by heavy weight, high-tire pressure aircraft. A trench 8-ft wide, 18-in deep was cut across the wheel path of Tyndall flexible pavement test sections which had been trafficked by simulated combat-ready F-15 C/D aircraft. Nuclear density, moisture content, bearing strength and gradation tests were performed at the various depths of trafficked and untrafficked areas of aggregate base and subgrade sand. A field CBR test was conducted at the top of compacted sand subgrade. Gyratory compaction tests were also performed on the base course aggregate and subgrade sand to determine ultimate dry densities. The results of field and laboratory tests indicated that there may be a correlation between ultimate gyratory density and field density after both construction and traffic compaction.

#### ACKNOWLEDGEMENTS

The Air Force office of Science Research is gratefully acknowledged for providing financial support for this research project. The author wishes to express his sincere appreciation to members of the Air Force Engineering and Services Center at Tyndall Air Force Base, Captain Charles Manzione and Mr Jim Murfee, for giving me the opportunity, support and the guidance necessary for the research.

Special thanks goes to the Laboratory staffs of Applied Research and Associates, Inc, who helped perform field and laboracory tests and plot figures for this report. I also would like to thank Ms Marilyn Flawn of the Air Force Engineering and Services Center for typing the entire manuscript

### I. INTRODUCTION.

In 1988 the Air Force Engineering and Services Center constructed flexible and composite pavement test sections at Tyndall AFB, Florida for use in a study on rutting of asphalt pavement under high temperature and tire pressure (Figure 1). One segment of test sections under this study consisted of a 6-in asphalt concrete layer placed over 12-in of compacted limestone aggregate base course. The aggregate base course was underlaid by a 16-in compacted subgrade sand over the natural sand subgrade

During construction of the Tyndall test sections, the aggregate base materials were compacted to a target average dry density of 140.8 pcf at 4.75% of moisture content. These were the maximum dry density and optimum moisture content of base materials as determined by modified proctor compaction test (ASTM D-1557).

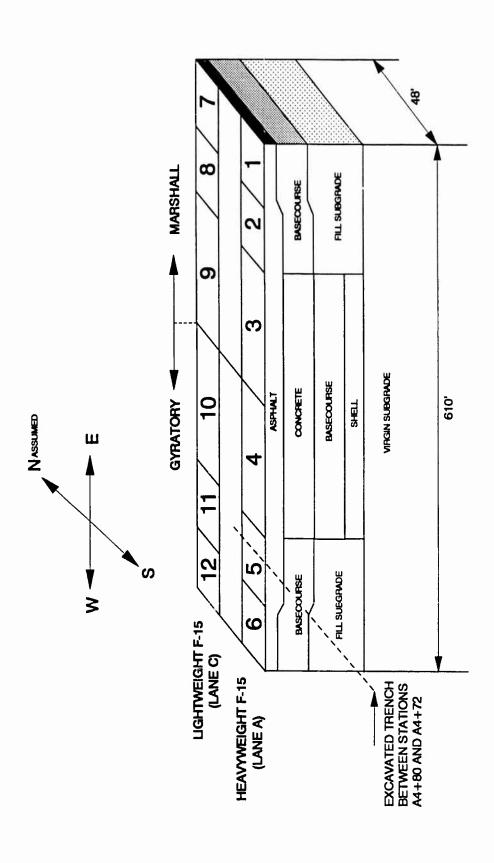


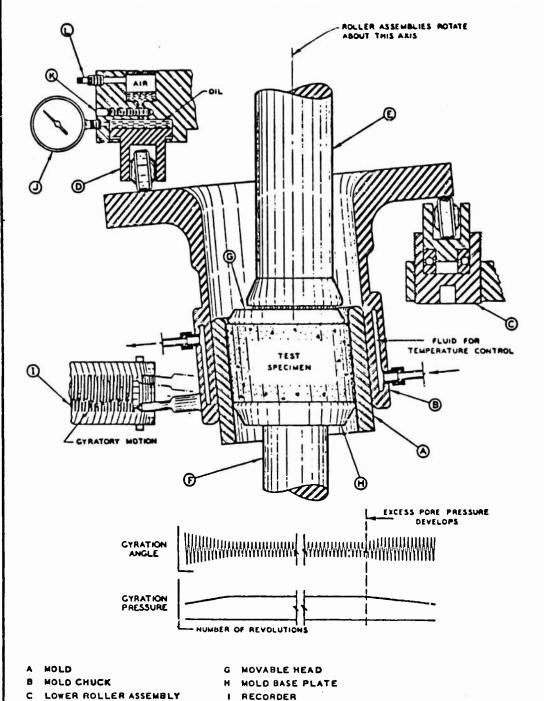
Figure 1. Test Sections Layout.

The test sections were trafficked with a load cart which was intended to simulate combat-ready F-15 C/D fighter aircraft (29,500 lb. single wheel load with 355 psi tire pressure). A considerable amount of rutting in the granular layers was detected by multi-depth deflectormeters installed at various depths in the test sections during construction.

Permanent deformation in a flexible pavement can be significantly reduced by increasing the degree of compaction of the granular base course (1). This writer theorized that the modified proctor test did not and could not provide sufficient target density for field compaction for this section to support the high tire pressure to be trafficked on the pavement. To substantiate this theory, a trench 8-ft wide, 18-in deep,  $90^{\circ}$  across wheel path was cut through Tyndall test sections between stations A 4+72 and A 4+80 in flexible pavement areas (Figure 1) to determine if traffic further densified or degraded the granular layers.

Nuclear density, sand cone density, moisture content and gradation tests were performed at various depths in the trafficked and untrafficked areas of the base course and subgrade. Field California Bearing Ratio (CBR) test were conducted on the compacted sand subgrade to evaluate the adequacy of 12-in of Alabama limestone placed as base course.

The Gyratory Testing Machine (GTM) was employed in this study to investigate the feasibility of using this machine for better control of field compaction of aggregate base. The GTM (Figure 2) developed by the Corp of Engineers has the capability to compact pavement materials using a kneading process that simulates the action of rollers during construction and rolling tires under traffic. The GTM has the



- UPPER ROLLER ASSEMBLY
- E UPPER FIXED PLUNGER
- LOWER MOVABLE PLUNGER
- J PRESSURE GAGE
- K OIL CUTOFF VALVE
- L AIR INTAKE VALVE

SCHEMATIC ILLUSTRATION OF FIGURE 2 GYRATORY MACHINE (2)

R 0:0038A

flexibility of setting various vertical ram pressure, gyration angle and number of revolution to simulate field compaction by construction equipment and subsequent compaction by traffic (3).

The objective of this study is to look into probable inadequacy of using modified Proctor test to provide a target density for field compaction and to explore the possibility of using the GTM to replace modified Proctor test as a tool in field control of compaction for flexible pavement airfields.

The three phases of this study include: (a) cutting a 8-ft trench through test sections at Tyndall AFB FL and performing field tests, such as sand cone, nuclear density, moisture content and field CBR tests on base materials and compacted subgrade. Grain-size analyses were conducted at the Tyndall AFB FL Laboratory, (b) Performing gyratory compaction tests using subgrade sand and the stockpile materials of the same aggregates existed in the base course of test sections. Gyratory samples for base materials were fabricated in the laboratory to conform with the stockpile gradation, and (c) evaluating and analyzing both field and laboratory data, and studying the feasibility of using the GTM to control field compaction.

# II. MATERIALS AND TEST PROCEDURE

#### A. MATERIALS

#### 1. Base Course Material

The base course materials of the flexible pavement at Tyndall AFB FL text sections were crushed limestone obtained from Trinity, Alabama. The various properties of base course aggregate are listed as follow (4):

# a. Specific Gravity

# i. Course Aggregate

Average Bulk Specific Gravity	=	2.619
Average Bulk Specific Gravity (SSD)	=	2.642
Average Apparent Specific Gravity	=	2.680

# ii. Fine Aggregate

Average Bulk Specific Gravity	=	2.648
Average Bulk Specific Gravity (SSD)	=	2.650
Average Apparent Specific Gravity	=	2.655

# b. Grain - Size Distribution

Table 1 listed gradation of base materials along with the USAF specification for No. 3 base material.

TABLE 1. GRAIN - SIZE ANALYSIS OF BASE MATERIALS FROM STOCKPILE

SIEVE SIZE	PERCENT PASSING	USAF SPECIFICATION
1"	100	100
1/2"	65.9	40–70
#4	33.7	20-50
#10	22.2	15-40
#40	12.4	5-25
#200	6.6	0-10

- c. Maximum Dry Density and Optimum Moisture Content (determined by ASTM D- 1557, commonly referred to as the modified proctor compaction test.)
  - i. Maximum Dry Density = 140.8 lb/cu ft
  - ii. Optimum Moisture Content = 4.76%
  - d. AASHTO and Unified Soil Classifications
    - i. AASHTO: A-1-a
    - ii. Unified: GW
  - 2. Subgrade Beach Sand (4)
    - a. Grain-Size Distribution

The analysis of the beach sand indicated that the subgrade materials was uniform, poorly graded sand. Table 2 listed gradation of sand subgrade

TABLE 2. GRAIN-SIZE ANALYSIS OF SUBGRADE SAND

Sieve Size	Percent Passing
#16	100
#40	98
<b>#</b> 50	82
#100	2
#200	0.06

- b. Maximum Dry Density and Optimum Moisture Content
  - i. Maximum Dry Density = 101.0 pcf
  - ii. Optimum Moisture Content = 4.0%
- c. AASHTO and Unfield Soil Classification
  - i. AASHTO: A-3
  - ii. Unified: SP

#### B. TEST PROCEDURES

Nuclear density and moisture content tests were performed in accordance with ASTM D-2922; sand cone density tests were conducted following ASTM D-1556 procedures. Grain-size analyses of base materials excavated from the test trench were determined in accordance with ASTM C-136 and C-117. Field CBR test was performed by following ASTM D-4429 procedures.

The gyratory testing machine was used to determine the ultimate density that would develop in the base course under both construction equipment and traffic. The GTM test procedures used in this study are briefly described as follows (2):

Thoroughly mix sufficient sample of test materials at the water during and immediately after construction. content Compact specimens from this sample in the GTM at a 1° initial gyratory angle setting using a vertical ram pressure in each case that corresponds to the theoretical vertical stress for the particular depth for which the required unit weight is to be established. Continue compaction while reading the vertical deflection of specimen height (i.e. the vertical movement of the compression ram) at 50, 100, 150, 200, 250, 300 or more resolutions until the rate of densification is not more than 1 pcf per 100 revolutions. Calculate the dry density based on vertical movement of GTM's compression ram. Prepare a plot of dry density versus number of revolutions curves for each selected ram pressure. On each of these curves identify the point where the following 100 revolutions produce an increase in dry density of 1 pcf or less. The unit weight at this point was considered the ultimate density at the selected depth having the same

distributed stress under the trafficked wheel load as the selected ram pressure.

### III. DATA ACQUISITION AND EVALUATION

#### A. FIELD DATA

Nuclear density readings and moisture contents were taken from both trafficked and untrafficked areas at a depth of 12 inches into the base course. This yielded an average density for the entire 12-in layer. The dry density of base course in untrafficked area (average of 12 readings) was found to be 146.1 pcf with an averaged moisture content of 2.1%. dry density of base course under the rutted area (average of 6 readings) was determined to be 148.5 pcf with an average moisture content of 1.8%. A sand cone test was performed on the surface of base course. Due to roughness and irregularity of base course surfaces, and the shallow depth of the test hole dug, the result of this test with a dry density of 133.8 pcf was considered to be inaccurate and was ignored. The in place averaged dry density of base materials under the rut (148.5 pcf) is slightly higher than the averaged dry density of untrafficked area (146.1 This phenomenon suggests that traffic densification had taken place in the base course (Figure 3). During the excavation of the trench, it was observed that the backhoe experienced more difficulty exavating the rutted area than the untrafficked areas.

Nuclear density tests were also performed on the top of the compacted subgrade inside and outside of the rutted areas. The dry density of 103.6 pcf (average of 6 readings) under the rutted area and the dry density of 102.5 pcf (average of 12 readings) outside the rutted area

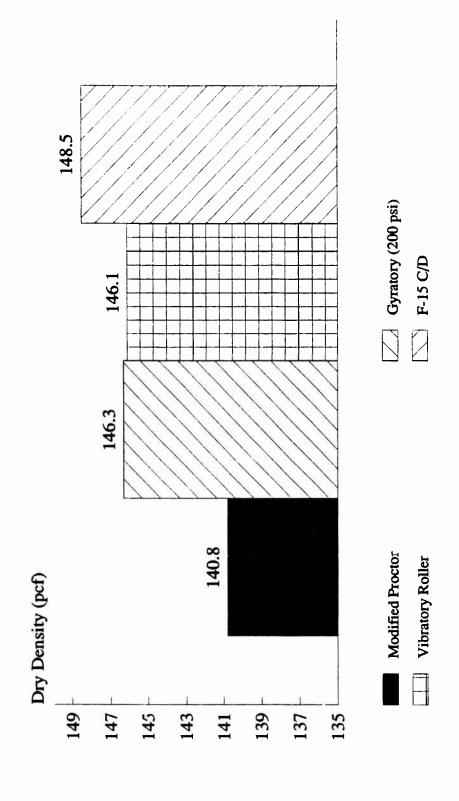


Figure 3. Effect of Compaction on Base Course

indicated that slight traffic densification might have happened at the top layer of compacted subgrade.

Field California bearing ratio tests were conducted on the subgrade sand approximately 25-inches below the pavement surface. The CBR values obtained from the test site were 34,34 and 42 with an average of 37.

#### B. LABORATORY DATA

# 1. Grain-Size Analysis

Aggregate samples under and outside of the rutted areas at various depth of base course were obtained from the excavated trench of the test sections. Grain-size analyses of these aggregates were conducted at Tyndall AFB FL laboratory and the results, along with gradation of stockpile materials were listed in Tables 3 and 4, and plotted in Figures 4 and 5. Table 3 and Figure 4 illustrate effects of the construction roller and possibly traffic on degradation of upper 6-inches of base course. Table 4 and Figure 5 demonstrate degradation of lower 6-inches of base materials. The effect of traffic seemingly apparent in the top lift of base course (Figure 4) is not evident in the bottom lift of base course (Figure 5). However, note that the gradation of the base course material from the botton lift (in the rutted area) was finer than that from the top lift. This indicates that there may not have been degradation under traffic. More data will likely settle this issue.

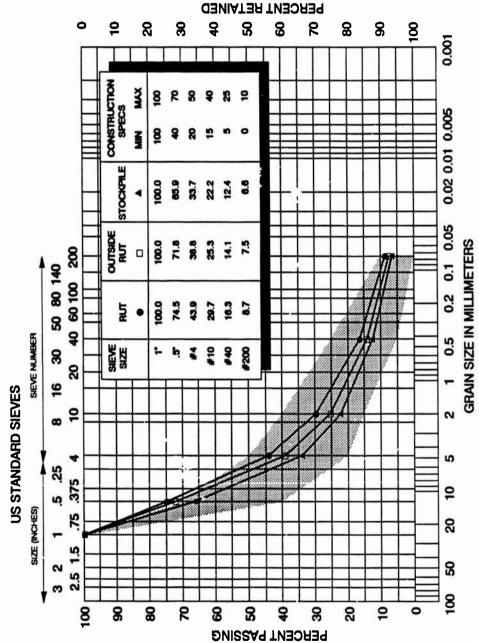


Figure 4. Effect of Roller and Traffic on Degradation of Upper 6-Inches of Base Course.

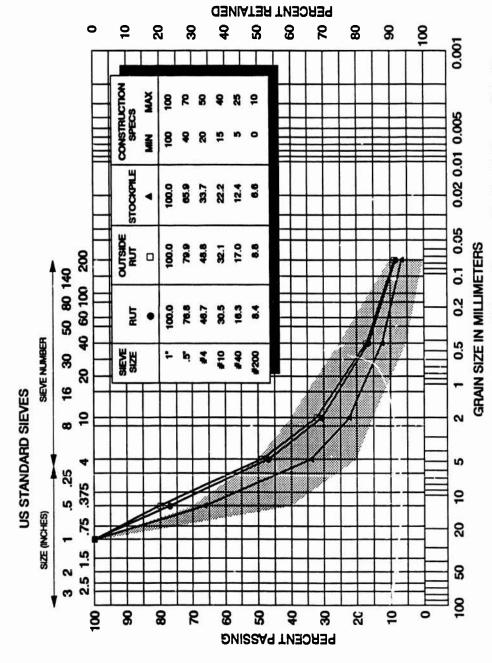


Figure 5. Degradation of Lower 6-Inches of Base Course Under Roller and Traffic.

TABLE 3. GRAIN-SIZE ANALYSIS OF UPPER 6-INCH OF BASE MATERIALS

SIEVE SIZE	STOCKPILE (% passing)	OUTSIDE RUTTED AREA (% passing)	UNDER RUTTED AREA (% passing)
1"	100	100	100
1/2"	65.9	71.8	74.5
#4	33.7	38.8	43.9
#10	22.2	25.3	29.7
#40	12.4	14.1	16.3
#200	6.6	7.5	8.7

TABLE 4. GRAIN-SIZE ANALYSIS OF LOWER 6-INCH BASE MATERIALS

SIEVE SIZE	STOCKPILE (% passing)	OUTSIDE RUTTED AREA (% passing)	UNDER RUTTED AREA (% passing)
1"	100	100	100
1/2"	65.9	79.9	76.8
#4	33.7	48.8	46.7
#10	22.2	32.1	30.5
#40	12.4	17.0	16.3
#200	6.6	8.8	8.4

# 2. GYRATORY DATA

Eight gyratory samples of base materials were obtained from the stockpile and were fabricated in the laboratory to conform to the stockpile gradation (Table 1). The gyratory compaction tests were conducted in accordance with the procedures described in Section II, Article B of this report. The results of gyratory compaction tests were listed in Table 5 and plotted in Figure 6.

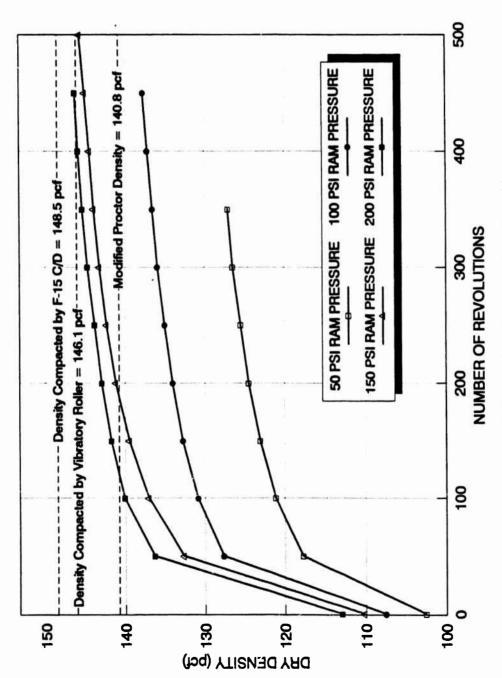


Figure 6. Correlation of Gyratory and Field Densities.

TABLE 5. GYRATORY COMPACTION DATA (AVERAGE OF 2 REPETITIONS)

RAM PRESSURE (PSI)	MAXIMUM (WET (PCF)	POST MOISTURE CONTENT (%)	MAXIMUM DRY (PCF)
50	134.1	4.17	127.1
100	143.5	3.86	137.7
150	151.4	3.92	145.7
200	152.1	3.97	146.3

McRae (2) suggested that the compaction (ram) pressures of the GTM be based on the theoretical vertical stresses produced at various depths of pavement by the anticipated wheel load. Under 355 psi of F-15 C/D tire pressure, the theoretical vertical stress at the top of base course according to the layered elastic program, WESLEA, was approximately 200 psi. The ultimate dry density at ram pressure of 200 psi was determined to be 146.3 pcf by GTM (Table 5). This density happens to be close to the dry density compacted by the vibratory steel wheel roller and 1.5% less than the dry density compacted by the F-15 C/D (148.5 pcf). The specimens for gyratory compaction tests were prepared in accordance with the stock pile gradation. After the GTM tests, specimens were then subjected to grain-size analysis in the laboratroy to determine degree of degradation due to the GTM compaction, and also to see if the degradation pattern is similar to the base course degradation due to construction and traffic compaction. These data are listed in Table 6.

#### IV. CONCLUSIONS

Based on the field and laboratory test data and subsequent evaluation on the test trench excavated between stations A 4+72 and A 4+80 of the

TABLE 6. GRAIN-SIZE ANALYSIS OF GTM SPECIMENS
BEFORE AND AFTER THE GTM TEST

SIEVE SIZE	BEFORE GTM (STOCKPILE) (% passing)	AFTER GTM (% passing)
1"	100	100
1/2"	65.9	77
#4	33.7	46.5
#10	22.2	31.5
#40	12.4	17.0
#200	6.6	9.5

Air Force 9700 test sections, the following conclusions can be drawn:

The base course dry density of 143.5 pcf under the rutted area is 2 to 3 pcf more than the dry density of 146.1 pcf outside the rutted area. This phenomenon suggested that traffic densification had taken place in the base course. The results of modified Proctor (ASTM D 1557) with a maximum dry density of 140.8 pcf and optimum moisture content of 4.76% were used to control the base course compaction of this project. Evidently the modified proctor is inadequate and unsuitable for controlling airfield compaction in the field because it would not simulate the field densities after field compaction (Figure 3).

The ultimate gyratory dry density at ram pressure of 200 psi averaged 146.3 pcf. This ultimate density was less than the 148.5 pcf density compacted by the F-15 C/D (Figure 3). However, it appears that the GTM has the capability for providing laboratory densities on the crder of those being produced by compaction equipment and subsequently by traffic.

Comparison of gradation from the stockpile, inside and outside the rutted areas indicated that degradation due to construction compaction took place in the base course (Figures 4 and 5). A similar pattern of degradation took place before and after the GTM compaction tests (Tables 3, 4, and 6). This implies that the GTM not only reproduces the densities found in the field, under traffic, but also may degrade the aggregate similarly.

All the laboratory and field data of this study indicate that the GTM may be able to replace the modified Proctor tests to provide an adequate target dry density for field compaction.

#### REFERENCES

- 1. Mark, C. R. "Compaction of Graded Aggregate Bases and Subbases,"

  <u>Transportation Engineering Journal</u>, January, 1977.
- 2. McRae, John "Gyratory Compaction Method for Determining Density Requirements for Subgrade and Base of Flexible Pavements, "U. S. Army Engineers WES Miscellaneous Paper No. 4-494, May, 1962.
- 3. Roberts, Kandhal, Brown, Lee and Kennedy, Hot Mix Asplalt Materials, Mixtures. Design. and Construction. NAPA Education Foundation. 1991.
- 4. Crockford, Bendana, Yang, Rhee and Senadheera, "Modeling Stress and Strain States in Pavement Structures Incorporating Thick Granular Layers," The Texas Transportation Institute Final Report to AFESC, Contract No. F08635-87-C-0039, April, 1990.
- 5. Timian, D. A. "Design and Construction of Pavement Test Sections for the Study of High Pressure Tire effects," <u>Applied Research Associated</u>

  Report to AFESC, Contract No. F08635-88-C-0067, Subtask 1.04, May, 1989.

# USE OF A CENTRIFUGE IN INVESTIGATION OF DYNAMIC PHENOMENA IN PARTIALLY SATURATED SANDS

Teresa Taylor, Assistant Professor Virginia Polytechnic Institute & State University

# **ABSTRACT**

Centrifuge tests were conducted to investigate different dynamic phenomena in partially saturated soils. The primary research effort involved studying the influence of degree of saturation on transmission of explosion-induced stress waves in compacted soils. Tests were conducted using different charge masses and g-levels to simulate different prototype explosive masses. In conjunction with these tests, the resulting explosion-induced apparent crater dimensions and volumes were measured; comparisons were made to full-scale test results and results of other investigators for centrifuge crater tests in dry sands. Finally, a limited number of the tests were conducted using different materials placed against the walls of the sample bucket to assess relative capabilities of minimizing reflected waves resulting from the explosions. These results are described in a separate report.

#### INTRODUCTION

This research effort was undertaken to provide centrifuge test support to Dr. Wayne A. Charlie, of Colorado State University (CSU), for his ongoing, separately funded, investigation of the effects of saturation on stress wave propagation through soils (Charlie, 1991). A series of 24 instrumented centrifuge tests in partially saturated soils were conducted specifically to support this project, and to complement a planned series of 1-g field tests to be conducted at CSU.

In addition to the tests in partially saturated soils, a series of 16 centrifuge tests were conducted in dry soils; of these, 5 tests were instrumented to provide a baseline comparison to the results of tests in the partially saturated soils. The remaining 11 centrifuge tests conducted in dry soil were undertaken as part of a secondary project investigating cratering. The cratering project utilized results from all of the centrifuge tests, as well as from six 1-g tests in both dry and partially saturated soils. This report summarizes the 10 week summer effort involving these two projects, and presents a brief preliminary analysis of the data obtained. Further in-depth analysis is underway, and more detailed analyses are anticipated.

In addition to the two projects introduced above, a limited number of the instrumented centrifuge samples were prepared using different boundary materials near selected gages. Results from these tests were used to assess relative effectiveness of the different materials in minimizing reflected waves. Details on the boundary materials and gage responses are reported by Olen (1991).

# DISCUSSION

Use of a centrifuge to simulate the self-weight stress variation in soil has been well-documented (Cheney and Fragaszy, 1984), and the importance of utilizing the centripetal acceleration-induced artificial gravitational field for correct experimental modeling of many soil phenomena is becoming increasingly clear to the geotechnical research community. The generally accepted centrifuge scaling relationships for explosive events in soils, assuming that all requirements for constitutive and dynamic similarity are met, require that the mass of the model explosive scale as  $1/n^3$ , where n corresponds to the number of g's. Thus, relatively small explosive charges are used in the centrifuge environment to

simulate large explosives in the field. A discussion of the limitations to centrifuge modeling and departures from similarity between model and prototype events is beyond the scope of this report. The reader is referred to discussions such as those by Schmidt and Holsapple (1980), Nielsen (1983), Cheney and Fragaszy (1984), and Goodings, et al. (1988).

Centrifuge tests were conducted using the Air Force Civil Engineering Support Agency (AFCESA; formerly AFESC) 15 g-ton capacity centrifuge at Tyndall Air Force Base (AFB), Florida. Since the machine's initial acquisition in 1986, AFCESA has developed a complete geotechnical centrifuge research facility, with the addition of such features as an on-board shuttered video camera and 32-channel data acquisition system, trained technician support, on-site instrumentation shop, etc.

Two soils were used in the current test program. The majority of the tests utilized beach sand obtained locally at Tyndall AFB (Tyndall sand). This sand is a fine-grained, uniform, subreaded to subangular quartz sand. Curves of grain size distribution and desaturation characteristics are presented as Figs. 1 and 2, respectively. Fig. 1 also shows the grain size distribution curve for Ottawa 20-30 sand, which was used for five of the centrifuge tests. Ottawa 20-30 sand is a commercially-available standard silica sand, also uniform, but somewhat more rounded and considerably coarser than the Tyndall sand. The desaturation curve for this sand is presented in Fig. 3.

Much of the 10 week effort was devoted to developing sample preparation, instrument placement and detonator burial techniques. Brief descriptions of such technique follow.

Samples were prepared in 18 inch diameter aluminum sample buckets to depths ranging between 10 and 12 inches, at a relative density of approximately

Fig. 1 -- Grain Size Distribution Curves for Test Solls

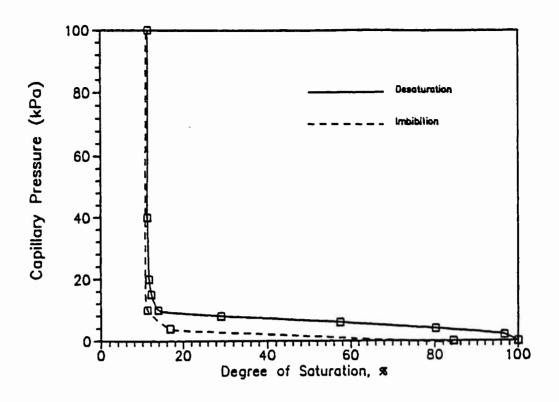


Fig. 2 - Saturation vs. Capillary Pressure, Tyndall Sand

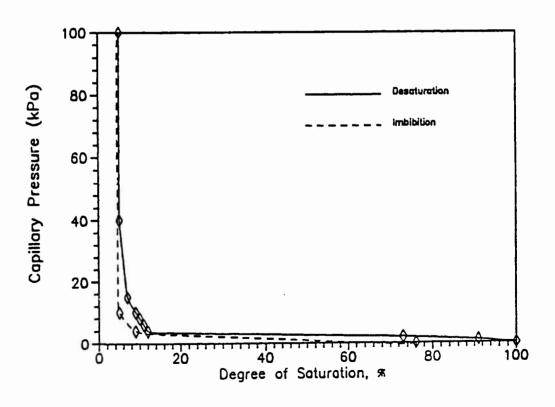


Fig. 3 - Saturation vs. Capillary Pressure, Ottawa 20-30 Sand

39% (95 pcf for Tyndall sand, 100.7 pcf for Ottawa 20-30 sand). The partially saturated soil samples were difficult to prepare at the target dry densities, particularly samples using the fine-grained Tyndall sand, in which the high capillary pressures resisted compactive efforts. Several different methods of sample preparation were attempted; the most successful involved vibrating samples in 2 inch lifts. For each lift, a pre-measured quantity of soil at the appropriate water content was placed in the sample bucket. A vibrator mounted on an aluminum plate slightly smaller than the diameter of the sample container was placed on top of the soil. The soil was then vibrated to the required final volume; for the Tyndall sand, this process frequently required the addition of large pseudo-static weights. Difficulties with desaturation during sample compaction were experienced with the Ottawa 20-30 sand, particularly at the higher water contents.

Instrumented dry samples were prepared through the same vibration process, although considerably less effort was required to compact each lift. Non-instrumented dry samples were prepared by pluviation (controlled dropping through air) using the large-scale pluviator at the AFCESA centrifuge facility. Description of the method is provided by Taylor, et al. (1988).

Although not as uniform or reproducible a method as pluviation, the vibration method used for preparing the partially saturated samples did allow the target dry densities to be obtained, and provided similarities with the vibratory compaction method planned for use in the 1-g field tests at CSU.

Accelerometers (manufactured by Endevco) and 1000 ohm carbon resistors were used to determine peak accelerations and peak stresses, respectively. Details on stress gage calibration are provided by Charlie and Walsh (1990) and Charlie (1991). Gages were manually located and placed

between lifts. Due to the primary focus on obtaining lateral stress wave propagation characteristics, and the extremely time-consuming nature of placing the instruments, gage placement after the first few tests was restricted to different radial spacings away from the center of the sample, at a constant depth corresponding to where the center of mass of the explosive would ultimately be located.

The explosives used in the test program were Model RP-83 electrical detonators manufactured by Reynolds. Four different explosives were available: 880, 660, 440 and 220 mg detonators, with corresponding total charge weights (output charge, pellet and initiating explosive) of 1.043, 0.823, 0.603 and 0.383 g. Because of the small difference in explosive masses available, a rigourous modeling-of-models program (see Cheney and Fragaszy, 1984) could not be carried out; centrifuge tests in the partially saturated soils were conducted using the 880 and 220 detonators, to maximize the available difference in masses.

Explosives were placed after the completed samples were loaded onto the centrifuge. A vooden drilling template with a provision for a guided rod at the center was placed in position over the sample bucket. For partially saturated samples, an appropriately sized drill bit was guided into the soil and used to remove soil to the desired depth. For dry samples, a glass rod was guided into the soil while a controlled vacuum was simultaneously applied to remove the soil. After placing the detonator, the hole was backfilled with dry soil. The partially saturated tests were conducted at a constant scaled depth of burial,  $\lambda_d$ , of 1.9, where

$$\lambda_{\rm d} = {\rm d}/{\rm M}^{1/3} \tag{1}$$

In this equation, d represents distance below the ground surface and M is the explosive mass. This value of  $\lambda_d$  was selected to maximize the ground shock

parameters (magnitude of stress and ground motions increase with explosive burial depth up to a limiting value; this relationship is frequently described by a coupling parameter, f, the ratio between ground shock magnitude for a near surface compared to a fully buried blast). For the cratering tests in dry soil, values of  $\lambda_d$  ranged between 0.59 and 3.5. This wide range of  $\lambda_d$  was selected to allow the variation of this parameter with apparent crater dimensions obtained in the centrifuge tests to be determined, as well as to allow more comprehensive comparisons with full-scale field tests conducted at different values of  $\lambda_d$  to be made. Relative data from the centrifuge tests are being reduced and compiled at CSU, and will be further analyzed as they are made available.

The centrifuge tests were conducted at g-levels between 21.3 and 66.7, corresponding to scaled explosive masses between approximately 15 lbs and 500 lbs. The on-board data acquisition system was used to collect and store data obtained during the tests. After the centrifuge was decelerated, records of voltage and acceleration were converted to stress and velocity, respectively (see Charlie, 1991).

Measurements of apparent crater dimensions and volume were obtained at the completion of each centrifuge test. Diameter and depth measurements were manually measured. Volumes were determined by filling the crater with a concrete mix, forming a cast of the crater. The cast was then covered with florist clay and supported by masking tape. The impermeable crater mold thus created was filled with water, and the mass of water was used to determine the apparent crater volume.

Since subjecting saturated soil samples to centrifugation is one of several methods that can be used to develop desaturation curves such as those in Figs. 2 and 3, it was anticipated that the upper nortion of the samples used in this

research would desaturate when subjected to accelerated g's. A series of tests were conducted for Tyndall sand in which samples prepared at different degrees of saturation were subjected to various g-levels, with water contents being measured both before and following centrifugation. Although it was not possible to actually determine water contents while the centrifuge was operating, the aftertest values in the upper desaturated zone of the sample were sufficiently close to the residual saturations predicted by Figs. 2 and 3 to generate confidence that any imbibition as the centrifuge decelerated was minimal. Fig. 4 presents water content/depth results for Tyndall sand at different degrees of saturation, both before and after centrifugation.

# **RESULTS**

Figs. 5a and 5b provide results related to stress wave transmission in Tyndall sand and Ottawa sand, respectively. A variation in the attenuation coefficient, n, with degree of saturation is clearly evidenced by these test results. This coefficient is used to define the slope of the logarithmic relationship between  $\lambda_d$  and different ground shock parameters. For the Tyndall sand (Fig. 5a), the attenuation is greater for completely dry and completely saturated samples, compared to partially saturated samples at the same dry density. A similar variation is seen for the coarse Ottawa sand (Fig. 5b), although insufficient data were collected to observe the behavior at degrees of saturation greater than 60%, due to the difficulties with desaturation during sample preparation previously discussed.

Similar trends are reported recently by Qian, et al. (1991) for resonant column tests in partially saturated sands. Their test results, reported in terms of shear modulus ratio (shear modulus for the moist sand normalized with respect to shear modulus for the dry sand) vs. saturation, describe a more bell-shaped

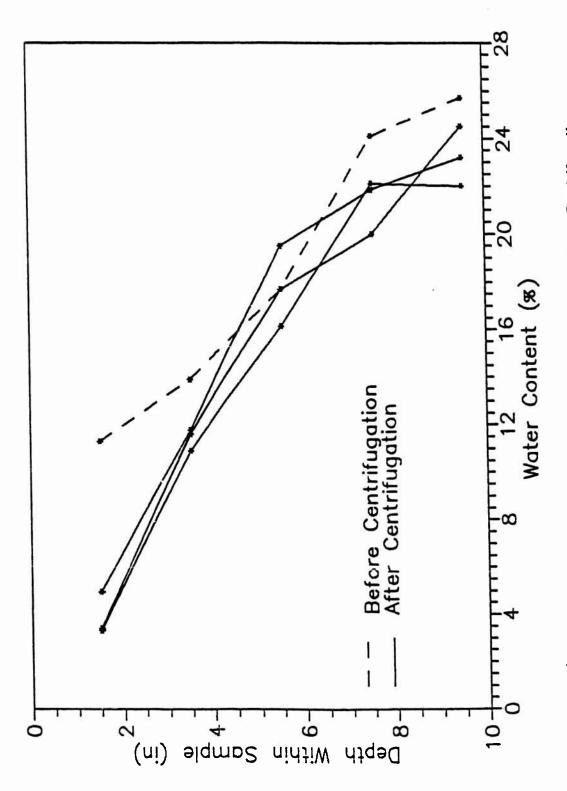


Fig. 4 -- Water Content Distribution in Test Samples Before and After Centrifugation

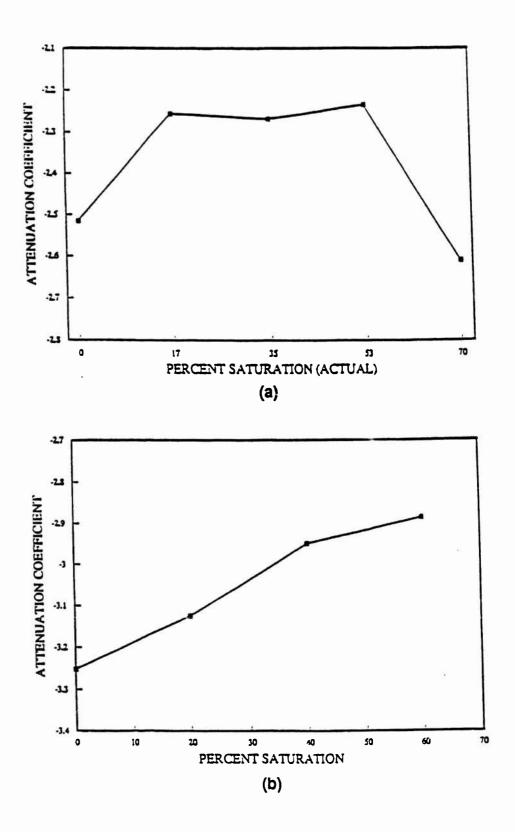


Fig. 5 -- Degree of Saturation vs. Attenuation Coefficient; (a) Tyndall Sand (b) Ottawa 20-30 Sand

curve than developed in the current research. This difference may be due to the greater number of data points obtained in their program. Alternatively (as discussed in connection with Fig. 4), although the centrifuge test samples were prepared at different degrees of saturation, all detonations occurred at or near residual saturation, which may have influenced the shape of the saturation/attenuation curve. A method for controlling water levels within a soil sample during centrifugation would be desireable.

Qian, et al. (1991) utilized 13 different sands in their resonant conlumn tests to study influence of such properties as angularity, grain size distribution, and void ratio on the observed increase in shear modulus for partially saturated conditions compared to dry and fully saturated. Their test program indicated a reduction in the shear modulus with increase in confining pressure, leading to the authors' conclusion that effects of capillarity are more pronounced at low confining pressures (shallow depths) than at high, due to the proportionately greater increases in effective stress attributed to capillarity at low confining pressures.

It is significant to note that the soil specimens used in the test program by Qian, et al. (1991) were all compacted by the same tamping technique, but with varying degrees of compactive effort. No discussion of the potential effects of compactive technique and/or effort was presented. Ross (1989) and Ross, et al. (1989) describe split Hopkinson bar test results for tamped soil specimens compacted moist and for tamped soil specimens compacted dry then wetted. An increase in stress wave transmission at partial degrees of saturation was observed only for the soils compacted moist. It was concluded that the effects of water content during the compaction process dominate over effects of capillarity in stress wave propagation characteristics.

As Figs. 5a and 5b indicate, the same trend is observed in the present work for vibratory compacted sand specimens; thus, the centrifuge work is in agreement with dynamic tests using both resonant column and split-Hopkinson bar techniques. It should be noted that this agreement between techniques spans a wide range of specimen sizes, and supports independence of the observed phenomena from test technique. In all of the test programs described above, compactive effort was necessarily varied with degree of saturation to maintain the same dry density. Additional work on compactive technique and compactive energy is warranted.

Preliminary results for the cratering data are presented in Figs. 6 and 7. These figures reflect apparent crater depth and radius data for the centrifuge and 1-g tests in moist Tyndall Beach sand (as of this writing, additional depth and radius data, as well as data for apparent crater volumes, are still being reduced at CSU). Until additional field tests are conducted at CSU and data become available for small explosive masses, the best-fit lines shown in these figures for the Tyndall sand are useful only in indicating general trends.

Fig. 6 is a plot of scaled explosive weight (TNT equivalent) vs. scaled apparent crater depth for the buried explosives in partially saturated Tyndall sand, and Fig. 7 is a plot of scaled explosive weight vs. scaled apparent crater radius. For comparison, a series of centrifuge tests in dry Ottawa sand is also presented in these figures. The dry test series, conducted by Goodings, et al. (1988), modeled after an earlier series of centrifuge work by Schmidt and Holsapple (1980), used surface and near-surface charges as opposed to the fully buried charges of the present research. In addition, direct comparisons between the dry tests and the current research are further complicated because the two soils were prepared at different absolute and relative densities. Nevertheless, the similar

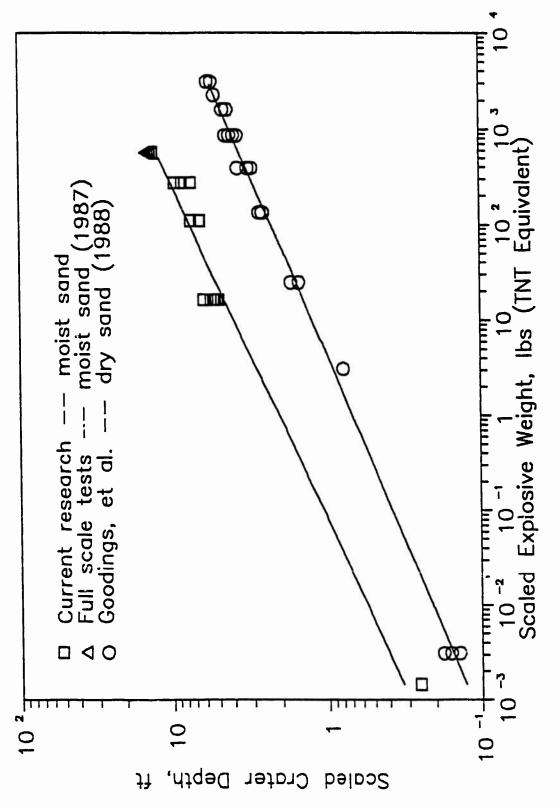


Fig. 6 -- Scaled Explosive Weight vs. Scaled Apparent Crater Depth for Different Explosive Tests

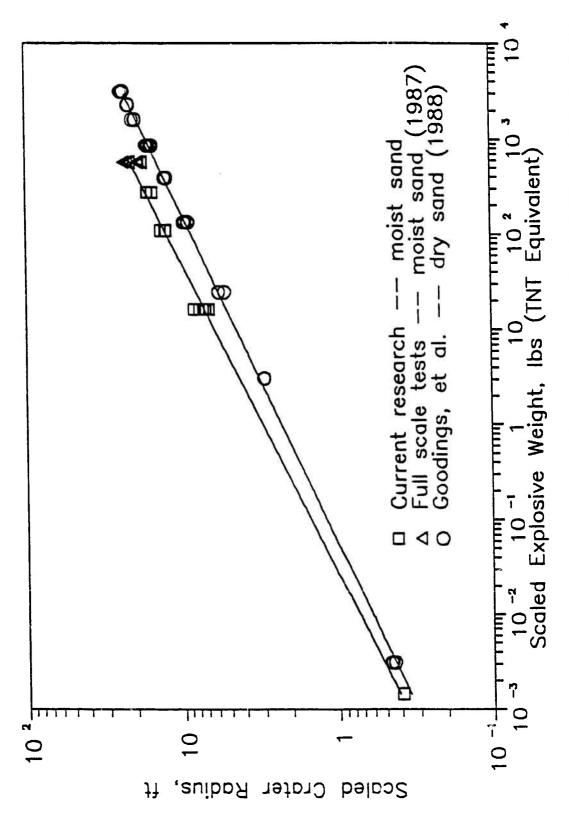


Fig. 7 -- Scaled Explosive Weight vs. Scaled Apparent Crater Radius for Different Explosive Tests

seen in both data sets is encouraging. Both Goodings, et al. (1988) and Schmidt and Holsapple (1980) reported crater depth proportional to explosive mass raised to an exponent of 0.28, and crater radius proportional to explosive mass raised to an exponent of 0.29 and 0.28, respectively. Although caution must be exercised in quantifying the exponential values for the current test program until additional data are obtained for small explosive masses, the preliminary results reflect exponents of 0.28 and 0.31 for similar depth and radius relationships.

Also presented in Figs. 6 and 7 are results from full-scale field tests conducted at Tyndall AFB using 1000 lb. bombs (Walter Buckholtz, AFCESA, personal communication, 1991).

Significant features to be noted with respect to Figs. 6 and 7 are as follow:

- a. Although only limited data are available as of this writing, preliminary correlations between scaled explosive weights and apparent crater dimensions are reasonable, and are consistent with other centrifuge test programs.
- b. In view of the considerably more difficult sample preparation involved with preparing moist samples compared to dry, scatter among replicate tests is surprisingly minimal.
- c. A greater difference between results of dry vs. moist centrifuge tests is seen for scaled crater depth, compared to radius, which is consistent with field data predictions (U.S. Army Engineering Waterways Experiment Station, 1960, 1961). Additional comparisons are underway.
- d. Of most significance is the fit of the field test data from full-scale tests conducted at Tyndall. These data are not included in the best-fit curve describing the centrifuge data, but fit the data remarkably well. Scaled burial depth for these field tests is approximately 1.2, compared to 1.8 for the centrifuge

tests. The field tests, in addition to being conducted in the same soil as the centrifuge tests and using fully buried charges, were also conducted in partially saturated soils. As is typical for most field tests, no quantitative information was obtained on soil density or moisture content; nontheless, these tests provide the best available validation for the centrifuge crater data of this research effort.

There is clearly a need for better quantified field data; however, the difficulties in obtaining such data and the wealth of field data that would be required to fully identify the recognized (but not quantified) soil property-dependent relationships between explosive weight and crater dimensions, provide strong arguments for the importance of conducting additional centrifuge work (perhaps in conjunction with numerical models) to better define these relationships.

Later analyses will include apparent crater volume results, as well as results from the 11 centrifuge tests in dry soils. The test matrix for the tests in dry soils was designed to compare:

- 1. successively larger scaled masses at constant values of  $\lambda_d$  using (a) the same model explosive, and (b) different model explosives;
- equivalent confining stresses using (a) the same model explosive
   and (b) different model explosives to simulate successively larger scaled
   explosive masses;
- 3. (a) equivalent and (b) successively larger scaled explosive masses over a range of  $\lambda_d$ .

To the best of the author's knowledge, these tests represent the first centrifuge program involving such a wide range of burial depths. The centrifuge cratering tests at residual or near-residual saturations are also unique to this research, and study of the effects of saturation on apparent crater formation is underway.

# CONCLUSION

Although analysis is not completed, results from the centrifuge tests conducted during this research effort appear to be of good quality. Preliminary analysis suggests that useful information has been obtained regarding both stress wave transmission in partially saturated soils, and cratering in both dry and partially saturated soils. For the stress wave transmission studies, results are comparable to those obtained by other researchers using very different test techniques (split Hopkinson bar and resonant column). This suggests that the increase in stress wave transmission ratio observed for partial degrees of saturation compared to that observed for dry and fully saturated conditions, is not unique to a particular test method and is likely a generally occurring phenomenon in partially saturated sands.

Although only preliminary analysis has been made of the centrifuge cratering results, data are consistent both with centrifuge results obtained by other researchers, and with limited field data, and clearly reflect strong, soil property-dependent correlations between apparent crater dimensions and explosive mass.

## REFERENCES

- Charlie, W. A., "Stress Wave Transmission from Contained Blasts in Moist Soils,"
  Interim Report, Contract No. FO-8635-90-C-306, AFCESA/RACS, Tyndall
  AFB, FL, September, 1991.
- Charlie, W. A. and Walsh, A. J., "Centrifuge Modeling of Explosive Induced Stress Waves in Unsaturated Sand," Final Report, USAF-UES Summer Faculty Research Program, sponsored by AFOSR, September, 1990, 21 pp.

- Cheney, J. A., and Fragaszy, R. J., "The Centrifuge as a Research Tool,"

  <u>Geotechnical Testing Journal</u>, ASTM, December, 1984, pp. 182-187.
- Goodings, D. G., Fourney, W. C., and Dick, R. D., "Geotechnical Centrifuge Modeling of Explosion Induced Craters--A Check for Scaling Effects," Final Report, AFOSR-86-0095, 1988.
- Nielson, J. P., "The Centrifugal Simulation of Blast Parameters," Report No. ESL-TR-83-12, AFESC, Tyndall AFB, FL, 1983.
- Olen, K. A., "Stress Wave Transmission in Partially Saturated Soils," Final Report,
  USAF-RDL Summer Faculty Research Program, sponsored by AFOSR,
  September, 1991.
- Qian, X., Gray, D. H., and Woods, R. D., "Resonant Column Tests on Partially Saturated Sands," <u>Geotechnical Testing Journal</u>, Vol. 14, No. 3, ASTM, September, 1991, pp. 266-275.
- Ross, C. A. (1989), "Split-Hopkinson Pressure Bar Tests," Final Report, AFESC/RDCM, Tyndall Air Force Base, FL, 1989.
- Ross, C. A., Thompson, P. Y., Charlie, W. A., and Doehring, D. O., "Transmission of Pressure Waves in Partially Saturated Soils," <u>Journal of Experimental Mechanics</u>, Society for Experimental Mechanics, Vol. 29, No. 1, March, 1989, pp. 80-83.
- Schmidt, R. M., and Holsapple, K. A., "Theory and Experiments on Centrifuge Cratering," <u>Journal of Geophysical Research</u>, Vol. 85, No. B1, Jan., 1980, pp. 235-251.
- Taylor, T., Meyer, M. R., and Fragaszy, R. J., "Design of a Soil Pluviator for Centrifuge Testing," <u>Proceedings</u>, 24th Symposium on Engineering Geology and Soils Engineering, Coeur D'Alene, Idaho, 1988, pp. 191-200.

- U.S. Army Engineering Waterways Experiment Station, "Cratering from High Explosives--Compendium of Crater Data, Report No. 1," Technical Report No. 2-547, Vicksburg, Mississippi, May, 1960.
- U.S. Army Engineering Waterways Experiment Station, "Cratering from High Explosives--Analysis of Crater Data, Report No. 2," Technical Report No. 2-547, Vicksburg, Mississippi, June, 1961.

# DRAFT TEST METHODS TO ASSESS THE PERFORMANCE OF EXTERNAL VAPOR-PHASE LEAK DETECTION DEVICES FOR UNDERGROUND STORAGE TANKS: A VALIDATION AND MODIFICATION STUDY

Brian S. Vogt, Ph.D., Research Associate
Headquarters Air Force Engineering and Services Center
Environics Division, Site Restoration Branch
(HQ AFESC/RDVW)
Tyndall AFB, FL 32403 0001

#### Abstract

Draft test methods for evaluating sensor devices to be used to monitor vapor-phase hydrocarbons in monitoring wells around underground storage tanks vere validated. Although the test apparatus specified by the draft methods was found to be basically sound in design, it was necessary to make some modifications so that device testing will be more realistic and thus better suited to Air Force needs. Most of the conclusions concerning any sensor device tested with the draft methods ultimately rely on accurately knowing the concentrations of hydrocarbon vapors in the test apparatus. For this reason it was necessary to eliminate several erroneous assumptions implicit in apparatus construction and data handling. Some changes were made in the apparatus and testing protocol to simplify testing. Several ways of presenting sensor device accuracy data were devised to permit quicker and more intuitive understanding of device response. Numerous other recommendations regarding apparatus construction, apparatus calibration and use, hydrocarbon test products, and calculations and data presentation were made. These are summarized toward the end of this report1.

The results of this study are on file at Headquarters Air Force Engineering and Services Center. The full summary of recommendations given in that report is included herein, but much of the supporting text (with associated figures) is omitted because of the format and length requirements of this report.

## Introduction

Although it is usually not possible to mathematically model the relationship between soil-gas and ground-water hydrocarbon concentrations, knowledge of soil-gas hydrocarbon concentrations is useful in determining whether or not a leak has occurred from an underground storage tank and, if such a leak has occurred, in determining how far the leak has spread reground. The detection and measurement of hydrocarbon vapors in the soil by means of sensor devices coupled to observation wells is thus an important component in monitoring the condition of underground storage tanks. Different devices may be based on different sensor technologies. Deciding which sensor device is most suitable for use in a given installation may be difficult because a wide array of commercially-built devices is available 5,6. Methodology has been developed to permit unbiased evaluation of the accuracy, response time, specificity, and lower detection limit of devices designed to detect liquid-phase and

<sup>&</sup>lt;sup>2</sup>D. A. Devitt, R. B. Evans, W. A. Jury, T. H. Starks, B. Eklund, and A. Gholson, Soil Gas Sensing for Detection and Mapping of Volatile Organics, Environmental Monitoring Systems Laboratory—Las Vegas Office of Research and Development—U. S. Environmental Protection Agency (EPA/EMSL), Report EPA/600/8-87/036, August 1987.

<sup>&</sup>lt;sup>3</sup>R. A. Scheinfeld, J. B. Robertson, and T. G. Schwendeman, *Ground Water Monitoring Review*, Vol. 6, No. 4, pp. 49-55, 1986.

<sup>&</sup>lt;sup>4</sup>J. D. Kotler, Leak Lookout: Using External Leak Detectors to Prevent Petroleum Contamination from Underground Storage Tanks, Office of Underground Storage Tanks—U. S. Environmental Protection Agency, Report EPA/530/UST-88/006, August 1988.

<sup>&</sup>lt;sup>5</sup>R. A. Scheinfeld et. al., op. cit.

<sup>&</sup>lt;sup>6</sup>J. D. Kotler, op. cit.

<sup>&</sup>lt;sup>7</sup>This methodology was developed through EPA/EMSL by Radian Corporation (P. O. Box 201088, Austin, TX 78720-1088) acting as a subcontractor to Camp Dresser & McKee (CDM) Federal Programs Corporation (13135 Lee Jackson Memorial Highway, Suite 200, Fairfax, VA 22030) under contract to EPA/EMSL (EPA contract No. 68-03-3409). The four methods referred to are drafts written by Radian Corporation in American Society for Testing and Materials (ASTM) format and dated June 29, 1990. The methods are entitled Standard Test Method for Accuracy and Response Time for Liquid-Phase Out-of-Tank Petroleum Detectors (designated X 0000), Standard Test Method for Specificity for Liquid-Phase Out-of-Tank Petroleum Detectors (X 0002), Standard Test Method for Lower Detection Limit for Liquid-Phase Out-of-Tank Petroleum Detectors (X

vapor-phase hydrocarbons<sup>8</sup>. Analysis of test results should permit objective comparison of different devices instead of relying on vendors' claims. The methodology referred to is, however, only in the draft stage. The goals of this research were to (1) validate the draft methods for evaluating vapor-phase sensor devices capable of detecting fuels leaking from underground storage tanks, (2) clarify and modify the draft methods so that they more adequately meet Air Force needs, and (3) provide vendor-hired contract laboratories and Air Force personnel with supplemental documentation to be used in conjunction with the original draft methods when testing devices of potential value to the Air Force.

#### Apparatus Construction

The apparatus in the original draft methods was described in part by schematics and in part by detailed drawings. Figure 1 is an overview showing the complete apparatus (except the air supply and sensor device) configured for testing an aspirated device<sup>9</sup>. The four divisions shown are slightly different from the three divisions in the draft methods—this was done to simplify describing how the apparatus functions.

The air supply manifold (Figure 2) provides a simple and quick way of supplying either dry or wet air to the remainder of the apparatus.

<sup>0005),</sup> and Standard Practice for Preparation of Synthetic Gasoline for Liquid-Phase Out-of-Tank Petroleum Detectors (X 0004).

<sup>8</sup>The three methods referred to are also drafts written by Radian Corporation under the same contract (EPA contract No. 68-03-3409) to CDM Federal Programs Corporation. These drafts were also provided in ASTM format and dated June 29, 1990. The methods are entitled Standard Test Method for Accuracy and Response Time for Vapor-Phase Out-of-Tank Petroleum Detectors (X 0001), Standard Test Method for Specificity for Vapor-Phase Out-of-Tank Petroleum Detectors (X 0003), and Standard Test Method for Lower Detection Limit for Vapor-Phase Out-of-Tank Petroleum Detectors (X 0006). All draft methods will hereafter be referred to by their Radian designations.

<sup>&</sup>lt;sup>9</sup>In this context an aspirated device is a device that includes an integral gas pump to acquire an air sample from a sampling well.

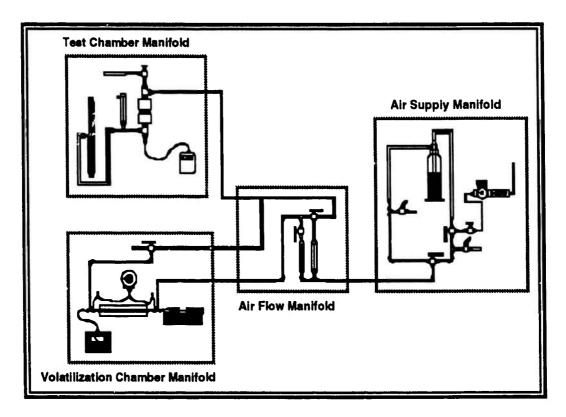


Figure 1 Overview of the entire apparatus.

There are four significant differences between the manifold shown in Figure 2 and that described in the draft methods:

- 1. The air supply is provided by a methane-fired pure air generator instead of ultra-high-purity air in cylinders. This was done to provide a less expensive, more convenient source of air. Adequate results were obtained with this source of air.
- 2. An impinger partially filled with purified water is used to provide wet air. The draft methods make no provision for wet air. It is generally accepted that underground hydrocarbon vapors are present in an atmosphere nearly saturated with water<sup>10</sup>. Furthermore, some

<sup>10</sup>M. A. Portnoff, R. Grace, A. M. Guzman, and J. Hibner, Carnegie Mellon Research Institute (4400 Fifth Avenue, Pittsburgh, PA 15213), Measurement and Analysis of Adsistor and Figaro Gas Sensors Used for Underground Stolage Tank Leak Detection, Reprint of poster board presentation at the Second International Symposium on Field Screening Methods for Hazardous Wastes and Toxic Chemicals, February, 1991.

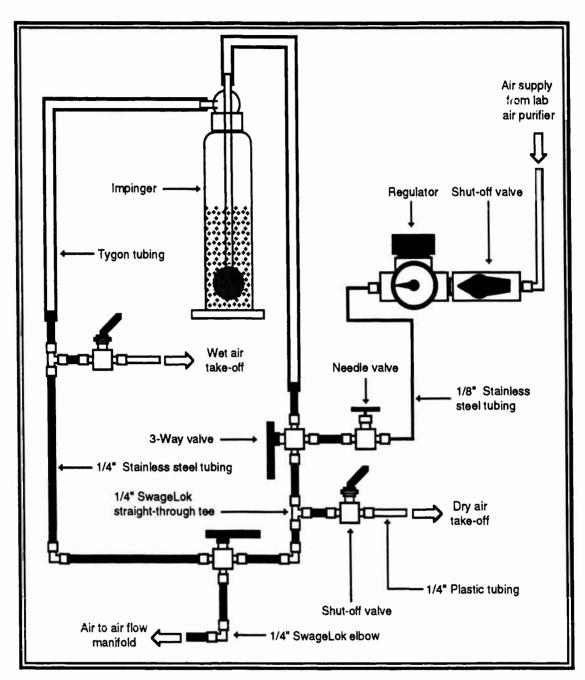


Figure 2 Detail of the air supply manifold.

sensors respond to a given concentration of hydrocarbons in wet air differently than to the same concentration in dry air.  $^{11}$  Realistic device testing must make use of wet air.

<sup>11</sup> Ibid.

- Two three-way valves are incorporated to facilitate switching between dry and wet air.
- 4. Dry air and wet air take-offs are provided to allow access to the purified air without detaching the manifold from the air source.

The air flow manifold is detailed in Figure 3 and is constructed identically after the schematic in the original draft methods.

The major difference between the volatilization chamber manifold used in this study (Figure 4) and that described in the draft methods is that in this study a thermocouple was inserted through a teflon ferrule in the straight-through tee at the exit end of the chamber to permit direct monitoring of the chamber temperature.

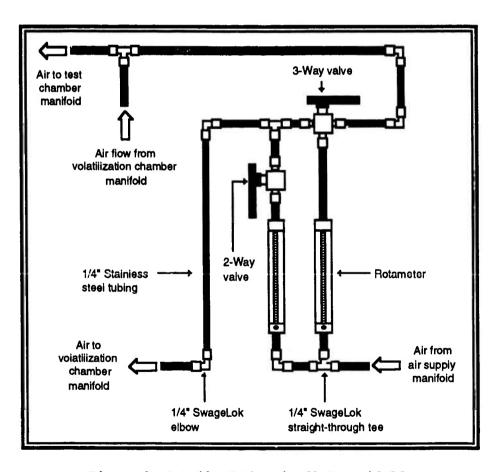


Figure 3 Detail of the air flow manifold.

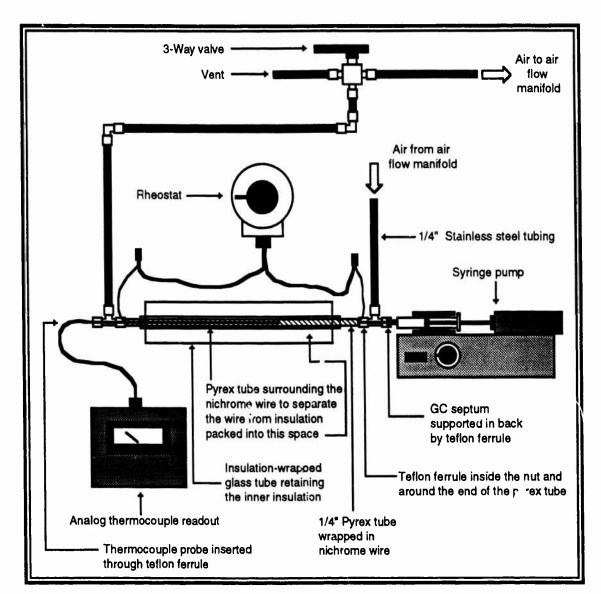


Figure 4 Detail of the volatilization chamber manifold.

The test chamber manifold is detailed in Figure 5. The configuration shown is for an aspirated sensor device that required some resistance to aspiration in order for it to function properly. The needle valve shown at the top of the apparatus was partially closed to provide this resistance.

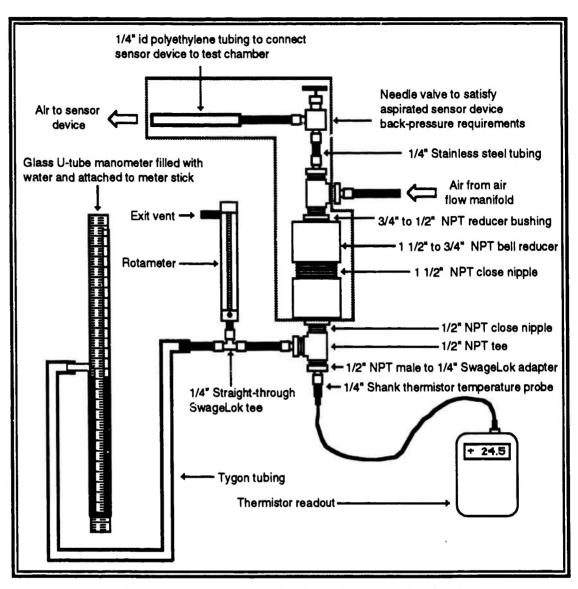


Figure 5 Detail of the test chamber manifold.

## Apparatus Calibration and Use

There were far to many details of apparatus calibration to include them here.

At the beginning of each day, both dry and wet air backgrounds should be checked with the device being tested 12. The background should also

<sup>12</sup> The actual readings may depend on the device being tested. Although not done in this study, device-independent estimates of background contamination could be obtained by analyzing test chamber air samples with gas chromatography.

be checked when switching from one test product to another to ensure that residual vapors are not present in the test apparatus. During this study it was observed that JP-4 and JP-8 jet fuel vapors lingered for periods of time that varied with concentration. Atypically high background readings were observed after testing these products at high concentrations. Consequently, extended periods of time were required to flush residual fuel vapors out of the apparatus. Time spent doing this can be minimized by systematically testing a device completely with a given test product before switching products 13.

### Test Products

All conclusions concerning any sensor device tested with the draft methods ultimately rely on accurately knowing test product vapor concentrations. There is some question as to whether the less volatile components of fuels such as JP-8 volatilize quickly enough to be able to state with confidence that all of the components of the product being injected into the volatilization chamber get to the test chamber at the same time. This casts doubt on whether the calculated vapor concentrations of such test products are very accurate. Furthermore, it is expected that any problem with volatility would be exacerbated by using wet air instead of dry air because the water in the wet air would tend to suppress the vaporization of low volatility substances. For this reason some gas chromatography (GC) analysis was done to compare dry and wet air hydrocarbon concentrations in the air flowing out of the test chamber. To permit sample removal, a glass gas sampling chamber was added to the test chamber rotameter exit vent (see Figure 12).

The compound chosen to be checked with this procedure was n-hexane because (1) it was felt that there would probably be no such

 $<sup>^{13}</sup>$ It is felt that this is justifiable even though the draft methods specify that testing be done in random order (see X 0001, p. 14; X 0003, p. 13; and X 0006, p. 17). The recommended steps are given in the HQ AFESC report.

volatilization problems with it and (2) quantitatively analyzing a complex mixture such as JP-4 or JP-8 by GC would be very time-consuming and more difficult to interpret. The hexane used was certified for gas chromatography/mass spectrometry (GC/MS) use. Four hexane standards were prepared in air by injecting small quantities of liquid hexane through septa into volume-calibrated 120 mL glass vials with a one µL syringe. The chromatograph used was a Hewlett-Packard (HP) 5890 fitted with a 10 meter, 0.1 mm bore diameter column coated with 0.34 micron thick HP5. The analysis was done isothermally at 40°C with a 1:2° solit of a one mL gas sample. Injection of one mL standard samples into the 250°C injection port was done with a 2.5 mL gas syringe. The flame-ionization detector (FID) was at a temperature of 270°C.

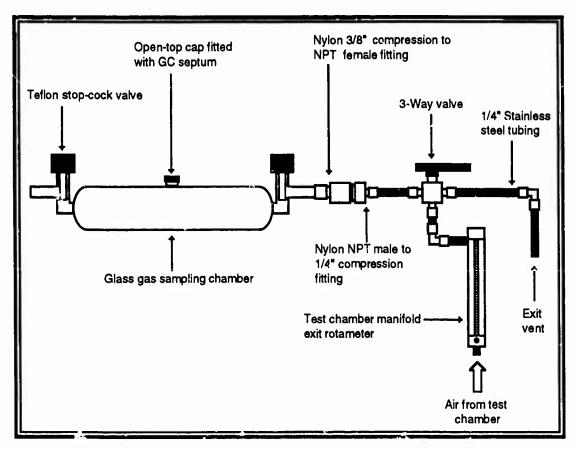


Figure 12 Test apparatus modified to allow removal of gas samples.

Four samples of air containing hexane at a nominal concentration of 926 ppm were obtained from the test apparatus: two with dry air and two with wet air. Each air sample was collected and analyzed between a different set of hexane standard calibration runs. It was observed that the chromatograms of the standards, dry air samples, and wet air samples were essentially identical except for, obviously, peak areas. Each chromatogram had three major peaks with average retention times of 1.61, 1.77, and 2.15 minutes representing averages of 4.0, 84.5, and 11.3 percent of the total chromatogram area, respectively. Data analysis was done using the largest peak, which was assumed to be that of n-hexane. The remaining 15.3 percent was assumed to be other hexane isomers. Brief additional analysis of the data indicated that comparable results could have been obtained by using the sums of the areas of the three major peaks instead of just the largest peak.

It was found that the estimated and calculated concentrations of hexane in the air samples from the test apparatus are within experimental error of each other. This suggests that the test apparatus was sound both in design and construction.

It was found that the peak areas of the two dry air samples were well within experimental error of each other, from which it is concluded that the water vapor in the wet air was not interfering with the volatilization of the hexane in the test apparatus. Undoubtedly this will be true at lower hexane concentrations and, because hexane is moderately volatile, it is probably true at somewhat higher concentrations as well. These findings suggest that hexane can be used as a reliable standard to which other test products can be compared under both dry and wet air conditions. For this reason it is suggested that n-hexane be used as a standard test product during device evaluation. The term standard test product refers to a test product that is to be subjected to the full battery of accuracy, response time, specificity, and lower detection limit tests. Since hexane is an

aliphatic compound, however, using it as an exclusive standard would bias test results in favor of devices that respond primarily to aliphatic hydrocarbons and against devices that respond primarily to aromatic compounds. Fuels are complex mixtures of both aliphatic and aromatic hydrocarbons. A device should not be ruled out because it responds primarily to aromatic compounds because such a device still has potential for being a useful sensor for detecting fuel vapors in monitoring wells. Unfortunately, there was insufficient time during this 10 week study to do a GC investigation of a pure aromatic compound like toluene or of any relatively simple aromatic-containing mixtures. Although toluene (boiling point  $110.6^{\circ}C^{14}$ ) is less volatile than nhexane (boiling point 68.95°C<sup>15</sup>), it is still a moderately volatile compound and it is expected that it would be efficiently volatilized in the test apparatus even with wet air. As such, it is recommended that toluene also be used as a standard test product 16. All jet fuels contain some low volatility components. JP-4 is no exception, but it should be retained as a standard test product anyway because (1) it is a real fuel and as such provides a realistic test of device capability and (2) it is reasonably well characterized. When evaluating test results, it might be wise to view reported concentrations of JP-4 with some skepticism just in case incomplete volatilization of any low volatility components resulted in the actual vapor concentrations being slightly lower than the calculated ones.

Using n-hexane and toluene as separate standard test products rather than using them in a mixture will reveal if a given sensor device is more sensitive to aliphatic hydrocarbons, to aromatic hydrocarbons, or

<sup>14</sup>CRC Handbook of Chemistry and Physics, 54th edition, 1973-74 (CRC Press, 18901 Cranwood Parkway, Cleveland, OH 44128).

<sup>&</sup>lt;sup>15</sup>Ibid.

 $<sup>^{16}</sup>$ The use of toluene is mentioned on p. 13 in X 0003 but is not mentioned in X 0001 or X 0006.

equally sensitive to both. The use of commercial or synthetic gasolines as standard test products would not result in separate aliphatic and aromatic responses. Device response to a mixture of aliphatic and aromatic hydrocarbons will be determined with JP-4.

It is recommended that sensor devices be tested with the standard test products at concentrations of (1) 50, 500, and 1000 ppm when doing accuracy and response time testing, (2) 500 ppm when doing specificity testing, and (3) either 10, 50, 100, 500, or 1000 ppm when doing lower detection limit testing (use the lowest concentration the device responds to). There are some inconsistencies in the draft methods pertaining to the maximum concentrations to be used  $^{17}$ .

It is further recommended that JP-8 and any other products that become of concern to the Air Force should be tested only for accuracy and specificity relative to the standard test products and should not be tested for response time or lower detection limit. These products will be referred to as nonstandard test products. It is felt that an adequate picture of response time and lower detection limit characteristics of a given sensor device will be obtained by testing with standard test products. Further testing of these device characteristics with nonstandard test products is unnecessary.

The draft methods specify that "cryoscopic osmometry" should be used to determine the average molecular weight of JP-4 jet fuel<sup>18</sup>. This probably means to use either cryoscopy (determination of freezing point) or osmometry (determination of osmotic pressure). In both cases the average molecular weight of a solute is determined from a solution colligative property. During the development of the draft methods the

<sup>&</sup>lt;sup>17</sup>Draft X 0001 indicates a maximum of 1000 ppm in some places (pp. 3, 23, and 28) but 1250 ppm in other places (pp. 21-22). Draft X 0006 specifies maximum test product concentrations of 1000 ppm in some places (pp. 3 and 20) but indicates a maximum of 500 ppm for JP-4 in another (p. 18).

<sup>18</sup>X 0001, p. 12; X 0003, p.11; and X 0006, p. 14.

average molecular weight of JP-4 "was measured at 128 g/mol." <sup>19</sup> In this study, however, the average molecular weight was estimated from an analysis of GC/MS data<sup>20</sup>. Only peaks comprising greater than one percent of the total original chromatogram area were considered. Of those 94 peaks, 76 were composed of only a single component<sup>21</sup>. They covered a retention time range of 1.47 to 48.75 minutes, and had a mass range of 58 to 212 amu. The peak-area-weighted JP-4 average molecular weight estimated from these peaks is 127.6 g/mole, which is remarkably close to that measured during the development of the draft methods. The average molecular weight of JP-4 is probably reasonably consistent from sample to sample because there are so many components to include in the average.

#### Calculations and Data Presentation

Equation (4) in the draft methods<sup>22</sup> was modified to incorporate the barometric pressure and the temperature of the gas in the apparatus test chamber. The modified equation is given here as Equation [1]:

Injection rate,  $\mu$ L/hr = F<sub>a</sub> x M<sub>f</sub> x C<sub>a</sub> x P x 0.73126 + (T + d<sub>f</sub>) [1]

where  $F_g$  is the test gas flow rate in L/min,  $M_f$  = test product average molecular weight in g/mole,  $C_g$  is the test gas concentration in ppm, P is the barometric pressure in atm, T is the test chamber temperature in

<sup>19</sup> Development of Procedures to Asses the Performance of External Leak Detection Devices: Draft Summary Report on Laboratory Evaluation of Liquid-Phase and Vapor-Phase Test Methods Using JP-4 Jet Fuel, dated July 5, 1990, p. 29, written by Radian Corporation (P. O. Box 201088, Austin, TX 78720-1088) acting as a subcontractor to CDM Federal Programs Corporation (13135 Lee Jackson Memorial Highway, Suite 200, Fairfax, VA 22030) under contract to EPA/EMSL (EPA contract No. 68-03-3409).

<sup>&</sup>lt;sup>20</sup>Data collected by Kristin McSwain during the summer of 1987 under the direction of Dr. Howard Mayfield (HQ AFESC/RDVC, Tyndall AFB, FL 32403-6001).

<sup>21</sup> Assessment of GC peak purity and assignment of masses relied on Dr. Mayfield's GC/MS experience ir. combination with component identification from probability-based matching software.

 $<sup>^{22}</sup>$ X 0001, p. 15; X 0003, p. 14; and X 0006, p. 19.

Kelvins, and  $d_f$  is the test product density in g/mL. The factor of 0.73126 in Equation [1] contains R, the molar gas constant, plus various factors to convert between different units.

Several graphical methods of presenting accuracy and response time data for quantitative sensor devices were devised. The visual cues provided by these graphs allow conclusions about any given device to be drawn mo: quickly and intuitively than from the data tabulations required by the draft methods.

# Summary of Recommendations

Recommendations are summarized below and are grouped under the same headings as those found in the body of the report. Furthermore, the recommendations within each heading are listed in the same order as they were addressed in that section of the main body of the report. These are intended to supplement and to be used in conjunction with the original draft methods when testing devices of potential value to the Air Force.

### Apparatus Construction

- For safety purposes the test apparatus should be assembled in a hood.
- 2. Leak test all connections with scapy water or a commercial leak detection solution and be sure to leak test all connections to the test chamber every time it is reconfigured for a different device.
- 3. Make sure that old fittings are cleaned before use to prevent any residual grease from acting as a hydrocarbon sink that could result in high blank readings and erroneously high standards concentrations when switching from a high to a low hydrocarbon concentrations.
- 4. After apparatus construction is complete, the entire apparatus should be purged with air over a weekend to ensure that the system is clean.

- 5. Permit the use of air from a lab pure air generator in place of ultra-high-purity air in cylinders.
- 6. Test devices with both dry and wet air, with the wet air being provided by a modified air supply manifold.
- 7. Incorporate a temperature probe into the volatilization chamber so that the temperature inside the chamber can be monitored easily and reliably.
- 8. In order to ensure that the gas flowing into the test chamber reaches ambient temperature, run a minimum length of 18 inches of quarter-inch tubing from the exit end of the volatilization chamber to the three-way valve found in the volatilization chamber manifold.
- Permit the use of thermister temperature probes as well as thermocouple probes for monitoring the temperature of the test chamber
- 10. Dispense with the test chamber manometer because the errors incurred by not having one are negligible.
- 11. Require that a mercury barometer be present with the remainder of the test apparatus to permit the easy elimination of unnecessary errors in the calculated concentrations of hydrocarbon test products.

### Apparatus Calibration and Use

- Calibrate the volatilization chamber temperature probe with any common lab thermometer that covers the appropriate temperature range as long as the thermometer is not defective.
- 2. Permit the use of a flow meter of any type for rotameter calibration rather than requiring the use of a soap bubble flow meter as long as the meter used is traceable to the National Institute of Standards and Technology<sup>23</sup> (NIST).

 $<sup>^{23}</sup>$ Formerly the National Bureau of Standards (NBS).

- 3. Check rotameter calibration with both dry and wet air. If a rotameter gives different readings when the air type is changed, then complete calibration should be performed with both dry and wet air.
- 4. All nonlinear rotameter calibration data should be curve fit with a computer program to help minimize inaccu: in air flow rates and calculated concentrations of test products in the test atmosphere.
- 5. The syringe pump should be calibrated with each syringe being used at the actual pump settings being used because the calibration behavior is not necessarily linear. Assuming that the syringe pump will have linear calibration behavior can lead to serious errors in calculated test product vapor concentrations.
- 6. If the accuracy of a syringe is questioned, its accuracy should be verified gravimetrically with distilled water and a four-place analytical balance.
- Calibration data fitted with nonlinear curve fits should not be extrapolated.
- 8. It is important that caution be exercised when mounting a syringe on the syringe pump and that sufficient time be allowed to pass so that the test product vapor concentration will reach the expected value. Failure to do so may result in erroneously high or low test product concentrations.
- 9. The syringe filled with test product should not remain inserted into the volatilization chamber for long periods of time unless the syringe pump is running. Doing so may result in erroneously low test product concentrations when the pump is started.
- 10. The temperature of the volatilization chamber should be monitored and permitted to stabilize while air is flowing through the chamber at the rate to be used during device testing. This is necessary because both the final temperature of the chamber and the amount of

- time it takes for the temperature to stabilize are very sensitive to the rate of air flow through the chamber.
- 11. Background testing should be performed as specified in the draft methods with both dry and wet air at the beginning of each test day. Background checks should also be performed when switching from one test product to another to ensure that residual vapors are not present in the test apparatus.
- 12. Test each product completely and systematically before switching products to minimize time spent on flushing residual vapors out of the test apparatus between test products.

#### Test Products

- Only three test products should be subjected to the full battery of accuracy, response time, specificity, and lower detection limit tests: n-hexane, toluene, and JP-4. These will be referred to as the standard test products.
- Do not use commercial or synthetic gasoline as standard test products.
- 3. Sensor devices should be tested with the standard test products at concentrations of (1) 50, 500, and 1000 ppm when doing accuracy and response time testing, (2) 500 ppm when doing specificity testing, and (3) either 10, 50, 100, 500, or 1000 ppm when doing lower detection limit testing (use the lowest concentration the device responds to).
- 4. JP-8 and any other products that become of concern to the Air Force should be tested only for accuracy and specificity relative to the standard test products and should not be tested for response time or lower detection limit. These products will be referred to as nonstandard test products.
- 5. Relative accuracy and specificity testing of nonstandard test products should be done by injecting them into the volatilization chamber at the same flow rates used when testing with JP-4.

- 6. The densities and average molecular weights of nonstandard test products are not needed and hence testing labs should not be required to determine them.
- 7. Use the tabulated values found in this report for the density and molecular weights of the standard test products instead of requiring that the testing labs determine them.

# Calculations and Data Presentation

- 1. The equation used to calculate standard test product vapor concentrations should contain the temperature and pressure of the test chamber gas as variables to eliminate unnecessary errors resulting from unrealistic assumptions. The modified equation is found in this report.
- 2. In addition to the tabulations required by the draft methods, accuracy data obtained by testing quantitative devices with the standard test products should be presented graphically. A separate graph showing dry and wet air response (given in units of ppm) versus actual test product vapor concentration (given in units of ppm) should be created for each standard test product.
- 3. Quantitative response data for each nonstandard test product should be plotted as response (given in units of ppm) versus nominal volume of liquid test product delivered per unit volume of air (given in units of  $\mu L$  of liquid test product per liter of air). Dry air response and wet air response should be shown on the same graph. These data should also be tabulated.
- 4. The response of each quantitative device (given in units of ppm) to both standard and nonstandard test products should be plotted versus nominal volume delivered per unit volume of air (given in units of  $\mu$ L of liquid test product per liter of air). All of the dry air response data should be shown together on one graph and all of the wet air response data should be shown together on another. These data should also be tabulated.

- 5. Testing of any quantitative device should be stopped if it is identified as an integrating device during accuracy and response time testing. This should be recorded on the data recording form.
- 6. The data recording form used to report the results of accuracy and response time testing should be modified to reflect the recommendations in this report.
- 7. There is no need to perform specificity testing separately because the specificity of a given device toward the standard test products can be calculated from data obtained during accuracy and response time testing.

### Conclusion

With the exception of response time behavior, all conclusions concerning any sensor device tested with the draft methods ultimately rely on accurately knowing test product vapor concentrations. It is for this reason that this report places such great emphasis on the accuracy of calculated vapor concentrations. None of the errors allowed by the original draft methods are by themselves of earth-shaking significance. When taken as a whole, however, they would lead to significant errors in calculated test product vapor concentrations and, therefore, to incorrect conclusions concerning the devices being tested. The modifications and recommendations arrived at through this study allow most of the inaccuracy permitted by the draft methods to be eliminated without much difficulty. Used in conjunction with the documentation provided in this report, therefore, the draft methods should provide adequate testing of vapor-phase sensor devices that are potentially useful to the Air Force.

# MICROBIAL CHLOROBENZENE DEGRADATION

In-Soon You

Associate Professor of Biology
California State University, Fresno

### ABSTRACT

Pseudomonas sp. strains JS6 and JS150 are able to use paradichlorobenzene as the sole source of carbon and energy. Catabolic genes involved in the metabolism of p-dichlorobenzene were studied by using hybridization. The dichlorobenzene catabolic genes of JS6 and JS150 did not appear to show any significant homology to known chloroaromatic catabolic genes including gene tfdC of the 2,4-dichlorophenoxyacetate plasmid pJP4. Dichlorobenzene (dcb) catabolic genes were further characterized by cloning in Escherichia coli and Pseudomonas putida. The upper-pathway genes (dcbA and dcbB) and/or the lower-pathway genes (dcbC, dcbD and dcbE) have been cloned as evidenced by the growth of recombinant clones on chlorobenzene or 3-chlorobenzoate.

## INTRODUCTION

The massive introduction of toxic chemicals such as chlorinated benzenes and polychlorinated biphenyls (PCBs) into the environment is

widely recognized as a major problem in the United States. Chlorinated benzenes are used as degreasing solvents for jet engines, pesticides and synthetic intermediates. Chlorinated aromatic compounds including chlorobenzenes are poorly biodegraded and thus tend to persist in the environment. The latter contributes to the contamination of groundwater as well as soil and surface water by these chemicals. An example: At Kelly Air Force Base in California, groundwater aquifers are contaminated by chlorobenzenes.

Like other chlorinated aromatics, the slow microbial degradation of chlorobenzenes is largely due to the presence of a chlorine atom(s) on the aromatic ring, i.e., ring chlorination. In general, the more chlorinated the compounds are, the more resistant they become to microbial attack. Several microorganisms have been recently described that are capable of growth on mono-, di- and/or tri-chlorobenzenes as sole carbon and energy sources (Schraa et al., 1986; Spain and Nishino, 1987; van der Meer et al., 1987; Haigler et al., 1988). A few such bacteria were isolated here at the Air Force Engineering and Services Center, Tyndall Air Force Base, Florida (Spain and Nishino, 1987; Haigler et al., 1988). Although the biochemical pathways for chlorobenzene degradation (Fig. 1) have been studied in detail by the Microbiology lab at Tyndall Air Force Base (TAFB) and other labs, the genetics of chlorobenzene degradation has been poorly understood (van der Meer et al., 1991a, b, c).

In light of the environmental importance, it is of interest to study the molecular and genetic basis of chlorobenzene degradation and to explore the utility of chlorobenzene degrading bacteria in the

treatment of toxic chemicals at waste sites. This report describes some preliminary findings of the genetic analysis of para-dichlorobenzene degradation by Pseudomonas sp. strains JS6 and JS150, i.e., TAFB isolates.

# MATERIALS AND METHODS

Bacterial strains, plasmids, and culture conditions. The bacterial strains and plasmids used in this study are listed in Table 1.

Pseudomonas sp. strains JS6 and 150 were grown in a selective medium at 30°C as previously described (Spain and Nishino, 1987). LB medium (Sambrook et al., 1989) served as a complete medium for growth of E. coli and other Pseudomonas strains.

DNA isolation and analysis. Plasmid DNA was prepared from *Pseudomonas* strains JS6 and JS150 grown on *para*-dichlorobenzene, using the procedure of Casse et al. (1979). The total DNA was prepared by the Mamur method (1961). Plasmid DNA was purified by two-cycle CsCl-EtBr density ultracentrifugation. DNA modifying enzymes and plasmid molecular weight markers were purchased from Gibco/BRL Life Technologies Inc. (Gaithersburg, MD). Restriction analysis and agarose gel electrophoresis were performed according to the Sambrook et al. procedures (1989).

DNA-DNA hybridization. For DNA hybridizations, DN7 restriction fragments were fractionated on agarose gels and transferred to GenScreen

plus membrane (Dupont, NEN Research Products, Boston, MA) by the method of Southern (1975). Hybridizations were carried out at  $68^{\circ}$ C and washings, at  $65^{\circ}$ C. DNA fragments were isolated using DEAE membrane (Schleicher & Schuell, Keene, NH) and labeled with [ $\alpha$  -  $^{32}$ P]dCTP (3,000 Ci/mmol: NEN, Boston, MA) using a nick translation kit obtained from the same company. The 2,4-D monooxygenase gene tfdA (Streber et al., 1987), dioxygenase gene tfdC (Ghosal and You, 1988a) and regulatory gene tfdR (I.-S. You, unpublished results) of plasmid pJP4 were used as labeled probes. Also used was the nahG gene of plasmid NAH7 (You et al., 1991) encoding salicylate hydroxylase.

Cosmid cloning. Both JS6 plasmid and JS150 total DNA were digested with restriction enzyme HindIII. Cosmid vector pCPl3 was also cleaved with HindIII. The vector and insert DNA were then ligated and packaged in vitro using packaging extracts obtained from Stratagen (La Jolla, CA). The in vitro packaging and subsequent transfection of E. coli HB101 cells were carried out according to the specifications of the supplier. Recombinant plasmids generated in E. coli were mobilized into either P. putida AC812 or P. cepacia 383, by a triparental mating (Ruvkun and Ausubel, 1981) using E. coli HB101/pRK2013. Pseudomonas strains carrying recombinant plasmids were subsequently selected on minimal agar containing tetracycline at 50 ppm. 3-Chlorobenzoate or chlorobenzene served as the sole carbon and energy source.

Analysis of plasmid DNA of Pseudomonas sp. strains JS6 and JS150.

Strains JS6 and JS150 were derived from the parent strain JS1 that was isolated from a mixture of sewage samples collected at Tyndall Air Force Base and Panama City for its ability to utilize para-dichlorobenzene as a growth substrate. Since the genetic capabilities of chloroaromatic degraders often reside in plasmids, we have studied the plasmid profile of dichlorobenzene degraders JS6 and JS150. The total plasmids were prepared and analyzed with the results summarized in Fig. 2. Strain JS6 (lane 2) appears to contain four plasmids and the JS150 strain (lane 1), three plasmids. Some of the plasmids (e.g., the smallest one) appear to be common for both JS6 and JS150, while others appear different in size.

The total plasmid DNA of JS6 and JS150 were digested with restriction enzymes EcoRI or HindIII, and subsequently fractionated on a 0.7% agarose gel. These results are shown in Fig. 3. The EcoRI digestion (lane 4) of JS6 plasmid DNA gave rise to three major fragments of ca. 7.5, 20, and 30 kb in size while the HindIII digestion (lane 3) showed four major fragments of 7, 8, 35, and >50 kb, respectively. The JS150 plasmid DNA, upon digestion with EcoRI or HindIII, similarly showed one (7.5 kb; lane 2) and two major fragments (7 and 8 kb; lane 1), respectively. In conclusion, the JS6 and JS150 total plasmids show different restriction patterns indicating that one or both plasmid DNA had undergone genetic rearrangements.

Hybridization analysis of JS6 and JS150 DNA. A recent report has described that the genes for trichlorobenzene degradation show 54 % homology to the well-characterized chlorocatechol catabolic gene tfdC of plasmid pJP4 (van der Meer et al., 1991b). Chlorocatechol is a key intermediate in the metabolism of chloroaromatics (see Fig. 1). In an attempt to locate genes encoding dichlorobenzene degradation of the JS6 and JS150 strains, DNA hybridizations were carried out. Both plasmid and total DNA were prepared and digested with EcoRI and HindIII, respectively. The restriction fragments were separated, immobilized and hybridized to known chloroaromatic catabolic genes. Our hybridization studies indicate that there is no significant homology of the dichlorobenzene (dcb) catabolic genes of JS6 and JS150 to the wellcharacterized chloroaromatic catabolic genes including the tfdC gene (data not presented). A plasmid containing cloned tfdC is shown in Fig. 3 (lane 5), which overexpresses chlorocatechol dioxygenase . In an analogous experiment, the nahG gene of naphthalene/salicylate catabolic plasmid NAH7, when used as a labeled probe, did not show any significant homology with the plasmid as well as total DNA of the JS strains.

Cloning of the genes encoding chlorobenzene metabolism. HindIII gene libraries of JS6 plasmid DNA and JS150 total DNA were constructed using a cosmid vector pCPl3 in E. coli. Upon en mass mobilization of E. coli gene libraries into two Pseudomonas hosts, several recombinant clones were obtained. When the JS150 library was transferred into P. putida AC812, four clones (YS1-4) were obtained that were able to grow on 3-chlorobenzoate. In order for a pseudomonad to utilize 3-chlorobenzoate

as the growth substrate, it requires a minimum three genes that encode chlorocatechol dioxygenase, cycloisomerase and hydrolase, respectively. It is known that benzoate dioxygenase and diol dehydrogenase encoded by the chromosomal genes of psudomonads may be recruited to carry out the initial reactions involved in 3-chlorobenzoate catabolism. We have also obtained a clone (YS100) that appears to grow on chlorobenzene as the sole carbon and energy source.

Based on the above observations, it was concluded that the genes coding for dichlorobenzene (i.e., dcbA and dcbB) and/or 3-chlorobenzoate degradation (i.e., dcbC, dcbD and dcbE) were cloned. We are currently in the process of characterizing the above recombinant clones.

#### LITERATURE CITED

- Casse, F., Boucher, C., Julliot, J. S., Michel, M., and Denare, J.

  1979. Identification and characterization of large plasmids in

  Rhizobium meliloti using agarose gel electrophoresis. J. Gen.

  Microbiol. 113:229-242.
- Chakrabarty, A. M., and Gunsalus, I. C. 1979. Chromosomal mobilization from a recA mutant of Pseudomonas putida. Mol. Gen. Genet.

  176:151-154.
- Darzins, A., and Chakrabarty, A. M. 1984. Cloning of genes controlling alginate biosynthesis from a mucoid cysticfibrosis isolate of Pseudomonas aeruginosa. J. Bacteriol. 159:9-18.
- Ghosal, D. and You, I.-S. 1988a. Nucleotide homology and organization of chlorocatechol oxidation genes of plasmids pJP4 and pAC27. Mol.

- Gen. Genet. 211:113-120.
- Ghosal, D. and You, I.-S. 1988b. Gene duplication in haloaromatic degradative plasmids pJP4 and pJP2. Can. J. Microbiol.
- Haigler, B. E., Nishino, S. F., and Spain, J. C. 1988. Degradation of 1,2-dichlorobenzene by a *Pseudomonas* sp. Appl. Environ.

  Microbiol. 54:294-301.
- Marmur J. 1961. J. Mol. Biol. 3:208-218.
- Ruvkun, G. B., and Ausubel, F. M. 1981. A general method for sitedirected mutagenesis in prokaryotes. Nature 289:85-88.
- Schraa, G., Boone, M. L., Jetten, M. S. M., van Neerven, A. R. W.,

  Colberg, T. J., and Zehnder, A. J. B. 1986. Degradation of 1,4
  dichlerobenzene by Alcaligenes sp. strain A175. Appl. Environ.

  Microbiol. 52:1374-1381.
- Southern, E. M. 1975. Detection of specific sequences among DNA fragments separated by gel electrophoresis. J. Mol. Biol. 98:503-517.
- Spain, J. C., and Nishino, S. F. 1987. Degradation of 1,4-dichlorobenzene by a *Pseudomonas* sp. Appl. Environ. Microbiol. 53:1010-1019.
- Streber, W. R., Timmis, K. N., and Zenk, M. H. 1987. Analysis, cloning, and high-level expression of 2,4-dichlorophenoxyacetate monooxygenase gene tfdA of Alcaligenes eutrophus JMP134. J. Bacteriol. 169:2950-2955.
- van der Meer, J. R., Eggen, R. I. L., E. J., Zehnder, A. J. B., and de Vos, W. M. 1991a. Sequence analysis of the *Pseudomonas* sp.

- strain P51 gene cluster, which encoded metabolism of chlorinated catechols: evidence for specialization of catechol 1,2-diox,genases for chlorinated substrates. J. Bacteriol. 173:2425-2434.
- van der Meer, J. R., Frijters, Leveau, A. C. J., Eggen, R. I. L., F. J., Zehnder, A. J. B., and de Vos, W. M. 1991b. Characterization of the *Pseudomonas* sp. strain P51 gene \*cbR, a Lysp-type transcriptional activator of the tcbCDEF chlorocatechol oxidative operon, and analysis of the regulatory region. J. Bacteriol. 173:3700-3708.
- van der Meer, J. R., van Neerven, A. R. W., de Vries, E. J., de Vos, W. M., and Zehlder, A. J. B. 1991c. Cloning and characterization of plasmid-encoded genes for the degradation of 1,2-dichloro-, 1,4-dichloro-, and 1,2,4-trichlorobenzene of Pseudomonas sp. strain P51. J. Bacteriol. 173:6-15.
- You, I.-S., Ghosal, D., and Gunsalus, I. C. 1991. Nucleotide sequence analysis of the *Pseudomonas putida* PpG7 salicylate hydroxylase gene (nahG) and its 3'-flanking region. Biochemistry 30:1635-1641.

Table 1. Bacterial strains and plasmids.

Strain or plasmid	Relevant characteristics <sup>a</sup>	Source or reference
Pseudomonas sp. strair JS6	Dcb <sup>†</sup> Tol <sup>†</sup> Cb <sup>†</sup>	Spain and Nishino (1987)
Pseudomonas sp. strair JS150	n Dcb <sup>+</sup> Tol <sup>+</sup> Cb <sup>+</sup> Nah <sup>+</sup>	Spain et al., unpublished results
Pseudomonas putida AC812	RecA trp	Chakrabarty and Gunsalu (1979)
Pseudomonas cepacia 383	Sal <sup>+</sup> Tc <sup>r</sup> Km <sup>r</sup>	Ghosal and You (1988b)
Escherichia coli HBl01	Sm <sup>r</sup> recA13 leuB6 proA2 thi-1 hsdR17 hsdM	J. S. Karns
Escherichia coli HB101	Sm <sup>r</sup> recA13 leuB6 proA2 thi-1 hsdR17 hsdM, pRK2013	W. C. Suen
Escherichia coli AC80	Thr- leu- met- hsdR17 hsdM, pCP13	Darzins and Chakrabarty (1984)
Escherichia coli AC80	Thr- leu- met- hsdR17 hsdM, pYG1316	Ghosal and You (1988a)

<sup>&</sup>lt;sup>a</sup> Abbreviations: Dcb<sup>+</sup>, growth on p-dichlorobenzene; Tol<sup>+</sup>, growth on toluene; Cb<sup>+</sup>, growth on chlorobenzene; Nah<sup>+</sup>, growth on naphthalene; Sal<sup>+</sup>, growth on salicylate; r, resistance; Tc, tetracycline; Km, kanamycin; Sm, streptomycin.

# FIGURE LEGENDS

- Fig. 1. Proposed pathway, genes (left) and enzymes (right) for p-dichlorobenzene degradation by Pseudomonas sp. JS6. The pathway was adopted from the published work of Spain and Nishino (1987).
- Fig. 2. Agarose gel electrophoresis of JS6 and JS150 plasmid DNA.

  Lane 1, JS150; lane 2, JS6; lane 3, supercoiled DNA

  ladder; lane 4, phage lambda DNA digested with HindIII.
- Fig. 3. Agarose gel electrophoresis of DNA restriction fragments of various plasmids. Lane 1, JS150(HindIII); lane 2, JS150 (EcoRI); lane 3, JS6 (HindIII); lane 4, JS6 (EcoRI); lane 5, pYGl316 (HindIII); lane 6, lambda DNA (HindIII).

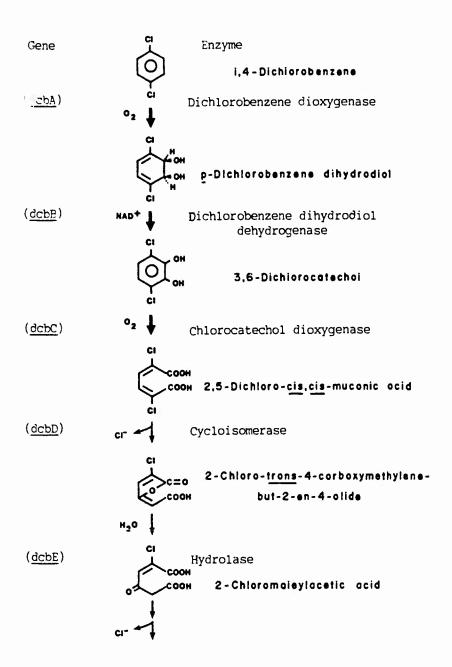


Figure 1

1 2 3 4

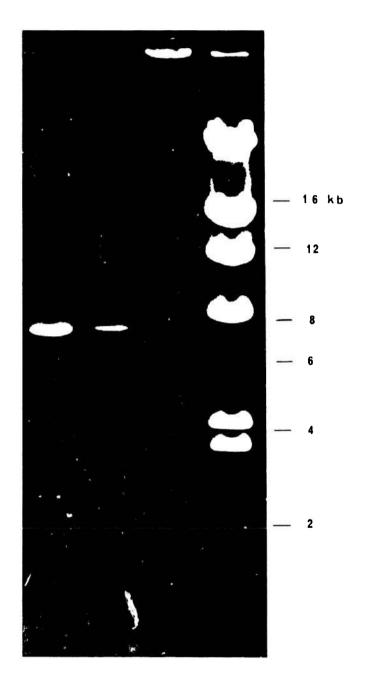


Figure 2

1 2 3 4 5 6

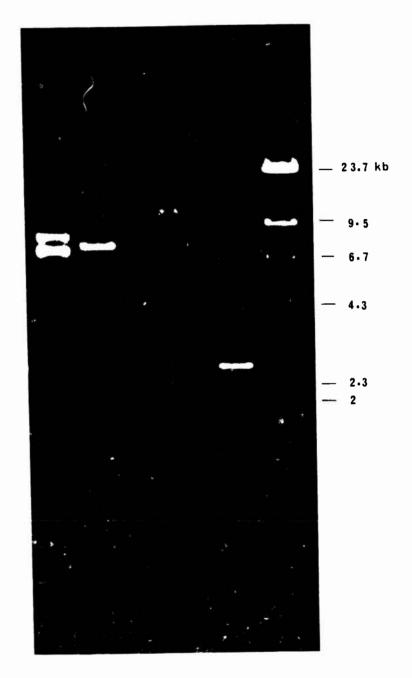


Figure 3